UC20
PFC/RR-81-31 DOE/ET-51013-27

COMPARATIVE STUDY OF FUNDAMENTAL AND SECOND HARMONIC ICRF WAVE PROPAGATION AND DAMPING AT HIGH DENSITY IN THE ALCATOR TOKAMAK

Marcel P. J. Gaudreau

Plasma Fusion Center
Massachusetts Institute of Technology
Cambridge, MA 02139

September 1981

This work was supported by the U.S. Department of Energy Contract No. DE-AC02-78ET51013.

COMPARATIVE STUDY OF FUNDAMENTAL AND SECOND HARMONIC ICRF WAVE PROPAGATION AND DAMPING AT HIGH DENSITY IN THE ALCATOR TOKAMAK

by

Marcel P. J. Gaudreau

D. E. C. CEGEP de La Pocatière
1972

B.S. Massachusetts Institute of Technology
1974

M.S. Massachusetts Institute of Technology
1975

Submitted in Partial Fulfillment
of the Requirements for the
Degree of Doctor of Science

at the

Massachusetts Institute of Technology

September 1981

Signature of Author ______________________
Department of Electrical Engineering
and Computer Science
August, 1981

Certified by ______________________
Dr. Ronald R. Parker
Thesis Supervisor

Accepted by ______________________
Arthur C. Smith
Chairman, Departmental Committee of Theses

COMPARATIVE STUDY OF FUNDAMENTAL AND SECOND HARMONIC ICRF WAVE

PROPAGATION AND DAMPING AT HIGH DENSITY IN THE ALCATOR TOKAMAK

by

Marcel P. J. Gaudreau

Submitted to the Department of Electrical Engineering and Computer Science in August 1981 in partial fulfillment of the requirements for the Degree of Doctor of Science

ABSTRACT

This thesis presents a comparative study of the theoretical foundations and experimental results of the ICRF heating experiment on the Alcator A tokamak at the MIT Plasma Fusion Center and Francis Bitter National Magnet Laboratory. Due to the versatility of the high power apparatus, the fast magnetosonic branch is used with $\omega_o = 1,2,3,4\ \omega_{ci}$, unlike most other ICRF experiments. Unusually high magnetic field (B_o= 40-80 kG), plasma density ($n_e = 10^{13} - 5 \times 10^{14}/cm^3$), generator frequency ($f_o$ = 90-200 MHz) and transmitter power, with shielded and unshielded antennas, are the key parameters of the experiment. This wide parameter range allows a direct comparison between fundamental and second harmonic regimes, and shielded and unshielded antennas, our prime goals. The real and imaginary parts of the parallel and perpendicular wave numbers are measured with extensive magnetic probe diagnostics for a spectrum of plasma parameters and compared with theory. Qualitative and quantitative evaluations of the wave structure and scaling laws are derived analytically in simple geometries and computed numerically for realistic plasma parameters and profiles. General figures of merit, such as radiation resistance and quality factor, are also derived and compared with the experiment. Secondary effects of the high power wave launching, such as changes in plasma current, density, Z_{eff}, energetic neutral flux, soft X-rays, neutron flux, and impurities are also discussed. Most important, a general synthesis of the many engineering, physics, and experimental problems and conclusions of the Alcator A ICRF program are inspected in detail. Finally, the derived and experimentally determined scaling laws and engineering constraints are used to estimate the ICRF requirements, advantages, and potential pitfalls of the next generations of experiments on the Alcator tokamaks.

Thesis Supervisor: Dr. Ronald R. Parker

Title: Professor of Electrical Engineering and Computer Science, Assistant Director of the Plasma Fusion Center, and Assistant Director of the Francis Bitter National Magnet Laboratory

ACKNOWLEDGEMENTS

This report was prepared at the Francis Bitter National Magnet Laboratory and the Plasma Fusion Center, and was sponsored by DOE under contract DE-AC02-78E T 51013.A002. The author is grateful to the Department of Energy for providing financial and technical support. The author is also thankful to the Department of Defense, the Air Force, and in particular, Master Sergeant Philip Keysor for acquisition of the Shemya Alaska Air Force Base FPS-17 transmitter, and guidance throughout the logistic operations.

Much of the experimental hardware was built by a number of M.I.T. students, in particular, Doug Gearson, Randy Fahey, Gary Spletter, Matthew Besen and Brian Abbanat who received Bachelor of Science Thesis credit for their work. Several professionals also worked many long hours on the project. Especially helpful were Faith Knowlton for her work on numerical simulations, and Dr. Boyd Blackwell for the many instructive discussions.

The author is indebted to Dr. D. Bruce Montgomery, Assistant Director of the National Magnet Laboratory and to Dr. James Melcher, the author's academic advisor, for their continued encouragement during the many difficult phases of the author's education and experimental work at M.I.T.

The author is grateful to Cornelis Holtjer, Donald Lavoie, Peter Besen, and Don Shulsinger, some of the best engineers in the field, for their unfailing technical help.

The author had the privilege of working under the supervision of Dr. Ronald R. Parker, Professor of Electrical Engineering and Computer Science, and Associate Director of the Plasma Fusion Center and Francis Bitter

National Magnet Laboratory. Ron was always the primary instigator and energy source of my effort during and even before this project.

Finally, the author is deeply indebted to Michael Sansone,who was the single most important designer, builder and co-investigator with the author on this project and many other enterprises not mentioned in this thesis.

To My Parents

Joseph and Françoise

TABLE OF CONTENTS

Page

I. INTRODUCTION

I-1. Motivation

Since the early 1950's, extensive work in the area of plasma physics has been undertaken to achieve controlled thermonuclear fusion, which may be the ultimate source of energy for the next century[1]. There are two main steps to demonstrate scientific feasibility of controlled thermonuclear fusion power. The first is to achieve sufficient levels of the product of plasma density n, and energy confinement time τ, known as Lawson's criterion $n\tau = 10^{14}$ sec/cm^3 . Many schemes for attaining these high levels of $n\tau$ have been proposed, an example being the Alcator tokamak[2]. Lawson's criterion is expected to be achieved within the next decade of large scale experiments.

The second step, which certainly has not been achieved, is to attain the formidable temperatures required for fusion ($\simeq 10^8$ °K). Again, several schemes have been proposed and tried with some success. Ohmic heating of the plasma by intense currents has achieved consistently high temperatures in tokamaks[3], but fails in the thermonuclear regime since the plasma resistivity[1] drops as $T_e^{-3/2}$. Injection of high energy neutral particles[5] has so far been successful in low density plasmas,but may be impractical in a high density reactor because of the low efficiency of the extremely high energy beams required for good penetration to the plasma center[4]. For many years, radio frequency heating of these plasmas has appeared attractive. A wide spectrum of wave frequencies is available at high power and good efficiency with current technology. Several specific frequency regimes have been tested, in particular, low frequency ($\simeq 10^6$ Hz)

Alfvén heating[6], medium frequency ($\approx 3 \times 10^7$ Hz) Ion Cyclotron Range of Frequencies heating (ICRF)[7], high frequency ($\approx 10^9$ Hz) lower hybrid[8], and ultra high frequency ($\approx 3 \times 10^{10}$ Hz) electron cyclotron heating[9]. Each regime has its specific theoretical and practical advantages, disadvantages and, especially, unknowns.

For the moment, the Ion Cyclotron Range of Frequencies is the prime candidate because of the relatively good agreement between theory and experiment, and compatibility with engineering constraints[10]. Even within the Ion Cyclotron Range of Frequencies, there are fundamentally different regimes of wave propagation and absorption, which can be broadly classified in terms of harmonic number of the ion gyrofrequency.

For the present work, we will investigate ICRF heating in a high density tokamak, and attempt to identify the most promising wave launching structures, wave frequency, and plasma parameters for efficient heating[21].

Almost all recent ICRF work has been in one particular regime: the minority fundamental ion gyrofrequency regime[11,12]. Furthermore, the conditions have always been in tokamak plasmas in similar regimes, $n_e \approx 3 \times 10^{13}/cm^3$, $B_o \approx 20$ kg, $f_o \approx 25$ MHz, all being significantly short of the high field and high density thermonuclear regime. The Alcator ICRF experiment[13] in these respects is different since it is a high field (≈ 60 kG), high central current density ($\approx 1{,}500$ amps/cm^2), high density ($\approx 3 \times 10^{14}/cm^3$) and high frequency ($f_{ci} = 100$ MHz) experiment[14,15]. Fortunately, for comparison, the experiment can also be run at moderately low fields, current density, plasma density, and frequency. The wide range of parameters and their proximity to the reactor regime[16] make Alcator an almost ideal test machine for RF heating.

I-2. Methodology and Overview

The main goals of this ICRF program are to identify the proper parameter regime which produces efficient heating. The single most important parameter is the harmonic number, i.e., fundamental, second harmonic or even higher harmonics of the ion gyrofrequency. The harmonic number, coupled with working gas and toroidal field, fully determine the transmitter chain and antenna operating frequency, a non-trivial amount of expensive and complicated hardware to be adjusted to a particular regime. A prime objective is to be able to change the parameters of the experiment and still satisfy $\omega_o = n \frac{eB}{M}$ for different harmonic numbers n. Two frequencies, 183.5, 92 MHz, four gases, H^1, D^2, He^3, He^4 and toroidal fields from 30-90 kg enable n to be changed over a wide range (n = 1, 2, 4, 8) in different parts of parameter space.

The second issue is the selection of proper launching structure. This is an especially sensitive topic in the fusion RF community, and considerable controversy exists over fundamental issues, in particular, whether or not the antenna should be shielded [17]. Many other secondary but nevertheless essential issues are the choice of location, insulation, and method of RF feeding of the antenna[18]. As far as achieving this second goal, the Alcator experiment has a severe handicap; almost total lack of space for insertion, access, and location of antenna near the plasma[2]. However, several all metal shielded and unshielded antennas (Section III-2) were built and tested, and experimental results showed small but accceptable loading resistances of a few ohms[13]. An innovative all metal antenna and matching system with the vacuum breaks at a point where there is little reactive power is also proposed (Section III-2-6), and could be a great step forward in Alcator ICRF antenna technology and performance.

To achieve the above goals, a clear understanding of the basic physics is necessary as well as a quantitative evaluation of the theory (Chapter IV). First, a more or less complete review of the current theory[7,19-22] is warranted to ensure that the approximations are still valid at high field, high frequency, and in particular, high density.

The physics of the problem may be divided broadly into three areas[7, 89]; wave launching and propagation, wave damping, and the physics of heating. There are three basic aspects of the wave propagation problem:

(1) the dielectric tensor, wave equation, dispersion relation and polarization[7,45];

(2) the homogeneous and inhomogeneous plasma cylindrical wave field solutions[21,22,45,46]; and

(3) stochastic mode stacking[24].

The above aspects are first treated in conventional rigorous analytical ways with approximations justified quantitatively in the Alcator regime[3]. Successively more complicated models (Sections IV- 1-7) are developed starting with cold uniform infinite plasma with a single ion species and zero electron mass. The final theory includes hot plasma effects to first order, finite electron mass, two ion species, cylindrical geometry, 1/R toroidal field, and inhomogeneous density profile[21,22,26,27]. A tangible physical explanation of the mathematical results is given whenever possible.

Second, the wave fields are numerically evaluated with realistic plasma parameters and profiles[28,29] and compared with experimental observations. A multitude of important measurable quantities is also calculated in the same manner. Two prime examples are antenna loading resistance and RF signals from magnetic probes distributed around the torus.

The second facet of the problem is wave damping. The many wave damping mechanisms[7,21,26,30,31] are derived in the high density regime, and again we try to draw simple, intuitive, qualitative understanding as well as a quantitative evaluation and comparison with the experiment. Damping depends on the theoretical and experimental results of wave propagation. Damping may also significantly modify the propagation picture, especially on sensitive parameters such as radiation resistance[32].

The last theoretical aspect is the physics of heating, and we will concentrate on the parameters that directly affect the plasma diagnostics used for monitoring heating, or the parameters that are likely to modify the wave propagation or damping. A few good examples are the ion distribution function as inferred from the fast neutral spectrum monitored by charge exchange analyzer[3,33-38], neutron flux[39], plasma current and density[73], soft X-ray radiation[39], edge temperature, and density as measured by Langmuir probe[29].

The actual experiment is in the form of multi-dimensional scans to map out the different functions of the multitude of RF and plasma parameter combinations. This results in experimental scaling laws[40] that are compared with theory. A good example of this is that, experimentally, antenna loading resistance R_R linearly increases with electron density[13]. Loading resistance also increases with mass density, i.e., R_R is larger in deuterium than in hydrogen, but on the other hand, He^3 or He^4 loading resistance is very small[41,42] (Chapter II). Until now, there has been no theory that satisfactorily explains these effects, and they have not been seen in any other experiment. Plausible new explanations are discussed in detail, especially in light of "Stochastic Mode Stacking" (Section IV-6), a new concept developed in this work that refers to simultaneous excitation of a number of randomly phased toroidal eigenmodes, which may profoundly affect the wave structure at high density[23-25,93].

The conclusion to this work will consist of a tentative synthesis of the many interacting processes and parameters of the experiment,as well as recommendations for further investigation.

I-3. Summary of Related Work

The relatively new Ion Cyclotron Range of Frequencies (ICRF) regime[43] has evolved out of the Ion Cyclotron Resonant Heating (ICRH) scheme in the older magnetic confinement devices like the stellarator[44]. Much of the theory for wave excitation and propagation was then summarized in two books by T.H. Stix[45] and Allis et al.[46], and the formulation and notation are still widely accepted.

The fundamental difference between ICRH and ICRF is that they each use a different branch of the wave dispersion relation[7]. ICRH used the slow branch, also called the ion cyclotron wave, at frequencies near or below the ion cyclotron frequency. The new (1970)[43] ICRF uses the fast branch, also called the fast wave or fast magnetosonic wave, and the wave is usually carried by a majority ion component at some low harmonic number. The ion cyclotron wave is evanescent under these conditions[7].

Many national laboratories and universities throughout the world are involved in ICRF, but the most important are located in the U.S. (Princeton University, Princeton, NJ), France (TFR, Fontenay- aux- Roses), and Japan (Japan Atomic Energy Institute Tokai, Ibaraki). Princeton has been in the field of RF heating for about two decades, and has developed both ICRH and ICRF through the Model C Stellarator[44], the Adiabatic Toroidal Compressor (ATC)[11], and finally, the Princeton Large Torus (PLT)[12]. Much of the literature is by T.H. Stix[7,93,45], F.J. Paoloni[19,47], F.W. Perkins[48], J.C. Hosea[49-50], P.L. Colestock[51], and D.G. Swanson[20]. The TFR group is newer, but has been producing consistently good experimental data and theory, and is headed by J. Adams[21,52,54] and J. Jaquinot[22,53,55]. Several other institutions[56] also have published good work, particularly the

University of Wisconsin (Madison, WI)[16,59,26,27], but their confinement device's plasma parameters are usually remote from the high density regime[57].

For this work, three review publications broadly define current theory and technology, and contain the foundations of this program:

- The Theory of Plasma Waves, T.H. Stix, McGraw-Hill, New York (1962).
- "Fast Wave Heating of a Two Component Plasma," T.H. Stix, Nuclear Fusion 15, 737 (1975).
- "Eigenmode Field Structure of the Fast Magnetosonic Wave in a Tokamak and Loading Impedence of Coupling Structures," J. Adams and J. Jaquinot, EUR-CEA-FC-886 (April, 1977).

State of the art in ICRF is well summarized in a number of papers presented at the 8th International Conference on plasma physics[101-106] (Brussels, July, 1980), and the Fourth Topical Conference on RF Heating in plasma[107-115] (University of Texas, February, 1981).

II. EXPERIMENTAL RESULTS

II-1. Available Parameter Space and Principal New Results

II-1.1. Available parameter space

The experiment was usually run in the form of multi-dimensional parameter scans. The basic methodology was to map out the various plasma and wave processes by independently varying each parameter at a time over as wide a range as possible, with as many other different parameter combinations as possible,while monitoring all the diagnostics. The main parameters that could be independently varied were:

(1) RF power from .1 W to 100 kW

(2) Toroidal field from 40 to 80 kG

(3) Resonance layer position from 30 to 70 cm

(4) Plasma density from 10^{13} to $5 \times 10^{14}/cm^3$

(5) Wave frequency 90, 180 (50, 360) MHz

(6) RF spectrum width up to 2 MHz

(7) Plasma current from 50 to 250 kA

(8) Working gas, H^1, D^2, He^3, He^4

(9) Minority concentration from 1 to 100%

(10) Plasma radius from 9 to 10 cm

(11) Antenna loop area from 5 to 25 cm^2

(12) Probe radial position from 9 to 13 cm

(13) Shielded or unshielded antenna

(14) Antenna phasing m = 0 or m = 1

This represents considerable amounts of machine time, and efficient, judicious choices of parameter scans are necessary. Theory and gradual increase in experience guide these choices to enable formulation of reasonably sound scaling laws, maximization of machine time, and better understanding of the many interacting physical processes. Nevertheless, only a fraction of all parameter space was explored.

Figure 1 shows a plot of resonant frequency with respect to magnetic field for typical Alcator, TFR and PLT regimes and different hydrogen and helium isotopes. As we stressed in the introduction, Alcator stands out as very different from other tokamaks in many directions of parameter space. We also note from Figure 1 how several resonant regimes may be present at the same time. This effect is further emphasized in Figure 2 and Table 1 where we note how partially ionized impurities may scan the whole width of the plasma and cause edge heating (large concentrations of impurities are most likely confined to the plasma edge).

Table 1

Normalized cyclotron frequencies and refractive indicies

gas (n_e, B_o = constant)	$\omega_c \propto \frac{Z}{\mu}$	$n_A \propto \frac{\sqrt{\mu}}{Z}$
H^1	1.	1.
D^2	.5	1.41
He^3	.667	.866
He^4	.5	1.
Fully Ionized Impurities	$\sim .5$	$\sim \left[\frac{2}{\sqrt{\mu}}\right]$
Partially Ionized Impurities	$\frac{1}{\mu}$ to .5	$\left[\frac{2}{\sqrt{\mu}} \text{ to } \sqrt{\mu}\right]$

ICRF Wave Regime In ALCATOR A

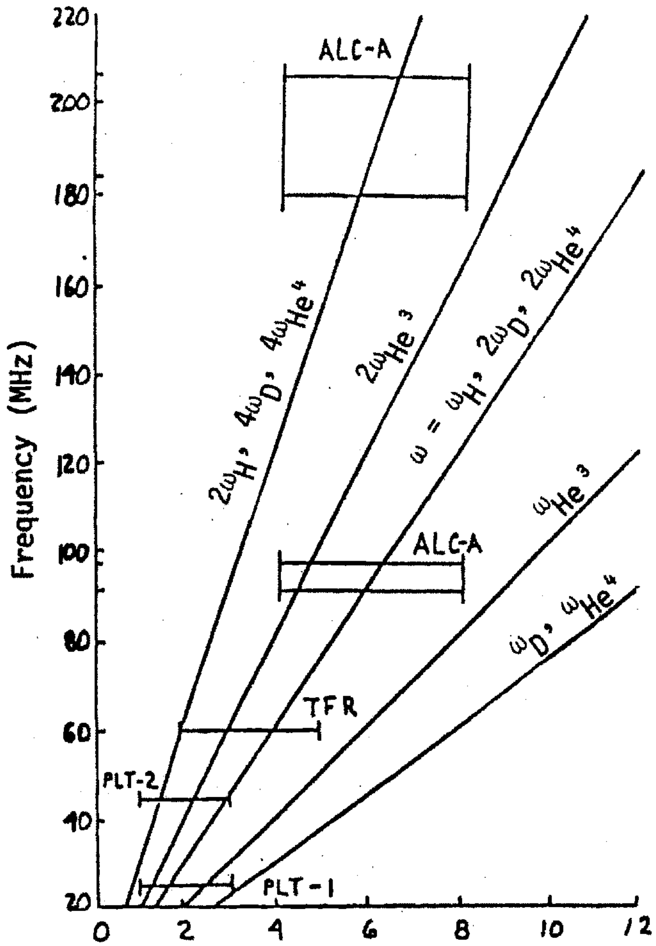

Figure 1

Cyclotron Harmonic Resonance Position
Vs Toroidal Field

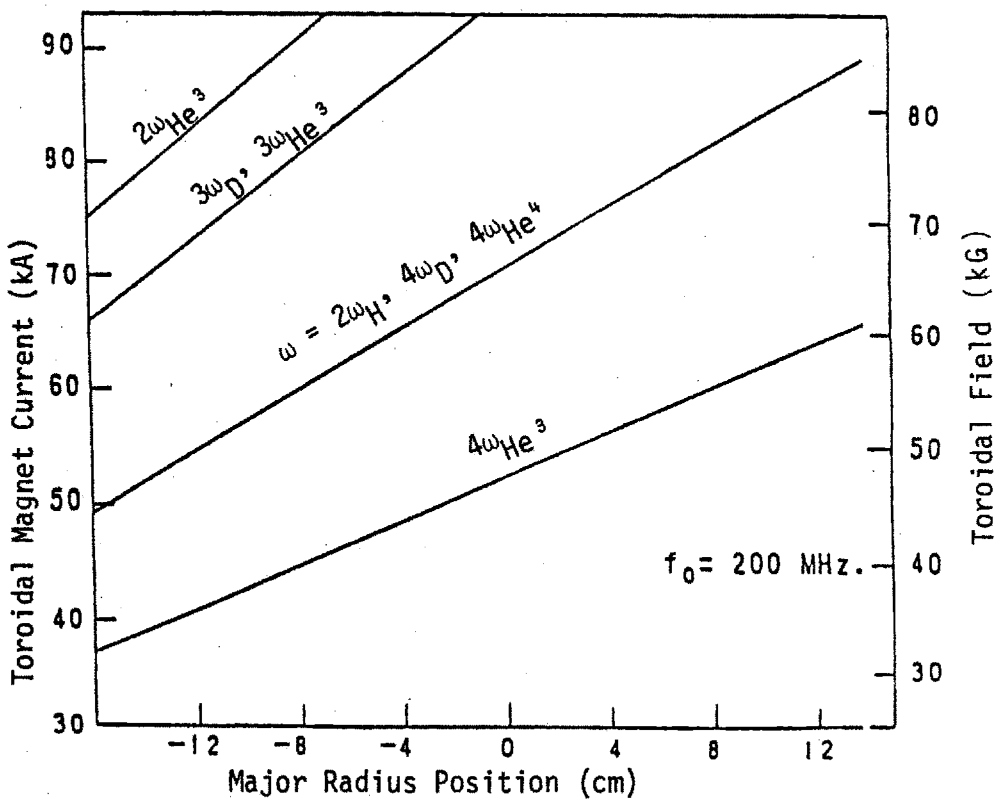

Figure 2

II-1.2. Principal new experimental results

The most important products of this research are sound experimental results that preferably can be explained by theory. To date, there are many important questions that need to be answered, most of which are still unexplored in the high field, high frequency, and high density regime.

The first question is whether or not the minority or second harmonic regime should be used. This is a far reaching question and needs much consideration, many parameter scans and is, of course, answered with best heating and engineering compatibility.

The second question is whether the antenna should be shielded or not. This is answered for Alcator A by comparing the performance of the A_1, A_2, and A_4 antenna over a wide range of experimental conditions.

Third, also of utmost importance, and closely related to the first two questions, is the effect of density, working gas, frequency. antenna loop area, shielding, RF power and wave Q on antenna loading Also correlations between R_R, H_α light, impurities, disruptions, X-rays, etc., are important and not well understood.

Fourth, what are the predominant wave damping mechanisms, near-field power losses, and power deposition profiles? This can be answered by changing the most critical parameters of particular processes, and noting changes in field structure and heating efficiency. A prime example is the effect of the resonant layer position on antenna loading, RF probe signals, and the charge exchange neutral spectra. Wall losses can be directly calculated from probe signals. Near-field losses could be affected by antenna shielding, etc.

Fifth, what is the wave field structure? In particular, what modes are predominantly excited, and how are they affected by other parameters such as toroidal field, ion mass, and electron density. Is the cold plasma dispersion relation valid? What is the role of surface waves? This set of questions will be answered by detailed study of the RF probe signal phase measurements and comparison with theory.

Sixth, is what is the role of stochastic mode stacking ? How many modes are excited simultaneously ? What are their Q's? Does it explain the increase in radiation resistance and the saturation of probe signals with density? This will be tentatively answered by extensive simulations and comparison with experimental values of R_R and probe signals and phases. Finally, does large $k_\parallel$ mean small $k_\perp$, making second harmonical damping small, leading to a natural selection of undamped modes of high Q and R_R?

All these questions, and many more omitted here, are not fully answered, but much light is shed on the basic issues. Tables 1 to 4 summarize some of the basic experimental results that will be discussed in this chapter. The results are broadly categorized as wave propagation (Table 1), wave coupling (Table 2), wave damping (Table 3) and heating (Table 4). In this chapter, voltages and currents will always be referred to by their RMS value $(\frac{\text{Peak to Peak}}{2\sqrt{2}})$.

Table 1

Wave Propagation Measurements from Magnetic Probes Around Torus

- Large number of high Q, closely packed eigenmodes
- Apparent mode cutoff below $n_e \simeq 10^{13}/cm^3$
- No significant decrease in amplitude in the toroidal direction
- Magnitude compatible with radiation resistance and stochastic mode stacking
- B_θ, B_r, B_z, at edge, all have roughly same magnitude (3 axis probes in ceramic thimble)
- 20 cm long, $k_\parallel$ array shows nonuniform wave structure along torus (short wavelength stochastic mode stacking)
- Large apparent $k_\parallel \simeq .5\ cm^{-1}$, hence significant evanescent region at the edge
- $k_\parallel$ fringes show positive going sawteeth
- Electrostatic probe may not contain same phase information (tentative)
- Small k_θ from relative phases between probes at different poloidal positions

Table 2

Antenna Loading Resistance

- Three antennas tested

  A_1 electrostatically shielded

  A_2 bare metal, slotted limiters each side

  A_4 electrostatically shielded, slotted limiters each side

- R_R increases linearly with density
- R_R essentially independent of I_p, B_0, RF power
- R_R roughly increases as ω_o^2
- R_R roughly unaffected by Faraday shield (taking into account antenna geometry)
- At 180 MHz, H_2 and D_2 show similar resistances (D_2 slightly larger than H_2) and He exhibits a much smaller resistance
- R_R sensitive to plasma position (R_R decreases at end of shot when plasma moves inward)
- R_R and H_α light have similar time evolution
- Multipactor regime is very wide in the new large ceramic breaks (5W - 500W)
- R_R is roughly proportional to antenna length squared
- R_R is roughly independent of antenna phasing (m = 0,1)

Table 3

Comparison of Fundamental and Second Harmonic Regimes

($n_e = 3 \times 10^{14}$ cm^{-3}, $B_o = 60$ kG, $I_p = 150$ kA)

	Experimental Regime	90 - 100 MHz (ω_{CH}, $2\omega_{CD}$) Minority $n_H/n_D \approx .05$	180 - 200 MHz ($2\omega_{CH}$, $4\omega_{CD}$) H, D, and H & D
Typical Radiation Resistance	Shielded (A_1) Unshielded (A_2) Shielded (A_4)	≈ 0.5 Ω ≈ 2 Ω ≈ 2 Ω	2 - 3 Ω 7 - 10 Ω 5 - 8 Ω
Magnetic Field Dependence	Radiation Resistance	- Background component unchanged - Eigenmode structure disappears with layer inside plasma	Independent of toroidal field (40 - 80 kG)
	Probe signals	Modes remain, but with reduced amplitude when layer is at plasma center	Probe signal decreases slightly when layer is near probe position (preliminary)

Table 4

Medium Power Heating Experiments

High Density:

Typical Parameters	$\bar{n}_e = 2 - 3 \times 10^{14} cm^{-3}$, $I_p = 150$ KA
	$B_o = 60$ kG, 50% H, 50% D (also 100% H or D)
	$f_o = 180$ MHz $= 2F_{CH} = 4F_{CD}$
	$P = 30 - 100$ kW

Results

- Energetic H & D tails (>5 Kev) with short decay times (<100 μs)
- 30 - 50% increase in soft X-rays
- Bolometric measurement indicates an increase in (fast particles/radiation) flux proportional to the RF input power
- 30% increase in H_α light both at the antenna and around the torus
- Some evidence of light impurities (extreme UV spectra)
- Small dip in neutron production
- No significant change in I_p, V_{loop}, hard X-rays, $\bar{n}_e$
- With carbon limiter:
  - 10% density increase
  - carbon deposit on antenna
  - no consistent increase in energetic neutrals

Low Density:

- $\bar{n}_e = 5 \times 10^{13}$ cm^{-3}, deuterium ($4\,\omega_{cD}$)
- Very energetic ion tail formation (both early and at peak of discharge)

II-2. Low Power Wave Measurements

II-2.1. High Q eigenmodes

In every case examined, except those at high density in the minority regime, high Q closely packed eigenmodes were observed. An apparent mode cutoff was also observed at about 10^{13}/cm. Density measurements below $3 \times 10^{13}/\mathrm{cm}^3$ were very crude since the resolution of the alcohol interferometer was about $10^{13}/\mathrm{cm}^3$. Particle recycling usually keeps the density above $2 \times 10^{13}/\mathrm{cm}^3$. As expected, cutoff was much easier to reach at 90 MHz than at 200 MHz because $k_A \propto \omega_o$.

Figure 1 shows the plasma current (~150 kA), electron line average density (10^{14} cm^{-1}/fringe), RF pulse timing, forward (58 KW) and reflected voltages (9 kW), antenna current (150 Amps RMS) and a probe signal from the Thomson port for a typical high density shot at 180 MHz ($2\omega_{cH}$, $4\omega_{cD}$). Figure 2 shows the antenna current, probe signal and square law detected $k_{\parallel}$ array probe signals for a medium density shot. Several important conclusions can be drawn from these two Figures. First, we obviously see dozens of eigenmode peaks in as little as 8 msec (in agreement with IV-6.3.). Second, these eigenmodes are very closely packed, overlap, and constitute a virtual continuum. Nevertheless, some resonances are larger than others (because of higher Q or coherent stacking of two modes), and cause dips in the antenna current. The peaks in the probe signal do not necessarily line up with the dips in the antenna current because, with many eigenmodes, fields add differently at different locations around the torus. This effect is further emphasized in Figure 2, where the different probes are only a few centimeters apart along z (III-3.2), and show qualitatively the same behavior, but with some small but clearly discernable differences, implying the presence of stochastic stacking of relatively short wavelength eigenmodes (≃ array length).

Figures 3 and 4 show probe signals at very low density ($\simeq 10^{13}/cm^3$) where the eigenmode resonances are well separated, and can be compared to Figures IV-6.7(3) - (9). From Figure 3 (Min/Max ≃ 7) and equation IV-6.2(7), we can calculate the damping length as

$$(1) \qquad 1/k_i = \pi R\sqrt{\frac{F_R}{F_A}} \simeq 4.5 \text{ meters}$$

The eigenmode Q can be crudely estimated from equations IV-6.4.(6) and IV-6.4(21) as

$$(2) \qquad Q \simeq \frac{k_A}{4k_i} \simeq \frac{.2}{4 \times 2 \times 10^{-3}} \simeq 25 \text{ at low density}$$

$$\simeq 100 \text{ at high density}$$

$$(3) \qquad Q \simeq \frac{2n_e}{\Delta n_e} = \frac{2n_e}{\left(\frac{\partial n_e}{\partial t}\right)\Delta t} \simeq \frac{2 \times 10^{13}/cm}{\left(\frac{10^{13}/cm^3}{10^{-2}\ sec}\right)10^{-4} sec} \simeq 200 \text{ at either low or high density}$$

Although these two methods should be redundant, the large discrepancy is easily justified by the crudeness of IV-6.4.(6) ($k_\parallel$ is not known), and the gross inaccuracy of $\partial n/\partial t$. F_R/F_A is also underestimated, since the antenna current dips (F_R is underestimated), and several modes exist (skirts overlap and thus F_A is overestimated).

Figure 3 also shows an A cos ϕ signal of two $k_\parallel$ array probe signals. Although the magnitude of probe 76 is almost identical to 77, their phases are considerably different, as expected.

Figures 4 and 5 show probe signals at 10^{14} and $2 \times 10^{14}/cm^3$ line average densities and 200 MHz. At $10^{14}/cm^3$, the eigenmodes are still quite discrete, and mode stacking is only partial. At $2 \times 10^{14}/cm^3$

and above, the individual modes are more difficult to discern, and radiation resistance spikes disappear, in agreement with IV-6.7., where we concluded that probe signals would always be "noisier" than R_R. Figure 5 also shows a 23 kHz heterodyned probe signal for phase measurements (III-3.3. and II-2.3).

Figure 6 shows a low density, pure hydrogen, 90 MHz ($\omega = \omega_{cH}$) plasma shot. Very high Q eigenmodes occur early in the discharge. At very low density, late in the discharge, there is an apparent mode cutoff, in agreement with simple theory (this may not be a real cutoff, and Section IV-5.4. showed that no cutoff should occur for the $m > 1$, $\mu = 1$ modes).

Figures 7 and 8 show evidence of possible mode splitting (IV-3.3) in a very low and a medium density plasma. This effect could also be caused by density fluctuations, or simply by two different perpendicular eigenmodes.

Following the theory of Section IV-6.3, we are now faced with the dilemma of labeling these eigenmode resonances (Figures 1-8). Are they onsets, large R_R eigenmode resonances (i.e., $m = 0 \pm 1$ $\mu > 3$), or simply particularly high Q eigenmodes ($m > 1$)? Onset has the largest radiation resistance, and probably accounts for the thirty or so larger peaks. For a quality factor as large as 1000, the energy pump time (decay time, IV-6.4.(12))

$$\text{(4)} \qquad \tau = \frac{1}{\omega_i} = \frac{2Q}{\omega} = 1.6\ \mu\text{sec}$$

is much less than any experimental resonance width. From Figures IV-5.4.(3-14), we can approximately write

(5) $\frac{\partial k_{\parallel}}{\partial n} \simeq 10^{-14}\ \text{cm}^2$

$\rightarrow 0$ for $\mu = 1,\ m > 1$

$\rightarrow \infty$ for $\mu > 1$

(6) $\frac{\partial k_{\parallel}}{\partial t} = \frac{\partial k_{\parallel}}{\partial n}\ \frac{\partial n}{\partial t} \simeq 50\ \text{cm}^{-1}\ \text{sec}^{-1} \quad \left(\frac{\partial n}{\partial t} \simeq 10^{14}\ \text{cm}^{-3}\ \text{sec}^{-1}\right)$

and for

(7) $\Delta k_{\parallel} = k_i \simeq 10^{-3}/\text{cm} \quad (1/k_i = 10\ \text{meters})$

we have

(8) $\Delta t \approx \left[\frac{\partial k_{\parallel}}{\partial t}\right]^{-1} \Delta k_{\parallel} \approx 20\ \mu\ \text{sec}$

which is much longer than the pump time.

Until now, we have assumed $R_R \propto \frac{1}{k_{\parallel}}$ near onset. Taking into account $k_{\perp i} \simeq k_{\parallel i} \simeq 10^{-3}$, and substituting $k_{\parallel i}\ 2\pi R \rightarrow k_{\perp i} 4a$ and $z \rightarrow r$ in IV-6.2.(5), we have instead a coherent, perpendicular stacking, limiting factor of the form

(9) $R_R \propto \frac{1 + e^{-k_{\perp i} 4a}}{1 - e^{-k_{\perp i} 4a}} \approx 50$

and R_R does not go to infinity even for $k_{\parallel} = 0$.

Away from onset, toroidal resonance radiation resistance peaks are critically dependent on the evanescent edge and Q. Large perpendicular mode numbers have smaller $k_{\parallel}$ (small evanescence), but also larger damping (small Q), and the two effects compete. The $m > 0$ modes have larger Q (IV-5.3), but cannot be discerned from the $m < 0$ by probes at the plasma edge. Some peaks may also be beats between different perpendicular eigenmodes (even for $k_i R > 1$).

Eigenmodes at High Density

P13, B4, S50
Hydrogen 183 MHz

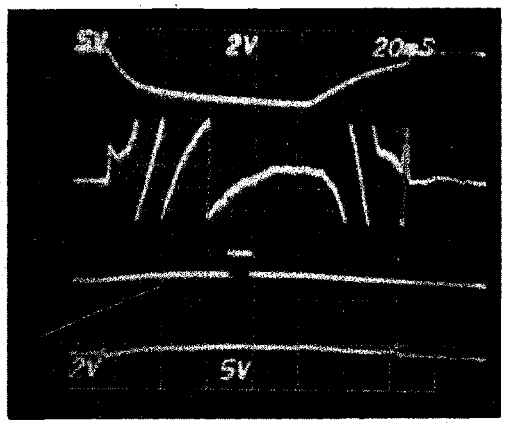

I_p

n_e

t

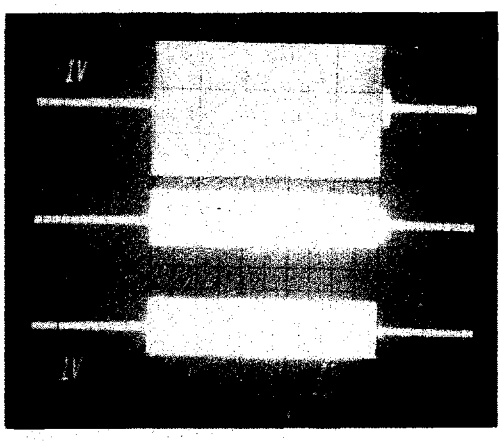

V_F 57.7 kW

V_R 8.9 kW

I_a 149 amps

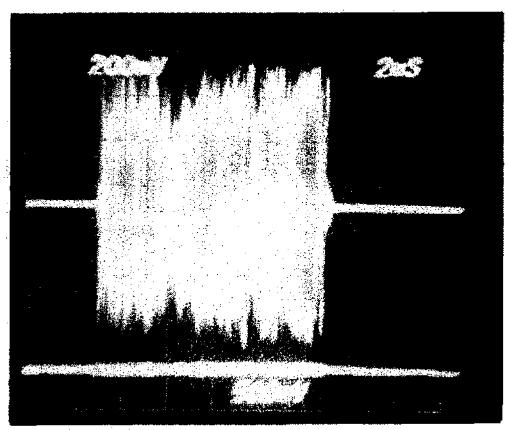

P_{74}

Figure 1

Radiation Resistance and Probe Signal at Medium Density

S47,B2,P9
D_2, 183 MHz

Figure 2

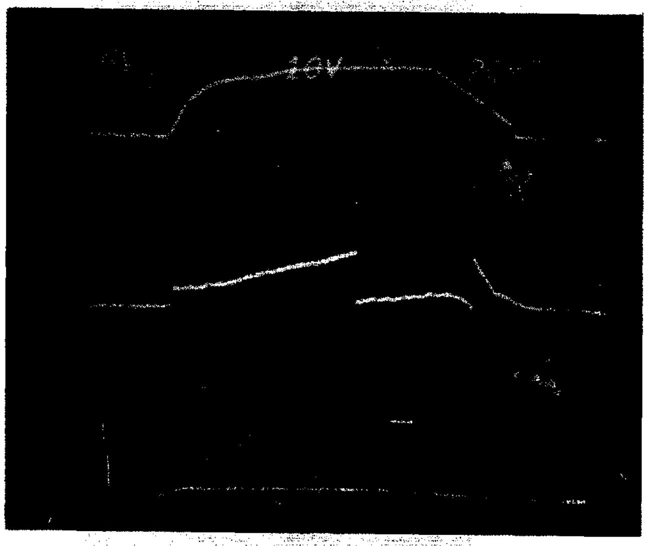

I_p

n_e

t

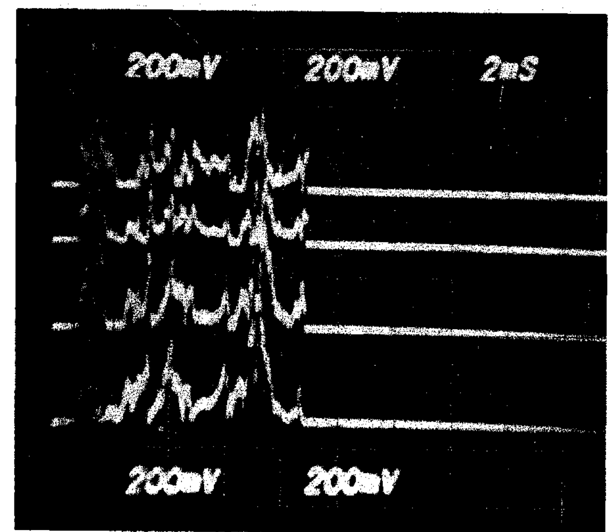

P_{70}

P_{71}

P_{72}

P_{73}

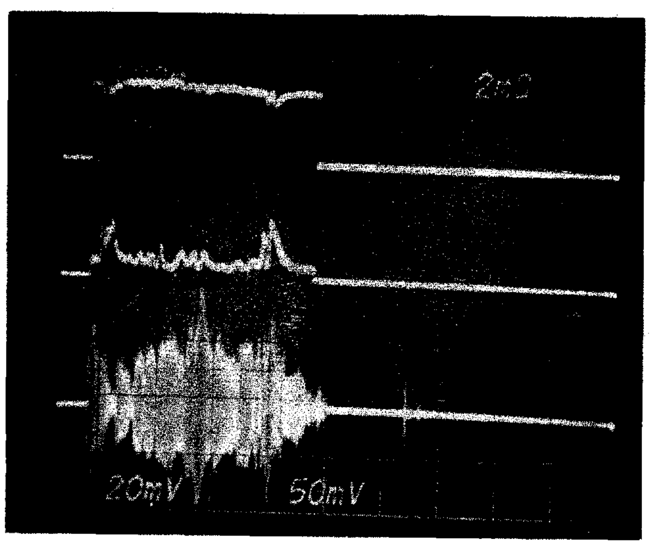

V_F (14.2 kW)

V_R (1.1 kW)

P_8

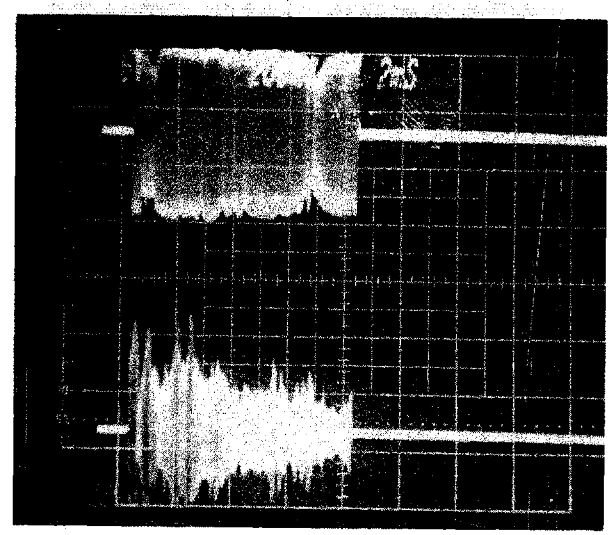

I_a
(96 amps)

$R_R = 1.4\Omega$

P_{79}

Low Density Phase and Magnitude Eigenmode Measurements

B4, P9, S39
Hydrogen, 183 MHz

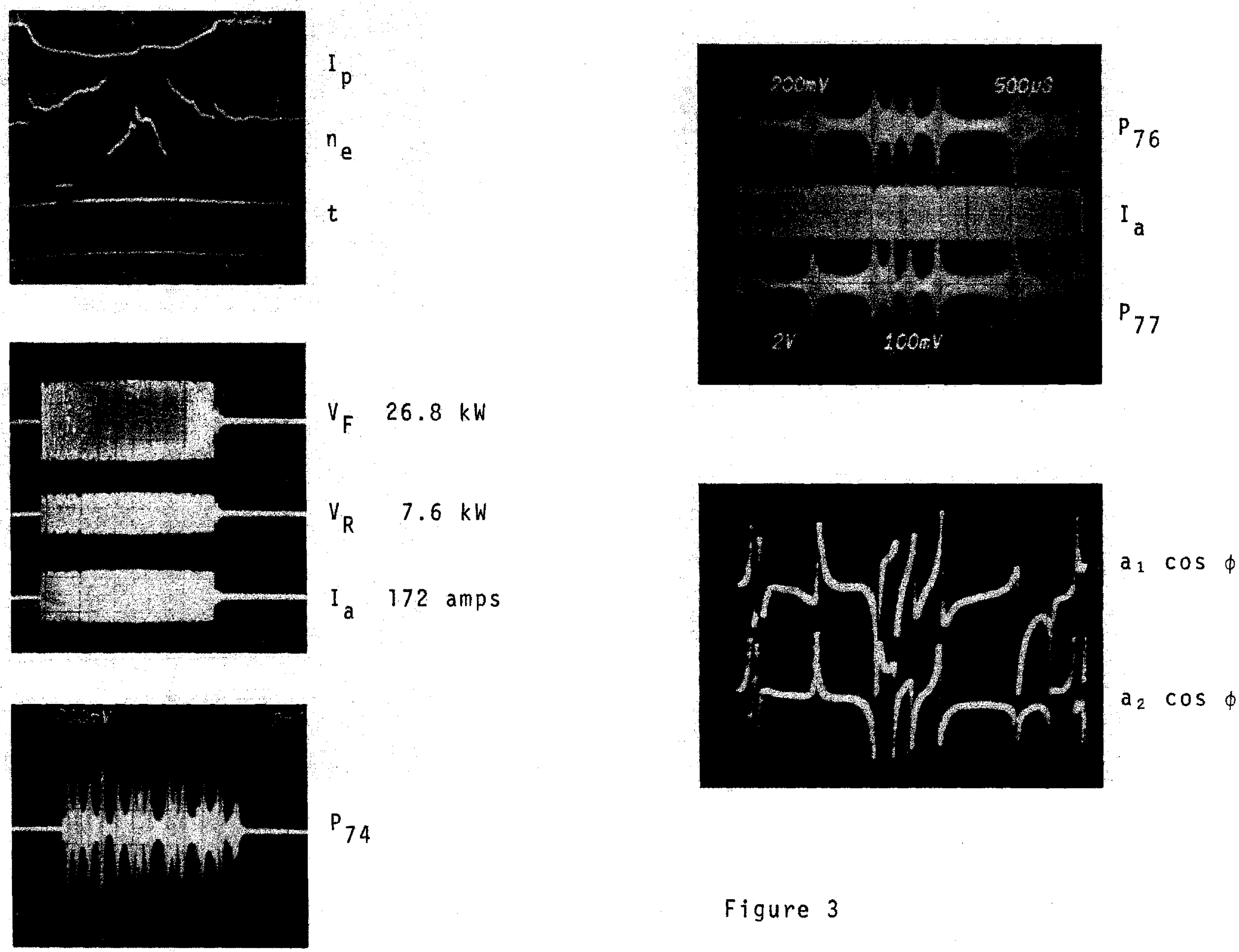

Figure 3

S32, P6, B4

200 MHz at
Medium Density

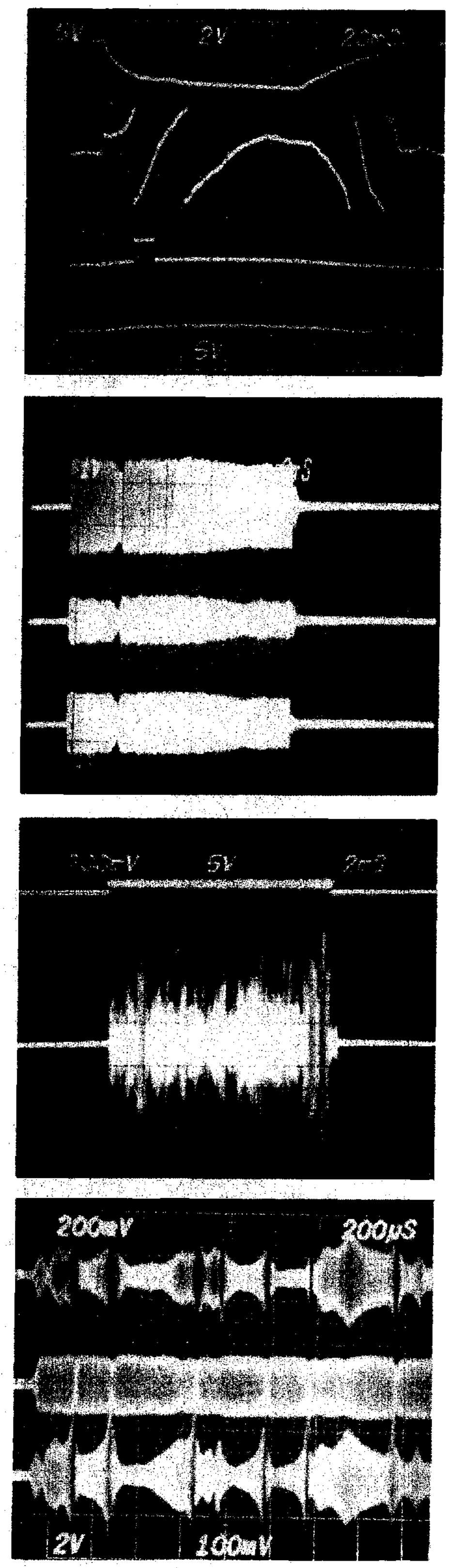

I_p

n_e

t

V_F

V_R

I_a

t

P_{74}

P_{76}

I_a

P_{77}

Figure 4

Eigenmode Detail
at Medium Density

S61, P69, B1
Deuterium

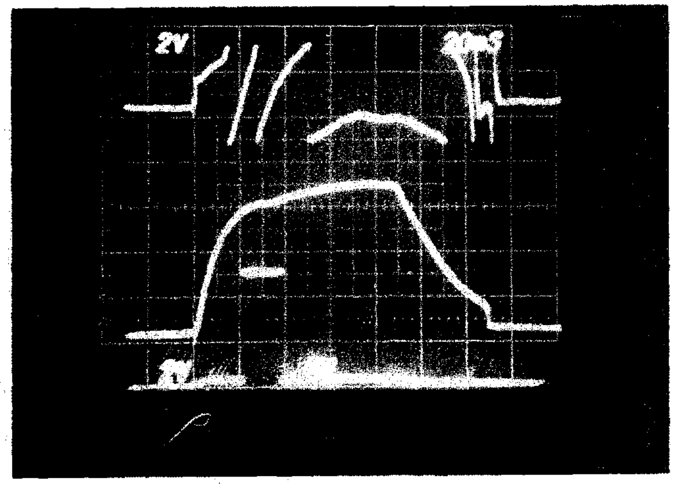

n_e

I_p

t

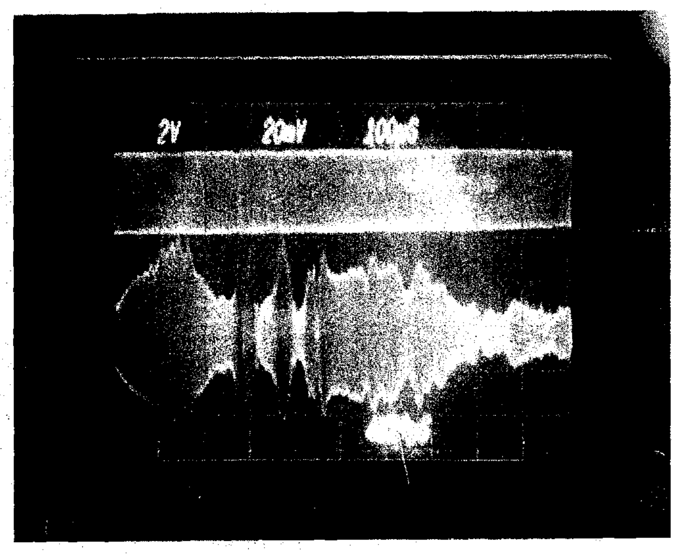

I_a

P_t

Figure 5

S41, P52, B2
Heterodyne
to 23 kHZ

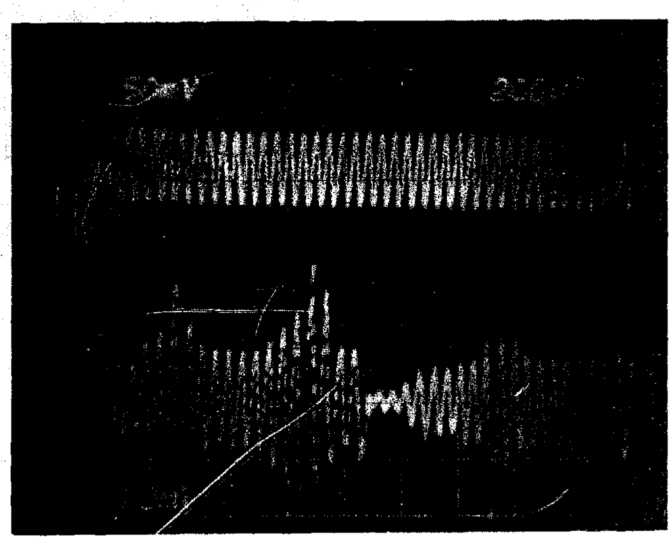

I_a

P_8

S7, P2, B8

Hydrogen at 90 MHz

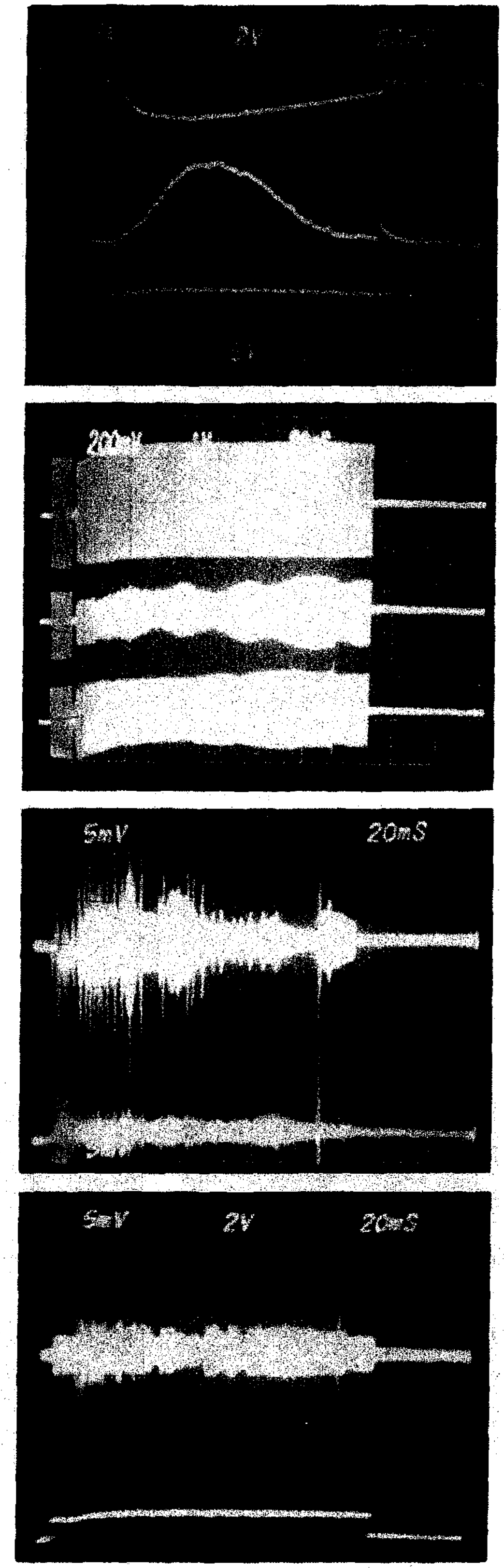

I_p

n_e

t

V_F

V_R

I_a

70 HCN

71 HCN

2 Near field

Figure 6

Evidence of Mode Splitting

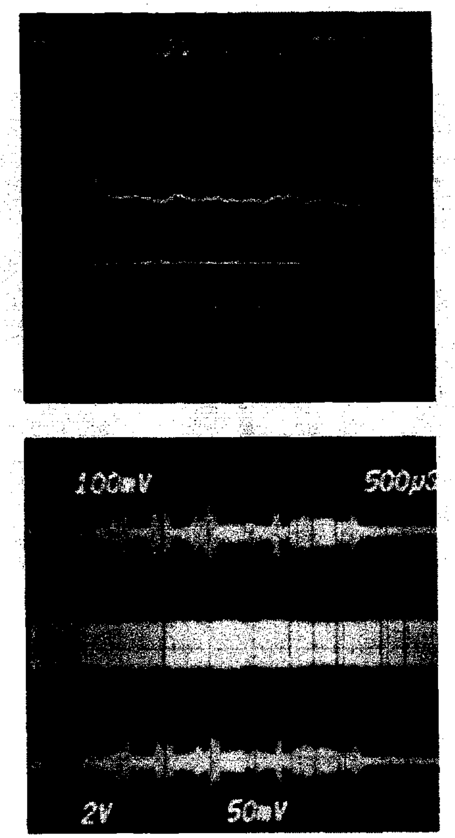

I_p

n_e

t

76

I_p

77

S20, P30, B4

H_2, 200 MHz

Figure 7

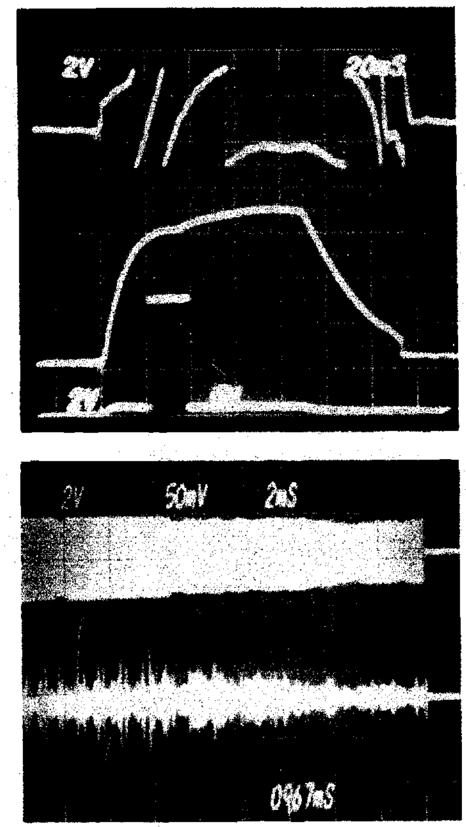

n_e

n_e

t

I_p

P

S64, B1, P70

Figure 8

II-2.2. Wave amplitude measurements

Neglecting near-field power absorption, we show in IV-6. that, for high Q toroidal resonances and many overlapping eigenmodes, the probe signal average is proportional to $\langle R_R \rangle / \sqrt{\bar{n}}$.

Figure 1 shows a standard high density low power shot with the forward and reflected voltage, antenna current and probe signal at HCN port. Figure 2 shows the radiation resistance $\left(\frac{P_F - P_R}{I^2}\right)$, antenna current, antenna electric field $\left(\frac{IR}{\ell}\right)$ and probe signal for the same shot. Note how the radiation resistance and electric field increase with density, but the probe signal saturates and even decreases with density. Figures 3 and 4 are similar shots, and we notice (Figure 3) the top and bottom antenna currents are loaded in an almost identical manner (good balance in push-push mode). Probe signals around the torus (68 HCN top, 69 HCN bottom and 67 top limiter), on the other hand, have significantly different time histories (Figure 4). Many of these different behaviors are believed to be due to the wandering plasma position. Radiation resistance is usually lower at the end of the shot (for the same density), and is most likely due to the plasma moving inward, since there is usually too much vertical field for the decreasing plasma current. In all cases examined (hundreds of shots in almost all directions of available parameter space) except the fundamental regime (with the cyclotron layer in the center of the plasma), probe signals around the torus (±90°, 180° from antenna) were all about the same magnitude (probe position in the complicated port geometry is critical). These measurements were done very carefully,and are strong evidence of long damping length.

Figures 5 and 6 show radial probe scans with a large magnetic probe (Figure III-3.2.(3)) and a standard small unshielded probe

(Figure III-3.2.(2)). With the large probe fully inserted, it becomes a good model of a short section of the A_2 antenna, and we can write (without mode stacking)

$$(1) \quad V_{\text{Probe Theoretical}} = \frac{A_{\text{probe}}}{A_{\text{antenna}}} I_{\text{antenna}} R_R$$

$$\simeq 3 \quad V_{p\text{ experimental}}$$

and the discrepancy could be explained by some 9 eigenmodes or, of course, by near-field or single toroidal pass power absorption. Figure 6 shows similar results, but at three different power levels, and also showing a discrepancy factor of three or so. If mode stacking is not invoked, this means that only some 10% of wave power reaches 90° away from the antenna. The measurement is very crude because of the extreme sensitivity of the probe and plasma position (evanescent edge), and the mere fact that power is proportional to voltage squared (50% error can easily be due to the average probe signal value estimation from the oscillograph).

Figures 5 and 6 are indicative of large $k_{\parallel}$, since, for small $k_{\parallel}$, the edge magnetic field should be roughly independent of distance from the wall, which is clearly not the case here. For large $k_{\parallel}$ ($\simeq$ .5/cm), the edge B_z vs r should be either linear or exponential, in agreement with experiment. (Note again the extreme sensitivity of the port geometry.)

The results shown in Figures 5 and 6 can also be used to estimate wall power losses as

$$(2) \quad P_{\text{wall}} = \frac{A_{\text{wall}} J^2_{\text{wall}}}{\sigma\ \delta} \simeq \left(\frac{V_p}{A_p}\right)^2 \left(\frac{1}{f_o \mu_o}\right)^{1.5} \left(\frac{\pi}{\sigma}\right)^{.5} a\ R \simeq 1.0 \text{ Watt}$$

$$(3) \quad \frac{P_{in}}{P_{\text{wall}}} \simeq \frac{500 \text{ W}}{1 \text{ W}} = 500$$

and wall losses can be totally neglected in any power balance calculation (this is a lower limit due to the bellows convolutions and port geometry).

High and low power experiments showed exactly the same results (except obviously, during multipactor), and all processes (coupling, damping, etc.) were linear over six orders of magnitude (.1 W to 100 kW) (except perhaps some preliminary measurements of low level and frequency parametric activity at the 50 kW input power level).

Figures 7 and 8 show low and high density shots with predominantly H_e^4 plasma composition. The eigenmodes are High Q and very similar to those for H_2 or D_2 plasmas. R_R, on the other hand, is very small (II-2.4). The lower traces of Figures 7 and 8 show RF pickup by the electrostatic Langmuir probe at the HCN port (Figure III-3.2.(5)). The probe signal was shunted by a 1 μH inductor acting as a high pass filter. At low density, the electrostatic and magnetic probe signals show the same behavior (high Q eigenmodes), but differ considerably at high density (activity continues even after RF is shut off).

Radiation Resistance and Probe Signal at High Density

B2, P61, S58

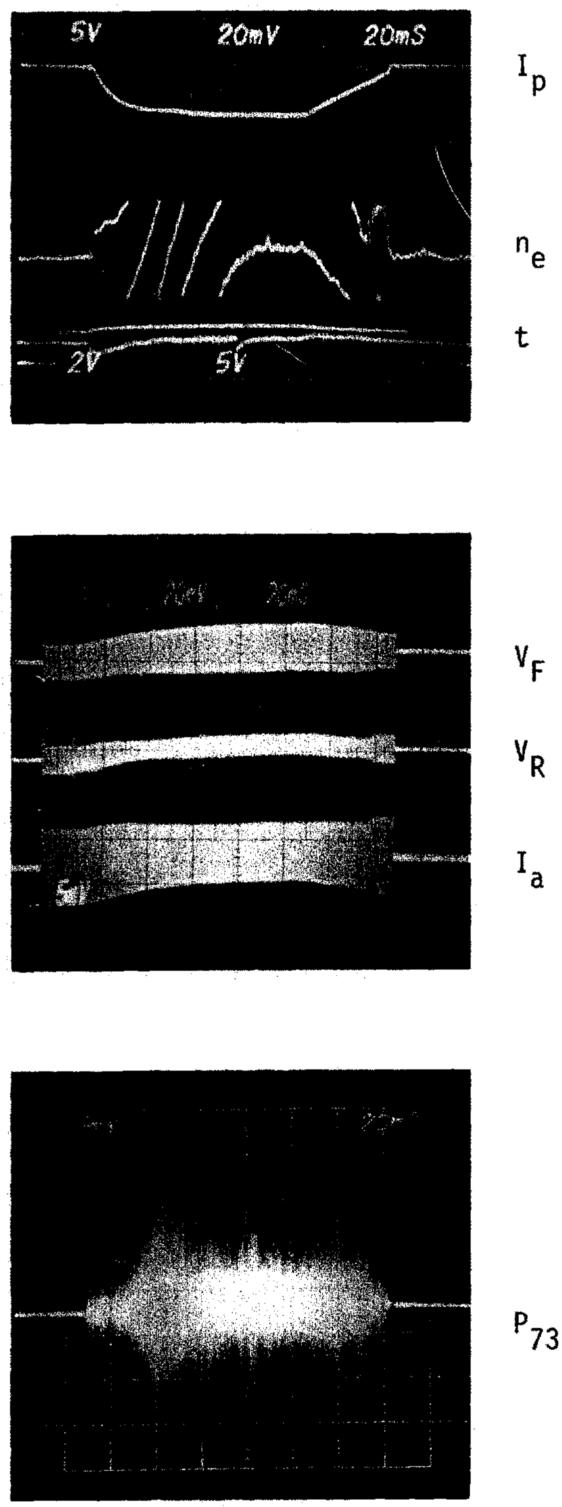

Figure 1

Radiation Resistance, Antenna Electric Field, and Probe Voltage as a Function of Density

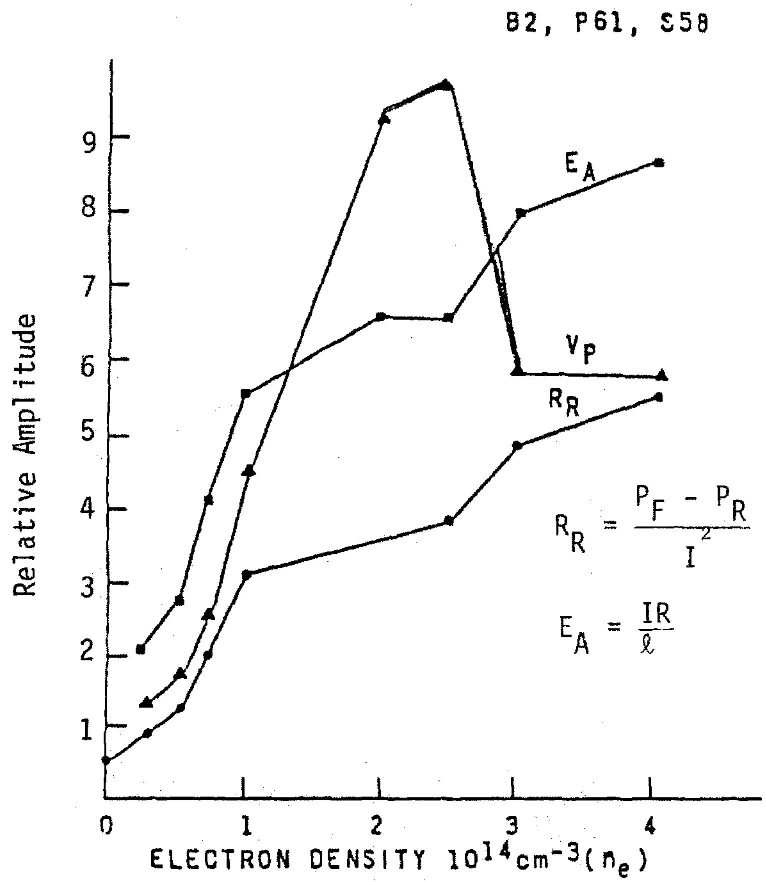

Figure 2

S17, B15, P57

Low Power with A_2 Fed
in Push-Push Mode

H_2, 67.5 kA
200 MHz

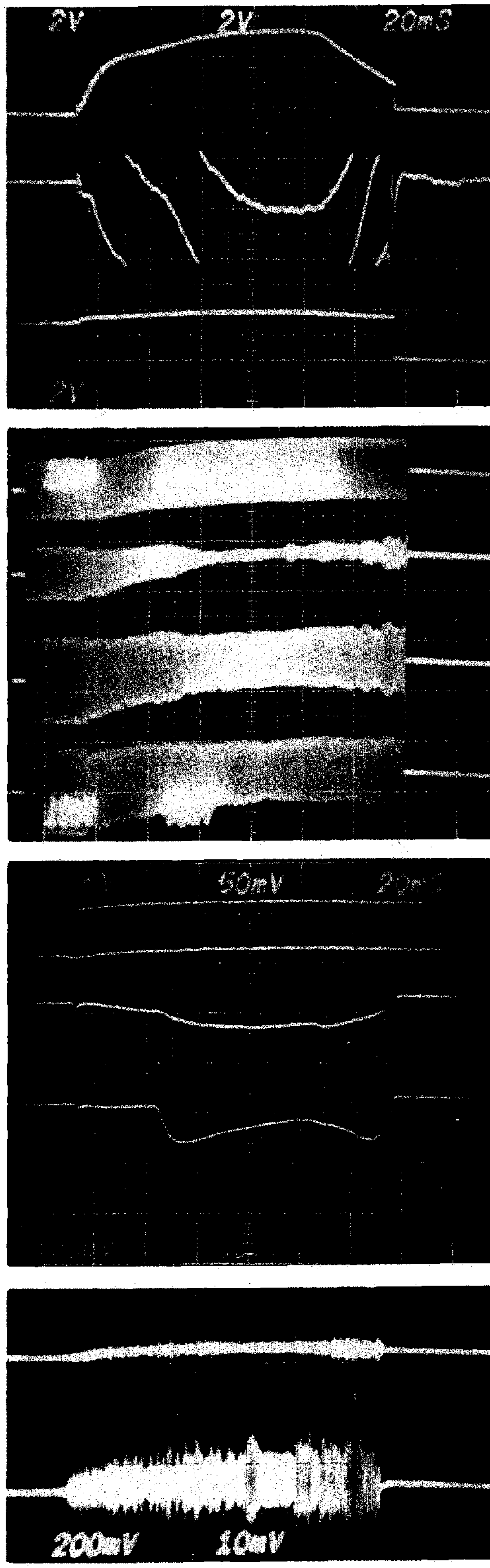

I_p

n_e

t

V_F 1.6 W

V_R

I_T .46 A

I_B R_R = 7.6Ω

L_T

L_B

pin

H_α

68 HCN top

69 HCN Bot.

Figure 3

S52, P20, B13

D_2 and He^4 Mixture

at 183 MHz

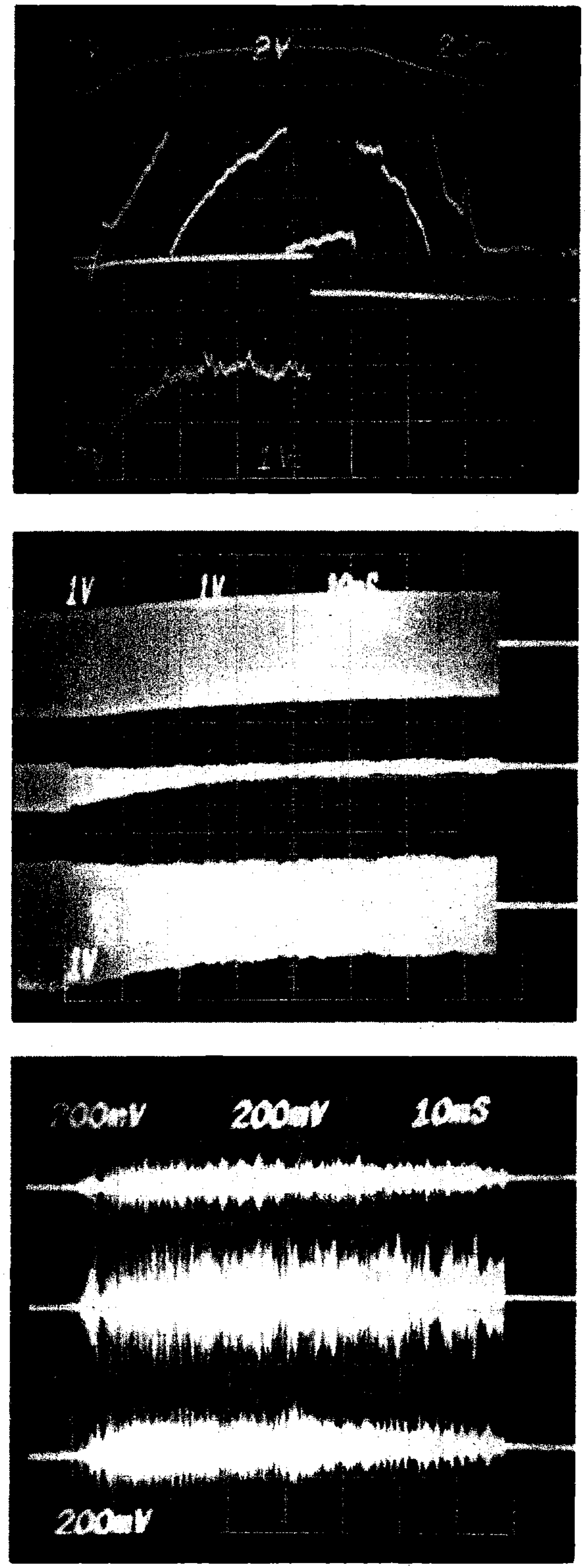

I_p

n_e

t

R_R

V_F

V_R

I_a

68 HCN top

69 HCN bot

67 Limiter top

Figure 4

PROBE SIGNALS VS RADIAL POSITION

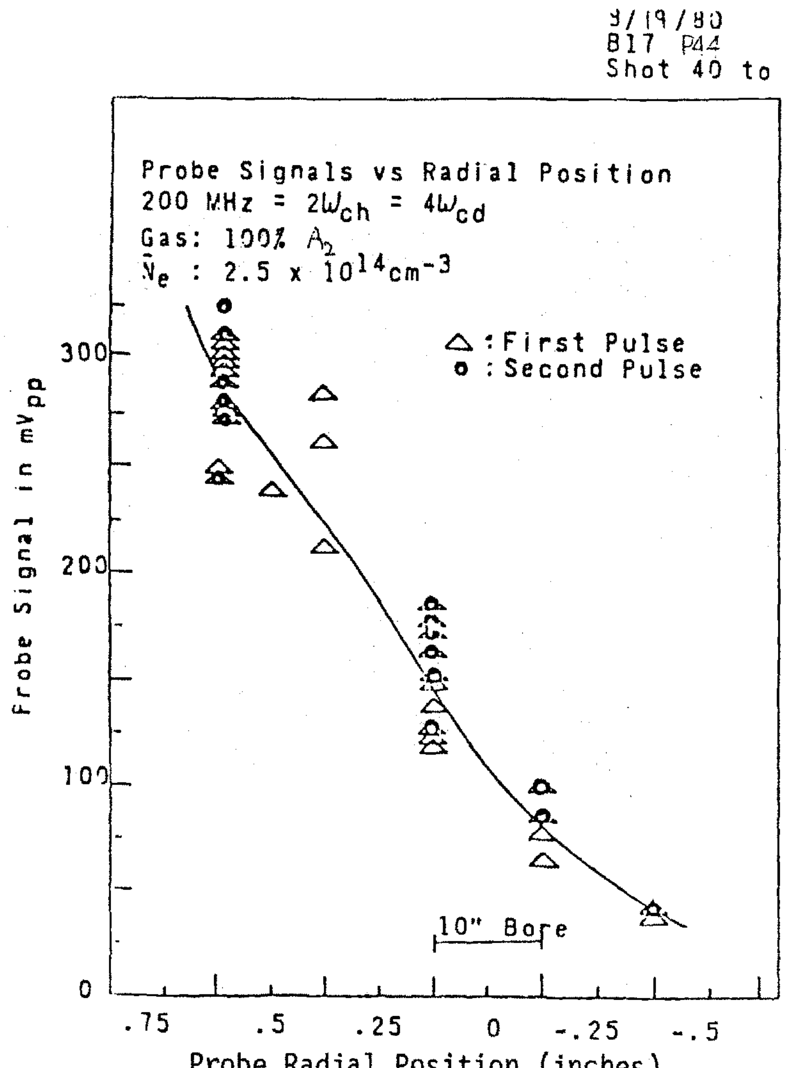

Figure 5

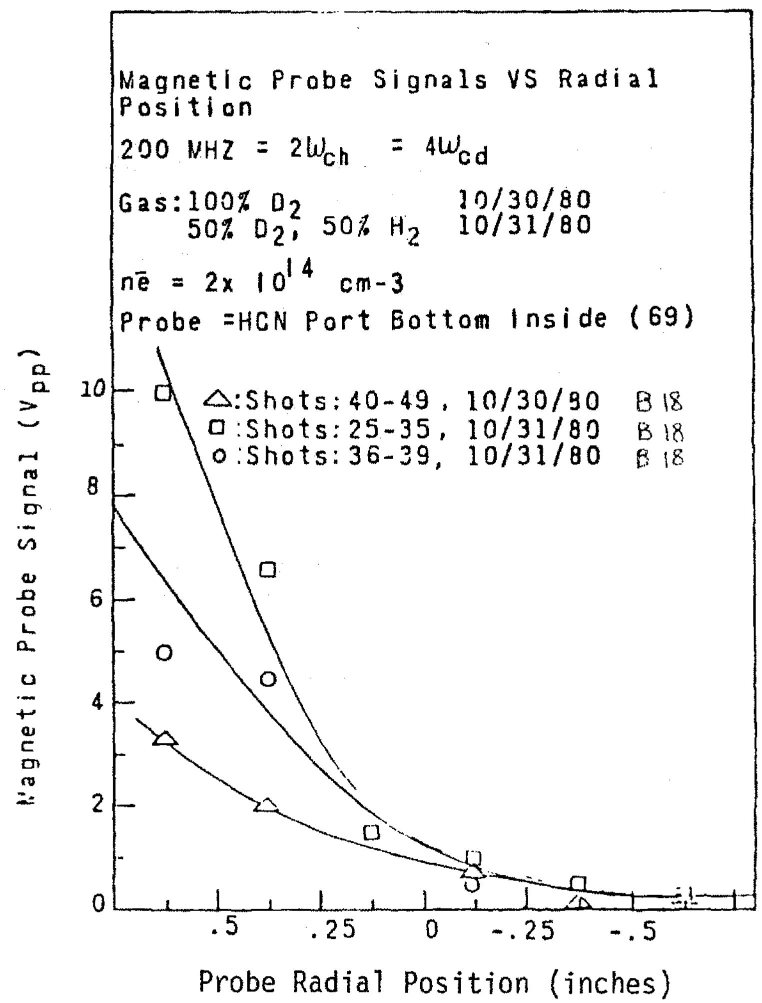

Figure 6

D_2 and He^4 Mixture at 183 MHz

S43, & 45, P16, B13

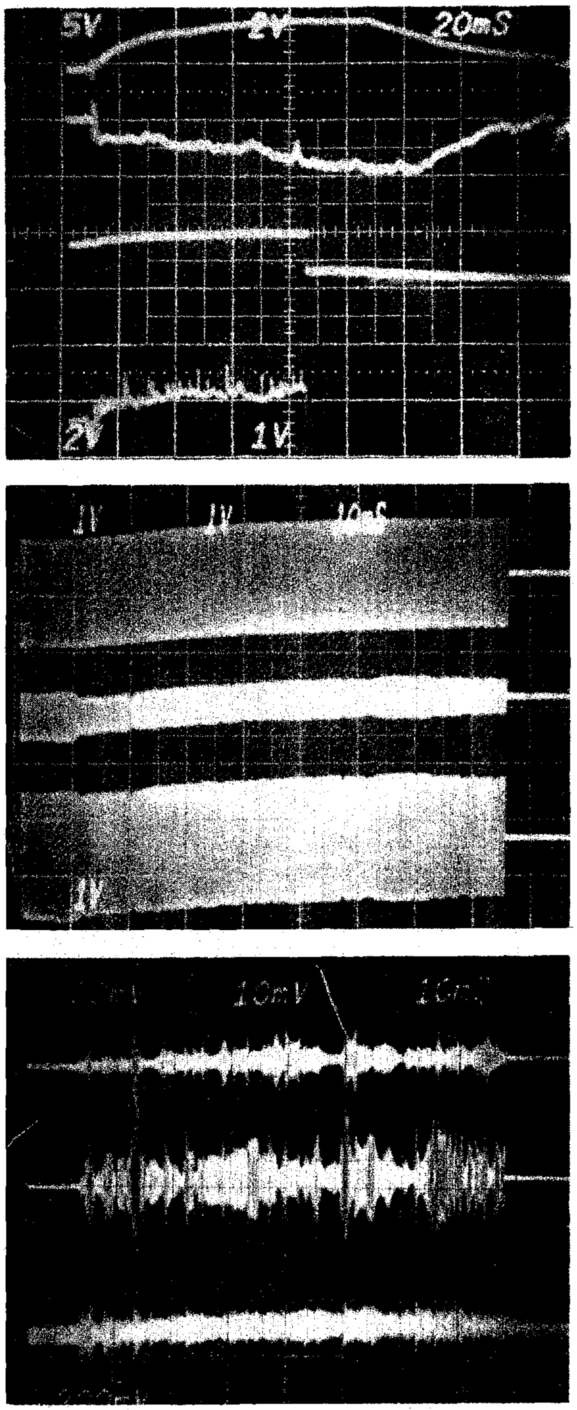

S45

Figure 7

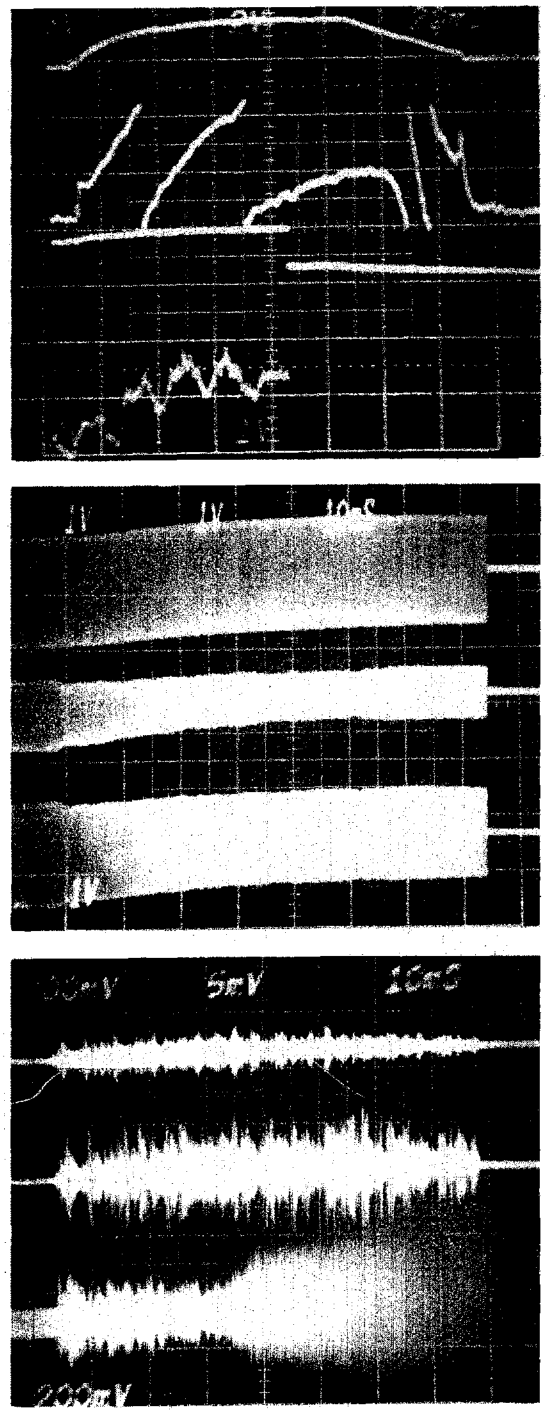

S43

Figure 8

II-2.3. Wave phase measurements

As outlined in III-3.3., extensive probe phase measurement schemes were used to estimate parallel and perpendicular wavelengths. Figure 1 shows a typical high density shot with 50% H_2 and 50% D_2. The lowest trace is the phase (2π/fringe) between the oscillator ($\simeq$ antenna current) and a magnetic probe 90° away from the antenna. For a finite Q system and large dynamic range, the phase is never lost, and the phase difference simply increases as $k_\parallel$ ($\propto \sqrt{n_e}$). Thus

(1) $$k_\parallel = \frac{\phi}{\ell} = \frac{4N}{R} = .61/\text{cm at } 2.2 \times 10^{14}/\text{cm}^3 \qquad (N = 8.3)$$

and from IV-2.2. the maximum $k_\parallel$ ($k_\perp = 0$) is

(2) $$k_\parallel = \frac{k_A}{\sqrt{1+\Omega}} = \frac{\Omega}{\sqrt{1+\Omega}} \frac{\omega pi}{c} = 4.4 \times 10^{-8} \frac{\Omega}{\sqrt{1+\Omega}} \sqrt{\frac{n}{\mu}} \simeq .78/\text{cm}$$

where

(3) $$\begin{aligned} \frac{\Omega}{\sqrt{1+\Omega}} \frac{1}{\sqrt{\mu}} &= 1.15 \quad \text{for} \quad \Omega = 2 \quad H_2 \\ &= \ .82 \quad \text{for} \quad \Omega = 2 \quad D_2 \\ &= 1.26 \quad \text{for} \quad \Omega = 4 \quad D_2 \\ &\simeq 1.2 \quad \text{for} \quad 50\%\ H_2,\ 50\%\ D_2 \end{aligned}$$

and the eigenmodes could be very near cutoff. Note that including an initial phase shift ($\phi_o \simeq \frac{\pi^2 R}{\lambda_o} \simeq \pi$) and perhaps one to three initial fringes at breakdown ($n_e \simeq 10^{13}/\text{cm}^3$)

(4) $$\phi_{10^{13}} = k_\parallel\ .5\pi R \simeq 4 \times 10^{-6} \sqrt{n} \simeq 2\pi$$

would give $k_\parallel = .76 \simeq k_\parallel$ ($k_\perp = 0$).

At this point, we must caution the reader that, according to Figure IV-2.2.(4), even for a large $k_{\parallel} = .8\ k_{\parallel cutoff}$, $k_{\perp} = .5\ k_A$, and many radial and poloidal mode numbers are still possible at high density.

Figure 2 shows an expanded view of a pure deuterium shot ($k_{\parallel} \cong .5$/cm at $2 \times 10^{14}/cm^3$) with the phase difference between the HCN port and antenna (68/ref), top and bottom of HCN (68/69) and HCN and limiter (68/67). Although more difficult to read (due to the large dynamic range on both inputs to the phase correlator), the phase difference between the HCN and limiter is the same as between the antenna and HCN ports. Of course, the phase difference between the antenna and limiter was twice as large as between the antenna and HCN ports (Figure 3). The shots shown in Figures 2 and 3 were at the 40 kW level, and the antenna broke down after 60 msec.

The phase difference between the top and bottom of the HCN (68/69, Figure 2) does not indicate any average increase in phase, and is very noisy, as expected with a mixture of many randomly phased eigenmodes. Eigenmode identification at high density would clearly be very difficult if not impossible.

Fringe measurements during a single run were also done at 90 and 180 MHz, and as expected from (3)

$$(5) \qquad \frac{\phi_{180}}{\phi_{90}} = \frac{1.26}{.82} \cong 1.54$$

and there were about twice as many fringes at 180 MHz as at 90 MHz for about the same experimental conditions. A similar effect was observed by changing the magnetic field from 40 to 80 kG in II-2.4.

Figures 4 and 5 show phase measurements between the reference and a near-field probe (5/2) and reference and HCN (5/68), with a linear and cosine phase correlator for He^3 and He^4 plasmas at 183 MHz. Note how the linear correlator is easier to read. The cosine correlator had a bandwidth of about 10 MHz. As expected, the near-field phase deviation was less than $\pm\pi$, and was highly dependent on eigenmode resonances. The radiation resistance for these He shots was much lower than for H_2 or D_2 at the same density, in agreement with the accepted belief that helium profiles are much narrower. ($k_{AHe} \cong k_{AH}$, but evanescent edge is much larger). $k_\parallel$ is also very large ($\cong$.6/cm), even for medium density ($n_e \cong 1.6 \times 10^{14}/cm^3$).

Figure 6 shows an expanded view of phase measurement at medium power ($\cong$50 kW). Note the slight phase difference between the top and bottom HCN probes, and the usual slight dip in the thermonuclear neutron production rate.

Figure 7 shows a close up of fringes and soft X-rays, where we note the correlation between the "positive going" fringe sawteeth and the central soft X-rays. This correlation could be an argument supporting the hypothesis that these measurements represent bulk $k_\parallel$.

Phase Measurements at 206 MHz and D_2 50%, H_2 50%

B18, P66, S49

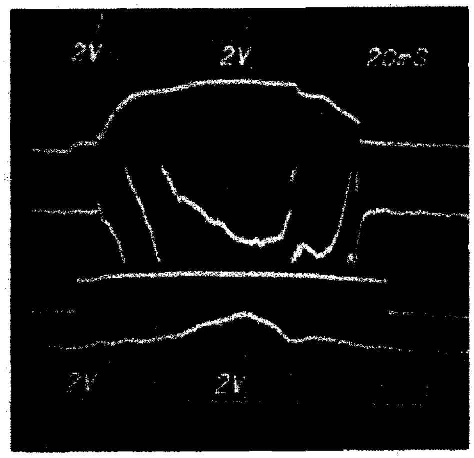

I_p

n_e

t

Neutrons

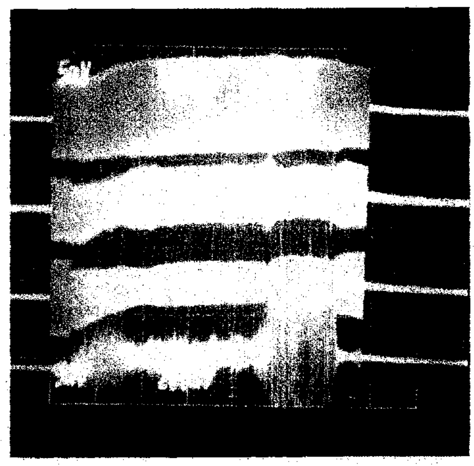

V_F

V_R

I_a

HCN Bottom, 69

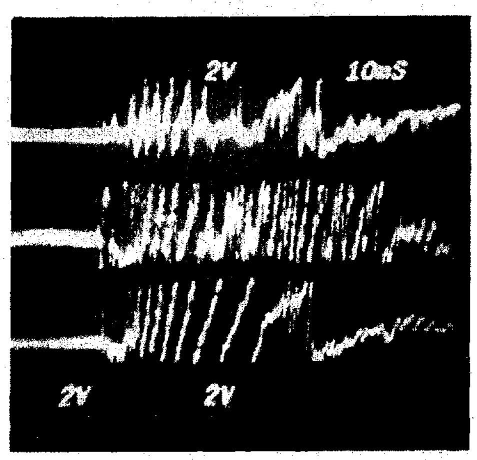

Ref/HCN Top, 68

Ref/HCN Bottom in., 69

Ref/HCN Bottom out., 70

Figure 1

Phase Measurements at 183.5 MHz and D_2

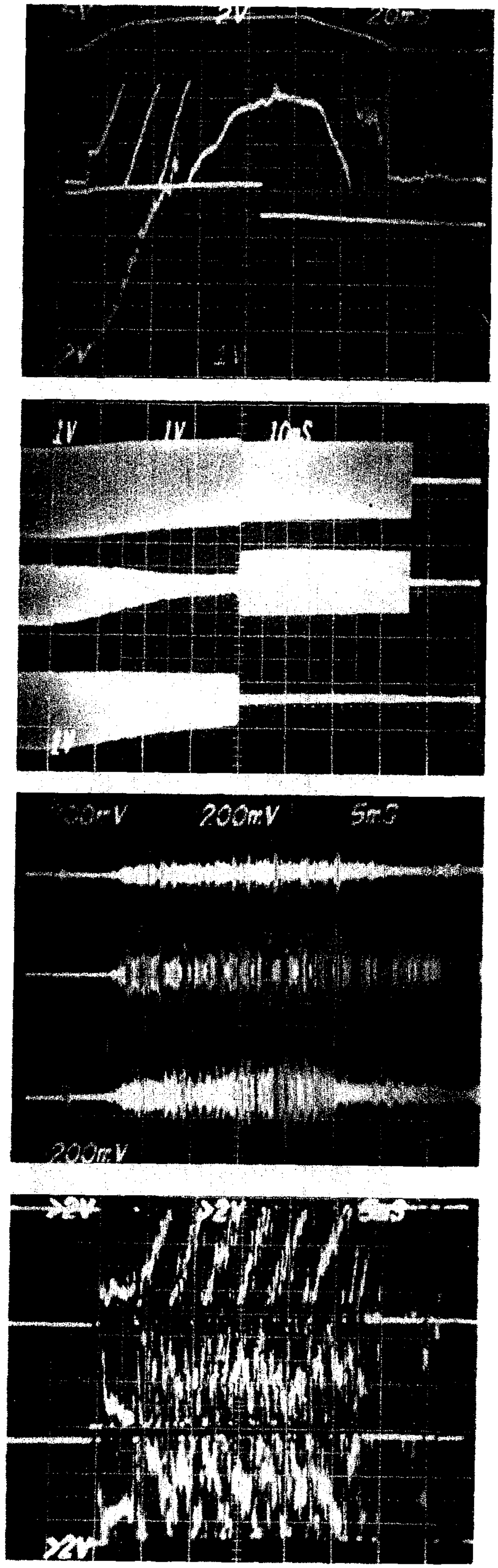

I_p

n_e

t

R_R

V_F

V_R

I_a

HCN Top 68

HCN Bottom 69

Limiter 67

68/REF

68/69

68/67

Figure 2

Phase Measurements Between MW, HCN and Limiter Ports

B13, P4, S12

Deuterium

183.5 MHz

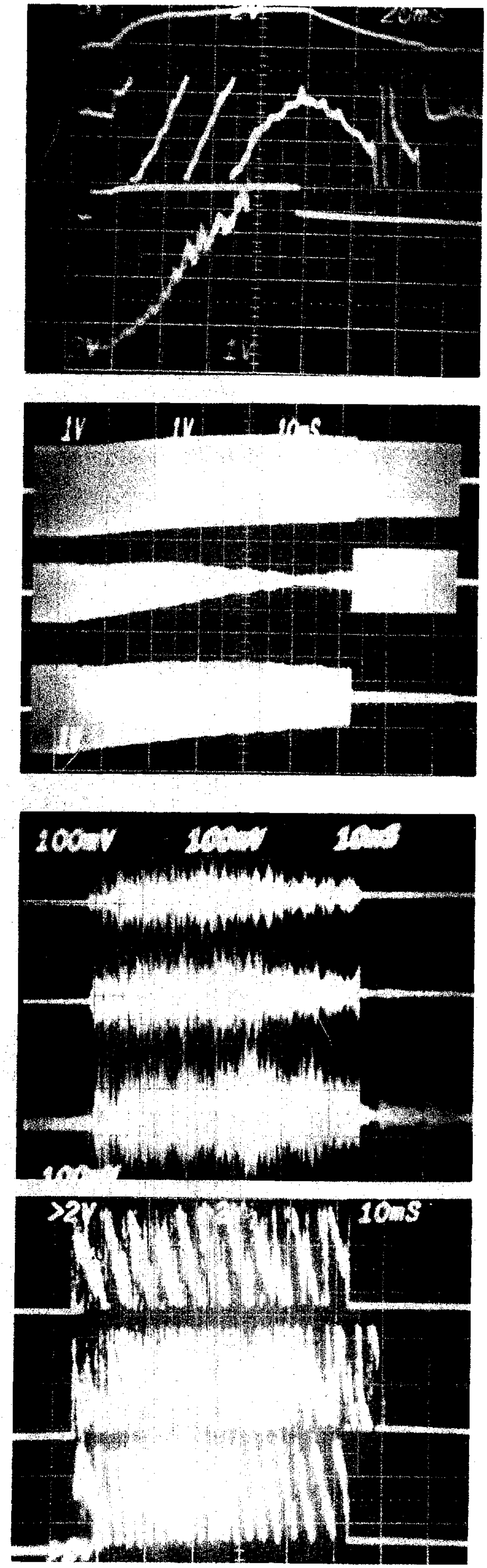

Figure 3

Phase Measurements at 183 MHz and He^3

P33, B10, S37-38

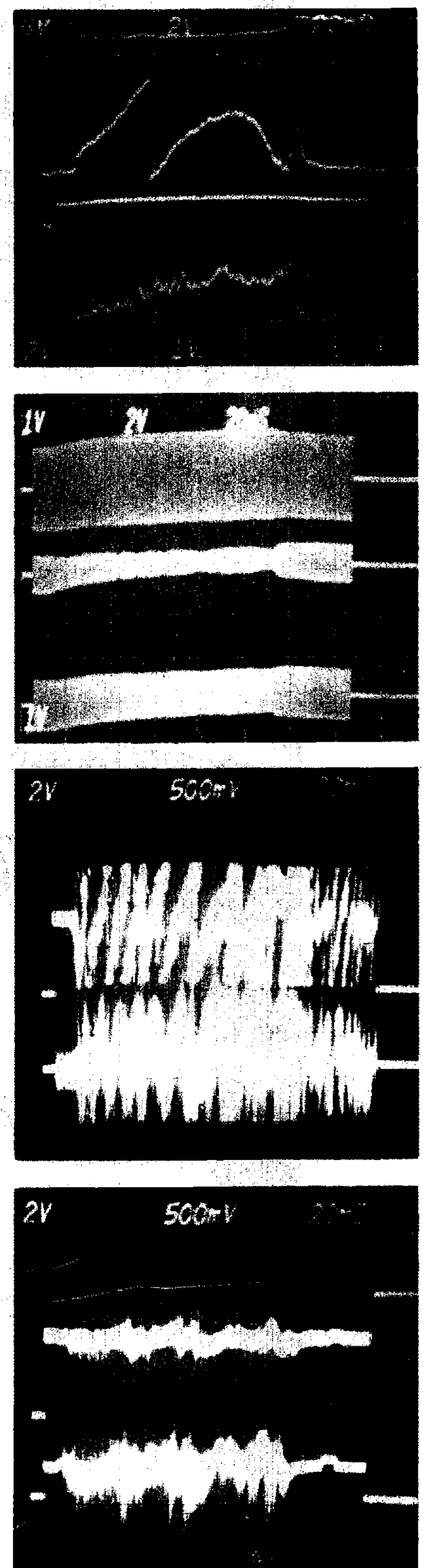

I_p

n_e

t

R_R

V_F

V_R

I_a

5/68

S37

5/68

5/2

S38

5/2

Figure 4

Radiation Resistance and Probe Measurements in He^4 at 183 MHz

S53, B10, P58

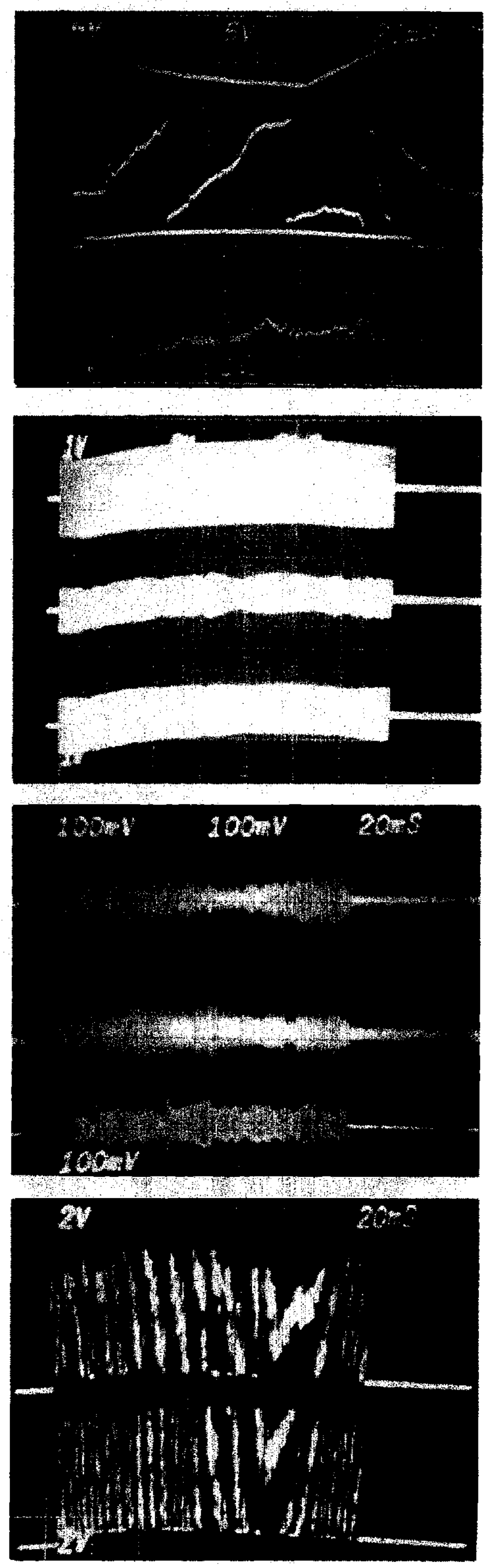

I_p

n_e

t

R_R

V_F

V_R

I_a

68 HCN

67 Limiter

2 Near-field

osc/68

osc/67

Figure 5

Phase Measurements at 206 MHz and D_2

B18, P51, S53

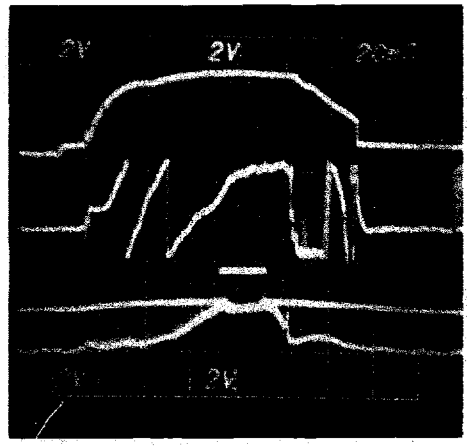

I_p

n_e

t

neutrons

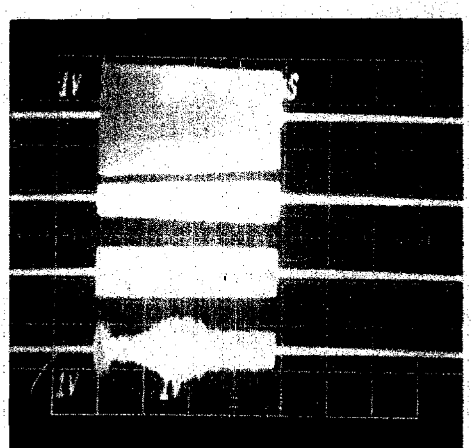

V_F

V_R

I_a

HCN Bottom inside 69

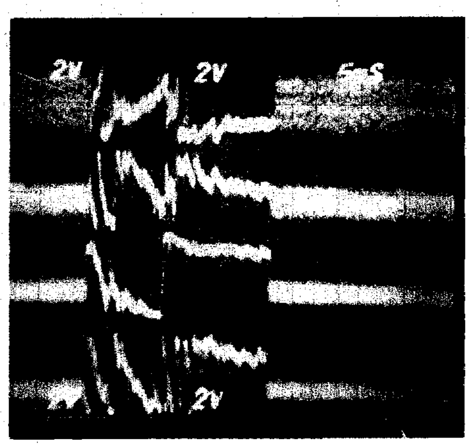

68/69

REF/HCN Top outside 68

REF/HCN Bot. inside 69

REF/HCN Bot. outside 70

Figure 6

Sawteeth on
$k_\parallel$ Measurements

205.5 MHz
100% D_2
65.3 kA

B18, S45, P64
11/1/80

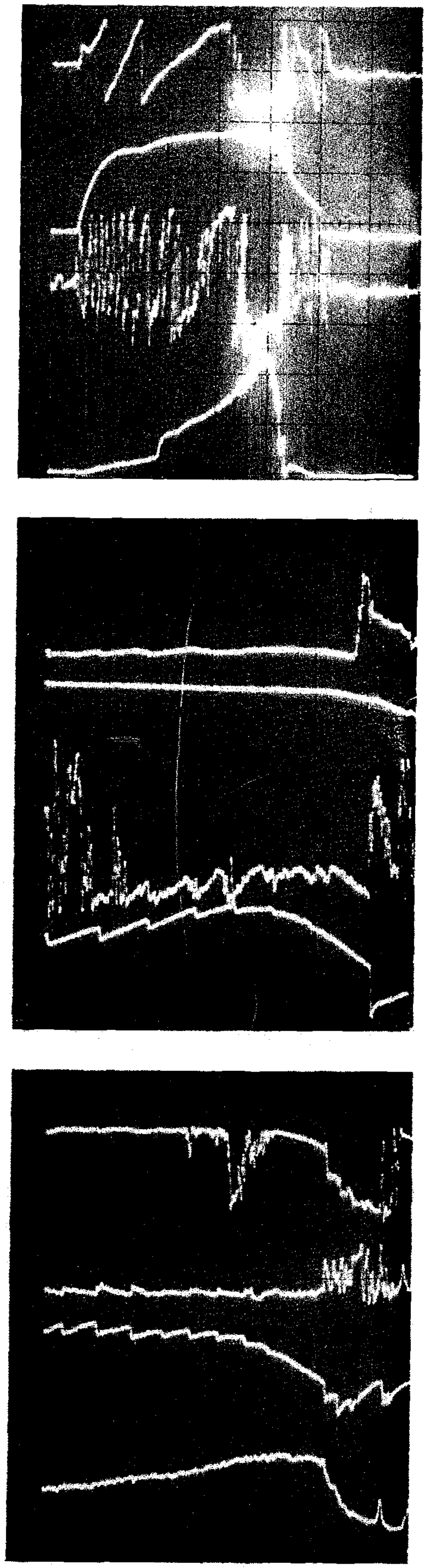

Figure 7

II-2.4. Radiation resistance and magnetic field scans

Radiation resistance is the single most important parameter to characterize ICRF wave coupling. Figure 1 shows how R_R roughly increases linearly with density, and is slightly higher for deuterium than hydrogen. Although R_R is usually quite repeatable within a given run, significant changes were noted from run to run with roughly similar experimental conditions. R_R background seemed essentially independent of plasma currents and magnetic field. Plasma in out position is believed to be responsible for much of the variations, but this was not confirmed, since all the position loops on Alcator were inoperative (Figure 2).

Most of the data in this work was taken with the A_2 unshielded antenna but R_R behaved essentially the same for the A_1, A_2 and A_4 antennas, except of course, for their relative value. At 200 MHz and $3 \times 10^{14}/cm^3$, A_1 was about 3 ohms while A_2 and A_4 were typically 8 ohms. At 90 MHz, R_R was lower by a factor of about 4, so that A_2 could only couple 30 kW or less.

Figures 3 and 4 show typical 90 MHz shots with D_2 fill and H_2 minority (recycling), and with the resonant layer either in (65.4 kA) or outside the plasma (79.2 kA). The radiation resistance was calculated with a high speed on-line analog computer (III-3.1.). R_R background is independent of magnetic field, but the eigenmode spikes on R_R and probe signal are very sensitive to layer position. Figure 5 is a plot of probe signal versus layer position, and unambiguously exhibits strong magnetic field dependence in agreement with theory. The minority concentration was small (<5%), so the TIIH layer was very near the cyclotron layer. Also note the difference between the field probe signals for the two resonant layer positions. This may suggest that eigenmode spikes are due to toroidal resonances rather than onsets, because even with short damping lengths (no probe spikes), R_R and near-field should still exhibit large onsets (which they do not in Figure 3).

Figures 6 to 9 show the results of similar experiments at 180 MHz. Only three fields were used in this case (smaller increments were used in other experiments), but many shots were averaged to gain good statistics. No significant field dependence was found on either the probe signals or radiation resistance (except for the expected $k_\parallel \propto 1/B_o$ dependence). Medium power field scans (II-3.3.) were also done in 50% H_2 and 50% D_2 plasmas, again with about the same result (except for the neutral flux dependence), indicating that second harmonic damping is weak. R_R background is not necessarily expected to change (both single perpendicular pass and high Q average R_R are independent of damping), but eigenmode peaks should be inversely proportional to damping if they are representative of the bulk power and second harmonic damping (the most important unknown).

Figure 10 shows a high density D_2 fill and He^4 pulse shot, where we again note (II-2.3.) how R_R stays small with a predominantly helium plasma. Figures 11 and 12 show H_α and total light in front (MW bottom) and inside (through holding pins) the antenna for two low power, high density, disruptive plasma shots. Note in particular, the close resemblance between the R_R and the light signals. The increase in R_R could be due to a broader profile (thinner evanescent layer) or increased near-field losses (also edge density). At medium power, this light increases by 30% (II-3.3) all around the torus. Also note (Figure 12) the close resemblance between the alcohol interferometer fringes ($\phi \propto n_e$) and the ICRF $k_\parallel$ fringes ($\phi \propto \sqrt{n_e}$).

Radiation Resistance vs. Density

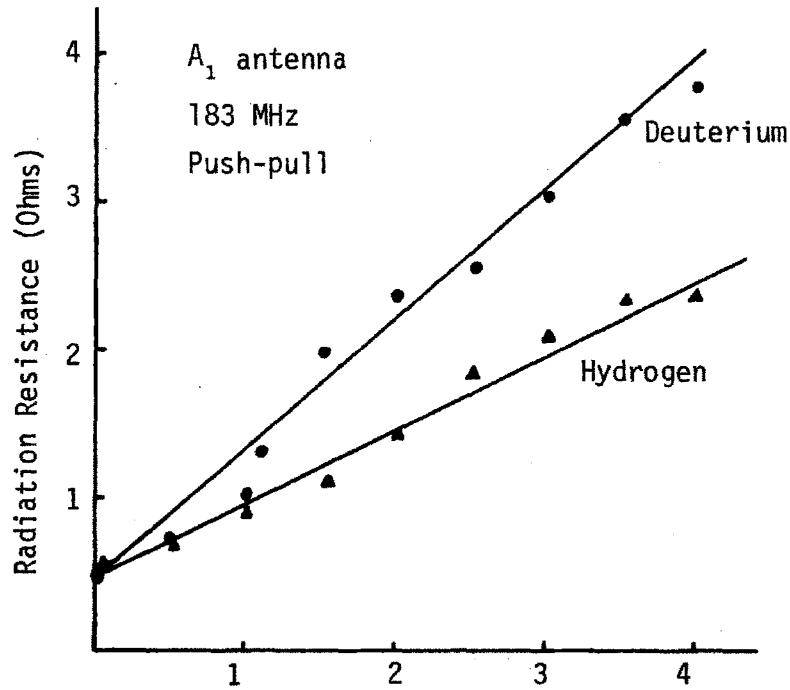

Line Average Density (10^{14} cm^{-3})

Figure 1

Radiation Resistance vs. Density

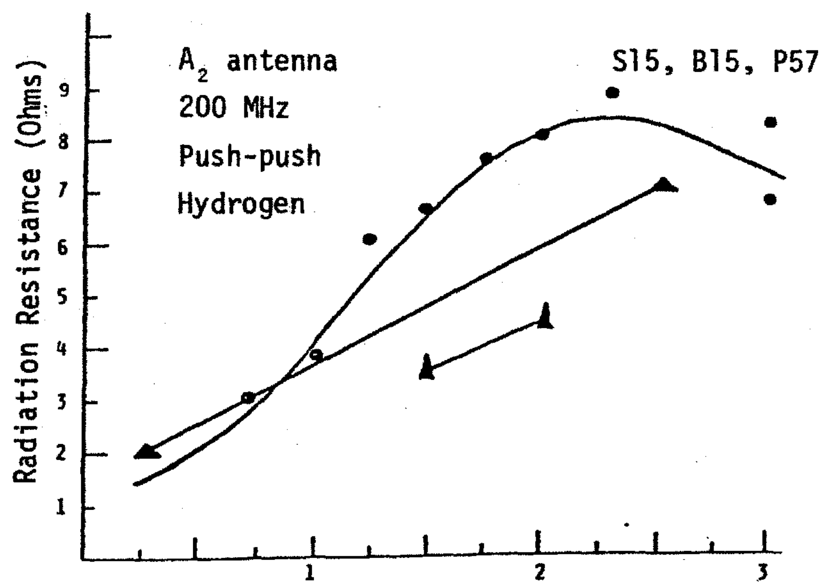

Line Average Density (10^{14} cm^{-3})

Figure 2

Radiation Resistance with Resonant Layer at Plasma Center

B9, P7, S21

90 MHz

D_2 fill

H_2 minority

65.4 kA

2.3 at 2 fringes

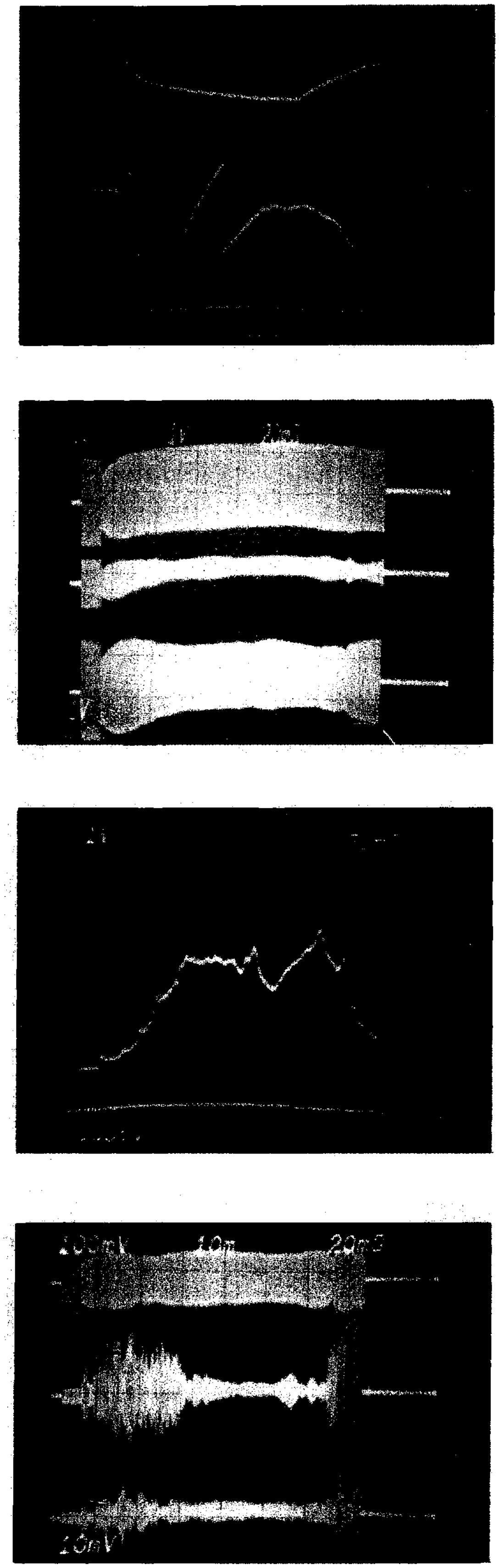

I_p

n_e

t

V_F

V_R

I_a

R_R

Near-field 2

Limiter 67

HCN Top 68

Figure 3

Radiation Resistance with Resonant Layer Outside Plasma

B9, P7, S32

90 MHz
D_2 fill
H_2 minority
79.2 kA
2.3 at fringes

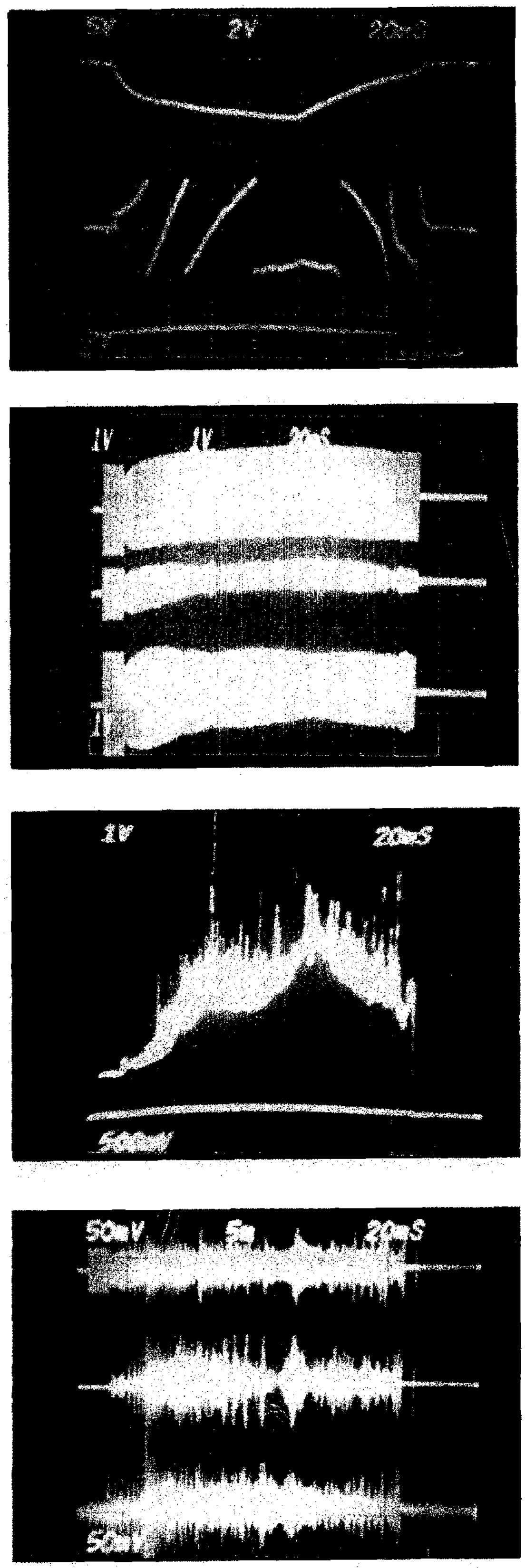

I_p

n_e

t

V_F

V_R

I_a

R_R

Near-field 2

Limiter 67

HCN Top 68

Figure 4

Probe Signals and Radiation Resistance as a Function of Toroidal Magnetic Field

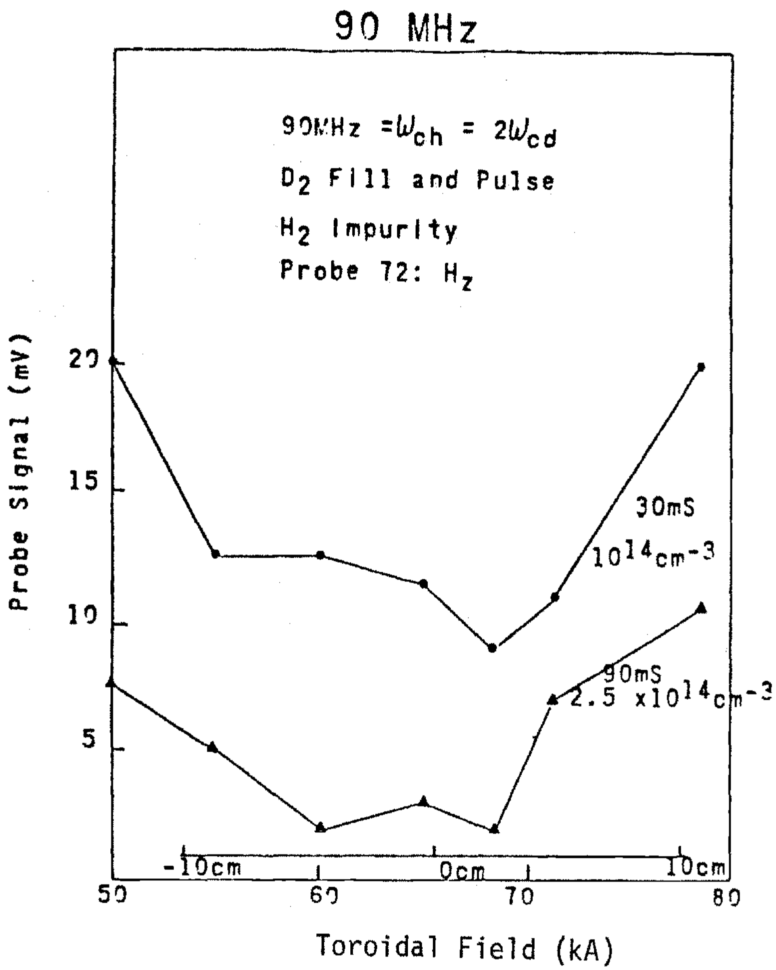

Figure 5

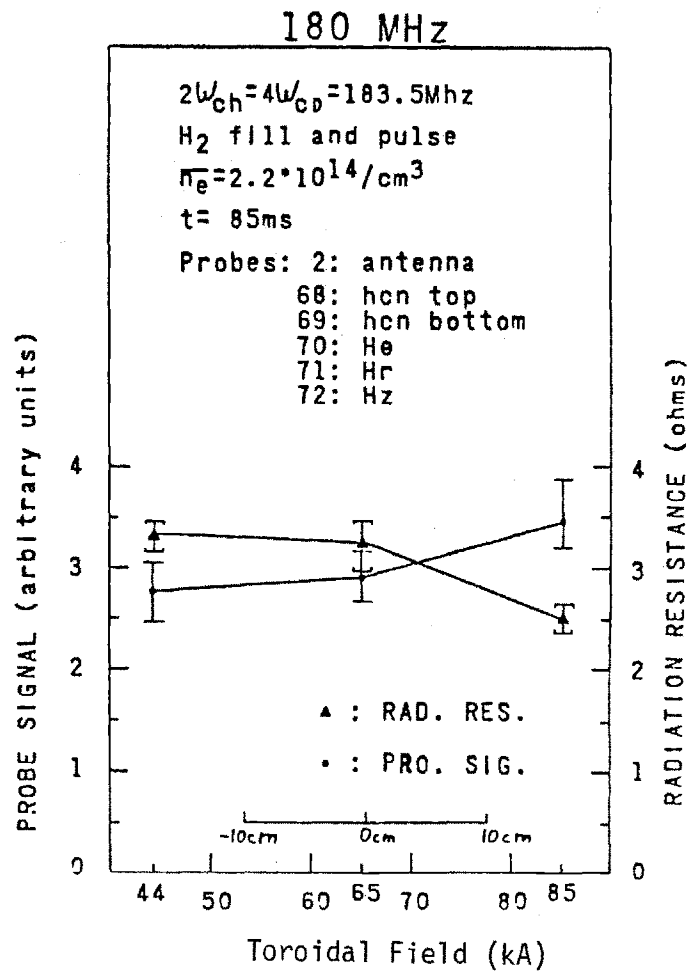

Figure 6

Resonant Layer on High Field Side

B10, P16, S50
2/13/80

Hydrogen
183.5 MHz
I_B = 44 kA
3 Ω at 2 fringes

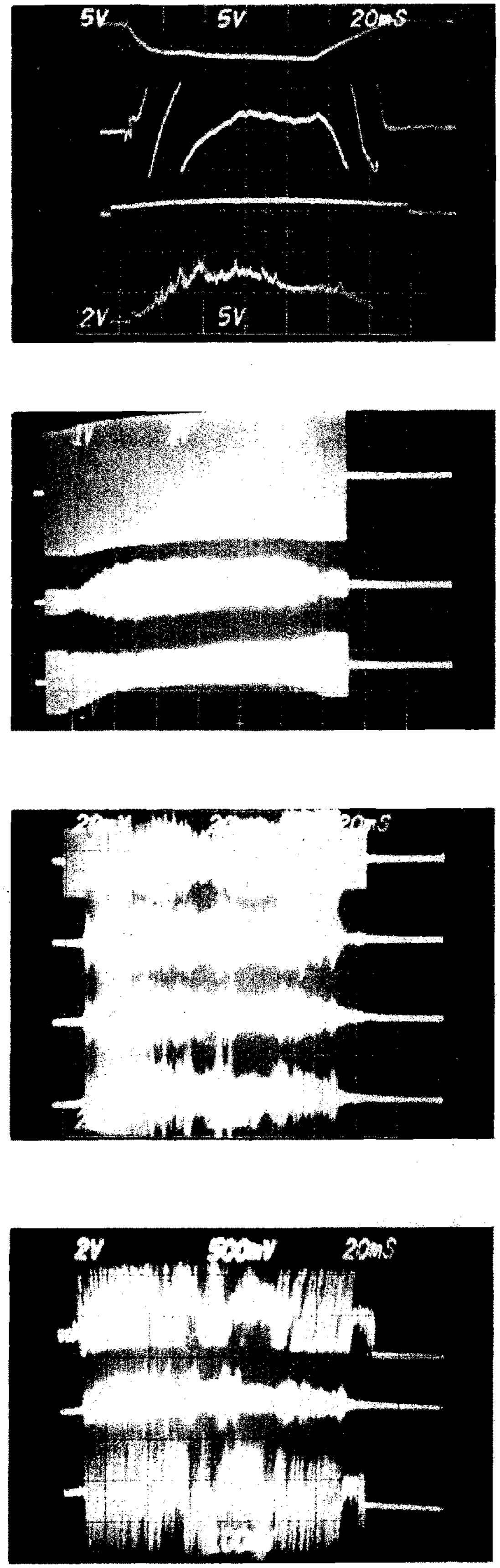

I_p

n_e

t

R_R

V_F

V_R

I_a

P 2

P 70

P 71

P 72

osc./72

5/72

Figure 7

Resonant Layer at Plasma Center

B10, P19, S57

2/13/80

Hydrogen

183.5 MHz

I_B = 65 kA

3 Ω at 2 fringes

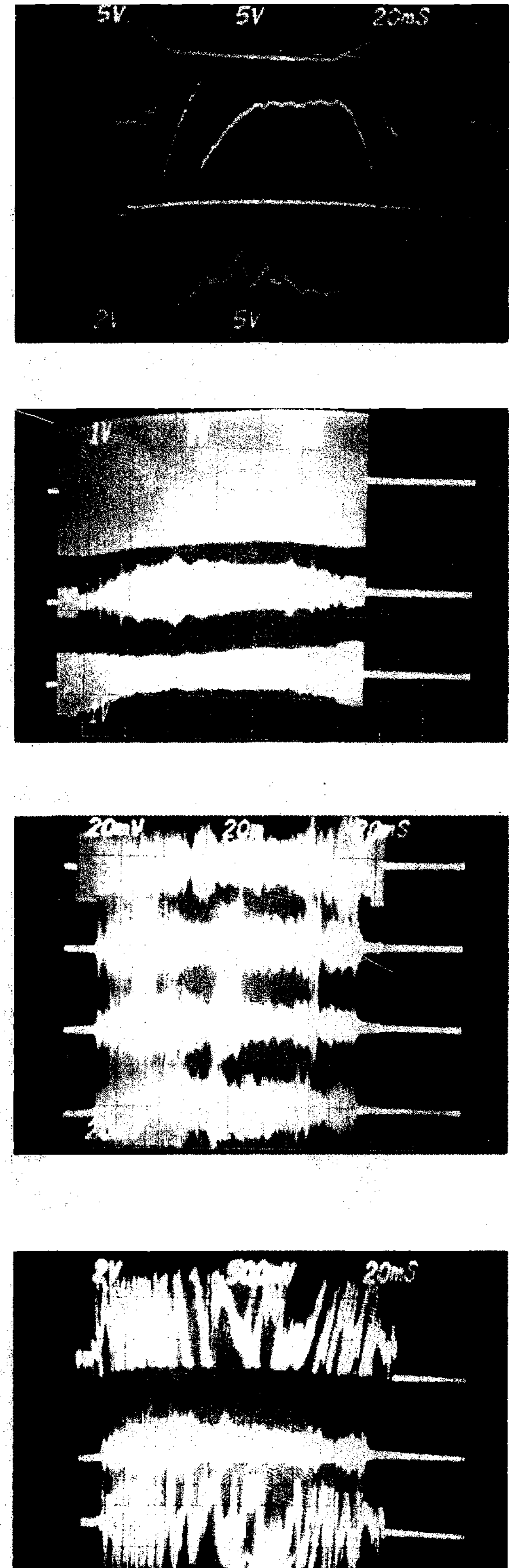

I_p

n_e

t

R_R

V_F

V_R

I_a

P 2

P 70

P 71

P 72

osc./72

5/72

Figure 8

Resonant Layer on Low Field Side

B10, P18, S55
2/13/80

Hydrogen
183.5 MHz
I_B = 85.8 KA
3 Ω at 2 fringes

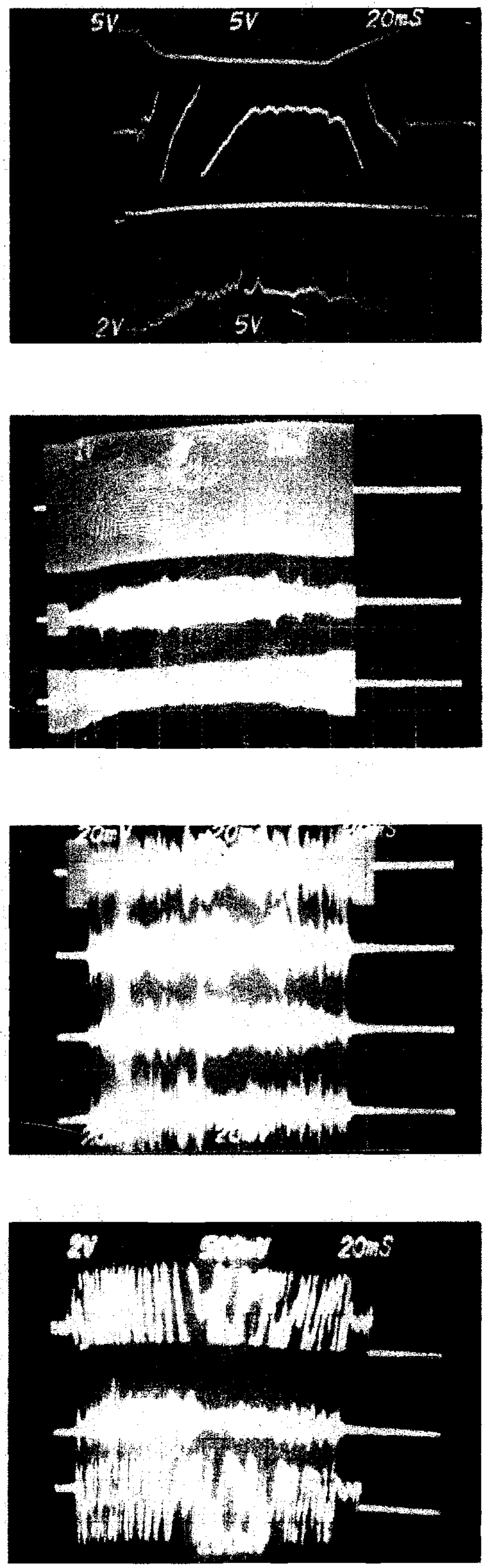

Ip
n_e
t
R_R

V_F
V_R
I_a

P 2
P 70
P 71
P 72

osc./72

5/72

Figure 9.

Radiation Resistance at 183.5 MHz with D_2 Fill He^4 Pulsed

B9, P41, S6

65.2 Ka
1.6 Ω at 2 fringes

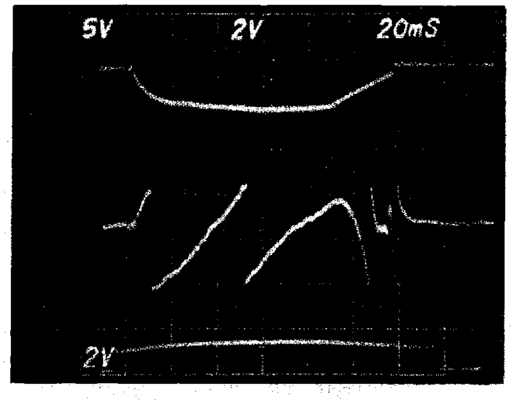

I_p

n_e

t

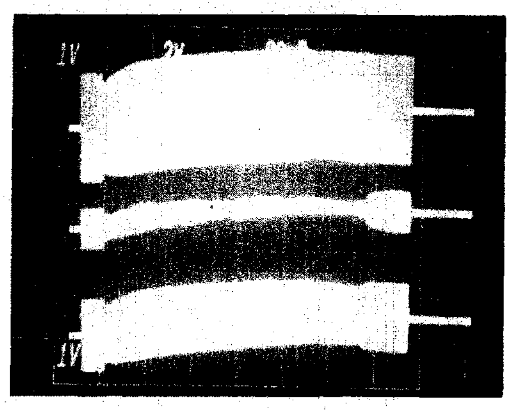

V_F

V_R

I_a

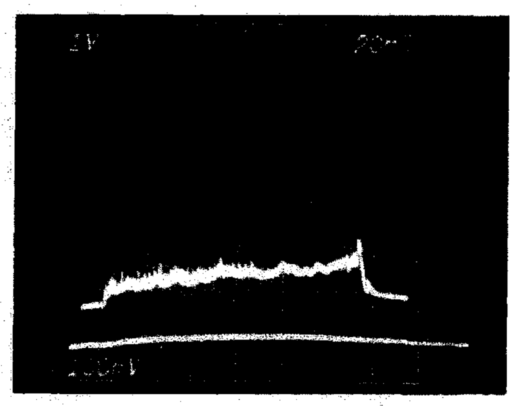

R_R

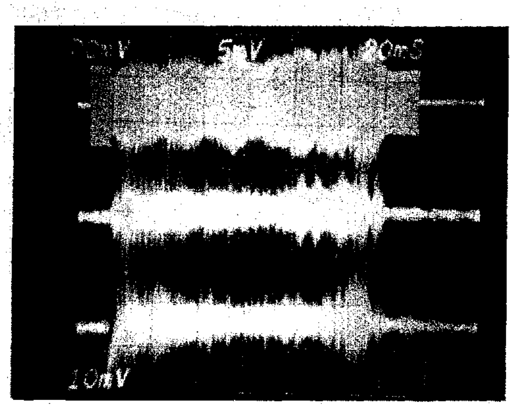

Near-field 2

Limiter 67

HCN Top 68

Figure 10

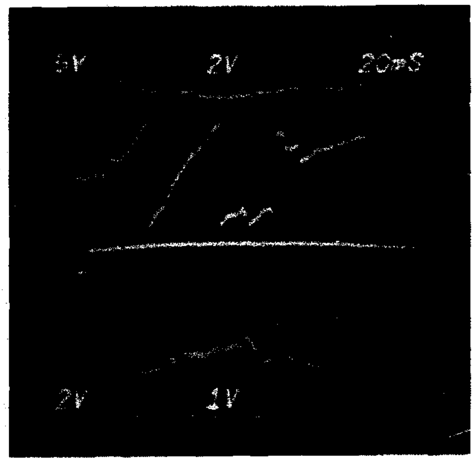

I_p

n_e

t

R_R

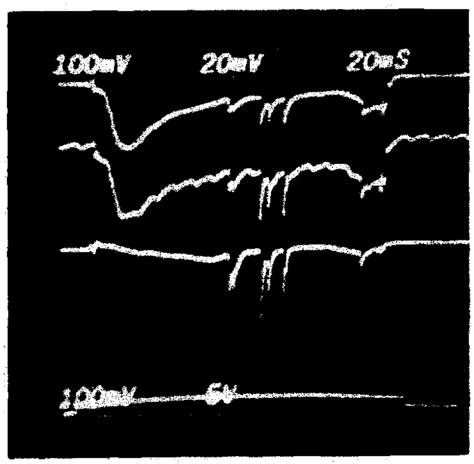

H_α

L_t

pin

t

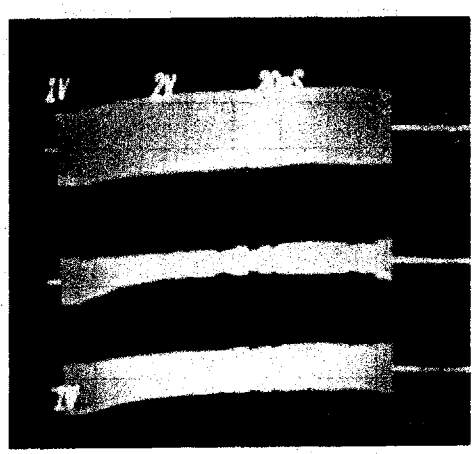

V_F

V_R

I_a

Figure 11

Effect of Disruptions on H_α, total light and R_R

B9, P71, S50

2/10/80 D_2, 183 MHz

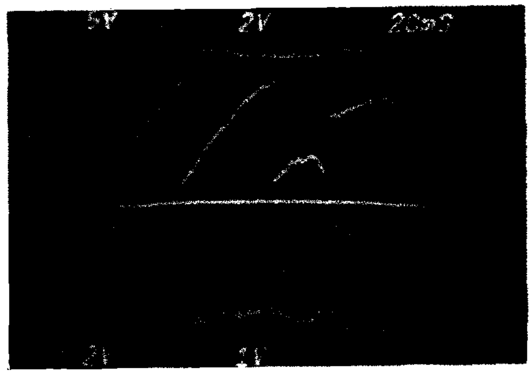

I_p

n_e

t

R_R

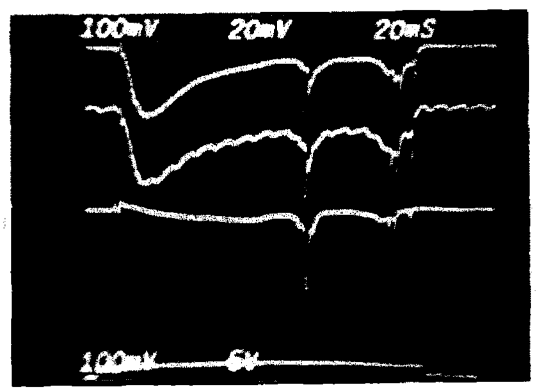

H_α

Total Light

Arc Det

t

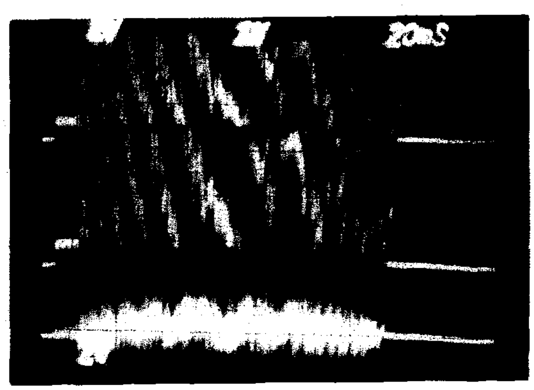

OSC./68

OSC./68

2/5

Figure 12

II-2.5. Wave coupling experiments

Aside from the carefully controlled A_1, A_2 and A_4 antenna coupling experiments, many other simple preliminary measurements were also performed. Energizing only half of the antenna produced between half and a quarter of the original R_R, in rough agreement with IV-1.3, IV-6.5, and IV-7.1. R_R also seemed independent of phasing, further supporting IV-6.5.

It was most unfortunate that $R_R \propto d^2$ scaling (center conductor to wall distance) was not proven (a + d remained constant), but the antenna was kept as close as possible to the plasma to maximize coupling (both the A_1 Faraday shield and the A_2 side limiters showed some minor plasma erosion). The Faraday shield did not affect coupling, as A_2 and A_4 proved to be almost identical in all respects (slightly lower R_R as expected from bench tests III-2.5.).

Figure 1 shows capacitive probe (III-3.2.) coupling at high density and 180 MHz. The front of the 1.2 inch diameter molybdenum block was about 3/4 inch from the chamber wall. Note how the probe impedence was almost exactly 50 Ω without any matching network, in plausible agreement with Section III-3.2.

$$(1) \quad Z_p = \frac{V_F + V_R}{V_F - V_R} 50\ \Omega \simeq R_R$$

From shot to shot during a single run, it was consistently noted that, for a given power (≃10 watts), the capacitive probe and the A_2 antenna produced roughly equivalent probe signals around the torus. Although very easily performed, radial probe scans were not done because the probe had to be removed for the new $k_{\parallel}$ array (the first array was destroyed by electron runaways). Note the discrete eigenmode structure of the probe signal at extremely low density after the plasma shot. These afterglow effects were never observed with A_1, A_2 or A_4 (probe singals are 50 msec/div).

The main tokamak limiter (Figure III-3.2.(13)) was also used as a transmitting antenna and receiving probe. Although the RF connection was very inductive, the limiter provided a reasonably good match. Crudely assuming $E_r \approx E_\theta$, and monitoring the received voltage on the limiter, produced roughly consistent results with magnetic probe signals and R_R (II-2.2).

Capacitive Probe Measurements at 200 MHz

S31, B19, P18
D_2, 200 MHz

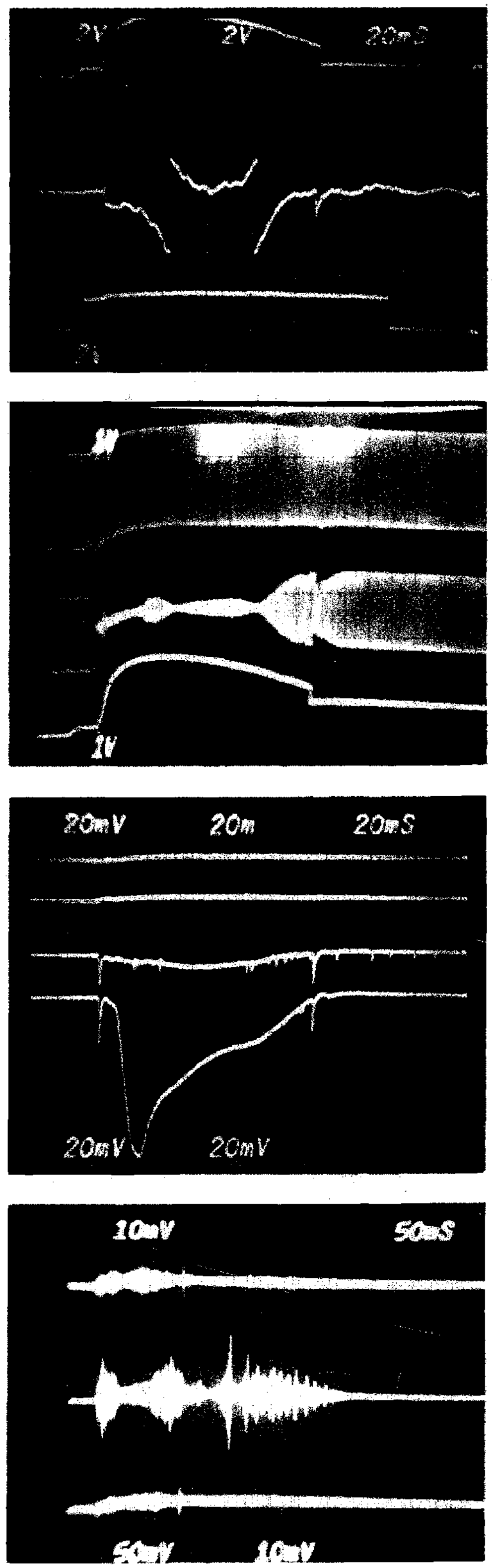

I_p

n_e

t (not used)

V_F

V_R

I_p

Light

Magnetic
Probes

Figure 1

II-3. Medium Power Heating Experiments

II-3.1. High density regime

Most of the medium power heating experiments were done in the $2\omega_{cH}$ and $4\omega_{cD}$ regimes, for either pure or mixed (50/50%) hydrogen or deuterium plasmas at $2.5 \times 10^{14}/cm^3$ and 65 kG.

Experimental conditions (disruptive plasmas and lack of diagnostics and machine time) were not the most favorable, and most of the following results were obtained with the A_2 unshielded antenna. Figures 1 and 2 show typical pure hydrogen shots with 40 kW. Note how the plasma current and density remain unchanged (loop voltage and plasma position also remain constant), while the plasma edge light (H_α and total light) at the antenna increases by 30%. Figures 3-5 show the fast neutral fluxes for the shots shown in Figures 1 and 2. Figure 5 shows the fast neutral spectra for the third RF pulse of Figures 1 and 3, which has an "effective temperature" of about 300 eV above background (the spectrometer was uncalibrated in these runs). Unfortunately, the flux rise and fall time is less than 100 μsec, and is not indicative of bulk heating. Figures 1 to 5 are for two consecutive shots of the same run, and show the close repeatability of the RF effects on the plasma. From run to run, on the other hand, repeatability was not nearly as good, especially for the usual but inconsistent soft X-ray increase (sometimes only center, then edge also, and ranging from 0 to 50%). Almost identical results were also obtained with pure deuterium, but with a very repeatable slight dip in the neutron rate (Figure II-2.3.(6)). Edge Langmuir probe diagnostics showed no measurable effect on either the plasma edge temperature or density (II-3.3).

Figures 6 to 17 show the basic results of a carefully executed field scan between 50 and 80 kG, for a 50% H_2 and 50% D_2 plasma at 200 MHz, 55 kW and with the A_2 antenna. Figures 6 and 7 show the high (5 keV) and low (500 eV) energy components of the deuterium fast neturals versus magnetic field (resonant layer position). Note how the low energy component doubles independently of layer position, while the high energy component increases by an order of magnitude when the layer is at the plasma center. Figures 8 and 9 show similar results for the hydrogen spectra, except for a very large increase in both the low and high energy components when the resonant layer is at the low field side of the plasma in the antenna near-field. Figures 10 to 13 show the unreduced neutral fluxes, as well as the neutral spectras for the resonant layer at the plasma center.

Figures 14 to 17 show the radiation resistance and probe signals at the HCN bottom inside (high field side), bottom outside and top outside (Figure III.3.(1)). Radiation resistance is again (II-2.4) independent of layer position (within experimental repeatability), and probe signals are only weakly dependent (slight changes in plasma position could produce even greater differences). One could possibly argue that a slight dip in probe signal exists when the resonant layer is at the center and high field side of the plasma(at the particular probe position that is monitored).

To lowest order and for bulk heating, we can typically calculate

(1) $P_{OH} = IV \simeq 150\text{ kA} \times 2.0\text{ V} \simeq 300\text{ kW} \simeq 10\, P_{RF}$

(2) $t_{RF} \geqslant \tau_E \simeq 10\text{ msec}$

(3) $T_{RF} \simeq T_{OH}\left[1 + \frac{P_{RF}}{P_{OH}}\right] \simeq 770$ eV

and the high energy (5 keV) neutral flux is

(4) $J \;\alpha\; e^{-E/T}$

(5) $\frac{J_{RF}}{J_{OH}} = e^{E\left(\frac{1}{T_{OH}} - \frac{1}{T_{RF}}\right)} \simeq 1.9$

and we can unequivocally conclude that no such bulk temperature increase was observed. (Of course, one might argue that it is not clear that the spectra is itself representative of the plasma bulk temperature).

In the minority heating regime, we can rewrite (3) (again to zeroth order) for the minority species (5% H_2)

(6) $T_{RF} \simeq T_{OH}\;\; 1 + \frac{n_D}{n_H}\frac{P_{RF}}{P_{OH}}\Big] \simeq 3\; T_{OH}$

(7) $\frac{J_{RF}}{J_{OH}} \simeq 117$

Although medium power 90 MHz heating experiments were only preliminary (R_R is 4 times smaller, and charge exchange was only available late in the experiment), no such increases in the minority tail were observed in any form (even 1 kW could produce $\Delta J \simeq J$). From available evidence (n_e, I_p, CX, etc.), 90 MHz unfortunately behaved much like 200 MHz at high density.

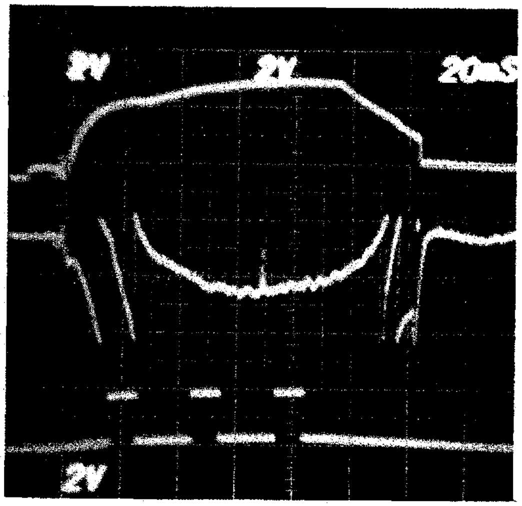

I_p

n_e

t

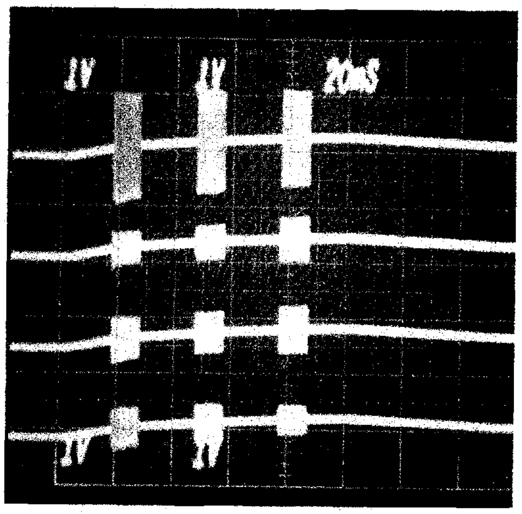

V_F

V_R

I_T

I_B

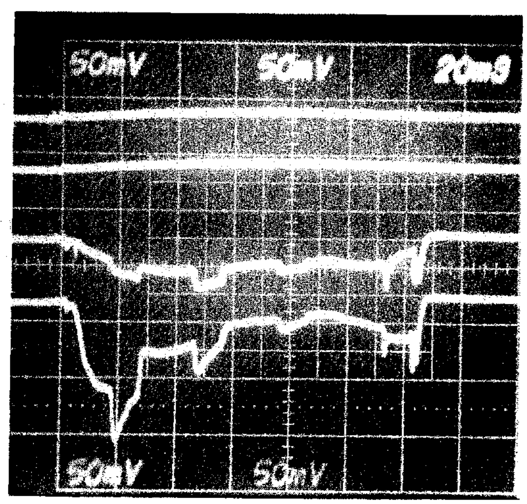

L_T

L_B

L_a

H_α

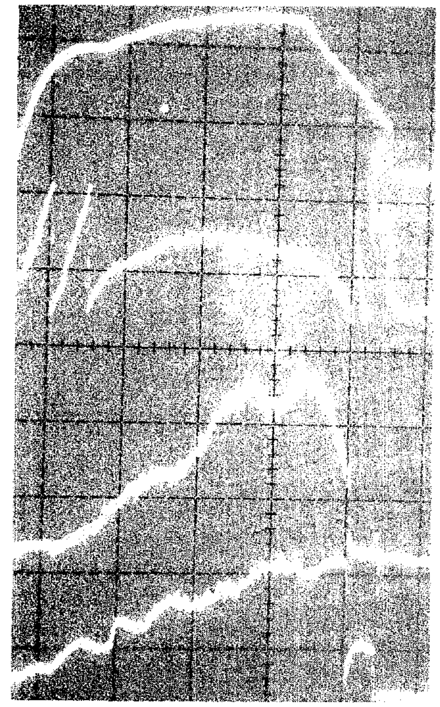

I_p

n_e

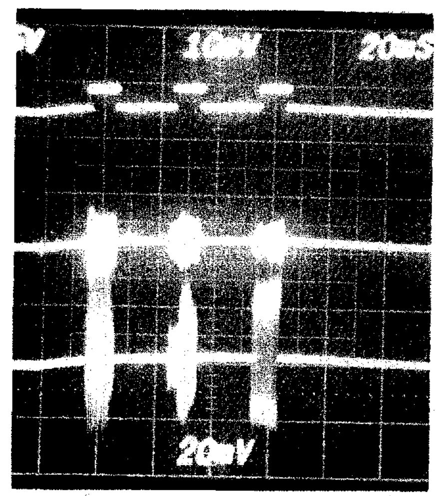

t

69 HCN top

68 HCN Bot

Medium Power Shot 42

S42, P28, B15

H_2, 67 kA, 200 MHz

Figure 1

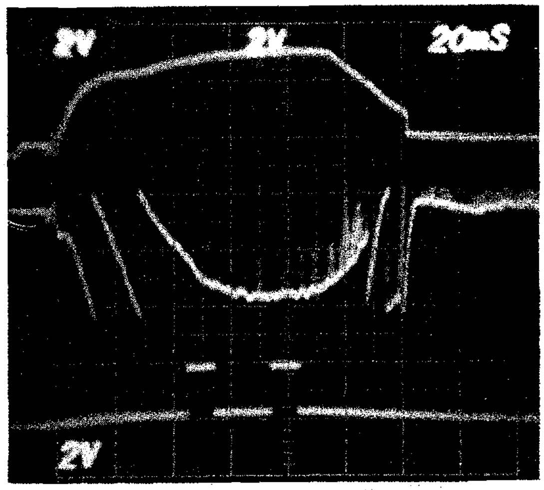

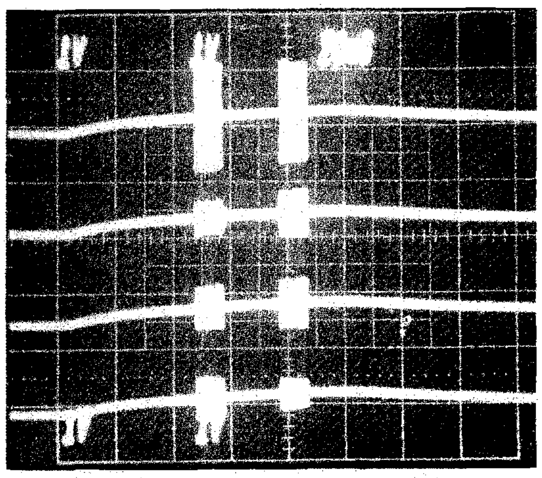

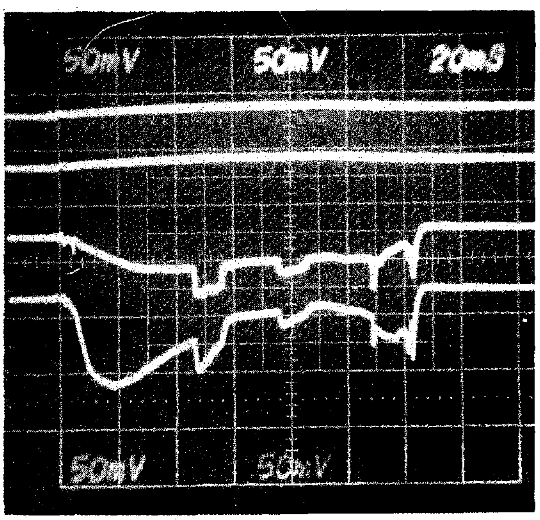

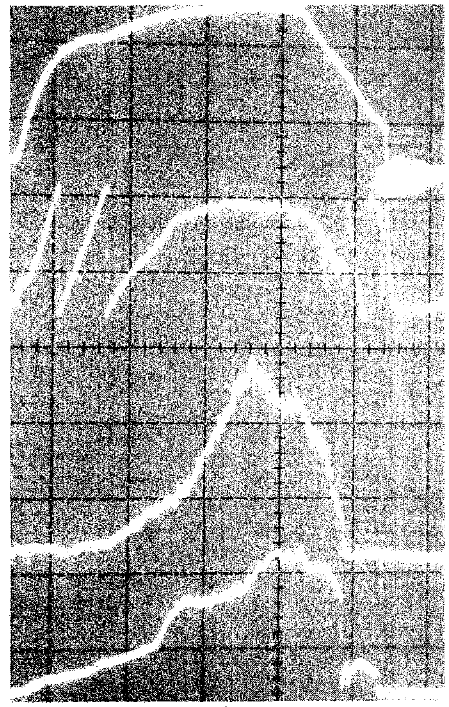

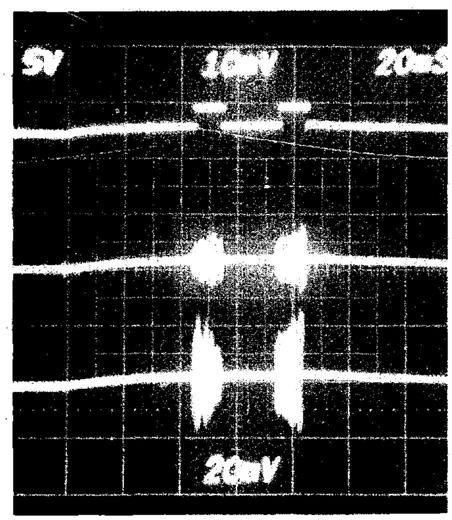

Medium Power Shot 43

S43, P29, B15

H_2, 67 kA, 200 MHz

Figure 2

Hydrogen

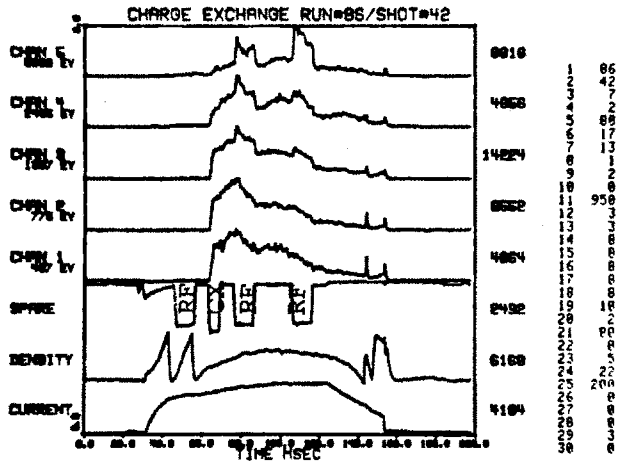

Figure 3

Hydrogen

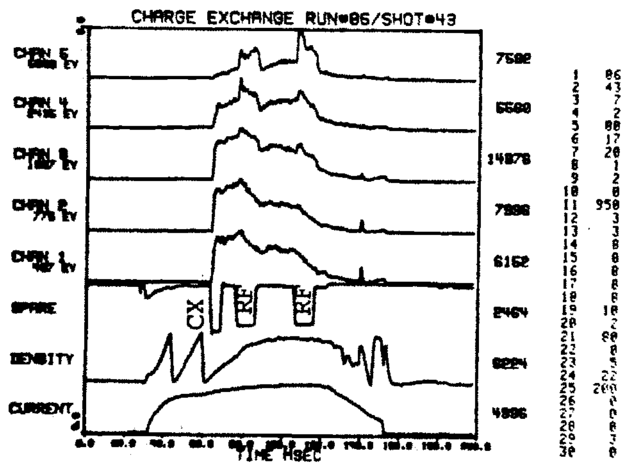

Figure 4

Neutral spectra at third RF pulse for shot 42

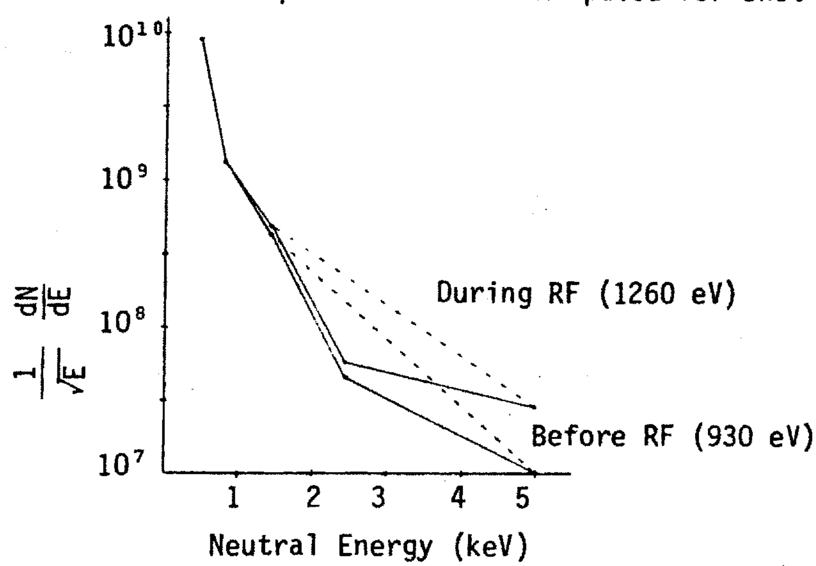

Figure 5

DEUTERIUM NEUTRALS VS TOROIDAL FIELD

5Kev

10/31/80
B18, pp46-51
S43-53

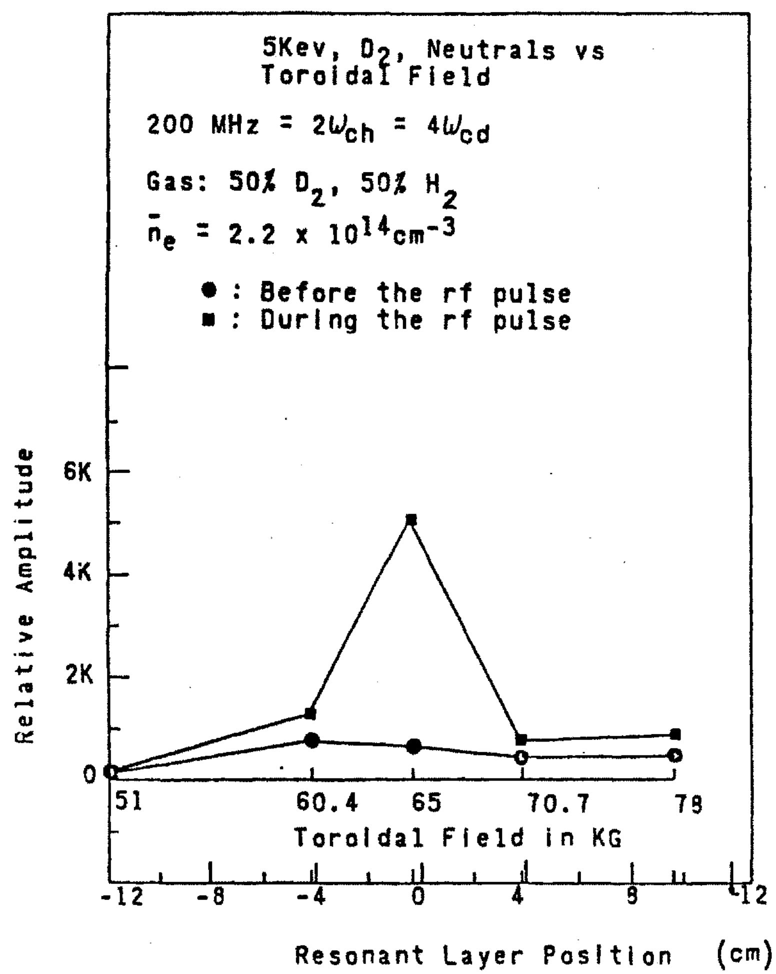

Figure 6

487ev

10/31/80
B18 pp 46-5
S43-53

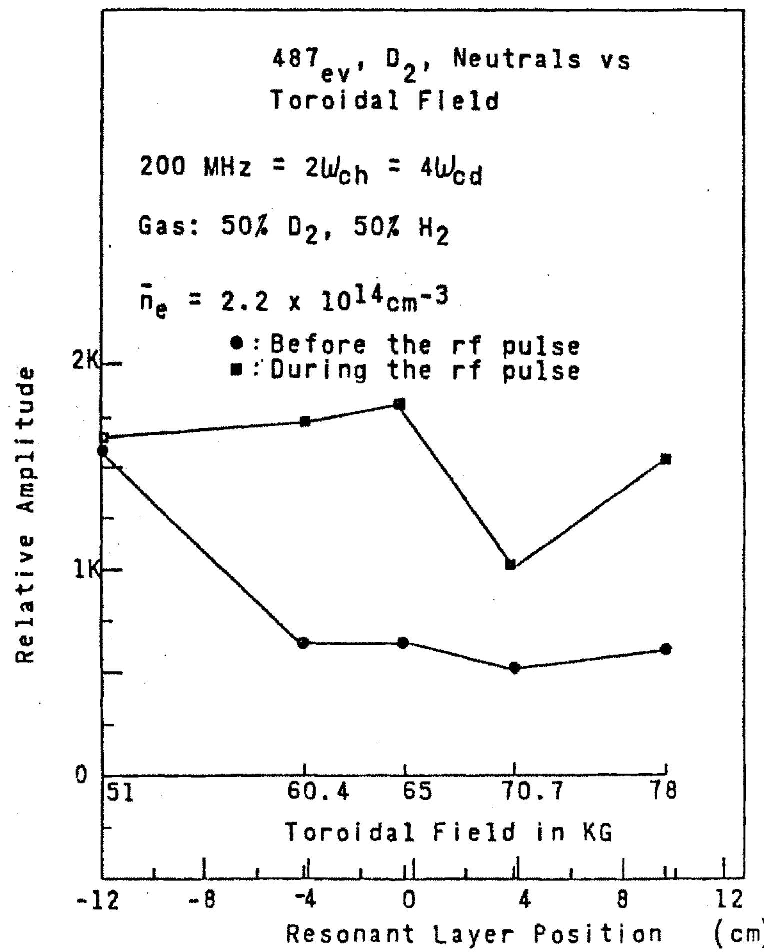

Figure 7

HYDROGEN NEUTRALS VS TOROIDAL FIELD

5Kev

10/31/80
B18, pp46-51,
S43-53

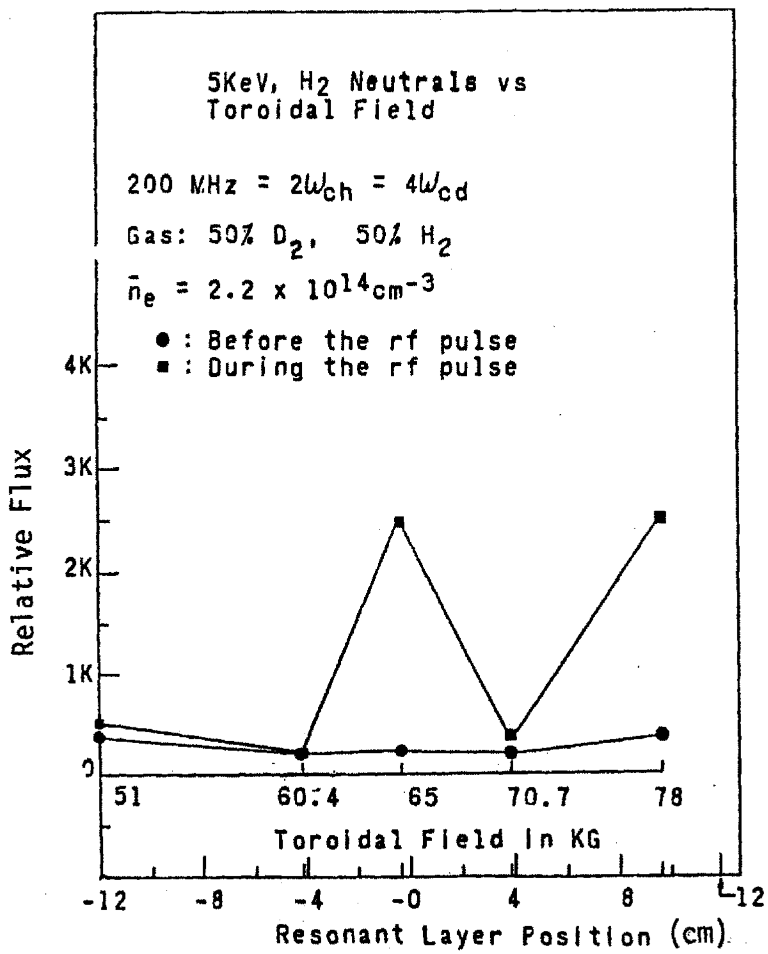

Figure 8

487ev

10/31/80
B18, pp46-51
S43-53

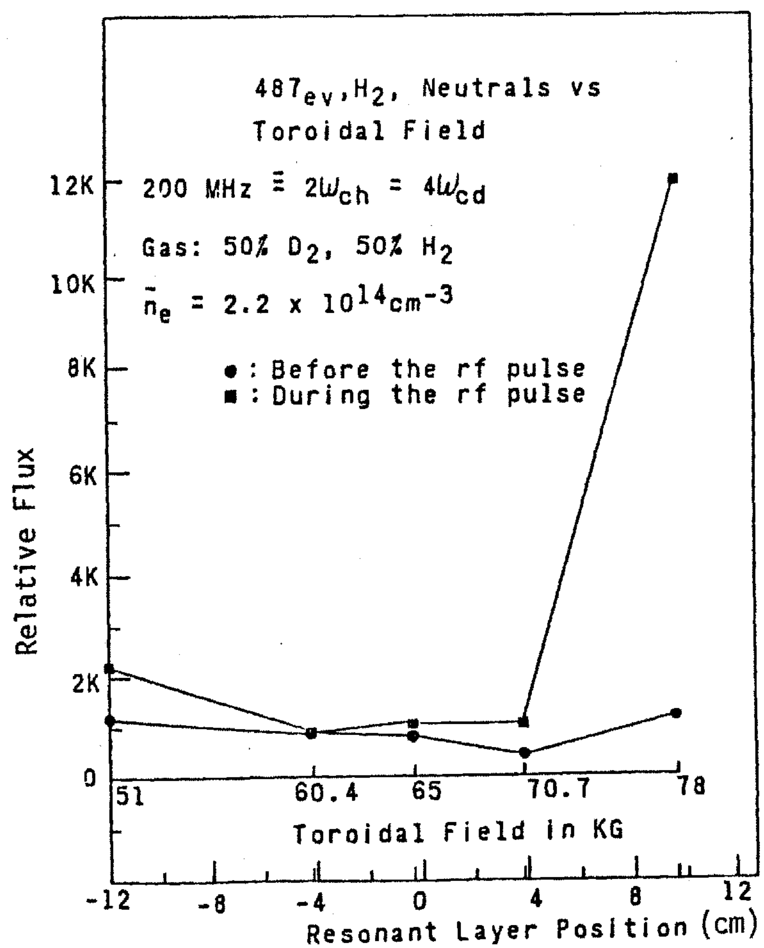

Figure 9

FAST NEUTRALS SPECTRA

DEUTERIUM

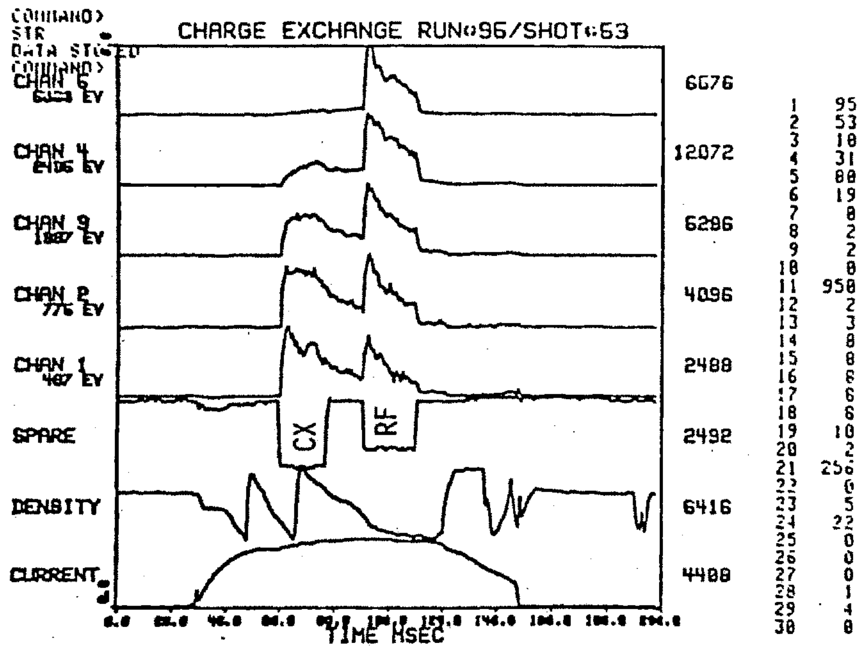

Figure 10

HYDROGEN

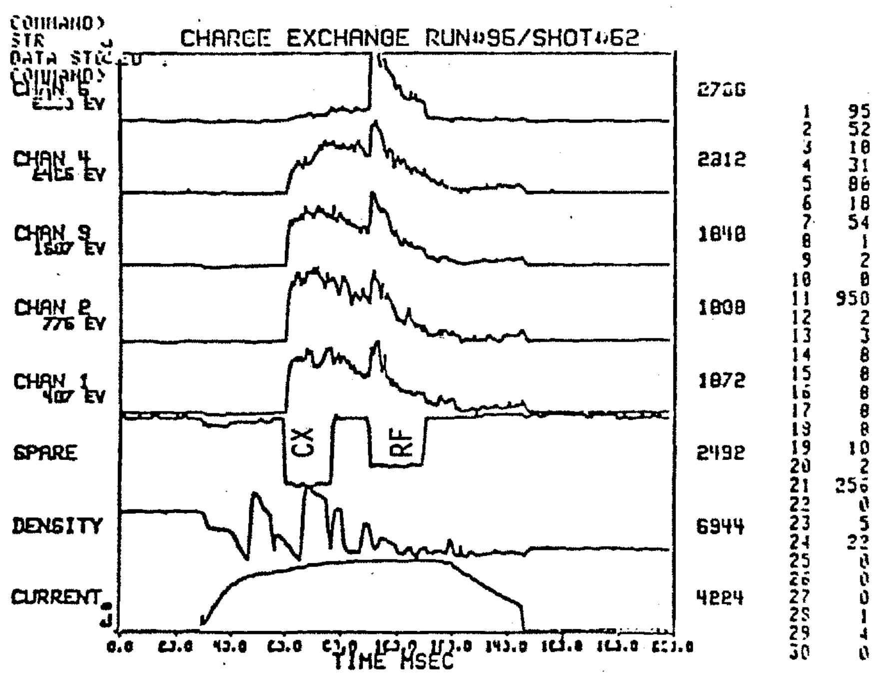

Figure 11

Deuterium

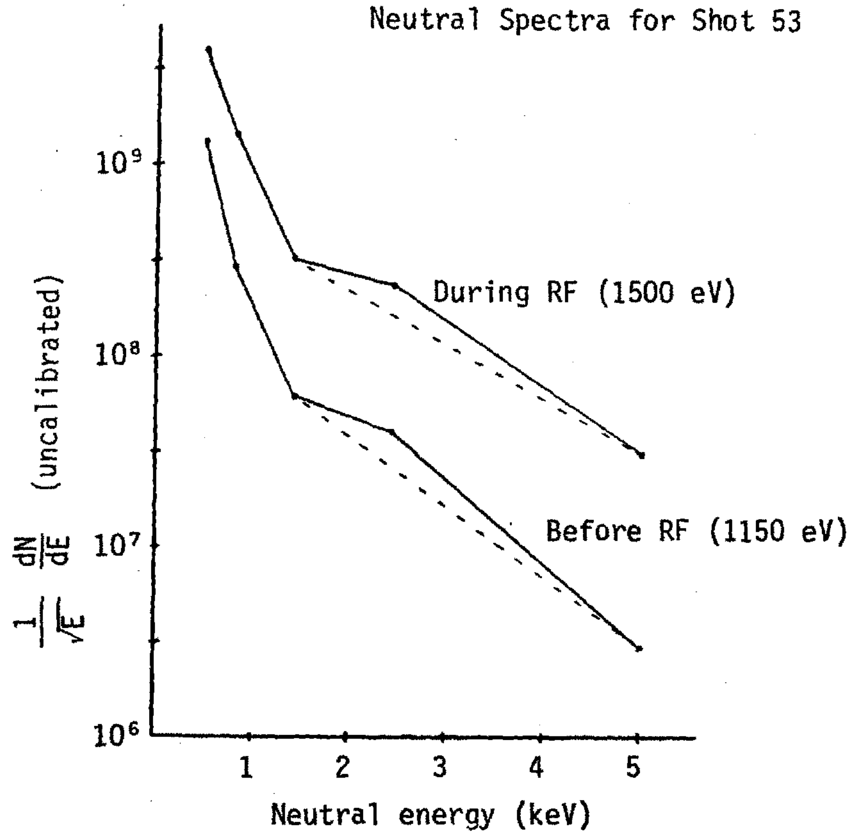

Figure 12

Hydrogen

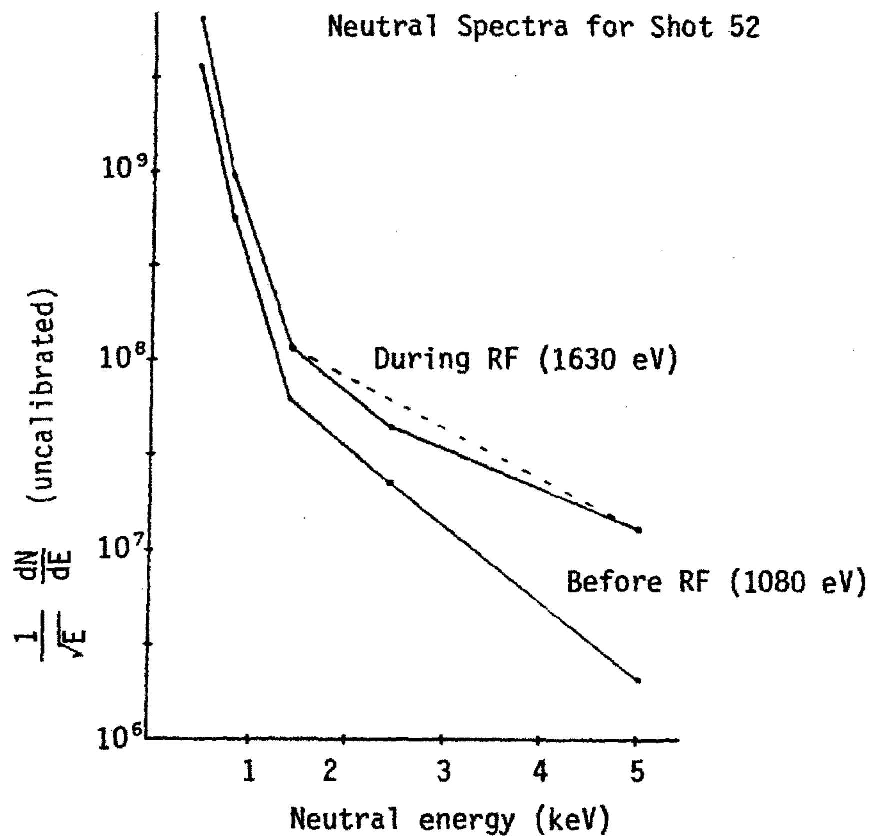

Figure 13

RADIATION RESISTANCE & PROBE SIGNALS VS TOROIDAL FIELD

B18, pp46-51
S43-53

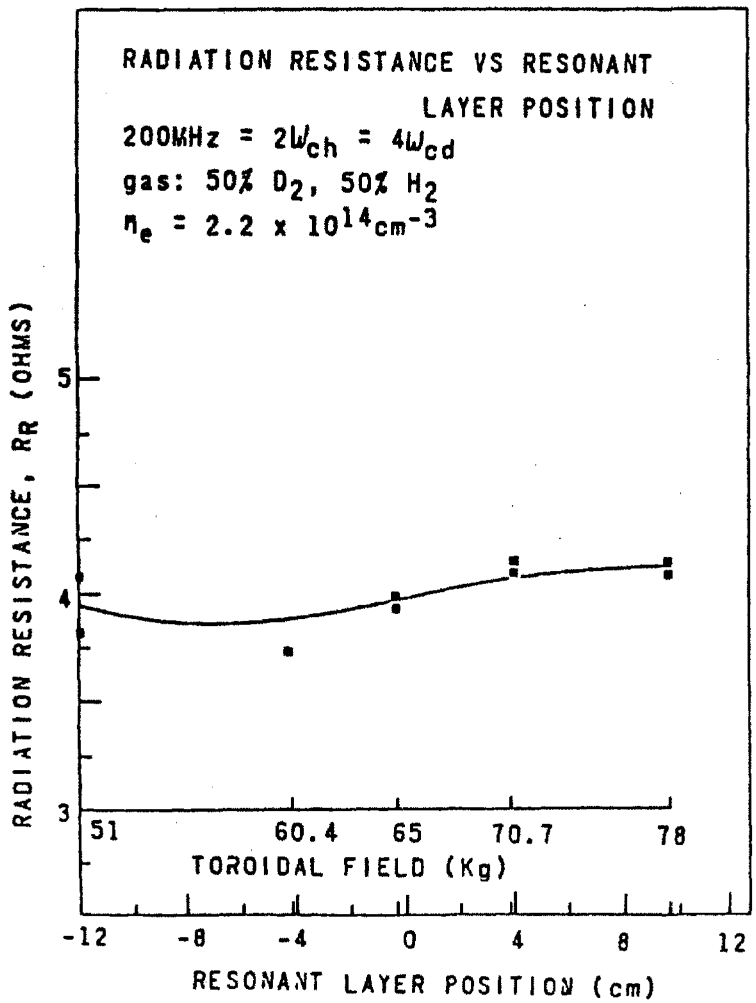

Figure 14

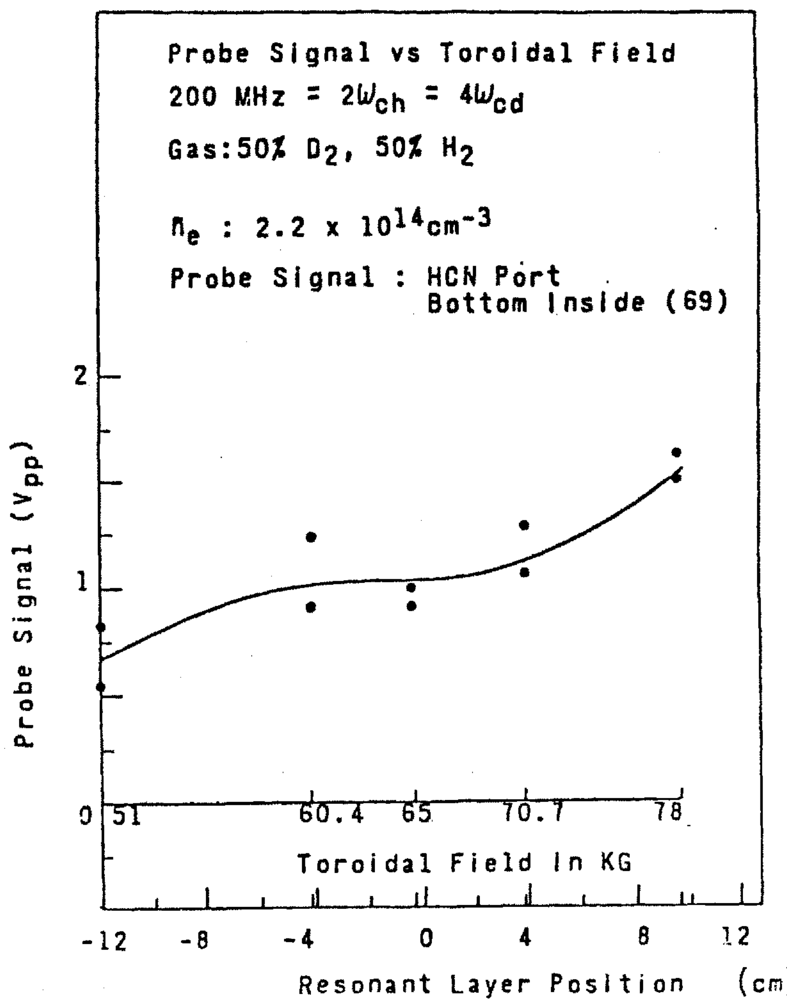

Figure 15

PROBE SIGNALS VS TOROIDAL FIELD

top outside

10/31/80
B18, pp46-51
S43-53

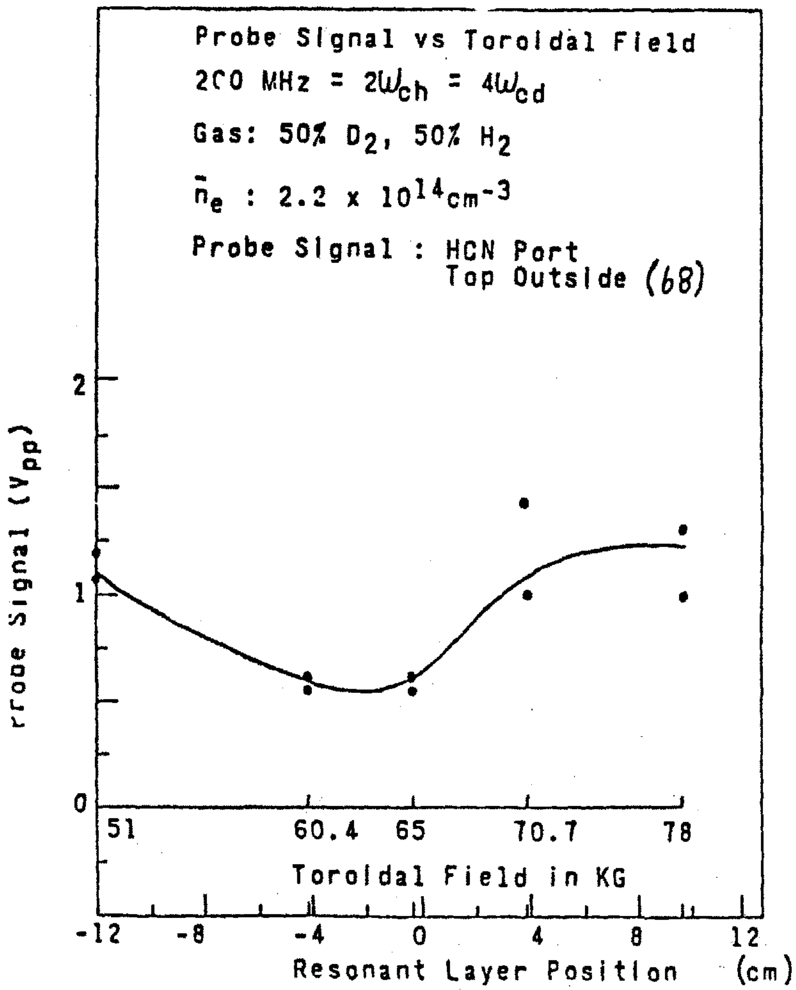

Figure 16

bottom outside

10/31/80
B18, pp46-51
S43-53

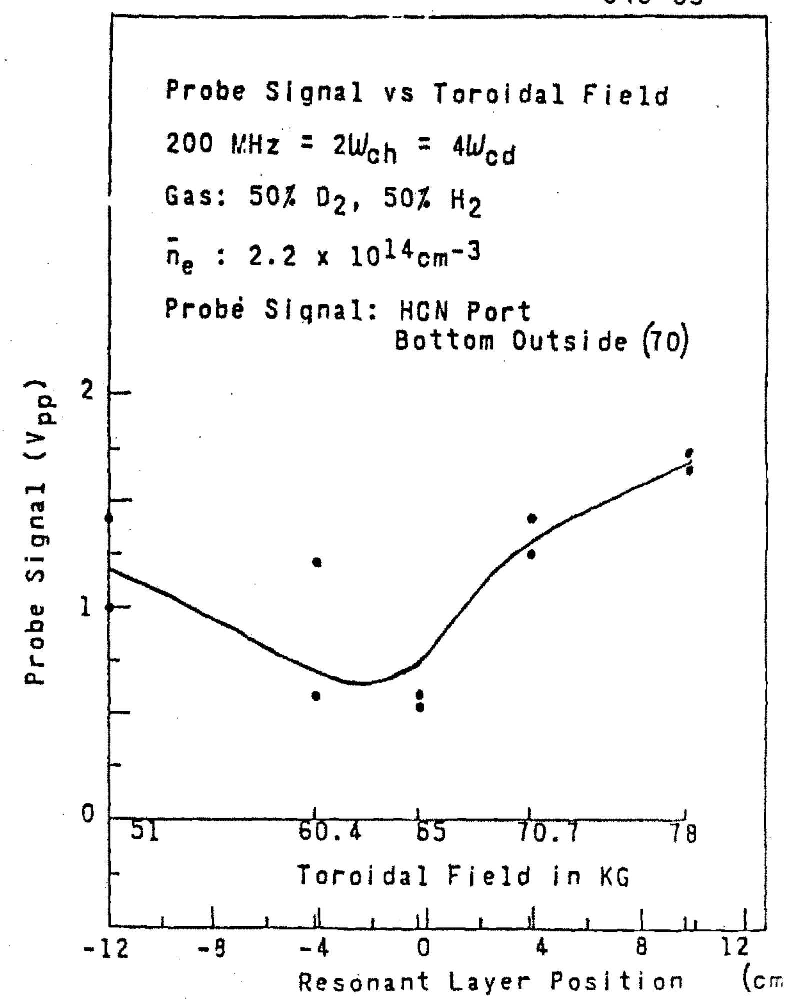

Figure 17

II-3.2. Low density regime

After the difficulty in heating high density plasmas was clearly observed, some very preliminary heating experiments were performed at low density ($5 \times 10^{13}/cm^3$ is still considered high density for other tokamaks). Note that $R_R \propto n_e\omega^2$ scaling is very unfavorable for low density coupling, expecially at 90 MHz where $R_R < R_{losses}$. Fortunately, fewer particles need to be heated, but on the other hand, P_{OH} remains approximately the same.

Figures (1) and (2) show the dramatic neutral flux increase for a medium power $5 \times 10^{13}/cm^3$, pure hydrogen and 200 MHz shot with the A_2 antenna. Neutral flux up to 10 keV with tail temperature 250 eV above background, were observed in this regime. Early in the discharge, the apparent flux decay time seemed to be due to the density increase since pulsing 5 msec later gave only a very small increase. However, similar pulses were also done at the density maximum of low density shots ($< 5 \times 10^{13}/cm^3$) with similar energetic neutral tails but without the decay time.

LOW DENSITY REGIME

HYDROGEN

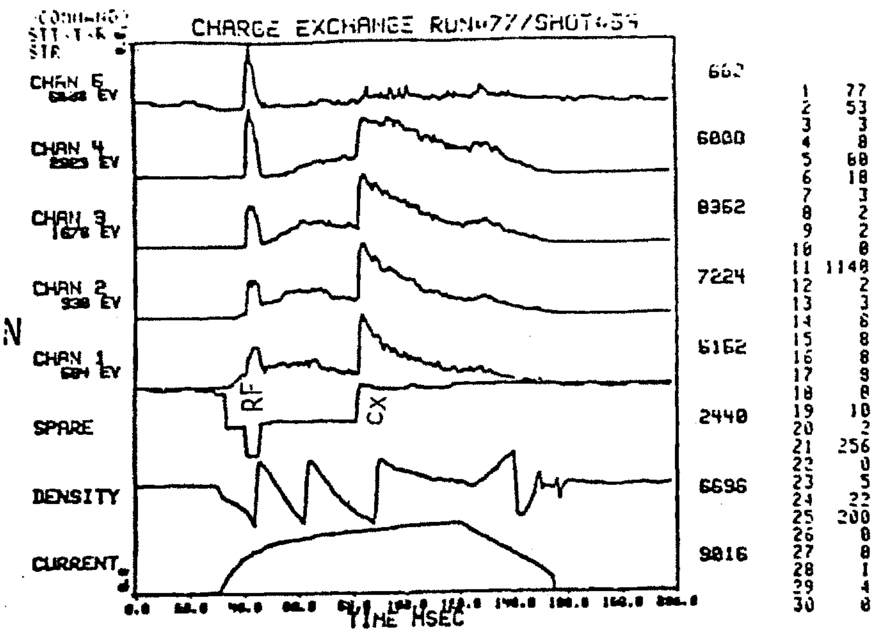

Figure 1

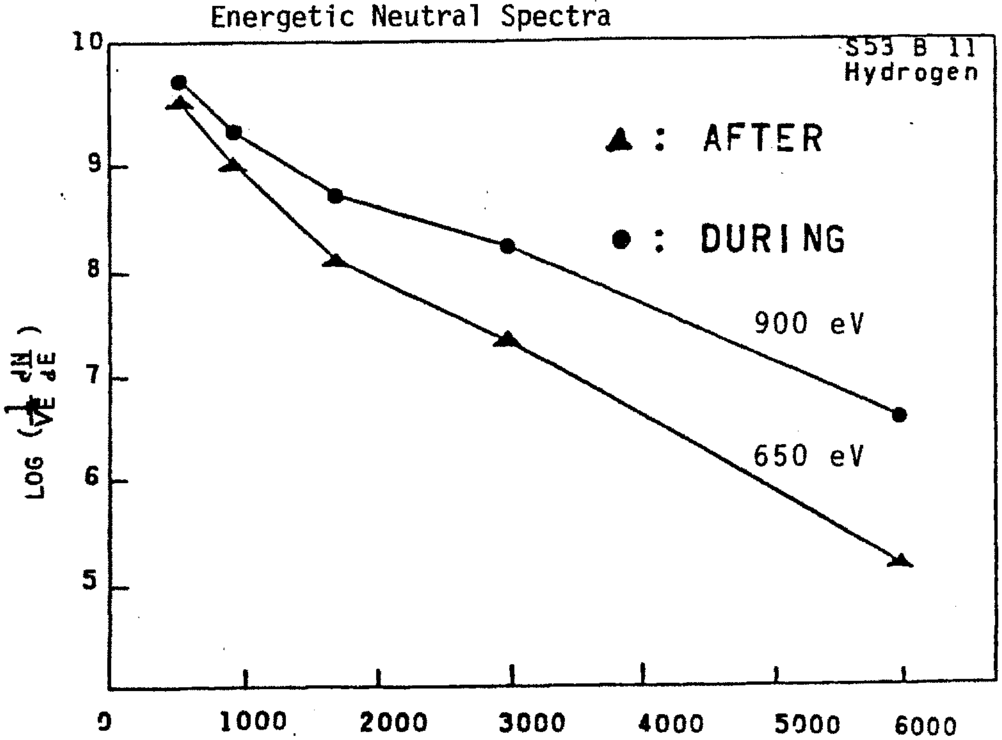

Figure 2

Neutral Energy (eV)

II-3.3. Impurities and radiation measurements

Figure 1 shows a typical disruptive high density plasma shot with mixed hydrogen and deuterium. Note how the basic parameters (I_p, n_e, I_a, V_{probe}, H_α, pin light) are well behaved and consistent over all three 40 kW pulses. The soft X-rays and thermonuclear neutrons, on the other hand, show a clear increase and flattening, respectively, over all three pulses (this effect was reproduced over several shots).

Figure 2 shows a similar plasma shot, where we note that the top electrical break broke down (L_T = 250 mV, I_T = 0) without affecting the plasma current and density, but, nevertheless, causing the usual increase in H_α, antenna light and fast neutral flux.

Figure 3 shows a similar shot where the current from an edge Langmuir probe (HCN top) is also displayed. No significant change in the edge temperature or density could be measured. Figures 4 and 5 show a reduced edge density and temperature radial scan for a typical high density shot. Considerable variation was observed from shot to shot, and even more from run to run, as expected from the steep density and temperature profile and the uncontrolled plasma position.

Figure 6 shows the extreme ultra violet spectrum (550 to 1600 Å) before and during a particularly bad RF pulse (typically there is no discernable increase in radiation). This small increase in radiation is most likely produced by light impurities (O, N, C) at the plasma edge ($r > 8$ cm), where $T_e < 40$ eV and $n_e < 10^{14}/\mathrm{cm}^3$, and also indicates no significant edge heating. The increase in central (and not edge) soft X - rays may be indicative of electron heating, but was not accompanied by any decrease in loop voltage or increase in electron cyclotron harmonic emission. Hard X-rays were never affected by the RF.

All previous measurements were done with molybdenum limiters. Surprisingly, completely different plasma behavior with RF was observed with a carbon limiter (although R_R and probe signal behaved the same). Returning to a different molybdenum limiter immediately reproduced the original results (so conditioning and exact limiter radius and geometry factors can be ruled out as the cause).

Figures 7 and 8 show the results of a dramatically affected (by RF) plasma shot, with a carbon limiter (although not very repeatable, no such behavior was ever encountered with a molybdenum limiter). Note how the electron density, central soft X-rays and total radiation (pyrometer) unambiguously increase with a long time constant during the medium power RF pulse. The Langmuir probe electron current was also greatly reduced, possibly indicating an increased plasma potential (ion saturation remained unchanged, III-3.4). Significant increases in the neutral tail were never observed either in this mode, as shown in Figure 7. Visual inspection of the antenna showed carbon deposits at high electric field points in the antenna, but not anywhere else near the antenna, which is far away from the limiter.

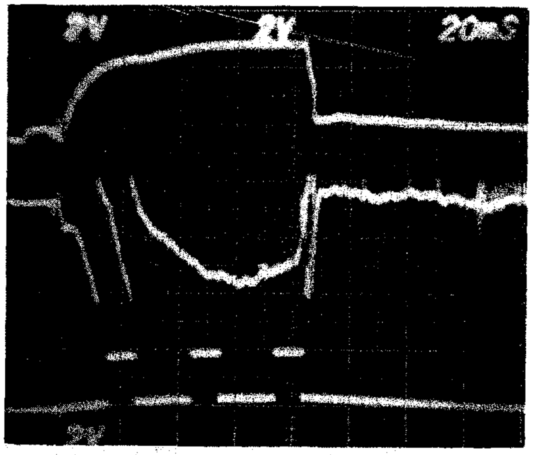

I_p

n_e

t

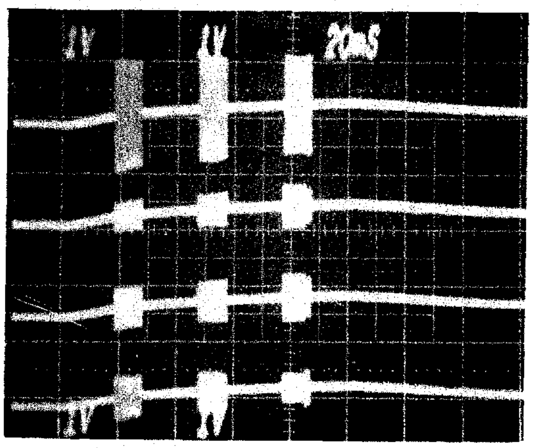

V_F

V_R

I_T

I_B

L_T

L_B

L_a

H_α

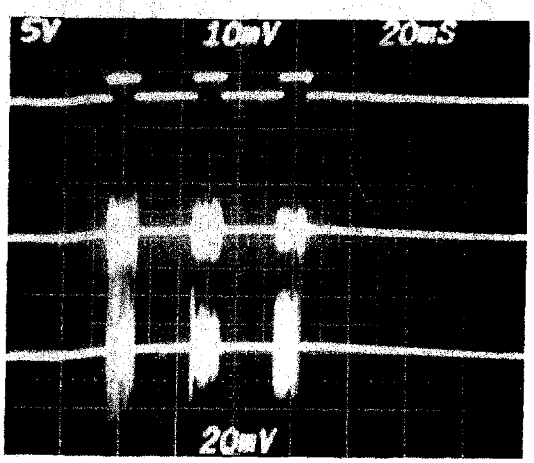

t

69 HCN
Bot

68 HCN
Top

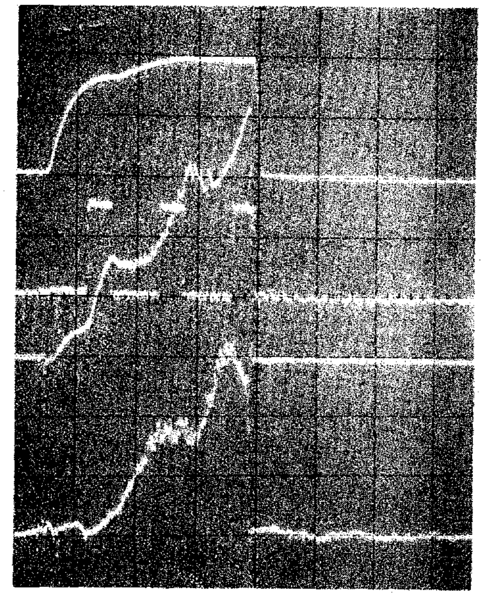

I_p

X-rays

neutrons

Hydrogen

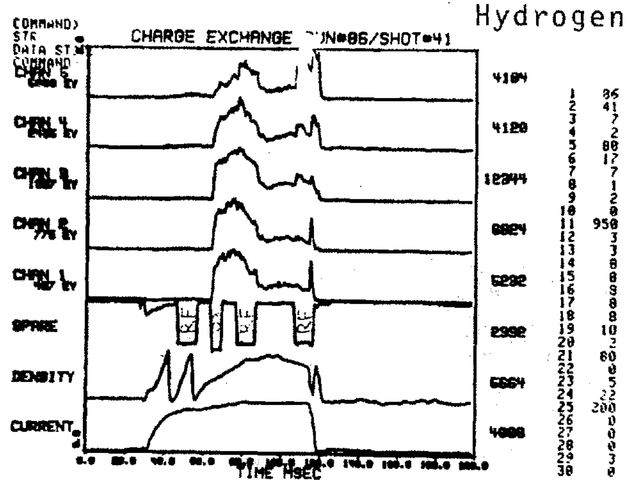

Disruptive Plasma

S41, P28, B15

D_2/H_2, 67 kA, 200 MHz

Figure 1

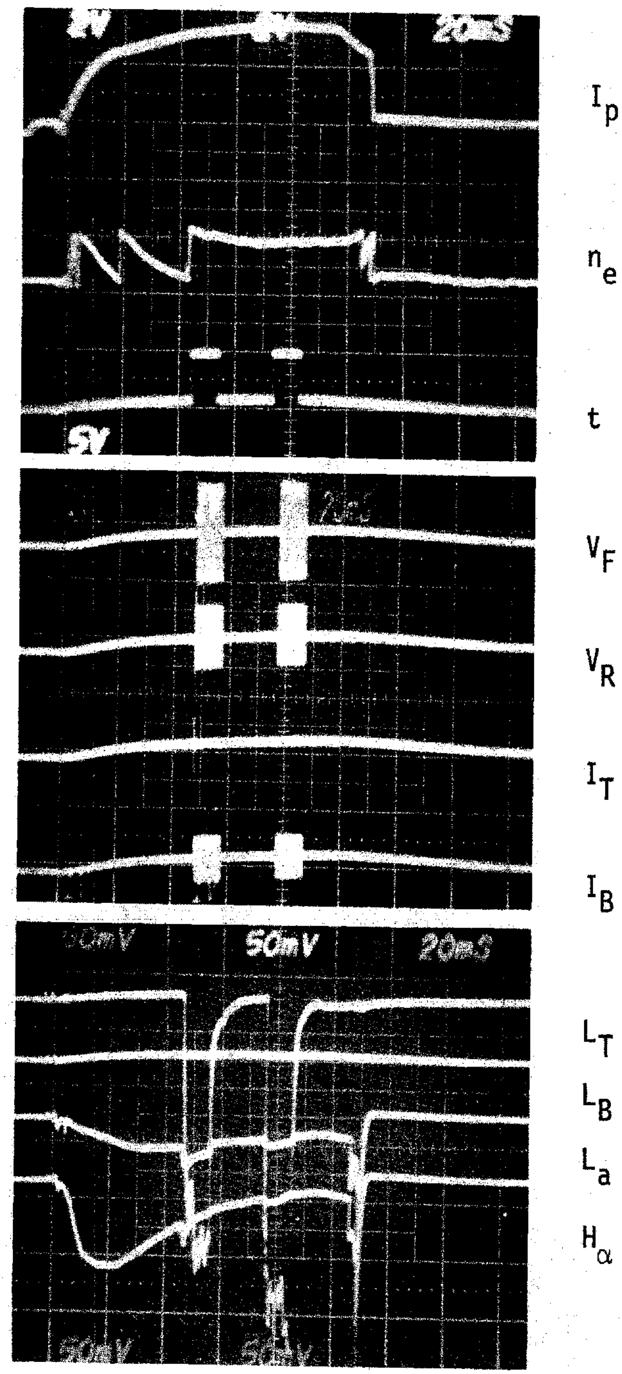

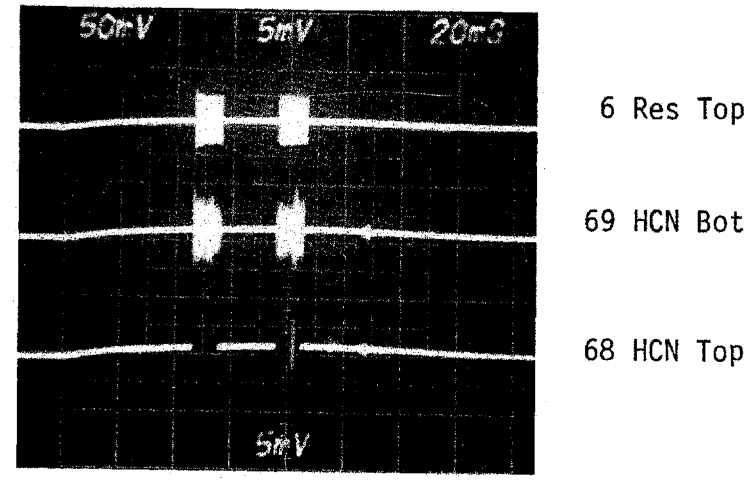

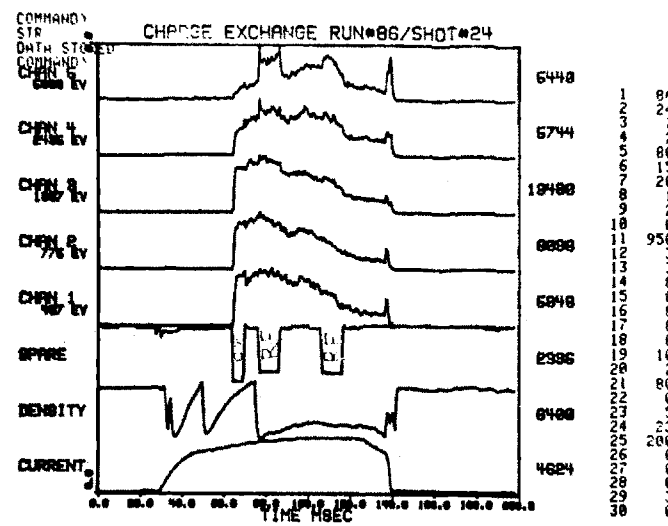

Breakdown in Top Coax

S24, P23, B15

H_2, 67 kA, 200 MHz

Figure 2

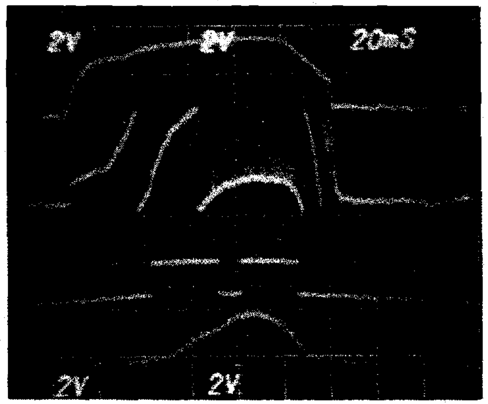

I_p

n_e

t

n

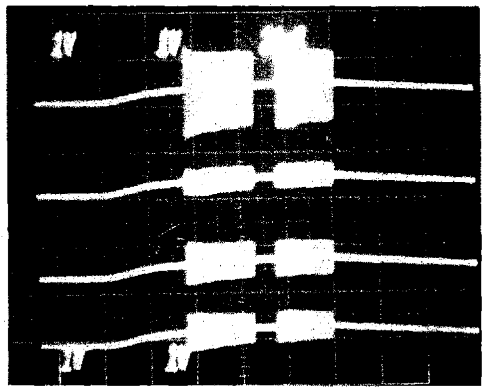

V_F

V_R

I_T

I_B

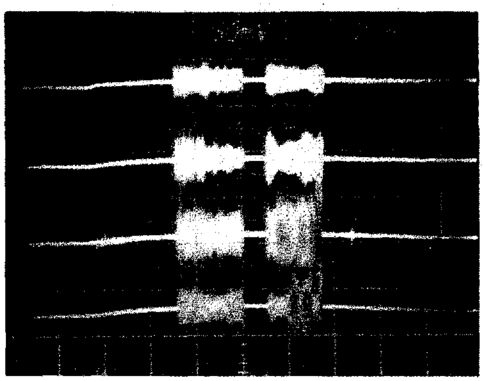

HCN

&

Limiter

Probes

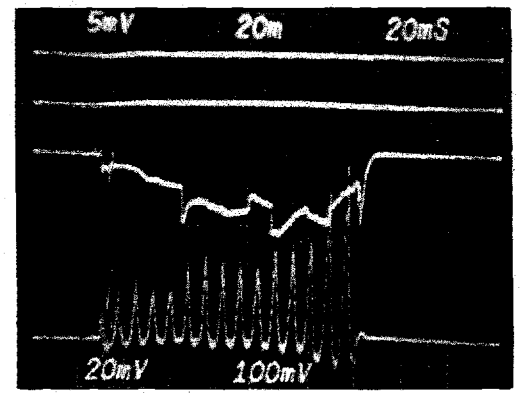

L_T

L_B

L_{pin}

I_L

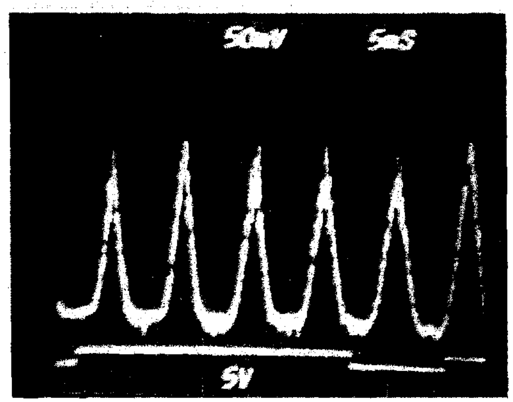

I_L

t

Typical Langmuir Probe Raw Data

Figure 3

50% H_2, 50% D_2, 200 MHz, 65.5 kA

S60, P15, B18

Edge Temperature and Density Profiles (Langmuir Probe)

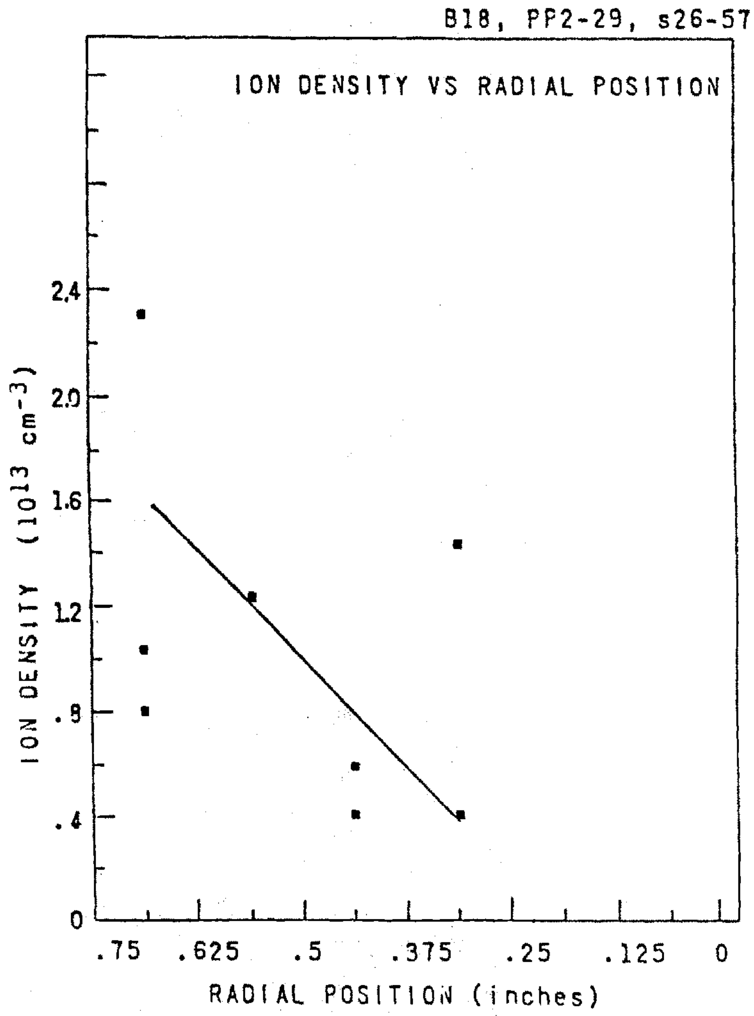

Figure 4

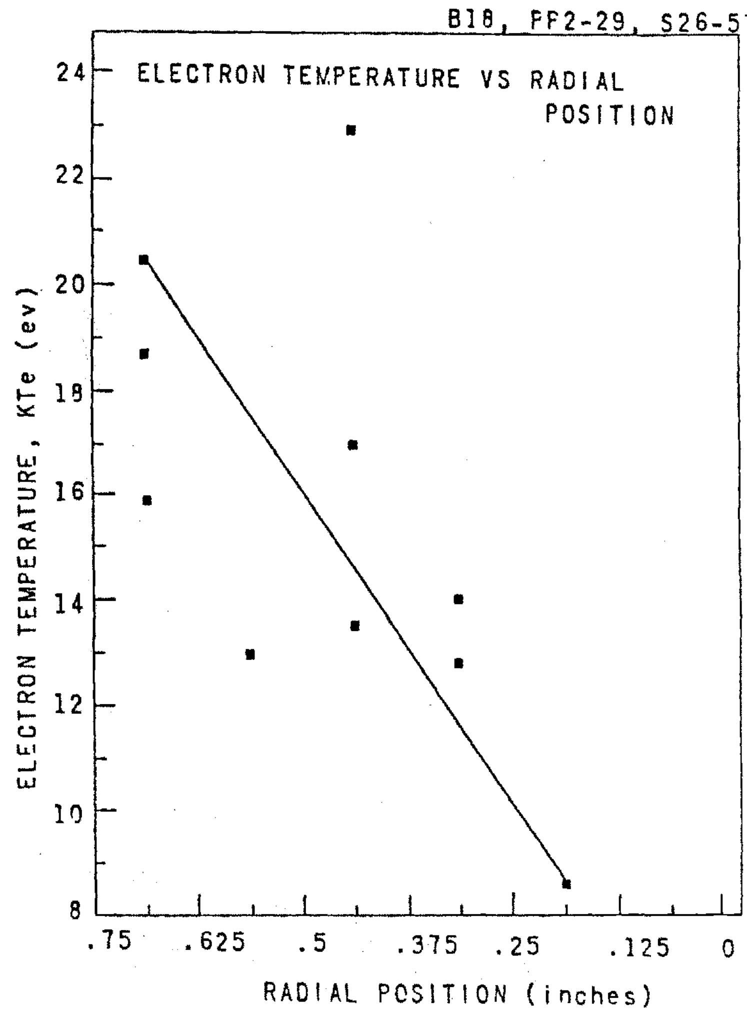

Figure 5

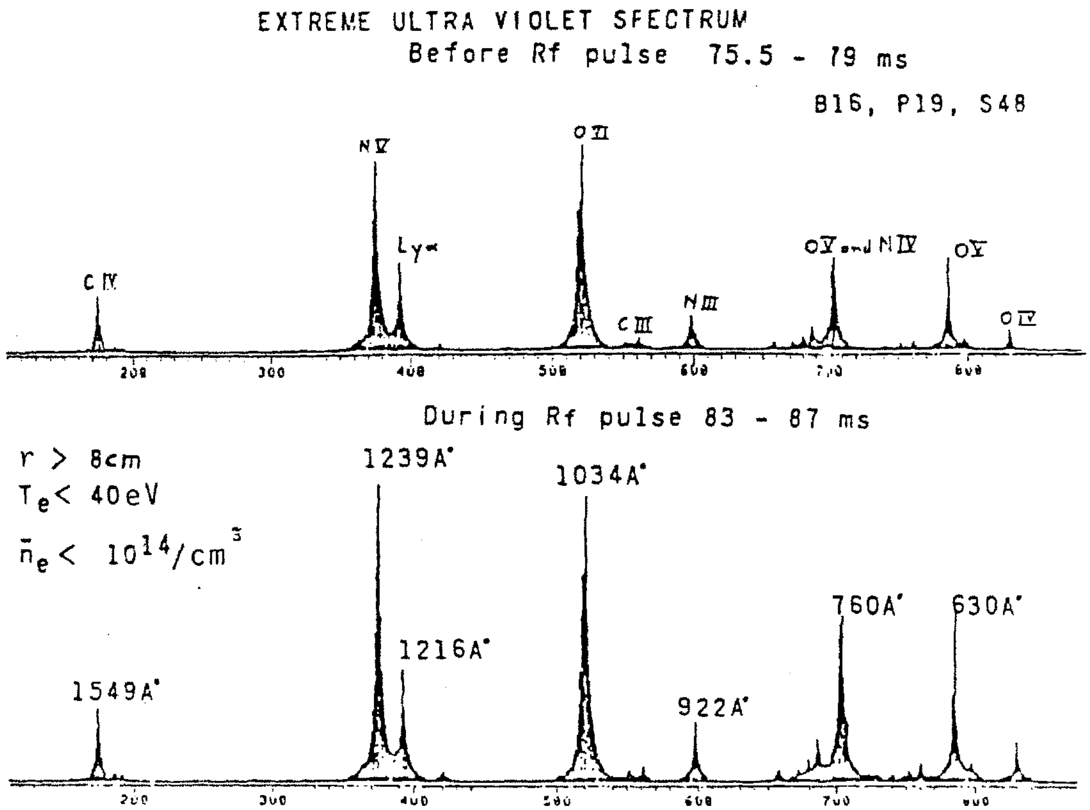

Figure 6

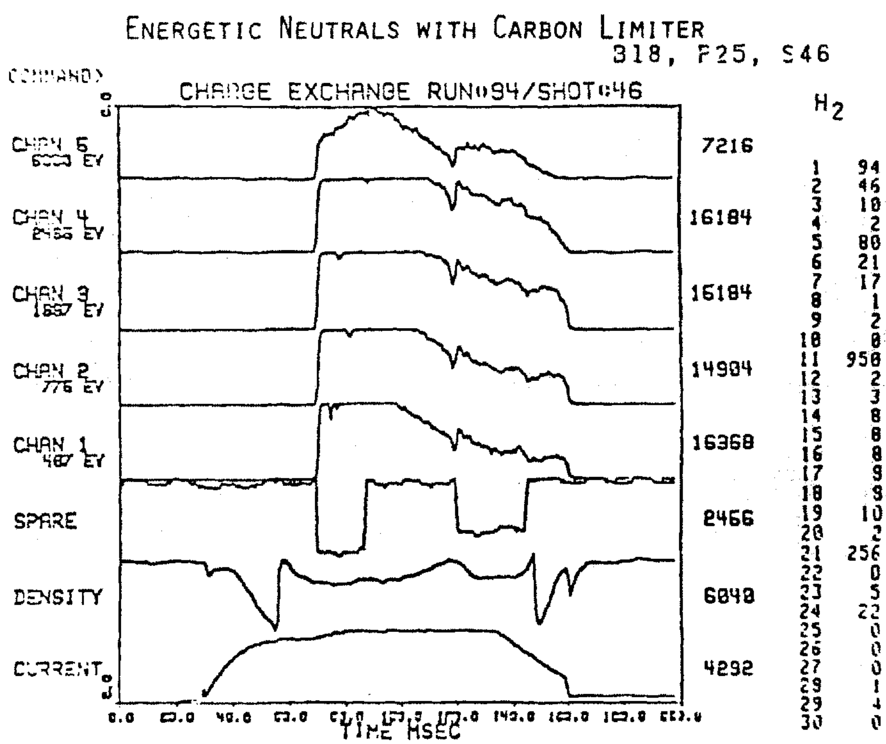

Figure 7

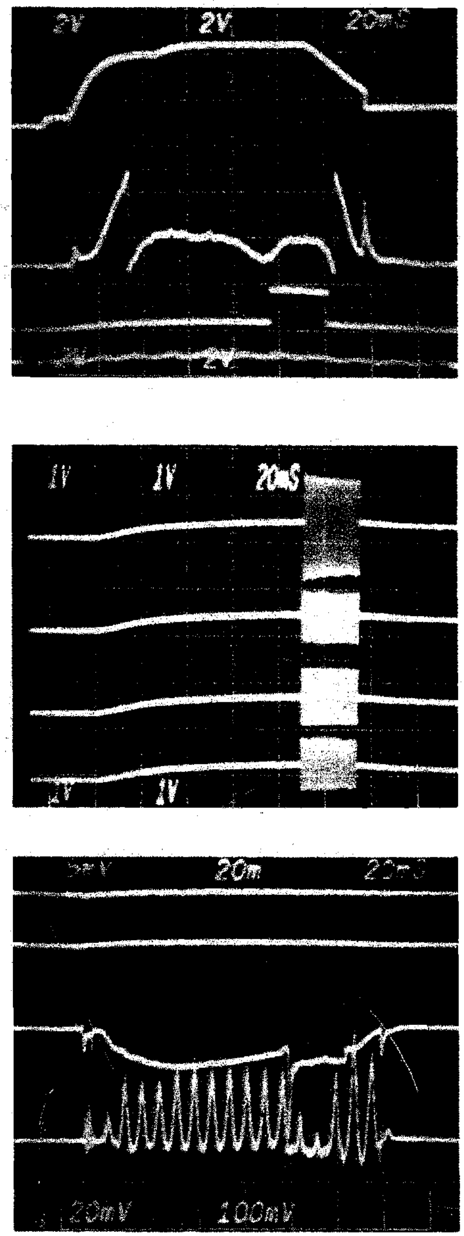

I_p

n_e

t

V_F

V_R

I_a Top

I_a Bottom

T Up

T Down

Pin

I_L

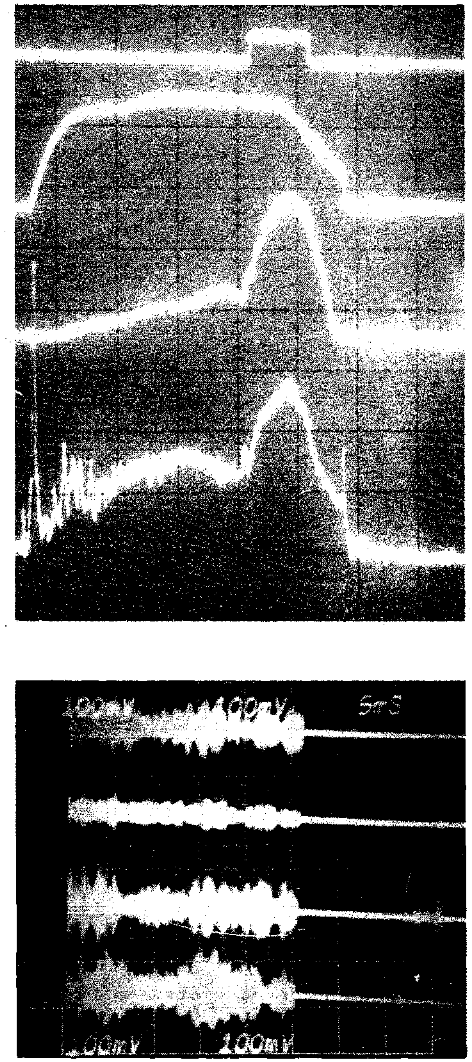

t

I_p

center
soft X-rays

Pyro

P67 Limiter

P68 HCN-top

P69 HCN-Bot-Out

P70 HCN Bot-In

Medium Power Experiments with Carbon Limiter.

B18, P25, S46

200 MHz, H_2, 62.2 kA

Figure 8

III - EXPERIMENTAL APPARATUS

III-1. Transmitter Chain and Engineering Support

III-1.1. Transmitter chain

Usually, the largest investment in any high power RF heating experiment is the transmitter chain and its engineering support.[66] In this case, we were fortunate enough to acquire most of the high power components as a gift from the Air Force, making the present installation the largest of its kind in the world (Figure 1,2). The system was built in view of a multimegawatt experiment on Alcator C, making the apparatus a gross over-kill for Alcator A.

Four "A^2" high power amplifiers [67] and "B^2" driver amplifiers were installed, yielding a maximum power of 6 MW, at 180 MHz. One of the B^2 was also operated at 90 MHz with major modifications. Figure 2 shows the initial basic transmitter chain from the oscillator, then exciters, B^2, A^2, RF switch gear, dummy loads, resonator, and finally, antenna. An RF feedback control system was built to stabilize either the antenna current or forward power. An auto-tune processor and double-stub tuner with stacked 9" transmit-receive switches as shorting elements was also planned to dynamically match the antenna during a plasma shot. Fortunately, since[134]

(1) $$.33 < Z/Z_o < 3$$

(2) $$\frac{P_{reflected}}{P_{forward}} = \left| \frac{Z - Z_o}{Z + Z_o} \right|^2 < .30$$

and this system became unnecessary since, for practical purposes, R_R never varied over much more than a factor of 3 during a given plasma shot. Figure 3 shows the simplified version of Figure 2 that was actually used during the Alcator A experiment. A broad-band 1 kW distributed transmission line amplifier was used instead of the exciters and the narrow band 5894, and the 4cx250 stages of the B^2 were bypassed (Appendix 12). Any power level from a fraction of a Watt to 500 kW could be injected into either Alcator or a 2MW dummy load through a network of motorized type-N, 3" and 9", single pole double throw coaxial switches.

Figures 5 and 6 are very simplified diagrams of the A^2 and the B^2. The B^2 uses an RCA 2041 high power tetrode mounted on a $\lambda/2$ plate coaxial cavity with an output coupling tap angle of about 30°. The input resonator is a simple 3/4 λ delay line with variable tap angle adjustment, and can be operated at either 90 or 200 MHz without modifications. For 90 MHz operation, the plate cavity is extended some 2', and less tuning flexibility is possible, due to the smaller relative size of the output tuning slug. The B^2 is keyed on by a small screen modulator very similar to the A^2 grid modulator.

The A^2 uses an RCA 6950 coaxial super tetrode. The A^2 grid is much more complicated than the B^2's, because the 200 lb tube is $\lambda/4$ long, and the voltage maximum must be tuned to the center of the tube grid. The $\lambda/2$ plate cavity is 30Ω and 4 feet in diameter. Four magnetic output coupling loops at the top of the cavity then combine to a single output 9" coax. A fifth output coupling loop is used to provide positive feedback, that is combined with the B^2 output, through a variable delay line and a 4 port hybrid ring. This feedback system was bypassed for more stable operation in varying loads.

At conservative power levels, the B^2 generates 100 kW of RF with 12 kVdc at 15 amps, and the A^2 generates 1.5 MW with 20 kVdc at 100 amps. One 6950 alone requires 8 kW of filament power and 150 gallons per minute of plate cooling water. All the tuning elements of the A^2 and B^2 are motor operated, and the transmitter cabinets are thoroughly RF leak tight. The A^2 and B^2 DC plate supply leads are brought through two high power LC RF feedthroughs.

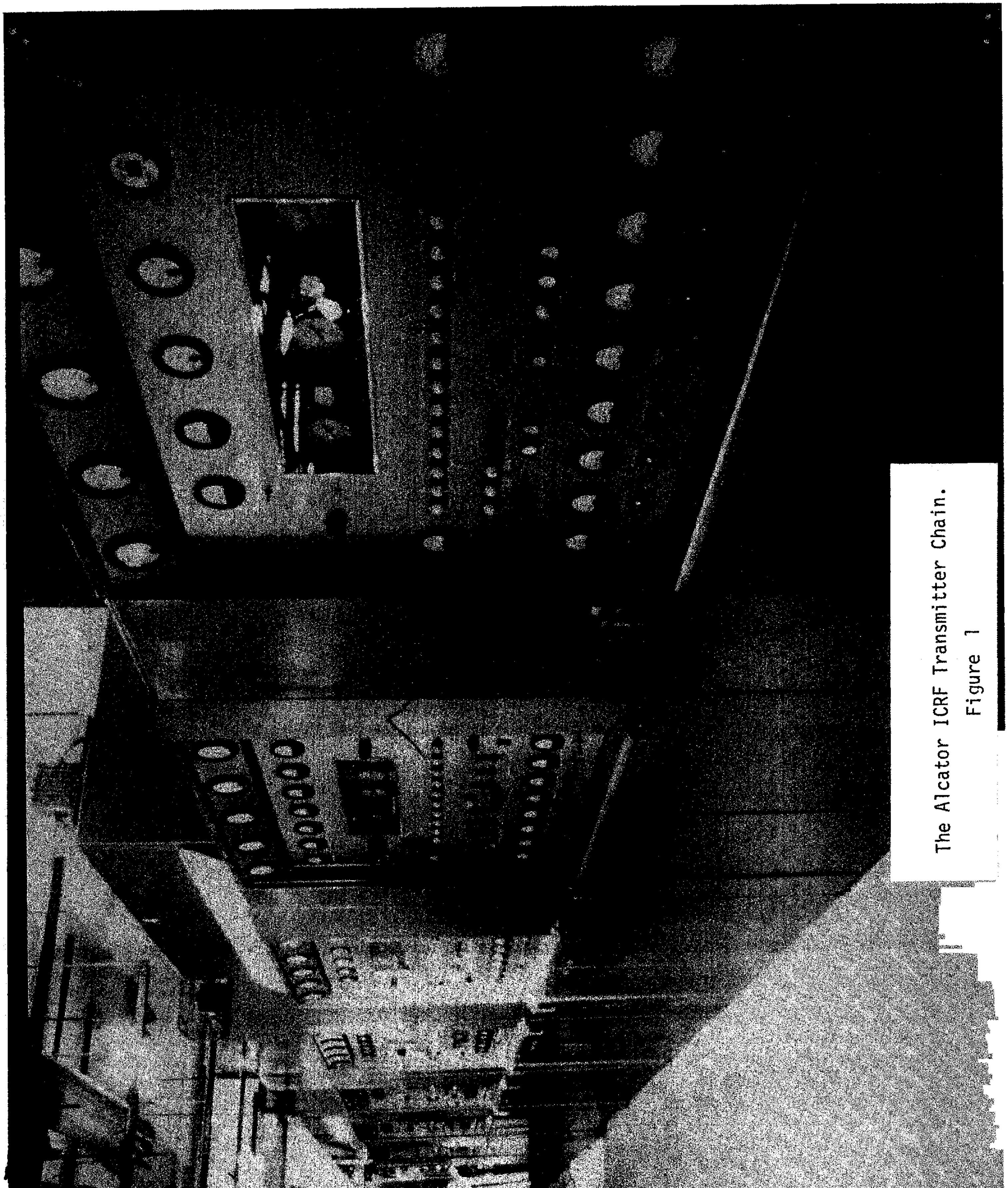

The Alcator ICRF Transmitter Chain.

Figure 1

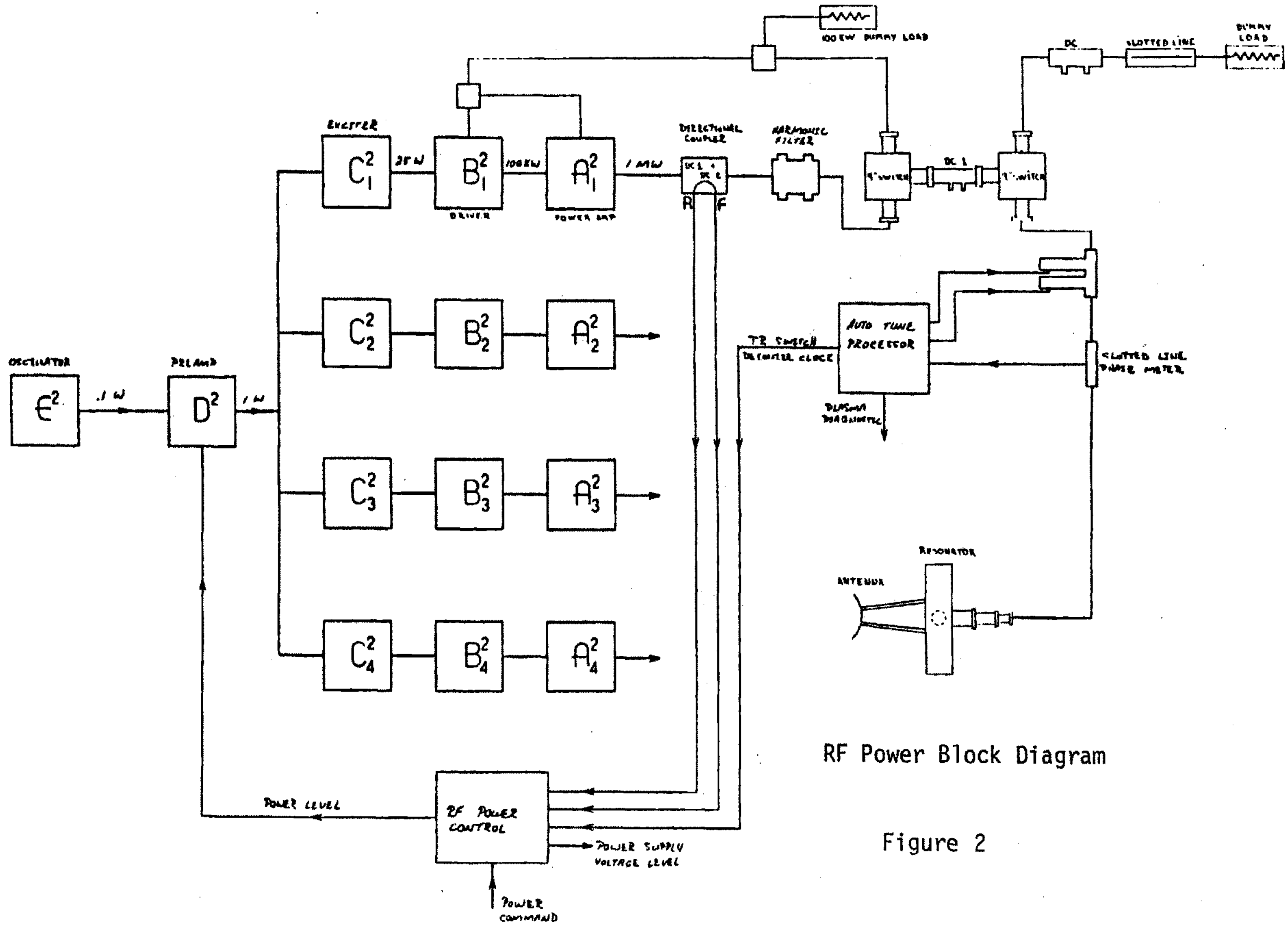

RF Power Block Diagram

Figure 2

Simplified Alcator A ICRF RF Power System

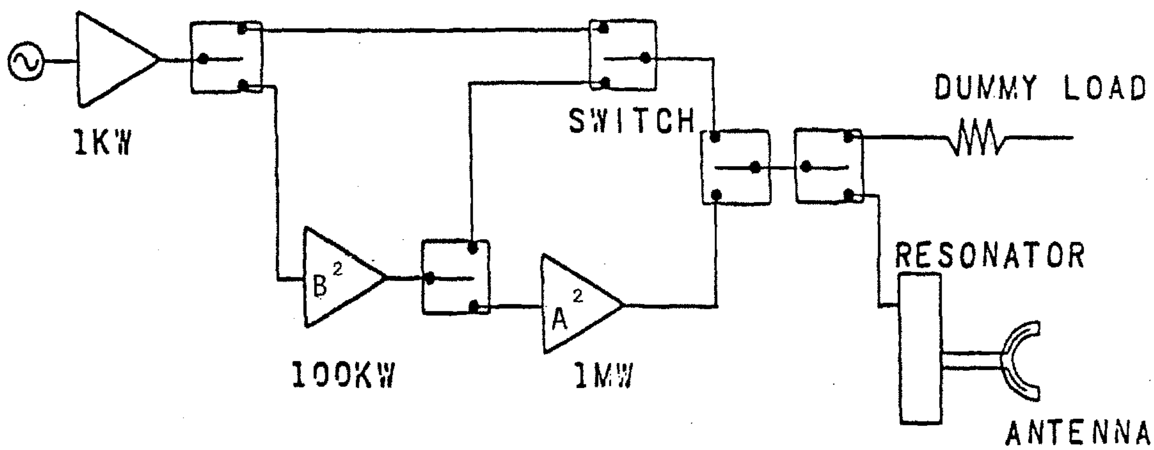

Figure 3

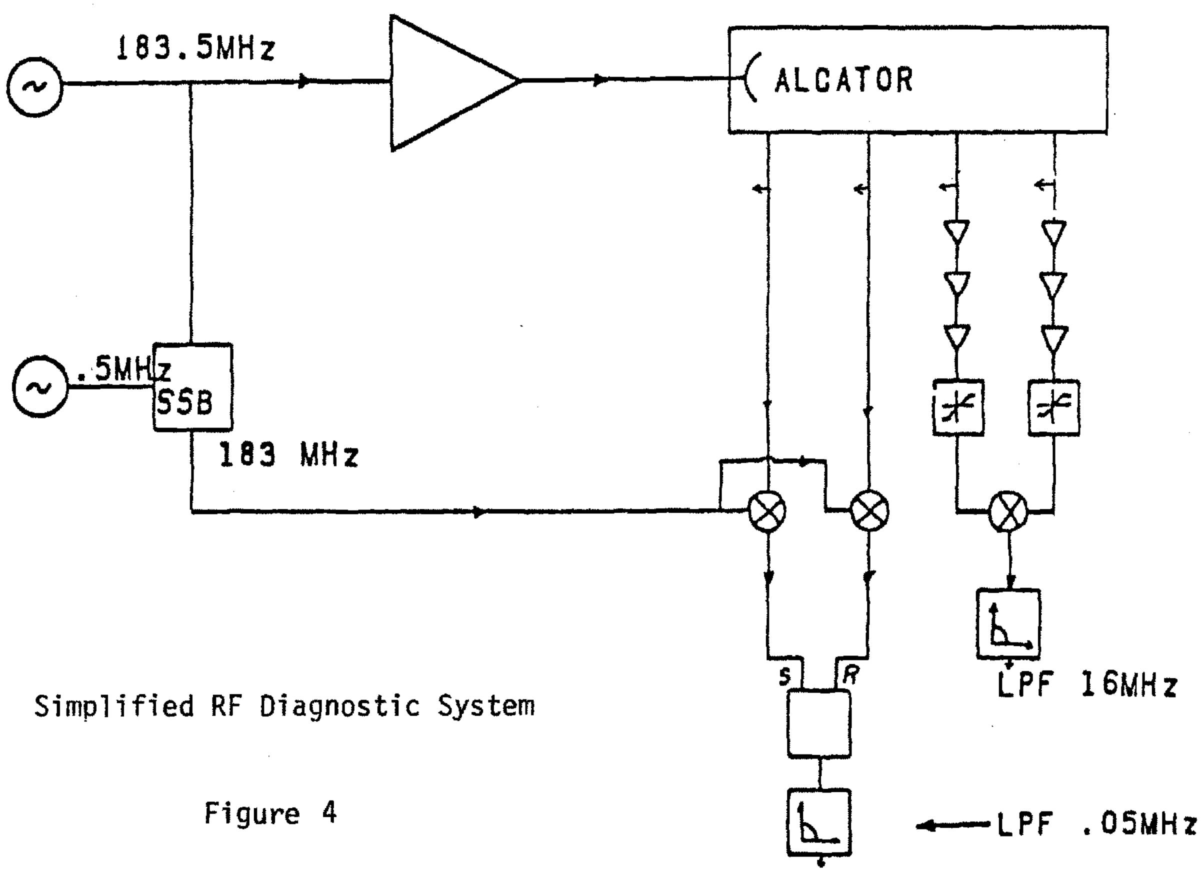

Simplified RF Diagnostic System

Figure 4

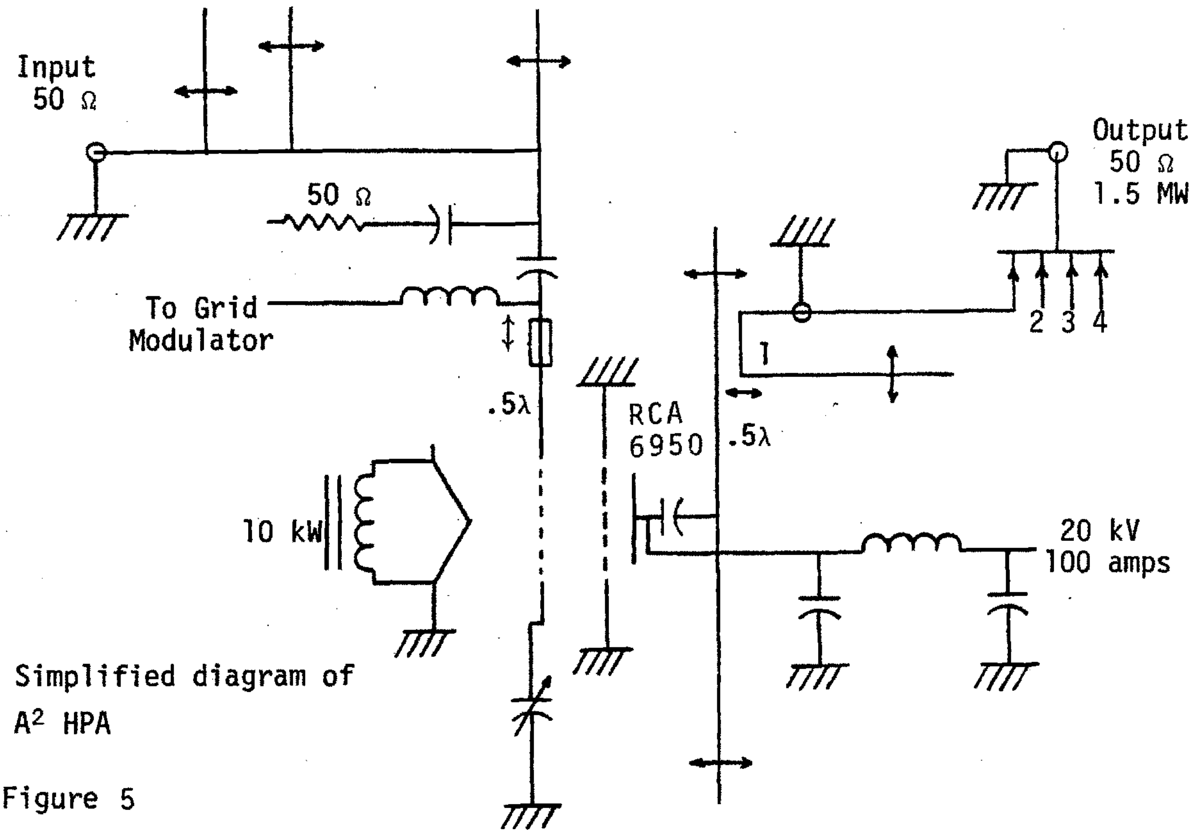

Simplified diagram of
A^2 HPA

Figure 5

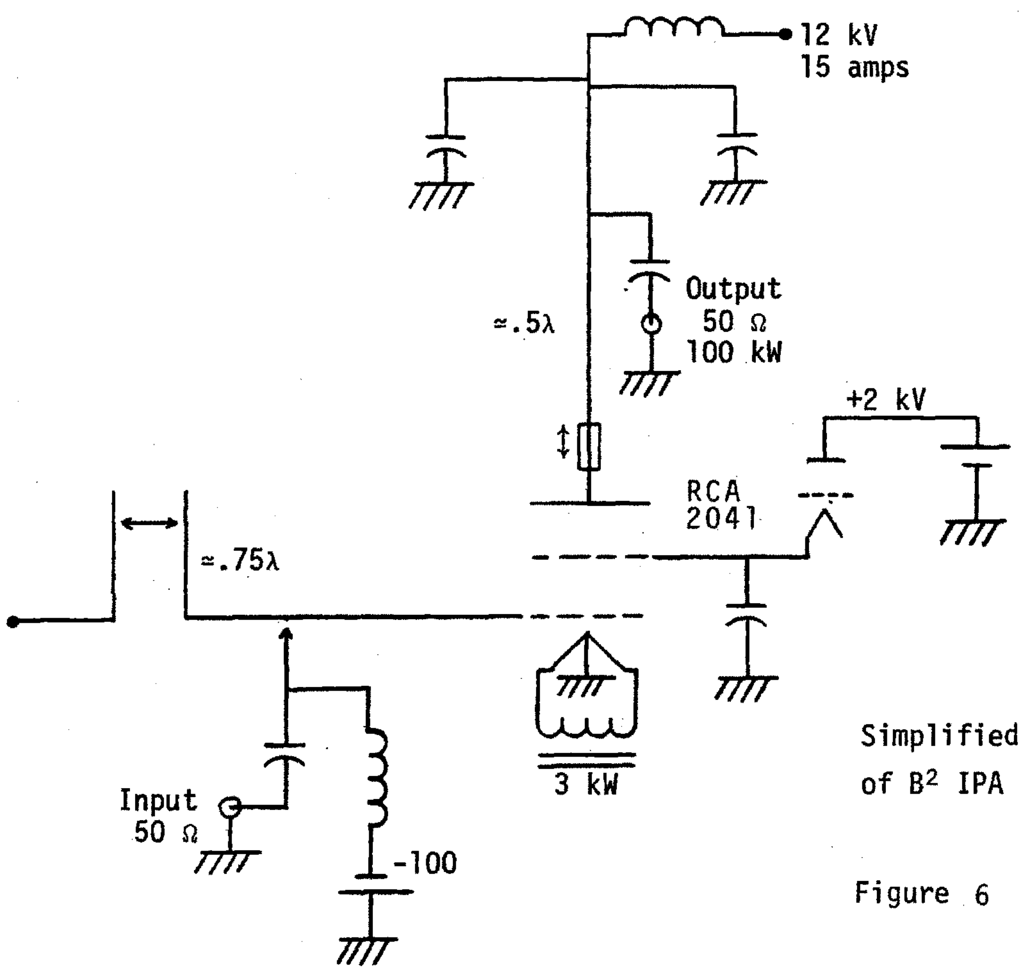

Simplified diagram
of B^2 IPA

Figure 6

III-1.2. High power DC and control systems

Two multi-megawatt DC power schemes could be used to feed the B^2 plate with 12 kV, and the A^2 plate with 20 kV, as can be seen from the simplified schematic of Figure 1. All four power supplies are located underneath the transmitter room in an explosion and fire proof vault (Appendix 12). In the first and simplest scheme, two 3 ampere DC power supplies are used to charge the 600 μF and 400 μF capacitor banks to produce a 40 ms, 500 kW RF pulse.

$$(1) \quad W = \frac{4 \times 10^{-4}\ F}{2}\ (20^2 - 15^2\ kV^2) = 35\ kJ$$

$$(2) \quad P = \frac{W}{T} = 875\ kWdc$$

Both capacitor banks are split in half, isolated with critically damped current limiting RL networks (not shown in Figure 1), and equipped with mechanical and ignitron crowbars. 1000 μF could also be installed in the vault permitting up 1.25 MW RF for 40 ms.

The second scheme uses 2 custom made long pulse 300 and 100 ampere ignitron power supplies powered from the 4160 volt ac 1200 ampere Magnet Laboratory bus system. Figure 2 is a simplified block diagram of this system. The main sequencer triggers the "domino block generator", which in turn, sequentially closes the 4160 Limitamp breakers feeding each of the A^2 and B^2 high voltage transformers. The sequencer also triggers the rectifier phase controller, the grid modulator and the fast crowbar system. The ignitron phase control system is very simple, since this is basically a predictable capacitive-resistive load and no power inversion is necessary. The phase control can be run either open or closed loop. The rectifier is a full wave, three phase array of 12 GL-5630 ignitrons (Appendix 12). These high voltage ignitrons are rated 30 coulomb, 30 kVdc, with gradient and screen grids, and one holding and two triggering anodes.

The 500 gallons per minute at 80 psi of highly demineralized cooling water is provided by a custom made heat exchanger unit using Charles River water as primary coolant.[69]

A multitude of control and safety systems was built to manage the complex high power apparatus. The safety system can be broken down into four basic blocks operating at different speed levels (Figure 3). First, a number of kirk key and panic button interlocks are located throughout the system and, in particular, at the main control panel, vault, RF switch yard, Limitamps, Alcator A sequencer and cell, physics station and matching system. These interlocks, combined with literally hundreds of relay contacts, monitor the status of everything from slow, high voltage overcurrents to a low water flow in an A^2 grid. In the event of a fault, the main high voltage interlock relay K_3 is opened, thus disabling all power systems operating above one kilovolt. Smaller interlock loops will shut down only subsets of the system to protect a particular part of the equipment.

The next two faster levels are solid state, monitor fast current, voltage or reflected power transients, and disable the main sequencer, which in turn, triggers the crowbars and cuts off the RF drive. At the fastest speed level, some twelve short dipoles located near the transmitters along the transmission line and in the Alcator cells monitor RF leakage, and, for power levels exceeding OSHA recommendations, the RF drive to the exciters is quickly cut off.

The most important control element is the central high power control unit (Appendix 12), which can be divided into three subsets, K_1, K_2, K_3. For all practical purposes, K_1 enables all non-solid state systems (as long as the safety circuits are satisfied). K_2 enables the 4160 Alcator starters, and K_3 enables all high voltage DC systems above 1 kV.

The main sequencer,[68] fast crowbar system, grid modulator and RF leakage detector system[70] were custom built in house. Many channels, remote control and the recyclable features were necessary for the sequencer, so that during a run, different RF scenarios could be quickly implemented between shots, (i.e., low power long pulse for tuning, three short interspaced pulses for high power heating, or simply a short medium power pulse every second for antenna conditioning).

Even when measured with a half wavelength 50 ohm matched dipole, RF leakage signals of, at most, one volt were measured under the most adverse conditions (i.e., a panel left off the resonator, and $P_f \simeq 50$ kW). The Poynting flux,

$$(3) \quad S = \frac{P}{A} \cong .07 \text{ W/m}^2 = 7 \ \mu\text{W/cm}^2$$

where

$$(4) \quad P = \frac{V^2_{rms}}{50\Omega}$$

$$(5) \quad A = \frac{1.65 \ \lambda^2}{4\pi}$$

was much less than the OSHA recommended 10 mW/cm^2, and the system was not needed. Normal readings in the cell were at the nanowatt/cm^2 level. Nevertheless, the system should be used with high power A^2 experiments.

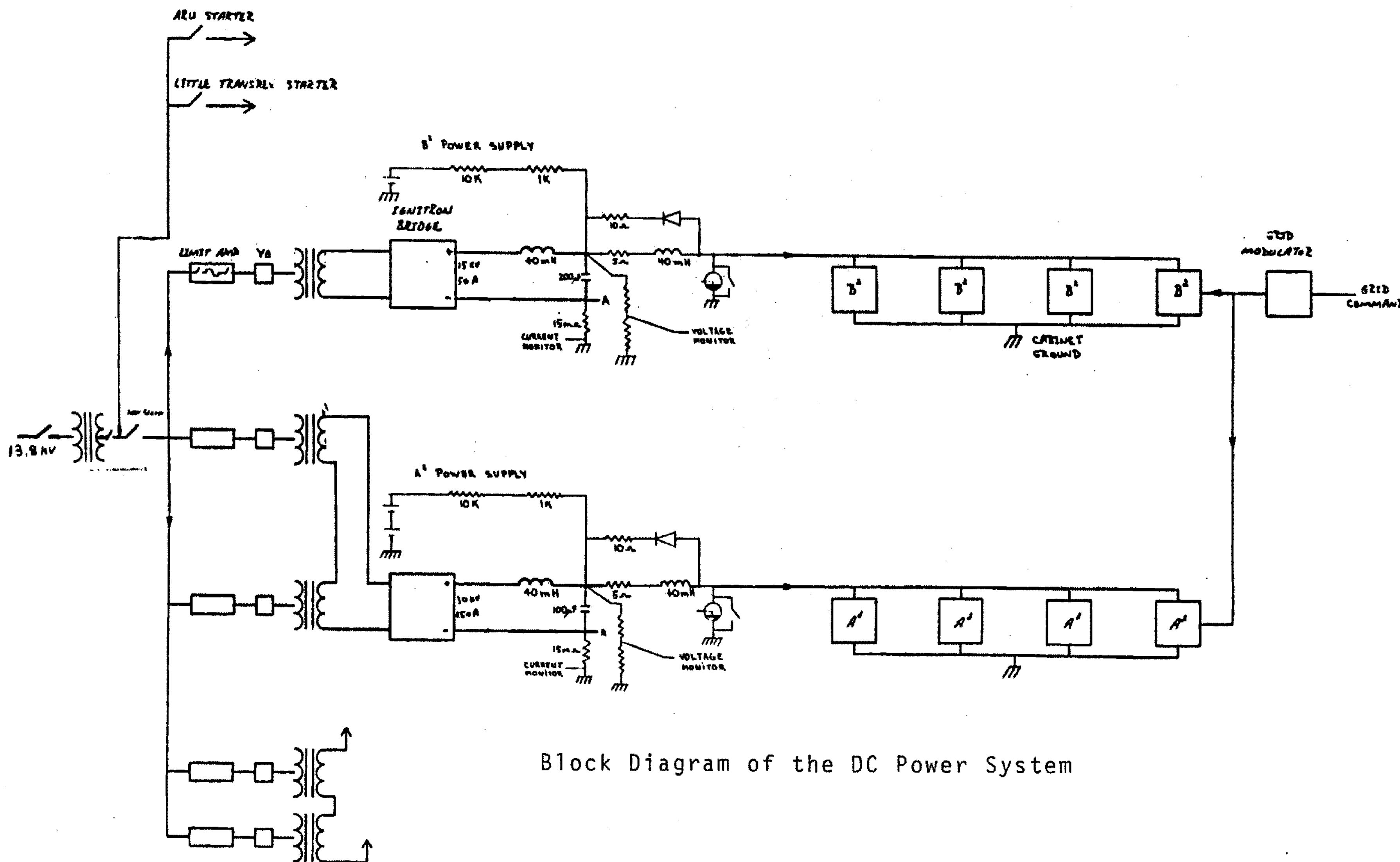

Block Diagram of the DC Power System

Figure 1

Ignitron A^2 and B^2 Phase Control Block Diagram

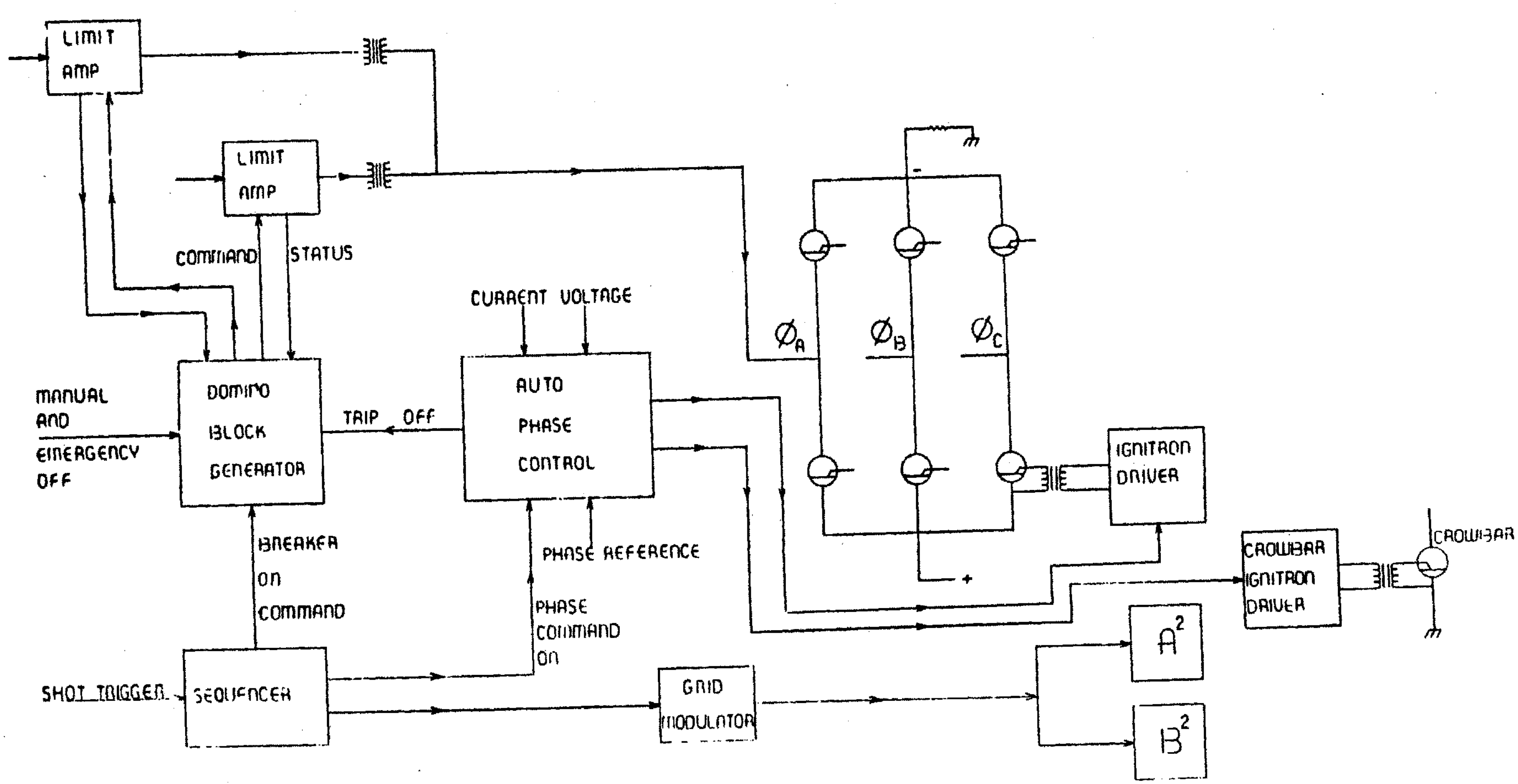

Figure 2

Simplified Flow Diagram of Safety System

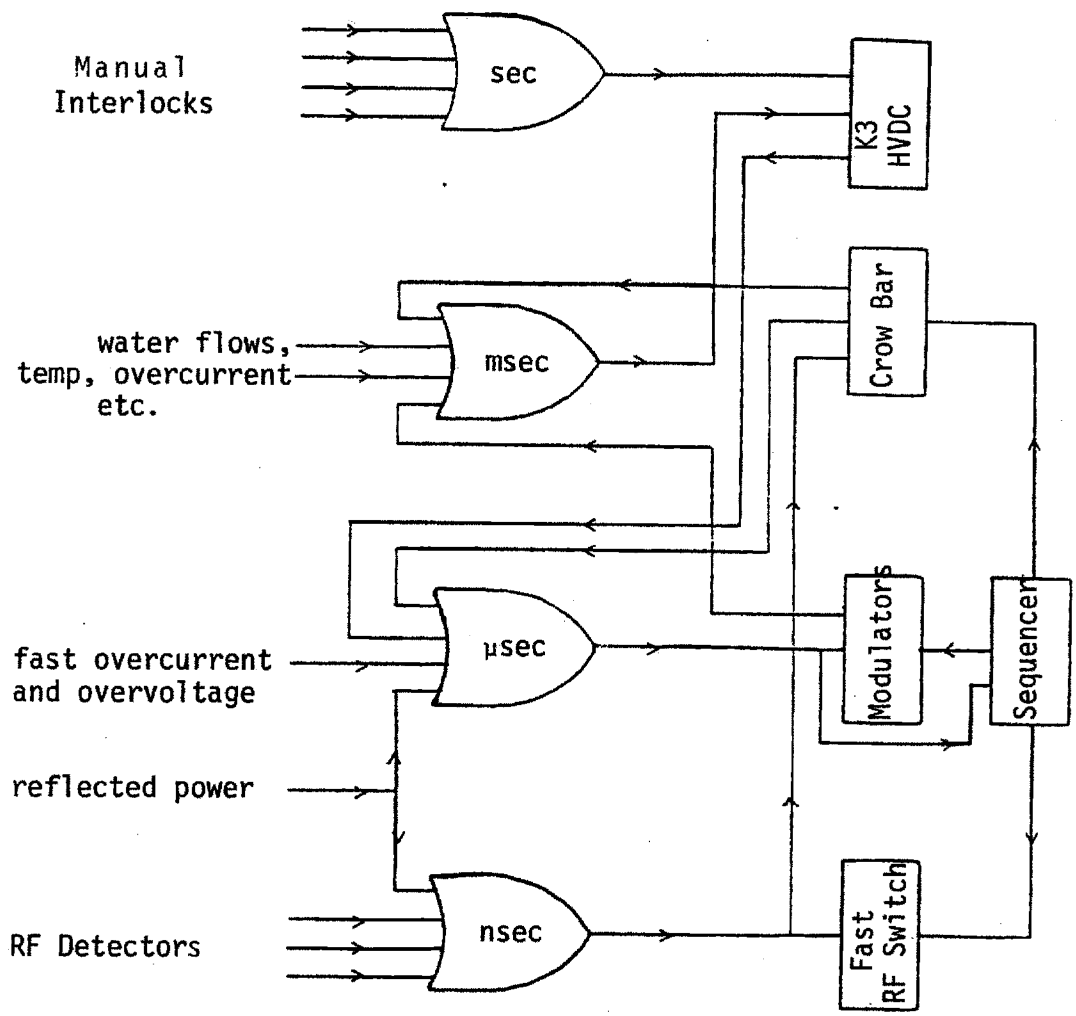

Figure 3

III-2. Matching and Launching Structures

III-2.1. Basic matching and launching system

As we mentioned earlier, a series of three antennas, A_1, A_2 and A_4 were designed and tested (Figure 1). The first, A_1, is an all metal ultra compact shielded antenna. Significant attention was given to RF properties, cooling, and especially to the stringent mechanical constraints of the Alcator tokamak [71] (Section III-2.2.). The second antenna, A_2, is unshielded, also all metal, and has 2.5 times more loop area (Section III-2.4.). The A_2 antenna structure with side virtual limiters is more than an order of magnitude larger than the tiny 1.25 x 3.4 inch access port, and extensive use of "Boat in the Bottle" technique was necessary to install these unfolding structures inside the Alcator vacuum chamber (Figure 2).

A_4 is a combination of A_1 and A_2, with an increased loop area, more finely slotted Faraday shield and side limiters, and a Langmuir probe mounted in the front of the shield. Figure 3 is a simplified diagram of the basic antenna structure.

All three antennas were located on the low field side of the plasma, with their back plane electrically connected to the vacuum vessel (r(wall) = 12.5 cm). The antennas were made with two current loops ($\Delta\theta = 65°$) that could be fed so their magnetic fluxes added (m = 0 mode, I_T out of phase with I_B, push-pull drive), or cancelled (m = 1 mode, I_T in phase with I_B, push-push drive). All three antennas also had internal RF current probes near the voltage minimum, thus making possible direct calculation of loading resistance, an advantage not usually seen in other experiments.

A high power 20 foot, 1200 lb. coaxial resonator system[72] was built to match, balance, and electrically isolate the antenna (Figure 4). The extremely versatile resonator could match almost any reactive or resistive load down to a fraction of an ohm, from 45 to 360 MHz, and up to the megawatt power level. Figure 5 is a simplified sketch of the vacuum antenna feeder. The m = 1 capacitive coupler is shown in solid lines, while the m = 0 magnetic coupler is shown in dashed lines. The vacuum breaks are shown with their CCl_4 and teflon sleeves. A late version, two stage dc break is also shown. The resonator and coupler box are at ground potential while the antenna and vacuum feeder hardware are at machine potential. Note also how the antenna feeder center conductor is supported only at each end, the antenna current maximum ground, and the vacuum breaks.

Considerable time was spent developing satisfactory high power vacuum electrical breaks. Many materials and geometries were tested at very high RF voltages using a modified panel at the voltage maximum in the resonator. Liquid carbon tetrachloride was found to have superior dielectric and cooling properties for high power, low loss RF insulation.

Finally, two innovative antenna structures and matching systems, A_3 and A_6, were proposed and designed (Section III-2.6). These last RF launching systems could be a full 360° around the plasma, m = 0 or m = 1, all metal, and shielded or unshielded. The resonator would be only a half wavelength long at Alcator vacuum, and the vacuum breaks would be at a real power feed point. The A_6 launching system would, theoretically, have superior power handling capability and loading and versatility characteristics.

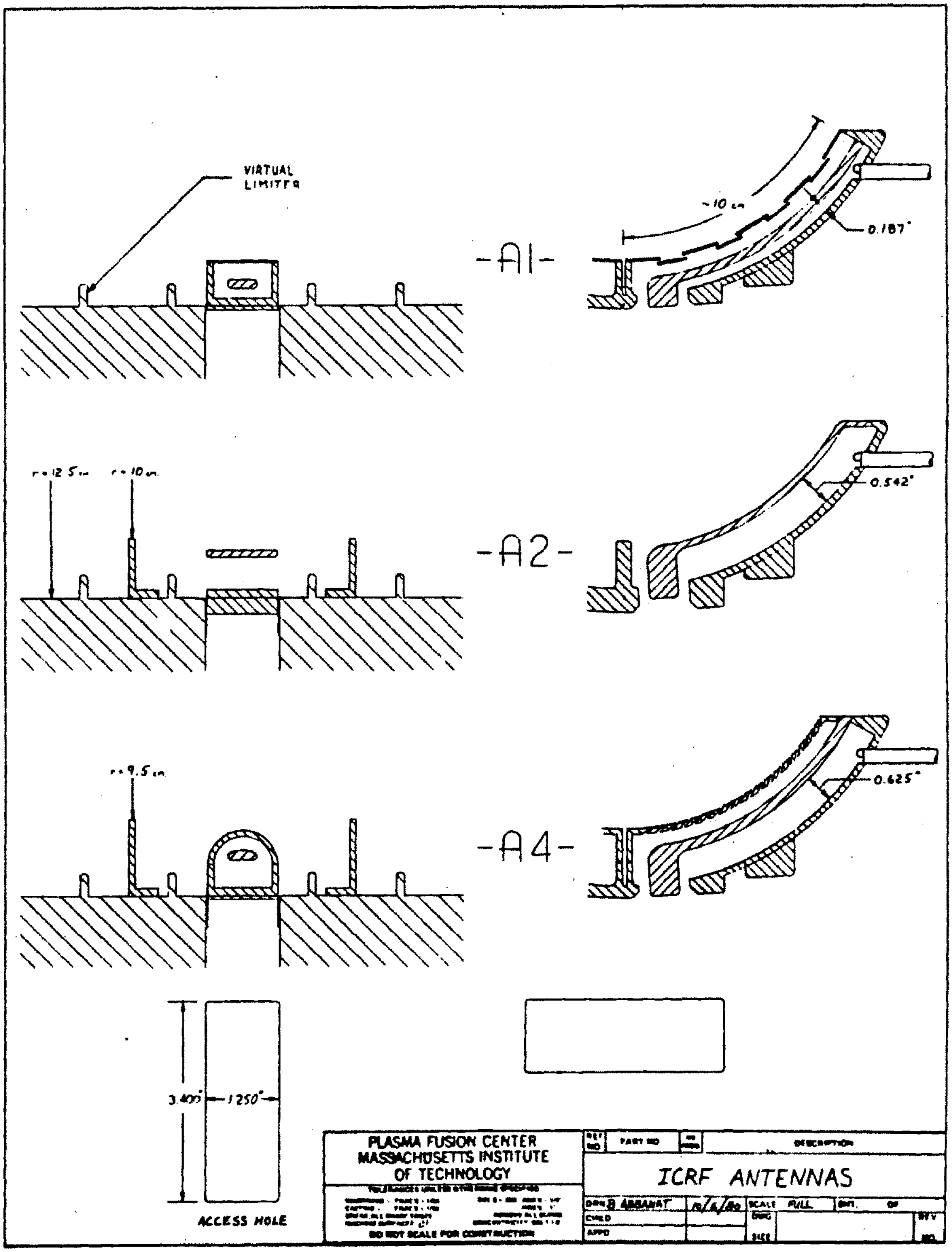

Alcator A ICRF Antennas

Figure 1

"A Boat in the Bottle" Technique

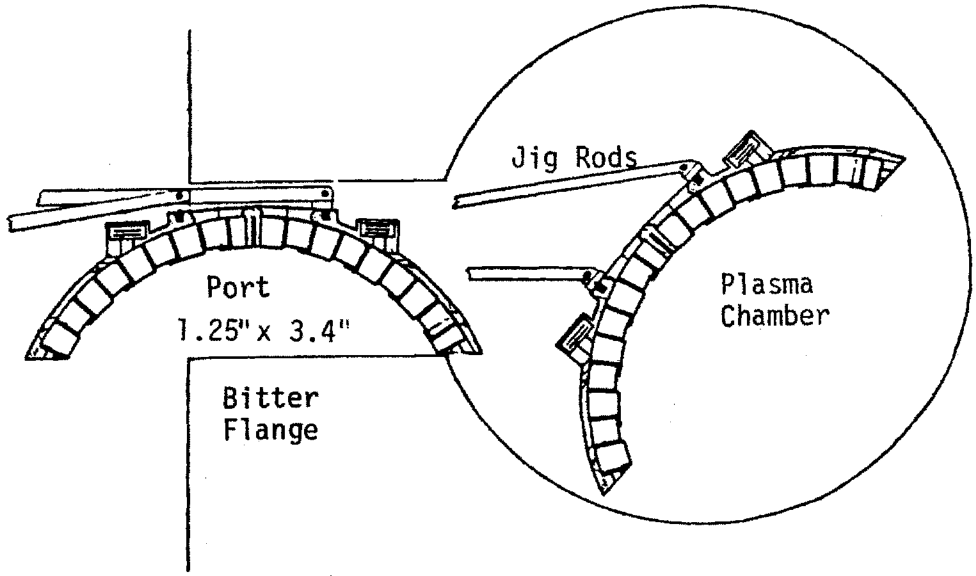

Figure 2

Nomenclature and Coordinate System

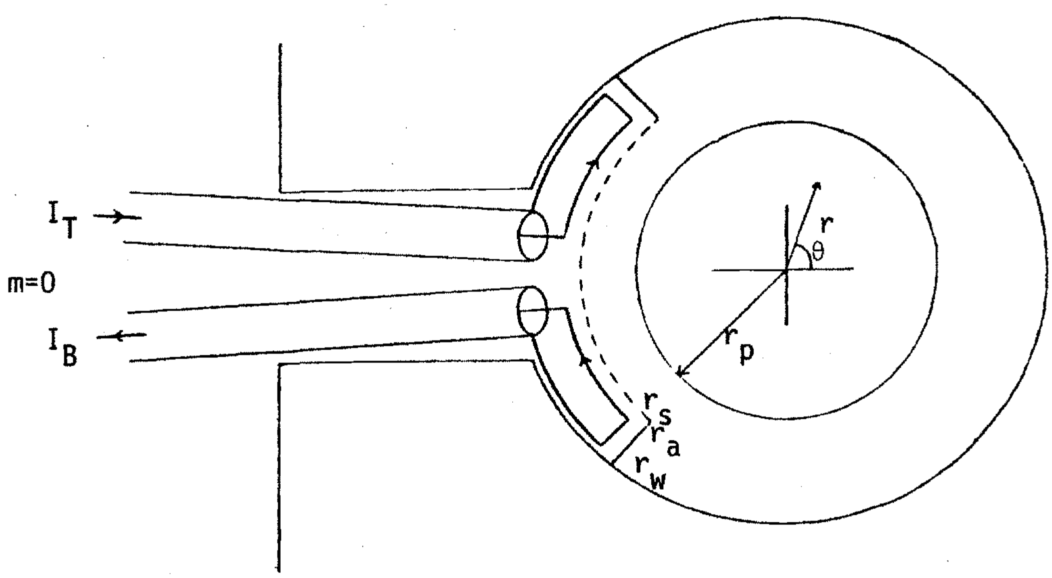

Figure 3

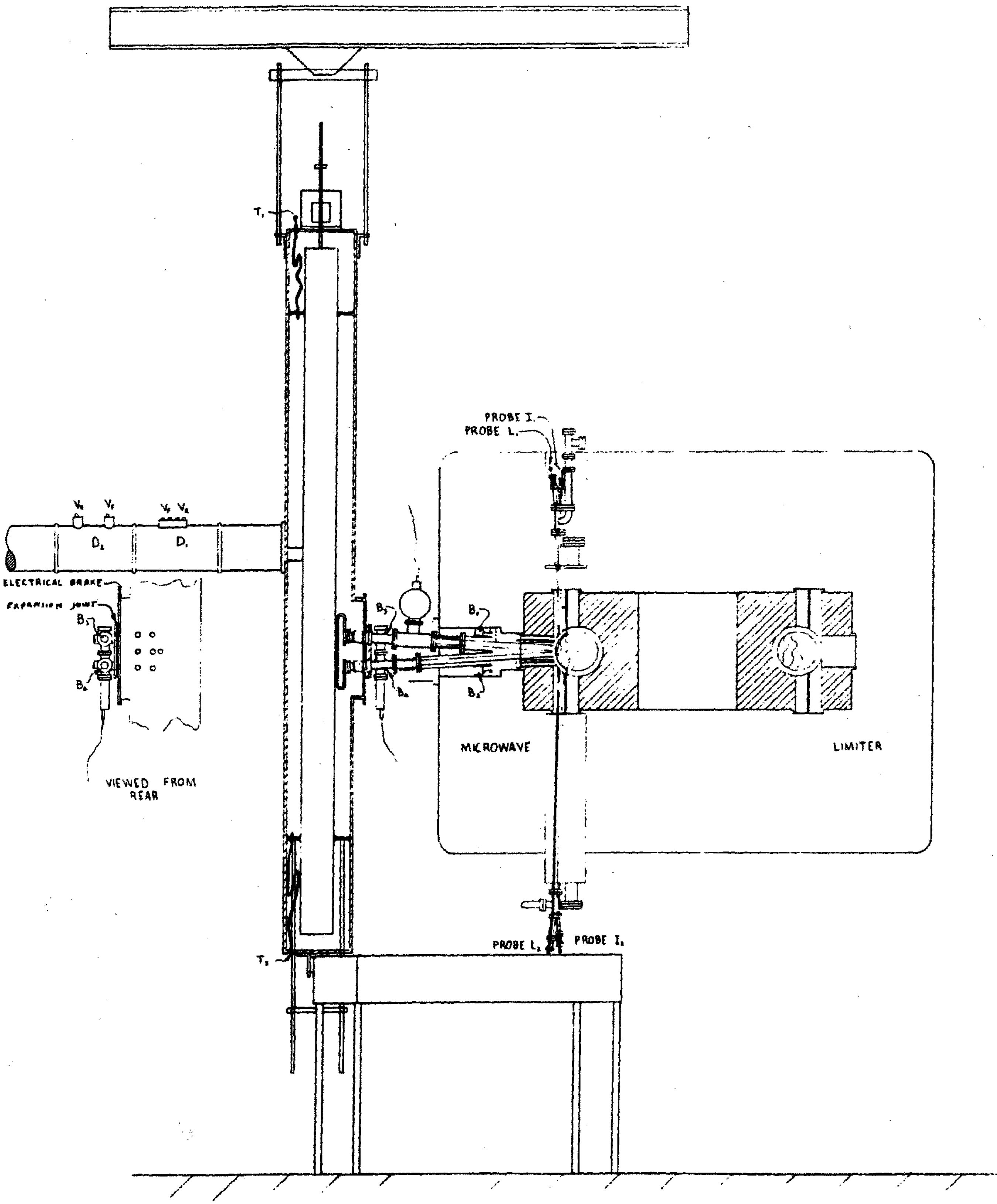

Alcator A ICRF Matching and Coupling System

Figure 4

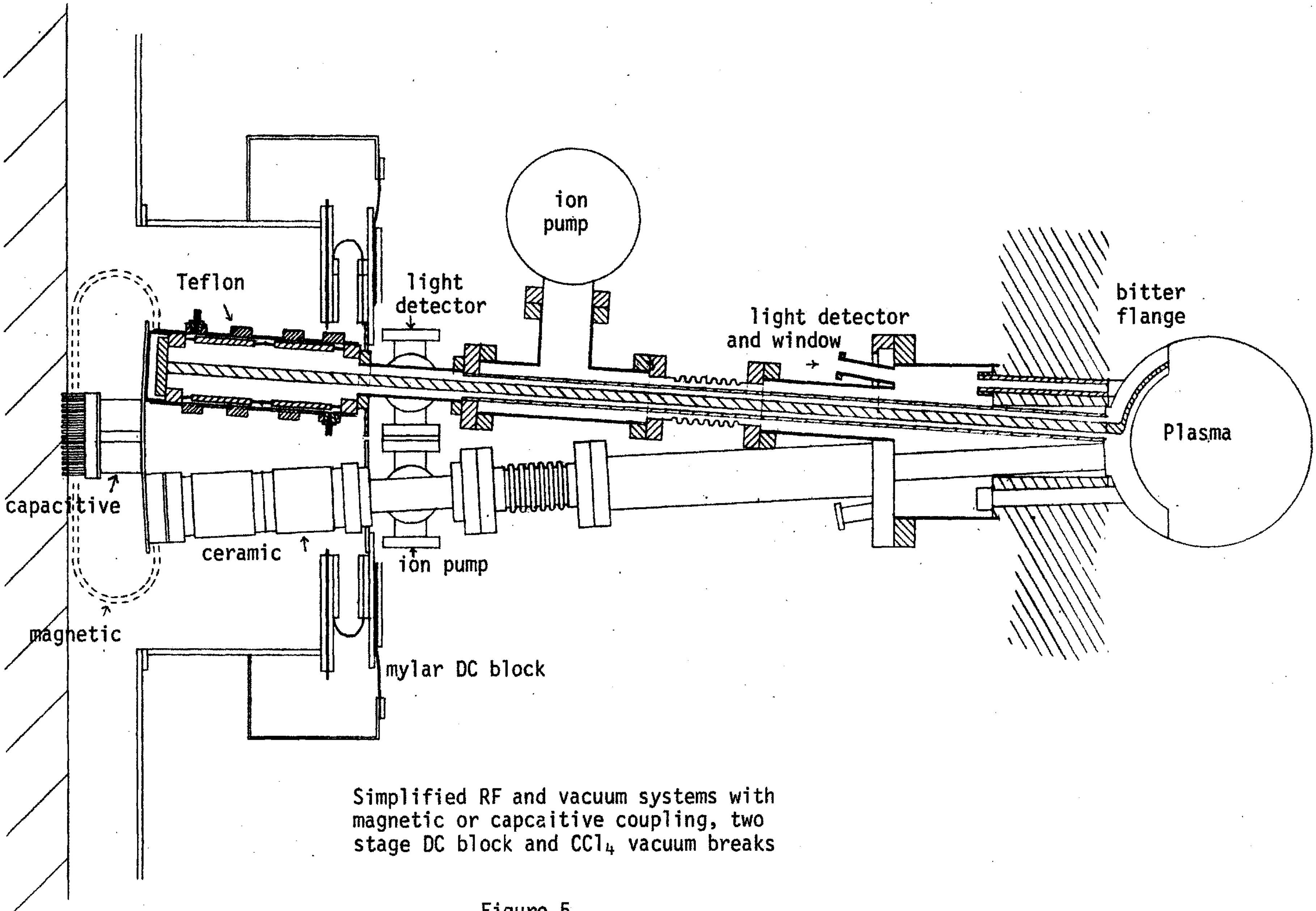

Simplified RF and vacuum systems with magnetic or capcaitive coupling, two stage DC block and CCl_4 vacuum breaks

Figure 5

III-2.2. A_1 antenna system and engineering constraints

The Alcator A access ports were made by milling holes and slots in a 3" thick solid block of 304 stainless steel (Bitter flange), which is part of the high compressional strength Bitter magnet. The plasma is actually located in a ten inch hole in this stainless steel block. Figure 1 is a mechanical drawing of the A_1 antenna mounted in the Bitter flange. Two hollow pins hold the antenna firmly against the vacuum wall. The treaded ends that screw in the antenna are locally weakened, so the pins can be broken in case of galling. Light inside the antenna can be monitored through a line of sight path between the antenna center conductor and a window mounted on the main 10 inch spool piece.

The feeder outer conductor is one inch in diameter, and has a "valve seat" fit to the back of the antenna. For comparison, this outer conductor is smaller than the TFR and PLT antenna center conductors, and A_1 is small enough to fit inside the center conductor of nine inch coax. The inside conductor is only half an inch in diameter, giving an impedence of about 40 ohms. 40 ohms is optimum for power carrying capability [18], and is a good mechanical compromise between a sagging small center conductor, and a large stiff one requiring too much dimensional stability.

The A_1 antenna was "carved" out of a solid block of 304-L stainless steel, as can be seen from Figure 2. Only the center conductor and front Faraday shield clips were welded in afterwards. Five almost symmetric pairs of holes were drilled in the backplane of the antenna. (Figures 2 and 3). Starting at the center of the antenna, we have the one inch feeder coax seat, then the insertion rod holding threads, the holding pin threads, the Langmuir probe seat and finally, at the end of the antenna, the antenna current probe seat.

The rugged Faraday shield is an integral part of the back plane, and was formed by slicing the side limiters at a 60° angle. The front overlapping clips were then electron beam welded to the back plane (Figure 4). Note how the vacuum vessel radius is only 12.5 cm, while the plasma limiter is 10 cm, so the Faraday clips are less than 1 cm from the relatively (to TFR and PLT) high power density plasma edge.

Figures 5 and 6 are mechanical drawings and assemblies of the vacuum RF antenna feeder. All components are standard 4.5 and 2.75 inch stainless steel hardware with knife edge and copper gasket seals. The ceramic vacuum breaks are high grade alumina (Al_2O_3) with high temperature brazing, so the whole antenna assembly is of ultra high vacuum quality (10^{-9} torr) and fully bakable.

The two 4.5 inch bellows enable the outer coax conductors to press firmly on the antenna seats. Two 30 liter/sec high-Q ion pumps, mounted on the 2.75 and 4.5 inch "T's" pump the coax feeders and the large trapped volume in the port behind the antenna. Note from Figure III-2.1.(4) how the main ten inch spool piece is at the bottom of a deep tunnel inside the Alcator liquid nitrogen dewar, considerably limiting access to the Bitter flange.

All RF carrying surfaces are electroplated with .001 - .003 inches[71] of pure silver (i.e., no organic brighteners). The skin depth at 200 MHz is[134]

(1) $$\delta = \sqrt{\frac{2}{\omega\mu_o\sigma}} = 4.6 \times 10^{-6} \text{ m} = 1.8 \times 10^{-4} \text{ inches}$$

where, for silver, $\sigma = 6.1 \times 10^7$ mho/meter, and δ is much less than the silver thickness.

About half of the easily calculatable system resistive losses comes from the two meters of half inch diameter center conductors

(2) $R_L = \frac{L}{\sigma\ \delta\ 2\pi r} \approx .18$ Ohms

With 200 amperes in these conductors, some

(3) $P/cm = \frac{I^2\ R_L}{L} \approx 36$ watts/cm

$P/cm^3 = \frac{P/cm}{\pi r^2} \approx 28$ watts/cm^3

and a final temperature of 830°K would be reached after (T_o = 270°K)

(4) $\Delta t = \frac{(T_f - T_o)\ \rho\ c_\rho}{P/cm^3} \approx 80$ sec

where for stainless steel, $\rho = 7.9$ g/ cm^3, $c_\rho = .504 \frac{J}{g\ °K}$ and $k = .16 \frac{W}{cm\ °K}$

This corresponds to about two hours of antenna conditioning, with sixty 10 msec pulses a minute. The 830°K was chosen for a 10^{-8} torr silver vapor pressure calculated from the approximate empirical formula[128]

(5) $\log_{10} p(\text{torr}) = 8.865 - 14058/T(°K)$

From the one dimensional heat diffusion equation in a solid

(6) $\frac{\partial T}{\partial t} = \alpha \frac{\partial^2 T}{\partial x^2}$

where for stainless steel, $\alpha = \frac{k}{\rho c_\rho} = .04$ cm^2/sec

we can calculate the approximate heat penetration depth for a 200 msec RF pulses as[139]

(7) $\Delta x \approx \sqrt{\alpha\ \Delta t} \approx .09$ cm << r

and the heat is deposited only on the surface of the conductors. In fact, the surface temperature of a semi-infinite solid exposed to a heat flux is[140]

(8) $\Delta T = \frac{P/cm}{2\pi r} \cdot \frac{1}{k} \sqrt{\frac{4\ \alpha \Delta t}{\pi}} \simeq 5.7°K$

Similarly, the heat diffusion time out each end of the center conductors can be estimated from equation (7)

(9) $\Delta t = \frac{\Delta x^2}{\alpha} \simeq 17$ hours

which is much longer than any run, and the heat simply piles up as in equation (4).

For sufficiently large surface temperature (≈830°K), black body radiation[141]

(10) $P/cm^2 = \sigma\ \varepsilon\ T^4\ (°K) \simeq .27\ W/cm^2$

where $\sigma = 5.67\ 10^{-12}\ \frac{W}{cm^2\ °K^4}$ and $\varepsilon \simeq .1$, radiation becomes important ($P/cm^2 \simeq .09\ W/cm^2$ during conditioning), and the surface temperature is not likely to reach the 10^{-8} torr vapor point.

Three basic types of electrical breakdowns can occur in the vacuum feeder: electron cyclotron, multipactor, and avalanche breakdown. Electron cyclotron breakdown occurs in high electric fields where

(11) $f_o = \frac{2\pi eB}{M} \cong 100$ MHz at $B_o \simeq 36$ gauss

The Alcator fringe fields are greater than 36 G, but in any case, a simple coil could easily be wound around the feeders (B parallel to the feeders) to increase the magnetic field. 200 dc amperes pulsed could also be injected in the center conductors (from an RF feedthrough in the resonator) to produce a "poloidal" field, also possibly increasing the threshold of avalanche and multipactor breakdown. The drawback is the significant IXB force on the antenna center conductor. For 200 amperes, 60 kG, and 10 cm, the force is

$$(12) \quad F = IB\ell \simeq 120 \text{ newtons} \simeq 27 \text{ lbs}$$

and the average poloidal magnetic field is

$$(13) \quad B_p = \frac{I\,\mu_o}{2\pi r} \simeq 42 \text{ gauss}$$

The time varying tokamak magnetic fields also induce voltages and currents in the antenna feeders,

$$(14) \quad V = -A\,\frac{\partial B}{\partial t} \simeq .03 \text{ Volts}$$

$$(15) \quad I = \frac{V}{R} = \frac{V\,\sigma\,\pi\,r^2}{L} \simeq 2.0 \text{ amperes}$$

where we assumed $A \simeq 50\ \text{cm}^2$, $\frac{\partial B}{\partial t} \simeq 6\text{T/sec}$, $\sigma_{ss} = 1.1 \times 10^6$ mho/meter, and therefore, are unimportant.

Multipactor occurs when the accelerated electron path length in an RF electric field becomes comparable to the electrode spacing.

$$(16) \quad m\ddot{x} = -e\,E_o \cos \omega t$$

$$x = \frac{e\,E_o}{m\omega^2} \cos \omega t$$

$$(17) \quad E_o = \frac{d\,m\,\omega^2}{2e} \simeq 900 \text{ V/cm}$$

$$P = 160 \text{ watts}$$

where we assumed $d = 2$ cm, 200 MHz, 50 Ω coax, and $R_R = 1\ \Omega$. The electrode must also have a secondary emission coefficient greater than one at about $W \simeq 2\,E_o d$, which is generally true for insulators, and in particular, for Al_2O_3, which has a peak coefficient of about 5, around 1 keV.[142] At low energy, the electrons cannot "knock out" secondary electrons, and at high energy, the electrons are buried too deeply in the material. Conductors and, in particular, silver, do not secondary emit easily, and the problem is most likely to occur only in the ceramic vacuum breaks.

For multipactor coefficients greater than one, the electric field[18] need not be in phase with the electron motion, and a whole range of electric fields are possible. In practice, multipactor can occur over several decades in power (α E^2), especially with long electrical breaks where several different multipactor regions are possible. Figure 8 is a dramatic example of how the antenna current can be almost totally suppressed by slightly lowering the power into the multipactor regime. Figure 7 compares the approximate experimental results with a more sophisticated multipactor model that takes into account the electron phase and the multipactor coefficient. A static magnetic field can greatly modify the electron motion, and thus multipactor. Insulating coatings with low secondary emission coefficient have been developed but were not necessary, since the effect could be circumvented with reasonably low (< 1 watt) and high (> 1 kW) powers.

The more commonly known avalanche breakdown can occur either inside or outside the vacuum, when electrons or ions are literally pulled out of the surfaces, forming large quantities of highly conducting ionized gas. The worst pressure region is in the high militorr range, slightly above the Alcator backfill pressure. To ensure high vacuum integrity and keep as much as possible of the RF feeder at high vacuum, a 30 liter ion pump was installed near the electrical breaks. The coax gas conductance in the molecular flow regime[80]

(18) $\lambda_{mfp} \approx 50$ cm >> D at 10^{-4} torr

(19) $U_c \approx 12.2 \frac{D^3}{L} \approx .44$ 1/sec << 30 liters/sec

where D ≈ 1.9 cm = average diameter, L ≈ 100 cm, and therefore the vacuum break pressure will be about an order of magnitude below the torus pressure.

On the other hand, the Faraday shield conductance is large

(20) $U_s \cong 11.7\ A_s$ liters/sec $\cong 100$ l/sec $>> U_c$

and the antenna remains at the torus pressure.

Figure 9 shows typical arcing conditions inside and outside the vacuum feeders. Arcs outside the vacuum are usually "stiff", and quickly crowbar the antenna current. Vacuum arcs can be either "stiff" or "soft", and are accompanied by large amounts of light inside the feeders.

A$_1$ Antenna Assembly in Alcator

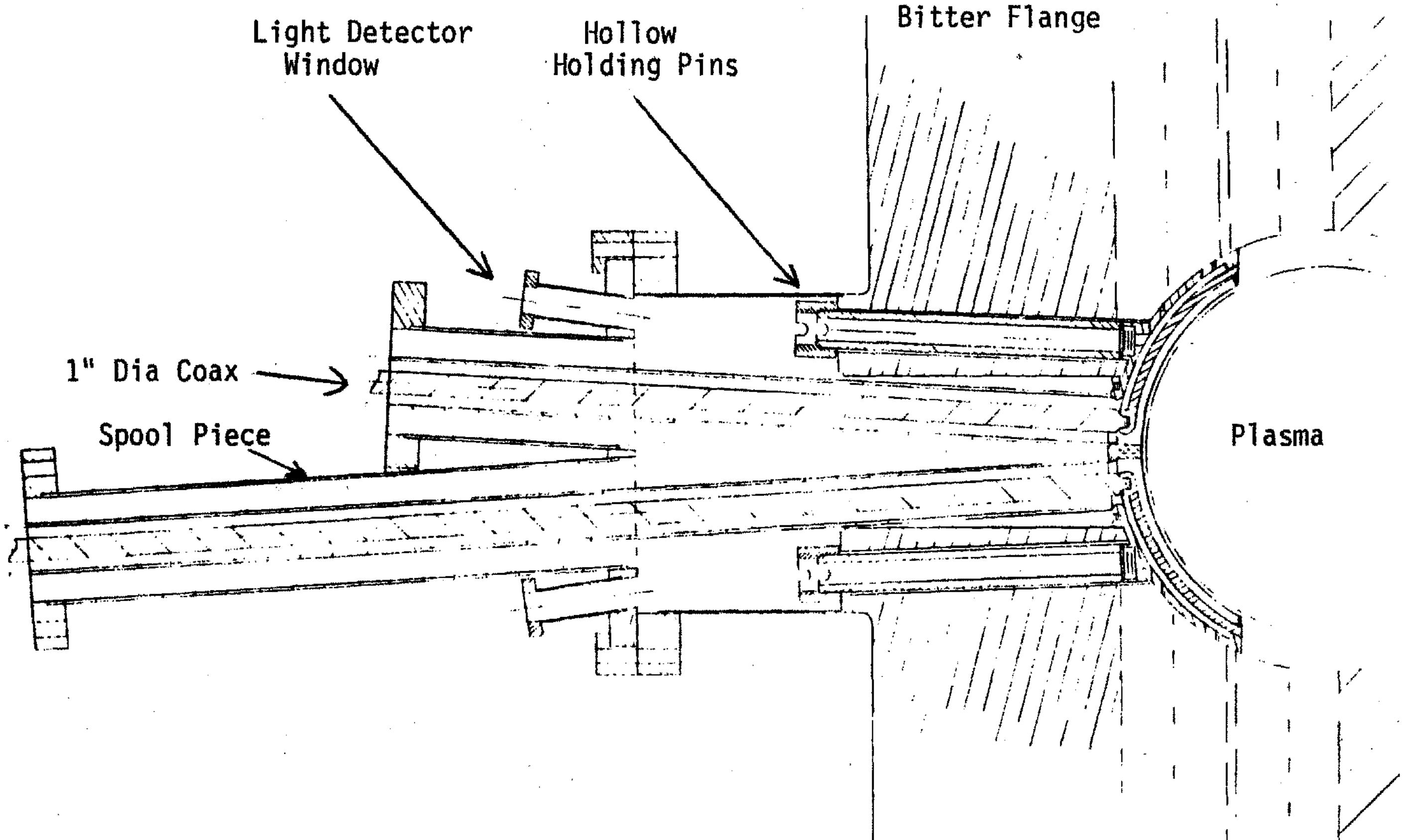

Figure 1

Mechanical Drawing of the A_1 Antenna

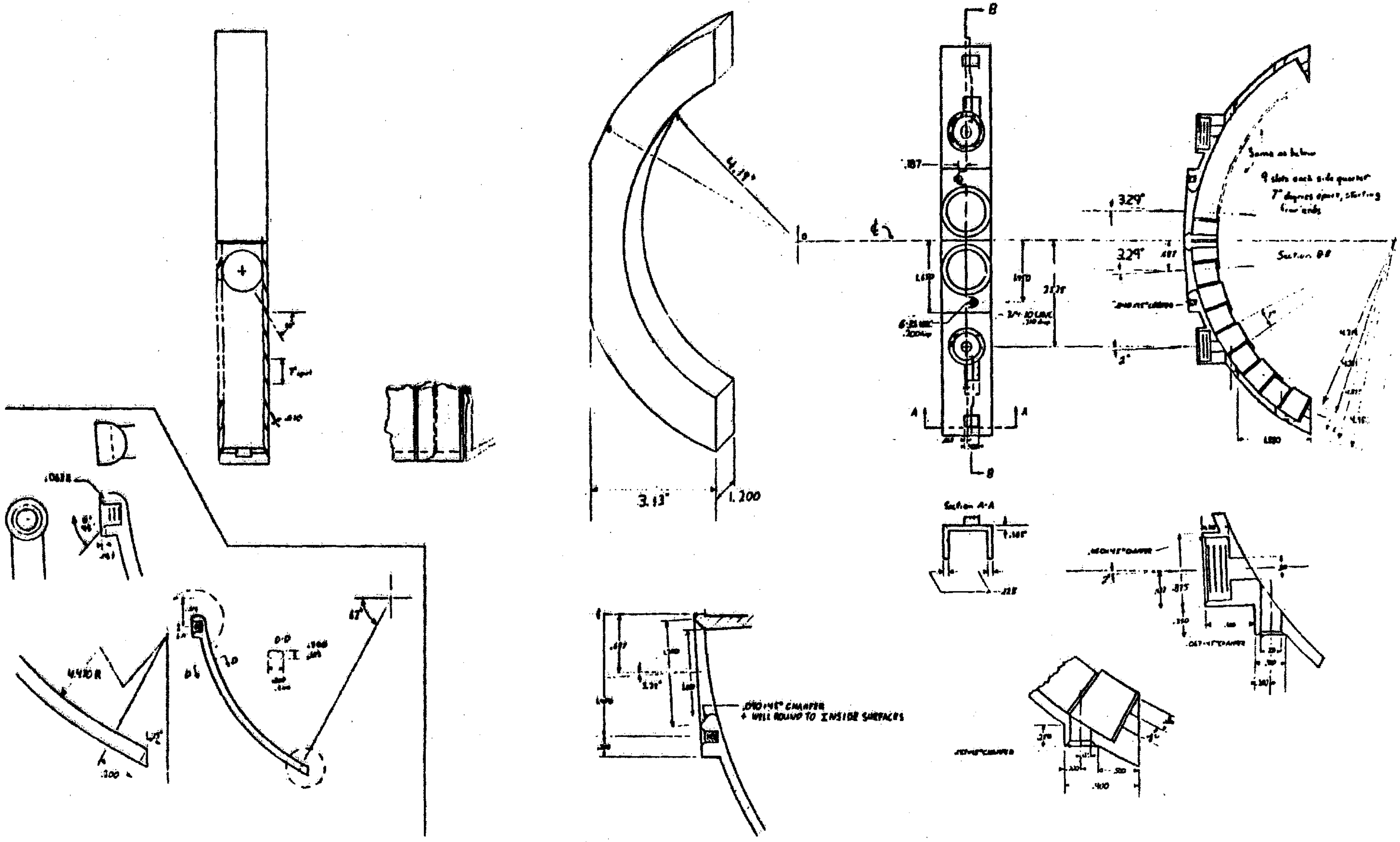

Figure 2

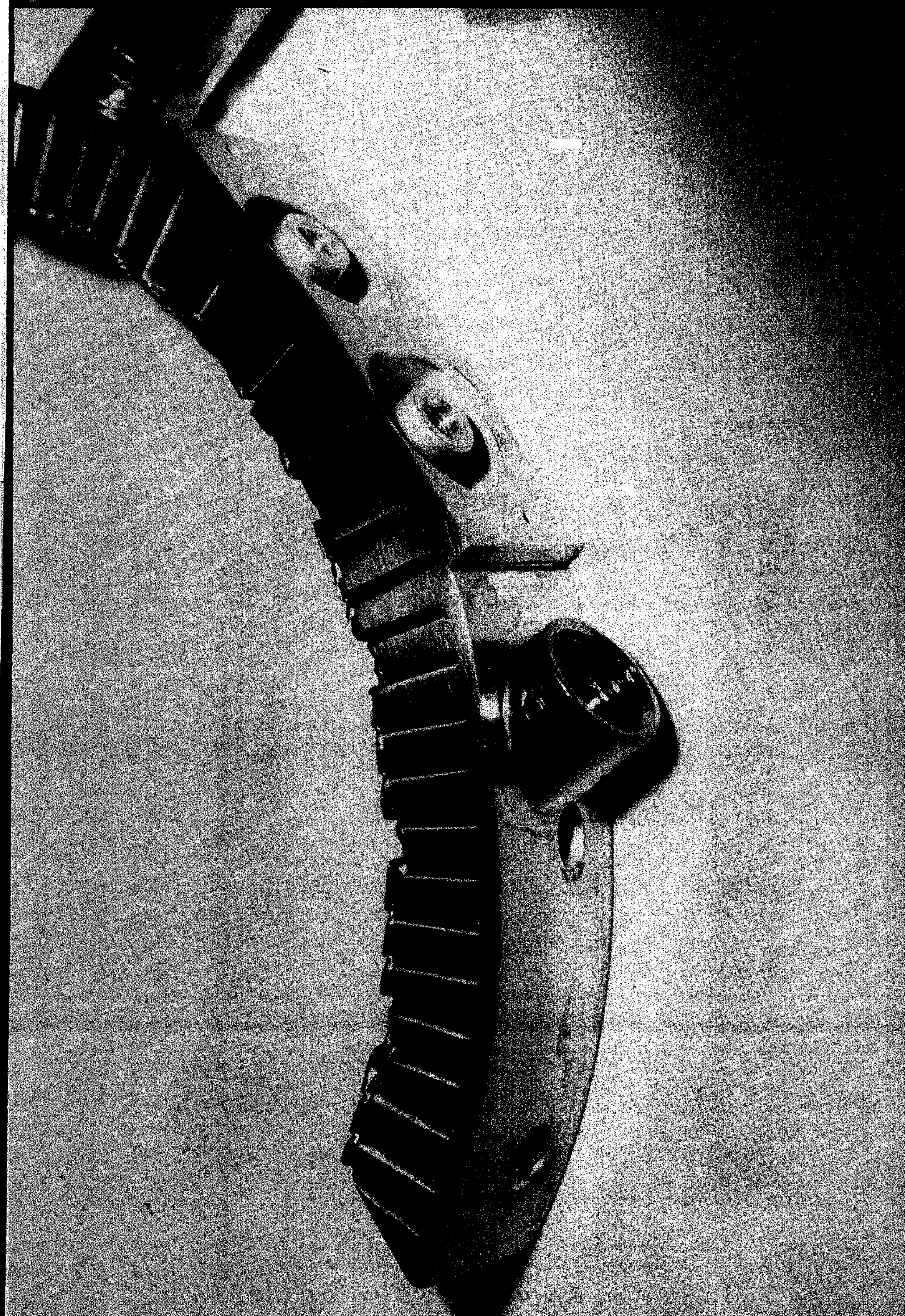

Backview of A_1 Antenna.

Figure 3

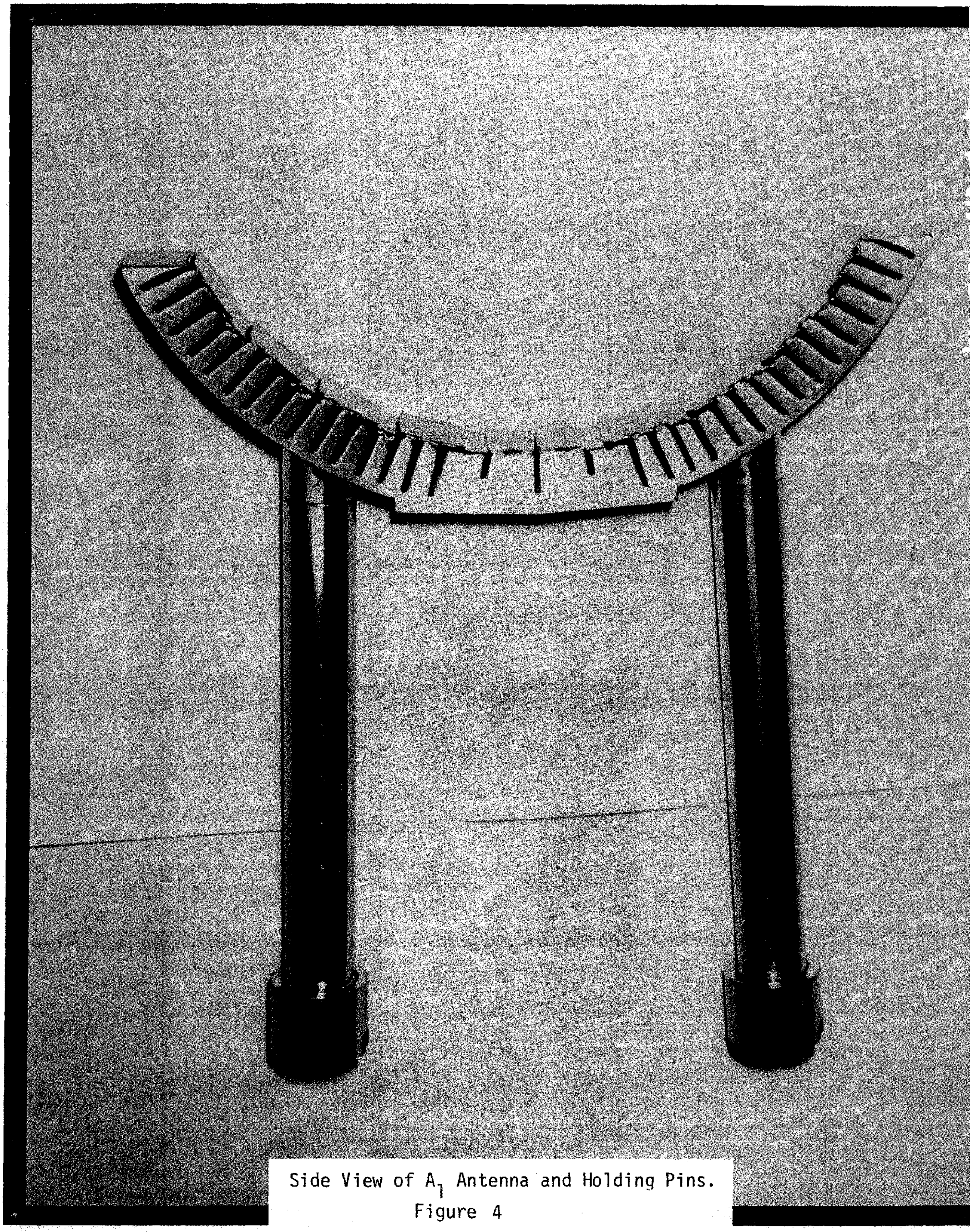

Side View of A_1 Antenna and Holding Pins.
Figure 4

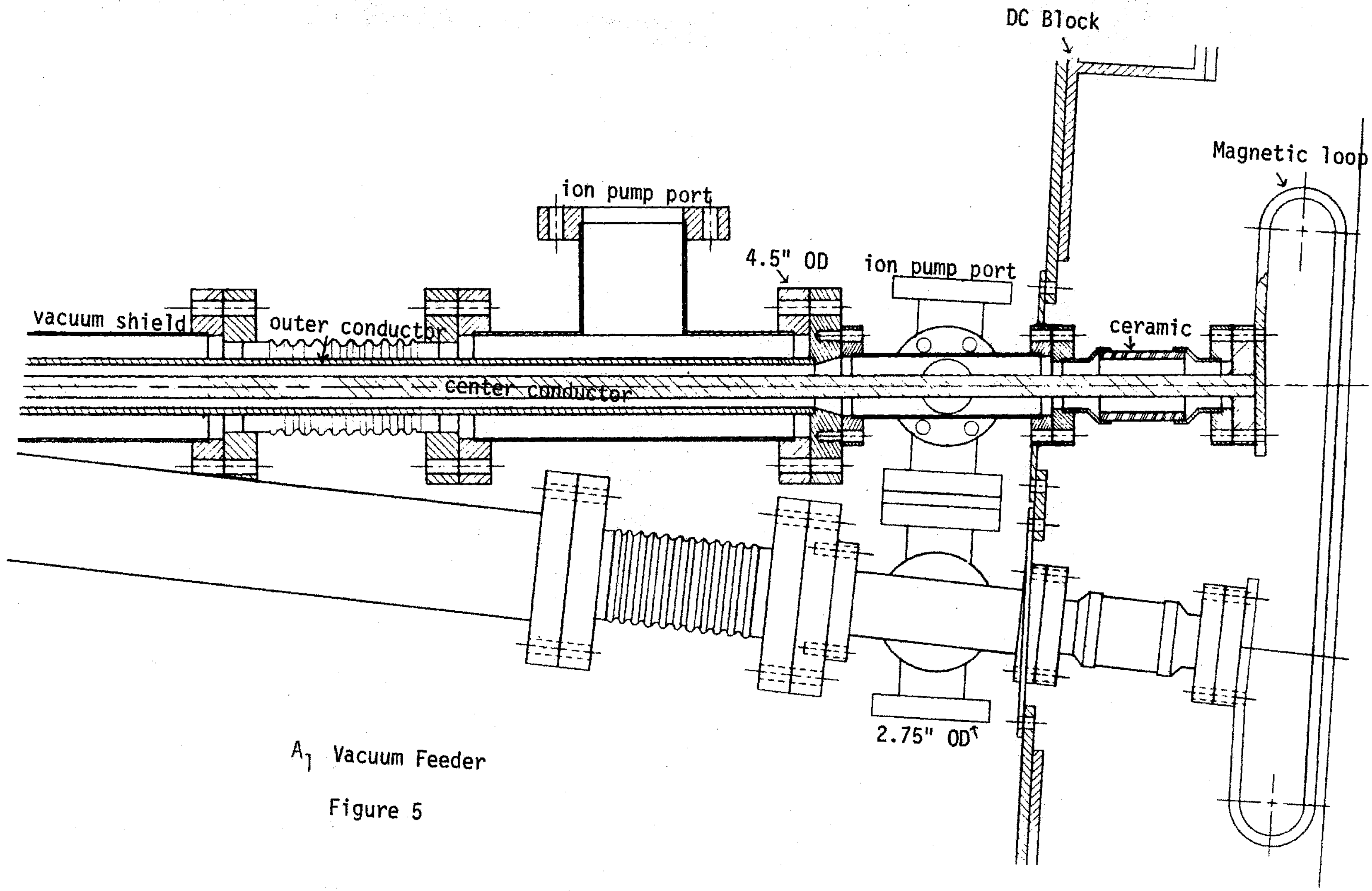

A_1 Vacuum Feeder

Figure 5

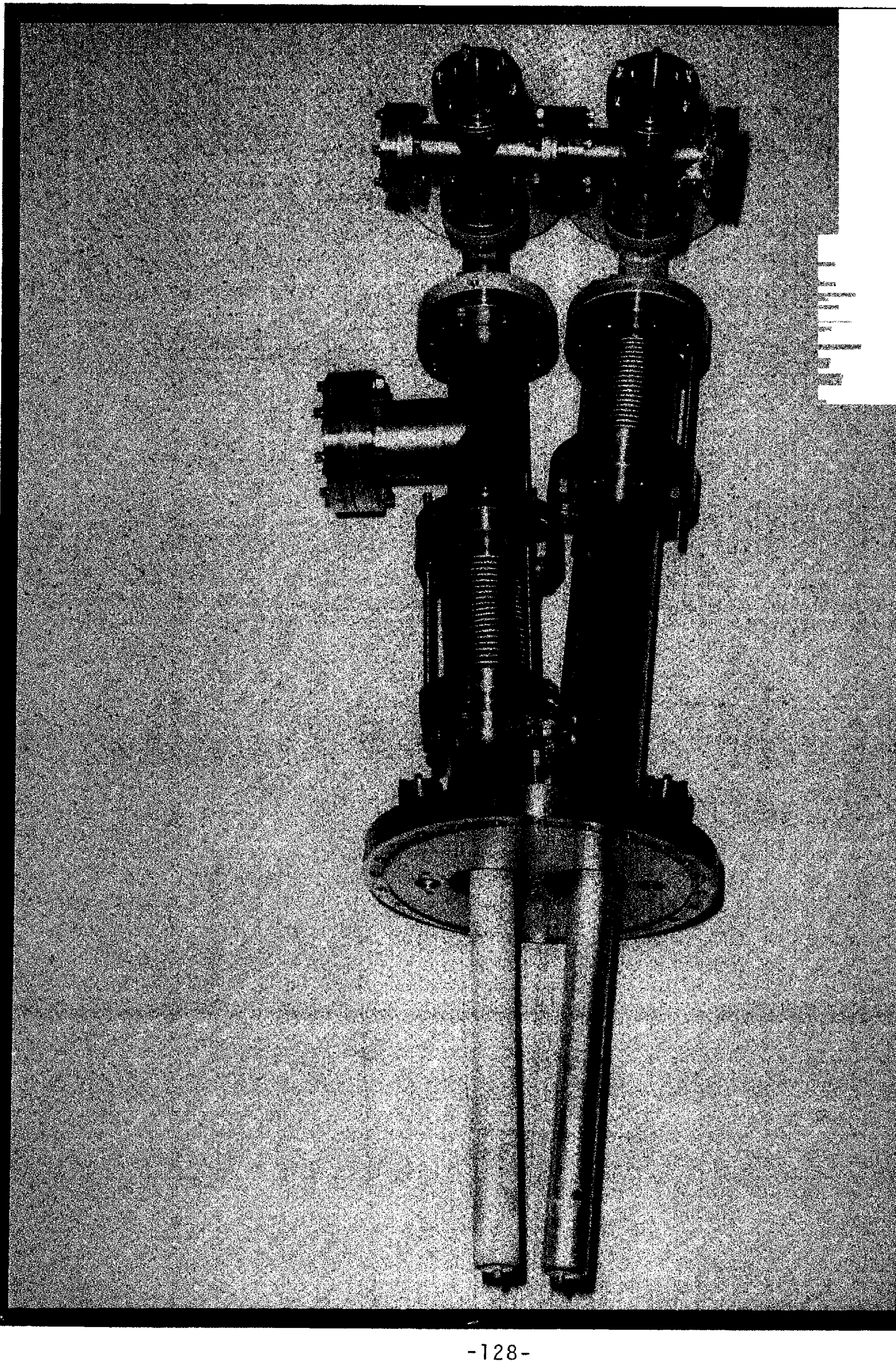

A_1 Vacuum Feeder Without Electrical Breaks.

Figure 6

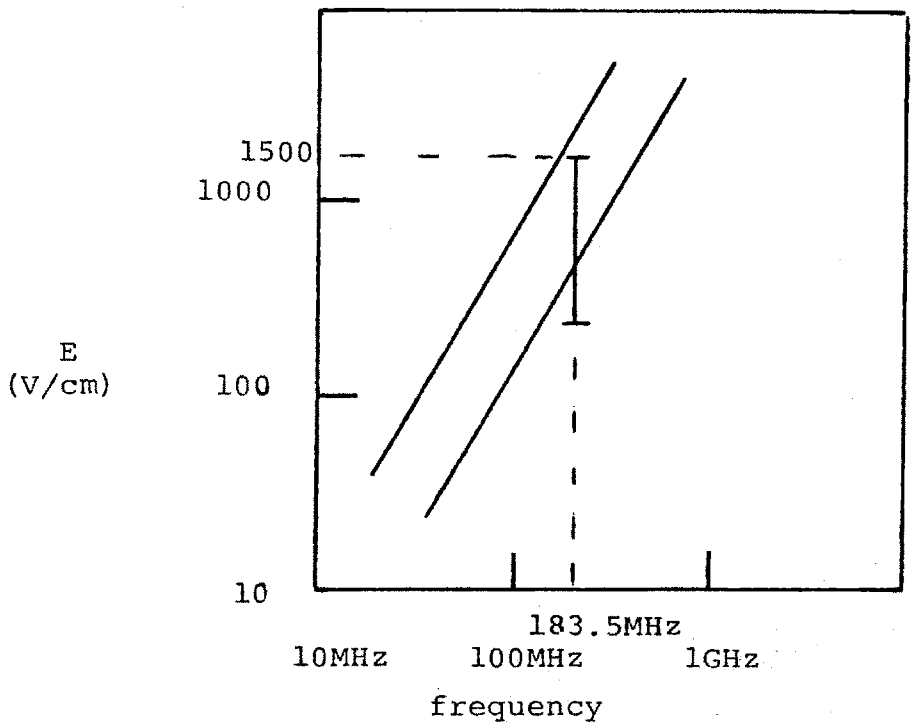

MULTIPACTOR REGIME

from TEPR-1

PPPL 1977

Figure 7

ABOVE MULTIPACTOR REGIME

BELOW MULTIPACTOR REGIME

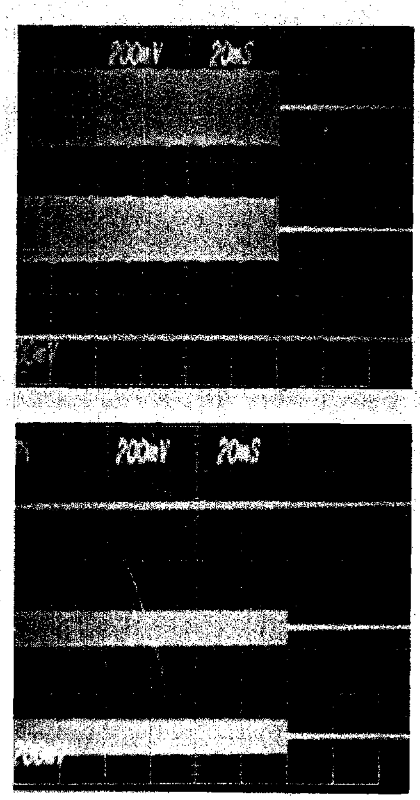

I = 32 amperes rms

V_F = 350 watts

V_R

I_A

V_F

V_R

Figure 8

Electrical Break
Arcs with New
Long Breaks

3/20/80

Normal Operation

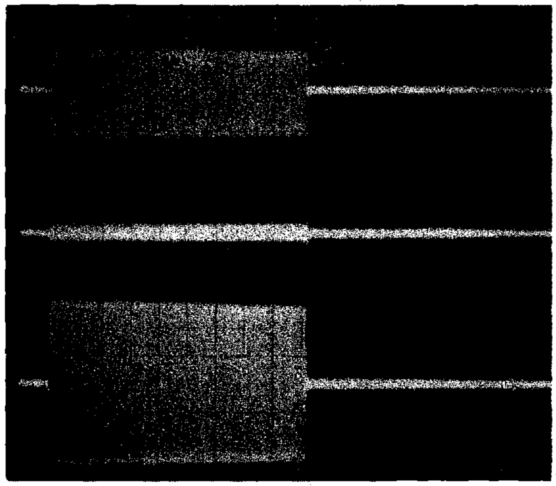

V_F

V_R

$I_a = 6V_{pp} \times 32.5\ A_{rms}/V_{pp}$
$= 195\ A_{rms}$

Arc Outside Coax

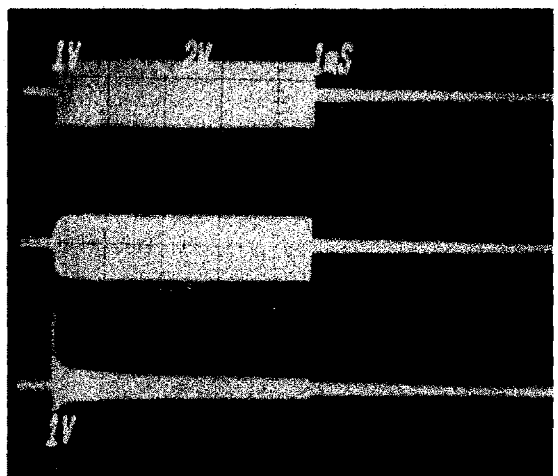

V_F

V_R

I_a

Arc Inside Coax

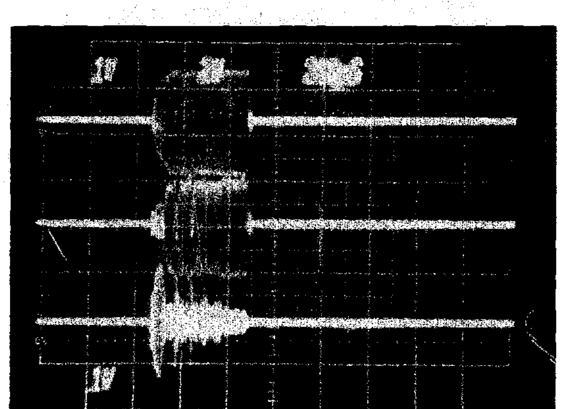

V_F

V_R

I_a

Figure 9

III-2.3. Matching resonator

The Alcator A matching system used a simple high power resonator (Figure 1).[72] Since space was not a constraint, the 13" square coaxial resonator was built large enough to accommodate almost any frequency (45-360 MHz), any resistive or reactive loading resistance (.5 Ω to 50 Ω), and either m=0 or m=1 phasing for powers up to the megawatt level. The resonator was also used as a high RF voltage test stand for electrical break development.

The basic matching system can be illustrated with a simple,half wavelength resonator (Figure 2) with a load R at $z = \lambda/2$. The field components are then[72]

(1) $V(z) = V_o \sin kz \cos \omega t$

(2) $I(z) = \frac{-V_o}{Z_o} \cos kz \sin \omega t$

At resonance, the impedence at the tap point z = d is purely resistive. From conservation of power and proper match,

(3) $\frac{V^2(d)}{Z_o} = I^2 (\lambda/2) R$

and substituting (1) and (2) into (3), we have

(4) $\frac{V_o^2 \sin^2 kd}{Z_o} = \frac{V_o^2 R}{Z_o^2}$

and the tap point angle

(5) $kd \simeq \sqrt{\frac{R}{Z_o}} \simeq 8° \text{ for } R = 1\ \Omega \text{ and } Z_o\ 50\ \Omega$

$\simeq 26° \text{ for } R = 10\Omega \text{ and } Z_o\ 50\ \Omega$

The actual resonator used was a combination of three overcoupled resonators as shown in Figures 3 and 4. At 200 MHz, the vacuum feeders are about a wavelength long, and a voltage minimum in the main resonator is tuned to half way between the antenna feeders. The input tap angle is calculated again from (5). Three conditions must be met for proper tuning. First, the system must be resonant, second, the top and bottom currents must be roughly equal, and third, the tap angle must be set for proper match. These three conditions can be met by the three moveable components; top plate, bottom plate, and tap angle. Unfortunately, the three degrees of freedom are not orthogonal, and expertise must be developed for quick, accurate tuning. A number of diagnostic current loop and capacitive probes are located in the matching system, in particular, on the top and bottom tuning plates, near the vacuum feedthrough and, of course, in the antenna.

At 90 MHz, the feeders are only $\lambda/2$, and the resonator is $3/4\ \lambda$, with the bottom shorting plate removed. Other similar resonant modes are also possible, especially at the higher frequencies.

Figure 5 is a much more general model of the resonator system that is valid, even off tune. Using the general lossless transmission line impedence transformation formula

$$(6) \qquad Z_x = Z_o \frac{Z_L + i\, Z_o \tan k\ell}{Z_o + i\, Z_L \tan k\ell}$$

the impedence of each half of the antenna, $Z_L = Z_1 = R_R/2$, is transformed over a distance $\ell = A$, to a new, complex impedence, $Z_x = Z_2$. Similarly, the lower circuit $Z_L = 0$ is transformed to Z_3. Z_3 and Z_2 are combined to give Z_4, which, in turn, is transformed to Z_5, and so on until Z_9, which will be pure, real 50 Ω if the system is in tune.

The vacuum feeders can also be run in the push-push mode by tying the two feeders together, coupling capacitively, and displacing the lower voltage node in the resonator. Balance is guaranteed by symmetry, only two degrees of freedom are necessary, and the system becomes much easier to tune.

Figure 6 shows the basic mechanical layout of the resonator box, coupler box, and the one stage capacitive DC break between the vacuum feeders and the grounded resonator. Figure 7 shows the top plate and center conductor tap angle remote control drive mechanisms. Figure 8 shows the top shorting plate and tap angle center conductor bellows. The resonator is built of 1/4 inch machined and silver plated copper plate. The resonator must be extremely RF leak tight, since for 200 amperes of push-push antenna current 400 amperes circulate in the resonator, corresponding to 20 kV RF and 8.0 megawatts of reactive power. Even under these circumstances, as we calculated earlier in Section III-1.2, the RF leakage is much less than 10^{-6} watts/cm^2.

Side View of 13 inch Diameter Coaxial Resonator

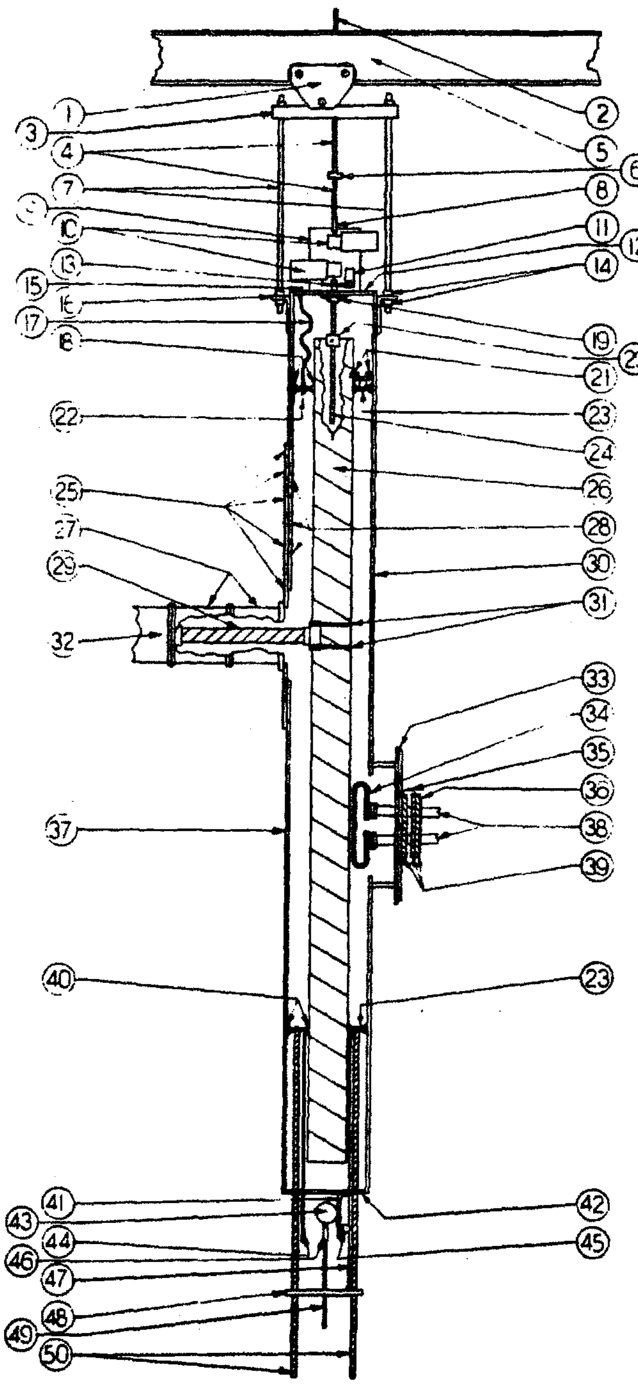

1. DOLLY
2. ROD TO TUNING PLATES - SEE 50
3. U-CHANNEL SUPPORT RAIL
4. THREADED ROD
5. I-BEAM: BOLTED TO CEILING
6. SEE 48
7. HANGING RODS
8. COUPLING PIECE: MOTOR TO THRD. ROD
9. MOUNTING BRACKET
10. A.C. MOTORS: 45 RPM
11. POTENTIOMETER
12. TOP PLATE
13. BELT: POT. TO MOTOR DRIVE SHAFT
14. LOCKING HEX NUTS
15. FEEDTHROUGH FOR RF PROBE
16. HANGERS OF RESONATOR BOX
17. RG8 50Ω FLEXIBLE COAX
18. FINGERSTOCK
19. BEARING
20. TAPPED BAR FIXED TO CEN. CONDUCTOR
21. TEFLON GUIDE BLOCKS
22. RF PROBE
23. UPPER, LOWER TUNING PLATES
24. THREADED ROD: TO MOTOR
25. COVER PLATES
26. CENTER CONDUCTOR
27. OUTER SHELLS OF 9 COAXIAL LINE
28. RF SEALING PLATES
29. FLEXIBLE BELLOWS (INNER CONDUCTOR)
30. SIDE PLATE
31. HOSE CLAMPS
32. 9" COAXIAL TRANSMISSION LINE
33. MYLAR ELECTRICAL BREAK
34. COUPLER
35. RF BELLOWS
36. ANTENNA/RESONATOR ADAPTOR
37. SIDE PLATE
38. ANTENNA FEEDING COAX
39. CLAMPING PLATES FOR RF BELLOWS
40. FINGERSTOCK
41. SEE 9
42. BOTTOM PLATE
43. SEE 10
44. DEFLECTION MEASURING STICK
45. POTENTIOMETER
46. SEE 8
47. LINE AROUND POT. TO TUNING PLATE
48. TAPPED BAR CLAMPS RODS (SEE 50)
49. THREADED ROD
50. RODS TO TUNING PLATES

Figure 1

Resonator Waveform

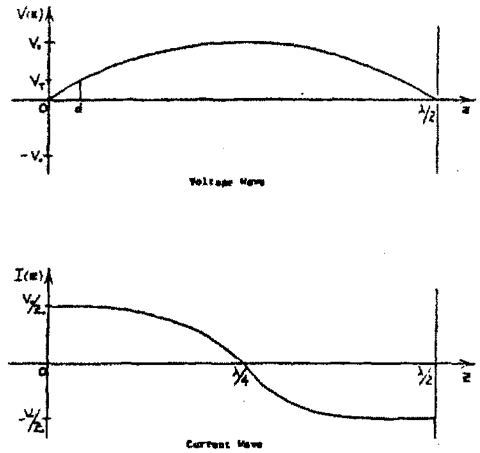

Figure 2

180 MHz Current Waveform

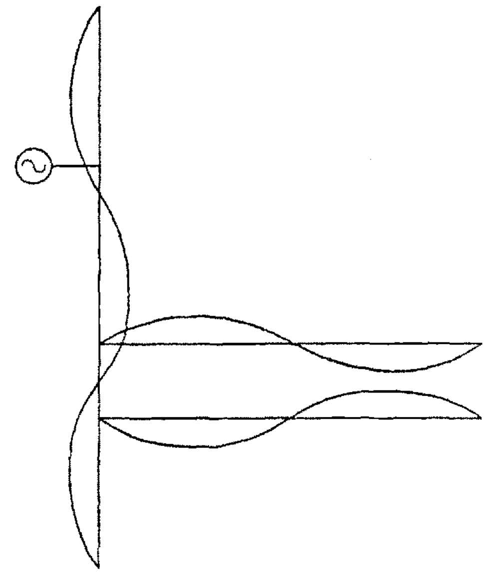

Figure 3

90 MHz Waveform

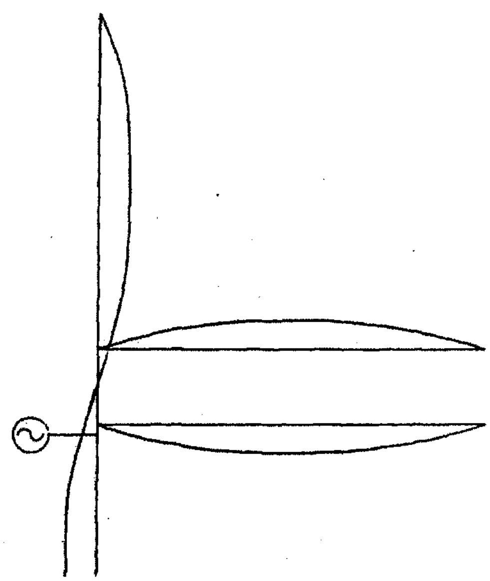

Figure 4

General Resonator Model

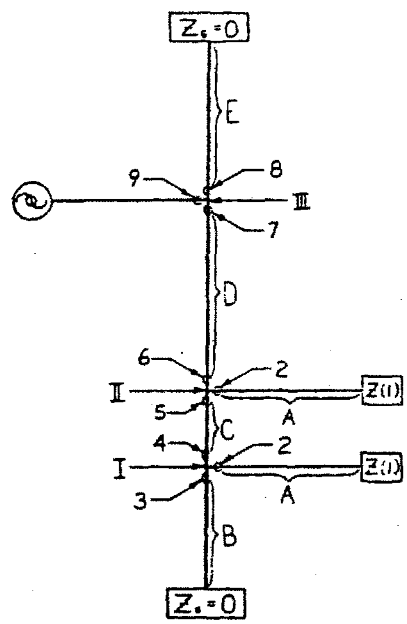

Figure 5

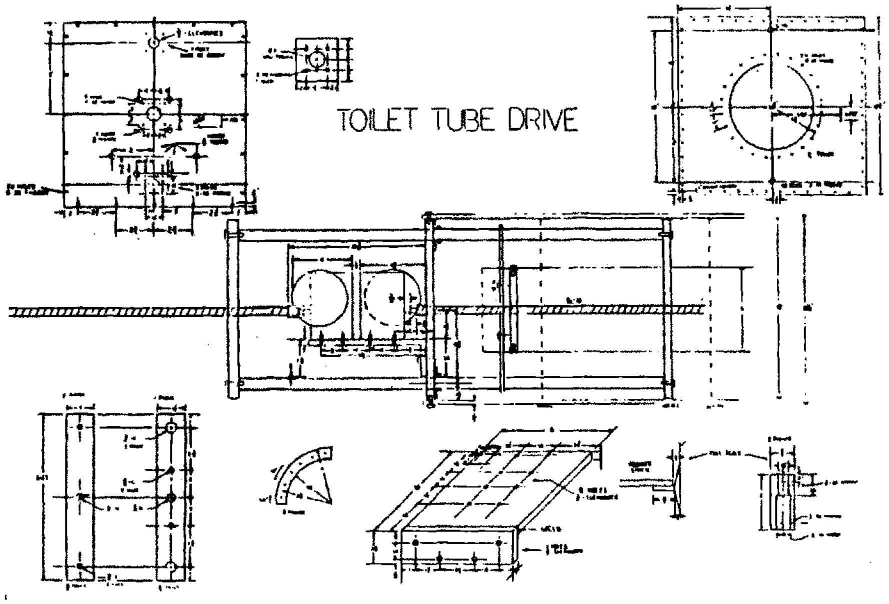

Resonator Drive Mechanism

Figure 7

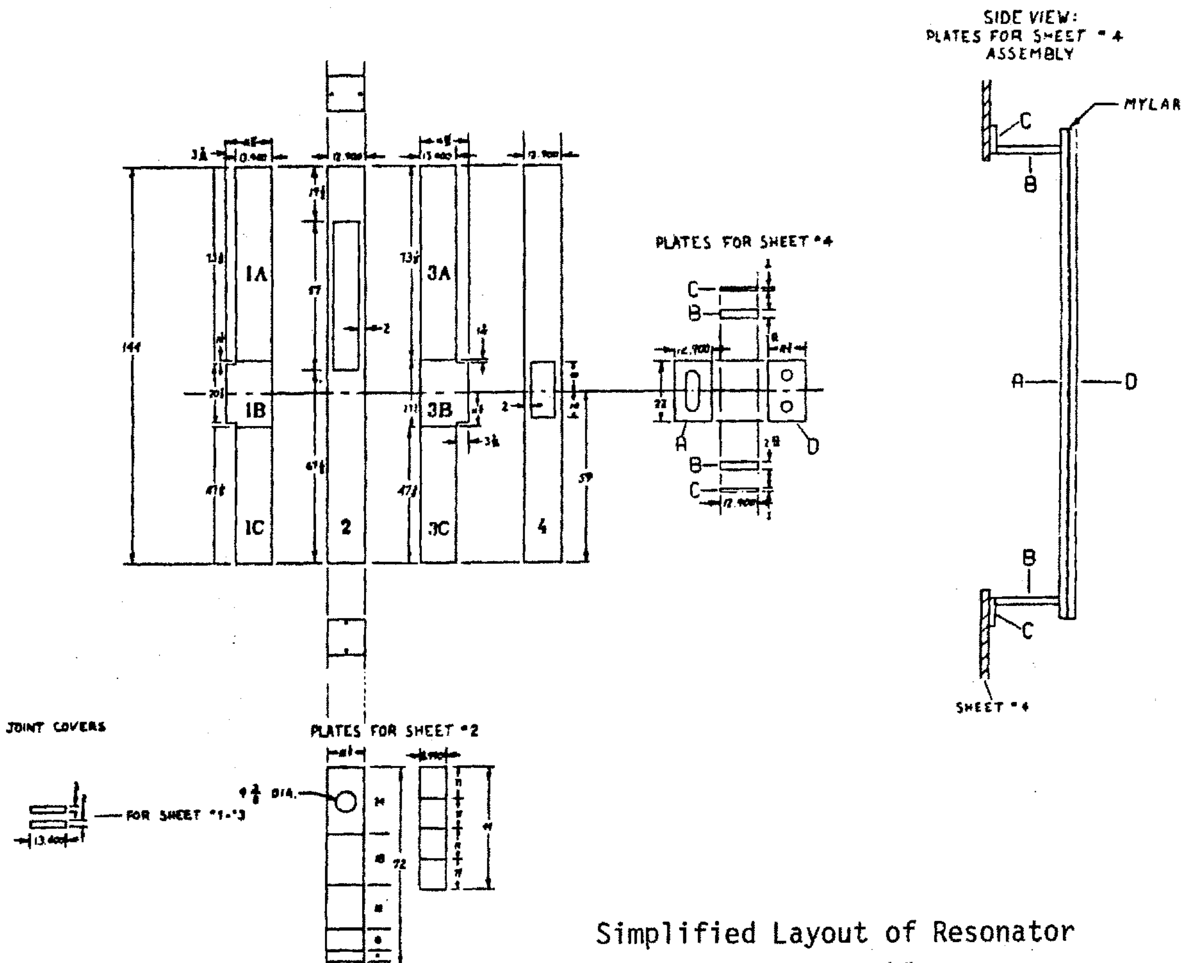

Simplified Layout of Resonator
and DC Block Assembly

Figure 6

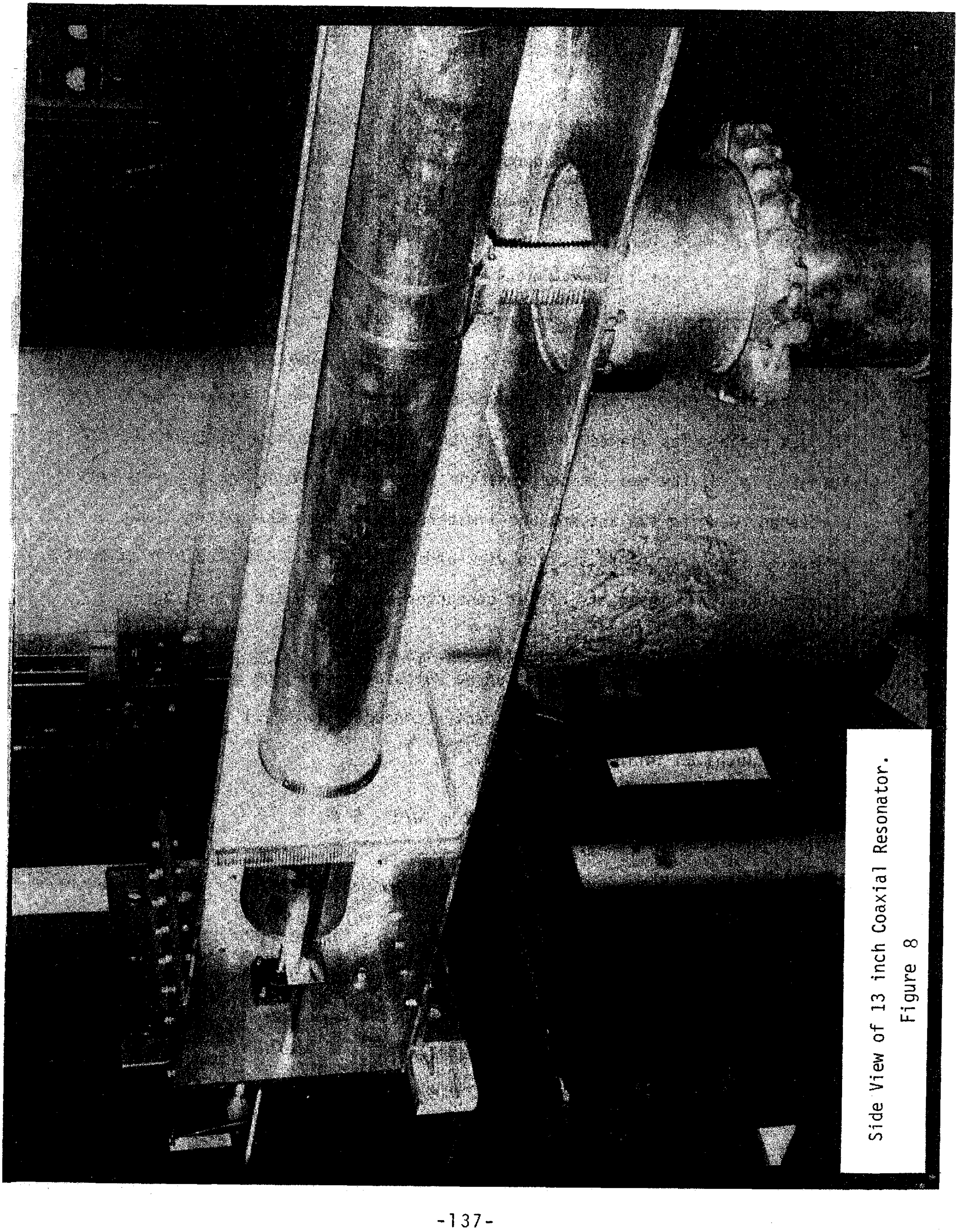

Side View of 13 inch Coaxial Resonator.
Figure 8

III-2.4. A_2 antenna system

To increase power coupling capability, a new antenna, A_2, was built with the same backplane and diagnostics as A_1, but with a loop area 2.5 times larger. The plasma radius was reduced from 10 cm to 9 cm, and slotted side limiters were installed on each side of the antenna, as can be seen in Figures 1, 2, 3, and III-2.1.(1).

The slotted side limiters were similar to the A_1 Faraday shield, and were held in place by thin flexible stainless steel arms. These limiters were installed first, then the antenna and current probes. When proper fit was reached (as viewed from a .5 inch flexible boroscope through the top keyhole Fig. 3), the two limiter arms and two hollow antenna holding pins were tightened, wedging the antenna and limiters securely to the Bitter flange, as can be seen from cross section view of Figure III-2.1.(1). The high current carrying region between the center conductor and back plane was silver-plated as A_1.

The impedence of the antenna can be calculated from the approximate semiempirical formula for a narrow center conductor ($w \simeq 1.1$ inch) over ($d \simeq .54$ inch) an infinite backplane.[135]

$$(1) \quad Z \simeq 125 - 116 \log_{10} (w/d) \text{ for } .2 < w/d < 5$$
$$\simeq 90\ \Omega$$

To calibrate the antenna current loop probes, the test set schematically shown in Figure 4 was used. The antenna with its limiters and probes were mounted in an aluminum cylinder simulating the vaccum vessel. A 50Ω terminated oscillator, directional coupler and coax were then connected to the antenna coax seat through a special adaptor.

The currents and voltages at the antenna are (Figure 4)

(2) $I_b = I_a \cos \theta_a$

(3) $V_b = I_a Z_a \sin \theta_a$

where $\theta_a = k\,\ell/2 \approx 22.5°$ at 200 MHz.

Similarly, on the coax side of the antenna-coax boundary

(4) $I_b = I_o \cos \theta_o$

(5) $V_b = I_o Z_o \sin \theta_o$

Equating (2) and (4), (3) and (5), and dividing the two results, we have

(6) $Z_a \tan \theta_a = Z_o \tan \theta_o$

(7) $\theta_o \approx 36.7°$

From (2), (4) and (7), we finally have

(8) $I_A = \frac{\text{Cos } \theta_o}{\text{Cos } \theta_a} I_o = .86\ I_o \cong I_o$

For practical purposes, we will assume

(9) $I_a \approx \frac{V_f + V_r}{50} \approx \frac{2V_f}{50}$

and the calibration factor

(10) $C_p = \frac{I_a}{V_p} \approx \frac{V_f}{25\ V_p} \approx$ 6.7 amps/volt at 200 MHz (typical)

To increase the voltage and power capability, a much larger (compared to the first version (Figure 6)) pair of electrical breaks was also installed (Figure 7). Although several times longer, these new feedthroughs could only carry about twice the power, since the thin, long exposed center conductors in the electrical breaks had a very high impedence, and unnecessarily increased the local RF potential. It is believed that the power capability could have been increased by simply enlarging the center-conductors of the new electrical breaks. The electrical breaks were "effectively" shortened (as in Figure 8) by shorting the first half of the electrical break with aluminum foil, resulting in an almost identical current carrying capability.

After elaborate testing of many electrical breaks, materials and geometries, it was consistently found that RF breakdown was several times more severe than DC (arcs 6 inches long between feeders were common), and always occurred on sharp edges. The most common and difficult to solve problem was at the metalized surface of the insulator, where the brazing thins out to a sharp knife edge. Several epoxies and corona rings were tested with some success (factors of 1.5 - 2 in antenna current) to cover these edges, but the main drawback was that, once breakdown occurred, the voltage standoff was greatly decreased, and the breaks were very difficult to clean.

Another important factor is keeping the electric field at the metalized joints, into the ceramic, so that particles cannot acquire kinetic energy before colliding. Figure 9 shows a ceramic break compatible with the A_1 and A_2 feeders using this principle, and where the brazing is down in a groove at the end of the ceramic sleeve. High power RF electron tubes are usually built this way.

Several liquids were also tested to wet these edges, or even completely submerge the ceramic electrical break inside a leak tight teflon sleeve. The liquid had to be of very high dielectric strength, low Z, volatile solvent (in case of contamination of the tokamak), lossless (which, for all practical purposes, meant nonpolar), and nonflammable. Carbon tetrachloride met all these specifications with no major drawbacks, except that it is a known carcinogen, and great care must be taken to avoid personnel exposure.

Figure 10 is a simplified sketch of a flexible version of A_2 that could be used for low power tests, and inserted in any of the much smaller HCN or Thompson port side keyholes.

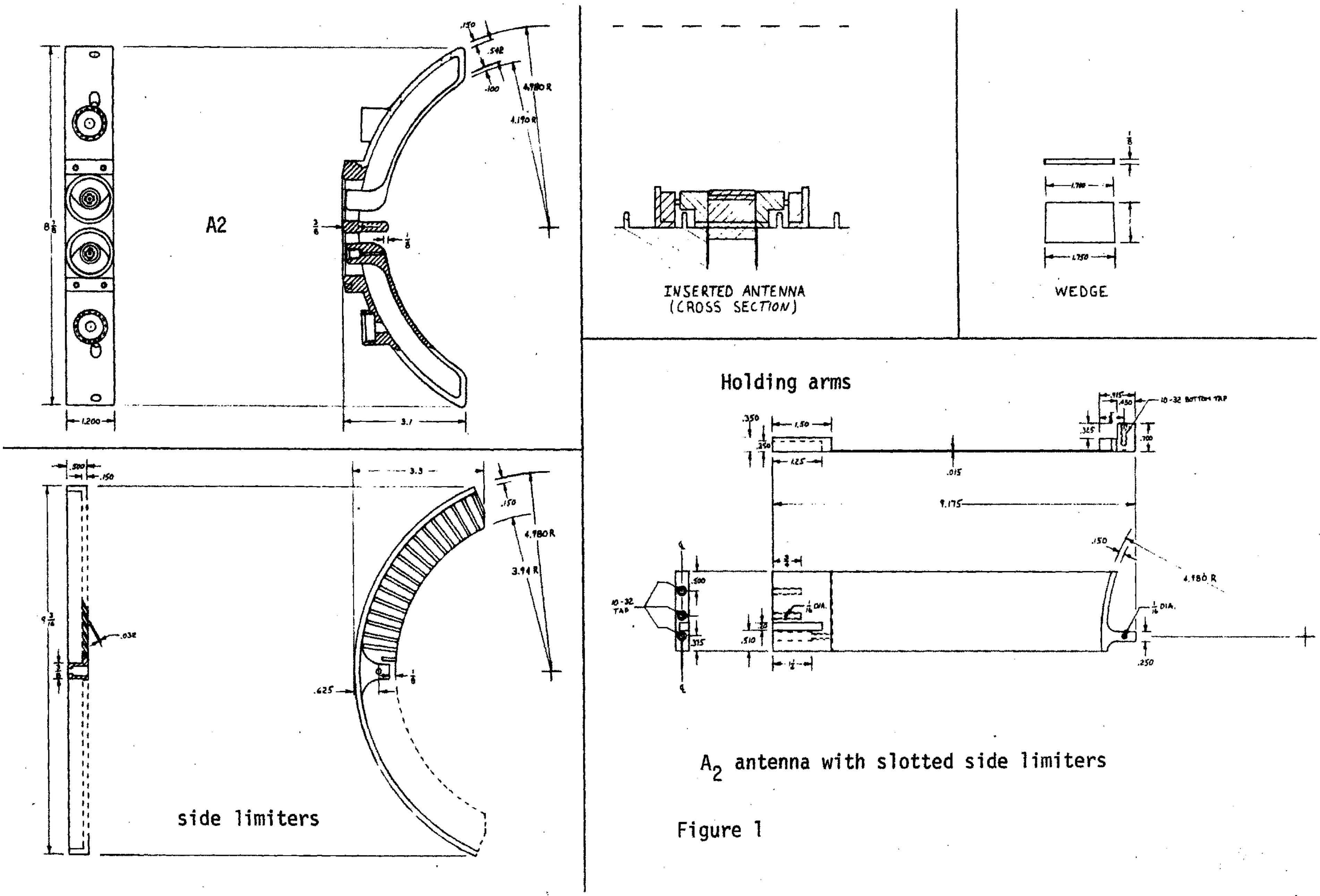

A_2 antenna with slotted side limiters

Figure 1

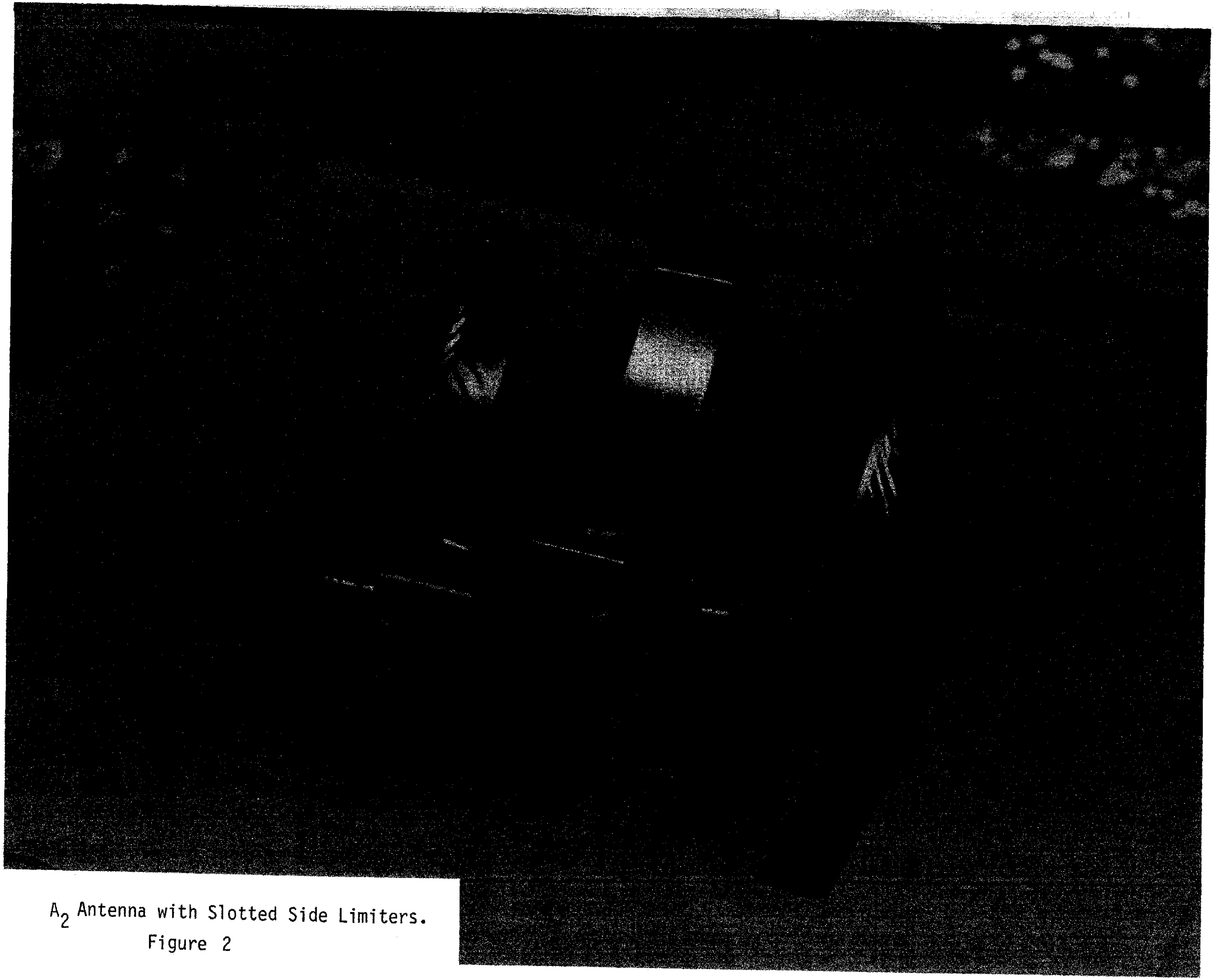

A_2 Antenna with Slotted Side Limiters.

Figure 2

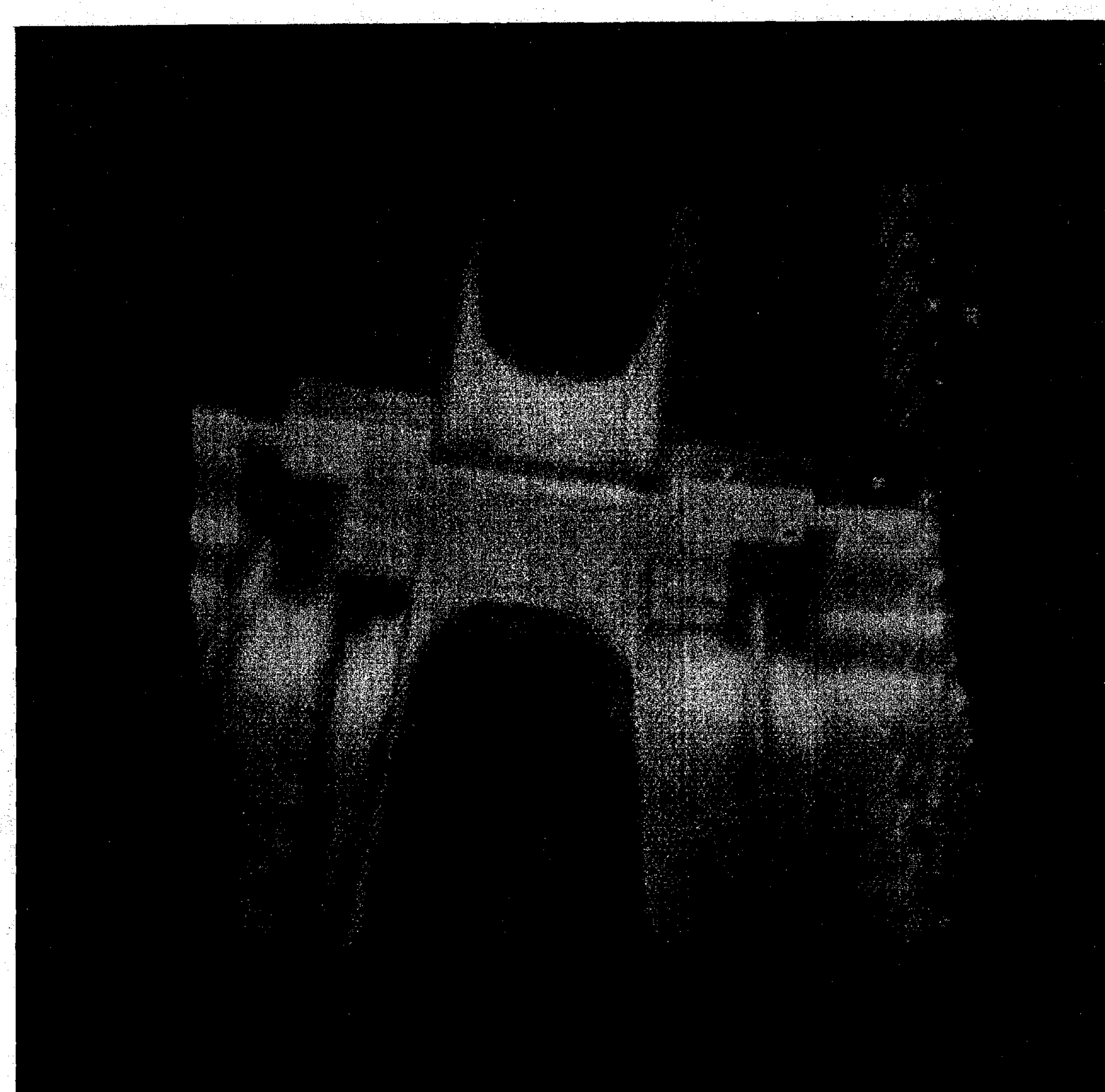

Boroscope View of A_2 Bridge Assembly Inside Alcator.

Figure 3

Antenna test stand model

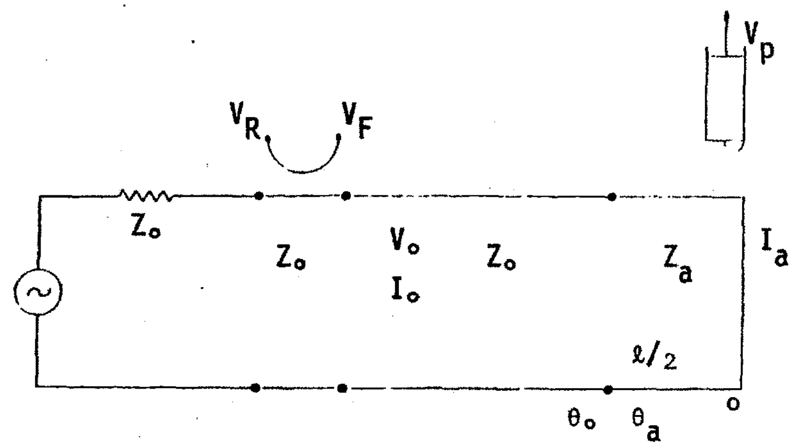

Figure 4

Probe test stand assembly

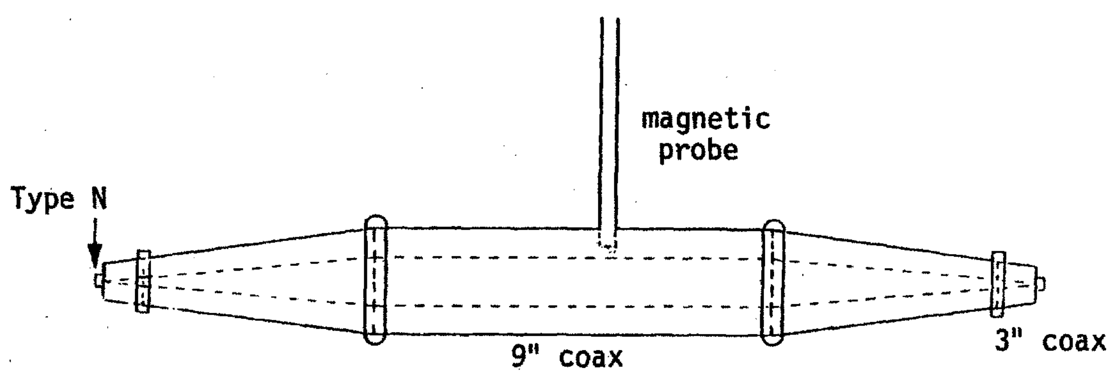

Figure 5

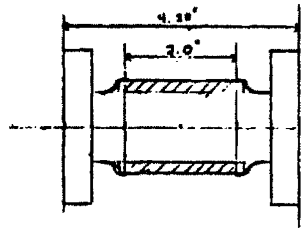

A_1 Vacuum Break

Figure 6

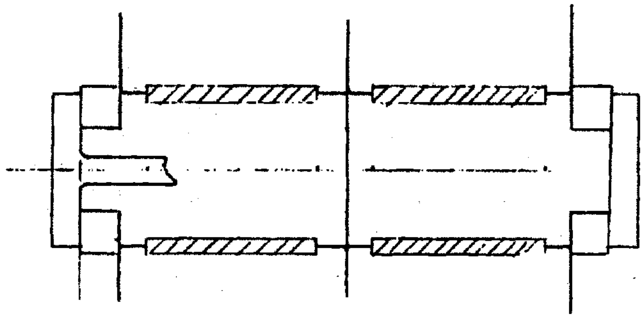

A_2 Vacuum Break

Figure 7

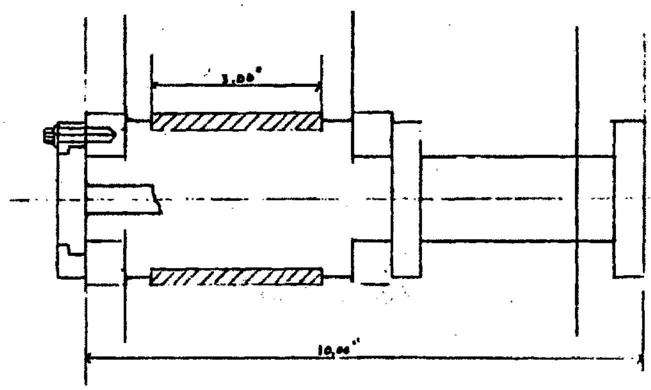

Short Vacuum Break

Figure 8

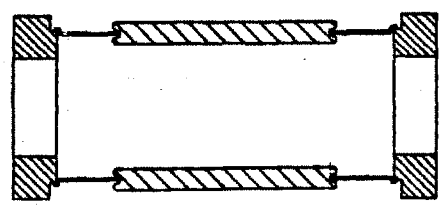

Improved Vacuum Break

Figure 9

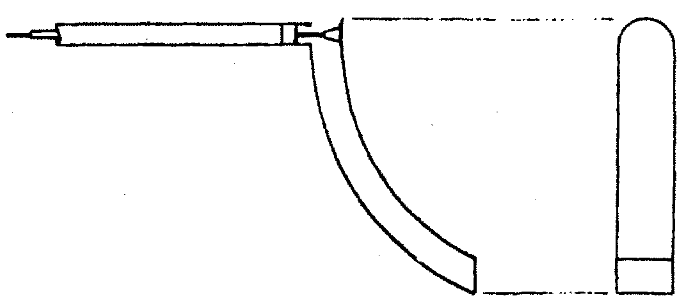

Flexible A_2 type antenna

Figure 10

III-2.5. A_4 antenna system and Faraday shields

The third antenna tested, A_4, is shown in Figures 1, 2 and III-2.1.(1). The backplane and side Faraday shield are from the old A_1 antenna. The center conductor was moved out like A_2, and a thick, dome-type Faraday shield front was added instead of the thin A_1 clips. Slightly higher (than A_2) slotted limiters were also added.

A radially scannable Langmuir probe, peeking through the front of the Faraday shield, was installed to measure the tenuous plasma near the antenna (Figure 1). The probe connections were made through an additional port on the already overcrowded 10 inch side port.

The purpose of the Faraday shield and side limiters is twofold. First, it keeps the tenuous plasma and, in particular, the particles streaming along the field lines out of the high electric field region of the antenna (kilovolts/cm), and second, it shorts out the unwanted E_z component of the antenna without affecting the E_θ components.

Two general rules of thumb can be formulated for the design of a Faraday shield that will not significantly shield out the desired B_z. First, the shield clip width should be much less than the center conductor to backplane distance. Careful examination of the clip geometry and the backplane currents shows that part of the backplane current will weave up the inside of the clip, about a distance equivalent to the clip width. This image current path will be unimportant only if it is low compared to the center conductor, and thus our first rule. In A_4, the clip width was 2.5 times less than d.

Second, the clip geometry must be designed so the magnetic energy stored in the gap between clips is less than the energy stored inside and outside of the shield. To see this we will, for simplicity, examine the magnetic energy of only the center conductor of a coaxial antenna. The stored energy is

$$(1) \quad W \equiv A \int_{r_1}^{r_2} (1/r)^2 \, dr = \left[\frac{1}{r_1} - \frac{1}{r_2}\right] A$$

where for typical Alcator values

inside shield	W_{in}	$= 2\,A$	$.25'' < r < .5''$
at shield	W_{at}	$= .33\,A$	$.5'' < r < .6''$
outside shield	W_{out}	$= 1.66\,A$	$.6'' < r < \infty$

For a good shield, the flux through the shield region is about the same as without the shield. With the same flux and a gap to width ratio, G, the energy density in the gap is increased by G^2, but the volume is decreased by G, so a net factor G remains. For A_4, $G = .25''/.032'' \simeq 8$, and the energy in the shield, W_{at}, becomes $8 \times .33 = 2.64 \simeq W_{in} \simeq W_{out}$, and a small reduction in flux can be expected as compared to A_2.

These rules came from a number of experiments on the simple, but very realistic, set up of Figure 3. Several stripline conductors of width w, length ℓ and height d above a large ground plane, were energized as in Figure III-2.4.(4). Several types of slotted and unslotted limiters and Faraday shields were also tested. Flux measurements at height h were made with a shielded magnetic probe (Figure III-3.2.(8).

Figure 4 shows how the magnetic field is independent of the center conductor width w, and decreases as $1/r^2$ as expected from the quasi-static near-field with $d << r << \lambda$

(2) $$B \propto \frac{1}{r_1} - \frac{1}{r_2} = \frac{1}{r - d} - \frac{1}{r + d} \simeq \frac{2d}{r^2}$$

Figure 5 shows the expected dramatic effect of Faraday shield clip width. Figures 6, 7, 8 and 9 are similar tests with A_1 and A_2 inside the cylindrical simulator. Figure 6 shows the weak effect of the slotted limiters spacing on A_2. Figures 8 and 9 show the flux ratio of A_1 to A_2 for carefully controlled conditions. Although the radiation resistance increases as flux squared ($4^2 = 16$), the plasma radius was decreased by a centimeter (from A_1 to A_2), and thus for large $k_\parallel \simeq .6$/cm, the evanescent edge layer is thicker and the resultant factor is only

(3) $$\frac{4^2}{e^{\cdot 6}} \simeq 8.8$$

A_4 had an effective flux about 30% less than A_2, as measured in the cylindrical simulator.

A side effect of a good Faraday shield is that the antenna becomes a slow wave structure. From transmission line theory,[134]

(4) $$V = \frac{1}{\sqrt{LC}}$$

(5) $$Z = \sqrt{\frac{L}{C}}$$

For a vacuum dielectric, A_4 geometry without the Faraday shield (Figure 1), and from equation III-2.4.(1) with w/d = .83

(6) $V = c = 3 \times 10^8$ m/s

(7) $Z = 134\ \Omega$

Combining (4) - (7) we have

(8) $C = \frac{1}{c\ Z} = 2.5 \times 10^{-11}$ F/m

(9) $L = \frac{Z}{c} = 4.5 \times 10^{-7}$ H/m

Adding the Faraday shield does not significantly change L, but the shield capacitance from Figure 1 is large

(10) $C_s \simeq 4.3 \times 10^{-11}$ F/m

The new phase velocity and impedence are now

(11) $V = \frac{1}{\sqrt{L(C + C_s)}} \simeq .6\ c$

(12) $Z = \sqrt{\frac{L}{C + C_s}} \simeq 81\Omega$

The impedence and phase velocity could be even further reduced by mounting large slotted knobs on the back plane or center conductor (the Faraday shield design rules apply here also) so as to increase the capacitance per unit length, but not the inductance and antenna loop flux.

Following the same procedure as in Section III-2.4.

(13) $\theta_a \simeq 37°$

(14) $\theta_o \simeq 51°$

(15) $I_{A4} = .79\ I_o = .92\ I_{A2} \simeq I_o$

and our current probe calibrations are still within reasonable error. Figure 7 is the calibration factor for the top and bottom A_4 current probes as a function of frequency. As expected, the calibration factor is nearly inversely proportional to frequency.

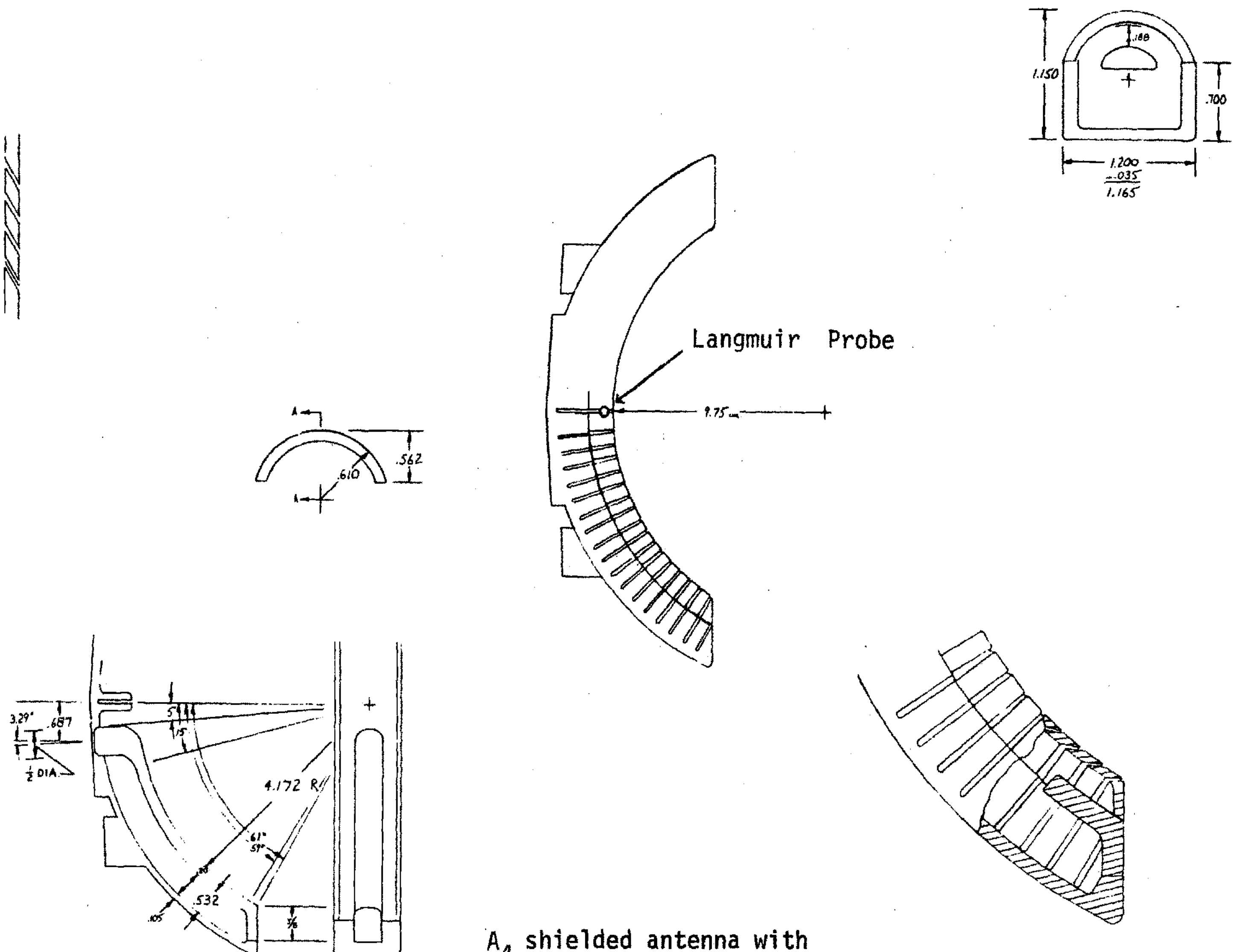

A_4 shielded antenna with
slotted side limiters

Figure 1

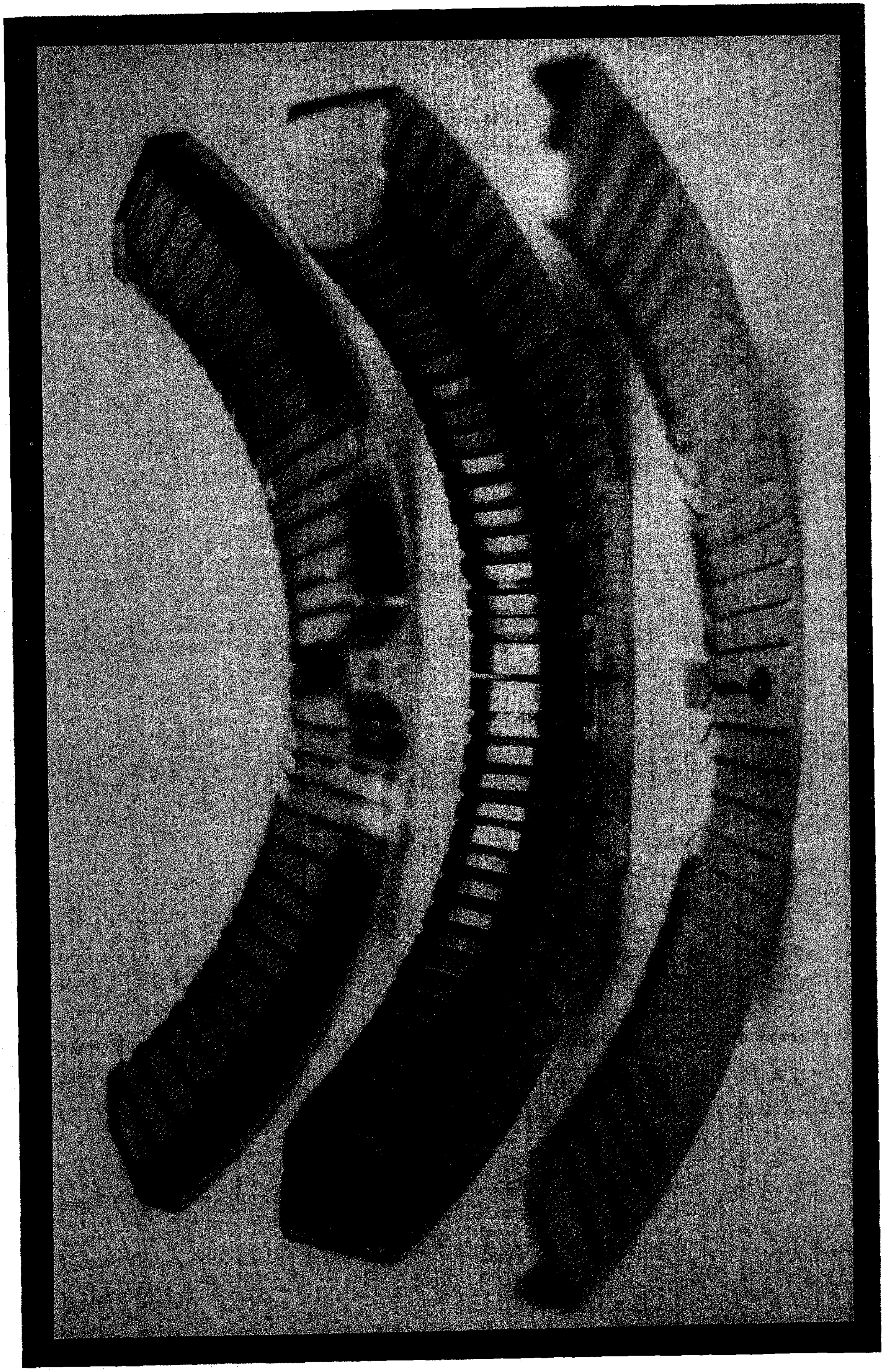

A_4 Antenna with Slotted Side Limiters

Figure 2

End View of Antenna Test Set

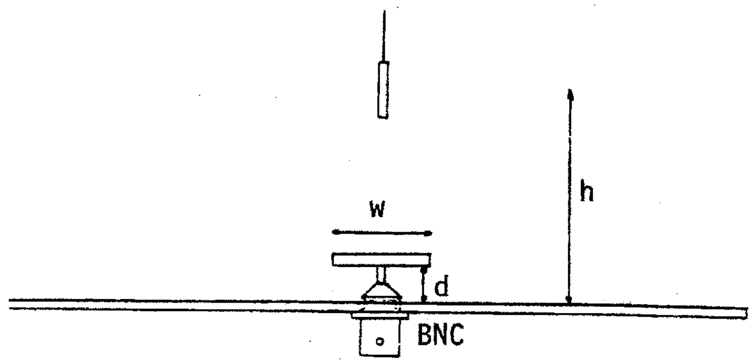

Side View of Antenna Test Set

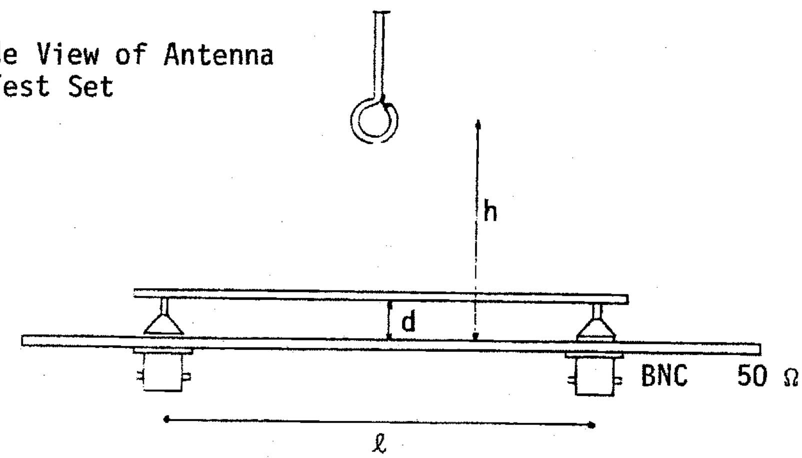

End View of Shields and Center Conductors

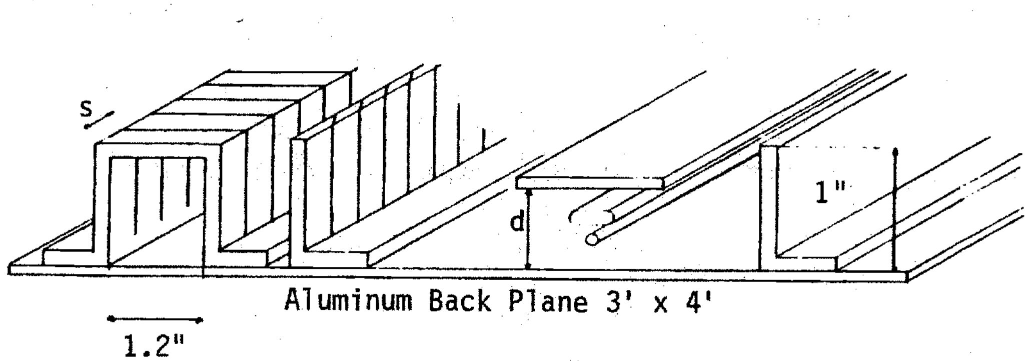

Figure 3

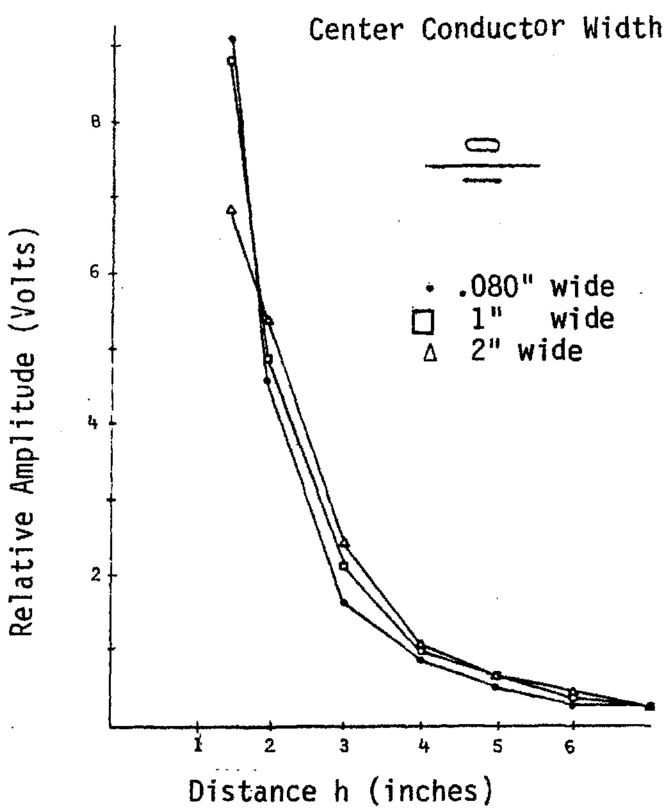

Figure 4

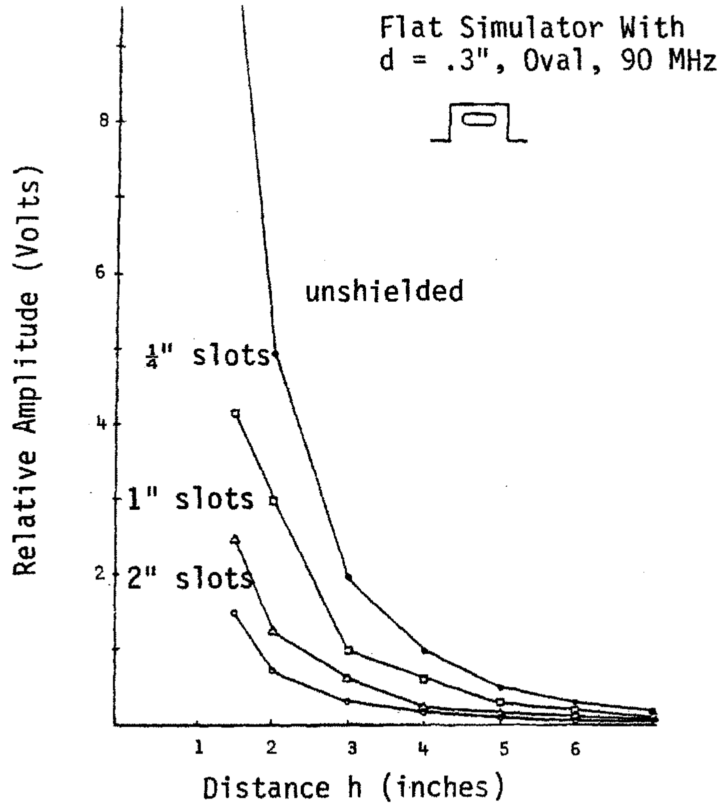

Figure 5

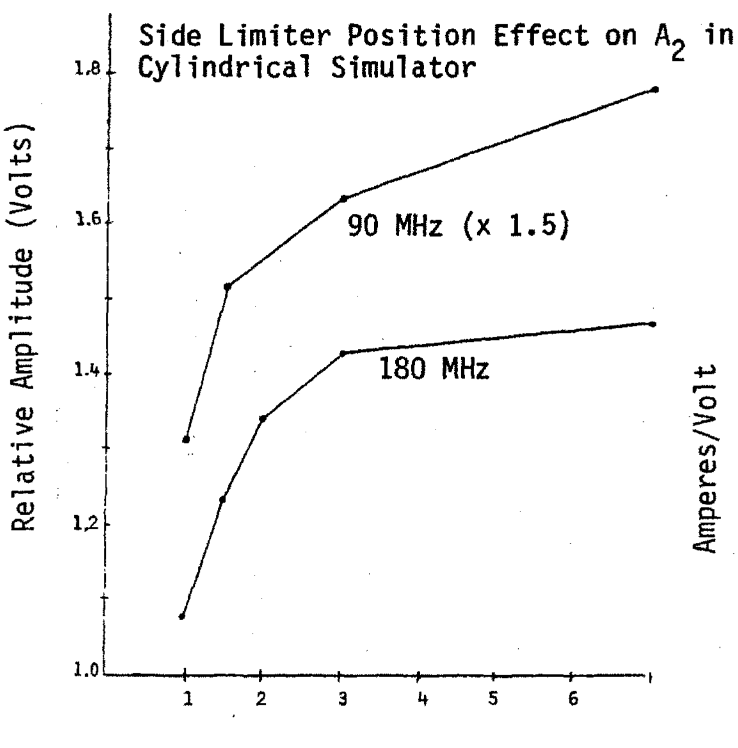

Figure 6

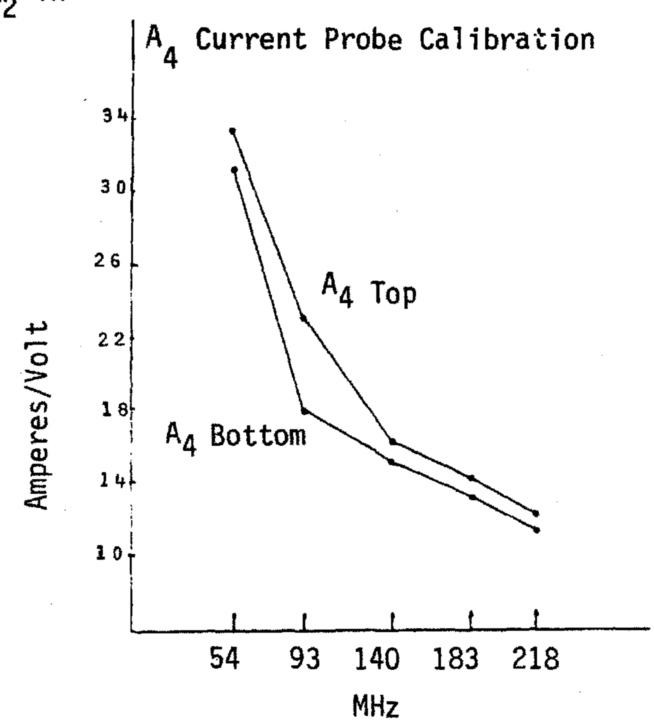

Figure 7

ANTENNA VACUUM FIELDS VS RADIUS

90MHz

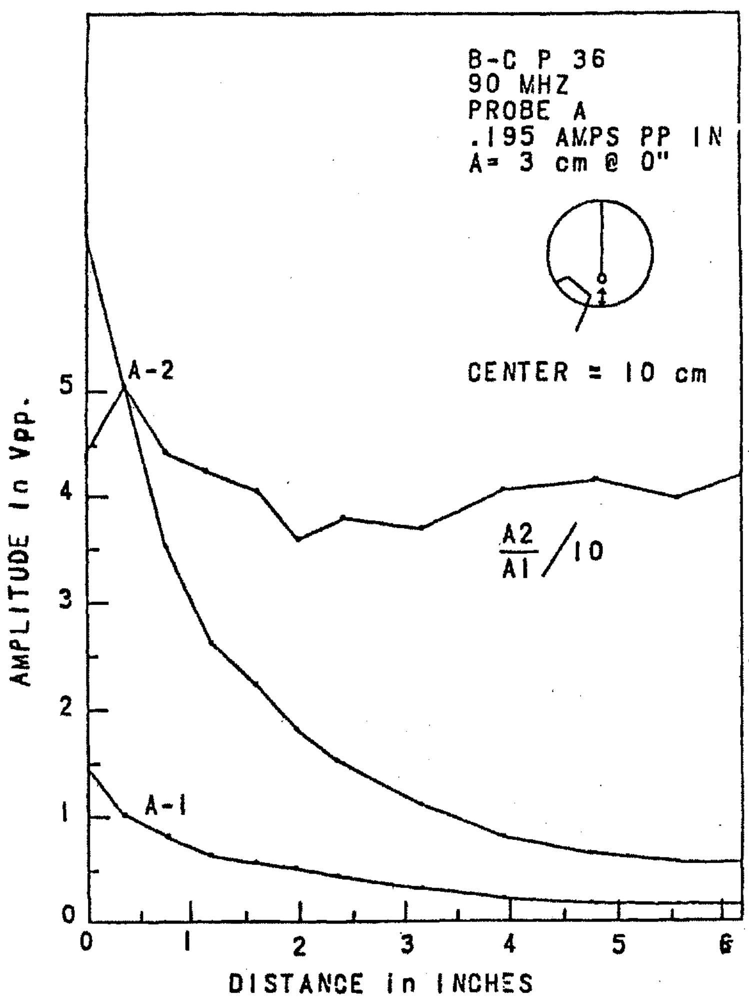

Figure 8

180MHz

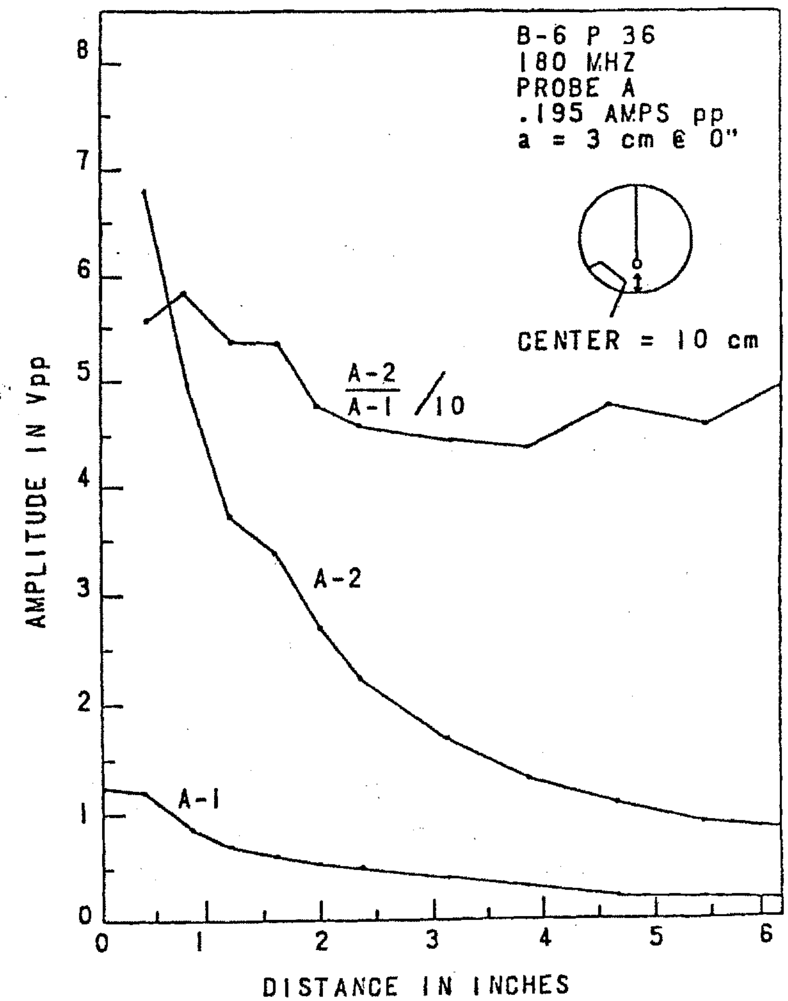

Figure 9

III-2.6. A_3, A_5, A_6 antenna systems

To further improve the power coupling capability of the A_2 unshielded type antenna, a longer and much higher current antenna system, A_3, was designed (Figure 1). The main new feature is that the matching is done in a vacuum, so the ceramic feedthroughs are at a pure real power point. Thus for a conservative 200 amperes, 800 kW can be coupled.

Figure 1 is a preliminary mechanical design of A_3. The antenna itself could be almost twice as long as A_2, and very easy to insert. Both antenna center conductors are hinged to the large, four inch diameter, hollow feeder conductor. Image currents run directly on the vacuum vessel, and the end of the conductors are held in place by threaded rods through the vertical keyholes. The large, stiff, hollow feeder is very rigidly cantilevered from the outer conductor behind the sliding tuning plate. The tuning plate is positioned by motor driven hollow control rods (at atmospheric pressure) with current loops at the plate surface. The entire matching and antenna system is the same size as the A_2 feeder, ($\lambda/2$ at 90 MHz, λ at 180 MHz). All parts are stainless steel, bakable and silver plated, as is A_1. Electrical breakdown can be monitored through windows mounted on the tuning and matching control flanges.

Tuning is done through a variable vacuum capacitor in a six inch "T" near the voltage maximum. From conservation of power when the system is in tune, and $R_R << Z_o$, we can approximately write

(1) $$P_{in} = I_{in} V_{in} = I_o^2 R$$

which can be rewritten as

(2) $$\frac{V_{in}^2}{Z_o} \approx \frac{V_o}{X_c} \cdot V_{in} \approx \frac{V_o^2}{Z_o^2} R$$

and solving for capacitor reactance

$$(3) \quad X_c \simeq Z_o\sqrt{\frac{Z_o}{R}} \simeq 160\Omega \quad \text{for } Z_o = 50\ \Omega \text{ and } R = 5\ \Omega$$

we find $C \simeq 5.0 \times 10^{-12}$ F at 200 MHz. This corresponds to a rather large capacitor disk four inches in diameter with a half inch spacing.

Two other major advantages of the A_3 system are that tuning and matching controls are nearly orthogonal, and the smaller and simpler matching system cannot contain as many parasitic modes. A_3 is thus much easier to tune and model accurately. A major possible disadavantage is that the high current carrying part of the antenna intersects the cyclotron resonance layer.

Figure 4 is a very preliminary conceptual design of a fully shielded 360° antenna similar to A_4. This antenna would be wider (1.6" instead of 1.2"), and of lower impedence than A_4. A_5 could be inserted in either (or both) the HCN or Thomson horizontal ports. The keyhole bridges in these side ports would be milled in place without lubricants and without dismanteling the tokamak, a tricky but nevertheless feasible task.

Finally, a no compromise realistic antenna was designed with all the technology developed through the A_1, A_2, A_3, A_4 and A_5 designs. Figure 2 is a simplified schematic of the A_6 RF components. The A_6 antenna is a slow wave, low impedence, 360° shielded antenna similar to A_4 and A_5 (Figure 4). Each half of the antenna is independently matched to 50 Ω by two short A_3 type vacuum resonators (Figure 3). The antenna halves can be easily and arbitrarily phased by a variable delay line (Figure 6) The 9" diameter coaxial power splitter (Figure 5) is of the long, linearly tapered type, which is relatively broadband (90 - 200 MHz) and free of parasitics. The 9 inch DC block is three stage, coaxial and similar to the two stage A_2 version.

Matching is mechanically most easily achieved by changing the frequency, since the A_3 tuning capacitor would be too large for the more compact A_6. The tap point (near the operating frequency) can be easily calculated and experimentally verified under bench test at atmospheric pressure. For gross tap changes, the standard 4.5" "T's" can be interchanged. The vacuum feedthroughs can be custom built, or the already available (FPS-17) high power 9 inch coaxial TR (Transmit-Receive) switch tube vacuum barriers could be used. The power splitter and delay line could also be built from available 9 inch "T's" (FPS-17 up-down switches) and already motorized A^2 feedback phase shifters.

The antenna itself could be secured in place by any combination of different ways, in particular, by horizontal back plane pins as A_1 A_2, A_4, vertical rods as A_3, or even screws into the Bitter flange as A_5. A_6 could also have the full line of RF, plasma and breakdown diagnostics. 360° slotted side limiters similar to A_2 and A_4 would also be installed.

For a sufficiently slow wave structure ($V \approx V_{A4} \approx .6$ c for Alcator C and 200 MHz), a voltage null in the antenna can be located slightly on the low field side of the major radius. This produces a nearly ideal field pattern for the single perpendicular pass regime ($R_{TIIH} < R_{\omega cH}$) and a small near-field edge heating at the resonant layer.

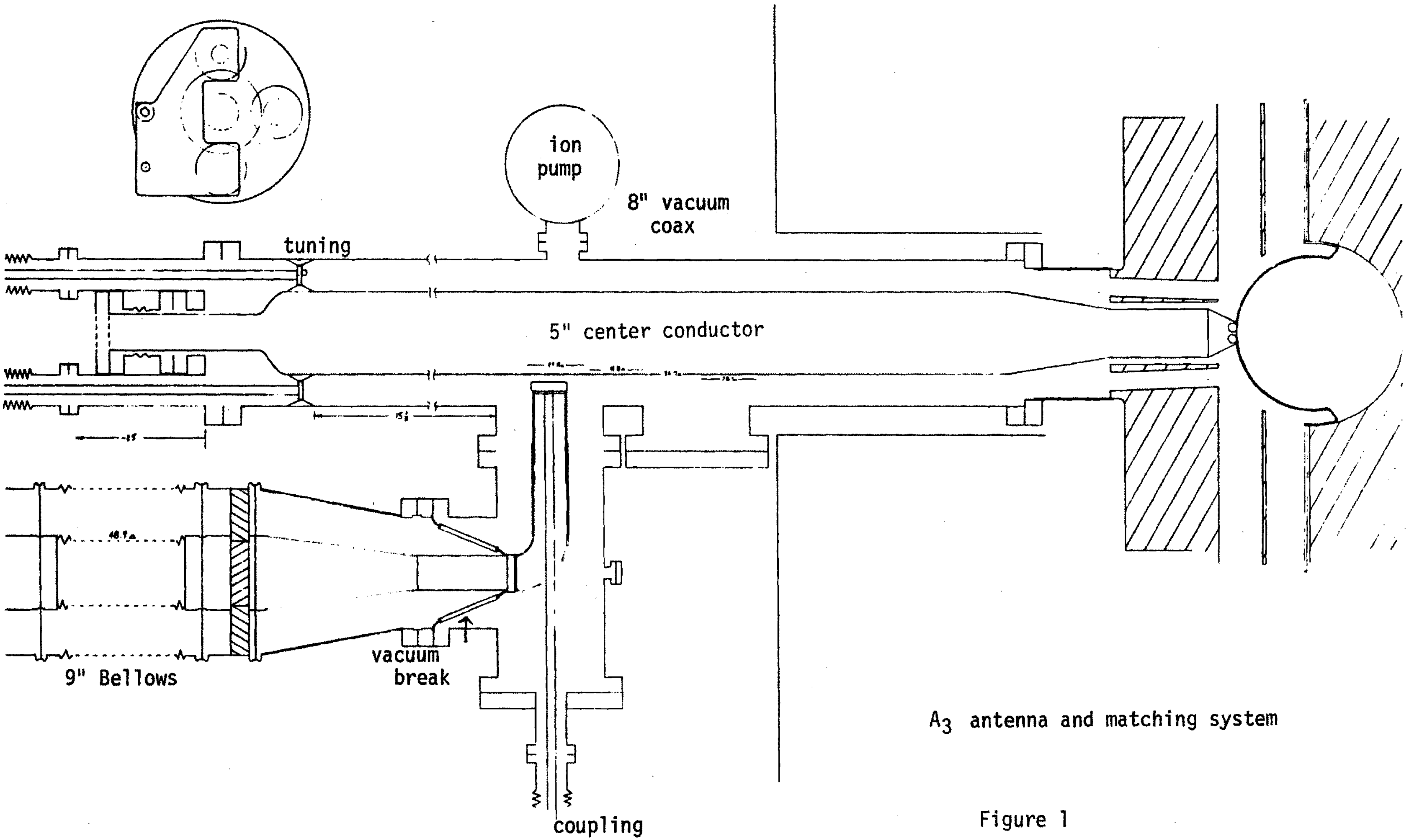

A_3 antenna and matching system

Figure 1

Simplified Schematic of A_6 System

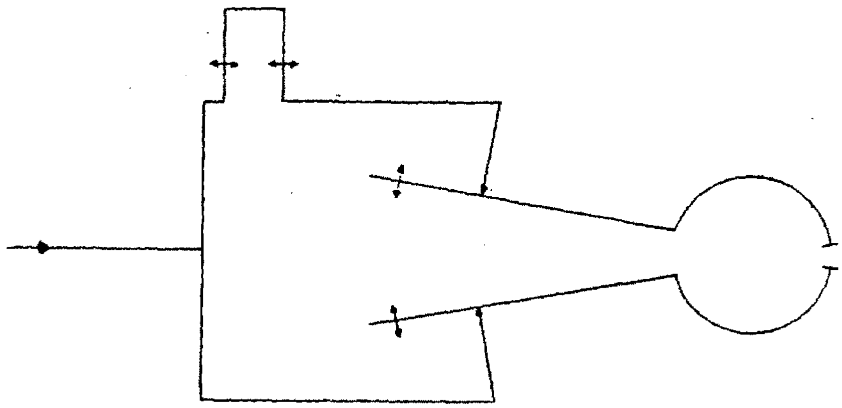

Figure 2

Simplified Mechanical Layout of A_6 System

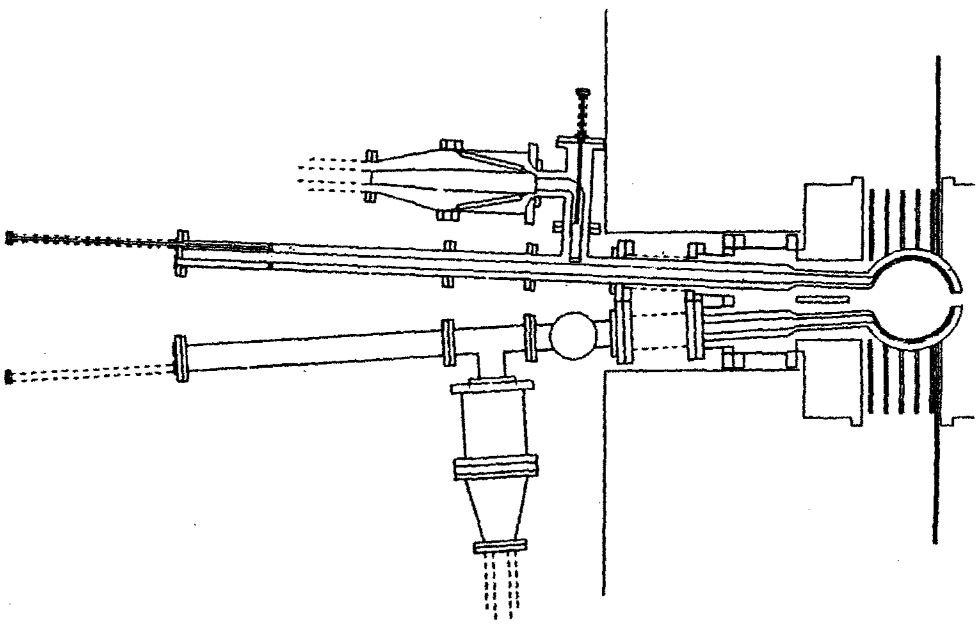

Figure 3

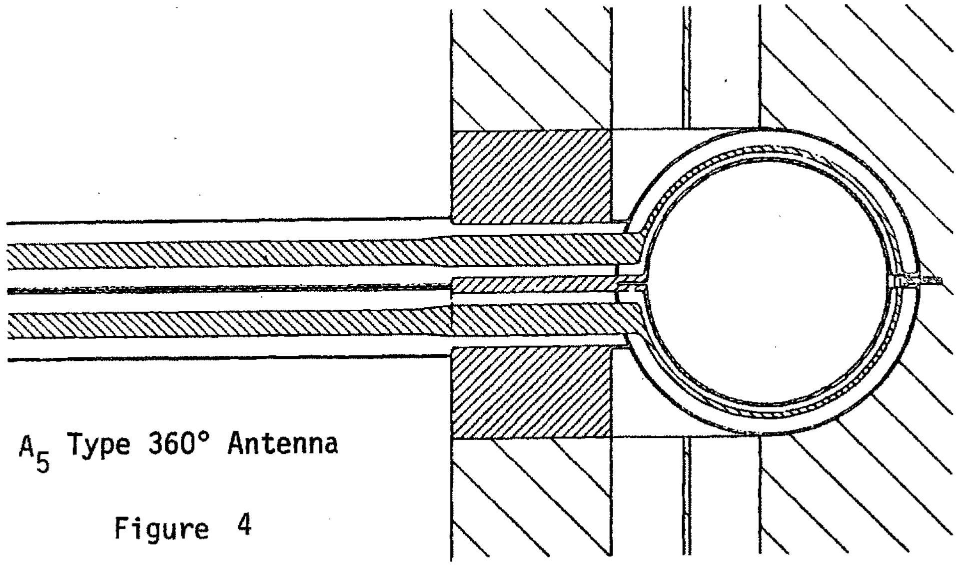

A_5 Type 360° Antenna

Figure 4

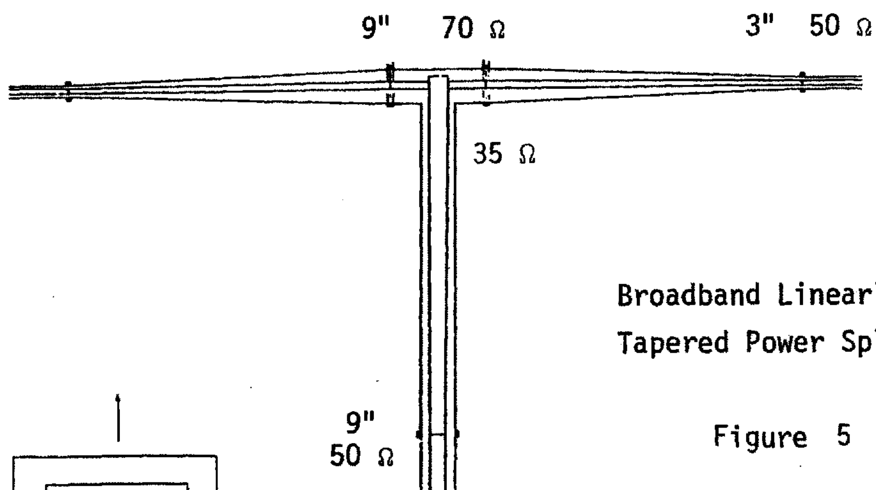

Broadband Linearly
Tapered Power Splitter

Figure 5

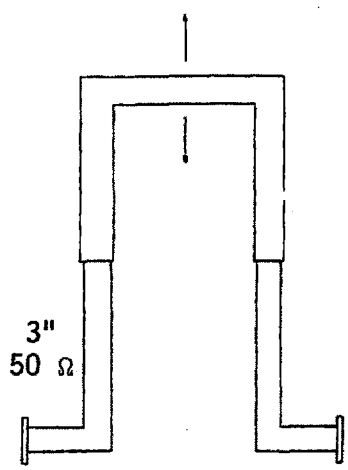

A^2 3" Coax Phase Shifter

Figure 6

III-3. Extensive Plasma and RF Diagnostics

One major objective of the experimental apparatus was to have as extensive RF diagnostics as possible. For this purpose, almost all easily implemented RF diagnostic schemes were used.

Forward and reflected power were measured at different points in the system with 9" coax directional couplers. Top and bottom resonator balance and antenna currents were measured with magnetic probes. A high speed dedicated analog computer calculated R_R in real time. Many unshielded RF probes were located around the torus, in particular, in the near-field of the antenna, in the opposite limiter port, and poloidally a quarter of the way around the torus. Ceramic thimbles were also built to house shielded probes and also a three component, B_θ, B_r, and B_z RF probe. Two $k_\parallel$ arrays of probes were used to measure the parallel wave length and field profile at the port.

Several increasingly sophisticated phase detection schemes were used to measure parallel and perpendicular mode numbers. These schemes include a high speed compressor and mixer, single sideband generated fringe correlators, and a sine cosine phase detector.

A number of plasma and RF breakdown diagnostics were also designed and used, among which were several high sensitivity light detectors monitoring the RF antenna feeder coaxes, the electrical breaks, and the inside and outside of the antenna (Figure 1). An H_α light detector, Langmuir probes, high speed bolometer and trapped particle detector were designed for measurements even in very high RF fields.

Finally, all the tokamak support diagnostics were used and, in particular, the alcohol laser interferometer[73*], mass selective charge exchange energetic neutral spectrometer[33-38*], soft X-ray detectors[39*], neutrons[39*], as well as all the usual magnetic diagnostics[2*].

*Stephen Wolfe and Jeffrey Parker were responsible for density measurements, Martin Greenwald and Catherine Fiore for charge exchange, Robert Granetz for soft X-ray, David Gwinn, Daniel Pappas and William Fisher for neutrons, and David Overskei and Bruce Lipschultz for magnetic diagnostics.

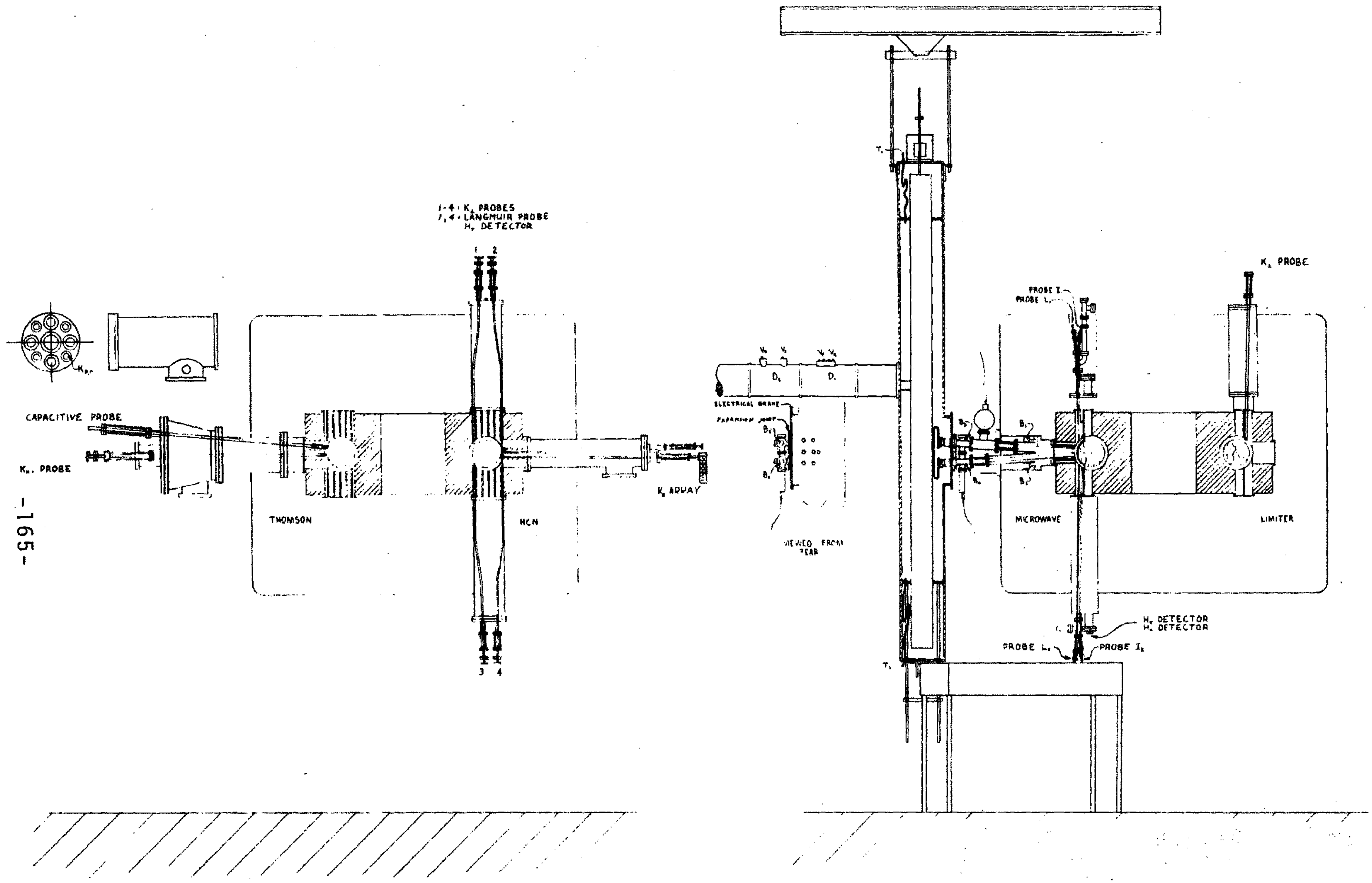

Alcator A ICRF Diagnostics

Figure 1

III-3.1. RF power, radiation resistance and data acquisition

Forward and reflected power were measured right at the matching resonator by 60.2 db (at 200 MHz), 9" directional couplers (Figure III-3.(1). Top and bottom antenna current were measured by calibrated current loops inserted through the top and bottom MW port.

Double shielded RG 55 coax ($\simeq$ 7 db/100 ft at 200 MHz) was used for all RF diagnostics. All lines were properly terminated to 50 Ω and shunted with high pass .2 microhenry inductors ($X_L \simeq 250\ \Omega >> 50\ \Omega$ at 200 MHz). Custom high voltage (>1 kV) DC blocks were installed at all RF sources.

Absolute RF measurements were made with 7A24, 400 MHz, 50 Ω terminated Tektronix plug-ins in two (7834), 400 MHz storage mainframes. Relative measurements at the base frequency and absolute measurements at lower frequencies were made with 7A18 plug-ins in five 7623A, 100 MHz mainframes (slew rate limited, $\simeq$ 3 db down at 100 MHz, 14 db at 200 MHz). RF voltages were usually measured at the base frequency as peak to peak measurements off oscillograms, and rarely by ordinary square law diode detectors.

Figure 1 shows the 100 kHz bandwidth on-line radiation resistance analog computer. Forward and reflected power and either top or bottom antenna current signals were 3 db split, displayed at the base frequency and square law detected. The diode signals were corrected for true square law over a 20 db range by diode networks, and then subtracted and divided to calculate loading resistance.

Most of the plasma diagnostic signals were recorded either on storage oscilloscopes, or on a slower CAMAC digital memory storage system interfaced to a PDP-11/55 computer.

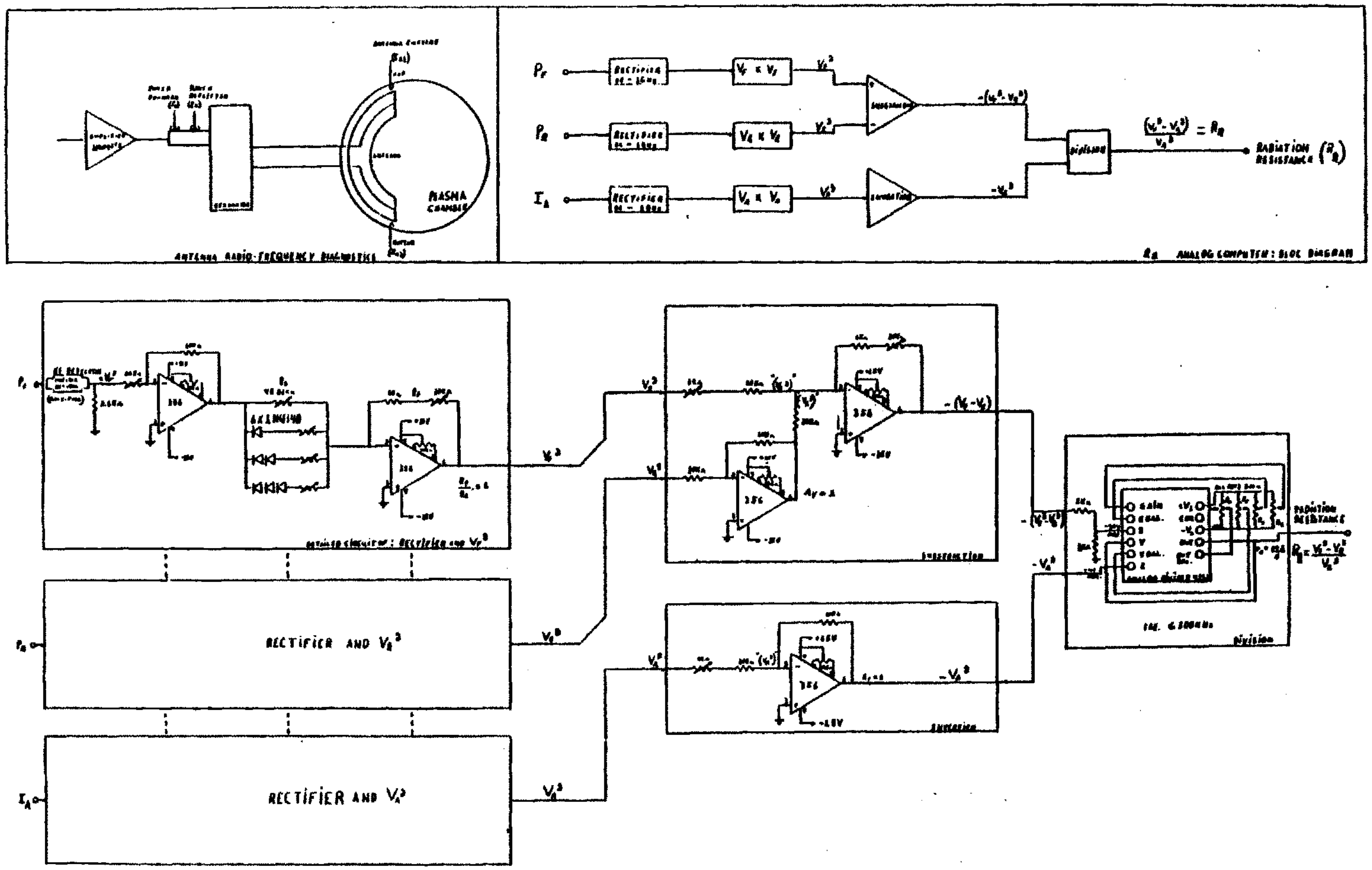

High Speed, On-line Radiation Resistance Analog Computer

Figure 1

III-3.2. RF wave probes and arrays

Many small unshielded RF wave probes were installed around the torus, as can be seen from the cross section view of Figure III-3.(1). Most of the probes were unshielded and similar to the ones shown in Figure 2 and the bottom of Figure 1. These probes were mounted on 3/8" OD pipe, with atmospheric pressure on the inside. Bakable .125" OD hardline coax and high temperature brazed alumina feedthroughs were used for high vacuum integrity. The feedthrough welds were electron beam welded and protected by side limiters. The Langmuir probe, A_2 flux model probe and $k_\parallel$ array of Figures 5, 4, and 1 were of similar construction. The array probe spacing was about 2 and 1 cm. A simple $k_\parallel$ array of 3 probes similar to Figure 1 was also used.

Figure 6 and top left of Figure 1 show a ceramic thimble that was used to house more complicated wave probes near the plasma, in an atmospheric environment. Among these probes were unshielded (Figure 7), shielded (Figure 8), differentially shielded (Figure 9), and three axis (B_θ, B_r, B_z), magnetic loop probes.

The inductance of the small probe loops can be approximated as[136]

$$(1) \quad L \approx \frac{R_p^2}{9 R_p + 20 r_p} \mu H \approx 4 \times 10^{-9} \text{ H}, \; R_p \approx .065", \; r_p \approx .025"$$

The effective area of the probe A_e, is larger than the estimated A_m (due to the reentrant geometry of the probe tip), and can be accurately calibrated in the nine inch diameter coaxial field simulator of Figure III-2.4.(5). The fields could be pure electric, magnetic, or both, depending on termination and location in the simulator.

(2) $I = \frac{V_0}{Z_0}$ for $z = z_0$

(3) $H = \frac{I}{2 \pi r_c}$

(4) $V_p = A_e \omega \mu_0 H$

(5) $A_e = \frac{V_p r_c Z_0}{V_0 f_0 \mu_0} \approx .19 \text{ cm}^2 > A_m \approx \pi r^2 = .086 \text{ cm}^2$

Capacitive coupling effects by the unshielded probes were similarly investigated. For simplicity, we will assume the probe tip has an effective capacitance area A_c exposed to a wave electric field. The current and voltage induced in the probe can be estimated as

(6) $I_c = A_c \omega \varepsilon E$

(7) $V_c = L \dot{I}_c = L \omega^2 A_c \varepsilon E$

and can be neglected even in the high dielectric plasma edge since

(8) $E \approx \frac{\omega}{k} B$

(9) $\frac{V_c}{V_p} = \frac{A_c}{A_p} L \frac{\omega^2 \varepsilon}{k} \approx \frac{\omega^2 \varepsilon}{k} L \approx .013$ for k_0, ε_0, 200 MHz

$\approx .016$ for $k \approx 1/\text{cm}$, $30\ \varepsilon_0$

Each half of the unshielded antenna can be modeled as shown in Figures 11 and 12. Power can be dissipated by four basic different mechanisms; First and second, the conventional inductively coupled R_R and circuit losses R_ℓ, third and fourth, resistive R_p, and capacitively coupled R_C losses, primarily at the high voltage (V_a) feeder area (A) of the antenna. The many possible pitfalls are best illustrated by a plausible, realistic numerical example.

(10) $P_{\ell/2} = I_o^2\ (R_R/2) \simeq 20$ kW for $I_o = 100$ amps and $R_R = 4\ \Omega$

(11) $E_{\theta w} = \dfrac{I_o\ R_R}{\ell} \simeq 20$ V/cm for $\ell = 20$ cm

(12) $\theta_{\ell/2} = 2\pi\ \dfrac{\ell/2}{\lambda_o} \simeq 24°$ for $f_o = 200$ MHz

(13) $V_a = I_o\ Z_o \sin\theta_{\ell/2} \simeq 3.7$ kV for $Z_o = 90\ \Omega$

(14) $E_z \simeq \dfrac{V_a}{d} \simeq 1.8$ kV/cm $>> E_{\theta w}$ for $d = 2$ cm

(15) $C_p \simeq \dfrac{\varepsilon_o A}{r_a - r_p} \simeq 10^{-12}$ F for $A \cong 10$ cm^2 and $r_a - r_p \cong 1$ cm

(16) $|X_C| = \dfrac{1}{\omega C} \simeq 800\ \Omega$

(17) $|X_L| \simeq \dfrac{V_a}{I_o} \simeq 37\ \Omega$

(18) $P_C \simeq \dfrac{(V_a/2)^2}{R_C} \simeq 4.3$ kW for $R_C \cong |X_C|$

(19) $P_p \simeq \dfrac{V_a{}^2}{R_p} \simeq 4.6$ kW for $R_p \cong 3000\ \Omega$

The root of the problem comes from the fact that the antenna electric near-field (eq. 14) is two orders of magnitude larger than the $E_{\theta w}$ (eq. 11) wave field (five orders larger than E_{zw}). This high voltage (eq. 13) combined with even large impedences, can give rise to substantial losses (eq. 18 and 19).

In equation (15), we assume a vacuum dielectric $\varepsilon \simeq \varepsilon_o$. If instead, we assumed a more tenuous plasma with $\varepsilon \simeq 30\ \varepsilon_o$, then $|X_C| \simeq |X_L|$, and substantial current could be diverted away from the antenna. Note also that $\varepsilon_{\parallel} \simeq 10^3\ \varepsilon_{\perp}$, and the problem is even more severe along the magnetic field lines.

To investigate these possible pitfalls, a medium power (<10 kW), capacitive antenna was installed. Figures 6 and 13 show this probe with a 1.5 inch diameter molybdenum electrode. Power was fed through RG 8 coax with custom-made high voltage connectors. The inside of the probe was gas cooled, so the probe could be inserted into the plasma past the limiter radius.

Since the tokamak main limiter radius had to be adapted to each antenna, several partial limiters, similar to Figure 13, and full 360° limiters were built and also energized with RF or used as RF probes.

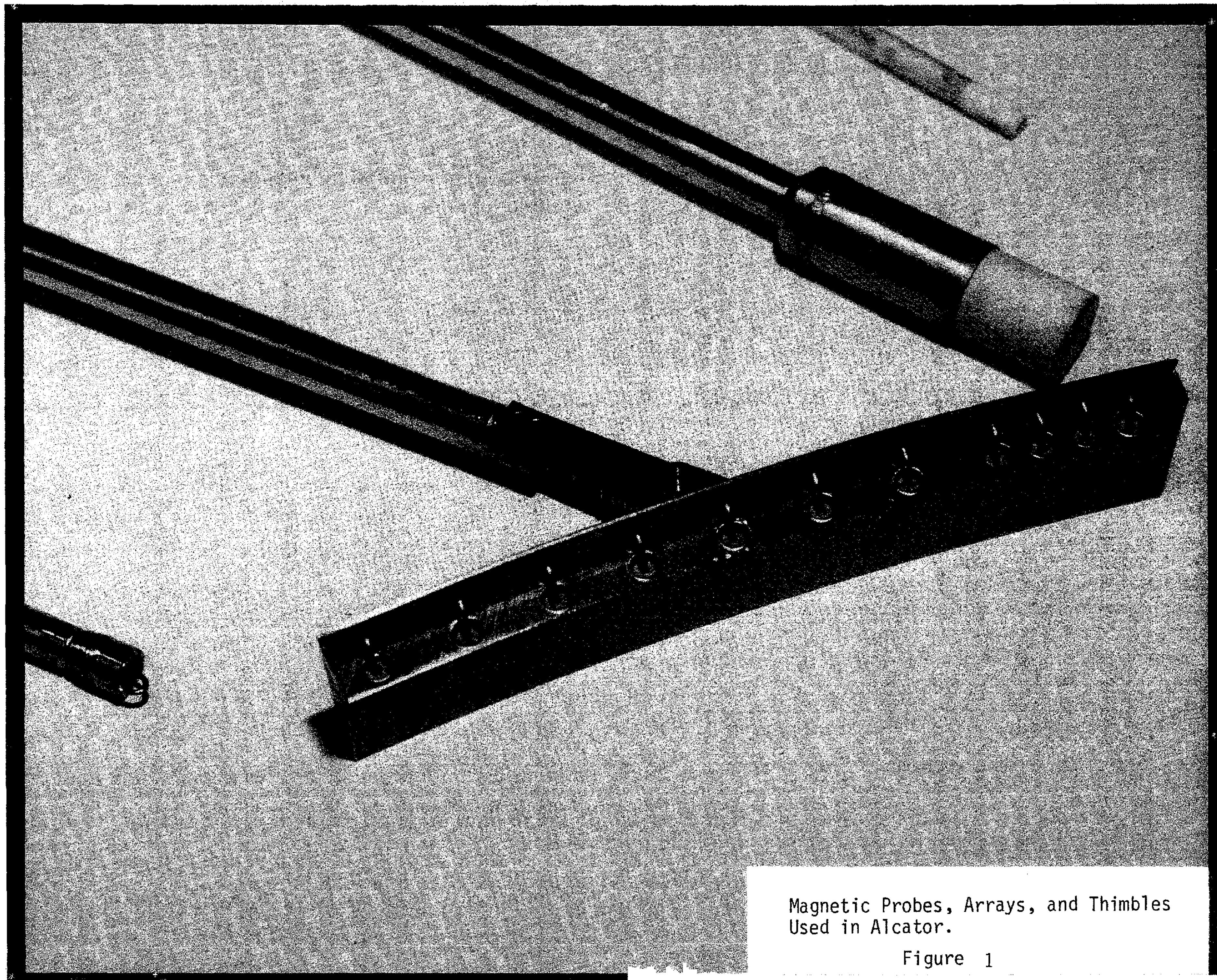

Magnetic Probes, Arrays, and Thimbles Used in Alcator.

Figure 1

RF Probe

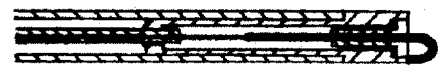

Figure 2

RF Probe

Figure 3

Thimble

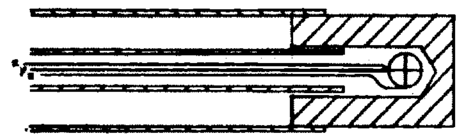

Figure 4

Langmuir Probe

Figure 5

Capacitive Probe

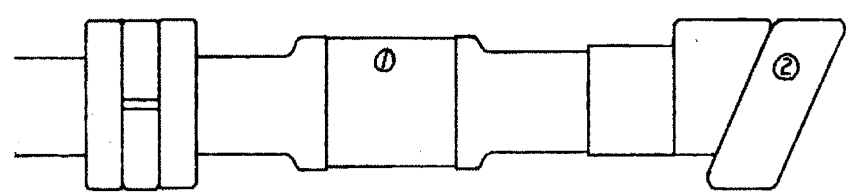

Figure 6

Simplified Mechanical Drawings of Magnetic Capacitive and Langmuir Probes Used in Alcator

Unshielded, Shielded and Shielded Balanced Magnetic Probes

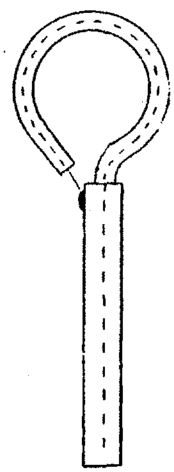

Figure 7

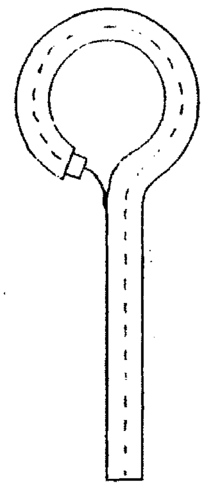

Figure 8

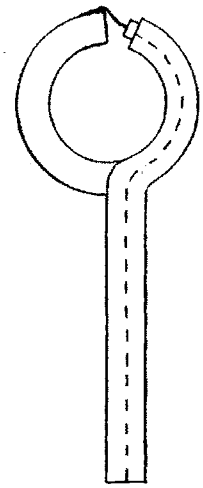

Figure 9

Top View of $k_{\parallel}$ Array and Access

Keyholes in Thompson and HCN Ports

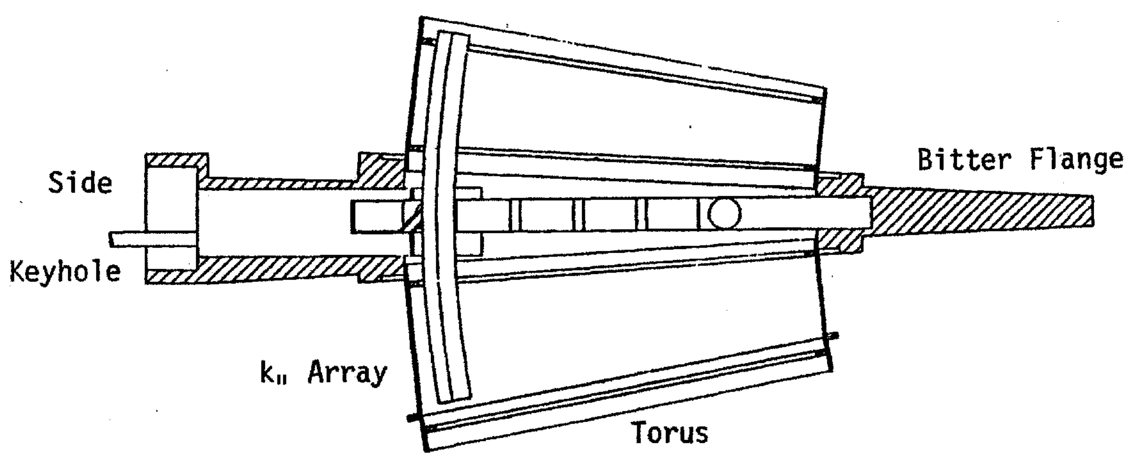

Figure 10

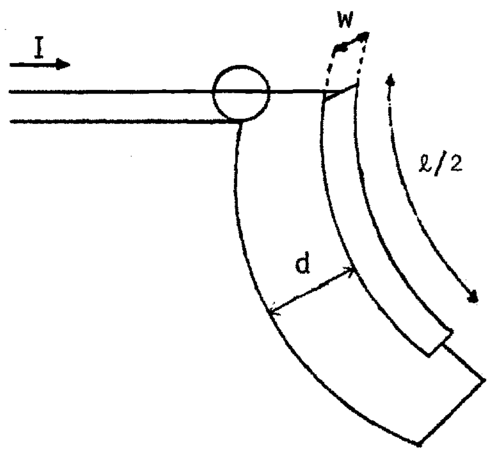

Simplified Model of A_2 Antenna

Figure 11

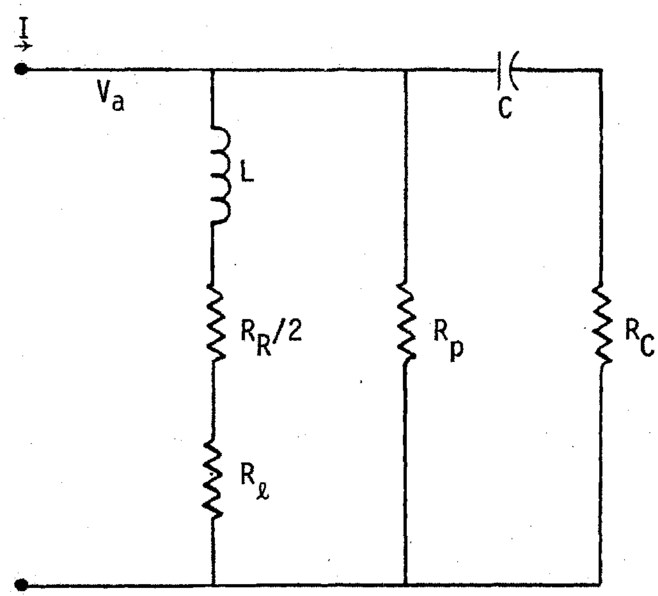

Simplified Electrical Model of A_2 Antenna

Figure 12

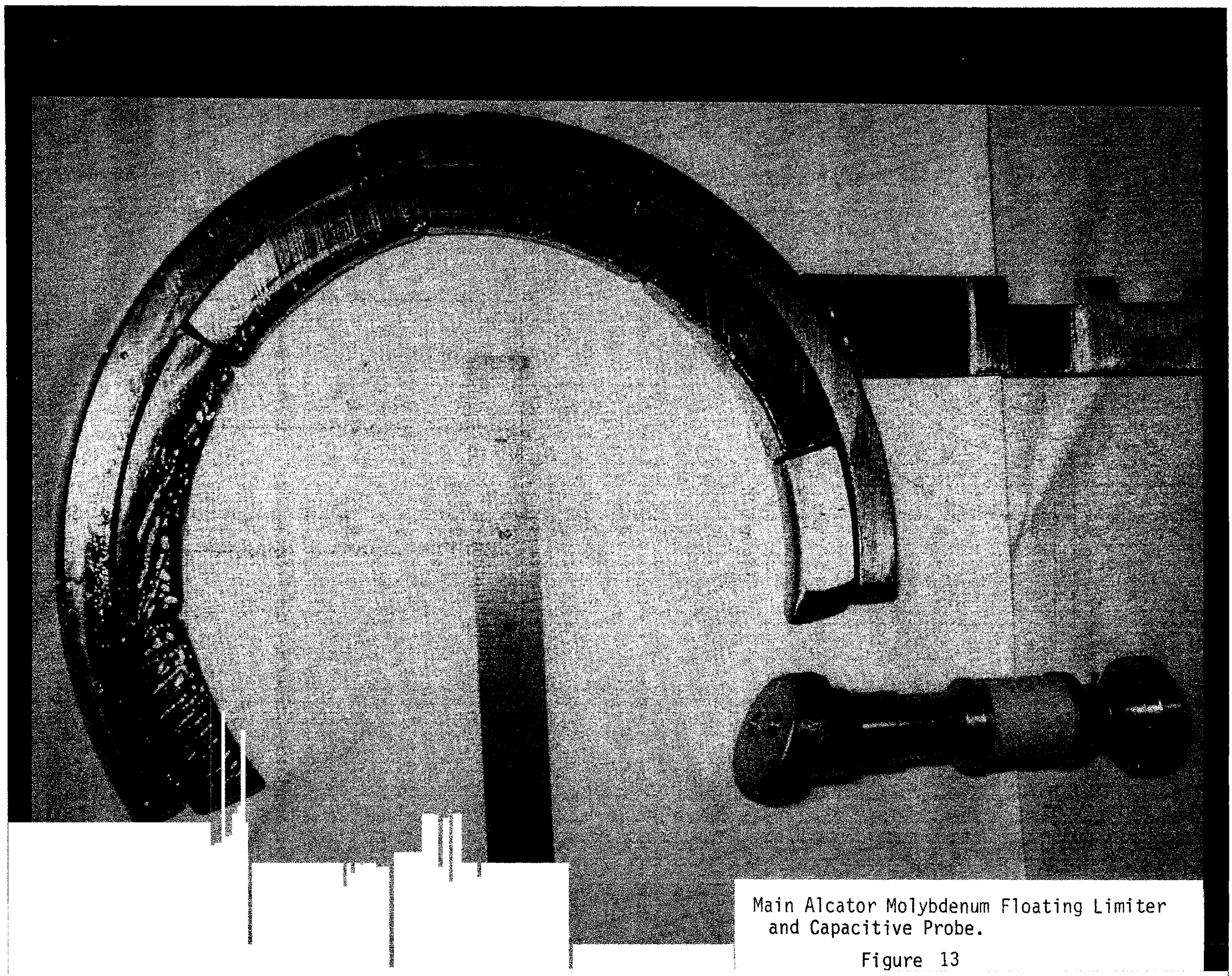

Main Alcator Molybdenum Floating Limiter and Capacitive Probe.

Figure 13

III-3.3. RF wave correlators

Several different schemes were used to measure the phase difference between various RF probes around the torus. The measurement difficulty comes from the large dynamic range necessary to continuously track the phase of the nearly 100% high frequency (up to 100 kHz) AM and PM modulated probe signals.

Figures 1 and III-1.1(5) show the most used basic techniques. Conceptually, the simplest scheme was to actively compress and limit the probe signals with cascaded 28 db RF amplifiers and diode limiters. These signals were then mixed at the base frequency with standard 7 dbm double balanced mixes to give a signal roughly proportional to cos $(\phi_1 - \phi_2)$. The main drawbacks are phase error and ambiguity. The advantage is, on the other hand, unlimited bandwidth. A more clever scheme, the sine-cosine method, did not require limiting, and is based on the simple trigonometric identities

$$(1) \quad A \cos \alpha \; B \cos \beta = \frac{AB}{2} \cos (\alpha - \beta) + \text{USB}$$

$$(2) \quad A \cos \alpha \; B \sin \beta = \frac{-AB}{2} \sin (\alpha - \beta) + \text{USB}$$

This method is implemented by mixing the A and B signal as in equation(1). The upper sideband (USB) is suppressed by a 16 MHz filter. The B signal also is phase-shifted with a 90° delay line and mixed with A as in equation(2). The phase difference can now be unambigiously resolved, given D cos γ and D sin γ, by either the PDP 11 or a high-speed analog computer (4 quadrant divider and arctan $(0 - 2\pi)$). The main disadvantages of this method are the high data storage rates for off-line digitally processing many probe signals, and the fact that the amplitude of the local port mixer signal must not be too modulated (the oscillator or antenna current are appropriate, but not an uncompressed probe signal).

All these problems can be circumvented by superheterodining the 200 MHz probe signals down to 500 kHz, and then using a linear set-reset type 0 - 2π phase correlator. Figure 1 is a detailed schematic of a later version of this method. The mixers can be operated in the linear range, since the local port signals are derived directly from the 200 MHz transmitter oscillator and a 200.5 MHz local oscillator. The USBs are removed by 16 MHz filters, and all lines, including the out ports, are properly terminated. 60 db amplitude dynamic range (5 mV to 5 V) is obtained by a high speed zero crossing comparator. High phase stability (in terms of local oscillator drift), 500 kHz, input RC filters were used for more accurate but smaller dynamic amplitude range tracking. Both positive and negative feedback were used to control the gain and hysteresis of the comparator. Without feedback and hysteresis, the correlator is unstable without signal. Simple first order and active fourth order 50 kHz output filters were also used to filter out the 500 kHz USB. An up-down counter could also have been used instead of the set-reset flip-flop, but the output can run away if tracking is lost.

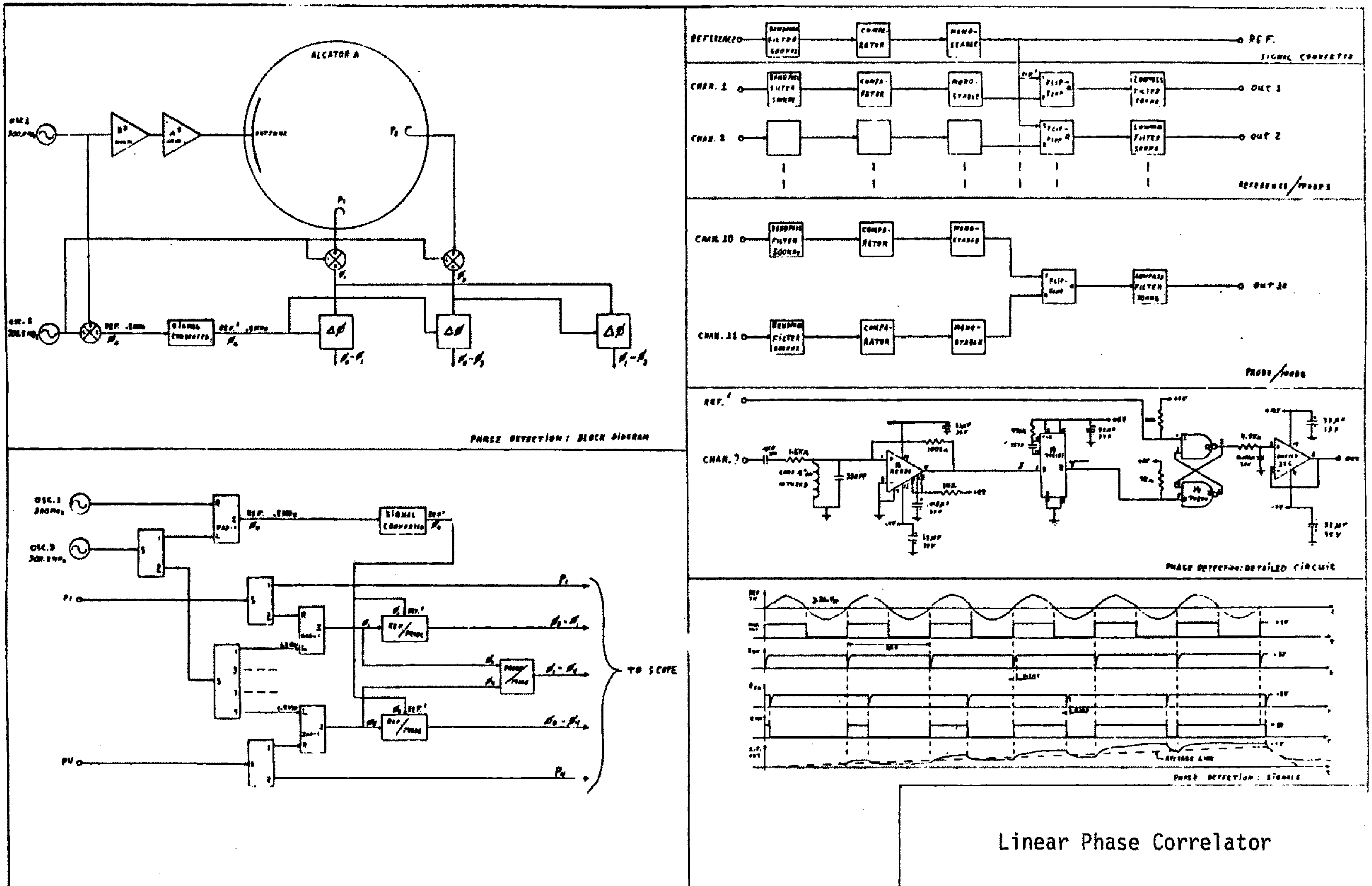

Linear Phase Correlator

Figure 1

III-3.4. Plasma edge and RF breakdown diagnostics

Three small Langmuir probes were installed in the HCN port and in front of the A_4 Faraday shield to estimate the density and temperature of the tenuous plasma edge (Figures 1 and III-3.2.(5)).

Although probe theory can be extremely complicated in the presence of high magnetic or RF fields, the basic physics is nevertheless the same.[77] For highly negative biased probe (with respect to the vacuum vessel and plasma potential),a thin sheath, depleted of electrons, is formed around the electrode. Ions in the nearby plasma acquire an energy

$$(1) \qquad -e\,V_s \simeq \frac{KT_e}{2}$$

from the leaking electric field (Debye shielding) before entering the sheath and free-falling onto the probe. Outside the sheath, quasineutrality and Boltzman relation are valid,so that

$$(2) \qquad n_e = n_\circ\, e^{\frac{e\,V_s}{KT_e}} \simeq n_i$$

The ion saturation current at the sheath boundary is thus simply ($A_s \simeq A_p$ since $r_p \gg \lambda_D$)

$$(3) \qquad I = e\,n_i\,v_i\,A_s = e\,n_\circ\,e^{-1/2}\sqrt{\frac{K\,T_e}{M}}\;A_p$$

Slightly above (in probe potential) the ion saturation regime, the dI/dV_p is mainly due to the electrons reaching the probe,and again from Boltzman relation

$$(4) \quad I_e \propto e^{\frac{e V_p}{KT_e}}$$

and the electron temperature can be inferred from the slope of the $\ln(I)$ vs. V_p curve.

The Alcator edge plasma has a very small $n_o \sqrt{T_e}$ scale length ($\approx$ .2 inches), so the .050 inch diameter stainless steel probe wire has an effective area $A_p \approx .2\ cm^2$. For a 10 eV, $5 \times 10^{13}\ cm^{-3}$ plasma, the ion saturation current will be about 3.0 amperes, and the electron temperature can be inferred from a 60 volt peak to peak triangular probe voltage and current trace. Figure 1 shows the basic circuit used, where care was taken to avoid standing waves in the probe coax by proper termination at 200 MHz.

A number of high sensitivity (0.4 A/W) silicon pin diodes were used to monitor visual light between 3,000 Å and 11,000 Å around the torus and antenna system, and in particular, through the antenna hollow holding pins, inside the electrical breaks and vacuum feeders, and in front of the antenna through the bottom MW keyhole. H_α filters (6520 - 6600 Å) were also used to estimate hydrogen ionization. The detectors were RF shielded, and multiple wave reflections were carefully suppressed to again avoid any possibility of RF pick-up (Figure 2).

To further investigate the intricate arcing and diffuse light production at the antenna, an optical viewer was designed to photograph (and later film) the antenna from the HCN or Thompson ports during a plasma shot. Figure 3 shows how a small pyrex window and polished stainless steel mirror attached to a 5/8 inch diameter pipe could be used with a high resolution, 1/2 inch diameter boroscope to image the plasma cross section (Figure 4). This diagnostic would also be used to monitor plasma edge position near the antenna.

Langmuir Probe Electronics

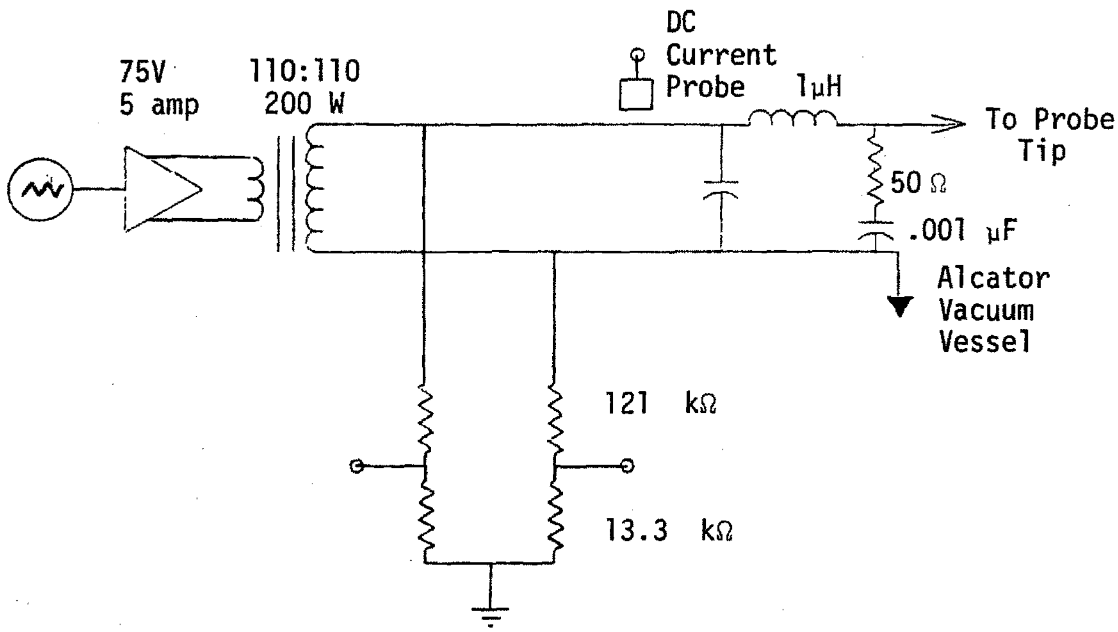

Figure 1

Optical Detector Electronics

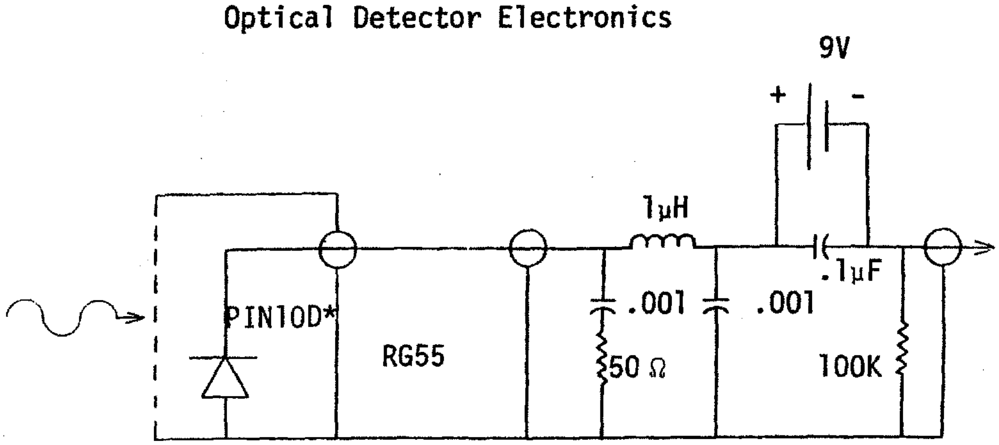

Figure 2

*United Detector Technology, Inc.

Top View of Optical Viewer Geometry

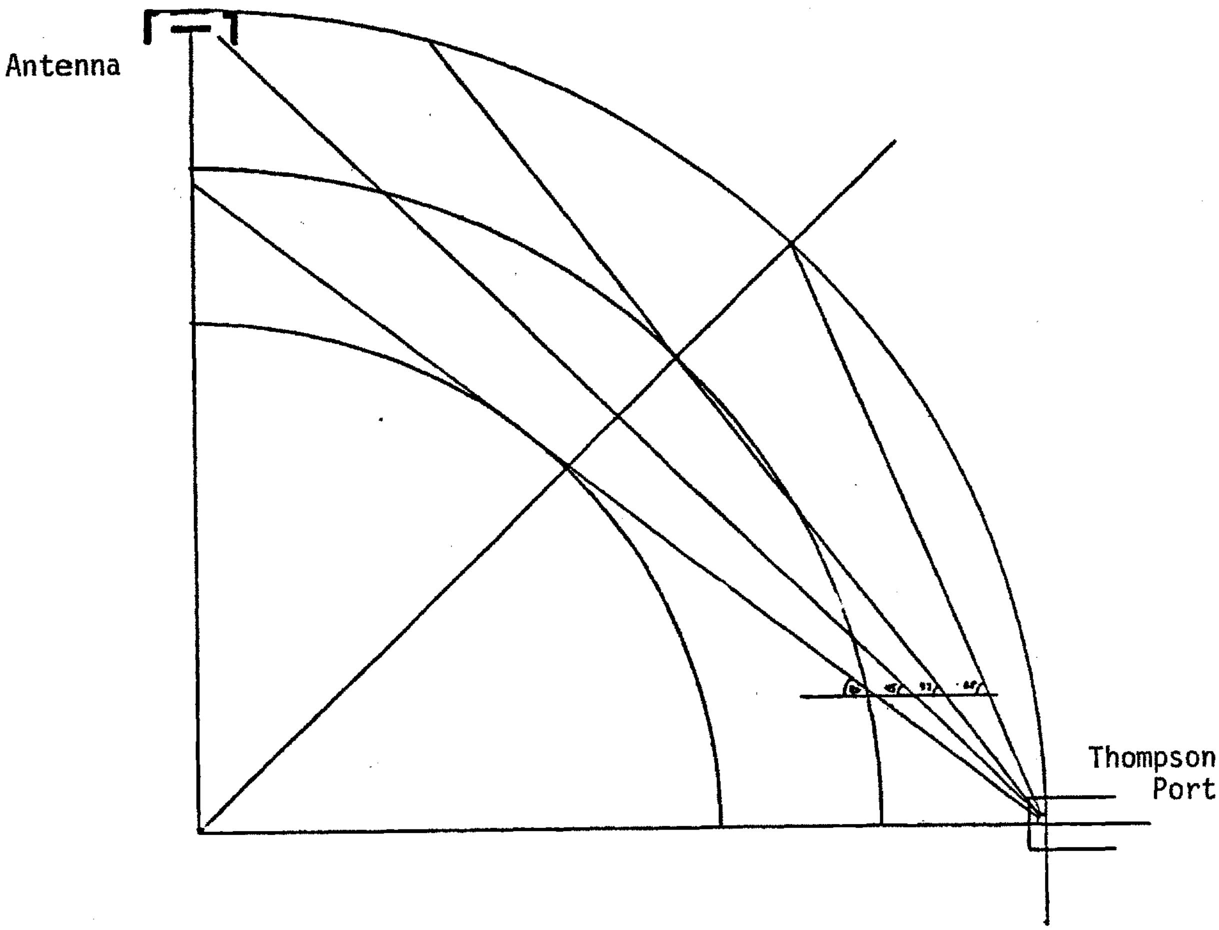

Figure 3

Detail of Stainless Steel Mirror and Boroscope Assembly

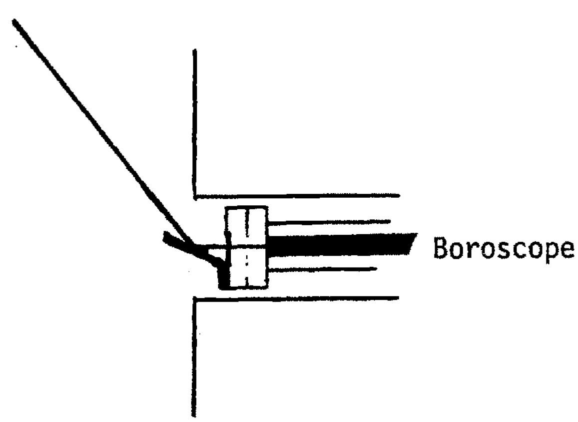

Figure 4

III-3.5. Charge Exchange Diagnostic

Charge exchange[33-38] was the single most important diagnostic for medium power heating experiments (Figure 1). Figure 2 is a simplified schematic of the fast neutral spectrometer. Energy selection is done by a series of electrostatic capacitor plates C_o - C_5. Mass selection is also made possible by replacing C_o by an electromagnet. At high plasma density, the energetic neutral flux is very small thus requiring high stripping cell efficiency. Either 10^{-4} torr of steady-state nitrogen or 10^{-2} torr of pulsed helium was used, with extensive use of baffles and differential pumps, to limit plasma contamination by the high pressure stripping gas. Figure 3 is a typical high density shot where both steady-state N_2 and pulsed He were used. The first 100 ms of flux is detected with background N_2, and then He is pulsed, giving a much higher sensitivity. The 20 ms decay time of the He signal is due to the gas pressure decay, and not a change in the neutral flux.

The fast neutral flux arriving at the spectrometer can be written as the product of three factors: collection, production and attenuation.

$$(1) \quad \frac{dN}{dE} = \underbrace{\frac{\Omega A}{4\pi} v_i}_{\text{collection}} \int_{-a}^{+a} \underbrace{\sigma_{cx} v_i n_n f_i (E)}_{\text{production}} \underbrace{\exp \left(- \int_r^a \frac{\gamma_{io} + \gamma_{cx}}{v_i} dr\right)}_{\text{attenuation}} dr$$

For low density and high energy neutrals, the flux is easy to calculate and interpret, since attenuation (ionization and charge exchange) is small, and since the neutral density in the center is not too many e-foldings lower than at the edge, and high energy ions are only produced in the hot center. The central temperature can then be simply estimated from the slope of the high energy neutral spectra.

At high density, and especially with RF in Alcator, none of the above is true. Attenuation can be several e-foldings, and the central neutral density is very low compared to the edge. Low energy neutrals from the surface ($n_n \simeq 10^{11} - 10^{12}$ cm^{-3}) have e-folding lengths of the order of a cm, and do not contribute to the central neutral density ($10^7 - 10^8$ cm^{-3}) which is sustained by electron-ion recombination. At high density, for well-behaved distribution functions and profiles, the high energy spectra will be colder than the central temperature. Figure 4 shows the neutral spectra for different times in a typical plasma shot. Note how the energetic neutral flux dramatically decreases with density. Figure 5 shows a typical ion temperature evolution with time.

Another major pitfall of charge exchange is that Alcator has a comparatively large port ripple (Figure 7), and only perpendicular viewing is possible, so only the ∇B drifting trapped particles are observed, and are, in many cases, not representative of the bulk of the distribution function. The mean free path for detrapping these particles out of the magnetic well is approximately (Figure 9)[1,35,85,86]

(2) $$\lambda \simeq \frac{v_{\nabla B}\ \theta^2}{\gamma_{ii}} \simeq 5.6 \times 10^{13} \frac{\sqrt{\mu}\ \theta^2\ E^{5/2}}{n\ R\ B}$$

where

(3) $$v_{\nabla B} = \frac{v_\perp^{\,2}}{2\ \omega_{ci}\ R}$$

(4) $$\theta^2 = \left(\frac{v_\parallel}{v}\right)^2 = \frac{\Delta B}{B} \simeq .04$$

(5) $$\gamma_{ii} = 1.8 \times 10^{-7}\ \mu^{-1/2}\ E^{-3/2}\ \ \Lambda\ n$$

This mean free path allows the higher energy trapped particles to drift upward significant distances ($\lambda_{mfp} \simeq a$) in the plasma. This effect is experimentally seen from Figures 6 and 8 where the asymmetric effective temperature and neutral flux are shown. This observed asymmetry is of course, reversed with reversed toroidal field, and closely tied to temperature and density profiles as can be seen from the difference between Figures 10 and 11, where the plasma current was changed from 100 kA to 225 kA. At high currents the profiles are broader, and the high energy production source becomes closer to the high neutral density edge, thus enhancing the asymmetry.

For high enough energies so the mean free path is larger than the plasma radius, the central chord distribution function can be completely depleted. This effect is also observed experimentally by a dramatic drop in neutral flux above 4 - 7 keV in medium density plasmas.

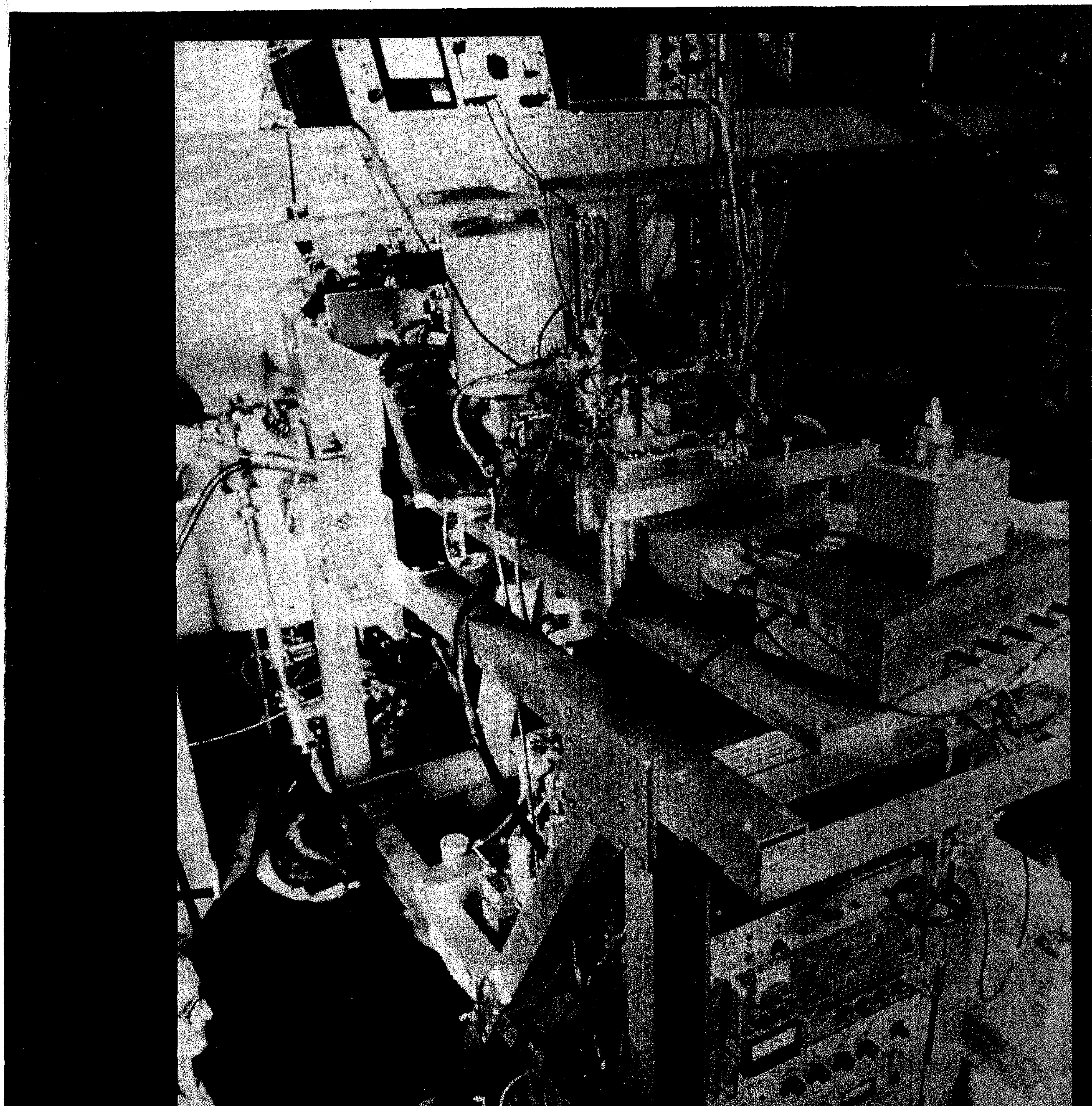

Change Exchange Apparatus
Figure 1

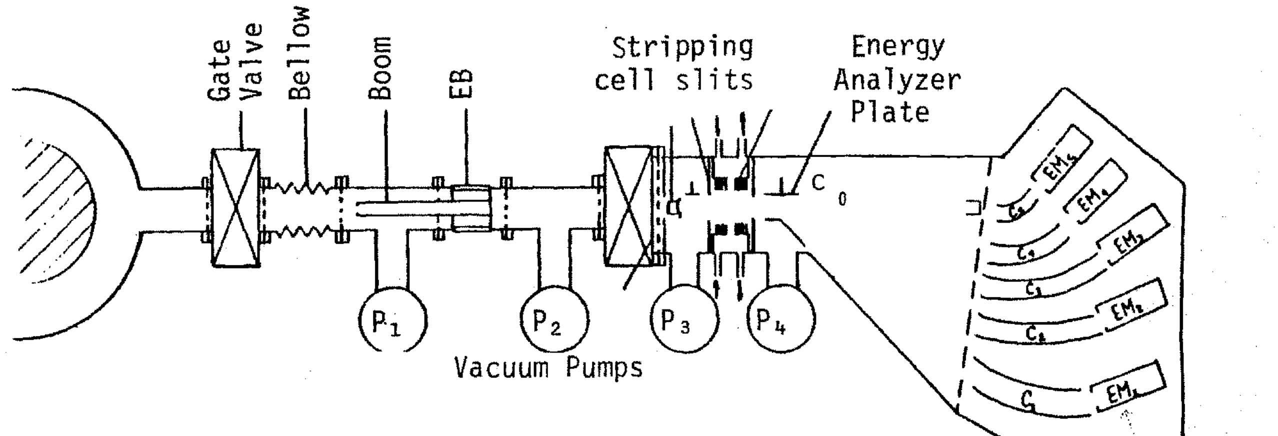

Charge Exchange Apparatus

Figure 2

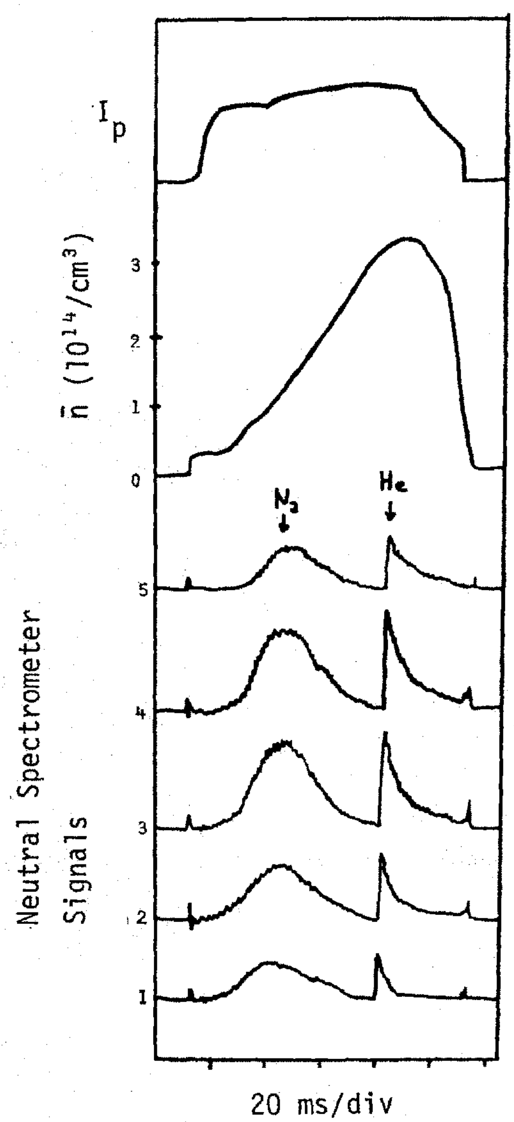

Typical Charge Exchange Data at High Density

Figure 3

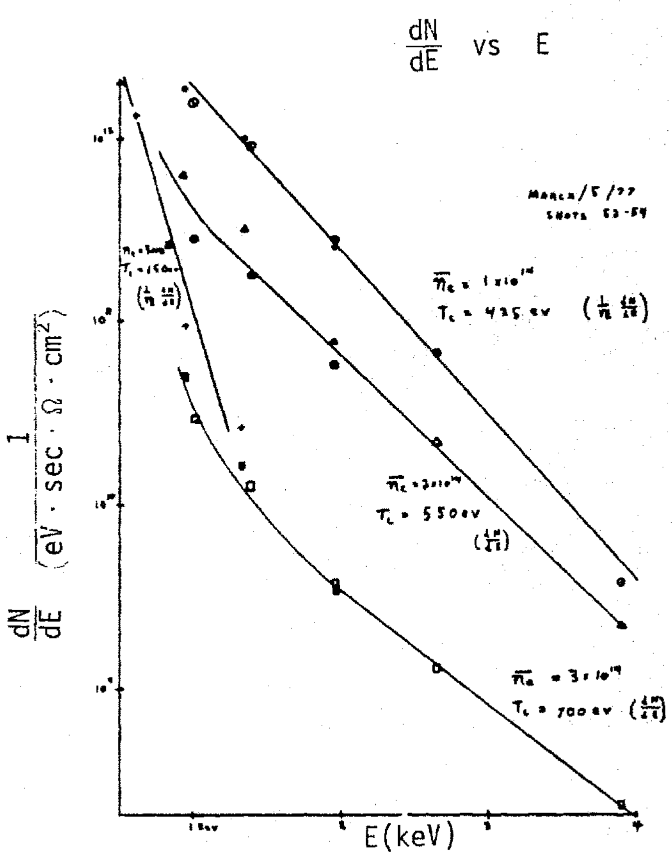

Neutral Spectra Change with Density

Figure 4

Typical Ion Temperature

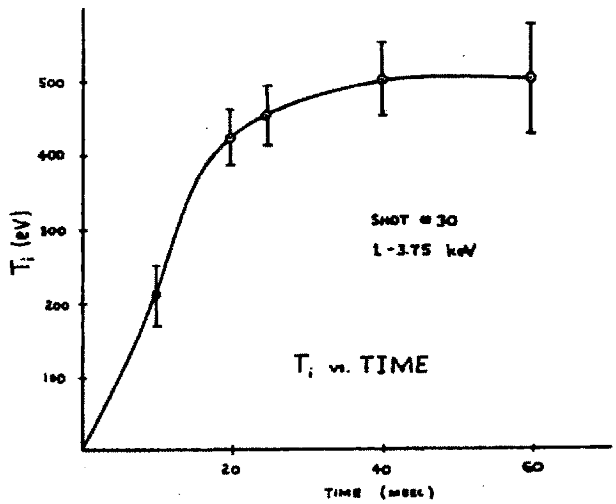

Figure 5

Typical Up-Down Spectra

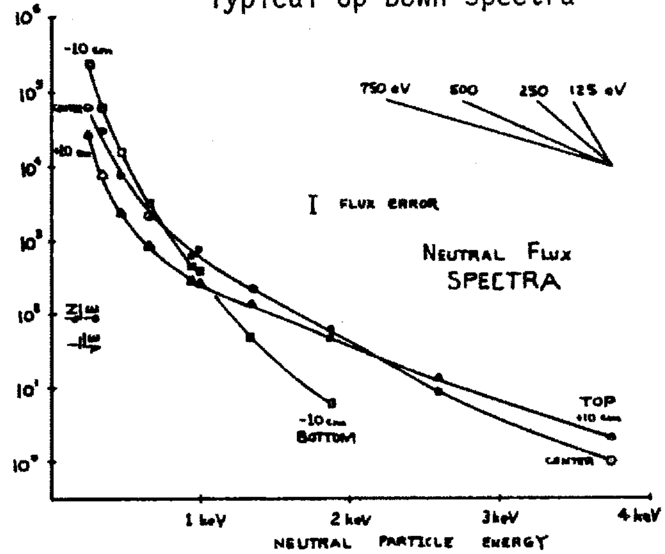

Figure 6

Alcator Port Ripple

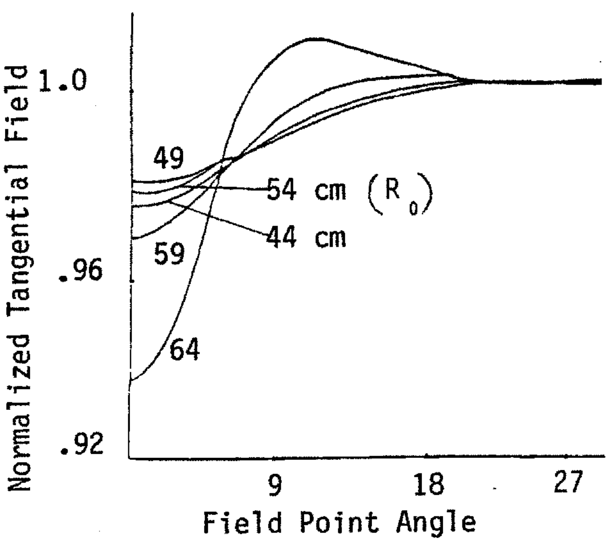

Figure 7

Typical Up-Down Spectra Temperature

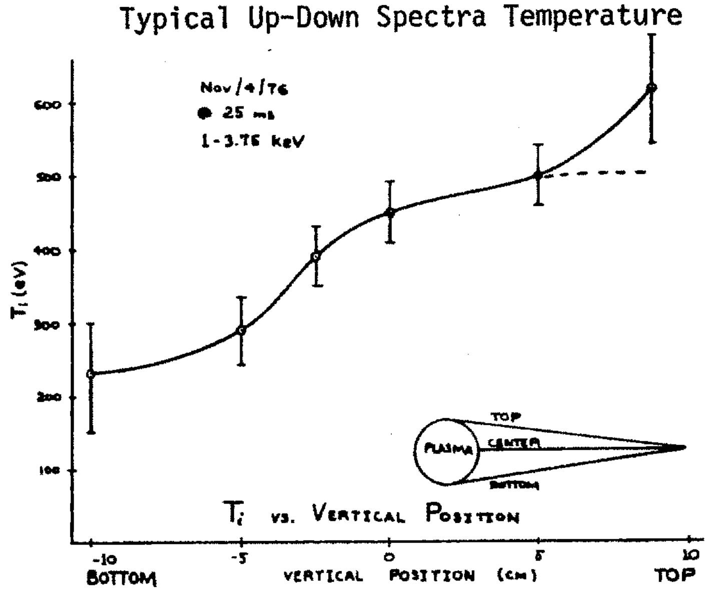

Figure 8

Ion Mean Free Path as a Function of Ion Energy

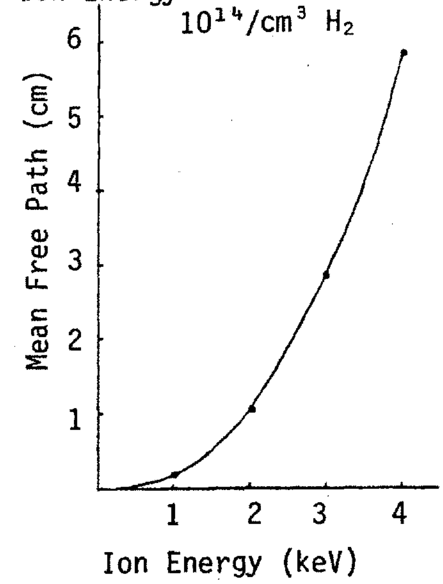

Figure 9

Neutral Flux vs. Up Down Position at High Plasma Current

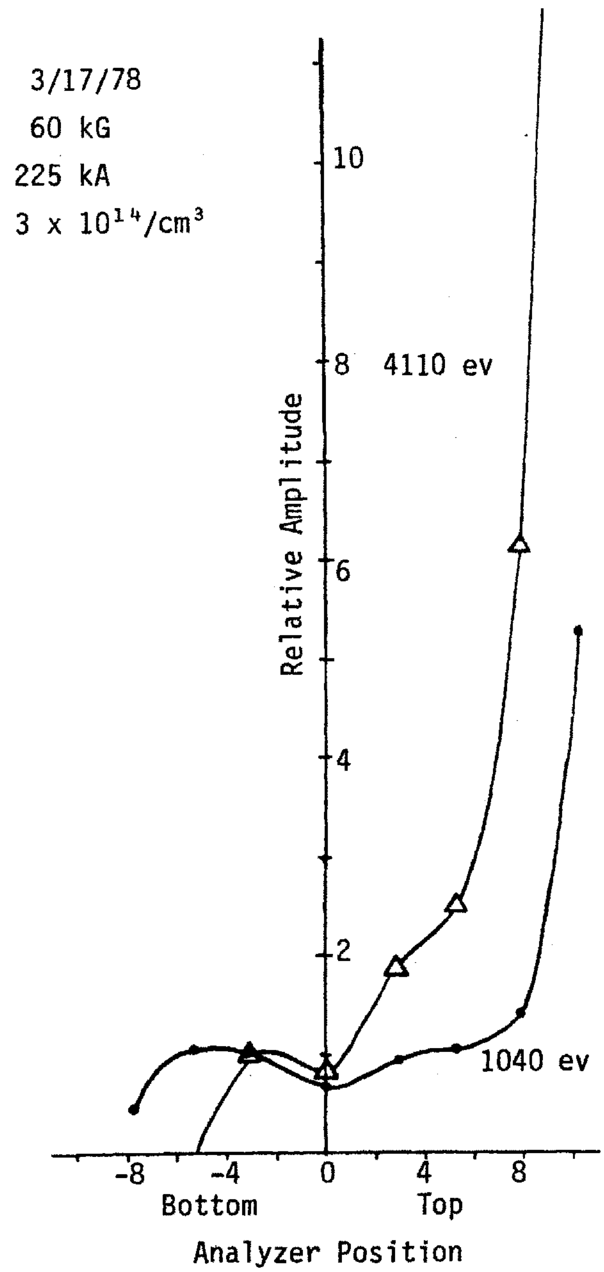

Figure 11

Neutral Flux vs. Up Down Position at Low Plasma Current

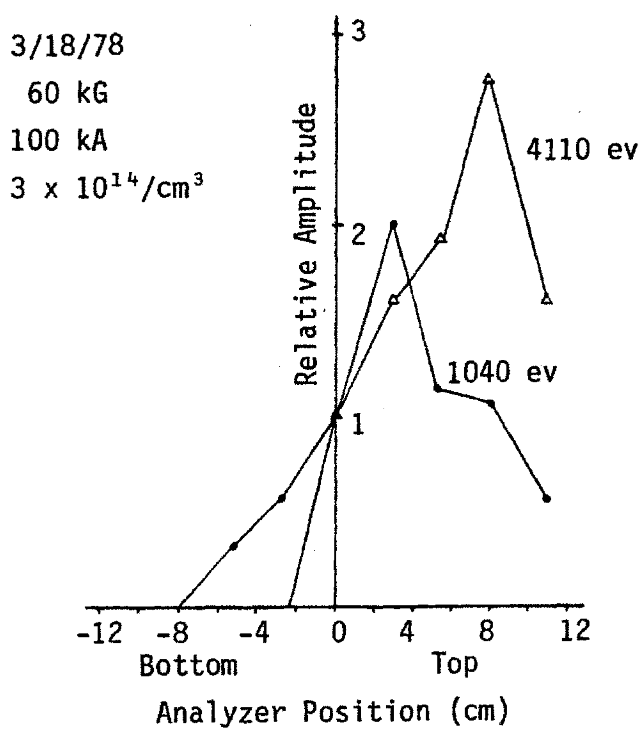

Figure 10

III-3.6. Bolometers and superbanana trapped particle detectors

In this Section, we present a zeroth order model to illustrate how trapped particles may also be an important power absorption loss. This discussion will be confined to the high energy particles at 5 keV, with $\omega_o = 2\,\omega_{ch} \simeq 2\,\pi\ 200$ MHz, 4% ripple, and $n_H = 10^{14}/cm^3$. The ICRF wave interacts with these trapped particles in a volume[103]

(1) $v_T = 4(\Delta R\ a\ \ell_T) \simeq 800\ cm^3 << 2\,\pi R\ \pi r^2 \simeq 10^5\ cm^3$

where

(2) $\Delta R \simeq 1$ cm (Eq. IV-4.2.(36))

(3) $a \simeq 10$ cm

(4) $\ell_T \simeq \frac{\pm 10°}{360}\ 2\,\pi R \simeq 20$ cm (Figure III-3.5.(7))

The trapped particles drift upward (or downward) at velocity

(5) $v_{\nabla B} = \frac{v_\perp^2}{2\,\omega_{ci}\,R} \simeq 1.4 \times 10^5$ cm/sec

and are confined a time

(6) $t_T \simeq \frac{a}{v_{\nabla B}} \simeq 7.1 \times 10^{-5}$ sec

before leaving the plasma. A large fraction of velocity space is trapped, so that

(7) $n_T \simeq n_o \frac{v_\parallel}{v} \simeq 2 \times 10^{13}\ cm^{-3}$

Since these trapped particles have large $v_\perp$ and bounce back and forth through the resonant layer, they can absorb much more power than the statistical average (over the plasma volume) calculated in Section IV-4.2. If 50 kW were absorbed by these ions, they would reach an energy

$$(8) \qquad W = \frac{P\, t_T}{n_T\, v_T} \simeq 1.4 \text{ keV}$$

before leaving the plasma. These ions would have a parallel velocity

$$(9) \qquad v_{\parallel} \simeq \sqrt{\frac{\Delta B}{B}}\; v_{\perp} \simeq 2 \times 10^7 \text{ cm/sec}$$

and pass some

$$(10) \qquad N = \frac{v_{\parallel}}{v_{\nabla B}} \; \frac{a}{\ell_T} \simeq 70$$

times through the resonant layer, acquiring

$$(11) \qquad \Delta W \simeq \frac{W}{N} \simeq 20 \text{ eV}$$

per pass. This very crude calculation is in reasonable agreement with the energy kick we calculated from equation IV-4.2.(20) where we can make the second harmonic substitution of equation IV-4.2.(34).

$$(12) \qquad \Delta W = \left(\frac{k_{\perp}\, \rho}{\sqrt{2}}\right)^2 \frac{e^2}{2m} E_+^2 \frac{2\pi}{\omega'} \cong 2.2\text{x}10^{-11} \text{ ergs} \cong 14 \text{ eV}$$

where we used[103]

$$(13) \qquad E \simeq 1 \text{ statvolt/cm (Section IV- 5.3)}$$

$$(14) \qquad \omega' \simeq 2\, \omega_{ci} \frac{v_{\parallel}}{\ell_T} \frac{\Delta B}{B} \simeq 5 \times 10^{13} \text{ sec}^{-2}$$

$$(15) \qquad \frac{k_{\perp}\, \rho}{\sqrt{2}} \simeq .05$$

Upon the realization of the importance of this possibly large power loss mechanism, a trapped particle detector and bolometer were designed and built.[103] These probes were small (3/8 inch diameter), and could be inserted in any port, but in particular, at the antenna port (through the top and bottom keyholes), under and over the resonant layer where trapping is most likely to occur.

Figures 1 and 2 show a simple, conceptual design where a poloidal screen and the machine virtual limiters are used to shield out streaming particles, but not the superbanana orbits. The circuitry is similar to Figure III-3.4.(1) and the probe current can be estimated as

(16) $I_p \simeq e\, v_{\nabla B}\, n_T\, \ell_T\, w_p \simeq 4.5$ amperes

The parallel and perpendicular energy can also be estimated from the probe characteristics

(17) $W_{\parallel} = W_{\perp} \frac{\Delta B}{B} \simeq 200$ eV

if the probe can sustain the high voltage ($V \simeq 2W_{\parallel}/e \cong 400$ V) needed to repel the ions without causing a plasma discharge in the probe tip.

The bolometer probe is a simple .002" thick stainless steel foil, with thin, flattened thermocouple wires tack-welded to the back of the foil (Figures 2 and 3). The ohmic heating power surface density averaged over the torus vacuum chamber is

(18) $P/cm^2 = \frac{I\ V}{2\pi\ R\ 2\pi\ a} \simeq 11\ W/cm^2$

and from equation III-2.2.(4), the bolometer temperature increase over a 150 millisecond shot is approximately

(19) $T = \frac{P/cm^2\ t}{\rho\ c_p\ \Delta x} = 41°C$

where

(20) $\Delta x \simeq .002"$ foil + .002" thermocouple

The detector reponse time can be calculated from equation III-2.2.(9) as

$$(21) \quad \Delta t \simeq \frac{\Delta x^2}{\alpha} \simeq 2.6 \text{ msec.} \ll t_{RF} \simeq 20 \text{ msec.}$$

41°C corresponds to 1.6 mV, with cromel-alumel, type k, .062" OD jacketed Omegaclad thermocouple wire, which is easily measurable during the plasma shot. Localized trapped particle fluxes could give rise to large temperature increases. A short 20 msec. 50 kW pulse, on the other hand, would only produce 36 μV, and the measurement becomes extremely difficult due to the large $\frac{dB}{dt}$ and RF fields near the plasma. Even with a small 1 cm^2 loop in a 1 KG, 30 msec. decay time magnetic field, the pick-up voltage would be 300 μV.

To make the measurement of such small signals possible, a triple differential measurement scheme was used, as shown in Figure 3. The input differential amplifiers have a gain of 1000, and were tested to discriminate a 10 μV, 1 kHz (-3 db) signal on top of a 1 volt 60 Hz common mode noise. A second reference signal is used to subtract background temperature and pick-up. The second differential stage is high pass (τ > 2 sec) to avoid saturation (total series gain is 10^5). The third differential stage is at ground potential in the control room.

The jacketed thermocouple wires are twisted and shielded inside an RF tight stainless steel tube. The electronics is in a RF tight aluminum box that is in a larger, half-inch thick, soft steel magnetic shield box. The steel box is electrically tied to the vacuum vessel, and acts as an electrostatic guard for the aluminum box. A heavy braid shield covers the thermocouple wires between the Conex vacuum feedthrough and the aluminum box. The thermcouples and electronics are oriented so as to have minimum coupling to the tokamak OH and vertical field.

Electrostatic Trapped Particle Detector

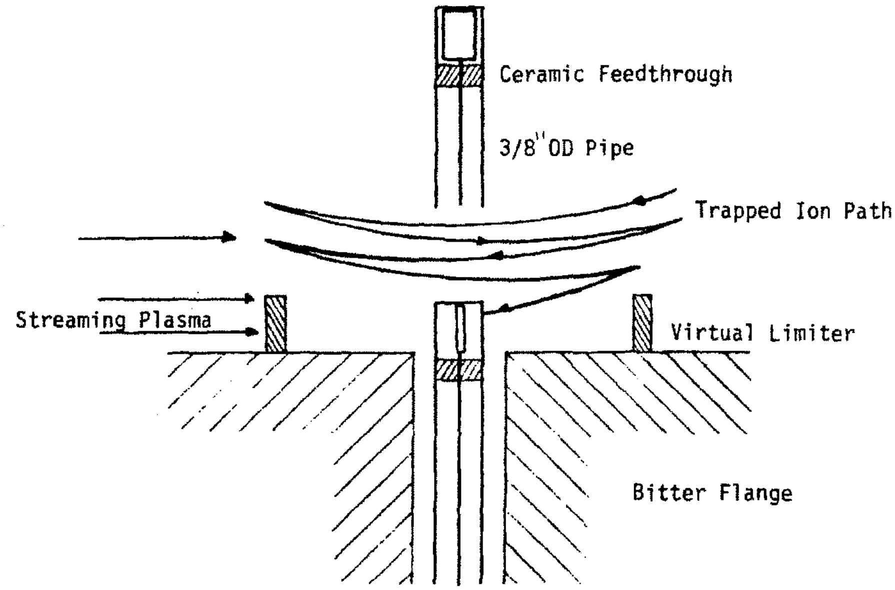

Figure 1

Electrostatic Trapped Particle Detector and Bolometer

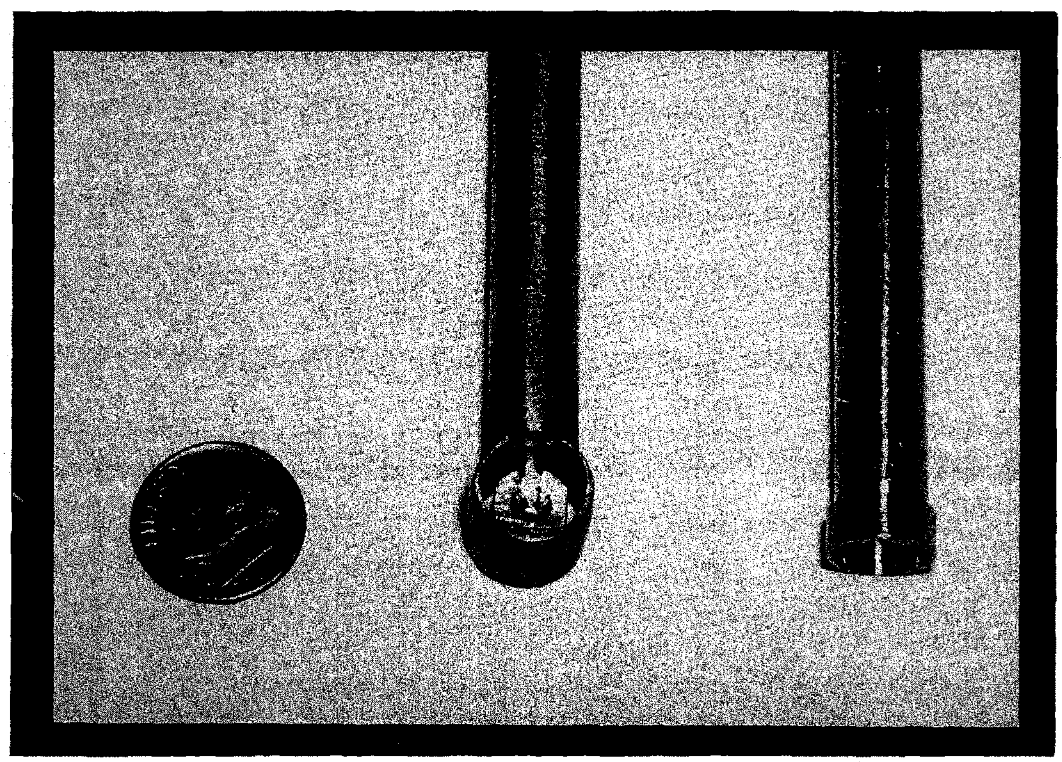

Figure 2

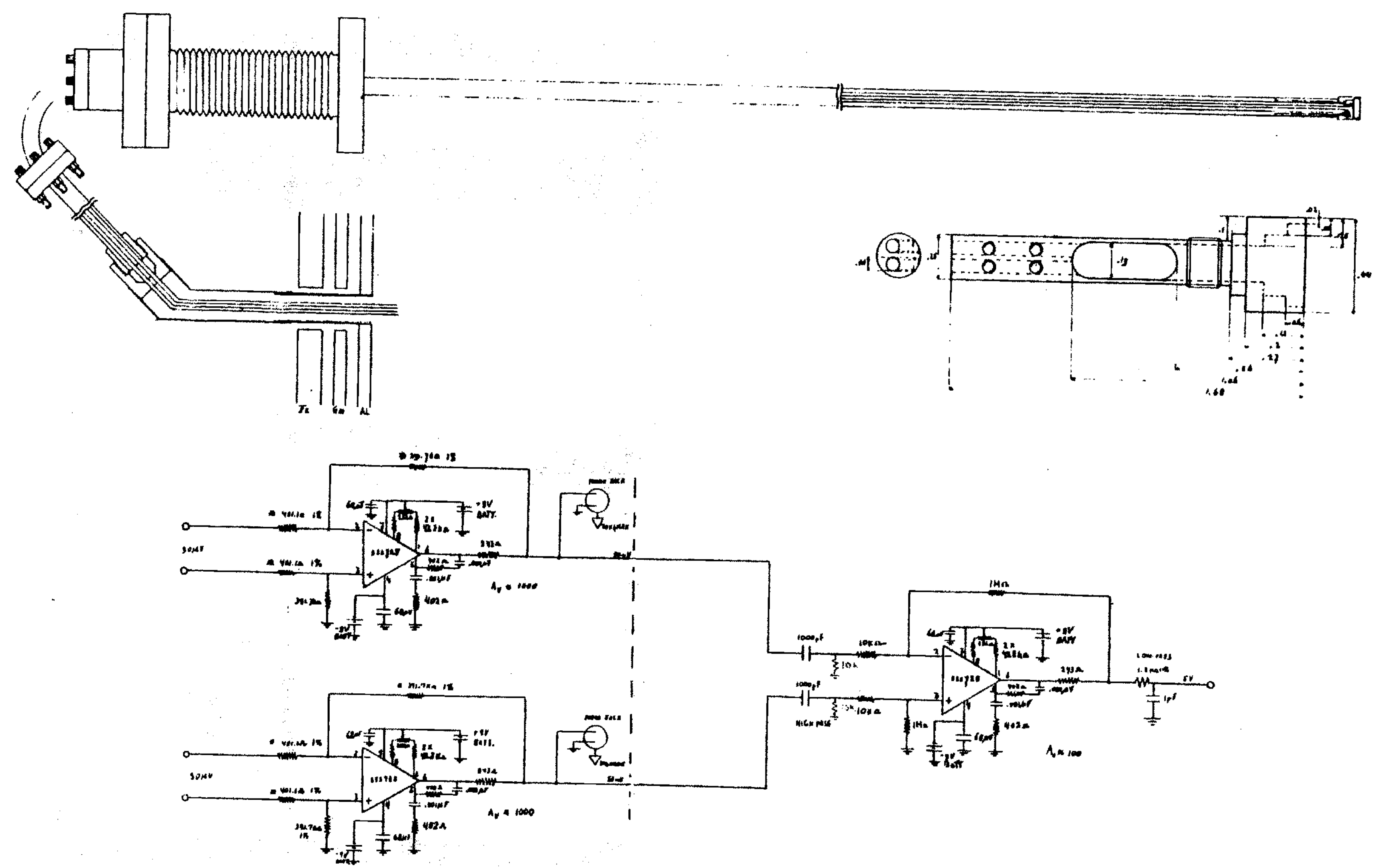

Mechanical and Electrical Drawing of Stainless Steel Foil Bolometer

Figure 3

IV. THEORETICAL WAVE MODELS AND COMPUTATIONS

IV-1. Introduction, First Order Models and Approximations

For the present work, many parameters and processes not fully discussed in the literature need to be defined[21,22,30-32] clearly in simple models to avoid confusion in the more complicated analytical or computational models. An intuitive feeling for the order of magnitude of most important parameters is derived from the most elementary foundations of physics. Among the processes that one must understand qualitatively and quantitatively, are Alfvén refractive index and wavelength[1], experimentally and theoretically derived radiation resistance[32], and wave quality factors[7]. The homogeneous[46] Cartesian waveguide is then usually sufficient to derive the most important scaling laws of the wave field structure and antenna design.

The reader more experienced in current ICRF work may wish to proceed directly to Sections IV-5., IV-6., and IV-7, where the more advanced models are discussed: inhomogeneous cylindrical plasma model, stochastic mode stacking, and single perpendicular pass regime.

IV-1.1. Eigenmode wave field approximations in toroidal geometry

In the toroidal geometry of the Alcator tokamak, the wave is bound by a highly conducting vacuum vessel. For wavelengths short enough to fit in the minor torus cross section, the wave will propagate and bounce around inside the toroidal cavity. Since the minor diameter is much less than the free space wavelength ($\lambda_o = 150$ cm at 200 mHz), we will have a density cutoff below which the wave cannot propagate. In Alcator we typically have

$$\omega_o \simeq 2\pi\ 200\ \text{MHz}$$

$$B_o \simeq 60\ \text{kG}$$

(1) $$n_e \simeq 3 \times 10^{14}/\text{cm}^3$$

$$\lambda_{\text{Alfvén}} \simeq 4\ \text{cm}$$

$$n_{\text{cutoff}} \cong 10^{13}/\text{cm}^3$$

For wave damping length smaller than the minor radius, no eigenmode is formed, a situation known as the single perpendicular pass regime (IV.7). For damping length of more than the minor radius, but less than the major radius ($R_o = 54$), we have perpendicular eigenmodes, but not toroidal ones. This situation is called the single toroidal pass regime. Since the Alcator aspect ratio ($R_o/a = 5.4$) is large, toroidal geometry maps out well into cylindrical geometry. (IV-3, IV-5, IV-6)

The basic physics of a perpendicular eigenmode can be illustrated with a simple TE_{10} mode (Transverse electric) in a rectangular waveguide along z, of width 2a, filled with an isotropic non-dispersive dielectric (Figure IV-1.2 (1)). The electric and magnetic fields (from Faraday's Law) are of the form (MKS)[134]

(2) $$E_y = E_o \sin(k_x x)\, e^{i(k_z - \omega t)}$$

(3) $$H_x = -E_y \frac{k_{\parallel}}{\omega\mu_o}$$

(4) $$H_z = E_\circ \frac{-ik_x}{\omega\mu_\circ} \cos(k_x x)\, e^{i(k_z - \omega t)}$$

with boundary conditions

(5) $$E_y\Big|_{x = 0,\ 2a} = 0$$

(6) $$k_x \simeq k_\perp \simeq \mu_\perp \frac{\pi}{2a}$$

where $\mu_\perp$ is the perpendicular mode number (typically $1 \leqslant \mu_\perp \leqslant 10$ for Alcator).

Similarly, in cylindrical geometry, using the usual coordinates r, θ, z, we have TE or TM eigenmode solutions of the form[134]

(7) $$A = A_\circ \cos(m\theta)\, J_m(k_\perp r)\, e^{i(k_\parallel z - \omega t)}$$

where m = 0, 1, 2...

For waves of the Alfvén class near the ion cyclotron frequency ($\omega \cong 2\omega_{ci}$), we notice (Appendix 1) two basic differences between a plasma and a "normal" dielectric. First, $\varepsilon_\parallel >> \varepsilon_\perp$, so $E_\parallel << E_\perp$, and thus the wave and its resulting eigenmode must be TE. Second, the wave is not allowed to be linearly polarized, so we must let the eigenmodes rotate (elliptically polarized) as they propagate along z. We then have wave field solutions of the form[46]

(8) $$A = A_\circ J_m(k_\perp r)\, e^{i(m\theta + k_\parallel z - \omega t)}$$

with $m = 0 \pm 1 \pm 2 \pm 3 \ldots$

We must allow m to be both positive and negative, since a field rotating with the ions "feels" a different dielectric constant than one rotating against the ions. The ion trajectory

(9) $$r_i = r_\circ \, e^{i(-\theta - \omega_{ci} t)}$$

and the m < 0 field patterns are left-handed. (The m < 0 electric fields are also predominately left-handed, as will be seen in IV-5.3.) The m > 0 modes are right-handed, and have a larger dielectric constant than the m < 0 modes (Section IV-5.3). The +m and -m modes thus have different $k_\parallel$, are orthogonal, and must be considered separately. For m = 0, equations (7) and (8) are equivalent since the mode field pattern is not rotating either way. For typical Alcator ICRF wave and plasma parameters, radial mode numbers (μ) up to 5 can be obtained with small m and $k_\parallel$ (Section IV-5.3).

With damping lengths larger than the major radius, both perpendicular and toroidal eigenmodes can exist. To zeroth order, we have a dispersion relation of the form

(10) $$k_\perp^2 + k_\parallel^2 = k_T^2 \cong k_A^2$$

combining (6) with (10) fully determines $k_\parallel$, and toroidal resonances will occur if

(11) $$\begin{aligned} 2\pi R_\circ &= n\lambda_\parallel \\ k_\parallel R_\circ &= n \end{aligned}$$

where n is the toroidal mode number (typically 1 < n < 60 for Alcator).

The orthogonality property of eigenmodes with different mode numbers enables these modes to propagate and be calculated independently without coupling to each other. For our simple TE modes, we can see easily that indeed TE_{mo} is independent of TE_{no}, since for $m \neq n$

$$(12) \qquad \int_0^{2a} \sin\left(m \frac{\pi x}{2a}\right) \sin\left(n \frac{\pi x}{2a}\right) dx = 0$$

Propagation along z is also orthogonal for $k_{\parallel 1} \neq k_{\parallel 2}$.

Physically, an eigenmode resonance is formed when two or more waves overlap coherently in space. The usual standing wave is found when a wave reflects off a boundary and adds to itself, (i.e. the perpendicular eigenmodes).

$$(13) \qquad \cos(kx - \omega t) + \cos(-kx - \omega t) = 2 \cos kx \cos \omega t$$

In toroidal geometry, a toroidal standing wave can be formed by two waves of the same $k_{\parallel}$ and perpendicular field structure circulating in opposite directions around the torus. If, on the other hand, the two $k_{\parallel}$ are not the same, but one of them satisfies (11), we have a resonant running mode

$$(14) \qquad \cos(kz - \omega t) + \cos(kz - \omega t) + \ldots = A \cos(kz - \omega t)$$

Physically, this amounts to a wave leaving the antenna, circulating in one direction around the torus, and adding coherently to itself. In this way, for small damping, and either standing or running waves, the circulating wave power can be many times the power coupled from the antenna.

IV-1.2. Theoretical radiation resistance

To calculate the effective radiation resistance (R_R) the plasma presents to the antenna, we assume for the moment a simple TE_{10} eigen-mode structure in a rectangular wave guide (Section IV-1.1) as seen in Figure 1, and the single toroidal pass regime.

$$(1) \qquad \frac{1}{R} < k_{\parallel i} << \frac{1}{a}$$

Since we have a lossless system except for the plasma, the power into the antenna, P_{in}, must equal the total wave Poynting flux flowing down the waveguide ($\pm$ z), $2P_{EXH}$. Thus (MKS)

$$(2) \qquad P_{in} = \frac{I^2 R_R}{2} = \frac{IV}{2} = 2P_{EXH}$$

where

$$(3) \qquad V = E_A \ell = E_o \ell \sin k_\perp d \cong E_o k_\perp d\ell$$

$$(4) \qquad P_{EXH} = \iint_S \frac{E_y X H_x}{2} \cdot ds = E_o^2 \frac{a^2 k_\parallel}{\omega\mu_o}$$

and combining (2), (3), and (4) we have

$$(5) \qquad R_R = \frac{V^2}{4 P_{EXH}} = \frac{E_a^2}{E_o^2} \frac{\ell^2}{k_\parallel a^2} \frac{\omega\mu_o}{4} = \frac{\beta_a^2 \ell^2}{k_\parallel a^2} \frac{\omega\mu_o}{4}$$

where we defined

$$(6) \qquad \beta_a = \frac{E_a}{E_o} \cong k_\perp d \cong \mu_\perp k_{o\perp} d$$

Equation (5) is the most important coupling scaling law. For typical ICRF in Alcator at high density

$$
(7) \quad
\begin{array}{ll}
n_e \cong 3 \times 10^{14}\ \mathrm{cm}^{-3} & d \cong 1\ \mathrm{cm} \\
f_\circ \cong 200\ \mathrm{MHz} & \ell \cong 20\ \mathrm{cm} \\
B_\circ \cong 60\ \mathrm{kG} & k_\parallel \cong k_A/3 \cong .5/\mathrm{cm} \\
\lambda_A \cong 4\ \mathrm{cm} & \beta_a \cong .16 \\
a \cong 10\ \mathrm{cm} & R_R \cong .8\ \mathrm{Ohms}
\end{array}
$$

Simply setting $k_\parallel$ of order $k_A{}^2/3$ is sufficient for rough calculations except at densities near the mode cutoff where $k_\parallel \rightarrow 0$ and R_R becomes momentarily large. The factor, $\beta_a{}^2$, is much more difficult to estimate correctly, since it can easily vary over more than two orders of magnitude due to the evanescent edge layer, as we shall see in Section IV-5.

Of course, many modes can exist at high density, and the total radiation resistance will be the sum over all the propagating poloidal and radial eigenmode number combinations

$$(8) \qquad R_T = \sum_\mu \sum_m R_{\mu m}$$

Calculating P_{EXH}, β_a and R_T accurately will require careful modeling of the antenna, and evaluation of the dispersion relation and wave fields in realistic geometry and profiles. This will be the subject of Section IV-5.3.

If we allow the damping to be very small and $k_\parallel R_\circ = n$ so as to have a toroidal eigenmode, another almost equivalent approach is to consider the back EMF produced by the wave in the antenna loop,

$$(9) \qquad V_{loop} = -\frac{d\Phi}{dt} = \omega\ \ell d\ \mu_\circ\ H_{edge}$$

and the usual definition of Q

(10) $$Q = \frac{\omega W}{P_{dis}}$$

where

(11) $$W \cong \left\langle \frac{1}{2} \mu_o H^2 \right\rangle \text{Vol} \cong \frac{1}{8} \mu_o H_o^2 \text{ Vol}$$

We have again from conservation of power

(12) $$P_{in} = P_{dis} = \frac{V^2_{loop}}{2 R_R}$$

and combining (9) to (12) we have[93]

(13) $$R_R = \left(\frac{H_{edge}}{H_o}\right)^2 (\ell d)^2 \frac{2\omega\mu_o}{\pi^2 a^2 R} Q$$

The importance of the antenna loop area and the evanescent edge are again emphasized, but a new factor, Q, has appeared. Physically, a high Q resonant toroidal eigenmode does not change the single pass Poynting flux P_{EXH} of eq. (4),but increases the antenna electric field, E_a, by a factor proportional to $\sqrt{Q}$.Thus at constant power and increased voltage, one has a large R impedence,R_R. Surprisingly, but quite correctly, weak damping produces a larger antenna loading and thus better coupling (Neglecting Parasitics, Section IV-2.6 and IV-4.5).

The above formulations, although simple and physically tangible, are very limited. Either one must be in a narrow window of damping length to have a single toroidal pass regime or to be on top of a narrow high Q toroidal resonance. We will treat this problem rigorously, with much more general and flexible formulations in Sections IV-5, IV-6 and IV-7.

Theoretical Radiation Resistance

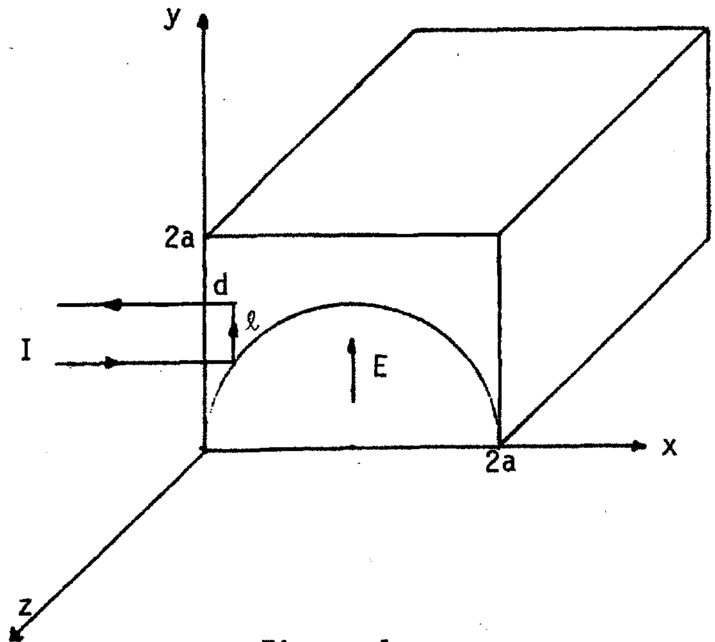

Figure 1

Experimental Radiation Resistance

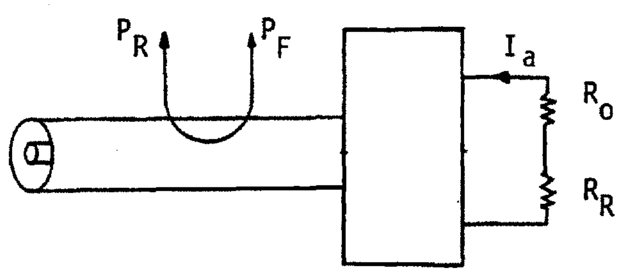

Figure 2

IV-1.3. Experimental radiation resistance

For typical loop antenna coupling systems, the real radiation resistance, R_R, is usually combined with a large reactance. To ease R_R measurements, and to allow efficient transfer of power between the transmitter and the antenna, a matching network system transforms the complex antenna load $R_R + iX$ into a real load of about the transmission line impedence (Figure IV-1.2.(2)). By measuring the antenna current with simple current loops inside the antenna, and the incoming and reflected power with directional couplers, we can use conservation of power to write:

(1) $P = I^2_{rms} R$

(2) $P_{forward} - P_{reversed} = I^2_{rms} (R_{losses} + R_{plasma})$

Coupling structure losses are easily measured by observing the loading resistance without plasma when the wave cannot propagate in the tokamak. Antenna matching system losses of the order of .5 ohms are common, and thus plasma radiation resistances of at least several ohms are necessary for efficient coupling.

IV-2. Cold Plasma Approximation and Cartesian Dispersion Relations.

The next step is to produce a rigorous, quantitative evaluation of the dispersion relation for the high density regime. Many approximations[7] are made,and must be justified quantitatively in view of the accuracy needed later.

The three main steps are the formulation of the dielectric tensor, wave equation, and dispersion relation[7,45]. All three are evaluated at high and low density and for the several harmonic numbers used in the experiment. Both branches, slow and fast[7,22], of the dispersion relation are also investigated over a range of wave $k_{\parallel}$, $k_{\perp}$ and frequency, and plasma parameters and profiles.

IV-2.1. Cold dielectric tensor wave equation and dispersion relation

To derive the general cold dielectric tensor and wave equation,we proceed exactly as in Appendix 1 ,except that we let E_z and E_y be variables as well as arbitrary $\vec{k}$.[45]

Assuming first order quantities proportional to

(1) $e^{i(\vec{k}\cdot\vec{r} - \omega t)}$

and a current density

(2) $\vec{J} = \sum_k n_k z_k \varepsilon_k e\vec{V}_k$

where

k = electrons, ions

z = charge magnitude

ε = charge signs

the equation of motion is

$$(3) \quad m_k \frac{d\vec{v}_k}{dt} = z_k \, \varepsilon_k \, e(\vec{E} + \frac{\vec{v}_k}{c} \times \vec{B})$$

For an ion,(3) becomes

$$(4) \quad v_x = \frac{e}{-i\omega M} (E_x + v_y \frac{B_\circ}{c})$$

$$(5) \quad v_y = \frac{e}{-i\omega M} (E_y - v_x \frac{B_\circ}{c})$$

Substituting (5) → (4)

$$(6) \quad v_x = \frac{\frac{i\omega_{ci}c}{\omega \; B_\circ} E_x - \frac{\omega_{ci}{}^2 c}{\omega^2 \; B_\circ} E_y}{1 - \frac{\omega_{ci}{}^2}{\omega^2}}$$

$$(7) \quad v_y = \ldots$$

and the expressions become overwhelmingly complicated as other species are added.

The problem can be greatly simplified by separating the components into left and right hand components. Thus,still being totally general,we assume

$$(8) \quad v\mp = v_x \mp i\varepsilon v_y \quad \text{and} \quad E\mp = E_x \mp i\varepsilon E_y$$

Equation (4) and (5) can now simply be added giving

$$(9) \quad v_k\mp = \frac{ic}{B_\circ} \frac{\varepsilon_k \, \omega_{ck}}{\omega \pm \omega_{ck}} E\mp$$

and just as before

$$(10) \quad v_{k,z} = \frac{ic}{B_\circ} \frac{\varepsilon \, \omega_{ck}}{\omega} E_z$$

Defining the dielectric tensor

(11) $\vec{D} = \vec{\vec{K}} \cdot \vec{E} = \vec{E} + \frac{4\pi i \vec{J}}{\omega}$

we need now only to substitute (9) and (10) in (2), and then finally into (11) to get the full, general cold plasma dielectric tensor. An important property of tensors is that they can simply be added. The total dielectric tensor can be represented as the sum of the free space tensor, (an identity diagonal tensor), the ion current tensor, and the electron current tensor. Each of the charge particle tensors have on-diagonal polarization drift terms ($K_{xx} = K_{yy}$), and off-diagonal $\vec{E}X\vec{B}$ drift terms ($K_{xy} = -K_{yx}$), and of course, an inertia term along B_o (K_{zz}).

When solving for a wave, we must always use the total dielectric tensor, but once the fields are found, we can look at each of the tensors individually to see what the velocities are. For example, two opposite cancelling currents do not affect the wave, but there is still kinetic energy stored in these velocities. Furthermore, each species tensor can be divided into a reactive part and a dissipative part. This formulation is particularly attractive in complicated situations near singularities, where the absorption mechanism is not well understood, and one wants to know which species are heated.

Furthermore, we will use the widely accepted notation introduced by Stix[45].

(12) $$\vec{\vec{K}} \cdot \vec{E} = \begin{bmatrix} S & -iD & 0 \\ iD & S & 0 \\ 0 & 0 & P \end{bmatrix} \cdot \begin{bmatrix} E_x \\ E_y \\ E_z \end{bmatrix}$$

where

(13) $S = \frac{R + L}{2}$

(14) $D = \frac{R - L}{2}$

(15) $R = 1 - \sum_k \frac{\pi_k^2}{\omega^2} \left(\frac{\omega}{\omega + \varepsilon\, \omega_{ck}}\right)$

(16) $L = 1 - \sum_k \frac{\pi_k^2}{\omega^2} \left(\frac{\omega}{\omega - \varepsilon\, \omega_{ck}}\right)$

(17) $P = 1 - \sum_k \frac{\pi_k^2}{\omega^2}$

The R and L notations stand for right and left hand polarized. If R and L are the same as in the very low frequency regime, then D for difference is zero, and the wave is linearly polarized as we noted in Appendix 1. If R and L are not the same, we generally have an elliptically polarized wave.

The wave equation and dispersion relation follow easily as before from Maxwell's equations.

(18) $\nabla \times \vec{E} = \frac{-1}{c} \frac{\partial \vec{B}}{\partial t}$

(19) $\nabla \times \vec{B} = \frac{4\pi \vec{J}}{c} + \frac{1}{c} \frac{\partial \vec{E}}{\partial t} = \frac{1}{c} \frac{\partial \vec{D}}{\partial t}$

(20) $\vec{k} \times (\vec{k} \times \vec{E}) + \frac{\omega^2}{c^2} \vec{\vec{K}} \cdot \vec{E} = 0$

Defining a refractive index

(21) $\vec{n} = \frac{\vec{k} c}{\omega}$

we have

$$(22) \quad \vec{n} \times (\vec{n} \times \vec{E}) + \overset{\leftrightarrow}{K} \cdot \vec{E} = 0$$

$$(23) \quad \begin{bmatrix} S - (n_y^2 + n_z)^2 & -iD + n_x n_y & n_x n_z \\ iD + n_x n_y & S - (n_x^2 + n_z^2) & n_y n_z \\ n_x n_z & n_y n_z & P + (n_x^2 + n_y^2) \end{bmatrix} \bullet \begin{bmatrix} E_x \\ E_y \\ E_z \end{bmatrix} = 0$$

We can usually choose our coordinate system so as to have $n_y = 0$, so that (23) becomes

$$(24) \quad \begin{bmatrix} S - n_z^2 & -iD & n_x n_z \\ iD & S - n^2 & 0 \\ n_x n_z & 0 & P - n_x^2 \end{bmatrix} \bullet \begin{bmatrix} E_x \\ E_y \\ E_z \end{bmatrix} = 0$$

Setting this determinant equal to zero gives the general dispersion relation.

IV-2.2. Zero electron mass dispersion relation and polarization

We now evaluate the dielectric tensor elements in the $\omega \ll \omega_{ce}$ regime for a two component plasma.

$$(1) \qquad R = 1 - \frac{\pi_e^2}{\omega(\omega - \omega_{ce})} - \frac{\pi_i^2}{\omega(\omega + \omega_{ci})}$$

We can make several important simplifications since

$$(2) \qquad \begin{aligned} &\pi_i^2 \ll \pi_e^2 \\ &\omega \ll \omega_{ce} \end{aligned}$$

$$(3) \qquad \frac{\pi_e^2}{\omega_{ce}} = \frac{\pi_i^2}{\omega_{ci}}$$

then

$$(4) \qquad R \cong 1 + \frac{\pi_i^2}{\omega_{ci}^2(1 + \Omega)}$$

where we defined

$$(5) \qquad \Omega = \frac{\omega}{\omega_{ci}}$$

For ICRF, the error in the tensor element will be of order $\frac{\omega}{\omega_{ce}} \approx \frac{m}{M} \ll 1$, a good approximation for any practical application.

Similarly,

$$(6) \qquad L = 1 + \frac{\pi_i^2}{\omega_{ci}^2\,(1 - \Omega)}$$

$$(7) \qquad S = \frac{R + L}{2} = 1 + \frac{\pi_i^2}{\omega_{ci}^2}\;\frac{1}{1 - \Omega^2}$$

(8) $D = \frac{R - L}{2} = \frac{\pi_i^2}{\omega_{ci}^2} \; \frac{-\Omega}{1 - \Omega^2}$

(9) $P = 1 - \frac{\pi_e^2}{\omega^2} - \frac{\pi_i^2}{\omega^2} \simeq 1 - \frac{\pi_e^2}{\omega^2}$

Since ω is of order ω_{ci}, and at high density

$\frac{\pi_i^2}{\omega_{ci}{}^2}$ is of order 10^3

$\frac{\Omega}{1 - \Omega^2}$ is of order 1

$\frac{\pi_e^2}{\omega^2}$ is of order 10^6

we can ,to a very good approximation, write

(10) $S = \frac{\pi_i^2}{\omega_{ci}^2} \; \frac{1}{1 - \Omega^2}$

(11) $D = -\Omega S$

(12) $P = - \frac{\pi_e^2}{\omega^2}$

For the moment, let's assume that we are looking for waves of the Alfvén type with $n_x \approx n_z \approx 40$ as we saw in Appendix 1. The third line of the wave tensor equation then reads

(13)
$$n_x n_z \, E_x + (P - n_x{}^2) \, E_z = 0$$
$$40^2 \, E_x \quad -10^6 \quad E_z = 0$$

and thus $E_z \ll E_x$, and E_z would have a negligible effect on the first two lines of the tensor. For practical purposes, we are now left with the 2 x 2 tensor equation

$$(14)\quad \begin{bmatrix} S - n_\parallel^2 & -iD \\ iD & S - (n_\perp^2 + n_\parallel^2) \end{bmatrix} \cdot \begin{bmatrix} E_x \\ E_y \end{bmatrix} = 0$$

Since this amounts to assuming $P \to -\infty$, or simply $m_e \to 0$, this formulation is usually referred to as the zero electron mass approximation, and requires $E_z = 0$. Solving the determinant

$$(15)\quad (S - n_\parallel^2)(S - (n_\perp^2 + n_\parallel^2)) - D^2 = 0$$

$$(16)\quad n_\perp^2 = \frac{(S - n_\parallel^2)^2 - D^2}{S - n_\parallel^2}$$

Defining an Alfvén refractive index

$$(17)\quad \vec{N} = \vec{n}\,\frac{\omega_{ci}}{\pi_i}$$

and multiplying both sides of (16) by ω_{ci}^2/π_i^2, we have [7]

$$(18)\quad N_\perp^2 = (A - N_\parallel^2) + \frac{A(1 - A)}{(A - N_\parallel^2)}$$

where we defined

$$(19)\quad A = \frac{1}{1 - \Omega^2}$$

Figures 1-4 are plots of $N_\perp^2$ vs $N_\parallel^2$, and $N_\perp$ vs $N_\parallel$ for different regimes. Several points are to be noted. First, one distinguishes clearly the fast wave from the slow wave, since the fast wave has a refractive index several times smaller than the slow wave. Second, the slow wave is evanescent for $\Omega > 1$, but the fast wave propagates both above and below ω_{ci}. Third, for propagation across B_o, $k_\parallel = 0$, then $N_\perp = 1$ independently of the frequency regime. Fourth, for fast wave propagation along B, $N_\perp = 0$, and

$$(20)\quad N_\parallel = \frac{1}{\sqrt{\Omega + 1}}$$

so one can then write the approximate simple dispersion relation

(21) $k_\perp^2 + (\Omega + 1)\, k_\parallel^2 = k_A^2$

From the first line of the dispersion relation (14),

(22) $$E_x = \frac{D}{S - n_\parallel^2}\, iE_y$$

we can calculate the ratio of the left hand E_+ to the right hand E_- polarized electric field components.

(23) $$\frac{E_+}{E_-} = \frac{E_x + iE_y}{E_x - iE_y} = \frac{D + S - n_\parallel^2}{D - S + n_\parallel^2} = \frac{R - n_\parallel^2}{-L + n_\parallel^2} =$$

$$= \frac{\frac{1}{\Omega + 1} - N_\parallel^2}{\frac{1}{\Omega - 1} + N_\parallel^2}$$

For perpendicular propagation ($N_\parallel = 0$)

(24) $\frac{E_+}{E_-} = \frac{\Omega - 1}{\Omega + 1} = .2$ for $\Omega = 1.5$

.33	"	2
.6	"	4
.78	"	8

For parallel propagation (20), $E_+/E_- = 0$ independently of Ω

If we allow $k_y \neq 0$ then (IV-2.1(23))

(25) $$E_x = \frac{D + i\, n_x n_y}{S - (n_y^2 + n_z^2)}\, iE_y$$

and

(26) $$\frac{E_+}{E_-} = \frac{\frac{1}{\Omega + 1} + i\, N_x N_y - N_y^2 - N_z^2}{\frac{1}{\Omega - 1} + i\, N_x N_y + N_y^2 + N_z^2}$$

and the polarization is a function of all three components of $\vec{k}$.

Fast and Slow Wave Dispersion Relations

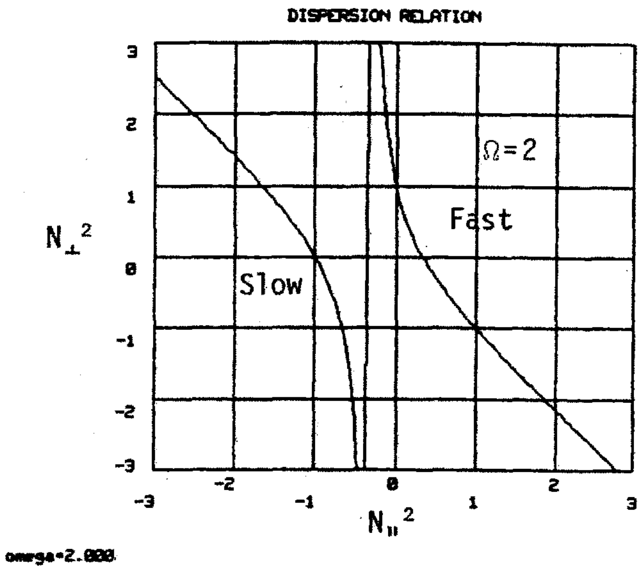

Figure 1

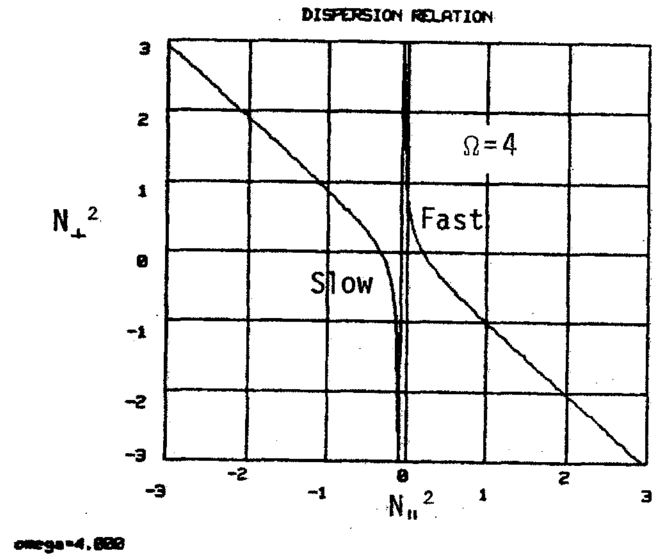

Figure 2

Fast and Slow Wave Dispersion Relations

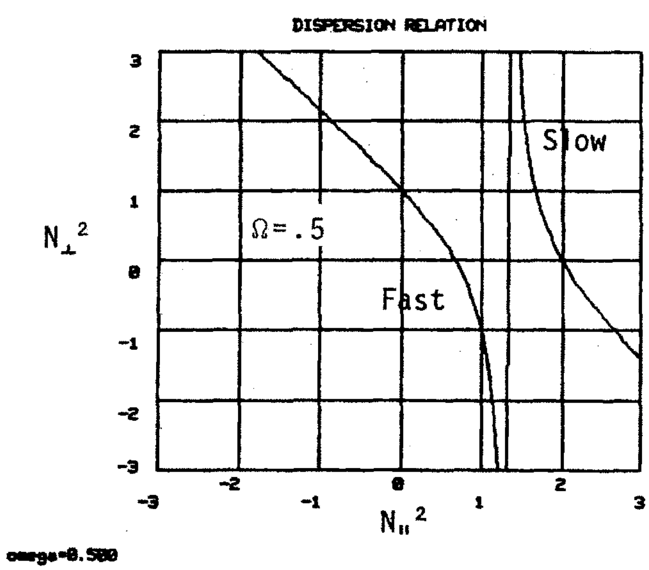

Figure 3

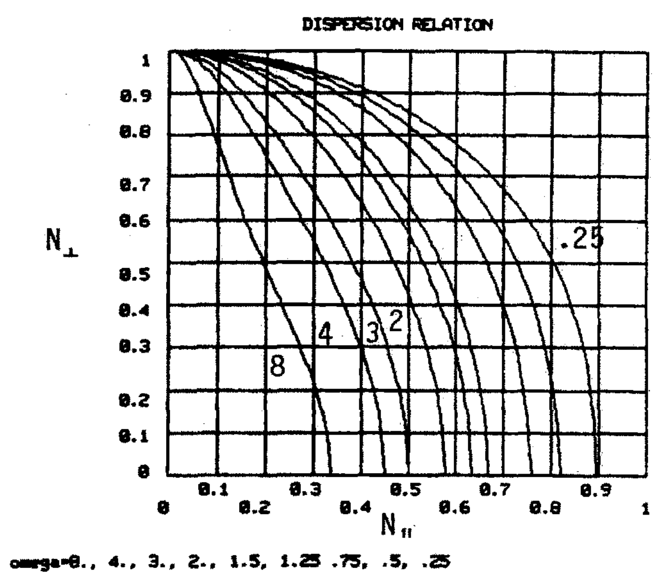

Figure 4

IV-2.3. Inhomogeneous Cartesian waveguide and WKB

We now assume realistic Alcator density and temperature profiles of the form (Figures 1, 2, 3).[28-29]

(1) $n = n_o\left[1 - \left(\frac{r}{9.7}\right)^2\right]$ $\qquad 0 < r < 9$ cm

$= n_o \; .139 \, e^{-12(r/9-1)}$ $\qquad 9 < r < 12.5$ cm

(2) $T = T_o \, e^{-r^2/a_T{}^2}$ $\qquad 0 < r < 12.5$ cm

where

$$a_T{}^2 = \frac{3}{2} a_1{}^2 \frac{q_o}{q_1}, \quad a_1 = 9 \text{ cm}, \; q_o \approx .9, \; q_1 \approx 5$$

Fixing $k_\parallel$ one can now calculate $k_\perp$ as a function of r using eq. IV-2.2(16) Figure 5 shows $k_\perp{}^2$ as a function of r for $k_\parallel$ = 0, .2, .4, .6, .8, 1.0, 1.2/cm, and for the standard condition

(3) f_o = 200 MHz

$n_o = 5 \times 10^{14}$ Hydrogen

$\Omega = 2$

One must note that, while in the center, the dispersion relation is of the type

(4) $k_\perp{}^2 + (1 + \Omega)\, k_\parallel{}^2 = k_A{}^2$

which allows $k_\perp$ to be of order unity; the dispersion relation in the near vacuum edge is of the type

(5) $k_\perp{}^2 + k_\parallel{}^2 = k_C{}^2 = 1.7 \times 10^{-3}/\text{cm}^2$

Thus

(6) $k_\perp = ik_\parallel$

and we have an evanescent layer at the edge. Making $k_\parallel$ larger not only makes the layer (d_e) thicker, but also decreases the decay length. A pessimistic example can be estimated from Figure 5 with

(7) $k_{\parallel} = .6/\text{cm}, \ d_e = 4 \text{ cm}$

$$e^{-kx} = e^{-4x.6} = .09$$

Of course, one could also propagate.

(8) $k_{\parallel} = .2, \ d_e \simeq 1 \text{ cm}$

$$e^{-.2} \approx .8$$

One can already see the difficulty in evaluating $\beta_a = \frac{E_a}{E_o}$ in the radiation resistance, due to the evanescent edge effect alone. This effect is much more pronounced in Alcator, since our antenna is narrow and thus has a wide $k_{\parallel}$ spectrum, the central density is very high and thus can support a very large $k_{\parallel}$, and the edge vacuum layer thickness is several centimeters. For low density tokamaks, typical parameters are

(9) $k_{\parallel} \simeq .05/\text{cm}, \ d_e \simeq 10 \text{ cm}$

$$e^{-.05 \times 10} \simeq .6$$

and almost complete tunneling occurs.

To evaluate the eigenmode wave field shape, we must use a numerical integration technique.

Assuming $k_y = 0$ and a wave field of the form

(10) $E(x,z,t) = E(x) \ e^{i(k_{\parallel}z - \omega t)}$

we have from Faraday's law

(11) $-k_{\parallel} \ E_y = \frac{\omega}{c} B_x$

(12) $k_{\parallel} \ E_x = \frac{\omega}{c} B_y$

(13) $\frac{\partial E_y}{\partial x} = \frac{i\omega}{c} B_z$

and, from the x and y components of Ampère's law, we have

$$(14) \quad k_{\parallel} B_y = \frac{\omega}{c} [SE_x - iDE_y]$$

$$(15) \quad ik_{\parallel}B_x - \frac{\partial B_z}{\partial x} = \frac{-i\omega}{c} [iDE_x + SE_y]$$

Substituting (11,(12→14),13)→15), we have

$$(16) \quad \frac{\partial E_y^2}{\partial x^2} = \frac{-\omega^2}{c^2} \left[\frac{-D^2}{S-n_{\parallel}^2} + S-n_{\parallel}^2 \right] E_y$$

which is recognized (from IV-2.2(16)) as

$$(17) \quad -k_{\perp}(x)^2 E(x) = \frac{\partial^2 E(x)}{\partial x^2}$$

Both sides of (17) can be integrated twice with respect to x

$$(18) \quad -\int_0^x\int_0^x k^2(x) E(x) d^2x = \int_0^x\int_0^x \partial^2 \frac{E(x)}{\partial x^2} d^2x = \int_0^x \left[\frac{\partial E}{\partial x} - \frac{\partial E}{\partial x}\bigg|_{x=0} \right] dx$$

$$= E(x) - E(x)\bigg|_{x=0} - \left[\frac{\partial E(x)}{\partial x}\bigg|_{x=0} \right] x$$

and assuming a symmetric mode

$$(19) \quad E(x) = 1 - \int_0^x\int_0^x k^2(x) E(x) d^2x$$

Figure 9 is a simplified block diagram of how one can easily calculate $n(x)$, $k^2(x)$, and $E_y(x)$ using a first order integration scheme. Although very crude, it gives excellent qualitative and quantitative results. Figure 6 is a typical example with $k_{\parallel} = .63$, $n = 5 \times 10^{14}$. To arrive at a physically valid solution, one must adjust $k_{\parallel}$ so as to have $E(x)\big|_{wall} = 0$. This is a tedious trial and error process that will be circumvented in Section IV-5.4. One can find the assymetrical solutions by changing the E and $\frac{\partial E}{\partial r}$ initial boundary conditions. Different radial mode numbers (μ) can also be found by drastically changing $k_{\parallel}$, and looking for a new solution.

Another way to solve equation (17) is to use WKB theory. To zeroth order, we can write[16]

(20) $E(x) = E_o e^{i\langle k\rangle \cdot x}$

to first order

(21) $E(x) = E_o e^{i\int k(x)\cdot dx}$

and to second order

(22) $E(x) = E_o \dfrac{e^{i\int k(x)\cdot dx}}{\sqrt{k}}$

WKB theory, although analytically appealing, must be used carefully, especially since the wavelength is of the same order as the density scale length. Zero order WKB is obviously very crude, and is only useful either along B_o or with flat density profiles. First order WKB (Fig. 7) is in good agreement with the exact solution, as it treats correctly the evanescent layer. Second order WKB, which one might expect to be better, has a singularity when $k_{\perp} = 0$, and is of no use for our purposes (Figure 8).

In Section IV-4 we will see that collisionless damping power deposition is proportional to either the temperature, (Fig. 1) or to some exponential factor of the temperature. These profiles are extremely peaked, with half power width of only a few centimeters. We then should expect the collisionless damping power to be deposited near the center of the plasma, almost independently of any reasonable electric field profile.

Temperature Profile

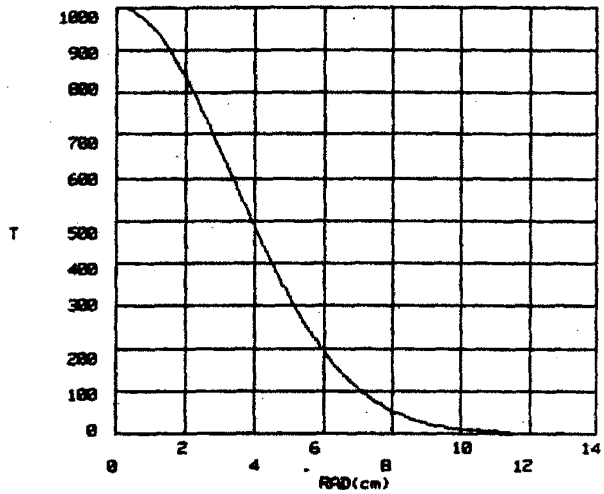

nprof= 1 t0= 1000.00 nhat=.50000E+15
f=.20000E+09 kpar(1)= 0.63032 mu= 1.00 omega= 2.00

Figure 1

TFR Type Density Profile

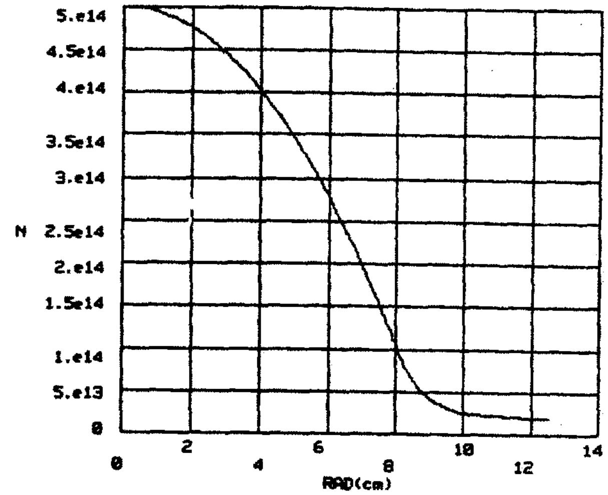

nprof= 1 t0= 1000.00 nhat=.50000E+15
f=.20000E+09 kpar(1)= 0.63032 mu= 1.00 omega= 2.00

Figure 2

Alcator Type Density Profile

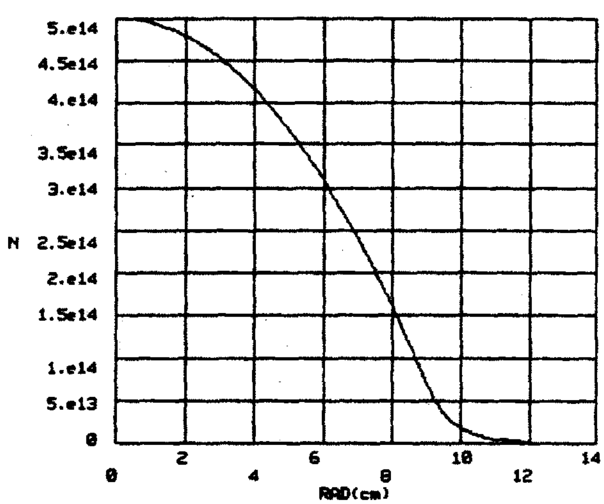

nprof= 2 t0= 1000.00 nhat=.50000E+15
f=.20000E+09 kpar(1)= 0.67200 mu= 1.00 omega= 2.00

Figure 3

Edge Density Profile

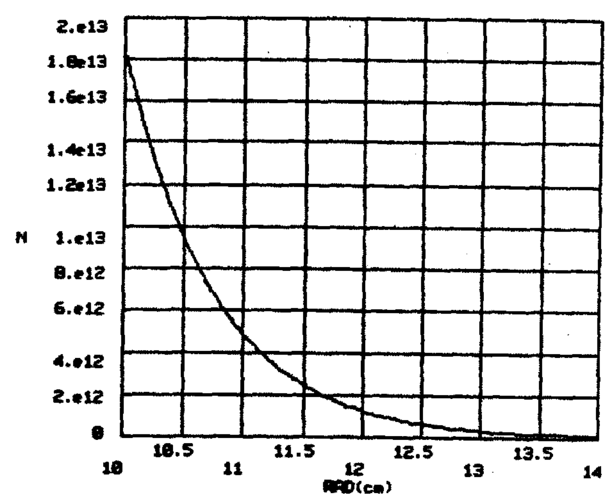

nprof= 2 t0= 1000.00 nhat=.50000E+15
f=.20000E+09 kpar(1)= 0.67200 mu= 1.00 omega= 2.00

Figure 4

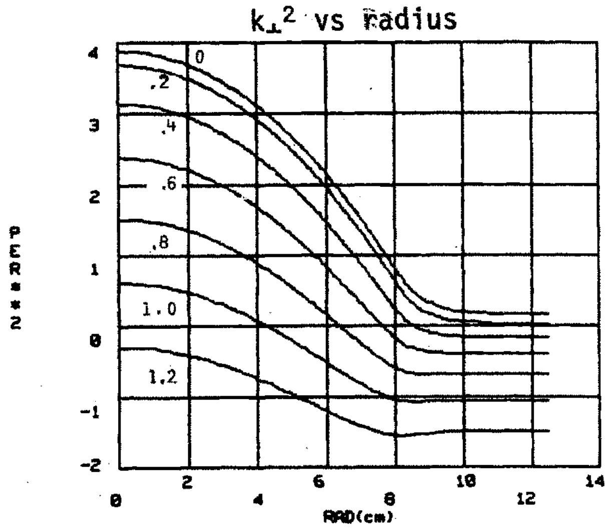

nprof= 1 t0= 1000.00 nhat=.50000E+15
f=.20000E+09 kpar(1)= 0.63032 mu= 1.00 omega= 2.00

Kpar= 0., .2, .4, .6, .8, 1.0, 1.2

Figure 5

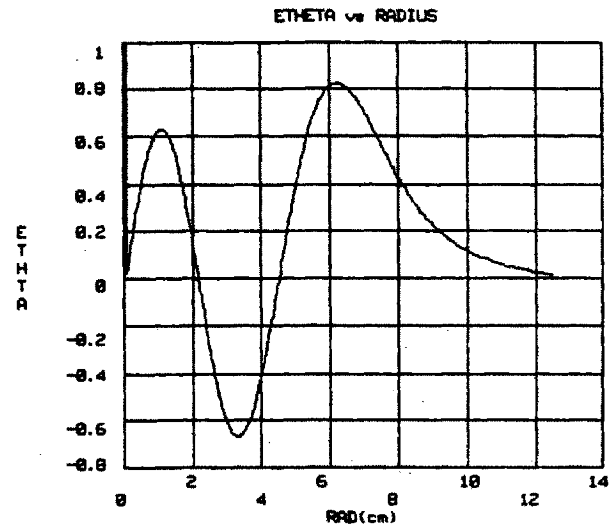

nprof= 1 t0= 1000.00 nhat=.50000E+15
f=.20000E+09 kpar(1)= 0.63032 mu= 1.00 omega= 2.00

Figure 6

First and Second Order WKB

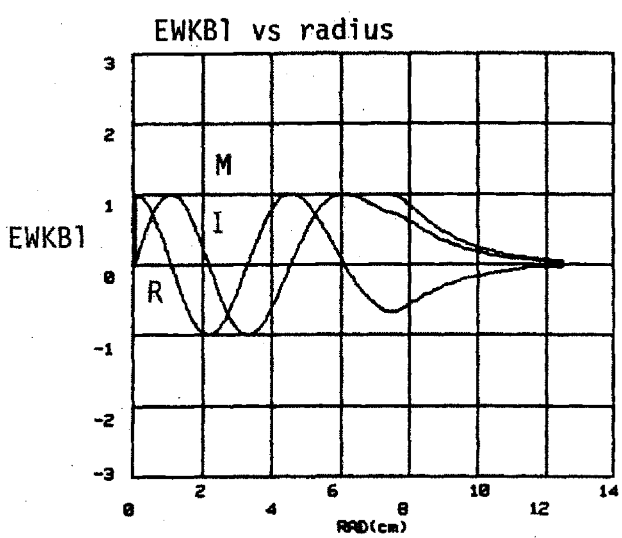

nprof= 1 t0= 1000.00 nhat=.50000E+15
f=.20000E+09 kpar(1)= 0.63032 mu= 1.00 omega= 2.00

Figure 7

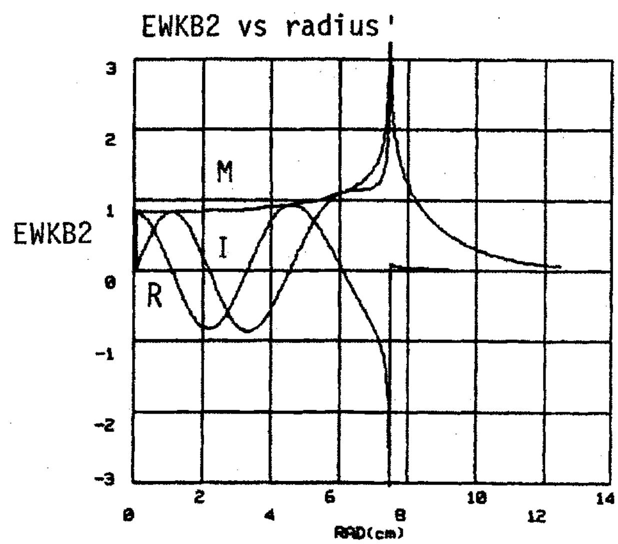

nprof= 1 t0= 1000.00 nhat=.50000E+15
f=.20000E+09 kpar(1)= 0.63032 mu= 1.00 omega= 2.00

Figure 8

Block Diagram of Heuristic Code

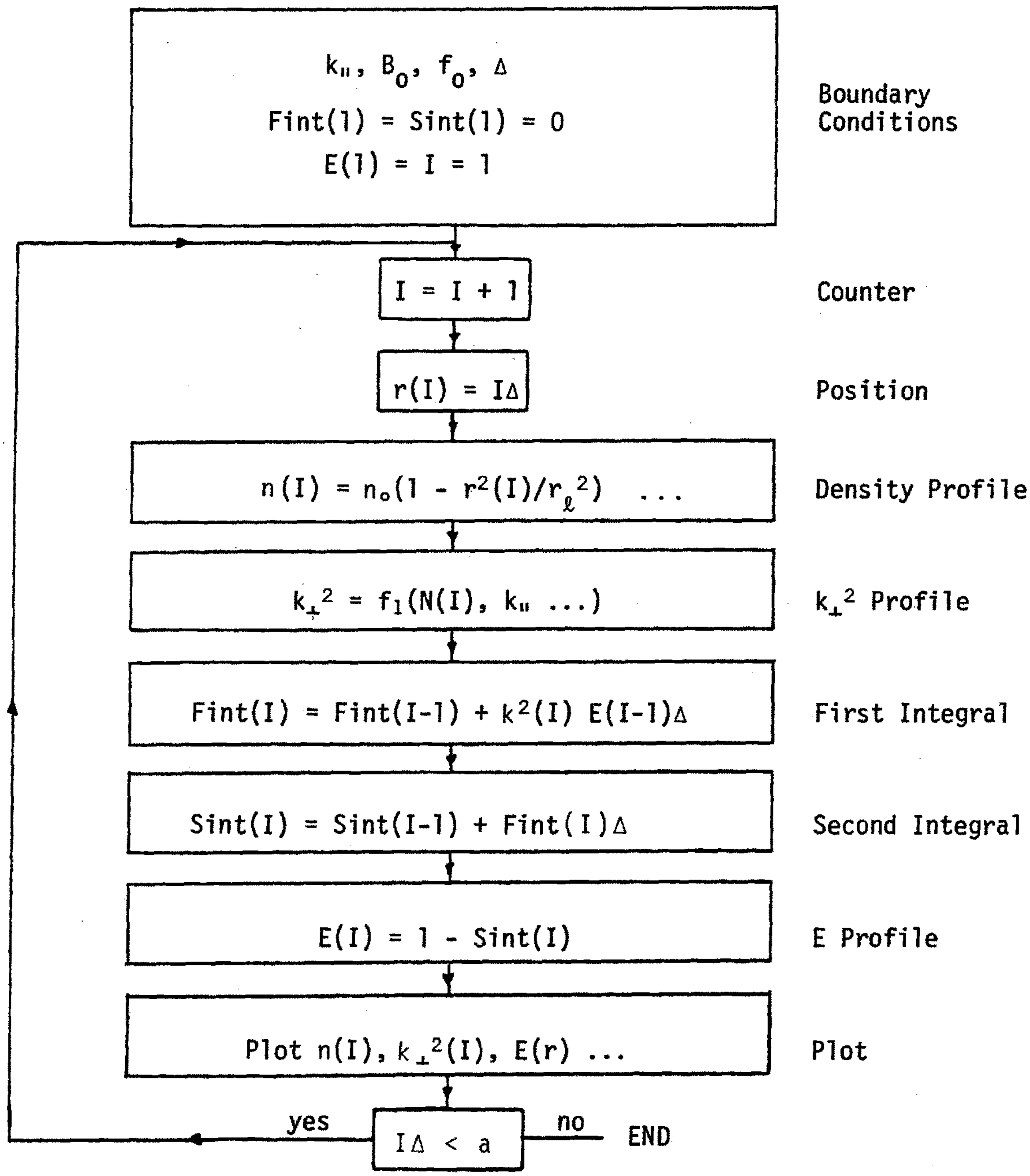

Figure 9

IV-2.4. Finite electron mass, fast and slow wave dispersion relations

If we now keep the full 3 x 3 dispersion relation tensor with $k_y = 0$ and solve for the determinant, we have

$$(1) \quad (S - n_{\parallel}^2)\,[(S - (n_{\perp}^2 + n_{\parallel}^2))\,(P - n_{\perp}^2)] - D^2\,(P - n_{\perp}^2) - n_{\perp}n_{\parallel}\,(S - n_{\perp}^2 - n_{\parallel}^2)\,n_{\perp}n_{\parallel} = 0$$

which,after some simple algebraic manipulations, can be written in the form

$$(2) \quad a\,n_{\perp}^4 + b\,n_{\perp}^2 + c = 0$$

where $a = 1$

$$(3) \quad \begin{aligned} b &= -\left(\frac{P}{S} + 1\right)(S - n_{\parallel}^2) + \frac{D^2}{S} \\ c &= \frac{P}{S}\,[(S - n_{\parallel}^2)^2 - D^2] \end{aligned}$$

Equation (2) has the fast wave root

$$(4) \quad n_{\perp+}^2 = \frac{-b + \sqrt{b^2 - 4ac}}{2a} \cong \frac{b}{2}\left(-1 + 1 - \frac{2c}{b^2}\right)$$

where we made the approximation $\sqrt{1 - \varepsilon} \simeq 1 - \varepsilon/2$, since, in our regime $b^2 >> 4ac$

and thus

$$(5) \quad n_{\perp+}^2 \simeq -\frac{c}{b} \simeq \frac{(S - n_{\parallel}^2)^2 - D^2}{S - n_{\parallel}^2}$$

which is the same as we found by solving the 2 x 2 determinant.

Similarly, we have the new slow wave root[22]

$$(7) \quad n_{\perp-}^2 \cong n_{\perp-}^2 = \frac{-b - \sqrt{b^2 - 4ac}}{2a} \simeq -b \simeq \frac{P}{S}\,(S - n_{\parallel}^2)$$

For $\Omega > 1$ and reasonable densities, $n_{\perp-}^2$ is of order $P = \frac{-\pi_e^2}{\omega^2}$, which means an extremely evanescent field. For this reason ,we are now confident that only the fast wave can propagate in Alcator. Figures 1 and 2 are the fast and slow wave $k_\perp^2$ profiles for standard condition B_o = 66 kG, f_o = 200 MHz, $k_\parallel$ = .5/cm and 5 x 10^{14} /cm^3 hydrogen central density.

Fast and Slow Waves at 200 MHz

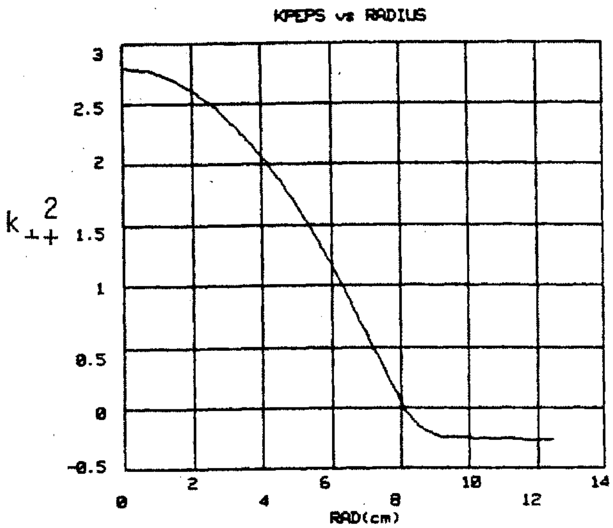

H_2, 66 kG, 200 MHz

Figure 1

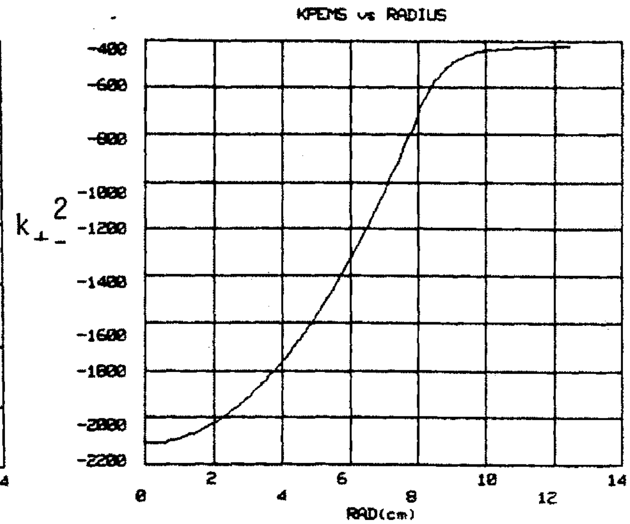

f=.20000E+09 oma= 2.000 b0=.65587E+05 kpar=0.5000 mu=1.00

nhat=.50000E+15 pp= 9.000 rmax=12.500

Figure 2

IV-2.5. 1/R Magnetic field, two ion species and the two ion-ion hybrid resonance

We now introduce a 1/R magnetic field, so that

(1) $$B = B_o \frac{1}{1 + r/R_o}$$

and let ω_{ci}, ω_{ce}, π_i, π_e, be functions of r. At this point, we also introduce several ion species, and numerically calculate R, L, S, D, and P directly in their unsimplified general form (IV-2.1.(13)-(17)). Figures 1 and 2 show the fast and slow wave for one ion species at second harmonic with 1/R magnetic field. We notice a slight shift of the $k_{\perp +}^2$ maximum towards the outside, which is simply explained by a lower magnetic field ($k_A \propto 1/B$). The effect of this is to make the wave effective major radius some 3% larger than R_o.

For a mixed hydrogen and deuterium plasma with

(2) $$\omega_o \simeq \omega_{cH} \simeq 2\,\omega_{cD}$$

and a smaller concentration of hydrogen than deuterium

(3) $$n_{oH} + n_{oD} = n_e$$

(4) $$\frac{n_H}{n_D} = \alpha < 1$$

we will encounter a singularity in the fast wave when

(5) $$n_{\perp +}^2 = \frac{(S - n_\parallel^2)^2 - D^2}{S - n_\parallel^2} \to \infty$$

or simply

(6) $$S - n_\parallel^{\ 2} = 0$$

a condition often called the Two Ion-Ion Hybrid (TIIH) resonance. Figures 3 and 4 show wave profiles for $k_\parallel = .3$/cm, $f_o = 90$ MHz, $n_H = 2.5 \times 10^{13}/\text{cm}^3$,

$n_D = 5 \times 10^{14}/cm^3$, and $B_o = 60$ kG. The $k_{\perp +}^2$ profile is now grossly non-symmetric since the resonance is critically dependent on the 1/R magnetic field.

Neglecting the small electron contribution, equation (6) becomes

$$(7) \quad n_{\parallel}^2 - 1 + \frac{\pi_D^2}{\omega^2 - \omega_{cD}^2} + \frac{\pi_H^2}{\omega^2 - \omega_{cH}^2} = 0$$

and for $n_{\parallel}^2 = 0$ and high density

$$(8) \quad \frac{\pi_H^2}{\pi_D^2} \approx - \frac{\omega^2 - \omega_{cH}^2}{\omega^2 - \omega_{cD}^2}$$

Combining (1), (2), (4) and (8), we have the simple formula

$$(9) \quad \Omega_H = \sqrt{\frac{1 + .5\alpha}{1 + 2\alpha}} \begin{array}{ll} = .97 & \text{for } \alpha = 5\% \\ = .82 & \text{for } \alpha = 20\% \end{array}$$

and the hybrid layer is some 1.5 to 6 cm on the high field side of the ω_{ci} resonance layer. Of course, for $\alpha = 0$, the resonance is right at the $\omega = \omega_{cH}$ layer.

For very low densities, when $\pi_i^2 \to 0$, equation (7) can only be solved for $\omega^2 \to \omega_{cH}^2$. Thus, for a parabolic density profile, the two ion-ion hybrid resonance layer meets the minority cyclotron layer at the plasma edge independently of α.

For the general case with finite $n_{\parallel}$, and π_i, we can write equation (7) in the form

$$(10) \quad n_{\parallel}^2 - 1 + n_e F(R, B_o, \alpha, \omega_o) = 0$$

$$(11) \quad n_e = \frac{1 - n_{\parallel}^2}{F(R, B_o, \alpha, \omega_o)}$$

Assuming a simple density profile

$$(12) \quad n_e(r) = n_{oe}\left(1 - \frac{r^2}{r_w^2}\right)$$

(13) $r = r_w \sqrt{1 - n_e(r)/n_{oe}}$

and a two dimensional Cartesian coordinate system centered on the plasma,

(14) $r^2 = x^2 + y^2$

(15) $y = \sqrt{r^2 - x^2}$

(16) $R = R_o + x$

Equations (11) and (12) can be numerically solved by slowly increasing x in (16)→(11) starting at $x = -r_w$, until the condition

(17) $0 < n_e < n_{oe}$

is met, at which point we have a resonance solution requiring a density $n_e(r) = n_e$ and radius r from (13).

Thus, substituting (16) → (11) → (13) → (15),

we have a resonance surface of the form

(18) $$(x,y) \equiv \left\{ x, \sqrt{r_w^2 \left[1 - \frac{1 - n_\parallel^2}{n_{oe} F(R_o + x,\ B_o,\ \alpha,\ \omega_o)}\right] - x^2} \right\}$$

and a vacuum vessel at

(19) $(x,y) = (x, \sqrt{r_w^2 - x^2})$

Figures 5 and 6 are typical two ion-ion hybrid resonance surfaces for α = .05, .1, .2, .3, .45, 1 and $k_\parallel$ = .1, .5 /cm, B_0=70 kG, and f_0=97 MHz. We see that at high density, $k_\parallel$ decreases the distance between the TIIH and cyclotron layers. For reasonable minority concentrations, the TIIH layer[17] will usually start near the dense plasma center and reach out to the cyclotron layer located in the low field side antenna.

Fast and Slow Waves at 200 MHz

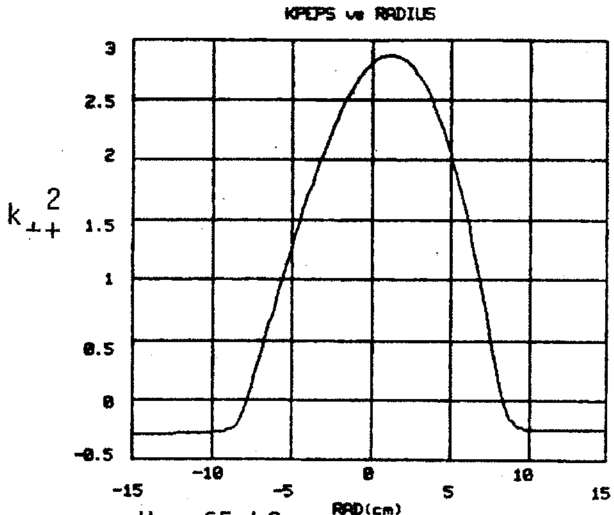

H_2, 65 kG

Figure 1

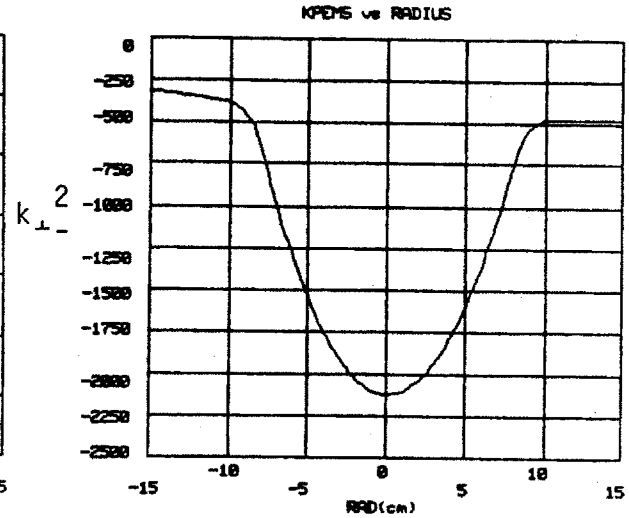

kpar= 0.500 f=.20000E+09 mua= 1.000 mub= 1.000 nprof= 1

nahat=.50000E+15 nbhat=.00000E+00 rmax=15.000 rmaj=54.000

nstep= 203 b0=.65587E+05 pp= 9.00

Figure 2

Fast and Slow Waves at 90 MHz

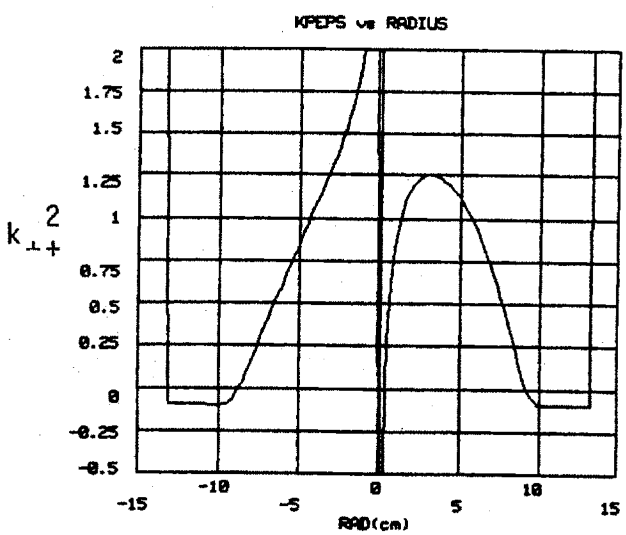

H_2, D_2, 60 kG

Figure 3

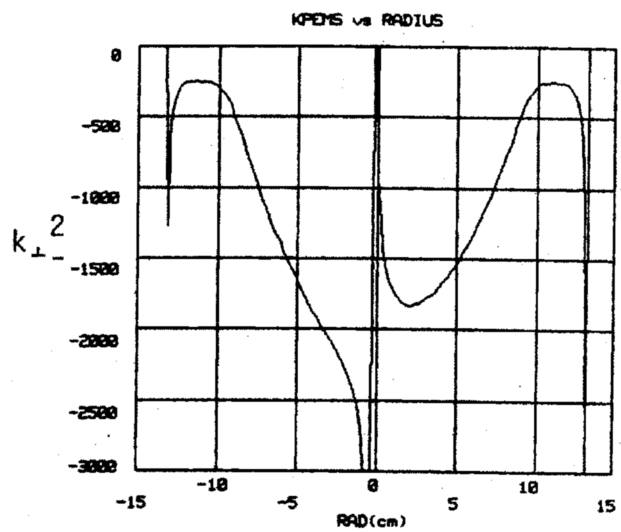

kpar= 0.300 f=.90000E+08 mua= 2.000 mub= 1.000 nprof= 2

nahat=.50000E+15 nbhat=.25000E+14 rmax=15.000 rmaj=54.000

nstep= 203 b0=.60000E+05 pp= 1000.00

Figure 4

TIIH Layer Position for $k_{\parallel}$ = .5/cm

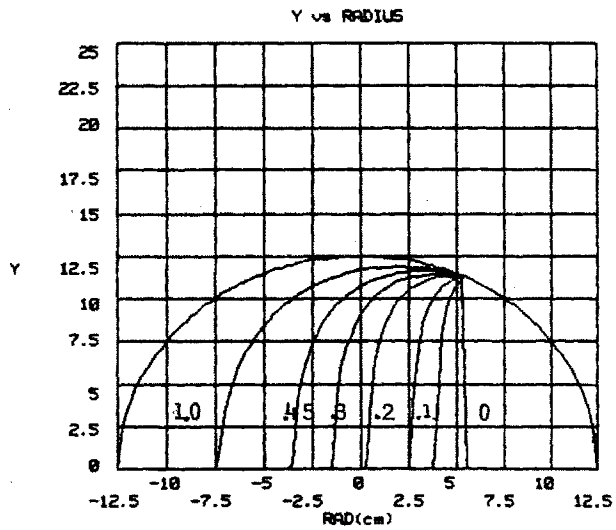

f0=.97000E+08 mua= 2.000 mub= 1.000 b0=.70000E+05 nehat=.50000E+15

rmax=12.500 rmaj=54.000 kpar= 0.500 nstep=100

alpha=.05, .1, .2, .3, .45, 1.0

Figure 5

TIIH Layer Position for $k_{\parallel}$ = .1/cm

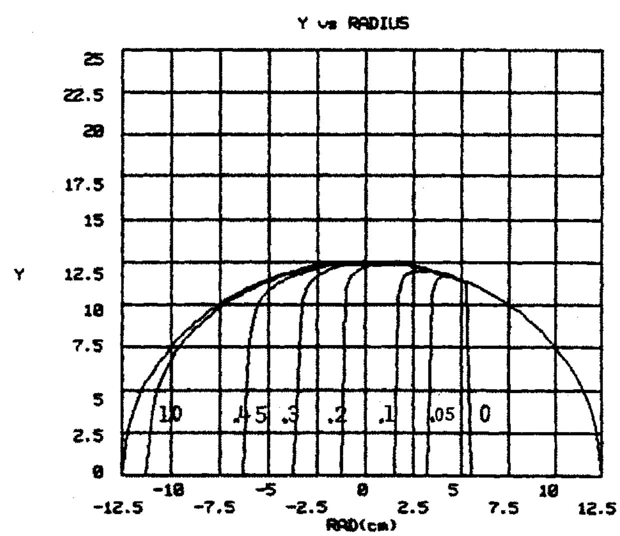

f0=.97000E+08 mua= 2.000 mub= 1.000 b0=.70000E+05 nehat=.50000E+15

rmax=12.500 rmaj=54.000 kpar= 0.100 nstep=100

alpha=.05, .1, .2, .3, .45, 1.0

Figure 6

IV-2.6. Plasma edge lower hybrid resonance and E_z

In Figures IV-2.5 (3-4), we noticed a singularity in $k_\perp^2$ when the density was decreased until the wave frequency was of the order of the ion plasma frequency. Specifically, close examination of Section IV-2.5 shows that this happens near

$$(1) \quad S = 1 + \frac{\pi_i^2}{\omega_{ci}^2} \frac{1}{1 - \Omega^2} \rightarrow 0^+$$

or simply

$$(2) \quad \omega^2 = \pi_i^2 + \omega_{ci}^2$$

From the usual definition of the lower hybrid wave[45]

$$(3) \quad \frac{1}{\omega_{LH}^2} = \frac{1}{\omega_{ci}^2 + \pi_i^2} + \frac{1}{\omega_{ce}\,\omega_{ci}} = \frac{1}{\omega_{ci}^2 + \pi_i^2} \quad \text{for } \pi_i^2 \ll \omega_{ci}\,\omega_{ce}$$

which is the same as (2), and we shall call this low density edge mode the lower hybrid resonance field. For the standard second harmonic condition in hydrogen at 200 MHz, this corresponds to $n_e \simeq 7 \times 10^{11}/cm^3$. Although very low, this edge density could be obtained with normal density profiles and a central density less than $10^{14}/cm^3$.

In cold plasma theory, we can easily calculate E_z from the third line of the full (3 x 3) wave tensor

$$(4) \quad n_\perp n_\parallel\, E_x + (P - n_\perp^2)\, E_z = 0$$

under normal fast wave circumstances, $n_\perp^2 \simeq n_\parallel^2 \simeq n_A^2 \simeq 40^2$, and $P \simeq 10^6$, so that

$$(5) \quad \frac{E_z}{E_x} = \frac{-n_\perp n_\parallel}{P} \cong 10^{-3}$$

and E_z is only a small perturbation to the overall TE electric field. (This is not true of the lower hybrid mode, since $|P|$ is of the order of n^2). Nevertheless, since S, D and n^2 are all of the same order, the parallel electron current

(6) $$J_{\parallel} = \frac{\omega}{4\pi i} PE_z \approx \frac{\omega}{4\pi i} n^2 E_{\perp}$$

is of the same order as the perpendicular currents

(7) $$J_{\perp} = \frac{\omega}{4\pi i} (S\ E_x - iD\ E_y) \approx \frac{\omega}{4\pi i}\ n^2\ E_{\perp}$$

IV-2.7. Fast Wave Energy Density

The total stored energy in the fast wave can be divided into magnetic, electric and kinetic energy components (MKS)

(1) $< W >_t = W_H + W_E + W_K = \frac{1}{4}\,\mu_o\, H^2 + \frac{1}{4}\,\varepsilon_o\, E^2 + \sum_k \frac{1}{4}\, n_k m_k v_k^{\,2}$

From Faraday's law,we can crudely write

(2) $$E \cong \frac{\omega}{k}\,\mu_o\, H \cong \sqrt{\frac{\mu_o}{\varepsilon_A}}\; H$$

(3) $$\frac{W_H}{W_E} \cong \frac{\varepsilon_A}{\varepsilon_o} >> 1$$

and the electric field energy can be neglected.

In any wave, energy is transferred back and forth between two or more energy storage mechanisms. A closer look at the different components of Faraday's law

(4) $$\begin{aligned} H_x &= -\frac{k_{\parallel}}{\omega\mu_o}\, E_y = -N_{\parallel}\, \sqrt{\varepsilon_A/\mu_o}\; E_y \\ H_y &= \frac{k_{\parallel}}{\omega\mu_o}\, E_x = N_{\parallel}\, \sqrt{\varepsilon_A/\mu_o}\; E_x \\ H_z &= \frac{k_{\perp}}{\omega\mu_o}\, E_y = N_{\perp}\, \sqrt{\varepsilon_A/\mu_o}\; E_y \end{aligned}$$

shows that for $k_{\parallel} = 0$,only H_z remains,and energy must be transferred between W_H and W_K, and

(5) $$W_H = W_K$$

For $k_{\parallel} \neq 0$, energy is shuffled between the different magnetic components and the particles velocities;so (5) is no longer valid.

Equation (1) may, in general, be rewritten for a lossless dielectric (CGS)[7]

$$
\langle W \rangle_t = \frac{1}{16\pi}\left[\vec{B}^*\cdot\vec{B} + \vec{E}^*\cdot \frac{\partial}{\partial\omega}(\omega\vec{\vec{K}})\cdot\vec{E}\right] \tag{6}
$$

$$
= \frac{1}{16\pi}\,\epsilon_A\,E_y^2\left\{\left[N_\parallel^2(F^2+1)+N_\perp^2\right] + \frac{1}{2(1-\Omega^2)^2}\left[(1+F)^2(1-\Omega)^2 + (1-F)^2(1+\Omega)^2\right]\right\}
$$

where the first bracket is the magnetic energy, and from the first line of the wave tensor

$$
F = \frac{iE_x}{E_y} = \frac{-D}{S - n_\parallel^2} = -\frac{1-\Omega^2}{\Omega}\left[N_\perp^2 + N_\parallel^2 - \frac{1}{1-\Omega^2}\right] \tag{7}
$$

Finally, substituting (4) and (7) into (6), we have

$$
\begin{aligned}
\langle W \rangle_t = 2W_H &= \frac{1}{8\pi}\,\epsilon_A\,E_y^2 && \text{for } k_\parallel = 0\\
&= \frac{1}{8\pi}\,\epsilon_A\,\frac{2+\Omega}{(1+\Omega)^2}\,E_y^2 && \text{for } k_\perp = 0\\
&= \frac{1}{8\pi}\,\epsilon_A\,.44\,E_y^2 && \text{for } k_\perp = 0 \text{ and } \Omega = 2\\
&\approx \frac{1}{8\pi}\,\epsilon_A\,E_y^2 && \text{in general}
\end{aligned} \tag{8}
$$

II-3. Homogeneous Plasma Cylindrical Waveguide Field Solution

For simple analytical purposes, the most important model is the homogeneous cylindrical waveguide[45,46,56,60]. The zero electron mass cold plasma dispersion relation[7], coupled with the electric field boundary conditions at the wall, gives the deterministic equation which in turn, uniquely defines k_z as a function of n_e, for the different values of radial and poloidal mode numbers[22]. This, furthermore, fully determines the cylindrical field solutions from which can be calculated the Poynting flux, antenna E_θ field, probe signals and the radiation resistance[21]. An estimate of the number of possible propagating modes[93] and mode splitting[22,52,55], due to the Ohmic current around the torus, is also calculated.

IV-3.1. Zero electron mass fast wave dispersion relation and mode cutoff

Proceeding exactly as in the previous chapter, we write Maxwell's equation and the equivalent dialectric tensor in cylindrical coordinates. From Faraday's law we have,

$$(1) \quad \nabla \times \vec{E} = \frac{-1}{c}\frac{\partial \vec{B}}{\partial t} = \frac{i\,\omega\,\vec{B}}{c}$$

from Ampère's law,

$$(2) \quad \nabla \times \vec{B} = \frac{1}{c}\frac{\partial \vec{D}}{\partial t} = \frac{-i\,\omega}{c}\,\vec{\vec{K}} \cdot \vec{E}$$

and from the dielectric tensor

$$(3) \quad \vec{\vec{K}} \cdot \vec{E} = \begin{bmatrix} S & -iD & o \\ iD & S & o \\ o & o & P \end{bmatrix} \cdot \begin{bmatrix} E_r \\ E_\theta \\ E_z \end{bmatrix}$$

where in cylindrical coordinates

$$(4) \qquad \nabla \times \vec{A} = \begin{vmatrix} \hat{r}/r & \hat{\theta} & \hat{z}/r \\ \partial/\partial r & \partial/\partial\theta & \partial/\partial_z \\ A_r & rA_\theta & A_z \end{vmatrix}$$

The basic methodology is to expand (1) and (2) in their r, θ and z components using (3) and (4). Then assuming [22]

$$(5) \qquad A = A_o \, e^{i(m\theta + k_{\parallel} z - \omega t)}$$

and a TE eigenmode ($E_z = 0$), so that

$$(6) \qquad B_z \propto J_m (k_\perp r)$$

we can write an equation of the type

$$(7) \qquad f(B_z) = g\,(E_\theta)$$

and using the boundary condition

$$(8) \qquad E_\theta \Big|_{wall} = 0$$

we have the deterministic equation and the dispersion relation.

We thus proceed with Faraday's Law,

$$(1r) \qquad \frac{-\partial E_\theta}{\partial z} = \frac{i \omega B_r}{c}$$

$$(1\theta) \qquad \frac{\partial E_r}{\partial z} = \frac{i \omega B_\theta}{c}$$

$$(1z) \qquad \frac{1}{r}\left[\frac{\partial r E_\theta}{\partial r} - \frac{\partial E_r}{\partial \theta}\right] = \frac{i \omega B_z}{c}$$

and Amperés law

(2r) $\frac{1}{r}\left[\frac{\partial B_z}{\partial \theta} - \frac{\partial r B_\theta}{\partial z}\right] = \frac{-i\omega}{c}(S\ E_r - iD\ E_\theta)$

(2θ) $\frac{-\partial B_z}{\partial r} + \frac{\partial B_r}{\partial z} = \frac{-i\omega}{c}(iD\ E_r + S\ E_\theta)$

and substituting (1θ) → (2r)

(9) $\frac{i\ m\ B_z}{r} + \frac{D\ \omega}{c} E_\theta = E_r\left(\frac{-i\omega S}{c} + ic\frac{k_\parallel^2}{\omega}\right)$

and (1r) → 2θ

(10) $\frac{\partial B_z}{\partial r} + E_\theta\left[\frac{ik_\parallel^2 c}{\omega} - \frac{i\omega S}{c}\right] = -\frac{\omega D}{c} E_r$

Finally, combining (9) and (10) we have

(11) $\frac{\partial B_z}{\partial r} + \frac{mD\omega^2}{r(c^2 k_\parallel^2 - \omega^2 S)} B_z = \left[\frac{i\ D^2\ \omega^3}{c(c^2 k^{\ 2} - \omega^2 S)} + \frac{i\omega S}{c} - i\frac{k_\parallel^2 c}{\omega}\right] E_\theta$

Using the Boundary condition (8)

(12) $a\left.\frac{\partial B_z}{\partial r}\right|_{wall} = -\frac{m\ D\ \omega^2}{(c^2\ k_\parallel^2 - \omega^2 S} \left. B_z \right|_{wall}$

and substituting (6) into (12), we have the dispersion relation

(13) $k_\perp\ a\ J_m'\ (k_\perp a) = \frac{m\ D\ \omega^2}{\omega^2\ S - c^2\ k_\parallel^2} J_m\ (k_\perp a)$

The mode cutoff can be found by setting $k_\parallel = 0$,and thus we have the simple deterministic equation

(14) $\frac{x\ J_m'\ (x)}{J_m\ (x)} = -m\ \Omega$

where

(15) $x = k_\perp a = k_A a$

For m = 0, x will be simply the zeroes of J_o'. Using the Bessel function identities[137]

(16) $$J_n'(x) = J_{n-1}(x) - \frac{n\,J_n(x)}{x}$$

(17) $$J_{-n}(x) = (-1)^n\,J_n(x)$$

we can calculate the ±1 mode cutoffs (Table 1) for hydrogen and $\Omega = 2$. We note that m = +1 has the lowest density cutoff, and is therefore the fundamental mode of the system.

We can now easily calculate the electric and magnetic field components. Of course from (6)

(18) $$B_z = A\,J_m(k_\perp r)\,e^{i(m\theta + k_\parallel z - \omega t)}$$

and substituting (17) → (11)

(19) $$E_\theta = B\,J_m'(k_\perp r) + C\,J_m(k_\perp r)$$

and (19) → (1r)

(20) $$B_r = \frac{-k_\parallel c}{\omega}\,E_\theta$$

and (18, 19) → (9)

(21) $$E_r = D\,J_m'(k_\perp r) + E\,J_m(k_\perp r)$$

and (21) → (1θ)

(22) $$B_\theta = \frac{k_\parallel c}{\omega}\,E_r$$

where A, B, C, D, E are constants proportional to the wave field, and functions of the plasma and wave parameters.

Table 1

μ \ m	-1	0	+1
1	.32	.19	.10 x $10^{14}/cm^3$
2	.89	.63	.42
3	1.71	1.34	.98
4	2.79	2.28	1.83
5	4.09	3.52	2.90

Eigenmode cutoff density for $m = 0 \pm 1$, $\mu = 1\text{-}5$, $\Omega = 2$, hydrogen and $a = 10$ cm

IV-3.2. Number of propagating eigenmodes at high density

Using equation IV-3.1(16), we can transform IV-3.1(14) to

$$(1) \quad J_{m-1} = \frac{m(1 - \Omega)}{\chi}$$

For reasonable values of m, Ω, and χ, i.e.

$$(2) \quad \begin{aligned} m &= 3 \\ \Omega &= 2 \\ \chi &= k_A a = 10 \end{aligned}$$

and, since J_{m-1} has roughly the same amplitude as J_m, we can approximate equation (1) as

$$(3) \quad J_{m-1}(\chi) = 0$$

From Figure 1 and IV-3.1(17), we can write the very crude but simple cutoff dispersion relation

$$(4) \quad k_\perp a = \mu(\pi + \frac{m}{2})$$

In a typical Alcator high density plasma with $\lambda_A = 3.8$ cm and $a = 10$ cm,

$$(5) \quad \frac{k_\perp a}{\pi} = \nu \simeq 5$$

and we can propagate as many as 45 perpendicular modes, as shown in Table 1.

Physically, we could have arrived at the same result by crudely assuming

$$(6) \quad \begin{aligned} k_\perp &= k_r + k_\theta \\ k_r a &= \mu\pi \\ k_\theta 2\pi\langle r\rangle &= m\, 2\pi \\ \langle r\rangle &= \leqslant a \end{aligned}$$

Of course, at large r, where 1/r effects can be neglected, we must have

(7) $$k_\perp^2 = k_r^2 + (\frac{m}{r})^2$$

At this point, we must use these simple relations for statistical purposes only. For example, in a normal dielectric, the lowest TE mode of a rectangular guide is TE_{01}. In a circular guide, the lowest mode is TE_{11}, not TE_{01}. Accordingly, a careful look at the electric field would have shown that the circular TE_{11} is only a slightly perturbed Cartesian TE_{01}, and would indeed require less $k_\perp$ than the more distorted circular TE_{01}. With an only slightly more sophisticated version of equation (4),[7] which includes a phase factor dependent on the sign of m, the mode spectrum would then be correctly symmetric about m = -1 instead of m = 0.

Cartesian fields (sin, cos) can be mapped into cylindrical coordinate fields (J_m, J_m') by using the crude approximation

(8) $$J_1(x) \cong \frac{\sin(x)}{\sqrt{1 + \pi x/2}}$$

as shown in Figure 2. Our corrected inhomogeneous Cartesian solution (IV-2.3) then becomes a very good approximation to the exact solution, as we will see in Section IV-5.3.

Table 1

Possible perpendicular eigenmodes for $k_\perp a = 5$.

μ	m
1	0 ± 1 ± 2 ± 3 ± 4 ± 5 ± 6 ± 7 ± 8
2	0 ± 1 ± 2 ± 3 ± 4 ± 5 ± 6
3	0 ± 1 ± 2 ± 3 ± 4
4	0 ± 1 ± 2
5	0

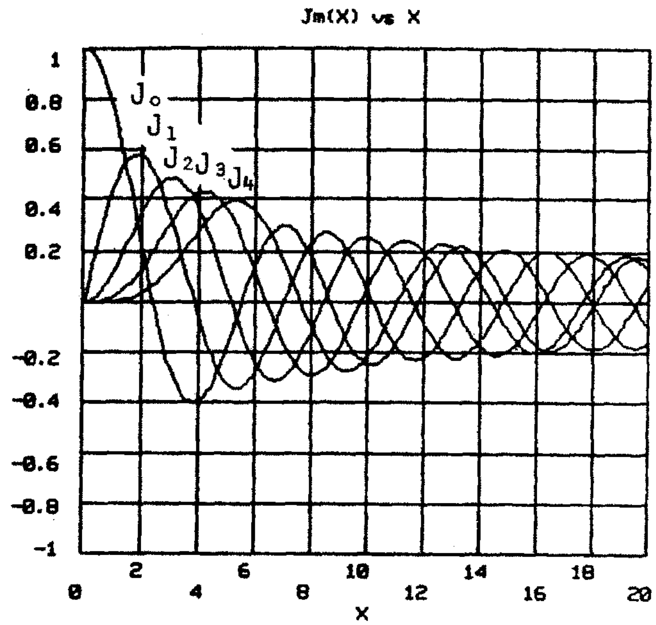

Figure 1

$J_1(x)$ and $\mathrm{Sin}(x)/\sqrt{1 + \pi x/2}$ vs. x

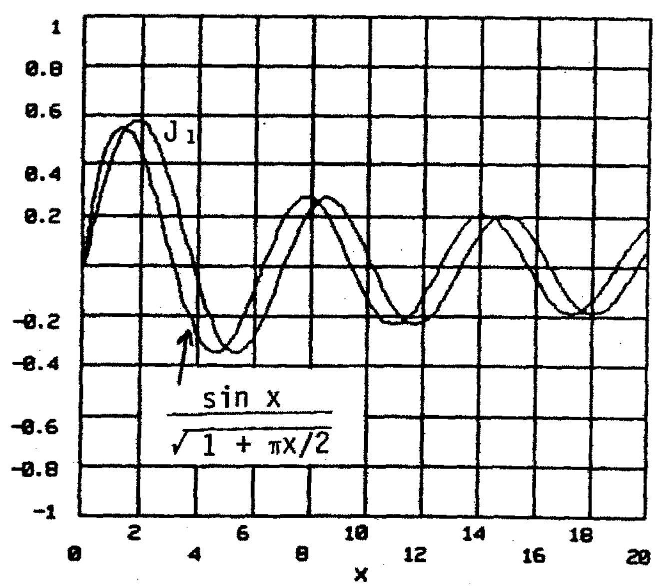

Figure 2

IV-3.3. Mode splitting

For a wave field of the form

(1) $e^{i(m\theta + k_{\parallel} z - \omega t)}$

we have a constant phase point at

(2) $\theta_W = \dfrac{-k_{\parallel} z}{m}$

So far, our wave field structure was always "tied" to a stationary magnetic field. If the magnetic field frame of reference is rotated, our field solutions are still valid in that reference frame. Unfortunately, we would like a solution in the laboratory frame of reference. In a tokamak, the confining field has a similar constant phase point (Figure 1)

(3) $\theta_B = \dfrac{B_\theta}{B_z} \dfrac{z}{r}$

Assuming $k_{\parallel}$ positive and $m < 0$, the wave field rotates with a typical parallel wavelength of a few centimeters. When positive B_θ is added, the wave field wraps around faster, and thus, as seen in the laboratory, has a shorter parallel wavelength.

(4) $y \simeq \lambda \quad \theta_B \simeq \Delta\lambda\theta_W$

and

(5) $\dfrac{\Delta\lambda}{\lambda} \simeq \dfrac{\theta_B}{\theta_W} << 1$

Substituting (2) and (3) in (5)

(6) $\Delta\, k_{\parallel} = \dfrac{B_\theta}{B_z} \dfrac{m}{r} = \dfrac{m}{qR}$

where q is the usual safety factor.[1,22] If we now simulate an identical wave going against B_o by simply reversing B_Θ, the wave wraps around more slowly, and thus has a longer parallel length. For typical Alcator experiments

(7) $k_{\parallel} = .5/\text{cm}$ $\qquad m = 2$

$q = 3$ $\qquad R = 54 \text{ cm}$

and

(8) $\frac{\Delta k_{\parallel}}{k_{\parallel}} \cong 2.5\%$

Mode Splitting

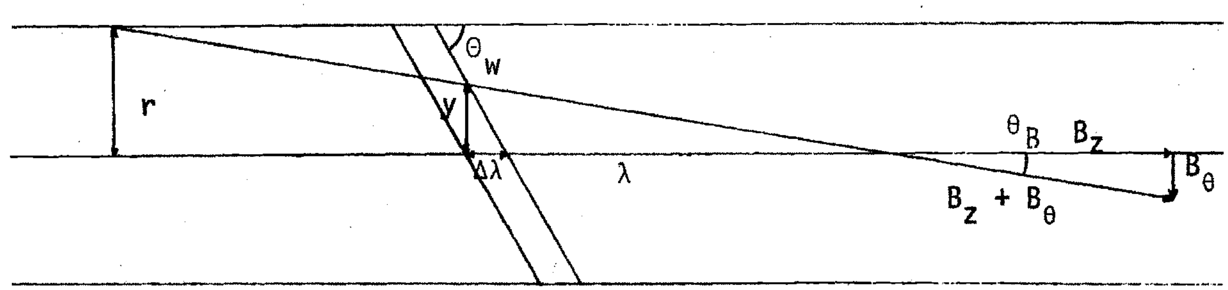

Figure 1

IV-4. Hot Plasma Model and Damping Mechanisms

Five basic damping mechanisms[32] of importance can be found in the Alcator experiment[20,26]. Each of the damping decrements depend heavily on the wave field structures and plasma parameter profiles. The first and simplest are wall losses,which are always present and give an upper bound on Q[32]. Wall losses are dependent on parallel and perpendicular mode numbers and, in particular, the edge H field. Second harmonic of the ion gyrofrequency damping can also be important if $k_\perp \rho_{ci}$ is large enough, which for practical purposes, means large radial mode numbers in the hot plasma center[30-32]. Fundamental and two ion-ion hybrid damping mechanisms have been discussed the most in the literature, and have the largest damping decrements[10,11,12,16,17,27,48,49].

Electron Landau Damping (ELD) and Transient Time Magnetic Pumping (TTMP) can be important in the high temperature center with large enough $k_\parallel$ and E_z in the absence of other strong damping mechanisms[30-32].

Finally, collisional and near-field damping may contribute to the[90,96] loading resistance, and remove power from the antenna. Also, a whole generation of non-linear effects and surface waves may, unfortunately, heat the plasma edge[17,32,74].

In this and the next Sections, all five types of damping mechanisms will be qualitatively evaluated in simple geometry, and then used in the weak damping approximation to numerically calculate wave damping length, radiation resistance and power deposition profiles for realistic experimental mode numbers, field strengths, plasma parameters and profiles.

IV-4.1. Wall damping

We now allow $k_{\parallel}$ to be complex, so the power flowing down our simple waveguide is

$$(1) \quad \begin{aligned} P_f &\propto [E_o\, e^{i((k_r + ik_i)\, z - \omega t)}]^2 \\ &\propto P_o\, e^{-2k_i z} \end{aligned}$$

The power dissipated per unit length is

$$(2) \quad -\frac{\partial P_f}{\partial z} = 2\, k_i\, P_f$$

and the wave damping length is

$$(3) \quad \frac{1}{k_i} = \frac{-2P_f}{\partial P_f/\partial z} = \frac{2 \text{ Power Flowing}}{\text{Power Dissipated}}$$

In Section IV-1.3, we calculated the power flowing down a simple wave guide as (MKS)

$$(4) \quad P_f = \frac{a^2 k_z}{\omega\mu_o} \quad E_o{}^2$$

For wall losses, the power dissipated per unit length can be calculated from the surface current resistive loss on the vacuum vessel

$$(5) \quad J_s \simeq \left.\frac{1}{\omega\mu_o}\frac{\partial E}{\partial x}\right|_{\text{wall}}$$

The power deposited per unit area and unit length are then[134]

$$(6) \quad P/m^2 = \frac{J_s{}^2}{2\,\sigma\delta}$$

$$(7) \quad P/m = 2\pi a\ P/m^2$$

where the skin depth is

$$(8) \quad \delta = \sqrt{\frac{2}{\omega\mu\sigma}}$$

Finally, substituting (4) - (8) into (3), we have

$$(9) \quad \frac{1}{k_i} = \frac{2\sqrt{2}}{\pi} \left[\frac{E_o}{\partial E/\partial x \Big|_{wall}} \right]^2 a\, k_\parallel \sqrt{\omega \mu_o \sigma} \cong 740 \text{ meters}$$

for high density (IV-1.3.(7)) and a stainless steel($\sigma = 1.1 \times 10^6$ mho/m) vacuum vessel.

We again see the critical importance of knowing the edge field. Physically, for a given central field, and thus flowing power, a smaller edge field will dissipate less power and have a longer damping length.

IV-4.2. Cyclotron damping

To first order, we can write the left handed particle trajectories and velocities (positive ions), as

(1) $x = r_o \sin \omega_o t$

(2) $y = r_o \cos \omega_o t$

(3) $v_x = r_o \omega_o \cos \omega_o t$

(4) $v_y = -r_o \omega_o \sin \omega_o t$

For a right handed electric field (E_-)

(5) $E_x = E_o \cos \omega_o t$

(6) $E_y = E_o \sin \omega_o t$

we can write the average power to the ion as

(7) $$P_- = \frac{\int_0^t q(v_x E_x + v_y E_y) dt'}{t} = r_o \omega_o q E_o [\langle \cos^2 \omega_o t \rangle - \langle \sin^2 \omega_o t \rangle] = 0$$

and, on the average, no power is coupled.

For a left handed electric field (E_+),

(8) $E_x = E_o \cos \omega_o t$

(9) $E_x = -E_o \sin \omega_o t$

and the power coupled to the ion is simply,

(10) $$P_+ = r_o \omega_o q E_o [\langle \cos^2 \omega_o t \rangle + \langle \sin^2 \omega_o t \rangle] = r_o \omega_o q E_o$$

Of course, negative power can be obtained by adjusting the phase of the electric field with respect to the ion velocity, but the right hand electric field component cannot couple power independently of phase, and can be ignored in the following power absorption calculations.

To understand this initial phase effect, we proceed directly to the tokamak geometry, where particles are streaming along the rotationally transformed field lines in a 1/R magnetic field. For ICRF, the electric field is a wave propagating along z, and the resonant condition is

(11) $\omega_\circ = \omega_{ci} + k_\parallel V_\parallel$

or simply, the cyclotron frequency in the ion's moving reference frame. Since the ions are moving along z in a slowly varying magnetic field, we can write.[7]

(12) $\omega_{ci}(t) = \omega_{ci} + t\,\omega'_{ci}$

and the equations of motion become

(13) $v_x - \omega_{ci}(t)\, v_y = q/m\, E_x \cos \omega_\circ t$

(14) $v_y + \omega_{ci}(t)\, v_y = -q/m\, E_y \sin \omega_\circ t$

Combining (13) and (14) in a rotating coordinate system

(15) $E\pm = \dfrac{E_x \pm E_y}{2}$

(16) $u = v_x + iv_y$

and neglecting the non-resonant right hand electric field, we have

(17) $\dfrac{du}{dt} + i\,\omega_{ci}\,(t)\;u = \dfrac{q}{m}\,E_+\,e^{-i\omega t}$

Equation (17) is linear, of first order, may be integrated using the integrating factor[132]

(18) $p = e^{i\omega_{ci}(t)}$

and has the solution[7]

(19) $u(t) = \exp(-\int_{-\infty}^{t} i\omega_{ci}(t)dt)\;\left[u(-\infty) + \dfrac{q}{m}\,E_+\sqrt{\dfrac{2\pi i}{\omega'_{ci}}}\right]$

The first factor in (19) is simply the phase angle of the velocity, and is analogous to WKB solutions, with $k(x)$ substituted by $\omega_{ci}(t)$, and x by t. Assuming that $u(-\infty)$ is randomly phased with respect to E_+, the average energy kick per pass through the resonant layer is

$$(20)\quad W = \frac{m}{2}\ \langle\ u(t)\ u(t)^* - u(-\infty)\ u(-\infty)^*\ \rangle\ = \frac{e^2}{2m}\ E_+^2\ \left|\frac{2\pi}{\omega'_{ci}}\right|$$

and is independent of initial phase and perpendicular energy. We can now integrate this energy kick over a distribution of resonant particles to find the power absorbed,

$$(21)\quad P/cm^3 = \frac{\pi q^2 E_+^2}{m\ k_\parallel} \iint dv_x\ dv_y\ f(v_\perp, V_{res})$$

where from (11)

$$(22)\quad V_{res} = \frac{\omega_o - \omega_{ci}}{k_\parallel}$$

Physically, the $1/k_\parallel$ factor is due to the fact that, for a given layer thickness Δx, perpendicular distribution function, etc., the integration interval width along $V_\parallel$ is proportional to $1/k_\parallel$.

Substituting a Maxwellian distribution function[1]

$$(23)\quad f_m = \frac{1}{\sqrt{\pi}\ v_{th}}\ e^{-\left[\frac{v}{v_{th}}\right]^2}$$

into (21), and making some changes in variables that cancel out the $1/R$ magnetic field dependence, gives the usual cyclotron power absorption formula[21,31,32]

$$(24)\quad P/cm^3 = \frac{\pi_i^2}{8\sqrt{\pi}}\ \frac{E_+^2}{k_\parallel\ v_{thi}}\ e^{-\left[\frac{\omega - \omega_{ci}}{k_\parallel v_{thi}}\right]^2}$$

We could have arrived at the same result in uniform B_o theory by an almost identical method, as in Section IV-2.1. First, we write the momentum equation including the parallel velocity, V.[45]

$$(25)\quad m\left[\frac{\partial\vec{v}}{\partial t} + \vec{V}\,\frac{\partial\vec{v}}{\partial z}\right] = q\left[\vec{E}_1 + \frac{\vec{v}X\vec{B}_o}{c} + \frac{\vec{V}}{c}\,X\vec{B}_1\right]$$

Again we assume

$$(26)\quad v_\mp = v_x \mp iv_y$$

$$E_\mp = E_x \mp iE_y$$

and solve for v adding the restriction v = 0 at t = 0

$$(27)\quad v_\pm = \frac{ie\,E_\pm\,(\omega - k_\parallel V)\,e^{i(k_\parallel z-\omega t)}}{m\omega}\,\frac{1-e^{i(\omega-k_\parallel V\mp\omega_{ci})t}}{\omega - k_\parallel V \mp \omega_{ci}}$$

Averaging (27) over a Maxwellian distribution and random initial phase, we can then write a dielectric tensor with complex elements similar to S and D which, themselves, are again functions of complex R (right hand) and L (left hand) components. The resistive parts of S and D then represent dissipative effects, since the current is now in phase with the electric field.
We can thus write[21]

$$(28)\quad K_{xx} = K_{yy} = S + i\gamma$$

$$K_{yx} = -K_{xy} = iD + \gamma$$

and

$$(29)\quad P/cm^3 = \frac{1}{2}\,R_e\,(\vec{E}^*\cdot\vec{J}) = \frac{1}{4}\,(\vec{E}^*\cdot\vec{J}) + cc = \frac{-i\omega}{16\pi}\,\vec{E}^*\cdot(\vec{\vec{K}} - 1)\cdot\vec{E} + cc$$

In equation (7) we assumed the ions were "free falling" in the resonant electric field, so the power delivered was proportional to $E_o t$. In practice, ions are not allowed to free fall, since the interaction time with the resonant field is finite, and phase incoherent from one pass to another through the resonant layer. This finite interaction leads to a collision type resistivity, and thus to an absorbed power proportional to E_o^2. The interaction force is, nevertheless, simply qE in the ion reference frame.

If we now assume an electric field at the second harmonic of the ion gyrofrequency, equation (7) becomes

(30) $P = r_o \omega E_o [\langle \cos\omega_o t \cos 2\,\omega_o t\rangle + \langle \sin \omega_o t \sin 2\,\omega_o t\rangle] = 0$

and no power can be coupled independently of polarization or initial phase. On the other hand, if we allow E to have a gradient,

(31) $E_x = E_o + \frac{\partial E}{\partial x} x = E_o\,(1 + k_\perp r_o \cos \omega_o t)$

power can be coupled through the non-linear term

(32) $\langle \cos \omega_o t \cos \omega_o t \cos 2\,\omega_o t\rangle \neq 0$

Our effective interaction force is now

(33) $\frac{k_\perp r_o}{\sqrt{2}} q\, E_o = \sqrt{\lambda}\, q\, E_o$

instead of simply qE_o, and all of our previous results can be upgraded for the second harmonic regime by simply replacing E_o, by $\sqrt{\lambda}\, E_o$ and ω_{ci} by $2\,\omega_{ci}$. Similarly, we could go to the nth harmonic by inserting the factors

(34) $\sqrt{\lambda}^{n-1}$ and $n\omega_{ci}$

From now on, we shall consider the second harmonic regime at high density in the tokamak geometry [21,31,32]

(35) $P/cm^3 = \frac{\pi_i^2}{8\sqrt{\pi}} \frac{\lambda}{k_\parallel V_{thi}} \left|E_+\right|^2 e^{-\left(\frac{\omega-2\omega_{ci}}{k_\parallel V_{thi}}\right)^2}$

In this case, the wave energy is deposited in the perpendicular component of the ion energy for predominantly large Larmor radii. At high power,this will lead to the formation of energetic perpendicular ion tails. If the resonant layer is at the center of the plasma,the resonant region will be a cylinder of radius R_o, height 2a and effective thickness ΔR (such that the exponent is negative one on each side of the resonance)[21]

(36) $\Delta R = \frac{k_{\parallel} V_{thi}}{\omega} \approx .6$ cm in the hot plasma center.

The heat transfer along θ is much greater than along r due to the rotational transform, and so we can write an average power per volume as a function of minor radius by integrating around θ at r and dividing by $2\pi r$.[21]

(37) $$P/cm^3 = \frac{\pi_i^2}{16\pi\omega} \frac{R_o k_\perp^2 \rho_i^2}{r} |E_+|^2 = \frac{\pi_i^2}{16\pi\omega} \frac{R_o}{r} \rho_i^2 |E_+'|^2$$

This result is independent of $k_{\parallel}$ and peaked at the center of the plasma (small r). The apparent singularity can be removed by displacing the resonant layer by ΔR ($r \to r + \Delta R$ in denominator). In any case, we will either want the power deposition profile or the power deposited per unit length, which removes the singularity altogether

(38) $$P/cm = \int_0^{a_{hot}} 2\pi r \; P/cm^3 \, dr \cong 1.7 \times 10^9 \frac{\text{ergs}}{\text{sec-cm}} = 170 \text{ W/cm}$$

where we assumed $a_{hot} = 5$ cm, $n_e = 5 \times 10^{14}/cm^3$, $E_+ = .16$ statvolt/cm and $k_\perp = 1/cm$. Also assuming $E \approx .5$ statvolt/cm and $k_{\parallel} = .5/cm$, the power flowing is approximately

$$(39) \qquad P_f = \int_S \frac{cEXH}{8}\, ds \simeq \pi a^2 \frac{c^2 k_\parallel}{\omega\, 8\, \pi} \cong 1.1 \times 10^{12} \text{ ergs/sec} = 110 \text{ kW}$$

The damping length is then

$$(40) \qquad \frac{1}{k_{\parallel i}} = \frac{2 P_f}{P_{dis}} = 13 \text{ meters}$$

which is several times the circumference of the torus, but is nevertheless much shorter than the wall damping length.

IV-4.3. Electron Landau damping and transit time magnetic pumping

The collisionless resonant damping condition $\omega - n\omega_c - k_\parallel V = 0$ can also be significant for $n = 0$ if the phase velocity is of the order of the parallel thermal velocity.[1] For electrons at high density in Alcator

$$(1) \qquad \alpha = \frac{v_{p_\parallel}}{v_{the_\parallel}} = \frac{2.5 \times 10^9 \text{ cm/sec}}{1.3 \times 10^9 \text{ cm/sec}} = 1.9$$

and we thus proceed to calculate what is usually called electron Landau damping. Considering only motions and fields along z, and without using complex variables, we can write the momentum equation and its solution just as in the previous Section.[1,45]

$$(2) \qquad \frac{m d\vec{v}_1}{dt} = e\vec{E} \cos\left[k\,(z_o + v_o t) - \omega t\right]$$

$$(3) \qquad \vec{v}_1 = \frac{e\vec{E}}{m}\;\frac{\sin\left[k\,(z_o + v_o t) - \omega t\right] - \sin kz_o}{kv_o - \omega}$$

The power absorption is then found by averaging the change in kinetic energy over the initial condition z_o and distribution function $f(v_o)$

$$(4) \qquad P/\text{cm}^3 = n_o \left\langle \frac{d}{dt}\;\frac{mv^2}{2} \right\rangle_{z_o,\, v_o}$$

$$= \frac{-\pi n_o \omega\; e^2 E_\parallel^2}{2\, m k_\parallel^2}\;\left.\frac{\partial f(v_o)}{\partial v_o}\right|_{v_o = \frac{\omega}{k_\parallel}}$$

Substituting a Maxwellian distribution function (IV-4.2(23)) and (1), we have

$$(5) \quad P/cm^3 = \frac{\sqrt{\pi}\, n_o\, e^2 E_z^2}{\omega\, m} \quad \alpha^2\, e^{-\alpha^2}$$

The difficulty is now in calculating E_z as a function of E_y. It is tempting to use the third line of the dielectric tensor, but as we shall see later, for the hot dielectric tensor when $1/\alpha$ is not small, the k_{zy} element can be of the order of n_A^2 instead of zero, and k_{zz} is $1/k_\parallel^2\lambda_D^2$ instead of $-\pi^2 e/\omega^2$.[7] To circumvent these problems, we shall assume the wave is more or less compressional ($k_\perp > k_\parallel$), and the electrons can keep quasi-neutrality through Debye shielding ($V_{te} \geq V_p$).[7] Both approximations are quite crude for Alcator, but will nevertheless give a reasonable answer. We can thus write from compressibility

$$(6) \quad \frac{n_{i1}}{n_o} = \frac{B_1}{B_o}$$

from quasi-neutrality

$$(7) \quad n_{i1} \simeq n_{e1}$$

from hot electron shielding

$$(8) \quad n_{e1} = n_o e^{\frac{e\phi}{KT_e}} = n_o \left(1 + \frac{e\phi}{KT_e}\right)$$

and from Ampère's law

$$(9) \quad \nabla X \vec{E} = -\frac{\partial \vec{B}_1}{c\partial t}$$

Substituting (7)→(6)→(8)→(9), we have

$$(10)\quad i\, k_x\, E_y = \frac{i\omega}{c}\, \frac{e\phi}{KT_e}\, B_o$$

and noting that

$$(11)\quad E_z = -\frac{\partial\phi}{\partial z} = -i\, k_\parallel\, \phi$$

then

$$(12)\quad E_z = -\frac{i\, k_x\, k_\parallel\, KT_e\, c}{\omega\, e\, B}\, E_y$$

Substituting (12) into (5) finally gives the compact form[130]

$$(13)\quad P/cm^3 = \frac{\omega\, \beta_e}{16\sqrt{\pi}} \left[\frac{k_\perp c}{\omega}\right]^2 \alpha\, e^{-\alpha^2}\, |E_y|^2$$

Note that, for Alcator, we could have achieved a similar result by blindly using the cold dielectric tensor, since

$$(14)\quad \frac{1}{k_\parallel^2 \lambda_D^2} = \frac{\pi_e^2}{\omega^2}\, \frac{v_p^2}{v_{the}^2} \simeq |P|$$

except that the phase of E_z would have been wrong (which is of no importance here).

Until now, we have only allowed qE forces on the particles, but we could also include $-\mu\nabla B$ forces, which would give rise to transit time magnetic pumping (TTMP). Careful analysis of the hot dielectric tensor[7] shows that ELD and TTMP are coherent, and cross terms cancel in the power deposition calculation (IV-4.2.(26)), thus leaving ELD (E_z) alone in the form of (13), which is half the TTMP power loss. We note also that the wave energy is deposited in the electron parallel velocity near the thermal velocity, unlike 2 ω_{ci} damping, which favors large Larmor radius ions. Using the same numbers as in Section II-4.2. ($E_\perp$ = 150 V/cm, a_{hot} = 5 cm, $k_\parallel$ = .5/cm, $k_\perp$ = 1/cm, α = 1.9, β_e = 5.6 x 10^{-3} and P_f = 110 kW)

(15) $$P/cm = \pi a_{hot}^2 \; P/cm^3 = 1.4 \times 10^8 \; \frac{erg}{sec \cdot cm} = 14 \text{ W/cm}$$

(16) $$\frac{1}{k_{i\parallel}} = \frac{2P_f}{P_{dis}} = 160 \text{ meters}$$

The damping length is then many times the circumference of the torus, but is, nevertheless, shorter than the wall damping length, and much longer than the 2 ω_{ci} damping length.

IV-4.4. The hot dielectric tensor and approximations

So far, we have looked into selected topics of hot plasma effects, just as in Appendix 1 we investigated selected simple wave regimes. Now we introduce a totally general wave propagation and damping formulation, the hot dielectric tensor and wave equation.[45,20] The basic constitution of the hot tensor is the same as the cold one, i.e., a sum of a vacuum, electron and ion terms, except that the elements can also be resistive. Unfortunately, as we saw in Section IV-4.2., the resistive and even reactive particle currents are much more difficult to calculate than in cold plasma theory. The basic trick is to calculate the field-particle interaction in the particle zeroth order trajectory reference frame, and then average over the particle velocity distribution function. The product of this formidable analytic computation is, even in its most compact form for Maxwellian distribution functions, a somewhat overwhelming series of infinite sums involving just about every plasma variable (T_e, k_x, λ ... V_d) and a particularly nasty integral, the dispersion function. Nevertheless, with a number of not too restrictive and quite accurate approximations at high density,[20,26]

(1) $V_{drift} = 0$

(2) $T_i = T_e$

(3) $k_y = 0$

(4) $j = e, i$

(5) $-5 < n < +5$

the formulation becomes manageable, and general trends become more apparent.

The basic expansion parameters are as one would expect from our simple treatment of collisionless damping:[20]

$$\lambda_j = \frac{k_\perp^2 \rho_j^2}{2} \tag{6}$$

$$\zeta_{nj} = \frac{\omega + n\omega_{cj}}{k_\parallel v_{thj}} \tag{7}$$

$k_y = 0$ is the most restricting approximation, since k_y affects the wave polarization, and thus the reactive and resistive components of the tensor elements. Although the dispersion relation is still found by simply setting the wave equation determinant to zero, we cannot write an equivalent biquadratic equation, since the tensor elements are infinite sums already involving k_x, k_y, $k_\perp$, $k_\parallel$. Without the further, major assumption that $\lambda_i \ll 1$, the many dispersion relation solutions can only be found by using sophisticated numerical methods. Restricting $\lambda \ll 1$ basically reproduces the cold (2 x 2) tensor with very small[26] changes in the reactive components due to ELD, TTMP and cyclotron damping, and does not allow any new wave solutions.

A realistic, comprehensive study of the effect of our approximations (equations (1) - (5)) can only be done on advanced algebraic manipulators such as MAXIMA. In particular, at low density in the runaway regime, the streaming parameter becomes appreciable ($V_D \neq 0$), $T_i \neq T_e$, discrete positive and negative m modes dominate ($k_y = 0$), $Z_{eff} > 1$ (j = e, i, impurities), and all approximations break down lamentably.

Fortunately, in Alcator, nearly pure hydrogen high density plasmas can be produced with very small drift velocities and nearly isotropic Maxwellian distribution functions. For simplicity and not necessity, we will also assume for now, that $k_y = 0$. The results of solving the cold and hot wave determinants for a hot, dense plasma center and cold edge, for the same $k_\parallel$ and roughly the same magnetic field are shown in Tables 1 and 2. As we suspected and assumed until now, the 2 X 2 part of the cold tensor is almost the same as its hot plasma counterpart for the fast wave branch, since indeed $\lambda \ll 1$, and so all our previous work is well founded. Also, as one would expect, at the cold edge, k_{xz} and k_{yz} are very small, and $k_{zz} = P$. Unfortunately, this is not the case with the hot plasma center, which led to our earlier difficulty in calculating E_z from the third line of the wave tensor. It is important to note here that, although the reactive components of the fast wave tensor elements are insensitive to the major radius position, that is, the magnetic field, the ion resistive components are dependent on the narrow harmonic resonant condition

(8) $$\omega - n\omega_c - k_\parallel V = 0$$

and the power deposition profile is very peaked at the resonant layer in a one dimensional plasma formulation.

It is also interesting to note that, for $k_y = 0$ ($m = 0$), from the first line of the wave tensor, we have

(9) $$\frac{E_y}{E_x} = \frac{E_\theta}{E_r} = \frac{S - n_\parallel^2}{-iD} \begin{array}{l} = 5.46 \text{ at the edge,} \\ = \ .60 \text{ at the center,} \\ = 1 \text{ at the cutoff layer} (k_\perp^2 = 0)\,. \end{array}$$

which means that, from a global point of view, the antenna couples to an E_θ edge wave that gradually transforms into an E_r wave in the center of the plasma.

The mere fact that the wave equation is of higher order than biquadratic means that other wave solutions exist. The most important solution (besides the slow wave which did not even depend on hot plasma effects, but was found evanescent in our regime and could be neglected) is the ion Bernstein wave. This new wave is critically dependent on λ and ζ, and thus cannot be coupled from the cold edge which does not allow such a mode, as we saw in cold plasma theory. Nevertheless, the wave can couple power from the fast wave near the center if the Bernstein wave $k_\perp$ becomes equal to the fast wave $k_\perp$. The two modes are then locally non-orthogonal, and power can be coupled between the waves giving rise to a telescopingly complicated problem. In the two ion-ion hybrid regime, even with cold plasma theory, we encountered singularities in $k_\perp$ which would have made $\lambda >> 1$, and new waves would have immediately appeared. In fact, hot plasma treatment of the two ion-ion hybrid regime would have removed the singularity, but the general location of the resonance would still be governed by the cold plasma $k_\perp$, which "controls" the hot plasma expansion parameter λ.

Table 1

Comparison of tensor elements in hot plasma center

Tensor Elements	Cold Plasma Fast Wave	Hot Plasma Fast Wave		Hot Ion Bernstein Wave	
K_{xx}, S	-735	+i184	-736	-i44.7	+151
K_{xy}, -iD	-i1471	-i1468	-184	-i582	+39.5
K_{zz}, P	-10^6	$+i1.4\times10^6$	-9.7×10^5	$+i1.4\times10^6$	-9.7×10^5
K_{xz}	0	+i.44	+4.99	-i39.9	-48.2
K_{yz}	0	+i1093	+1406	-i775	+3637
$k_\perp$	1.67	+i.04	+1.65	-i2.62	+2.47

Basic Parameters

200 MHz
65.8 kG
$k_\parallel$ = .5/cm
$n_e = 5 \times 10^{14}/cm^3$
Hydrogen

$k_y = 0$
$T_i = T_e = 1$ keV
$\Omega = 2$
$\omega_{pi}^2/\omega_{ci}^2 = 2207$

Table 2

Comparison of tensor elements in cold plasma edge

Tensor Elements	Cold Plasma Fast Wave	Hot Plasma Fast Wave		Hot Ion Bernstein Wave
K_{xx}, S	-13.7	-i.036	-13.6	
K_{xy}, -iD	-i29.4	-i29.3	+.036	No
K_{zz}, P	-2.0×10^{4}	$-i7.5\times10^{-9}$	-2.03×10^{4}	
K_{xz}	0	-9.7×10^{-5}	$+1.38\times10^{-8}$	Solution
K_{yz}	0	-5.0×10^{-6}	-.063	
$k_\perp$	i.511	+i.514	-4.05×10^{-5}	

Basic Parameters

200 MHz
65.8 kG
$k_\parallel$ = .5/cm
$n_e = 10^{13}/cm^3$
Hydrogen

$k_y = 0$
$T_i = T_e = 10$ eV
$\Omega = 2$
$\omega_{pi}^2/\omega_{ci}^2 = 44.1$

IV-4.5. Collisional Damping

To take into account collisional damping, we return again to the basic momentum equation, but including collisions [1]

(1) $$m_k n_k \frac{d\vec{v}_k}{dt} = q_k n_k \left(\vec{E} \times \frac{\vec{v}_k \times \vec{B}}{c}\right) - \gamma_k n_k m_k \vec{v}_k$$

Equation (1) can be cast in the form of equation IV-2.1.(3) with the substitution

(2) $$m_k \rightarrow m_k^{\dagger} = m_k \ (1 + i\ \gamma_k/\omega)$$

and

(3) $$\Omega \rightarrow \Omega^{\dagger}$$

(4) $$\frac{\pi^{\dagger 2}}{\omega_c^{\dagger}} = \frac{\pi^2}{\omega_c}$$

and our cold dielectric tensor is easily upgraded to include collisions. We will confine this derivation to ICRF, and assume

(5) $$\Omega_e << \Omega_i < \sqrt[4]{\frac{m_i}{m_e}} \cong 6.5$$

(6) $$\gamma_i = \sqrt{\frac{m_e}{m_i}}\ \gamma_e, \quad (T_i = T_e)$$

(7) $$\eta_s = \frac{E}{J} = \frac{m\ \gamma_{ei}}{n_e\ e^2}$$

(8) $$\frac{\gamma_k}{\omega} = \tau_k << 1$$

The new dielectric tensor elements are then calculated from IV-2.1 as

(9) $$P^{\dagger} = 1 - \frac{\pi_e^{\dagger\,2}}{\omega^2} - \frac{\pi_i^{\dagger\,2}}{\omega^2}$$

$$\cong - \frac{\pi_e^2\ (1 - i\ \tau_e) + \pi_i^2\ (1 - i\ \tau_i)}{\omega^2}$$

$$\cong P\ (1 - i\ \tau_e)$$

$$(10)\qquad R^{\dagger} = -\frac{\pi_e^{\dagger 2}}{\omega\,(\omega - \omega_{ce}^{\dagger})} - \frac{\pi_i^{\dagger 2}}{\omega\,(\omega + \omega_{ci}^{\dagger})}$$

$$= -\frac{\pi_i^{2}}{\omega\,\omega_{ci}}\left[\frac{1}{\Omega_e^{\dagger} - 1} + \frac{1}{\Omega_i^{\dagger} + 1}\right]$$

$$(11)\qquad L^{\dagger} = -\frac{\pi_i^{2}}{\omega\,\omega_{ci}}\left[\frac{1}{\Omega_e^{\dagger} + 1} + \frac{1}{\Omega_i^{\dagger} - 1}\right]$$

$$(12)\qquad \frac{1}{\Omega^{\dagger 2} - 1} \cong \frac{1}{\Omega^2 - 1}\,(1 - i\,2\tau\,\frac{\Omega^2}{\Omega^2 - 1})$$

$$(13)\qquad \frac{\Omega^{\dagger}}{\Omega^{\dagger 2} - 1} \cong \frac{\Omega}{\Omega^2 - 1}\,(1 - i\tau\,\frac{\Omega^2 + 1}{\Omega^2 - 1})$$

and using (12), (13) and (5),

$$(14)\qquad S^{\dagger} = \frac{R^{\dagger} + L^{\dagger}}{2} \cong S\,(1 + i\,\tau_i\,\frac{1 + \Omega_i^2}{1 - \Omega_i^2})$$

$$(15)\qquad D^{\dagger} = \frac{R^{\dagger} - L^{\dagger}}{2} \cong D\,(1 + i\,\tau_i\,\frac{2}{1 - \Omega_i^2})$$

Power absorption is then calculated as

$$(16)\qquad P_{\parallel} = \mathrm{Re}\,\frac{J_{\parallel}\cdot E_{\parallel}^*}{2} = \mathrm{Re}\,\frac{\omega}{i8\pi}\,P^{\dagger}\,E_z\,E_z^*$$

$$= \frac{\pi_e^2}{\omega^2}\,\frac{\gamma_e}{8\pi}\,E_z^{\,2} \cong \frac{\pi_i^{\,2}}{\omega_{ci}^{\,2}}\,\frac{\gamma_i}{8\pi}\sqrt{\frac{m_e}{m_i}}\;E_y^{\,2}$$

where we used (6), and assumed $E_z \simeq m_e/m_i\,E_y$, and

$$(17)\qquad P_{\perp} = R_e\,\frac{\omega}{i8\pi}\left[(S^{\dagger}\,E_x - iD^{\dagger}\,E_y)\,E_x^* + (iD^{\dagger}\,E_x + S^{\dagger}\,E_y)\,E_y^*\right]$$

$$= R_e\,\frac{\omega\,E_y}{i8\,\pi}\left[S^{\dagger}\left[\frac{D^2}{(S - n_{\parallel}^{\,2})^2} + 1\right] - D^{\dagger}\frac{2\,D}{S - n_{\parallel}^{\,2}}\right]$$

Further assuming $n_\parallel = 0$ and $D = -\Omega S$, we have

(18) $$P_\perp = \frac{\pi_i^{\,2}}{\omega^2_{ci}} \frac{\gamma_i}{8\pi} E_y^2 \cong \sqrt{\frac{m_i}{m_e}}\; P_\parallel$$

From Spitzer resistivity (7), and the ion-electron collision frequency (6)[75,82]

(19) $$\gamma_{ie} = 4.8 \times 10^{-8}\, n_e \lambda_c\, T^{-3/2}\, \mu^{-1/2} \cong 2.3 \times 10^6/\text{sec}$$

and the ion-neutral collision frequency[82]

(20) $$\gamma_{in} = n_n \sigma_n v_{thi} \cong 1.5 \times 10^6/\text{sec}$$

(21) $$\gamma_i = \gamma_{in} + \gamma_{ie} \cong 3.8 \times 10^6/\text{sec}$$

where we assumed $T_i = T_e = 10$ ev, $\sigma_n = 5 \times 10^{-15}$ cm^2, $n_n = n_e = 10^{14}/\text{cm}^3$.

The cold neutrals from the edge will have a short mean free path, due to ionization by electron impact [78]

(22) $$\gamma_{ion} \cong \langle \sigma v_e \rangle\, n_e \cong 1.9 \times 10^6/\text{sec}$$

(23) $$\lambda_{mfp} = \frac{v_{thi}}{\gamma_{ion}} = 1.1 \text{ cm}$$

where we assumed $T_n = 5$ ev, $T_e = 30$ ev and $n_e = 10^{14}/\text{cm}^3$.

Finally, the power deposition and damping length can be approximately calculated as

(24) $$P/\text{cm}^3 \cong P_\perp \cong 3.1 \times 10^6 \ \frac{\text{erg}}{\text{sec cm}^3} \simeq .31 \text{ W/cm}^3$$

(25) $$P/\text{cm} \cong 2\pi a \lambda_{mfp}\, P/\text{cm}^3 \cong 19.5 \text{ W/cm}$$

(26) $$\frac{1}{k_i} = \frac{2\, P_f}{P/\text{cm}} \cong 110 \text{ meters}$$

where we assumed from IV-4.2, $P_f = 110$ kW and $E_\perp \cong 60$ V/cm.

From (18) and (20) it is clear that

(27) $$P \propto n\, E_\perp^{\,2}\, T^{-3/2}$$

and

(28) $P_{center} < P_{edge}$

Even if the collisional damping length is much larger than the second harmonic damping length, it may have very detrimental effects since nT is much smaller at the plasma edge. Antenna near-fields can be several times larger than the wave fields (and E_z of the order of $E_\perp$ for unshielded antenna) giving rise to large power absorption, and even breakdown.

Collisional power absorption could also have been crudely estimated by simply writing [1,75,90,96,144]

(29) $P/cm^3 = \frac{J^2}{2} \eta_s$

where

(30) $J \simeq \frac{\omega}{4\pi} \epsilon_A E_\perp \simeq J_\perp \simeq J_\parallel$

and η is the Spitzer (or any other) resistivity. Note that this is very different from writing $P/cm^3 = E^2 \eta/2$ as in ohmic heating, since the resistivity is in "series" with a much larger wave reactance.[1]

(31) $X_W = \frac{E}{J} = \frac{1}{\omega \varepsilon_o \varepsilon_A} \simeq 100\ \Omega \cdot cm$

$$\gg \eta_s \simeq .08\ T^{-1.5} \simeq 10^{-4}\ \Omega \cdot cm$$

IV-5. Inhomogeneous Cylindrical Plasma Numerical Model

We now turn to a somewhat more sophisticated model, the inhomogeneous plasma-filled circular waveguide. The procedure for obtaining the field solutions is a combination of all our previous models, where we will sacrifice simplicity for more precise results, especially at the low density edge near the antenna. A numerical code[21] written by J. Adams (TFR, Fontenay - aux - Roses, France) and further extended to incorporate E_z and hot plasma effects, is used extensively. A similar code is also used to generate the full inhomogeneous plasma eigenmode dispersion relations. Using these codes, radiation resistance and probe signal components are calculated much more precisely.

IV-5.1. Inhomogeneous plasma eigenmode differential equations and large r approximation

In this Section, we will again start with Maxwell's equations and the dielectric tensor in cylindrical coordinates, as in Section IV-3.1., and assume a wave of poloidal, toroidal and temporal form

(1) $$A = A_o e^{i(m\Theta + k_{\parallel} z - \omega t)}$$

but leave the radial behavior unspecified. We will also solve for a second order differential equation in E_Θ, instead of B_z, so that the physical solution with $E_\Theta = 0$ at the wall can easily be recognized, just as in Section IV-2.3.

Starting with equation(2r) of Section IV-3.1. and substituting (1), we have

(2) $$\frac{im}{r} B_z - ik_{\parallel} B_\Theta = \frac{-i\omega}{c} (SE_r - iDE_\Theta).$$

Then substituting (1Θ) and (1z) into (2) and collecting terms, we have a first order differential equation in terms of E_Θ and E_r alone[21]

$$(3)\qquad i\, E_r \left[k_\parallel^2 + \frac{m^2}{r^2} - \frac{\omega^2 S}{c^2}\right] = \frac{m}{r} E_\Theta' + E_\Theta \left[\frac{m}{r^2} + \frac{\omega^2}{c^2} D\right]$$

where the prime denotes differentiation with respect to r. Similarly, we can also start with equation (2Θ), and substituting (1),

$$(4)\qquad -B_z' + ik_\parallel B_r = \frac{-i\omega}{c}\,(iDE_r + SE_\Theta)$$

and again, substituting (1r) and (1z) and collecting terms, we have

$$(5)\qquad E_\Theta'' + \frac{E_\Theta'}{r} + E_\Theta\left[\frac{\omega^2 S}{c^2} - k_\parallel^2 - \frac{1}{r^2}\right] = \frac{m}{r}\, iE_r' - iE_r\left[\frac{m}{r^2} + \frac{\omega^2 D}{c^2}\right]$$

Let's pause now from our general derivation and assume that $r \to \infty$ but m stays finite, which simulates a Cartesian coordinate system with $k_y = 0$. Equation (3) then becomes

$$(6)\qquad E_r\left[\frac{\omega^2 S}{c^2} - k_\parallel^2\right] - \frac{iD\omega^2}{c^2} E_\Theta = 0$$

which we recognize as the first line of the wave tensor equation. Similarly, equation (5) becomes

$$(7)\qquad E_\Theta'' + E_\Theta\left[\frac{\omega^2 S}{c^2} - k_\parallel^2 - \frac{\omega^4 D^2}{c^4}\,\frac{1}{\frac{\omega^2 S}{c^2} - k_\parallel^2}\right] = 0$$

where the factor multiplying E_Θ is easily recognized as the fast wave $k_\perp^2$ in agreement with our inhomogeneous plasma Cartesian waveguide treatment of Section IV-2.3.

Returning to our general derivation, we can rewrite (3) and (5) as

$$(8)\qquad AiE_r = B\,E_\Theta' + C\,E_\Theta$$

$$(9)\qquad E_\Theta'' + D\,E_\Theta' + F\,E_\Theta = BiE_r' - CiE_r$$

where A, B, C, D, and F are all functions of r.

By substituting (8) and the derivative of (8),

$$(10) \quad i\,E_r' = \frac{B}{A}E_\Theta'' + \left[\left(\frac{B}{A}\right)' + \frac{C}{A}\right]E_\Theta' + \left(\frac{C}{A}\right)' E_\Theta$$

into (9) and collecting terms, we have a second order differential equation in E_Θ alone,

$$(11) \quad E_\Theta'' = \frac{A}{A - B^2}\left[\left[-D + B\left(\frac{B}{A}\right)'\right]E_\Theta' - \left[F - B\left(\frac{C}{A}\right)' + \frac{C^2}{A}\right]E_\Theta\right]$$

where we note the possibility of a singularity at

$$(12) \quad A - B^2 = 0$$

which is simply our two ion-ion hybrid resonance condition, $S - n_\parallel^2 = 0$. Also, unlike equation (7), we must take derivatives of the plasma parameter functions, A', B' and C', which are trivial except for the dielectric tensor element factors S' and D', which can be written as

$$(13) \quad S, D \;\alpha\; n(r)$$

and these derivatives are easily calculated from the density profile $n(r)$ and $\frac{\partial n(r)}{\partial r}$.

Cold plasma E_z can be calculated from IV-3.1-(2z).

$$(14) \quad \frac{1}{r}\left[\frac{\partial r B_\Theta}{\partial r} - \frac{\partial B_r}{\partial \Theta}\right] = -\frac{i\omega}{c} P E_z$$

and substituting (1r) and (1Θ), we have

$$(15) \quad E_z = \frac{k_\parallel c^2}{P\omega^2}\left[\frac{iE_r}{r} + iE_r' - \frac{m}{r}E_\Theta\right]$$

IV-5.2. TFR-EZ code structure

We now wish to solve numerically equation IV-5. 1.(11), which can be rewritten as

(1) $E_\theta = F\ (r,\ E_\theta,\ E_\theta')$

and where we will use a density profile,

$$n(r) = n\ (1 - \frac{r^2}{a^2}) \qquad 0 < r < .9a \tag{2}$$
$$= n\ [.04 + .15e^{-12(r/a\ -\ .9)}] \qquad .9a < r < \text{wall}$$

and n_a, n_b, B_o, ω_o etc.,to calculate F.

In Section IV-2.3, we used a first order integration method to solve

(3) $y' = G\ (r,y)$

(4) $y_{k+1} = y_k + \frac{1}{6}\ (6a_1)$

with $a_1 = h\ G\ (r_k,\ y_k)$

h = step size

Quite similarly, we could have written to fourth order, using the Runge-Kutta method [132]

(5) $y_{k+1} = y_k + \frac{1}{6}\ (b_1 + 2b_2 + 2b_3 + b_4)$

with

$$b_1 = h\ G\ (r_k,\ y_k)$$

$$b_2 = h\ G\ (r_k + \frac{h}{2},\ y_k + \frac{b_1}{2})$$

$$b_3 = h\ G\ (r_k + \frac{h}{2},\ y_k + \frac{b_2}{2})$$

$$b_4 = h\ G\ (r_k + h,\ y_k + b_3)$$

Now solving equation (1) to fourth order, we similarly write

$$(6)\qquad \begin{aligned} E_{k+1} &= E_k + \frac{1}{6}\,(b_1 + 2b_2 + 2b_3 + b_4) \\ E'_{k+1} &= E_k' + \frac{1}{6}\,(b'_1 + 2b'_2 + 2b'_3 + b'_4) \end{aligned}$$

where we have successively calculated

$$(7)\qquad \begin{aligned} b_1 &= h\,E'_k \\ b'_1 &= h\,F\,(r_k, E_k, E'_k) \\ b_2 &= h\,(E'_k + \frac{b'_1}{2}) \\ b'_2 &= h\,F\,(r_k + \frac{h}{2}\,,\ E_k + \frac{b_1}{2}\,,\ E'_k + \frac{k'_1}{2}) \end{aligned}$$

and so on for b_3, b'_3, b_4, and b'_4.

To initialize the program,we need to specify E_θ and E'_θ at $r = 0$ for each poloidal mode number m, just as we needed to initialize FINT (first integral) and SINT (second integral) in Section IV-2.3. By judiciously varying $k_\parallel$,we can then solve for the desired radial mode number μ,while keeping E_θ (w) = 0. Since we now have E_θ, E'_θ, S, D, etc. for all r, we can successively calculate iE_r from Section IV-5.1.(3), E_z from IV-5.1.(15), B_r from IV-3.1.(1r), B_θ from IV-3.1. (1θ) and B_z from IV-3.1.(1z). We can calculate $|E_+|$, $|E'_+|$, $|E'_+|^2$ from

$$(8)\qquad E\pm = \frac{E_\theta \mp iE_r}{2} \qquad \text{(statvolts/cm)}$$

and the Poynting flux along +z and -z,as

$$(9)\qquad \Phi(r) = \frac{k_\parallel c^2}{4\omega}\int_0^r [|E_r|^2 + |E_\theta|^2]\, r\,dr \qquad \text{(ergs/sec)}$$

Similarly, power deposition per cubic centimeter and per unit length for ELD and second harmonic are calculated from IV-4.3. (13) and IV-4.2.(37) with a Gaussian temperature profile defined by IV-2.3.(2). Finally, the single pass radiation resistance can be found from (6), E_θ (r = antenna) and equation IV-1.2 (5).

Figure 1 is a simplified operational block diagram of TFR-EZ. Data can either be written directly in the beginning of the main program or through more convenient files. The initial data is then normalized and reduced to more compact forms,and proper initial conditions are set for E_θ and E'_θ as a function of m. ADIRKG is a general fourth order subroutine that sets up (6) and (7). SYDELC is a specific subroutine that calculates (7) from the initial reduced data. CALPI calculates n(r) and $\partial n(r)/\partial r$ from (2). The field components can then be calculated and printed as the main loop increases r to a maximum radius,where all the field components can be plotted as a function of minor radius.

Block Diagram of TFR-EZ

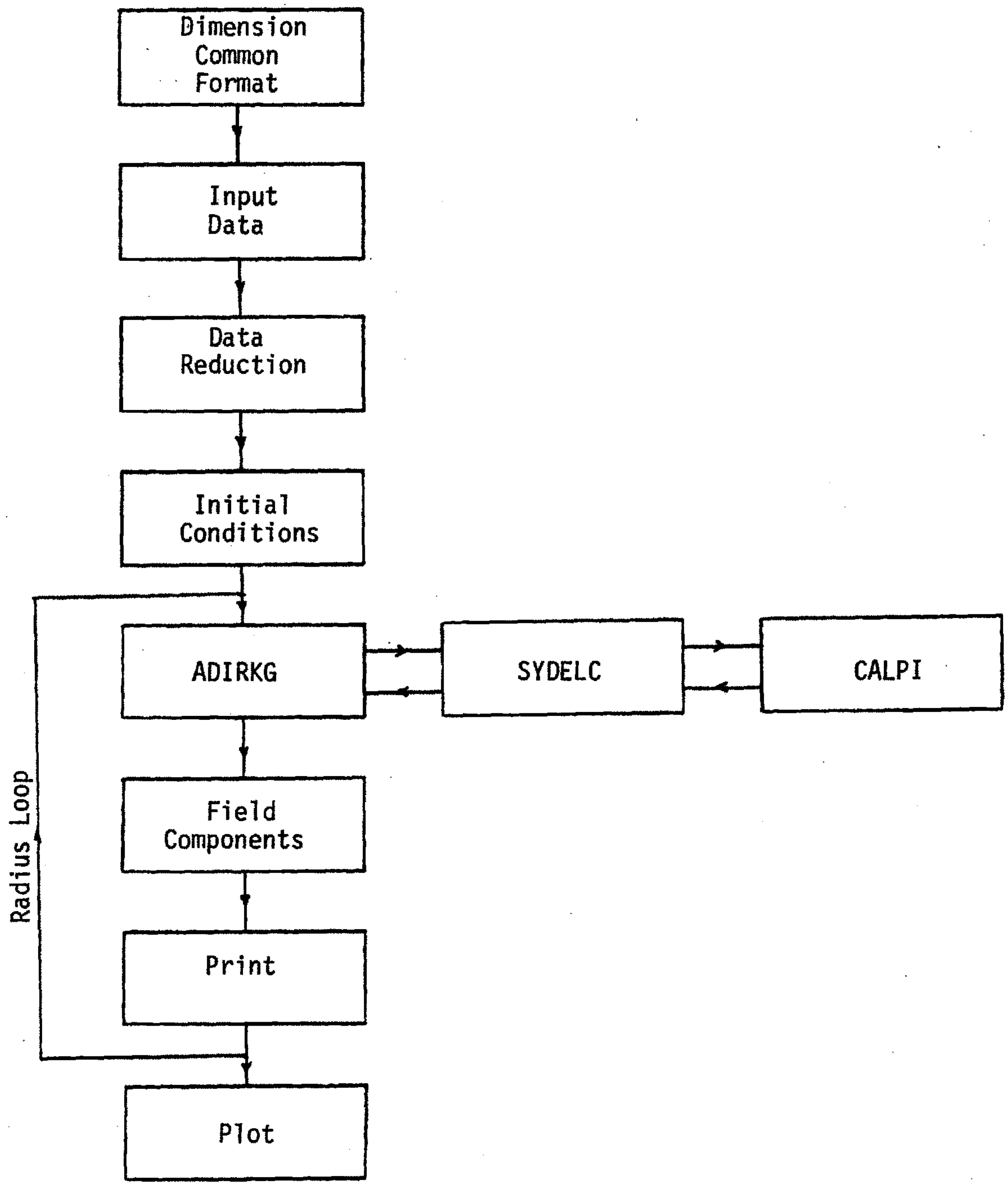

Figure 1

Similarly, power deposition per cubic centimeter and per unit length for ELD and second harmonic are calculated from IV-4.3. (13) and IV-4.2.(37) with a Gaussian temperature profile defined by IV-2.3.(2). Finally, the single pass radiation resistance can be found from (6), E_θ (r = antenna) and equation IV-1.2 (5).

Figure 1 is a simplified operational block diagram of TFR-EZ. Data can either be written directly in the beginning of the main program or through more convenient files. The initial data is then normalized and reduced to more compact forms,and proper initial conditions are set for E_θ and E'_θ as a function of m. ADIRKG is a general fourth order subroutine that sets up (6) and (7). SYDELC is a specific subroutine that calculates (7) from the initial reduced data. CALPI calculates $n(r)$ and $\partial n(r)/\partial r$ from (2). The field components can then be calculated and printed as the main loop increases r to a maximum radius,where all the field components can be plotted as a function of minor radius.

Block Diagram of TFR-EZ

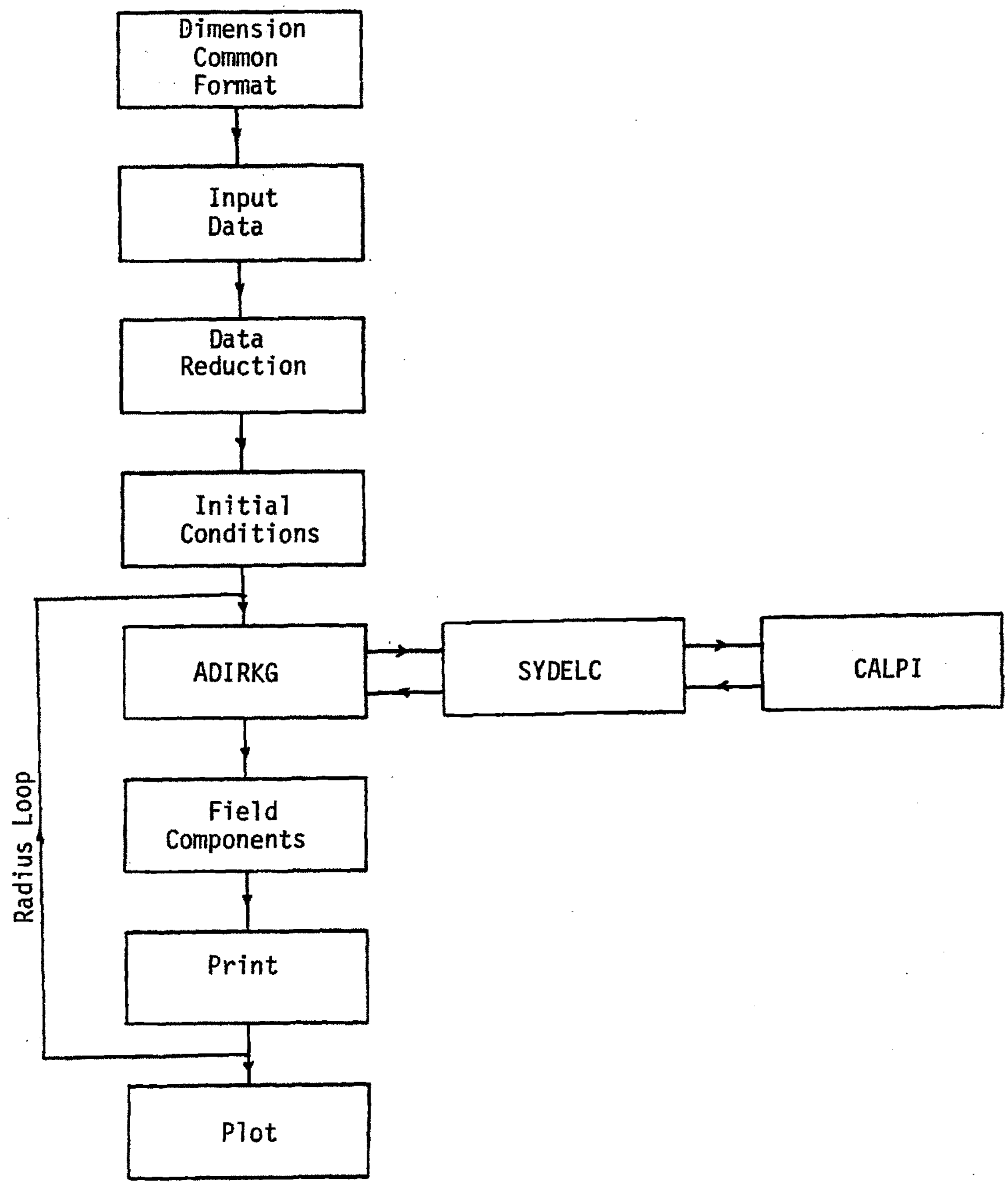

Figure 1

IV-5.3. Field profiles at high density

In this Section, we will discuss the Alcator ICRF field profiles for a hot ($T_e = T_i = 1keV$) high density ($\hat{n}_e = 5 \times 10^{14}/cm^3$) hydrogen plasma in the second harmonic regime ($f_\circ = 200$ MHz).

Figures 1-4 show E_Θ vs r for m = 0 and radial mode numbers $\mu = 1$-4. Note how Figure 3 is in excellent agreement with our simple Cartesian model of Figure IV-2.3.(6) (except for the Bessel function effect discussed in Section IV-3.2.). Note also the extreme importance of the evanescent layer for the smaller μ ($R_R \approx 10^{-3}\Omega$). The evanescent layer is, on the other hand, almost negligible for TFR, as can be seen from Figures 5 and 6, since $k_\parallel$ is of order .05/cm instead of .5/cm for Alcator.

Figures 7, 8, and 9 are the complete set of electric and magnetic fields and power absorption profiles, E_Θ, E_r, E_z, B_Θ, B_r, B_z, $S_{\pm z}$, E_+^2, $E_+'^2$, P_{eld}/cm^3, $P_{2\omega_{ci}}/cm^3$ $P_{2\omega_{ci}}/cm$, as well as the radiation resistance calculated from E_Θ (11.5 cm), for $\mu = 3$, m = 0, -1, +1. Many particularities need to be noted as follows.

The simplest mode to visualize is the asymmetric (E_Θ, about $\pm$ r) m = 0 mode shown in Figure 7. m = $\pm$ 1 are symmetric as shown in Figures 8 and 9. We must be careful with the definition of μ, since only B_z (in homogeneous plasma) is a pure Bessel function (E_Θ is the sum of two Bessel functions, IV-3.1.(19)), so that the number of zero crossings is different for E_Θ and B_z. We will use E_Θ in defining μ because of the wall boundary condition. Since the m = + 1 has the lowest density cutoff, it has the largest $k_\parallel$ for a given μ, and thus has the largest evanescent layer and smallest radiation resistance ($R_{+1} < R_0 < R_{-1}$).

In the plasma center, the magnitudes of E_r and E_Θ are comparable for all modes, and about three orders of magnitude larger than E_z (also $B_\Theta \approx B_r \approx B_z$). The phase between E_r and E_Θ, on the other hand, is very different for the different poloidal mode numbers, so that the $m < 0$ are essentially left-handed ($E_\Theta \approx -iE_r$), $m > 0$ are right-handed ($E_\Theta \approx iE_r$), and $m = 0$ is about half and half.[21] Second harmonic damping is dependent on the gradient of the left-hand component, so that the $m < 0$ will have shorter parallel damping length ($\approx$ 5 meters) than the $m > 0$ modes ($\approx$ 60 meters), as shown in Figure 10.

$$(1) \quad \frac{1}{k_i} = \frac{2P_f}{P_{2\omega_{ci}}/cm} = \frac{PHI}{P2WPL}$$

The effect of k_z on the damping length can be removed by dividing the Poynting flux (PHI α $E^2 k_z$) by k_z, also shown in Figure 10.

From Figures 7, 8, and 9, it is clear that it is not possible to discern the $m > 0$ from the $m < 0$ modes by the relative phases between field components in the evanescent plasma edge (from either E or B). Most of the wave fields are well confined to the plasma center, so that most of the Poynting flux is from $r_{PHI} < 8$ cm (Figures 7-9 and 11-14). The ELD and $2\omega_{ci}$ power deposition profiles are even more peaked, due to the narrow Gaussian temperature profile, so that $r_{ELD} < 3$ cm and $r_{2\omega_{ci}} < 4$ cm.

Figures 15 to 18 show the single parallel pass radiation resistance ($R_\circ$, IV-1.3.(5)), the toroidal resonance ($F_R R_\circ$, IV-6.2.(5)) and anti-resonance ($F_A R_\circ$, IV-6.2.(6)), corrected radiation resistance, $k_\parallel$, $\lambda_{2\omega C}$ and λ_{ELD} as a function of density for the $m = 0$, $\mu = 3$ and 4 eigenmodes (the singularities at cutoff are, of course, unphysical, and are removed by letting $k_{\perp i} \neq 0$ (Section IV-2.1.) .

m = 0, E_θ profiles in Alcator and TFR

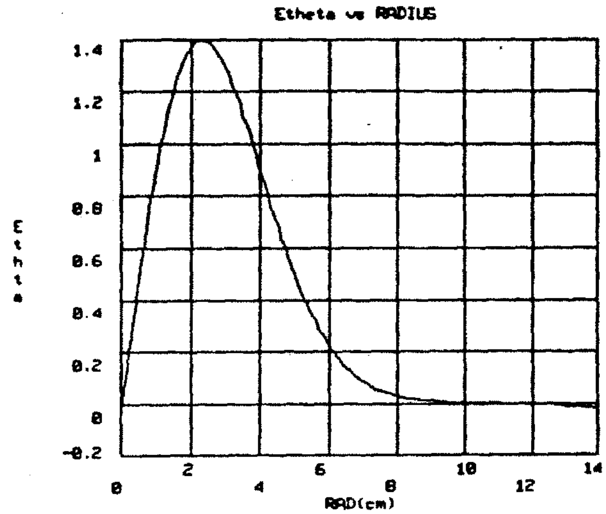

$\mu = 1$ Figure 1

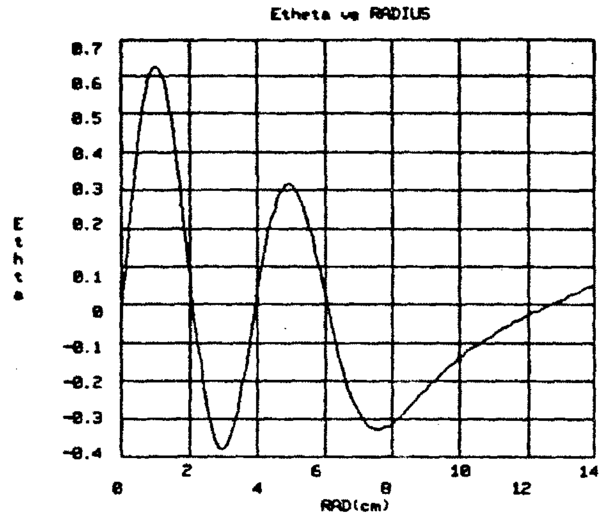

$\mu = 4$ Figure 4

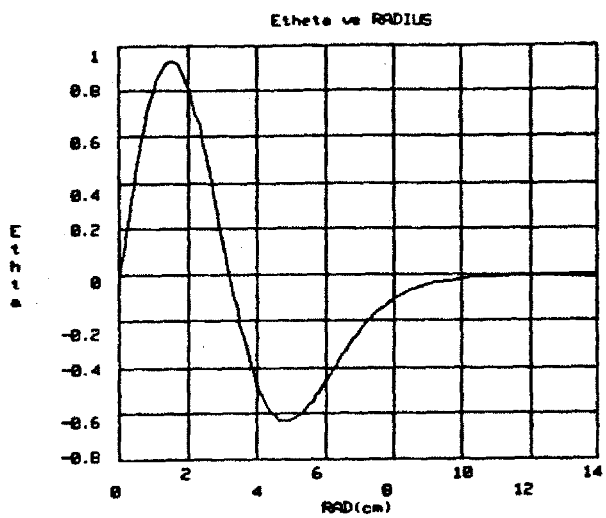

$\mu = 2$ Figure 2

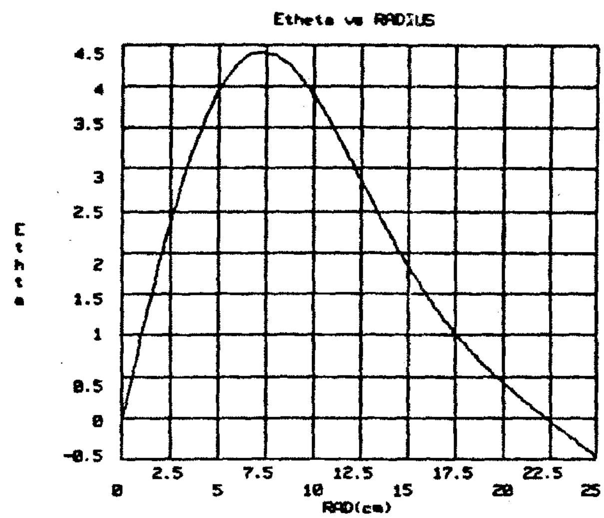

TFR $\mu = 1$ Figure 5

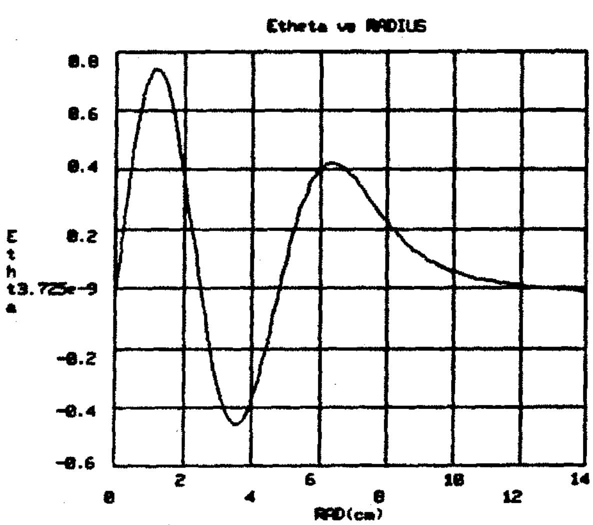

$\mu = 3$ Figure 3

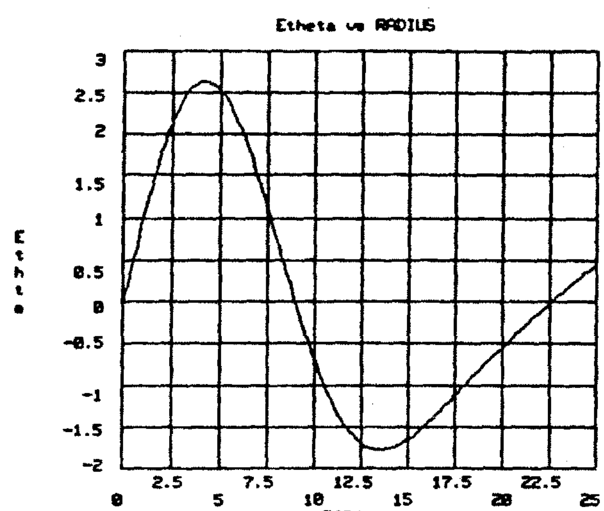

TFR $\mu = 2$ Figure 6

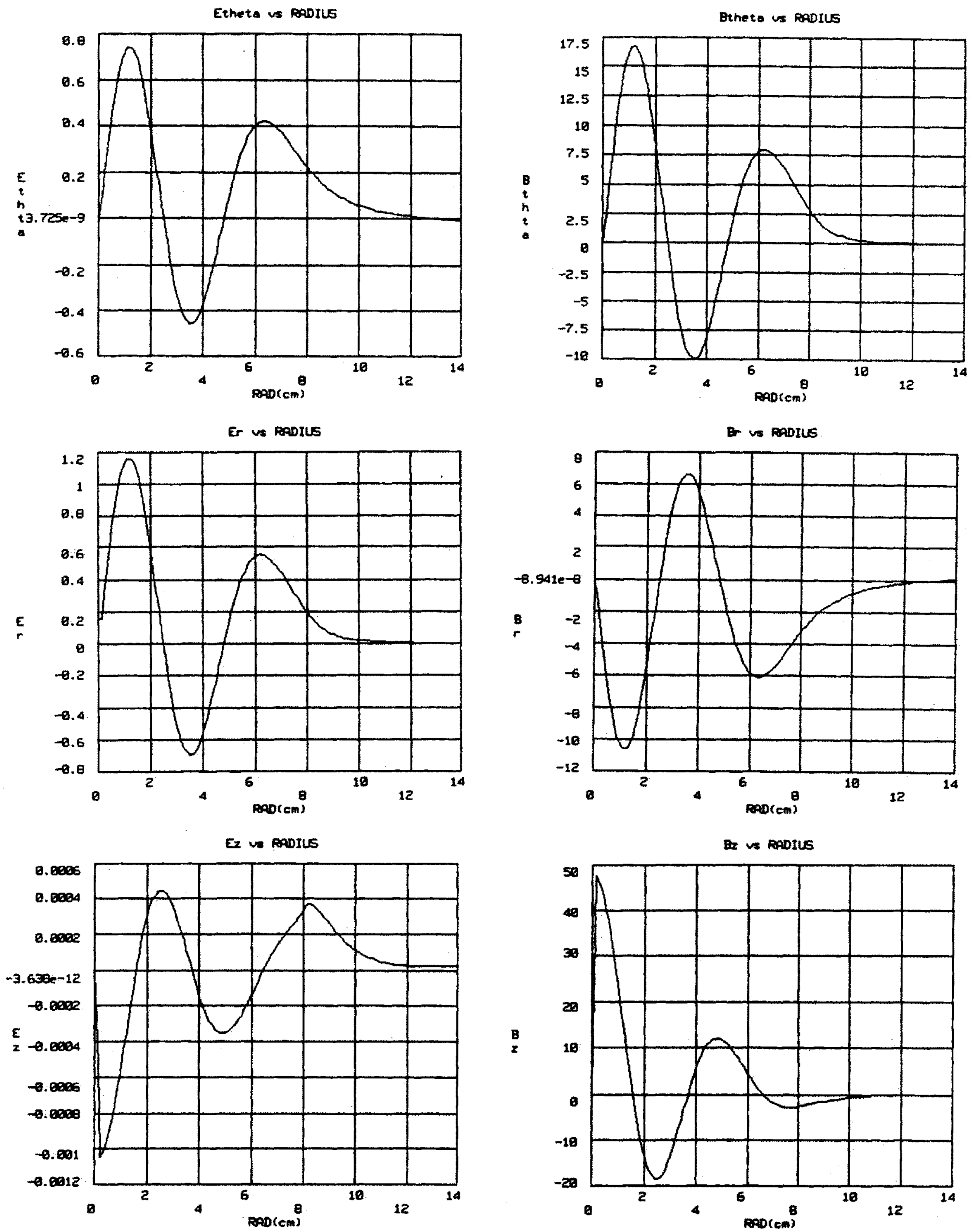

m = 0, μ = 3 field profiles
at high density

Figure 7

omega a= 2.0	omega b= 2.0	na=.50000E+15	nb=.00000E+00
ma=1.00	mb=1.00	Ti=1000.0	Te=1000.0
Kpar=.60291	m= 0.0	rmax=14.00	pp= 9.00
lant=20.00	f0=.20000E+09	rmaj=54.00	q0= 0.90
ql= 5.00	rant=11.00	pas=0.100	

Rr=.63408E-01 eldd l=.17296E+05 p2wdl=.22304E+04

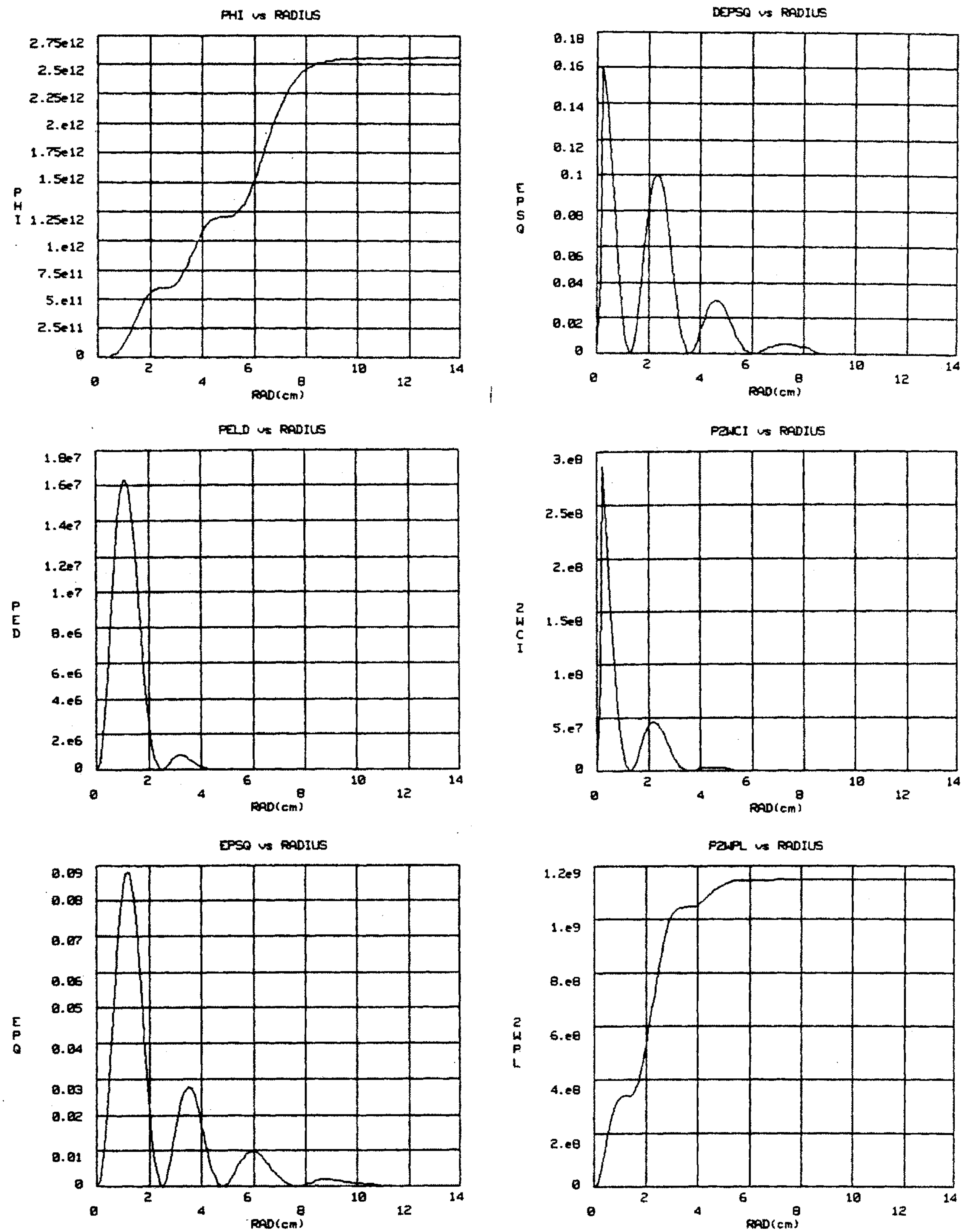

Figure 7 continued

omega a= 2.0	omega b= 2.0	na=.50000E+15	nb=.00000E+00
ma=1.00	mb=1.00	Ti=1000.0	Te=1000.0
Kpar=.60291	m= 0.0	rmax=14.00	pp= 9.00
lant=20.00	f0=.20000E+09	rmaj=54.00	q0= 0.90
ql= 5.00	rant=11.00	pas=0.100	

Rr=.63408E-01 eldd1=.17296E+05 p2wd1=.22304E+04

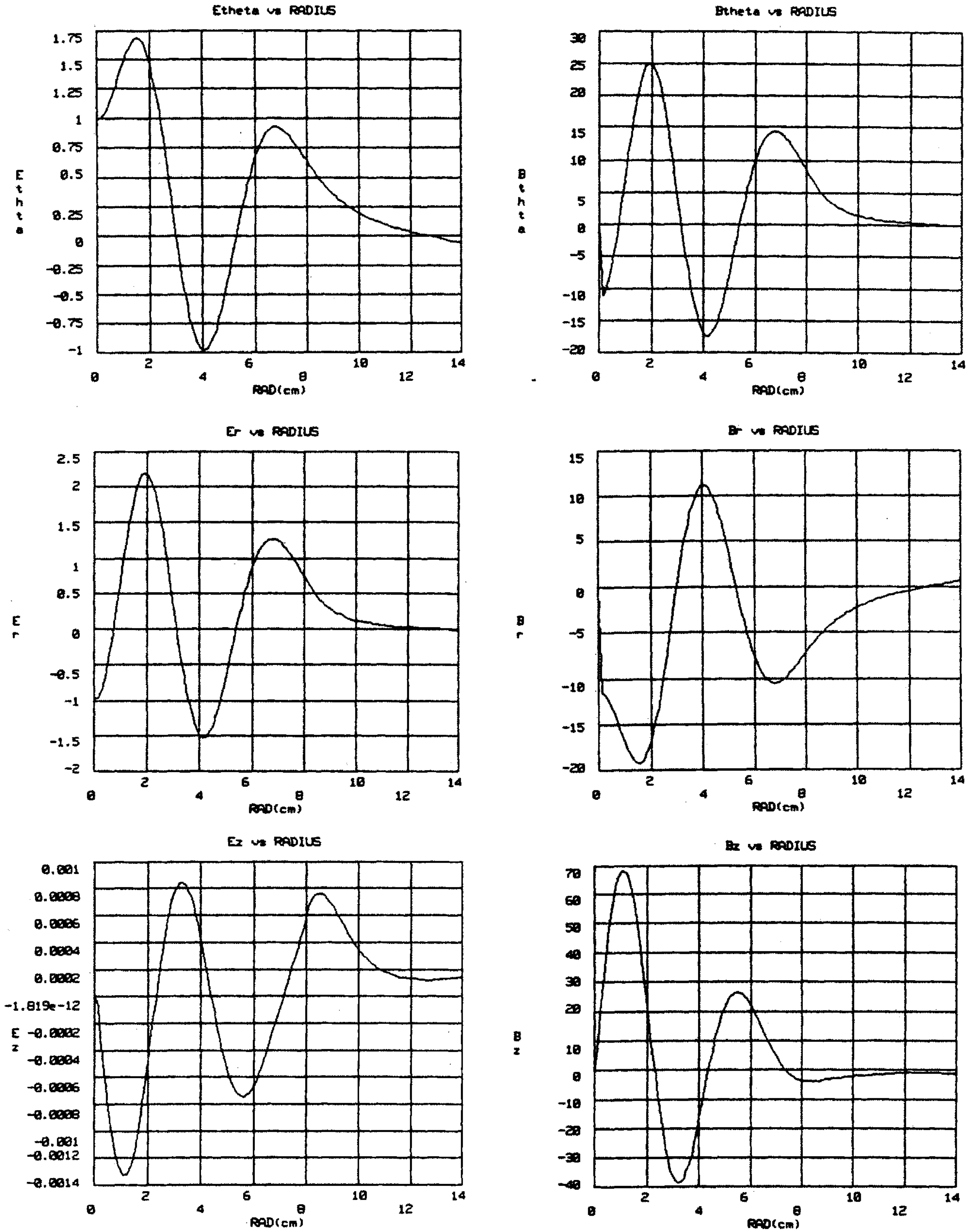

m = -1, μ = 3 field profiles
at high density

omega a= 2.0	omega b= 2.0	na=.50000E+15	nb=.00000E+00
ma=1.00	mb=1.00	Ti=1000.0	Te=1000.0
Kpar=.47800	m=-1.0	rmax=14.00	pp= 9.00
lant=20.00	f0=.20000E+09	rmaj=54.00	q0= 0.90
ql= 5.00	rant=11.00	pas=0.100	

Rr=.17400E+00 eldd1=.40135E+05 p2wd1=.65710E+03*

Figure 8

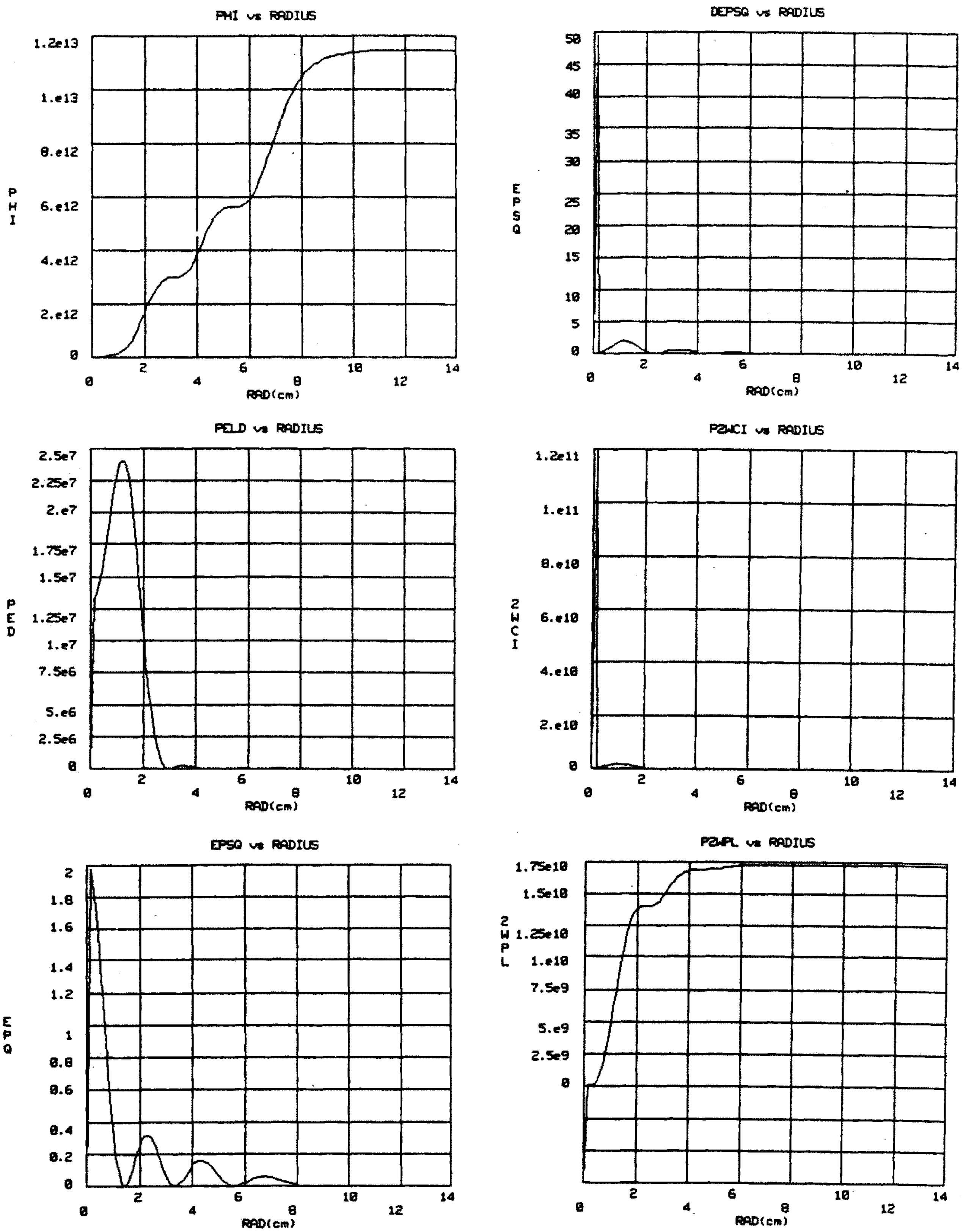

Figure 8 continued

omega a= 2.0	omega b= 2.0	na=.50000E+15	nb=.00000E+00
ma=1.00	mb=1.00	Ti=1000.0	Te=1000.0
Kpar=.47000	m=-1.0	rmax=14.00	pp= 9.00
lant=20.00	f0=.20000E+09	rmaj=54.00	q0= 0.90
ql= 5.00	rant=11.00	pas=0.100	

Rr=.17400E+00 eldd1=.40135E+05 p2wdl=.65710E+03 *

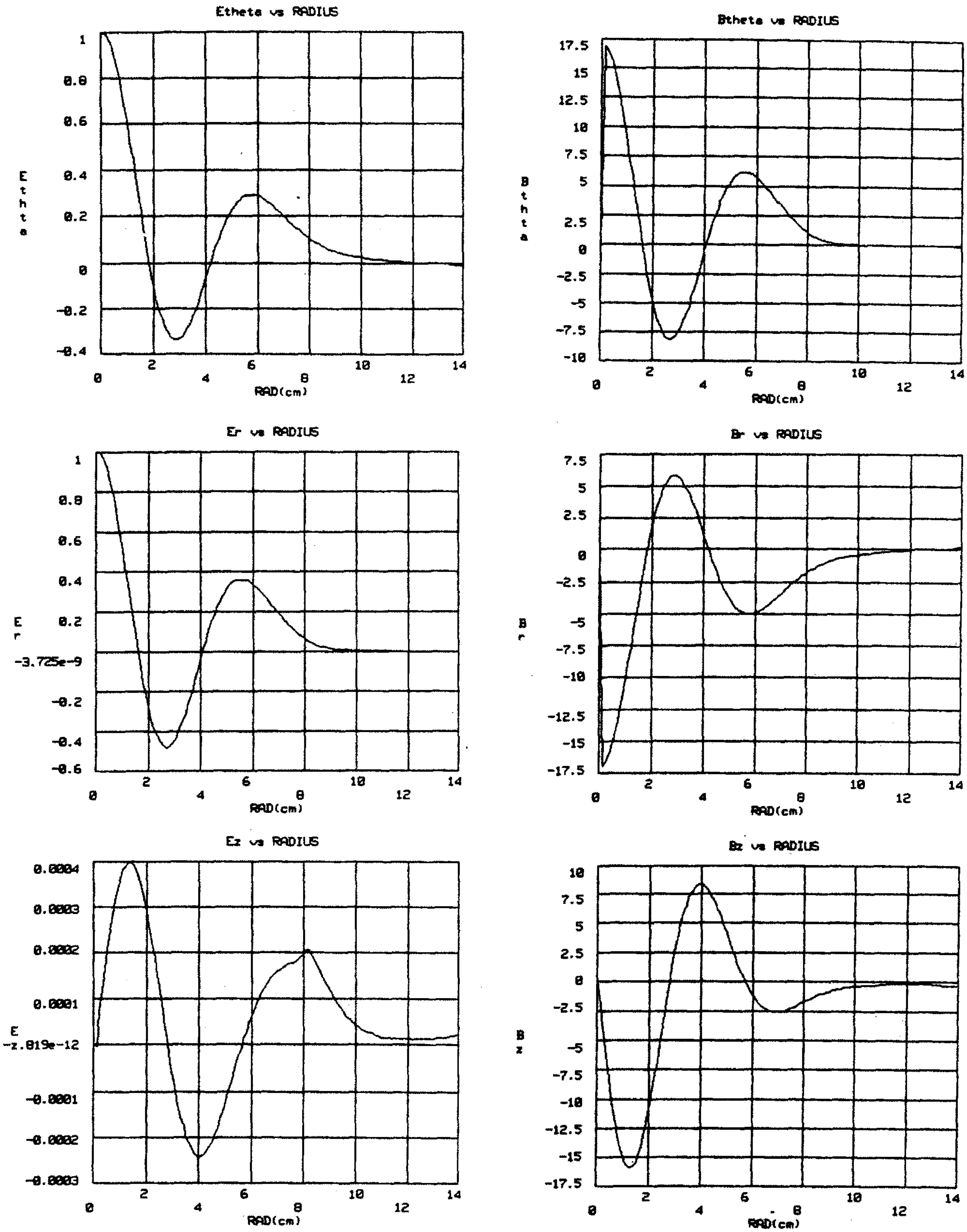

m = +1, μ = 3 field profiles
at high density

Figure 9

omega a= 2.0	omega b= 2.0	na=.50000E+15	nb=.00000E+00
ma=1.00	mb=1.00	Ti=1000.0	Te=1000.0
Kpar=.71288	m= 1.0	rmax=14.00	pp= 9.00
lant=20.00	f0=.20000E+09	rmaj=54.00	q0= 0.90
ql= 5.00	rant=11.00	pas=0.100	

Rr=.11944E-01 eldd1=.73785E+04 p2udl=.95003E+04

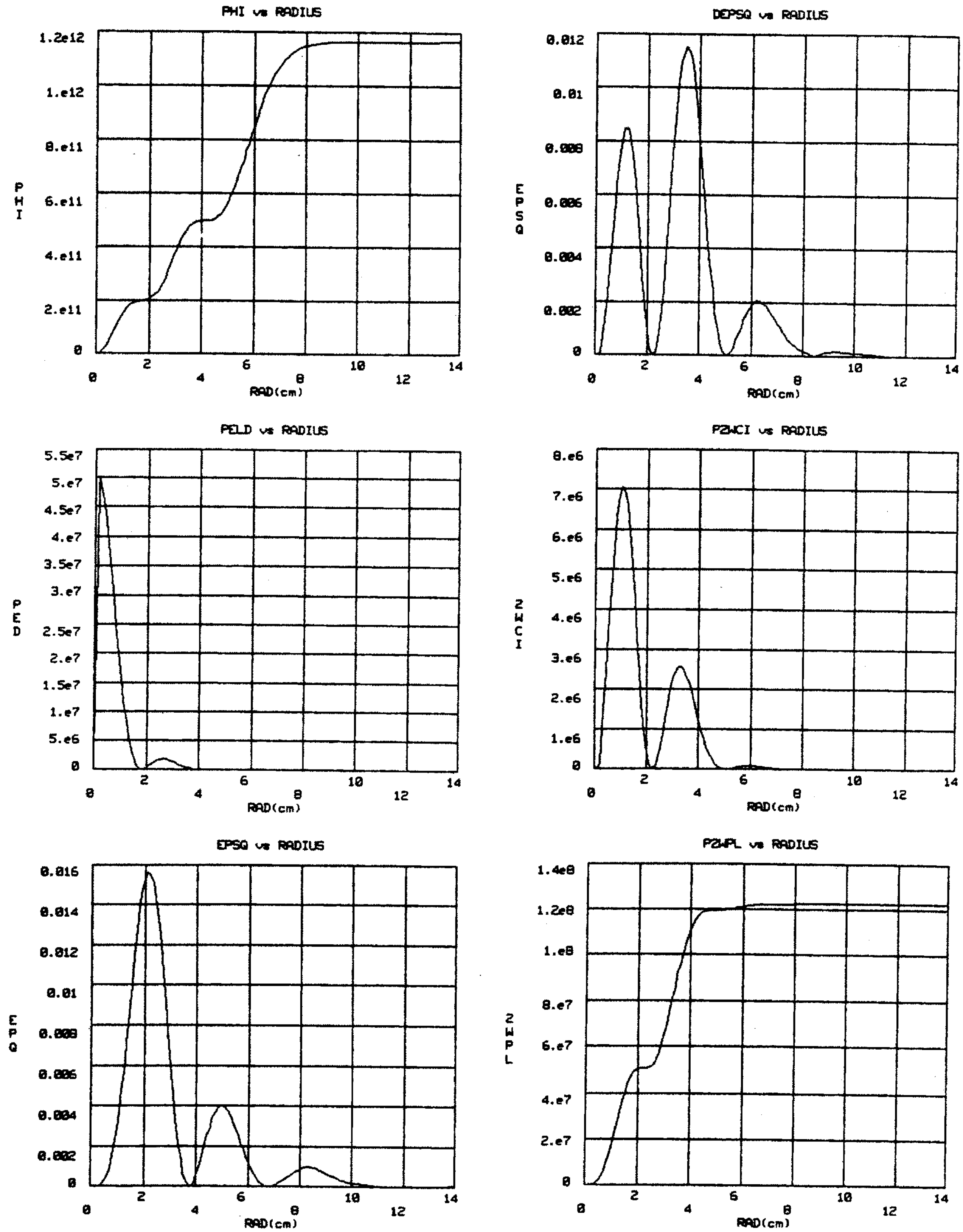

Figure 9 continued

omega a= 2.0	omega b= 2.0	na=.50000E+15	nb=.00000E+00
ma=1.00	mb=1.00	Ti=1000.0	Te=1000.0
Kpar=.71200	m= 1.0	rmax=14.00	pp= 9.00
lant=20.00	f0=.20000E+09	rmaj=54.00	q0= 0.90
ql= 5.00	rant=11.00	pas=0.100	

Rr=.11944E-01 elddl=.73785E+04 p2wdl=.95003E+04

Damping Length for $\mu = 3$, $-3 \leqslant m \leqslant +3$ at High Density

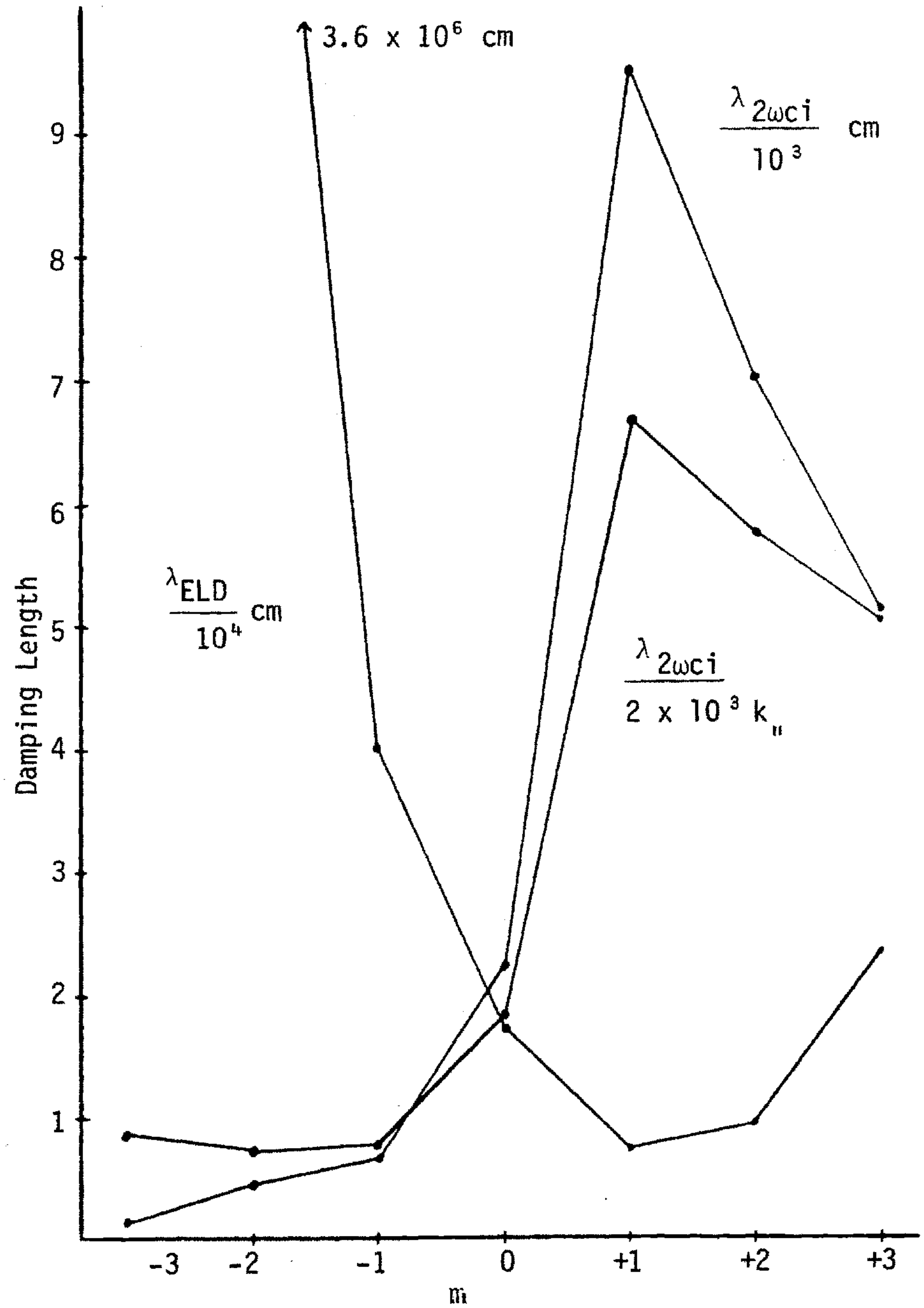

Figure 10

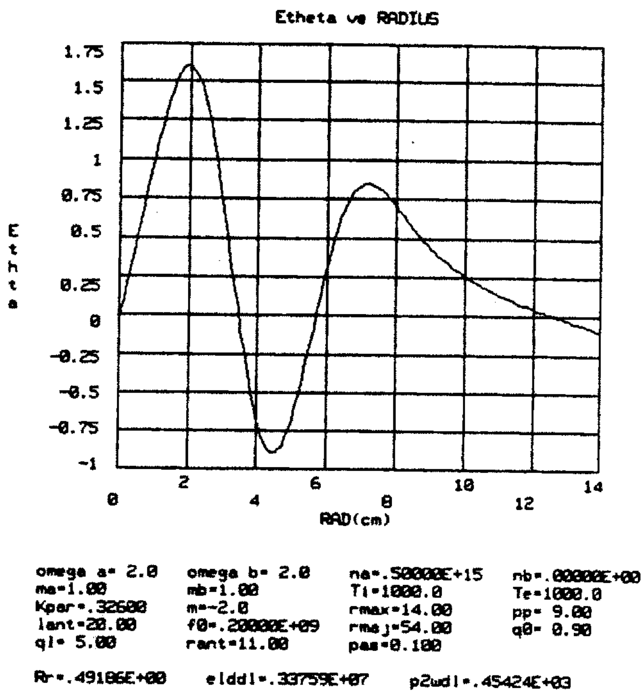

m = -2, μ = 3 at high density

Figure 11

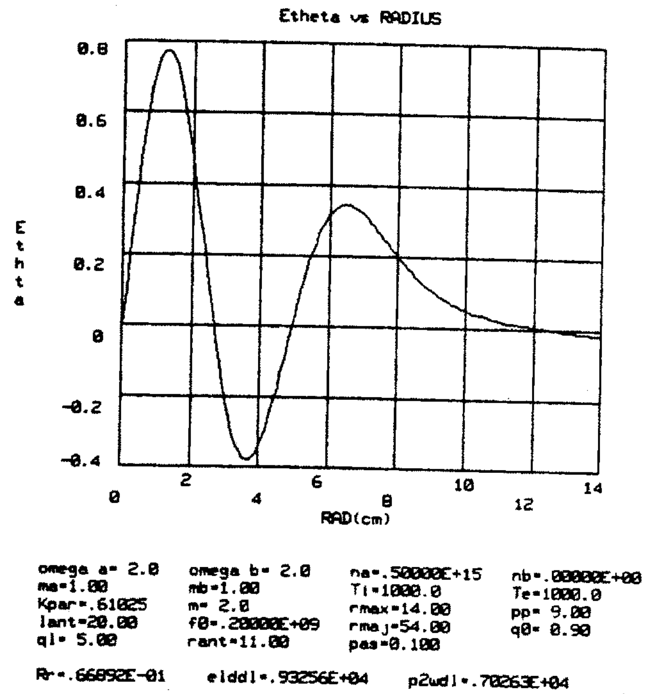

m = +2, μ = 3 at high density

Figure 12

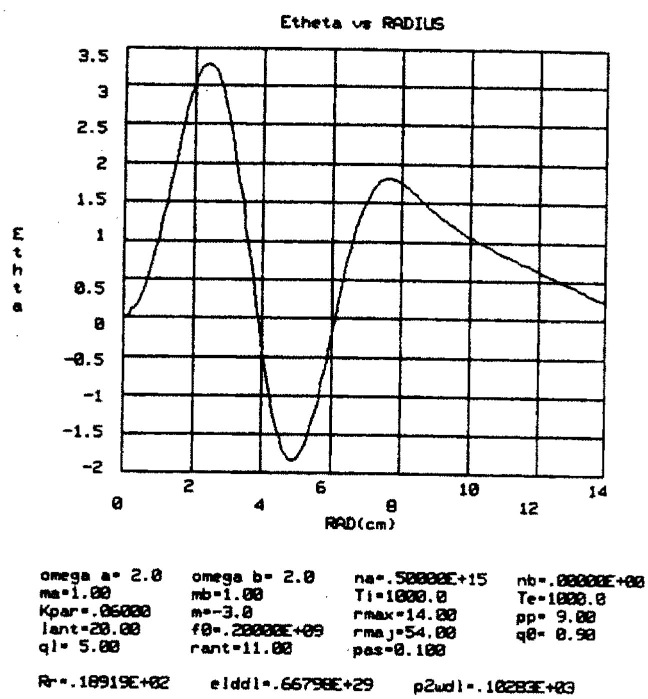

m = -3, μ = 3 at high density

Figure 13

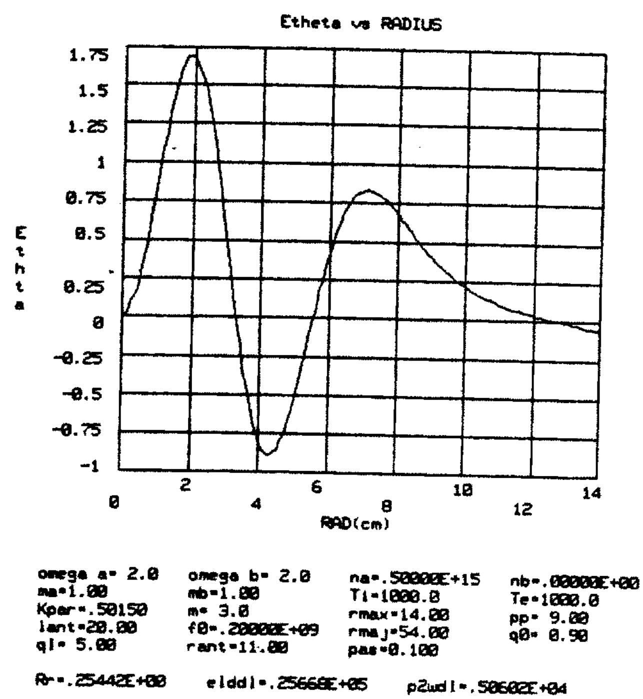

m = +3, μ = 3 at high density

Figure 14

Radiation Resistance and Damping Lengths for μ = 3 and m = 0
as a Function of Density

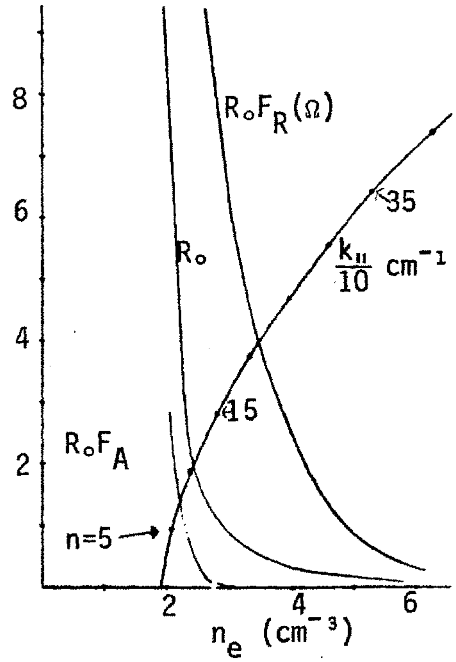

Figure 15

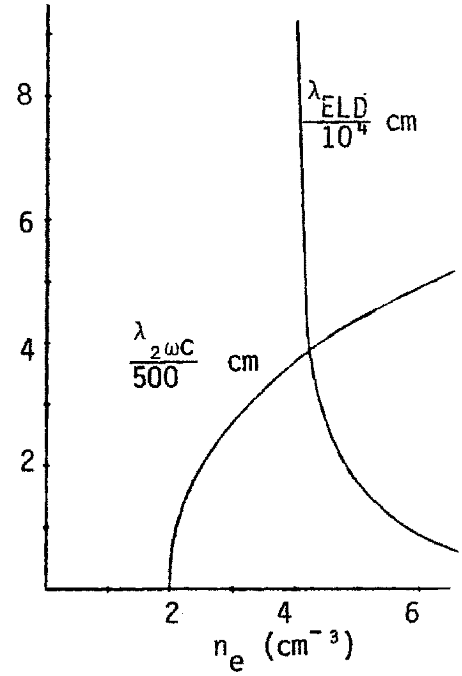

Figure 16

Radiation Resistance and Damping Lengths for μ = 4 and m = 0
as a Function of Density

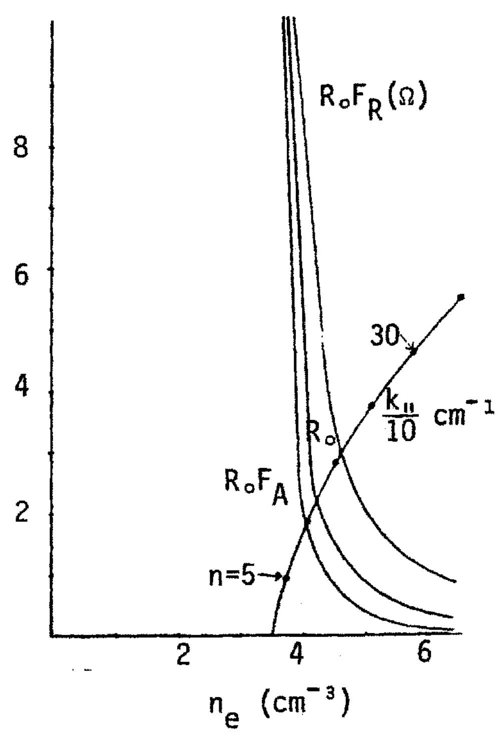

Figure 17

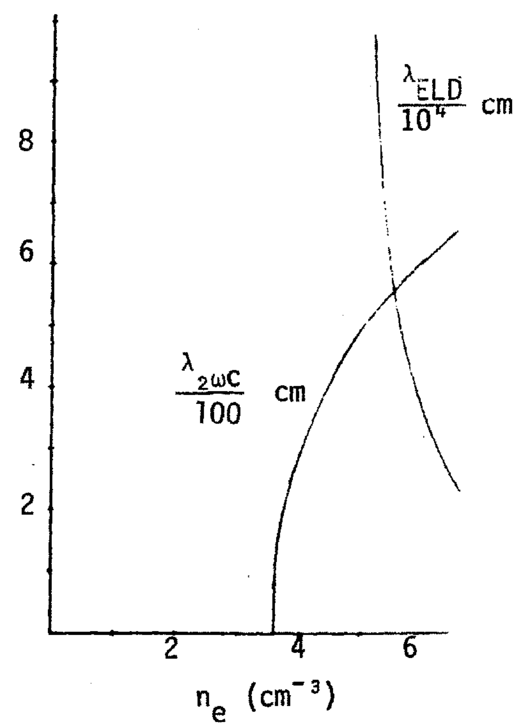

Figure 18

IV-5.4. Full inhomogeneous eigenmode dispersion relations

As we might expect, the full inhomogeneous eigenmode dispersion relation cannot be put in some simple form such as equation IV-3.1.(14). Numerically, however, TFR-EZ can be put in a loop that successively increases k_z and n_e, following the $E_\Theta(w) = 0$ boundary solution, and thus tracing the dispersion relation (Figure 1). Although simple in principle, this is a very large computation, and step sizes of the many nested loops must be judiciously chosen to ensure reasonable computation times, even on large computer systems such as Multics. The program is started with the usual boundary conditions (E_Θ, E'_Θ), but with a very small n_e and k_z. After each TFR-EZ integration from the plasma center to the wall, the wall E_Θ is multiplied with its previous value. If the product is positive, no solution was crossed, and we increase n and rerun TFR-EZ. At some value of n, an onset (cutoff) will occur, and the product will be negative. We then increase k_z until the product is again positive, and so on. To finder higher radial mode numbers, the program is simply started after a lower radial mode cutoff, but still with $k_z = 0$.

Figures 3-9 are the dispersion relation of the 0, $\pm$ 1, $\pm$ 2, $\pm$ 3 eigenmodes for 200 MHz, 67 kG, pure hydrogen and peak densities up to $6 \times 10^{14}/cm^3$. As we saw in our cruder model (IV-3.1.), the $m = +1$ is the fundamental mode, and can have a radial mode number as high as 5 at high density. k_z can also be as large as 1.2/cm, which corresponds to a toroidal mode number $n = 65$. Some 27 eigenmodes (Figure 10) are possible, which is in good agreement with Section IV-3.2. if we take into account that we did not include the poloidal modes with $|m| > 3$.

For the $m > 0$ modes, we note an apparent lack of cutoff due to the tenuous edge plasma layer. Figures 11-13 show the details of the low density end of the dispersion relations. The fundamental and higher toroidal resonances occur at

(1) $k_{\parallel} = \frac{1}{R}, \quad \frac{2}{R}, \quad \ldots$

$= .018, .037, .055, .074 \ldots /cm$

and further determine $k_{\parallel}$, so that densities of the order of $4 \times 10^{12}/cm^3$ are still necessary for the appearance of the lowest toroidal resonances.

(2) $\mu = 1, \quad m = \pm 1, \quad n = 3$

Note that this corresponds to edge and even central densities at or below the lower hybrid resonance, and these simulations are probably not meaningful.

Figure 14 shows the $m = 0$, $\mu = 1$ mode dispersion relation for pure hydrogen and deuterium plasmas, as well as a 50% H_2/50% D_2 plasma, in the $2\omega_{cH}$ regime.

Block diagram of inhomogeneous plasma eigenmode dispersion relation code

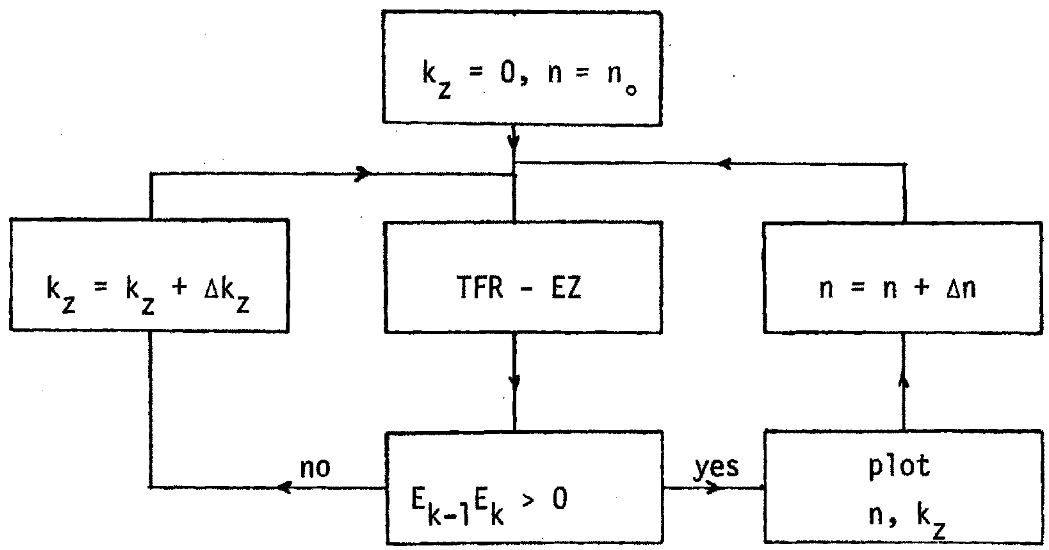

Figure 1

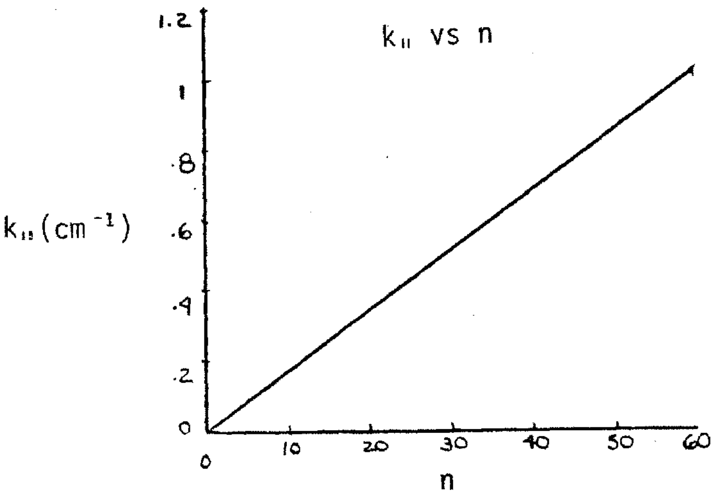

Figure 2

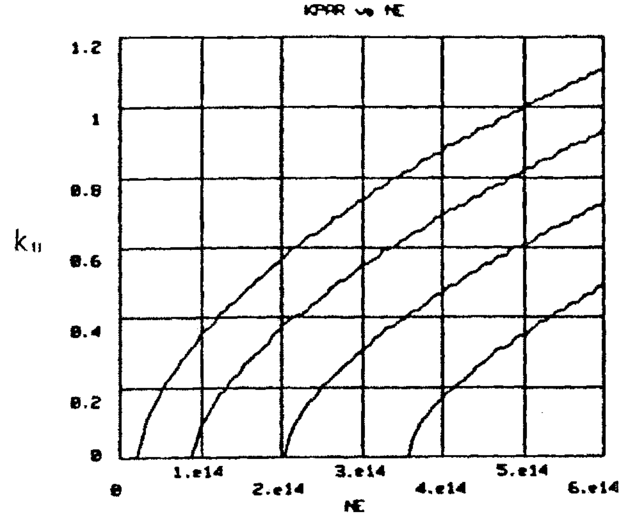

m= 0.000 pas= 0.500 nstep= 100

Figure 3

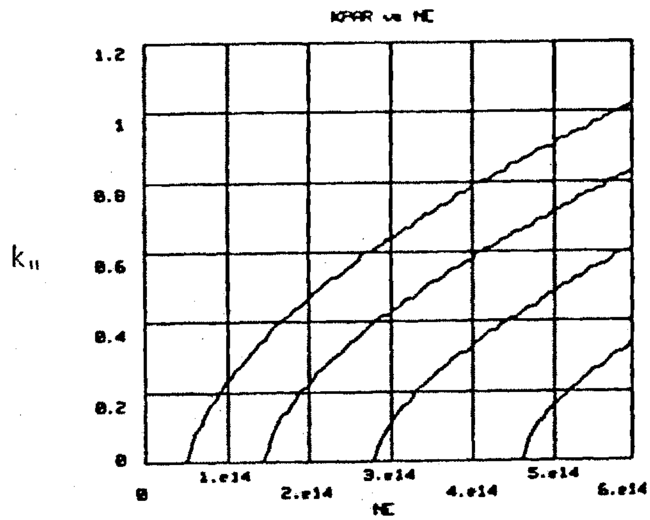

m=-1.000 pas= 0.500 nstep= 100

Figure 4

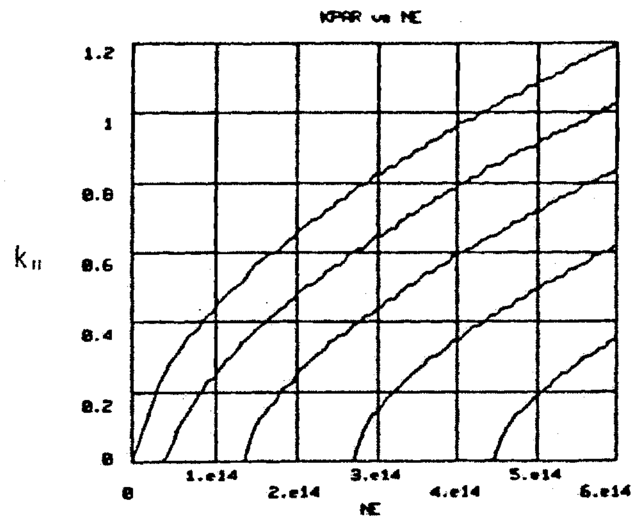

m= 1.000 pas= 0.500 nstep= 100

Figure 5

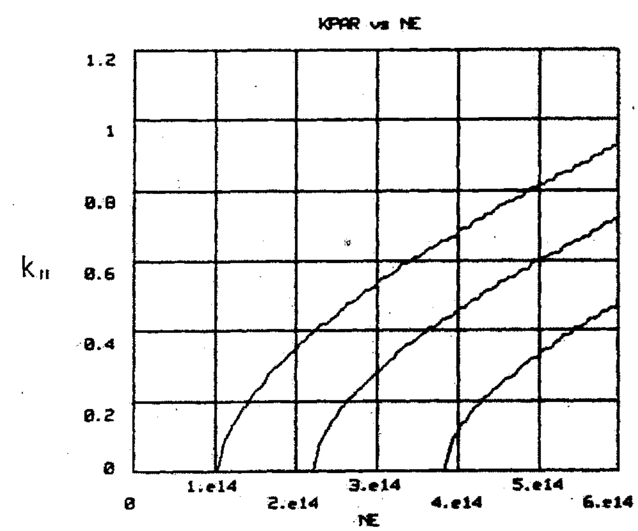

m=-2.000 pas= 0.500 nstep= 100

Figure 6

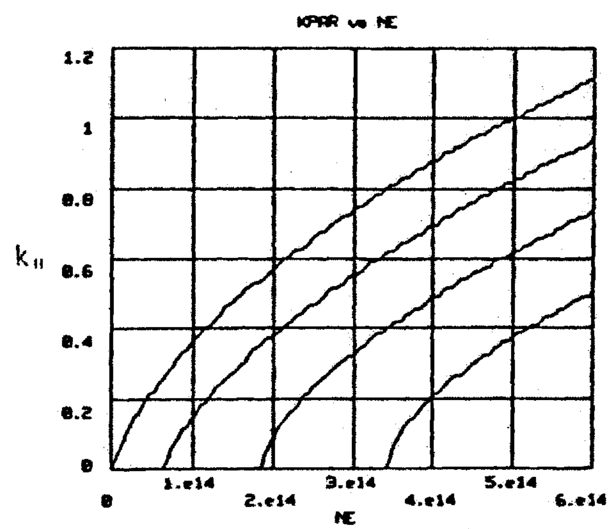

m= 2.000 pas= 0.500 nstep= 100

Figure 7

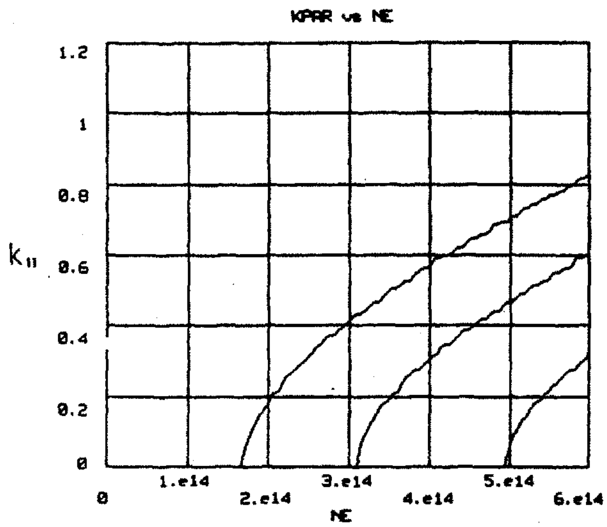

m=-3.000 pas= 0.500 nstep= 100

Figure 8

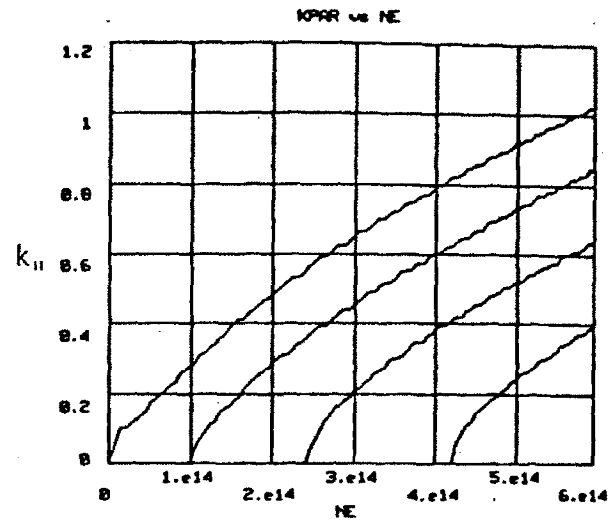

m= 3.000 pas= 0.500 nstep= 100

Figure 9

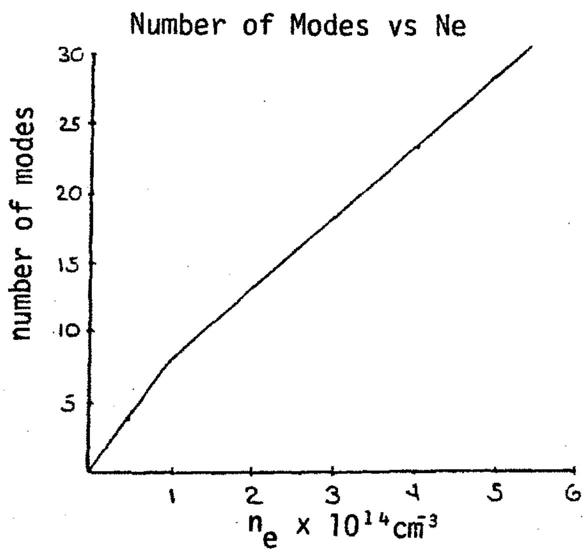

Figure 10

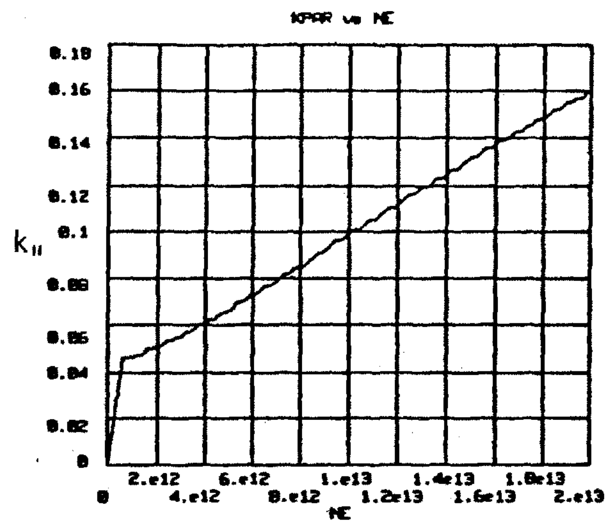

m= 1.000 pas= 0.500 nstep= 100

Figure 11

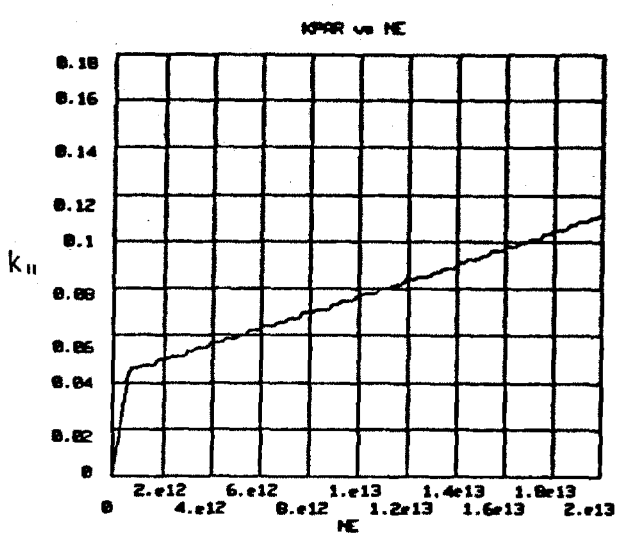

m= 2.000 pas= 0.500 nstep= 100

Figure 12

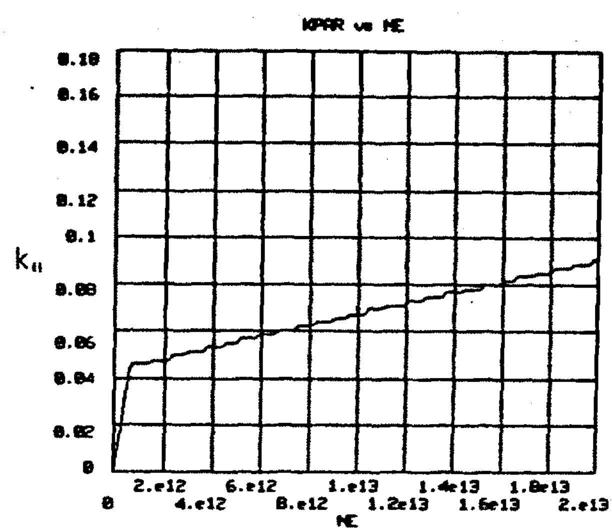

m= 3.000 pas= 0.500 nstep= 100

Figure 13

$m = 0$, $\mu = 1$ Dispersion Relations for Pure H_2, Pure D_2, and 50% H_2 / 50% D_2 Plasmas

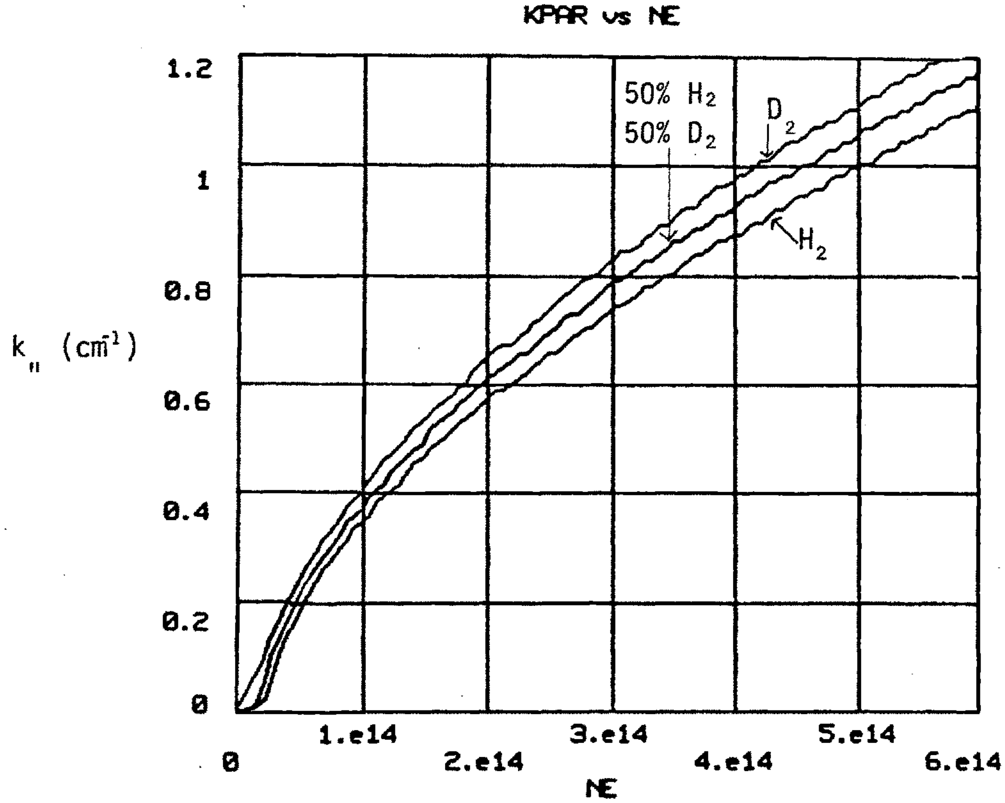

omega a=2.00 omega b=4.00 nb/na=1.000
ma=1.00 mb=2.00 pm=0.00
f0=.20000E+09 rmax=14.00 pp= 9.00 rw=12.50

Figure 14

IV-6. Stochastic Mode Stacking

IV-6.1. Introduction

The last theoretical aspect of eigenmode coupling, and one believed to be of importance at high density, is stochastic mode stacking in a multi-moded plasma cavity.[24] This somewhat new theory and original work, at least in the fusion field, is now discussed at length.[23-25,7,93]

In the Alcator program, our goal is to heat at high density, where a multitude of modes can propagate, many of which are coupled by the antenna, and several of which can be simultaneously resonant, due to their finite bandwidth in k space. This is fundamentally different from the regime of most previous experiments which were at low density, where only one mode at a time was important. Either a particular mode was actually tracked, or heating was efficient only for the short duration of the mode resonance.[52] Very large damping mechanisms can also be used to stop the toroidal resonances and stabilize the radiation resistance, but at a significant loss in antenna loading, a major engineering drawback.[30]

The first issue is the overlap of the skirts of the finite bandwidth modes. The coherent stacking of the many eigenmodes at the antenna will result in the radiation resistance increasing linearly with the number of modes present, whereas statistical interference away from the antenna will result in a less than linear increase in wave field and RF surface probe signal. This complicated multi-k wave structure can be analyzed in analogy to noise theory[63] with many random frequencies and phases.[64] The key issues reside in the judicious choice of distribution functions of the statistical parameters. All previous theories of propagation, coupling, and damping of the various field components are used in making this choice for various simulations.

The second major issue, which is closely related to the previous one, is the reactive component of the field structure and its effect on antenna loading and observed probe signal. The reactive wave components of the off resonance modes do not draw power from the antenna,and so do not contribute to radiation resistance, but are of utmost importance in the probe signal since, usually, only the magnitude is observed. If sophisticated phase detection is employed, the reactive skirts of the modes will be of importance in understanding the detailed phase structure of the measurements. This way, apparent magnetic probe signal phase jumps over a short time scale, as well as bulk continuous phase increase with density, are explained by the average phase increase of the finite Q toroidal modes. Appropriate analytical results from simplified models are backed up by detailed computational simulations.

The effect of internal plasma density perturbations[65] on effective Q is also discussed. The injection of a narrow spectrum of wave frequencies could also simulate lower Q,and increase the importance of the stochastic stacking.

It is also shown that,on the average,the total radiation resistance is independent of damping, is roughly proportional to the antenna length,and is independent of antenna phasing.

Finally, the above theory is used to tentatively explain three new experimental findings that cannot be explained satisfactorily without stochastic mode stacking. The first and most important is the somewhat linear increase of loading resistance with density.[13] The second is the saturation of the probe signal with electron density,[41,42] and the last is the noisy but monotonic phase increase between RF probes distributed around the torus. The first two findings could be explained somewhat by some near-field loading, but the fact that the probe phase is continuous is most likely of the realm of mode stacking.

A further, important, theoretically explained experimental finding is that the measurement of the bulk parallel and perpendicular phase (hence wave number) suggests a small propagation angle (referred to the toroidal field), which would make second harmonic damping small. A corollary to this effect is that these low $k_\perp$ modes will have large Q and enhanced resonant fields.

IV-6.2. Coherent and stochastic stacking

For a given perpendicular eigenmode field structure, two independent waves propagate away from the antenna along +z and -z around the torus, and add to the original electric field. Assuming (Figure 1)

(1) $k_{\pm} = k_{z\pm} + i\, k_{zi}$

(2) $l = 2\pi R$

we have the normalized electric field (z = 0 at antenna)[7,22]

(2)
$$
\begin{aligned}
F = \frac{E_T}{E_o} = \; & e^{ik_+ z} && + e^{ik_-(l-z)} \\
& + e^{ik_+(l+z)} && + e^{ik_-(2l-z)} \\
& \quad \cdot && \quad \cdot \\
& \quad \cdot && \quad \cdot \\
& + e^{ik_+(nl+z)} && + e^{ik_-(nl-z)} \\
= \; & \frac{e^{ik_+ z}}{1 - e^{ik_+ l}} && + \frac{e^{ik_-(l-z)}}{1 - e^{ik_- l}} \\
= \; & F_+ && + F_-
\end{aligned}
$$

where we used the binomial expansion

(3) $$\frac{1}{1 - x} = 1 + x + x^2 \ldots . x^n$$

Without mode splitting, $k_{z+} = k_{z-}$, and[56]

(4) $$F = \frac{e^{ikz} + e^{ik(l-z)}}{1 - e^{ikl}} = i\,\frac{\cos\,[(z - \pi R)\,k]}{\sin\,[\pi R k]} = i \text{ cotan } [\pi R k] \text{ for } z = 0$$

At a toroidal resonance, $k_z = n/R$, and $z = 0$

(5) $$F_R = \frac{1 + e^{-k_i\, 2\pi R}}{1 - e^{-k_i\, 2\pi R}} \cong \frac{1}{k_i\, \pi R} \quad \text{for } k_i 2\pi R \ll 1$$

$$\simeq \frac{2P_f}{P_{dis}\pi R} \quad \alpha \quad \frac{k_{\parallel}}{\sigma}$$

At antiresonance, $k_z = \frac{n + 1/2}{R}$ and

(6) $$F_A = \frac{1 - e^{-ik_i 2\pi R}}{1 + e^{-ik_i 2\pi R}} \cong k_i \pi R \text{ for } k_i 2\pi R << 1$$

Figure 2 is a plot of F_R and F_A for large damping. Finally, the ratio of the maximum to minimum is

(7) $$\frac{F_R}{F_A} = \left(\frac{1}{k_i \pi R}\right)^2 \text{ for } k_i 2\pi R << 1$$

The average value of F at the antenna between resonances can be calculated from (4) as

(8) $$\langle F \rangle = R \int_{n/R}^{(n+1)/R} F\, dk = \langle F_+ \rangle + \langle F_- \rangle$$

and using the integration formulas[137]

(9) $$\int \frac{dx}{a + b\, e^{px}} = \frac{x}{a} - \frac{1}{ap} \log_e(a + b\, e^{px})$$

$$\int \frac{e^{ax}\, dx}{b + c\, e^{ax}} = \frac{1}{ac} \log_e(b + c\, e^{ax})$$

we find

(10) $$\langle F_+ \rangle = 1$$
$$\langle F_- \rangle = 0$$

independently of k_i. The average of F_- is zero because F_- is negative half the time. F_+, on the other hand, is always positive. R_R is proportional to F (electric field), and thus $\langle R_R \rangle$ is also independent of damping.

Coherent Toroidal Wave Stacking Geometry

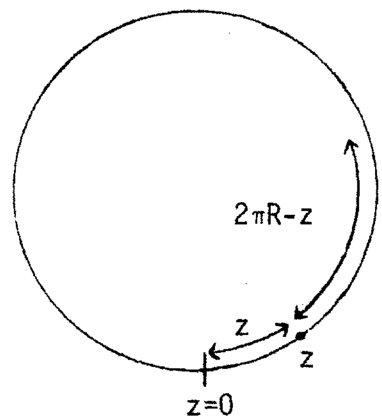

Figure 1

F_R and F_A as a Function of Damping

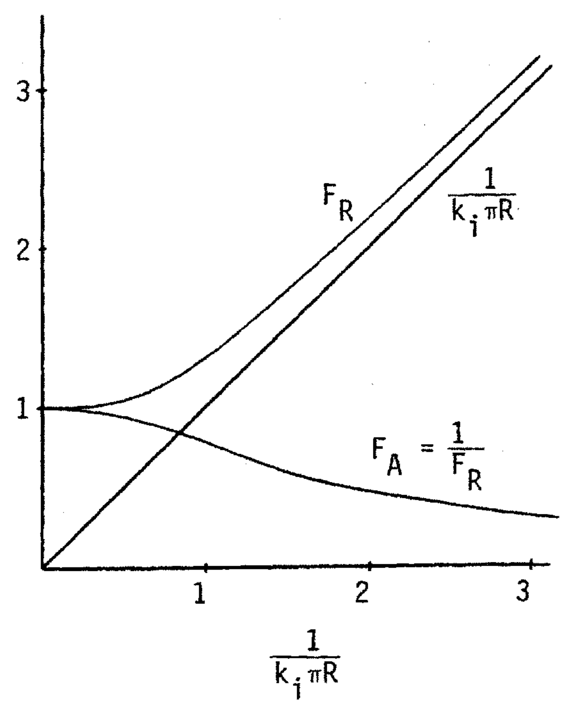

Figure 2

IV-6.3. Mode spacing and onset

From Section IV-3.2, equation (5) and Table 1, we can calculate the total number of possible perpendicular eigenmodes (onsets) as (Ω = 2, μ = 1, n_e = 3 x $10^{14}/cm^3$, a = 10 cm, R = 54 cm)

(1) $$N_{m_\perp} = \nu(2\nu - 1) \simeq 2\nu^2 \text{ for } \nu >> 1$$
$$\simeq 3.9 \times 10^{-16} \frac{\Omega^2 a^2}{\mu} n_e \simeq 45$$

Also recalling that

(2) $$k_\perp^2 + (1 + \Omega)\, k_\parallel^2 = k_A^2$$

(3) $$k_\perp = \frac{\pi\nu}{a}$$

(4) $$k_\parallel = \frac{N_{mT}}{R}$$

for a given perpendicular eigenmode with $k_\perp << k_A$, we calculate the number of toroidal eigenmodes as

(5) $$N_{mT} = \frac{k_A R}{\sqrt{1 + \Omega}} = 4.4 \times 10^{-8} \frac{\Omega\, R}{\sqrt{\mu(1+\Omega)}} \sqrt{n_e} \simeq 50$$

The total number of toroidal resonances is then approximately[93]

(6) $$N_{mS} \simeq \int_0^{\nu_{max}} 2\nu^2 N_{mT}(\nu)\, d\nu = \frac{2}{3\pi^2} \frac{R\, a^2}{\sqrt{1+\Omega}} k_A^3$$

$$= \frac{N_{m\perp} N_{mT}}{3} \simeq 5.75 \times 10^{-24} \frac{\Omega^3\, R\, a^2}{\sqrt{1+\Omega}\, \mu^{3/2}} n^{3/2} \simeq 750$$

The rate of onsets and resonances and spacing (ΔN = 1) in density is calculated as

$$(7)\qquad \frac{\partial N_{m\perp}}{\partial n_e} = \frac{N_{m\perp}}{n_e}$$

$$\Delta n_{em\perp} = 2.56 \times 10^{15} \frac{\mu}{\Omega^2 a^2} \simeq 6.4 \times 10^{12}/\text{cm}^3$$

$$(8)\qquad \frac{\partial N_{mT}}{\partial n_e} = \frac{N_{mT}}{2\ n_e}$$

$$\Delta n_{emT} = 4.5 \times 10^{7} \frac{\sqrt{\mu(1+\Omega)}}{\Omega\ R} \sqrt{n_e} \simeq 1.25 \times 10^{13}/\text{cm}^3$$

$$(9)\qquad \frac{\partial N_{mS}}{\partial n_e} = \frac{3}{2} \frac{N_{mS}}{n_e}$$

$$\Delta n_{emS} = 1.16 \times 10^{23} \frac{\sqrt{1+\Omega}\ \mu^{3/2}}{\Omega^3\ R\ a^2} \frac{1}{\sqrt{n_e}} \simeq 2.7 \times 10^{11}/\text{cm}^3$$

Finally, we can calculate the mode spacing in time (typically $\frac{\partial n}{\partial t}$ = 5×10^{15} cm^{-3} sec^{-1})

$$(10)\qquad \Delta t = \Delta n\left(\frac{\partial n}{\partial t}\right)^{-1} \simeq 1.3 \text{ msec for } m\perp$$

$$\simeq 2.5 \text{ msec for mT}$$

$$\simeq 54\ \mu\text{sec for mS}$$

IV-6.4. Quality factor

Wave or circuit quality factor is a criteria commonly used in electrodynamics and electrical engineering.[133,134] From first principles (previous Sections and IV-7.2), we have[144]

$$(1)\quad \frac{1}{k_i} = \frac{2\,P_f}{P_{dis}}$$

$$(2)\quad P_f = W v_{g_{\parallel}}$$

$$(3)\quad v_{g_{\parallel}} = \frac{1+\Omega}{1-\Omega N_{\parallel}^2/2}\, N_{\parallel} V_A \simeq 2V_A \qquad \text{for } N_{\parallel} = .5 \text{ and } \Omega = 2$$

$$(4)\quad Q = \frac{\omega W}{P_{dis}}$$

$$(5)\quad Q = \frac{\omega}{\Delta\omega}$$

Combining (1) to (4), and for the rest of this Section, assuming a plasma with $\Omega = 2$, $\mu = 1$, $n_e = 3 \times 10^{14}/\mathrm{cm}^3$, $a = 10$ cm, $R = 54$ cm, we have

$$(6)\quad Q = \frac{\omega}{2\,k_i\,v_{g_{\parallel}}} \simeq \frac{\omega}{2\,k_i\,N_{\parallel}\,V_A}\;\frac{1-\Omega N_{\parallel}^2/2}{1+\Omega} \simeq \frac{k_A}{4k_i} \quad \text{for } N_{\parallel} = .5$$

$$\simeq 250 \text{ for } k_A = 1/\mathrm{cm},\ 1/k_i = 10 \text{ meters}$$

In comparision, we would have for a "normal" dielectric[134]

$$(7)\quad \frac{1}{k_i} = \frac{2\,P_f}{P_{dis}} = \frac{\frac{2kE^2}{2\omega\mu}}{\frac{E^2}{2\eta}} = 2\eta\sqrt{\frac{\varepsilon}{\mu}}$$

$$(8)\quad Q = \frac{\omega W}{P_{dis}} = \frac{\frac{\omega\,\varepsilon\,E^2}{2}}{\frac{E^2}{2\eta}} = \eta\,\omega\,\varepsilon$$

$$= \frac{\omega W}{k_i 2P_f} = \frac{\omega}{k_i 2v_g} = \frac{k}{2k_i} \qquad \text{for } v_g = v_p$$

The quality factor can also be derived from the complex frequency

(9) $E = E_\circ\, e^{-i\,(\omega - i\omega_i)t}$

(10) $W = W_\circ\, e^{-2\omega_i t}$

(11) $P_{dis} = -\dfrac{\partial W}{\partial t} = 2\,\omega_i\, W_\circ$

(12) $Q = \dfrac{\omega}{2\omega_i}$

in agreement with (8) for nondispersive waves, where

(13) $\omega \;\; \alpha\; k$

$\omega_i \;\alpha\; k_i$

Further assuming $k_\perp = k_A$ and $T_e = T_i = 1$ keV, we can calculate (Section IV-4.2.) the second harmonic damping Q[7]

(14) $W/cm \simeq \dfrac{1}{8\pi}\;\varepsilon_A\, E_y^{\,2}\;\;\pi a^2$

(15) $E_+ = \dfrac{E_x + i\,E_y}{2} = \dfrac{\Omega - 1}{2i}\,E_y \;\; \simeq \dfrac{E_y}{2i}$

(16) $P_{dis}/cm = \displaystyle\int_s P_{dis}/cm^3\; ds = 2\pi a r\;\, P_{dis}/cm^3$

(17) $Q_{2\omega c} = \dfrac{\omega\;W/cm}{P_{dis}/cm} \;\simeq \dfrac{a\;\;2}{R\;\beta_i} \;\simeq 5 \times 10^{10}\;\dfrac{a\;\,B_\circ^{\,2}}{R\;n_e T_i} \;\simeq 110$

and assuming $\alpha = 1.9$, we have the electron Landau damping Q

(18) $Q_{ELD} = \dfrac{2}{\sqrt{\pi}}\;\dfrac{1}{\alpha e^{-\alpha^2}}\;\;\dfrac{1}{\beta_e}\;\simeq 6500$

$\geqslant \dfrac{2.63}{2}\;\;\dfrac{R}{a}\;\;Q_{2\omega c}$

Similarly, we can calculate collisional[90,96] and wall damping[93,134,144] Q as

$$(19)\quad Q_{coll} = \frac{\omega W}{P_{dis}} = \frac{\omega \varepsilon_A E^2/2}{\eta J^2/2} \approx \frac{1}{\omega \varepsilon_A \eta}$$

$$\approx \frac{k_A}{2k_i} \approx 5500$$

$$(20)\quad Q_w \approx \frac{\omega W}{P_{dis}} \approx \frac{a}{\delta} \frac{\langle B^2 \rangle}{B_{edge}}$$

$$\approx \frac{k_A}{2k_i} \approx 37{,}000$$

where we note the difference between equations (8) and (19).

From (5), we calculate the half power width in density as[10]

$$(21)\quad Q = \frac{\omega}{\Delta\omega} \quad \frac{\pi_i}{\Delta\pi_i} = \frac{2n_e}{\Delta n_e}$$

$$(22)\quad \Delta n_e = \frac{2n_e}{Q} \simeq 6 \times 10^{12}/\text{cm}^3 \quad \text{for } Q = 100$$

Mode stacking becomes important when the mode width is comparable to the mode spacing. Following the notation of IV-6.3., and using (20), we can calculate the maximum allowable Q for mode stacking (overlapping skirts).

$$(23)\quad Q_{m_\perp} = \frac{2n_e}{\Delta n_{em_\perp}} = 2\ N_{m_\perp} \simeq 90$$

$$(24)\quad Q_{mT} = \frac{2n_e}{\Delta n_{emT}} = N_{mT} \simeq 50$$

$$(25)\quad Q_{mS} = \frac{2n_e}{\Delta n_{emS}} = 3\ N_{mS} = 2250$$

Summarizing these results, we write

$$(26)\quad Q_{mT} < Q_{m_\perp} < Q_{2\omega e} < Q_{mS} < Q_{coll} < Q_{ELD} < Q_{wall}$$

and onsets and high radiation resistance perpendicular eigenmodes are expected to be distinguishable from the background. On the other hand, the average toroidal resonance is expected to be swamped out by stochastic mode stacking, especially with the resonant layer in the plasma center.

Finally, for a single mode, we can calculate the ratio of the maximum to minimum field from IV-6.2.(7), as

$$(27)\quad \frac{F_R}{F_A} = \left(\frac{1}{k_i \pi R}\right)^2 \simeq \left(\frac{4\ Q}{k_A \pi R}\right)^2 \simeq 5.6 \text{ for } Q = 100,\ k_A = 1/\text{cm}$$

IV-6.5. Poloidal mode stacking

From Section IV-1.3., we calculated that, in general,

$$(1) \qquad R_m = \frac{V_m^2}{4\,P_{fm}}$$

$$(2) \qquad R_T = \sum R_m$$

In this Section, we will consider the poloidal mode coupling effects of two independently fed antenna loops, as shown in Figure III-2.1.(3). Figures 1-4 show the usual discrete Fourier (sin, cos, m > 0) components[137] of a 360° (TFR) and 130° (Alcator) antenna, which is fed either in or out of phase (Section III-2.1.).

For simplicity, we will assume that the ratio of the Poynting flux to the square of E_θ at the antenna radius is independent of mode number ($\beta_{am} \simeq \beta_{an}$, Section IV-1.3.). For any particular set of eigenmodes, this may be a very crude approximation (especially due to the evanescent edge), but will lead to two simple, important, statistical scaling laws.

Allowing m to be both positive and negative (Section IV-1.2.), we have

$$(3) \qquad V_m = \int_{-\theta_a}^{+\theta_a} E_m\, \varepsilon_a \cos(m\theta - \omega t)\, a\, d\theta$$

where

(4) ε_a =

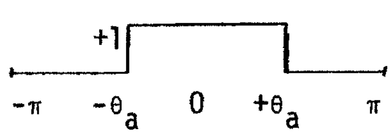

for push-pull

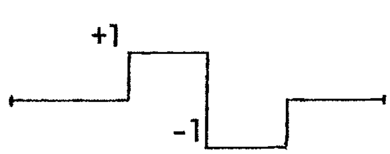

for push-push

Using the trigonometric identity

(5) $\cos(m\theta - \omega t) = \cos m\theta \cos \omega t + \sin m\theta \sin \omega t$

and assuming a push-pull fed antenna, we have

(6) $$V_m = a\, E_m\ 2 \int_0^{\theta_a} \cos m\theta\, d\theta\ \cos \omega t \qquad -\infty < m < +\infty$$

$$= 2\, a\, E_m \frac{\sin m\, \theta_a}{m} \qquad m \neq 0$$

(7) $$R_T = \frac{a^2 E_m{}^2}{P_{fm}} \left[\theta_a^2 + 2 \sum_{m=1}^{\infty} \frac{\sin^2 m\theta_a}{m^2} \right]$$

$$\alpha \quad \theta_a^2 + 2 \sum_{m=1}^{\infty} \frac{\sin^2 m\theta_a}{m^2} \simeq 9.87 \text{ for } \theta_a = 180°,\ m < 10$$

$$\simeq 3.47 \text{ for } \theta_a = 65°\ ,\ m < 10$$

Similarly, for push-push we have

(8) $$R_T = \frac{a^2 E_m{}^2}{P_{fm}}\ 2 \sum_{m=1}^{\infty} \left[\frac{1 - \cos m\theta_a}{m} \right]^2$$

$$\alpha \quad 2 \sum_{m=1}^{\infty} \left[\frac{1 - \cos m\theta_a}{m} \right]^2 \simeq 9.47 \text{ for } \theta_a = 180°,\ m < 10$$

$$\simeq 3.29 \text{ for } \theta_a = 65°\ ,\ m < 10$$

and we note that the total radiation resistance is independent of antenna phasing. A closer look at (7) and (8) further shows that

(9) $$R_T \simeq \frac{a^2 E_m{}^2}{P_f}\ \pi\ \theta_a$$

Of course, the radiation resistances of the low poloidal mode numbers still increase as $\theta_a{}^2$ (or even $\theta_a{}^4$), but the spectrum width decreases with θ_a, resulting in $R_T \; \alpha \; \theta_a$.

Antenna k_θ Spectrums for 360° and 130° Antennas

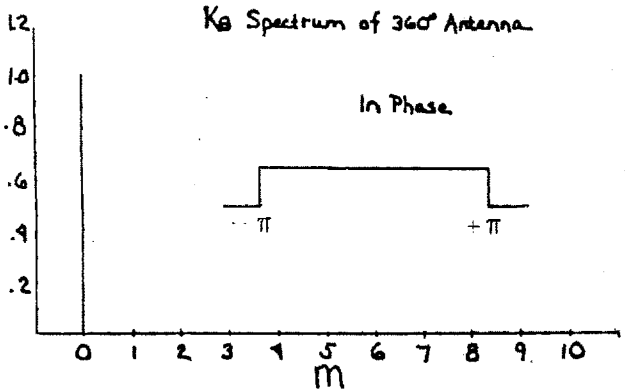

Figure 1

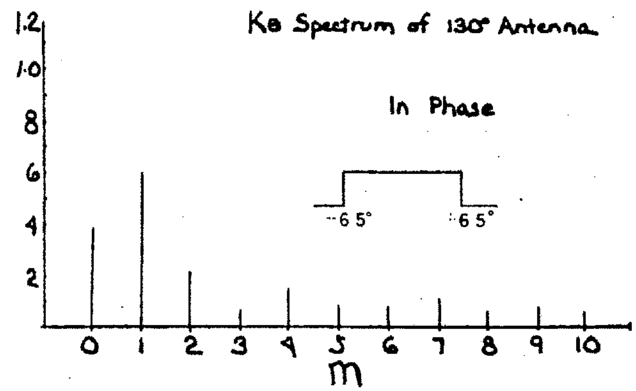

Figure 3

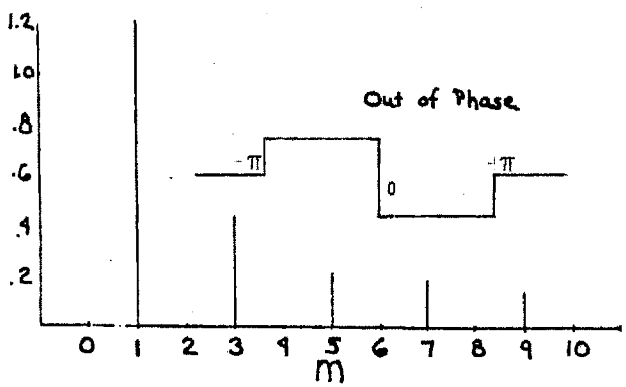

Figure 2

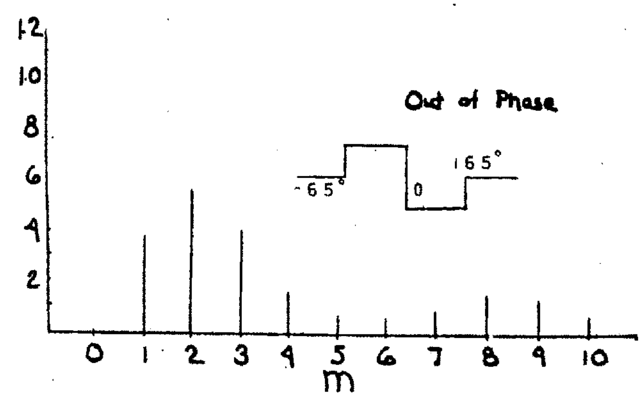

Figure 4

IV-6.6. Stochastic mode stacking

In this Section, we will examine the stochastic stacking of orthogonal eigenmodes, at and away from the antenna. At the antenna (E_a), the eigenmodes are coherent (all in phase), and the electric fields simply add. Away ($k_{\parallel} z \gg 1$) from the antenna (E_p), the modes become randomly phased with respect to each other (incoherent), and statistically interfere.

For perpendicular eigenmodes ($k_{\perp i} = 0$) and high Q toroidal standing eigenmodes, the electric fields are either in phase or out of phase with respect to the antenna (for the same poloidal angle θ). This random phase can be modeled by a simple coin toss with heads = 1 and tails = -1. Thus for 1 coin (1 mode), two possibilities exist ($2^1 = 2$), and

$$(1) \quad \langle E_a \rangle = \langle E_p \rangle = \frac{|1| + |-1|}{2} = 1$$

$$(2) \quad \frac{\langle E_p \rangle}{\langle E_a \rangle} = 1$$

For 2 coins, there are four possibilities (2^2) and

$$(3) \quad \frac{\langle E_p \rangle}{\langle E_a \rangle} = \frac{|1+1| + |-1-1| + |-1+1| + |+1-1|}{\big[|+1| + |+1|\big] + \big[|-1| + |-1|\big] + \big[|-1| + |+1|\big] + \big[|+1| + |-1|\big]} = \frac{1}{2}$$

For 4 coins[64]

$$(4) \quad \frac{\langle E_p \rangle}{\langle E_a \rangle} = \frac{4\left[\binom{4}{4} + \binom{4}{0}\right] + 2\left[\binom{4}{1} + \binom{4}{3}\right] + 0\left[\binom{4}{2}\right]}{4(2^4)} = \frac{3}{8}$$

where

$$(5) \quad \binom{n}{r} = \frac{n!}{r!(n-r)!}$$

and in general ,

$$(6)\quad \frac{< E_p >}{< E_a >} = \frac{\left\langle \left| \sum_{m=1}^{n} x_m \right| \right\rangle}{\left\langle \sum_{m=1}^{n} |x_m| \right\rangle} \qquad \text{for } x_m = \pm 1$$

$$= \frac{1}{\sqrt{n}} \qquad \text{for } n \to \infty$$

as shown in Figure 1.

Considering the problem from another angle, we may write

$$(7)\quad P_{antenna} = \frac{I_o \ell}{2} [\, E_1 + E_2 + \ldots .\ E_n] \approx \frac{n\, I_o\, E_o \ell}{2}$$

$$(8)\quad P_{dis} = \frac{E_p{}^2 \ell^2 Vol}{2n}$$

$$(9)\quad P_{antenna} = P_{dis}$$

and thus

$$(10)\quad E_a \propto n$$

$$(11)\quad E_p \propto \sqrt{n}$$

$$(12)\quad \frac{E_p}{E_a} = \frac{1}{\sqrt{n}}$$

in agreement with (6).

The electric field at the antenna is thus, on the average, $\sqrt{n}$ times larger than the electric field around the torus, and is much more likely to produce edge heating (the edge evanescence even further deteriorates the situation).

To further investigate the stochastic field structure of a set of random modes, we define the following statistical operators.

(13) Average (mean) = $<p> = \dfrac{\int p\,dq}{\int dq} = \dfrac{\sum p_n}{n}$

p = probe signal ($|p(z)|$), radiation resistance ($\mathrm{Re}\ p(z = 0)$)

$q = k_{\parallel}, t, n_e$

(14) Deviation = $p - <p>$

(15) Average Deviation = $<|p - <p>|>$

(16) Normalized Average Deviation = $\dfrac{<|p - <p>|>}{<p>}$

(17) Standard Deviation = $\sqrt{<(p - <p>)^2>}$

(18) Normalized Standard Deviation = $\dfrac{\sqrt{<(p - <p>)^2>}}{<p>}$

(19) Range = $p_{max} - p_{min}$

(20) Normalized Range = $\dfrac{p_{max} - p_{min}}{<p>}$

(21) Solidity[145] (normalized maximum) = $\dfrac{p_{max}}{<p>}$

To illustrate the basic issues, we will use the following simple heuristic model. Consider the field solidity near the antenna (coherent R_R) and away from the antenna (incoherent $|V_p|$).

		coherent	incoherent
(22)	$\langle p \rangle$ =	n	$\sqrt{n}$
(23)	p_{max} =	$\alpha Q + (n - 1)$	$\alpha Q + \sqrt{n - 1}$
(24)	Solidity (S) ≈	$\frac{\alpha Q + (n - 1)}{n}$	$\frac{\alpha Q + \sqrt{n - 1}}{\sqrt{n}}$

where n is the number of modes, and Q is the quality factor. Thus for the plausible cases

(25)	$n = 1, \alpha Q = 10$	$S_c = 10$	$S_i = 10$
	$n = 10, \alpha Q = 10$	$S_c = 1.9$	$S_i = 4.1$
	$n = 10, \alpha Q = 2$	$S_c = 1.1$	$S_i = 1.6$

and, in general,

(26) $S_i \geqslant S_c$

(27 $S_i \approx S_c \sqrt{n}$ for $\alpha Q \gg n$

which means that a probe signal (away from the antenna) will always have a "noisier" time history than the radiation resistance.

Although this simple model is a good approximation in the coherent case (since R_R is always positive), it does not take into account stochastic destructive interference (a high Q resonance with opposite phase can totally cancel out the background). The normalized range is a slightly more powerful operator (Range = p_{max} - $\langle p \rangle$ in coherent case), and further shows that the probe signal is statistically noisier than R_R. In the next Section, we will computationally use the average and standard deviations, again with the same results.

Simple Stochastic Mode Stacking Model

$$\frac{\text{Total } E_{probe}}{\text{Total } E_{antenna}} = \left\langle \frac{\left|\sum_{m=1}^{n} x_m\right|}{\sum_{m=1}^{n} |x_m|} \right\rangle, x_m = \pm 1$$

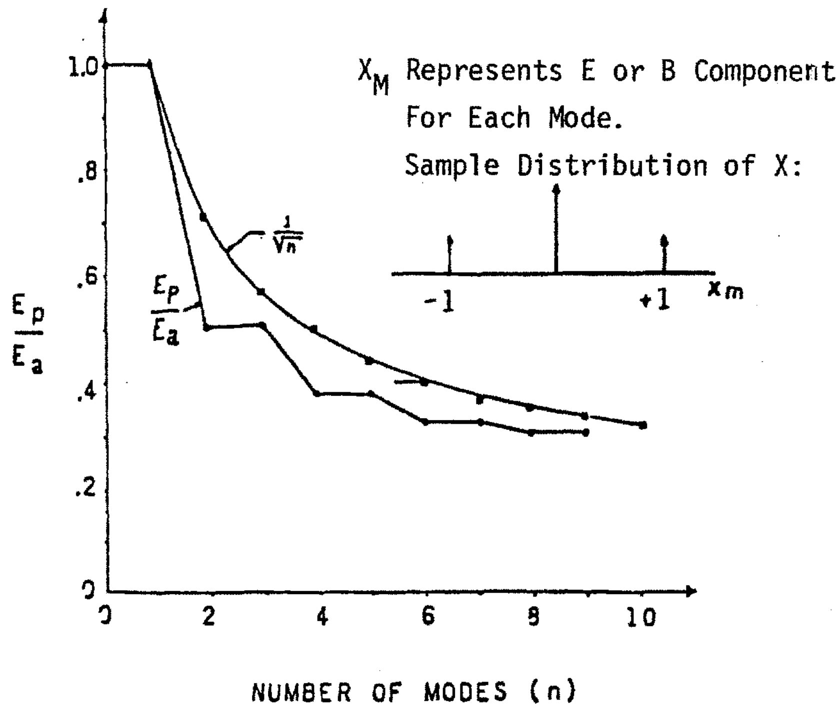

Figure 1

IV-6.7. Coherent and stochastic field simulations

In this Section, we will examine the results of realistic computer simulations of coherent and stochastic fields. A code called "Stochastic Mode Stacking" is listed in the appendix, and is versatile enough for almost any parameter scan. Figure 1 shows the many parameters that need to be chosen for a given set of simulations (multi-dimensional scans). Table 1 is an outline of the basic functions and variables used in the code, and is self explanatory with the code comments. Given the basic input data, the code calculates and plots the real, imaginary, magnitude and phase of the sum of s = 1, 3, 10 and 20 modes, as a function of linearly increasing k_z of z. k_{zo} is some random number (i.e., between .5 and .6/cm) with random or fixed initial phase, and z is the distance from the antenna. The average, average deviation, and standard deviation of the various parameters are also outputted.

Figures 4 to 7 show the real, imaginary, magnitude and phase of the electric field at the antenna (z = 0) versus $k_{\parallel}$(kzr), without mode splitting (p = 0) or fluctuations (kzfa = 0), and one mode (s = 1) and damping length = 10R. As expected from Section II-6.2, $\langle Re \rangle = ar \approx s = 1$, $\langle Im \rangle = ai \approx 0$ $\langle Mag \rangle = am > ar$ and $\langle \phi \rangle = ap \approx 0$.

Figure 3 is a magnified view of Figure 4, where the maximum (F_R), minimum (F_A) and half power width (Δk_z) are easily measured. Figure 8 shows eigenmode resonances produced by sweeping a multi-wavelength coax resonator through several resonances between 150 and 220 MHz (Figure 10). Figure 9 is similar, but with three different resonators in parallel.

Figures 11 and 12 are the same as 4 and 5, but with 1% mode splitting (p = .01). Figures 13 and 14 are z scans (scan k = 0) with large damping (kzi = 1/R). Note how the phase linearly increases near the antenna ($F_- << F_+$), but goes through nearly step-like transitions 180° around the torus ($|F_+| \approx |F_-|$). This effect is further investigated in Figures 15 to 20, where the damping length is varied from R to 100 R, and at a position near the HCN or Thompson ports (z = 60). Note again the phase increase difference between the small and large damping cases. At high Q, the fields are almost always either in phase or out of phase, and the parallel wavelength is most easily calculated by measuring the distance between phase jumps or magnitude nodes. This situation, of course, does not occur if the mode is highly split (running wave, Figures 53 to 58).

Figures 21 to 24 show the radiation resistance (Re, z = 0) for s = 1, 3, 10 and 20 and kzi = .1/R. Figures 25 to 30 show the same simulation, but with random initial phase, and z = 60. Note how the phase becomes progressively more difficult to measure with increasing number of modes. Table 2 summarizes the averages and normalized deviations, as a function of number of modes. Note, in particular, how the average of the magnitude of the probe signal ($\approx \sqrt{s}$) and radiation resistance ($\approx$ s) agree with analytical theory. Also note how the normalized deviation of the radiation resistance decreases with s, while the probe signal is independent of s. For many modes, the radiation resistance has a smaller normalized deviation than the magnitude of the probe signal (R_R is less "noisy" than a probe signal).

Figures 31 to 36 show similar simulations with 10 modes, but with $k_\parallel$ spectrum widths of .01, .1 and 1/cm. Figures 37 to 40 show the effects of 1% and 10% high frequency fluctuations on one mode.

Figures 41 to 46 show the probe signal (z = 60) for 10 modes as a function of increasing k_z, for k_i = 1/R, .1/R and .01/R (this is the same as Figures 15 to 20, but with scan k = 1). Figures 47 to 52 show the effect of 1% and 10% mode splitting on the probe signal (z = 60) and the radiation resistance (z = 0), for one mode and k_i = .1/R.

Table 1.

Outline of basic functions and variables used in the stochastic mode stacking code.

INPUT DATA

s = number of modes

$k = kzr + i(kzi)$ complex k

$k_- = k_+ (1 + p)$ mode splitting

$k = kzr[kzfa \cdot \cos(kzff \cdot kz)]$ fluctuations

$F = F_+ + F_-$ as calculated in II-6.2.

kzro and pha = random set of initial k and phase

scan k linearly increases k or z

kzro = kmult (kzro - ksubt) changes the initial spectrum width

OUTPUT DATA

Plot either real, imaginary, magnitude or phase.

ar = <Re> , ai = <Im> , am = <Mag> , ap = <ϕ>

adrs = $<|Re - s|>$; adrrs = $<|Re - \sqrt{s}|>$

sdrs = $\sqrt{<(Re - s)^2>}$; sdrrs = $\sqrt{<(Re - \sqrt{s})^2>}$

admrs = $(<|Mag - \sqrt{s}|>)$ <u>a</u>verage <u>d</u>eviation of <u>m</u>agnitude <u>m</u>inus <u>r</u>oot <u>s</u>

Table 2

Summary of averages and normalized deviations as a function of number of modes for $1/k_{zi} = 10R$.

	s = 1	3	10	20
z = 0				
$\langle Re \rangle \approx s$	1.0029	3.026	9.989	20.04
$\frac{\langle \lvert Re - s \rvert \rangle}{\langle Re \rangle}$	.715	.448	.212	.108
z = 60				
$\langle Mag \rangle \approx \sqrt{s}$	1.079	2.056	2.936	4.043
$\frac{\langle \lvert Mag - \sqrt{s} \rvert \rangle}{\langle Mag \rangle}$	.448	. 464	.476	.458

Multi-Dimensional Scans

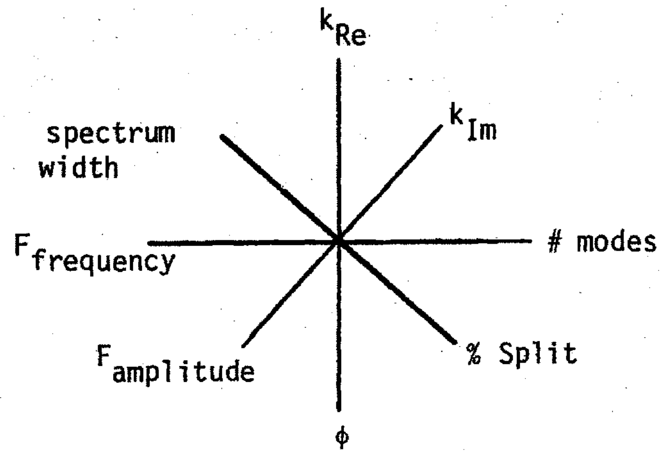

Figure 1

Measurements

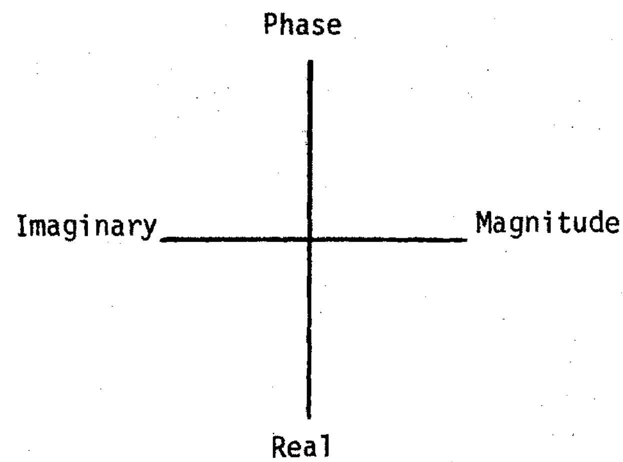

Figure 2

Low Q Eigenmode Waveform Detail

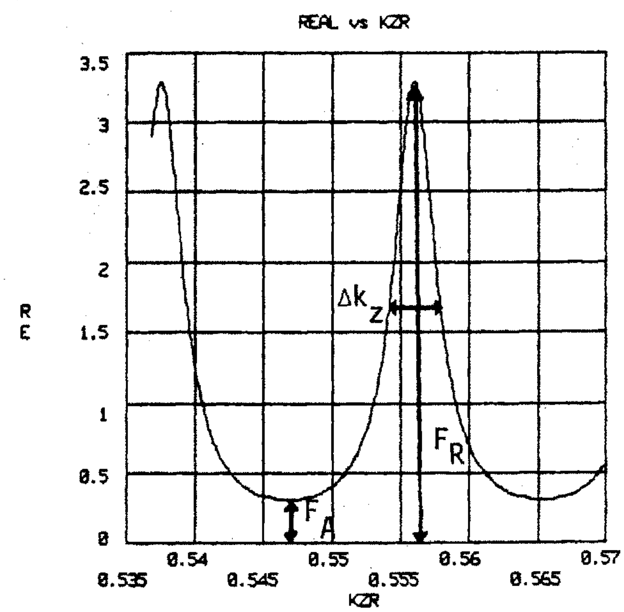


```
INPUT      scank=1.0  s= 1  phase=0.0  n= 500  r=54.0
DATA       kzi=0.001052  p= 0.00  z=  0.00  zmin=  50.00  zmax=  75.00
           kminf=0.970  kmaxf=1.030  kmult= 1.00  ksubt= 0.000
           kzfa=.000  kzff=.10000E+04  kzr0(1)=0.55340

AVERAGE    adr=  0.9597  adi=  0.1445  adm=  1.2480  adp=  0.0932
AVE DEV    adrs=  0.7351  adrrs=  0.7351  adms=  0.7458  admrs=  0.7458
STAND DEV  sdrs=  0.9077  sdrrs=  0.9077  sdms=  0.9762  sdmrs=  0.9762
```

Figure 3

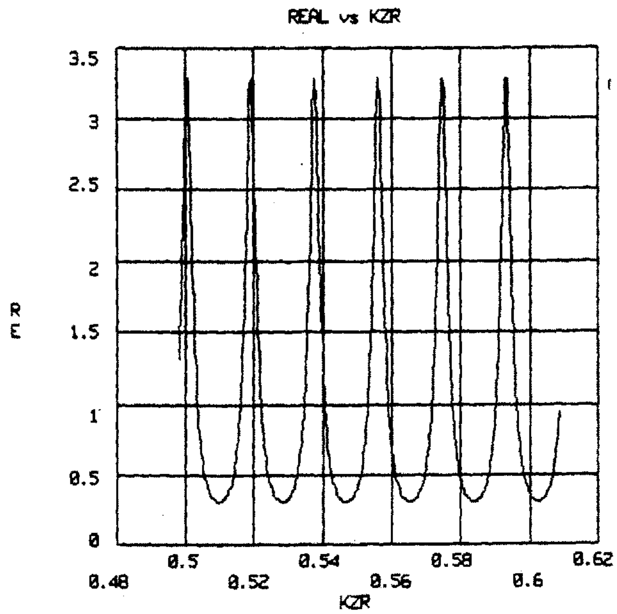

Figure 4

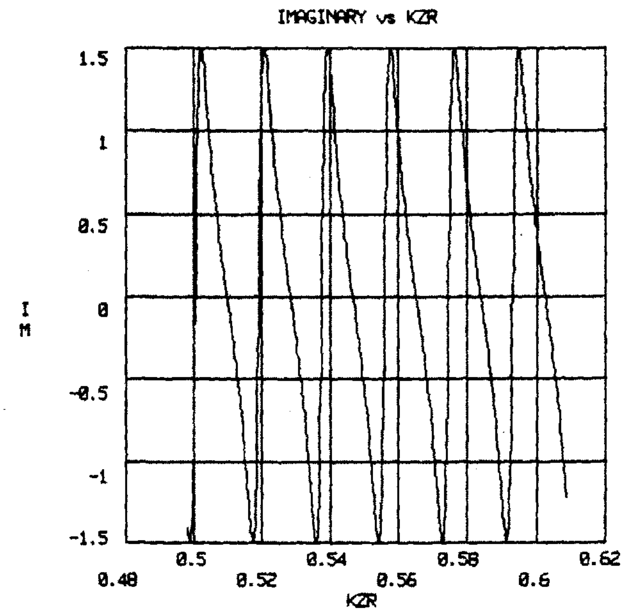

Figure 5

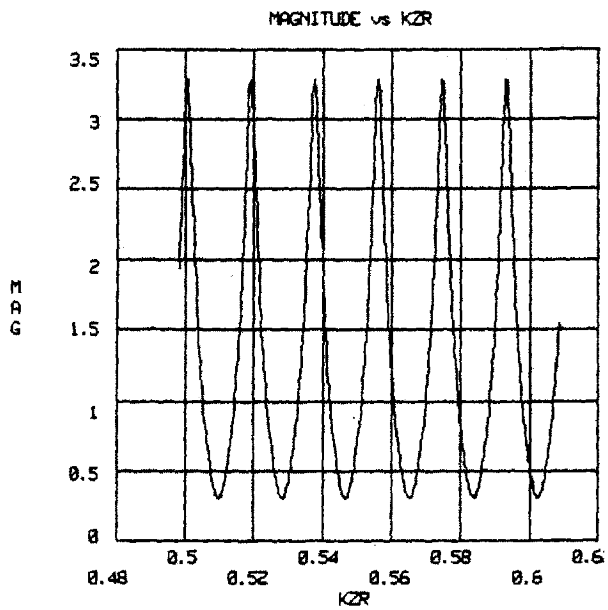

Figure 6

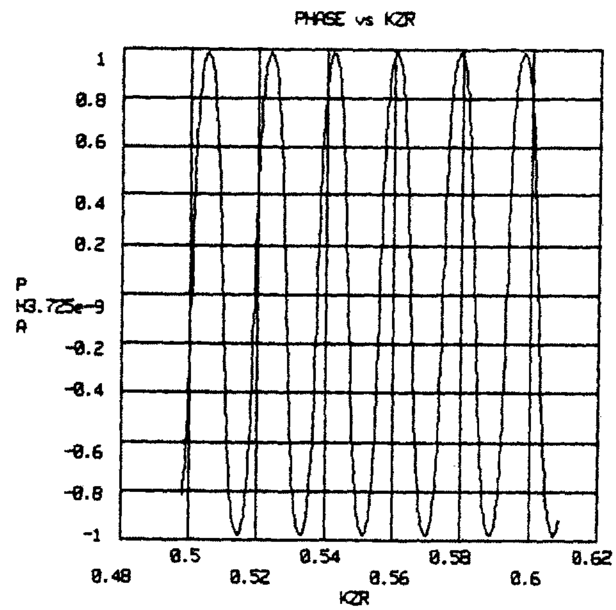

Figure 7

Real, Imaginary, Magnitude and Phase of one toroidal eigenmode at z = 0, k_i = .1/R, ϕ = 0 and no mode splitting

```
INPUT     scank=1.0  s= 1  phase=0.0  n= 500  r=54.0
DATA      kzi=0.001852  p= 0.00  z=   0.00  zmin=   0.00  zmax=  60.00
          kminf=0.900  kmaxf=1.100  kmult= 1.00  ksubt= 0.00
          kzfa=.000  kzff=.10000E+04

AVERAGE   adr=  0.9995   adi=  0.0063   adm=  1.3103   adp=  0.0042
AVE DEV   adrs=  0.7198  adrrs=  0.7198  adms=  0.7583  admrs=  0.7583
STAND DEV sdrs=  0.8948  sdrrs=  0.8948  sdms=  0.9856  sdmrs=  0.9856
```

Analog Eigenmode Simulations

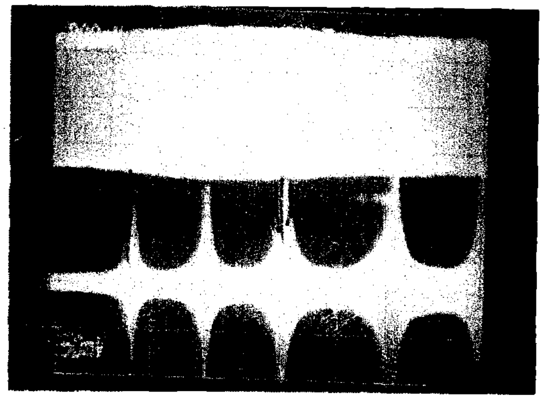

Vin (A)

1 mode (B)

Figure 8

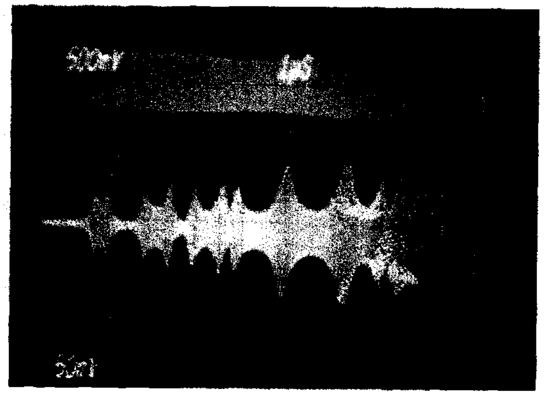

Vin (A)

3 modes (B)

Figure 9

Coax Eigenmode Simulators

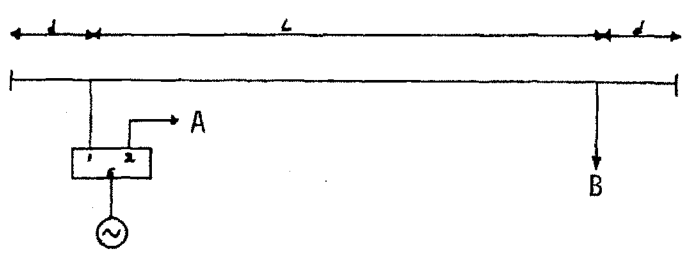

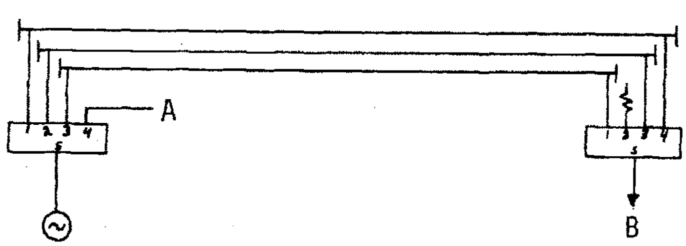

Figure 10

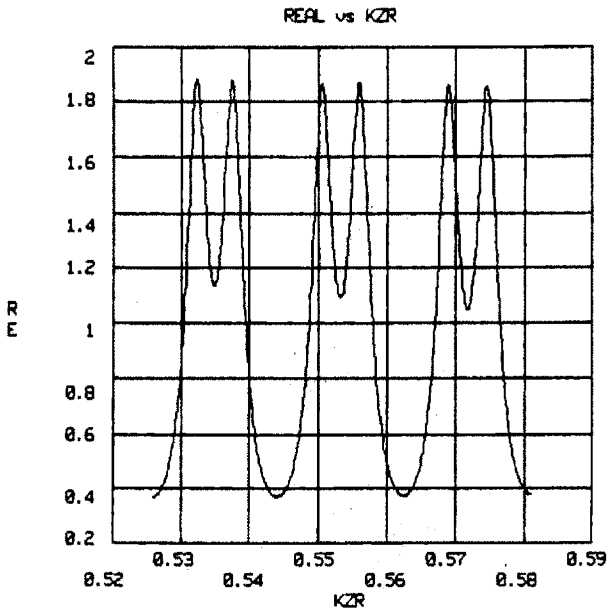

Figure 11

Same as Figures 4 and 5
but with 1% splitting

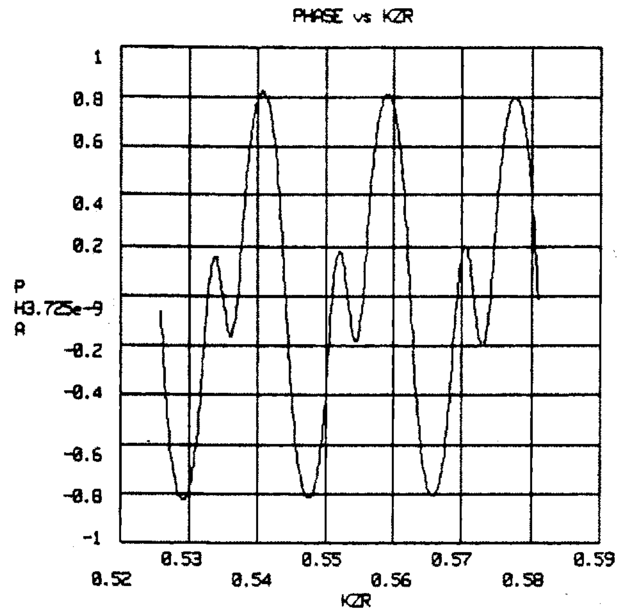

Figure 12

INPUT DATA scank=1.0 s= 1 phase=0.0 n= 500 r=54.0
kzi=0.001852 p= 0.01 z= 0.00 zmin= 0.00 zmax= 60.00
kminf=0.950 kmaxf=1.050 kmult= 1.00 ksubt= 0.00
kzfa=.000 kzff=.10000E+04

AVERAGE adr= 0.9999 adi= -0.0022 adm= 1.1302 adp= -0.0032
AVE DEV adrs= 0.4605 adrrs= 0.4605 adms= 0.4532 admrs= 0.4532
STAND DEV sdrs= 0.5153 sdrrs= 0.5153 sdms= 0.5200 sdmrs= 0.5200

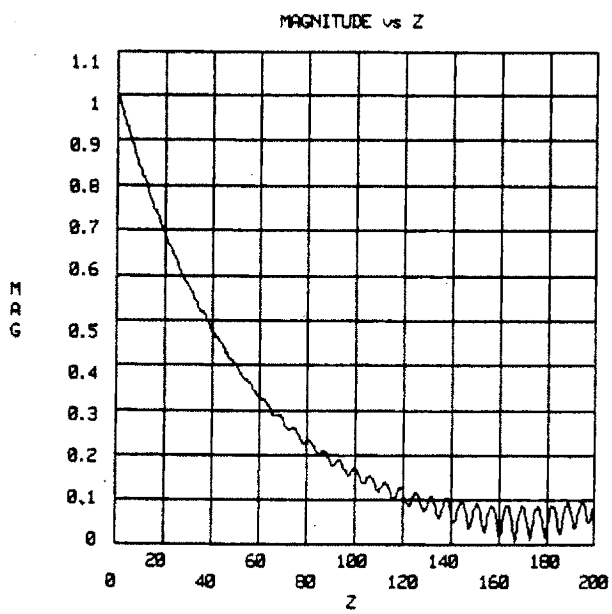

Figure 13

Toroidal position scan
with $k_i = 1/R$

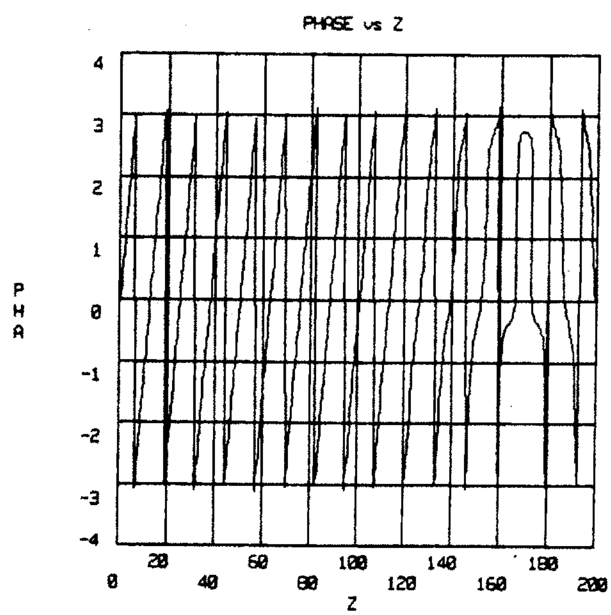

Figure 14

INPUT DATA scank=0.0 s= 1 phase=0.0 n= 500 r=54.0
kzi=0.018519 p= 0.00 z= 0.00 zmin= 0.00 zmax= 200.00
kminf=0.900 kmaxf=1.100 kmult= 1.00 ksubt= 0.000
kzfa=.000 kzff=.10000E+04 kzr0(1)=0.55340

AVERAGE adr= 0.0010 adi= 0.0106 adm= 0.2702 adp= 0.2649
AVE DEV adrs= 0.9990 adrrs= 0.9990 adms= 0.7298 admrs= 0.7298
STAND DEV sdrs= 1.0336 sdrrs= 1.0336 sdms= 0.7725 sdmrs= 0.7725

$k_i = 1/R$

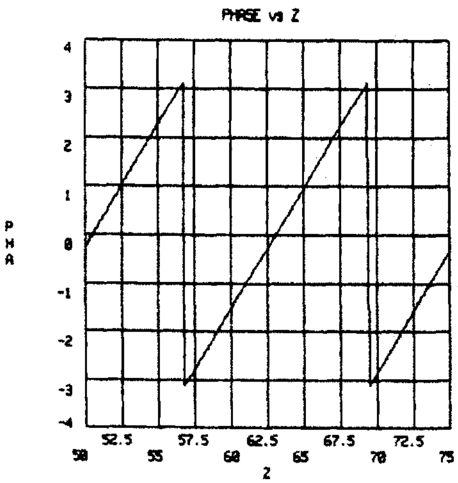

Figure 15

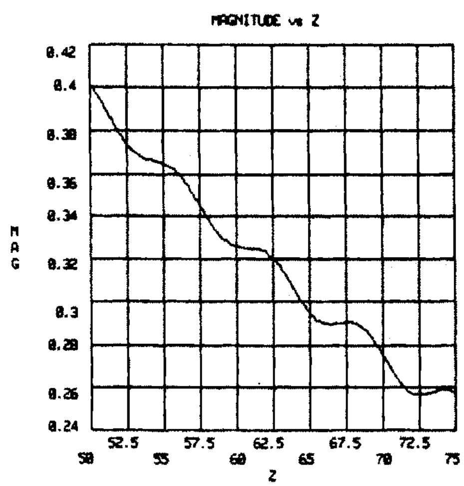

Figure 16

```
INPUT      scank=0.0  s= 1  phase=0.0  n= 500  r=54.0
DATA       kzi=0.010519  p= 0.00  z=  0.00  zmin= 50.00  zmax= 75.00
           kminf=0.900  kmaxf=1.100  kmult= 1.00  ksubt= 0.00
           kzfa=.000  kzff=.10000E+04

AVERAGE    adr=  0.0012   adi=  0.0123   adm=  0.3177   adp=  0.0139
AVE DEV    adrs=  0.9980  adrrs=  0.9980  adms=  0.6823  admrs=  0.6823
STAND DEV  sdrs=  1.0252  sdrrs=  1.0252  sdms=  0.6836  sdmrs=  0.6836
```

$k_i = .1/R$

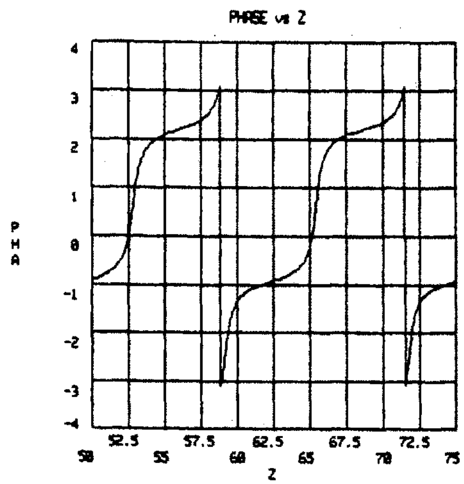

Figure 17

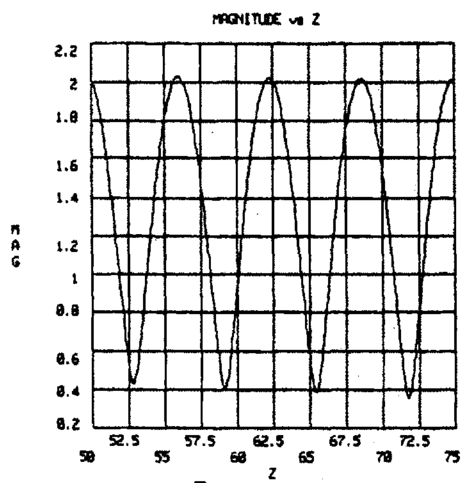

Figure 18

```
INPUT      scank=0.0  s= 1  phase=0.0  n= 500  r=54.0
DATA       kzi=0.001052  p= 0.00  z=  0.00  zmin= 50.00  zmax= 75.00
           kminf=0.900  kmaxf=1.100  kmult= 1.00  ksubt= 0.00
           kzfa=.000  kzff=.10000E+04

AVERAGE    adr= -0.0050   adi=  0.0193   adm=  1.3431   adp=  0.4996
AVE DEV    adrs=  1.0603  adrrs=  1.0603  adms=  0.5650  admrs=  0.5650
STAND DEV  sdrs=  1.3229  sdrrs=  1.3229  sdms=  0.6447  sdmrs=  0.6447
```

$k_i = .01/R$

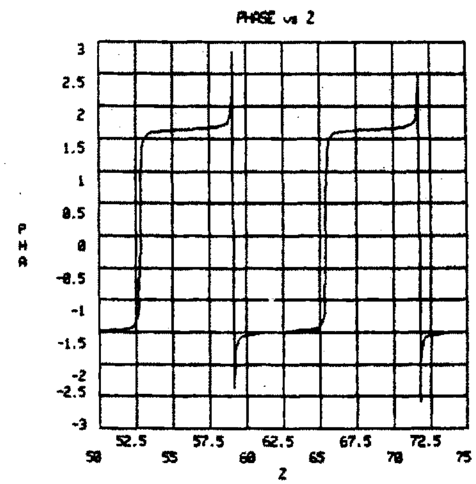

Figure 19

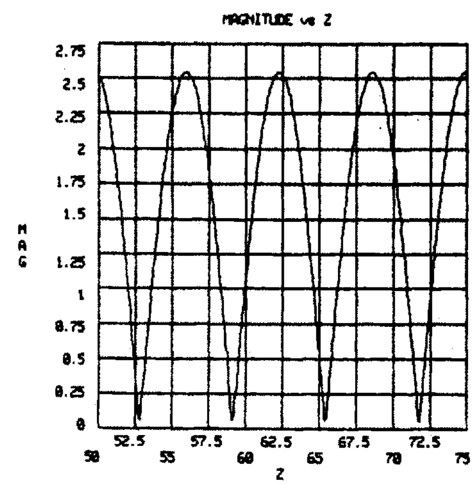

Figure 20

```
INPUT      scank=0.0  s= 1  phase=0.0  n= 500  r=54.0
DATA       kzi=0.000105  p= 0.00  z=  0.00  zmin= 50.00  zmax= 75.00
           kminf=0.900  kmaxf=1.100  kmult= 1.00  ksubt= 0.00
           kzfa=.000  kzff=.10000E+04

AVERAGE    adr= -0.0000   adi=  0.0234   adm=  1.6160   adp=  0.0891
AVE DEV    adrs=  1.0000  adrrs=  1.0000  adms=  0.8600  admrs=  0.8600
STAND DEV  sdrs=  1.0102  sdrrs=  1.0102  sdms=  0.9546  sdmrs=  0.9546
```

Phase and Magnitude Toroidal Position Scan for k_i = 1/R, .1/R and .01/R

1 Mode

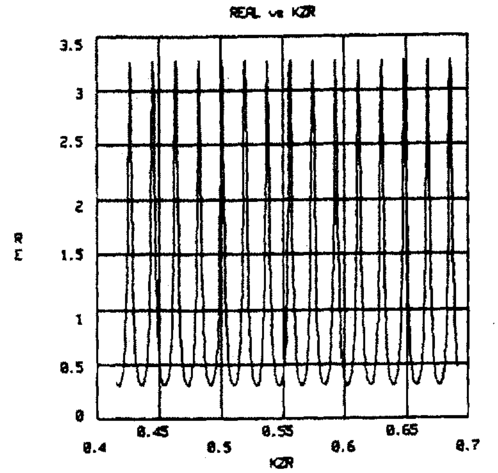

INPUT DATA scank=1.0 s= 1 phase=0.0 n= 500 r=54.0
kzi=0.001052 p= 0.00 z= 0.00 zmin= 0.00 zmax= 60.00
kminf=0.750 kmaxf=1.250 kmult= 1.00 ksubt= 0.000
kzfa=.000 kzff=.10000E+04 kzr0(1)=0.55340

AVERAGE adr= 1.0029 adi= -0.0023 adm= 1.3156 adp= -0.0042
AVE DEV adrs= 0.7174 adrrs= 0.7174 adms= 0.7599 admrs= 0.7599
STAND DEV sdrs= 0.8938 sdrrs= 0.8938 sdms= 0.9865 sdmrs= 0.9865

Figure 21

3 Modes

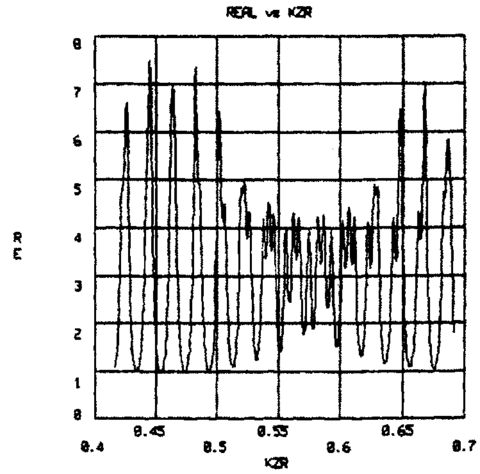

INPUT DATA scank=1.0 s= 3 phase=0.0 n= 500 r=54.0
kzi=0.001052 p= 0.00 z= 0.00 zmin= 0.00 zmax= 60.00
kminf=0.750 kmaxf=1.250 kmult= 1.00 ksubt= 0.000
kzfa=.000 kzff=.10000E+04 kzr0(1)=0.55340

AVERAGE adr= 3.0264 adi= -0.0124 adm= 3.4294 adp= -0.0078
AVE DEV adrs= 1.3575 adrrs= 1.5671 adms= 1.3561 admrs= 1.8519
STAND DEV sdrs= 1.5919 sdrrs= 2.0515 sdms= 1.6370 sdmrs= 2.3193

Figure 22

10 Modes

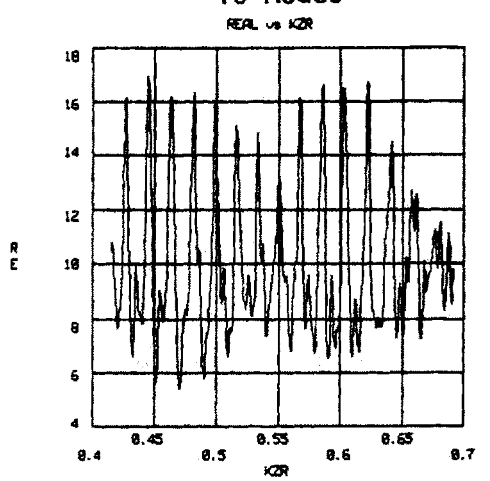

INPUT DATA scank=1.0 s=10 phase=0.0 n= 500 r=54.0
kzi=0.001052 p= 0.00 z= 0.00 zmin= 0.00 zmax= 60.00
kminf=0.750 kmaxf=1.250 kmult= 1.00 ksubt= 0.000
kzfa=.000 kzff=.10000E+04 kzr0(1)=0.55340

AVERAGE adr= 9.9892 adi= -0.0052 adm= 10.3204 adp= -0.0005
AVE DEV adrs= 2.1206 adrrs= 6.8270 adms= 2.1573 admrs= 7.1581
STAND DEV sdrs= 2.6486 sdrrs= 7.3227 sdms= 2.7218 sdmrs= 7.6514

Figure 23

20 Modes

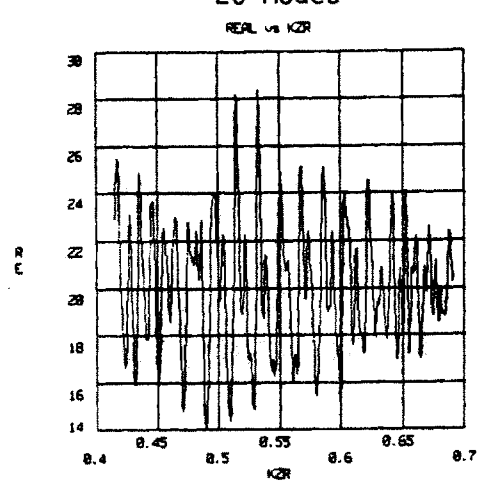

INPUT DATA scank=1.0 s=20 phase=0.0 n= 500 r=54.0
kzi=0.001052 p= 0.00 z= 0.00 zmin= 0.00 zmax= 60.00
kminf=0.750 kmaxf=1.250 kmult= 1.00 ksubt= 0.000
kzfa=.000 kzff=.10000E+04 kzr0(1)=0.55340

AVERAGE adr= 20.0391 adi= 0.0005 adm= 20.2136 adp= 0.0005
AVE DEV adrs= 2.1732 adrrs= 15.5669 adms= 2.1743 admrs= 15.7414
STAND DEV sdrs= 2.6640 sdrrs= 15.7932 sdms= 2.6710 sdmrs= 15.9650

Figure 24

Radiation Resistance of the sum of 1, 3, 10 and 20 modes for k_i = .1/R and no mode splitting

1 mode

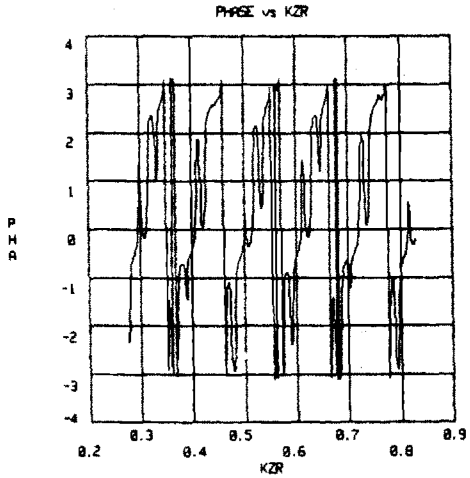

Figure 25

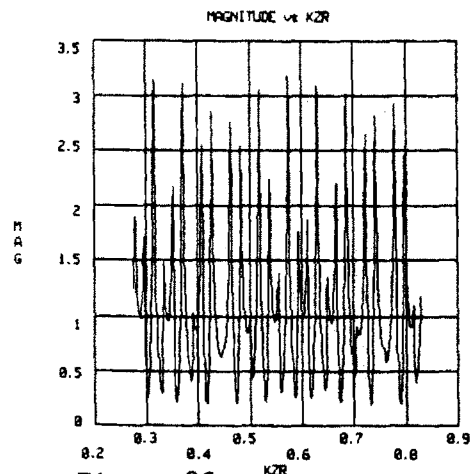

Figure 26

INPUT DATA scank=1.0 s= 1 phase=1.0 n= 500 r=54.0
kzi=0.001852 p= 0.00 z= 60.00 zmin= 0.00 zmax= 60.00
kminf=0.500 kmaxf=1.500 kmult= 1.00 ksubt= 0.000
kzfa=.000 kzff=.10000E+04 kzr0(1)=0.55340

AVERAGE ar= 0.0363 ai= -0.0234 am= 1.0700 ap= 0.3346
AVE DEV adrs= 1.0679 adrrs= 1.0679 adms= 0.4836 admrs= 0.4836
STAND DEV sdrs= 1.3140 sdrrs= 1.3140 sdms= 0.6604 sdmrs= 0.6604

3 modes

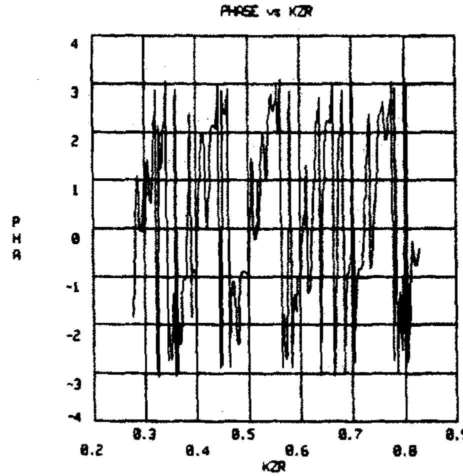

Figure 27

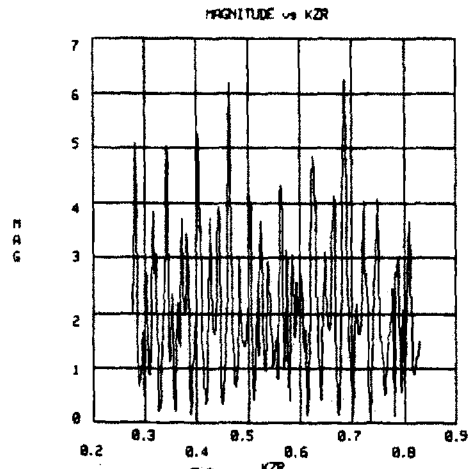

Figure 28

INPUT DATA scank=1.0 s= 3 phase=1.0 n= 500 r=54.0
kzi=0.001852 p= 0.00 z= 60.00 zmin= 0.00 zmax= 60.00
kminf=0.500 kmaxf=1.500 kmult= 1.00 ksubt= 0.000
kzfa=.000 kzff=.10000E+04 kzr0(1)=0.55340

AVERAGE ar= 0.0231 ai= -0.0120 am= 2.0560 ap= 0.1679
AVE DEV adrs= 3.0547 adrrs= 1.9637 adms= 1.3300 admrs= 0.9541
STAND DEV sdrs= 3.4243 sdrrs= 2.4050 sdms= 1.5436 sdmrs= 1.2635

10 modes

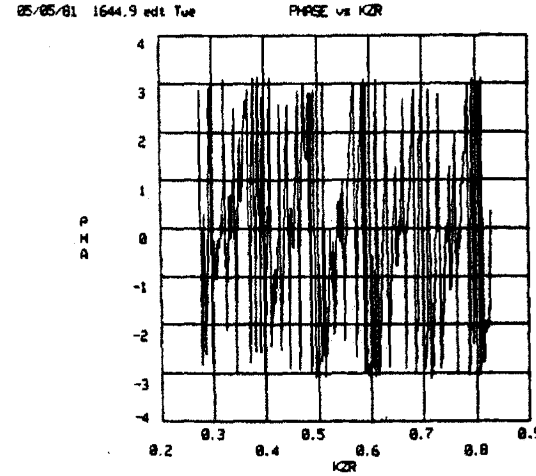

Figure 29

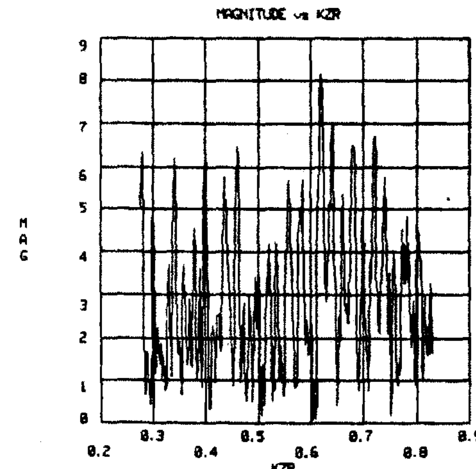

Figure 30

INPUT DATA scank=1.0 s=10 phase=1.0 n= 500 r=54.0
kzi=0.001852 p= 0.00 z= 60.00 zmin= 0.00 zmax= 60.00
kminf=0.500 kmaxf=1.500 kmult= 1.00 ksubt= 0.000
kzfa=.000 kzff=.10000E+04 kzr0(1)=0.55340

AVERAGE ar= -0.0160 ai= -0.0404 am= 2.9365 ap= -0.0977
AVE DEV adrs= 10.0160 adrrs= 3.3685 adms= 7.0635 admrs= 1.3975
STAND DEV sdrs= 10.2964 sdrrs= 3.9745 sdms= 7.2567 sdmrs= 1.6780

Phase and Magnitude of 1, 3, and 10 modes at r = 60, with Random Initial Phase, k_i = .1/R and No Mode Splitting.

Probe Signal Simulations for 10 modes and Spectrum Widths of .01, .1 and 1/cm

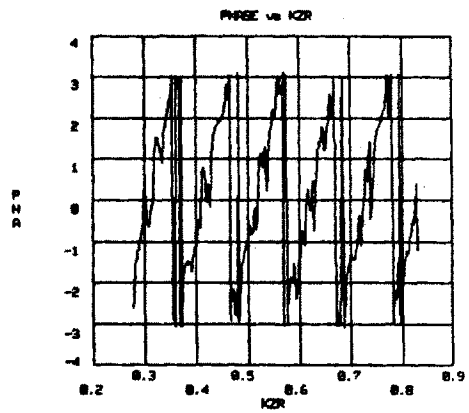

Figure 31

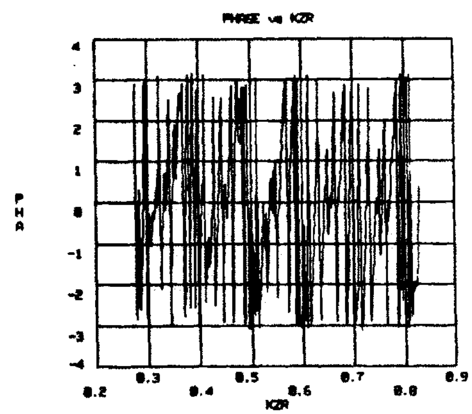

Figure 33

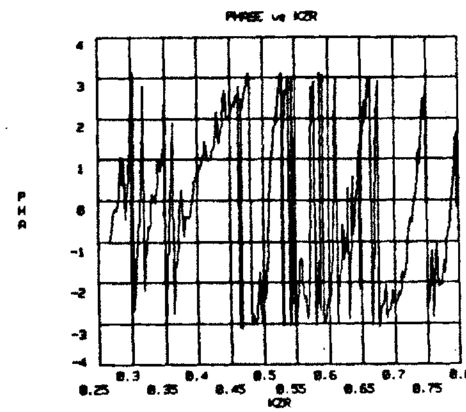

Figure 35

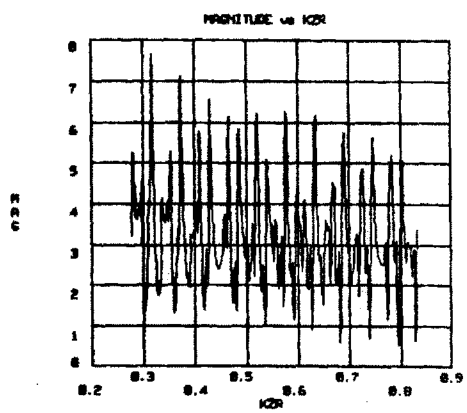

INPUT DATA
scank=1.0 s=10 phase=1.0 n= 500 r=54.0
kzl=0.001852 p= 0.00 z= 60.00 zmin= 0.00 zmax= 60.00
kminf=0.500 kmaxf=1.500 kmult= 0.10 ksubt=-5.000
kzfa=.000 kzff=.10000E+04 kzr0(1)=0.55340

AVERAGE ar= 0.0090 ai= -0.1217 am= 3.2472 ap= 0.0175
AVE DEV adrs= 9.9310 adrrs= 3.3260 adms= 6.7520 adwrs= 0.9497
STAND DEV sdrs= 10.2249 sdrrs= 3.9360 sdms= 6.8616 sdwrs= 1.2203

$\Delta k_{\parallel}$ = .01/cm

Figure 32

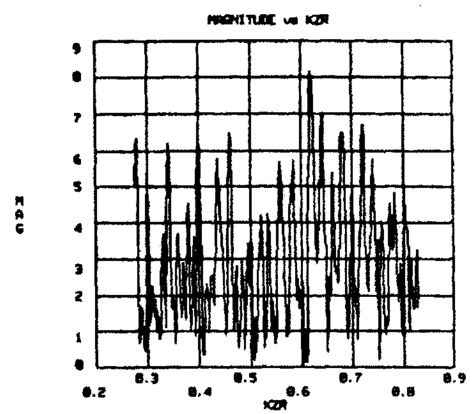

INPUT DATA
scank=1.0 s=10 phase=1.0 n= 500 r=54.0
kzl=0.001852 p= 0.00 z= 60.00 zmin= 0.00 zmax= 60.00
kminf=0.500 kmaxf=1.500 kmult= 1.00 ksubt= 0.000
kzfa=.000 kzff=.10000E+04 kzr0(1)=0.55340

AVERAGE ar= -0.0160 ai= -0.0404 am= 2.9365 ap= -0.0977
AVE DEV adrs= 10.0160 adrrs= 3.3605 adms= 7.0635 adwrs= 1.3975
STAND DEV sdrs= 10.2964 sdrrs= 3.9745 sdms= 7.2567 sdwrs= 1.6700

$\Delta k_{\parallel}$ = .1/cm

Figure 34

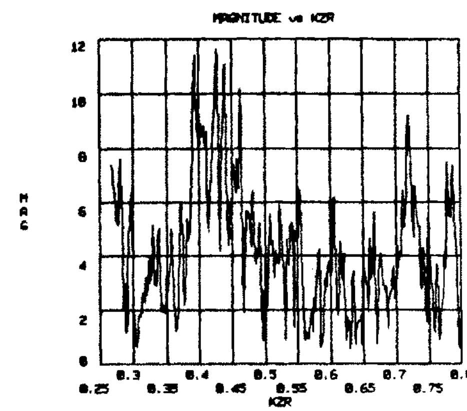

INPUT DATA
scank=1.0 s=10 phase=1.0 n= 500 r=54.0
kzl=0.001852 p= 0.00 z= 60.00 zmin= 0.00 zmax= 60.00
kminf=0.500 kmaxf=1.500 kmult=10.00 ksubt= 0.500
kzfa=.000 kzff=.10000E+04 kzr0(1)=0.55340

AVERAGE ar= 0.0460 ai= 0.1996 am= 4.1905 ap= -0.2125
AVE DEV adrs= 9.9615 adrrs= 3.9533 adms= 5.8400 adwrs= 1.0755
STAND DEV sdrs= 10.5279 sdrrs= 4.6332 sdms= 6.2499 sdwrs= 2.5234

$\Delta k_{\parallel}$ = 1/cm

Figure 36

Probe Signal Simulations for One Mode and 1% and 10% $k_{\parallel}$ Fluctuations

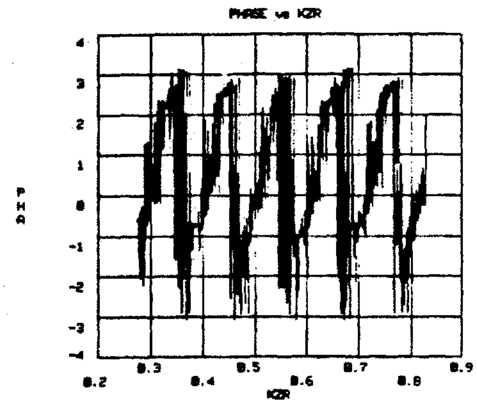

Figure 37

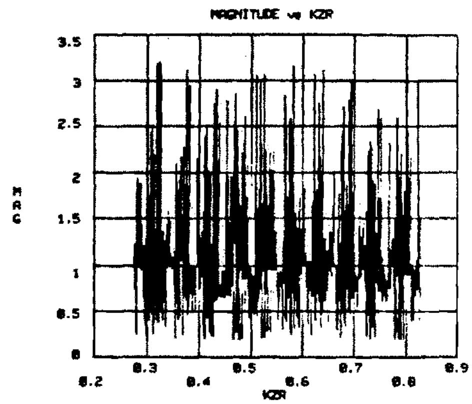

Figure 38

1% Fluctuations

```
INPUT      acank=1.0  s= 1  phase=1.0  n= 500  r=54.0
DATA       kzi=0.001852  p= 0.00  z= 60.00  zmin=  0.00  zmax=  60.00
           kminf=0.500  kmaxf=1.500  kmult= 1.00  ksubt= 0.000
           kzfa=.010  kzff=.10000E+04  kzr0(1)=0.55340

AVERAGE    ar=  0.0377   ai= -0.0052   am=  1.1220   ap=  0.3986
AVE DEV    adr=  1.0337  adrr=  1.0337  adm=  0.5245  admr=  0.5245
STAND DEV  sdr=  1.2557  sdrr=  1.2557  sdm=  0.7155  sdmr=  0.7155
```

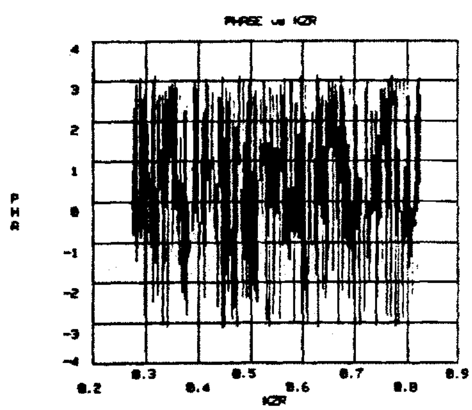

Figure 39

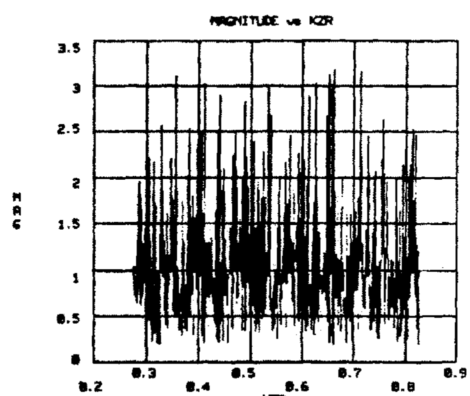

Figure 40

10% Fluctuations

```
INPUT      acank=1.0  s= 1  phase=1.0  n= 500  r=54.0
DATA       kzi=0.001852  p= 0.00  z= 60.00  zmin=  0.00  zmax=  60.00
           kminf=0.500  kmaxf=1.500  kmult= 1.00  ksubt= 0.000
           kzfa=.100  kzff=.10000E+04  kzr0(1)=0.55340

AVERAGE    ar=  0.0429   ai=  0.0126   am=  1.0529   ap=  0.4316
AVE DEV    adr=  1.0000  adrr=  1.0000  adm=  0.4722  admr=  0.4722
STAND DEV  sdr=  1.3002  sdrr=  1.3002  sdm=  0.6318  sdmr=  0.6318
```

Probe Signal Simulations for 10 modes and k_i = 1/R, .1/R and .01/R

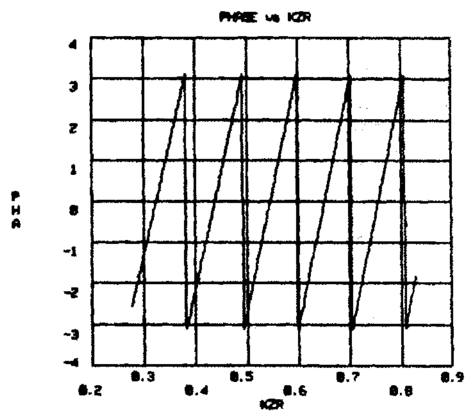

Figure 41

k_i = 1/R

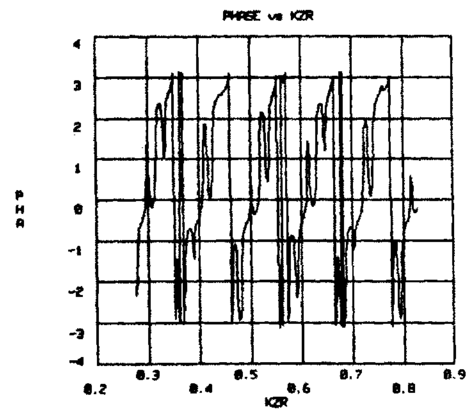

Figure 43

k_i = .1/R

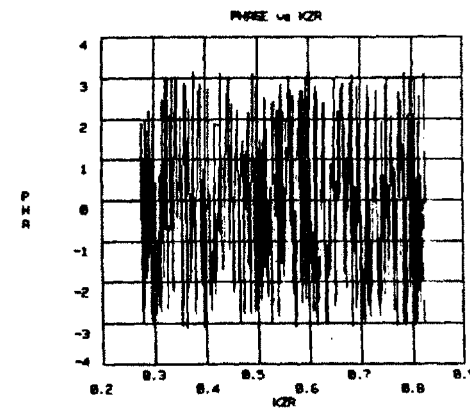

Figure 45

k_i = .01/R

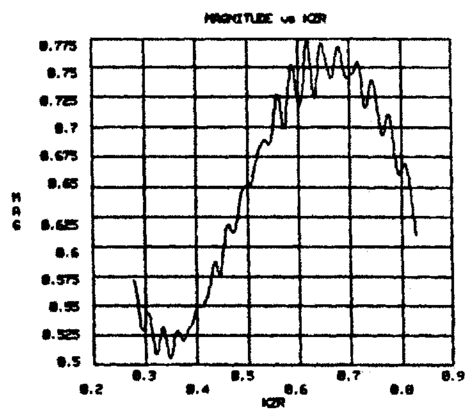

INPUT DATA scank=1.0 s=10 phase=1.0 n= 500 r=54.0
kzi=0.010520 p= 0.00 z= 60.00 zmin= 0.00 zmax= 60.00
kminf=0.500 kmaxf=1.500 kmult= 1.00 ksubt= 0.000
kzfa=.000 kzff=.10000E+04 kzr0(1)=0.55340

AVERAGE ar= -0.0091 ai= -0.0115 am= 0.6521 ap= -0.0011
AVE DEV adrs= 10.0091 adrrs= 3.1714 adms= 9.3479 admrs= 2.5102
STAND DEV sdrs= 10.0199 sdrrs= 3.2052 sdms= 9.3483 sdmrs= 2.5117

Figure 42

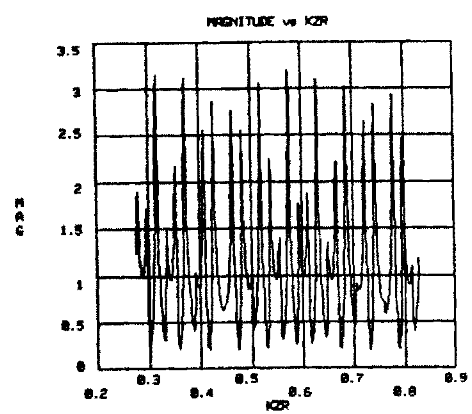

INPUT DATA scank=1.0 s= 1 phase=1.0 n= 500 r=54.0
kzi=0.001052 p= 0.00 z= 60.00 zmin= 0.00 zmax= 60.00
kminf=0.500 kmaxf=1.500 kmult= 1.00 ksubt= 0.000
kzfa=.000 kzff=.10000E+04 kzr0(1)=0.55340

AVERAGE ar= 0.0363 ai= -0.0234 am= 1.0788 ap= 0.3346
AVE DEV adrs= 1.0679 adrrs= 1.0679 adms= 0.4836 admrs= 0.4836
STAND DEV sdrs= 1.3148 sdrrs= 1.3148 sdms= 0.6604 sdmrs= 0.6604

Figure 44

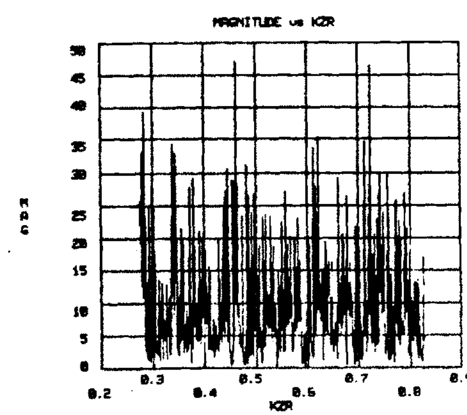

INPUT DATA scank=1.0 s=10 phase=1.0 n= 500 r=54.0
kzi=0.000105 p= 0.00 z= 60.00 zmin= 0.00 zmax= 60.00
kminf=0.500 kmaxf=1.500 kmult= 1.00 ksubt= 0.000
kzfa=.000 kzff=.10000E+04 kzr0(1)=0.55340

AVERAGE ar= 0.1164 ai= 0.0789 am= 9.4967 ap= -0.0055
AVE DEV adrs= 11.2596 adrrs= 6.8660 adms= 6.4856 admrs= 6.0841
STAND DEV sdrs= 13.3149 sdrrs= 9.4276 sdms= 0.2590 sdmrs= 10.3963

Figure 46

Effect of Mode Splitting on One Mode

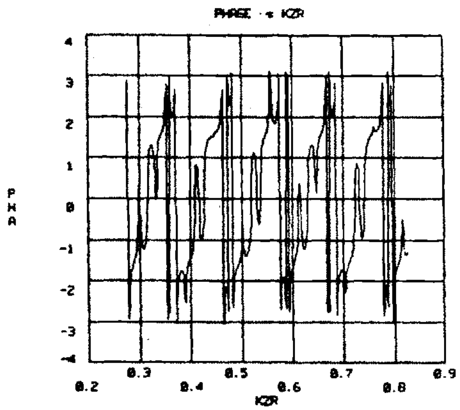

Figure 47

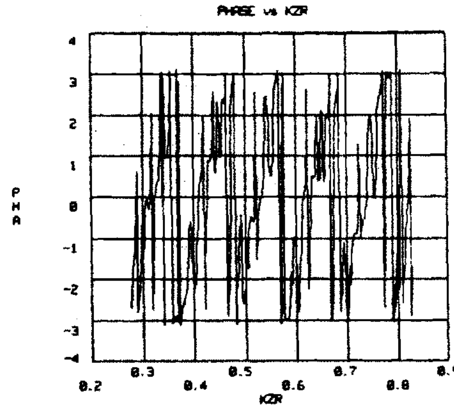

Figure 49

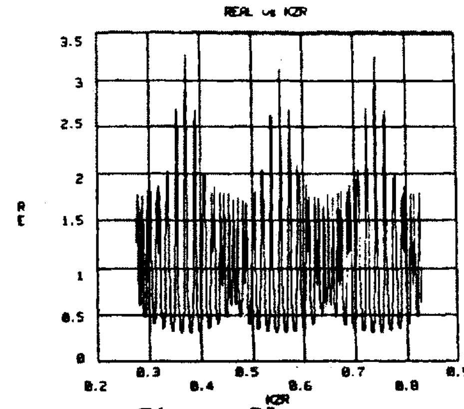

Figure 51

```
INPUT     scank=1.0  e= 1  phase=0.0  n= 500  r=54.0.
DATA      kzi=0.001852  p= 0.10  z=  0.00  zmin=  0.00  zmax=  60.00
          kminf=0.500  kmaxf=1.500  kmult= 1.00  ksubt= 0.000
          kzfa=.000  kzff=.10000E+04  kzr0(1)=0.55340

AVERAGE   ar=  1.0014   ai=  0.0014   am=  1.1783   ap=  0.0018
AVE DEV   adrs=  0.5300  adrrs=  0.5300  adms=  0.5372  admrs=  0.5372
STAND DEV sdrs=  0.6323  sdrrs=  0.6323  sdms=  0.6676  sdmrs=  0.6676
```

One Nonsplit Mode

One 10% Split Mode

Split and Nonsplit R_R with One Mode

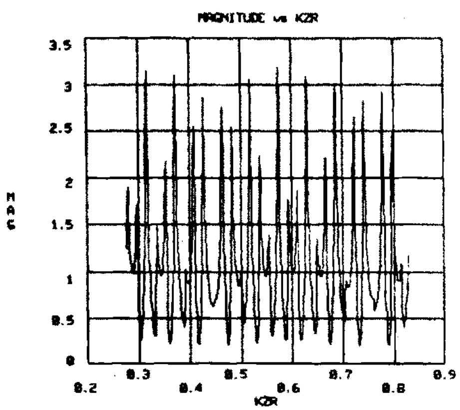


```
INPUT     scank=1.0  e= 1  phase=0.0  n= 500  r=54.0
DATA      kzi=0.001852  p= 0.00  z=  60.00  zmin=  0.00  zmax=  60.0
          kminf=0.500  kmaxf=1.500  kmult= 1.00  ksubt= 0.000
          kzfa=.000  kzff=.10000E+04  kzr0(1)=0.55340

AVERAGE   ar= -0.0022   ai= -0.0431   am=  1.0700   ap= -0.0348
AVE DEV   adrs=  1.1492  adrrs=  1.1492  adms=  0.4836  admrs=  0.483
STAND DEV sdrs=  1.3370  sdrrs=  1.3370  sdms=  0.6604  sdmrs=  0.660
```

Figure 48

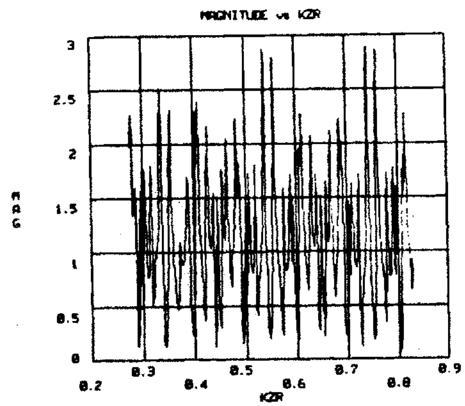


```
INPUT     scank=1.0  e= 1  phase=0.0  n= 500  r=54.0
DATA      kzi=0.001852  p= 0.10  z=  60.00  zmin=  0.00  zmax=  60.00
          kminf=0.500  kmaxf=1.500  kmult= 1.00  ksubt= 0.000
          kzfa=.000  kzff=.10000E+04  kzr0(1)=0.55340

AVERAGE   ar=  0.0050   ai= -0.0424   am=  1.1304   ap= -0.0963
AVE DEV   adrs=  1.1109  adrrs=  1.1109  adms=  0.4596  admrs=  0.4596
STAND DEV sdrs=  1.3376  sdrrs=  1.3376  sdms=  0.5097  sdmrs=  0.5097
```

Figure 50

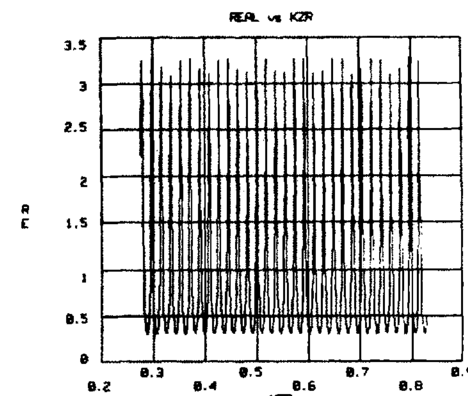


```
INPUT     scank=1.0  e= 1  phase=0.0  n= 500  r=54.0
DATA      kzi=0.001852  p= 0.00  z=  0.00  zmin=  0.00  zmax=  60.00
          kminf=0.500  kmaxf=1.500  kmult= 1.00  ksubt= 0.000
          kzfa=.000  kzff=.10000E+04  kzr0(1)=0.55340

AVERAGE   ar=  1.0001   ai=  0.0057   am=  1.3111   ap=  0.0043
AVE DEV   adrs=  0.7192  adrrs=  0.7192  adms=  0.7591  admrs=  0.759
STAND DEV sdrs=  0.8946  sdrrs=  0.8946  sdms=  0.9859  sdmrs=  0.985
```

Figure 52

Effect of Mode Splitting on One Mode for k_i = .01/R and S = 0, 1% and 100%

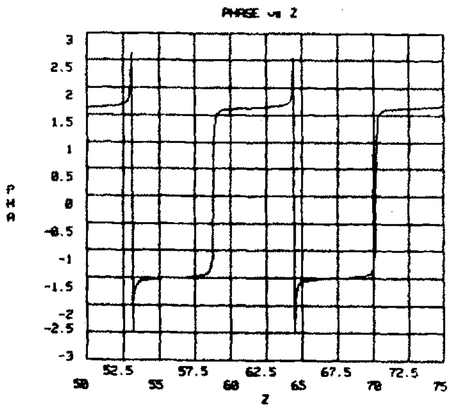

Figure 53

Nonsplit

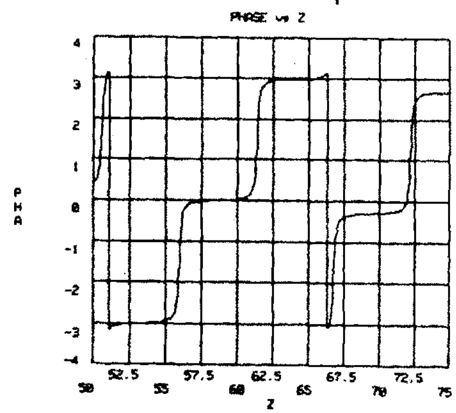

Figure 55

10% Split

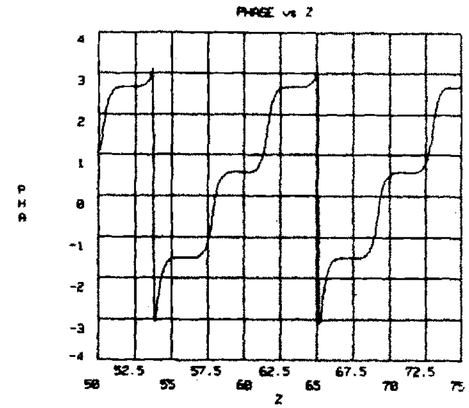

Figure 57

100% Split

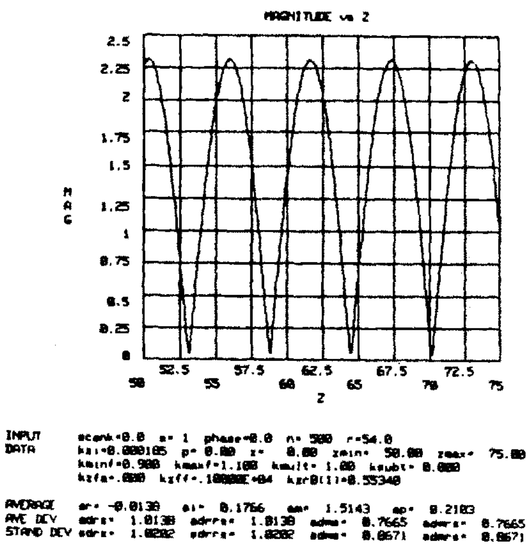

Figure 54

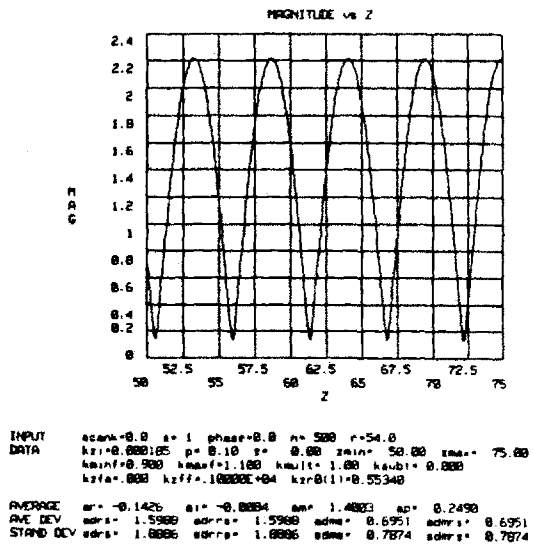

Figure 56

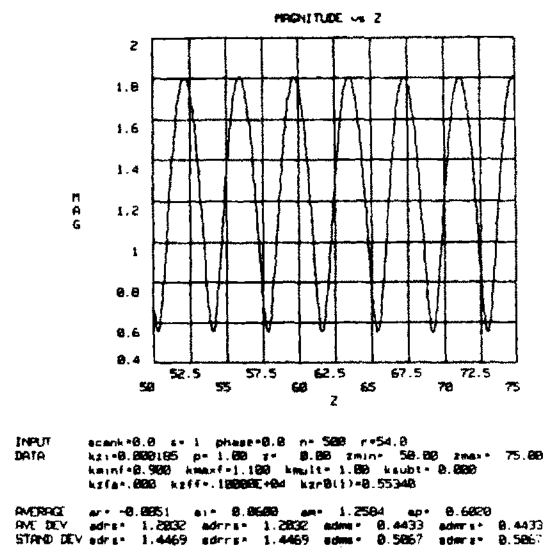

Figure 58

IV-7. The Single Perpendicular Pass Regime

In the presence of very strong damping mechanisms, neither parallel or perpendicular eigenmodes can occur. Our previous waveguide treatment must be significantly modified to account for the excited spectrum of the antenna. The concept of group velocity becomes an important analytical and intuitive tool for estimating energy propagation and deposition in this regime.

IV-7.1. Single perpendicular pass radiation resistance

To estimate the single perpendicular pass radiation resistance, we will model the antenna and plasma in the semi-infinite Cartesian geometry shown in Figure 1. The antenna is modeled as a Fourier transformed current sheet at r_a [126]

(1) $$J_k = J_o \, e^{i(kz - \omega t)}$$

backed by an infinitely conducting wall at r_w. The semi-infinite plasma is modeled as a flat density profile starting at r_c (cutoff radius), which will be a function of $k_{\parallel}$, as we shall see shortly. Only E in the direction of J needs to be considered, so that we define

(2) $$E_k = E_y \simeq E_\Theta$$

Neglecting vacuum displacement currents, the electric field in the three regions a, b, and c can be written as

(3) $$E_a = A \, e^{i k_r r}$$

(4) $$E_b = B \, e^{kr} + C \, e^{-kr}$$

(5) $E_c = D\,e^{kr} + F\,e^{-kr}$

where E_a is propagating and E_b and E_c are evanescent. From continuity in E_y, we have the boundary conditions

(6) $E_c(r_w) = 0$

(7) $E_b(r_a) = E_c(r_a)$

(8) $E_a(r_c) = E_b(r_c)$

From continuity in H_z ($H_z \propto \partial E/\partial r$), we have

(9) $\frac{d}{dr}[E_a(r_c) - E_b(r_c)] = 0$

(10) $\frac{d}{dr}[E_b(r_a) - E_c(r_a)] = \frac{4\pi\, i\, \omega\, J_k}{c^2}$

By making the judicious change of variables

(11) $\delta_1 = r_a - r_c$

(12) $\delta_2 = r_w - r_a$

(13) $\delta_3 = \delta_1 + \delta_2 = r_w - r_c$

equations (3) through (10) can be reduced to five compact equations and five unknowns.

(14) $D = -F\,e^{-2k\delta_2}$

(15) $E(r_a) = B + C = D + F$

(16) $Ae^{-ik_r\delta_1} = Be^{-k\delta_1} + Ce^{+k\delta_1}$

$$(17)\quad ik_r Ae^{-ik_r\delta_1} = kBe^{-k\delta_1} - kCe^{k\delta_1}$$

$$(18)\quad B - D + F - C = \frac{4\pi\, i\, \omega\, J}{kc^2}$$

which, after some lengthy algebra, can be solved to give the Fourier transformed electric field at the antenna (15).

$$(19)\quad E_k\,(r_a) = \frac{2\pi i\omega\, J_k}{kc^2}\,(e^{k\delta_2} - e^{-k\delta_2}) \times \frac{k(e^{k\delta_1} + e^{-k\delta_1}) + ik_r(e^{k\delta_1} - e^{-k\delta_1})}{k(e^{k\delta_3} + e^{-k\delta_3}) + ik_r(e^{k\delta_3} - e^{-k\delta_3})}$$

Fourier transforming the antenna current strip, we have

$$(20)\quad J_k = \frac{1}{2\pi}\int_{-w/2}^{+w/2} J_\circ\, e^{-ikz}dz = \frac{J_\circ w}{2\pi}\,\frac{\sin k\, w/2}{k\, w/2}$$

and

$$(21)\quad I_\circ = J_\circ w$$

The inverse transform of the electric field at the antenna radius is

$$(22)\quad E(r_a,\, z) = \int_{-\infty}^{+\infty} E_k(r_a)\, e^{ikz}\, dk$$

The Fourier spectrum of the antenna complex impedence is

$$(23)\quad Z_k = \frac{E_k(r_a)}{I_\circ}$$

and the inverse transform is

$$(24)\quad Z = \int_{-\infty}^{+\infty} \frac{E_k(r_a)}{I_\circ}\, e^{ikz}dk \approx 2\int_{0}^{+2} \frac{E_k(r_a)}{I_\circ}\, dk$$

Radiation resistance and impedence per unit length are then simply

(25) $R_R/\text{cm} = \text{Re}\,[Z]$

(26) $X/\text{cm} = \text{Im}\,[Z]$

In this model, we furthermore let k_r and δ_1 be functions of k, which is of course, k_z. Assuming a parabolic density profile, the cutoff ($k_\parallel = 0$) density and radius (r_c), and thus δ_1, can be found by equations IV-2.5.(12) and IV-2.2.(6) as

(27) $n_c = \frac{1+\Omega}{\Omega^2} 5.16 \times 10^{14}\ \mu\ k^2$

(28) $\delta_1 = \delta_\circ + r_p \left(1 - \sqrt{1 - \frac{n_c}{n_\circ}}\right)$

The plasma density in region a is then assumed to be

(29) $n_a = \frac{n_\circ + n_c}{2}$

so that k_r can be calculated from equation IV-2.2.(6), assuming $k_\parallel = k$ and $n = n_a$.

Figures 2 and 3 show the real and imaginary parts of the k spectrum for typical Alcator conditions

μ = 2 (Deuterium)	r_a = 11 cm
Ω = 2	r_p = 9 cm
f. = 97 MHz	w = 3 cm
r_w = 12.5 cm	$n_\circ$ = 0, .5, 1, 5 x 10^{14} x $10^{14}/\text{cm}^3$

The integral of the imaginary part of the spectrum for $n_\circ = 0$ (ZINTI = 2.2 Ω/cm) is in reasonable agreement with ωL, as calculated from equations III-2.4.(1) and III-2.5.(9)

(30) $\omega L = \frac{\omega Z}{c} = 1.83\ \Omega/\text{cm}$

The reactance is also slightly decreased, as expected, when the high dielectric constant plasma is brought near the stripline antenna. The real part of the spectrum is concentrated at low $k_{\parallel}$, and its integral (ZINTR $\approx$ .25 Ω/cm) is much smaller than the imaginary part, and is weakly dependent on density.

Figures 4 and 5 show the 200 MHz hydrogen case, where we note how the no-plasma reactance exactly doubled as expected. The real part also approximately doubled.

These computational findings can be more physically understood by separating the problem into three parts; wave production, attenuation and transmission. Wave production can be visualized as a wave from the antenna center conductor that interferes with a wave reflected from the wall.

$$(31) \quad E \propto 1 - e^{-2k_{\parallel}\delta_2} \approx 2k_{\parallel}\delta_2$$

Halving $\delta_2 = r_w - r_a$ thus halves the electric field, and reduces the coupled power and radiation resistance by a factor of four (ZINTR = .065), just as in eigenmode coupling. This effect is clearly shown in Figure 6 where r_a was increased from 11 cm to 11.75 cm. The antenna reactance also decreased according to equation (30).

The attenuation is simply the evanescence between the antenna and the plasma

$$(32) \quad E \propto e^{-k_{\parallel}\delta_1}$$

and limits $k_{\parallel} < 1/\delta_1$. Decreasing r_p from 9 to 8 cm decreased R_R by about 40%, as shown in Figure 7.

The transmission factor between the evanescent wave in the vacuum region and the propagating wave in the plasma comes about from the mismatch between the plasma and vacuum impedences. From continuity of E and H, we have (Transmitted, Incident, Reflected)

$$(33)\quad E_T\, e^{ik_\perp r} = E_I\, e^{-k_\parallel r} - E_R\, e^{+k_\parallel r}$$

$$(34)\quad E_T\, i\, k_\perp e^{ik_\perp r} = -E_I\, k_\parallel e^{-k_\parallel r} - E_R\, k_\parallel e^{k_\parallel r}$$

and assuming for simplicity $r = 0$ and $E_I = 1$, we find

$$(35)\quad E_T \;\alpha\; \frac{f(k_\parallel)}{ik_\perp - k_\parallel}$$

For constant $k_\parallel$, E_T is dependent on density when $k_\perp << k_\parallel$. On the other hand, at high density and small $k_\parallel$, $k_\perp >> k_\parallel$ and

$$(36)\quad E_T \;\alpha\; \frac{f(k_\parallel)}{ik_\perp} \;\alpha\; \frac{1}{\sqrt{n}}$$

Figure 8 shows a similar case, but with deuterium at high density ($1 - 5 \times 10^{14}/cm^3$). For small $k_\parallel$ ($\simeq .1/cm$), the cutoff layer is nearly fixed to the plasma edge ($r_c = r_p$), so that equation (36) is valid, and

$$(37)\quad R_R \;\alpha\; EXH \;\alpha\; k_\perp E_T^2 \;\alpha\; \frac{1}{k_\perp} \;\alpha\; \frac{1}{\sqrt{n}}$$

which is in good agreement with Figure 8.

If a density gradient were included, the transmission coefficient would be slightly larger, but since

$$(38)\quad \lambda = \frac{2\pi}{k_\perp} \gtrsim k_\perp \left[\frac{\partial k_\perp}{\partial r}\right]^{-1}$$

our computational model is a good approximation.

The last variable is the width of the antenna. Since $w < 1/k_{real}$, the width has little affect on R_R. On the other hand, decreasing w increases the high end of the imaginary part of the $k_\parallel$ spectrum (Figure 9), and thus the impedence, also in agreement with equation (30).

Single Perpendicular Pass Regime Fast Wave Coupling Model

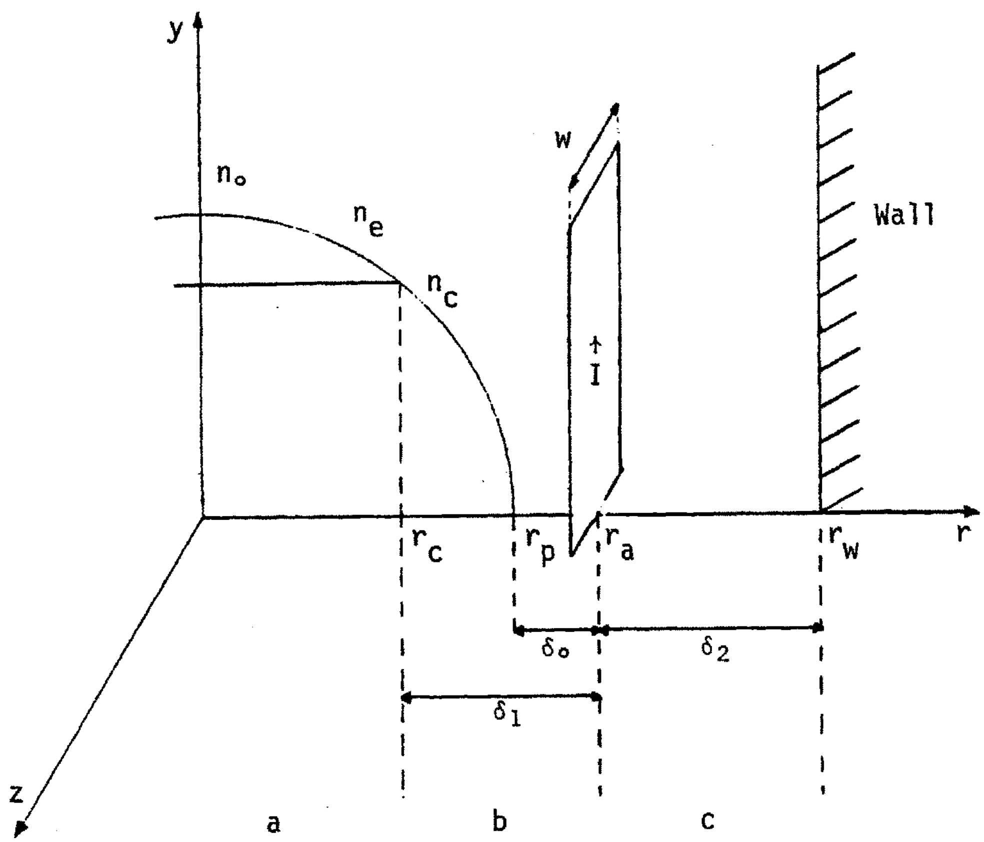

Figure 1

$k_{\parallel}$ Spectrum for D_2 at 97 MHz

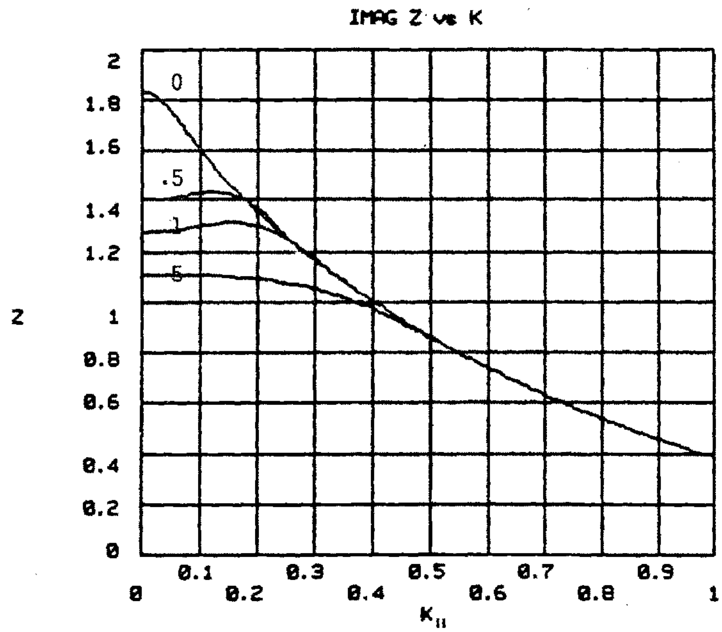

Figure 2

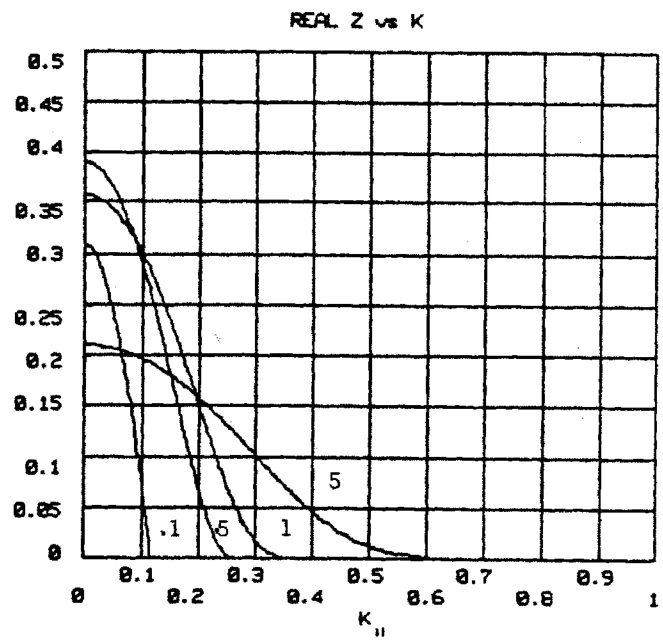

Figure 3

mu= 2.000 omega= 2.000 f=.97000E+08
rw=12.500 ra=11.000 rp= 9.000 ww= 3.000
n0=.00000E+00 zintr= 0.000 zinti= 2.204
n0=.50000E+14 zintr= 0.108 zinti= 2.131
n0=.10000E+15 zintr= 0.128 zinti= 2.081
n0=.50000E+15 zintr= 0.123 zinti= 1.952

$k_{\parallel}$ Spectrum for H_2 at 200 MHz

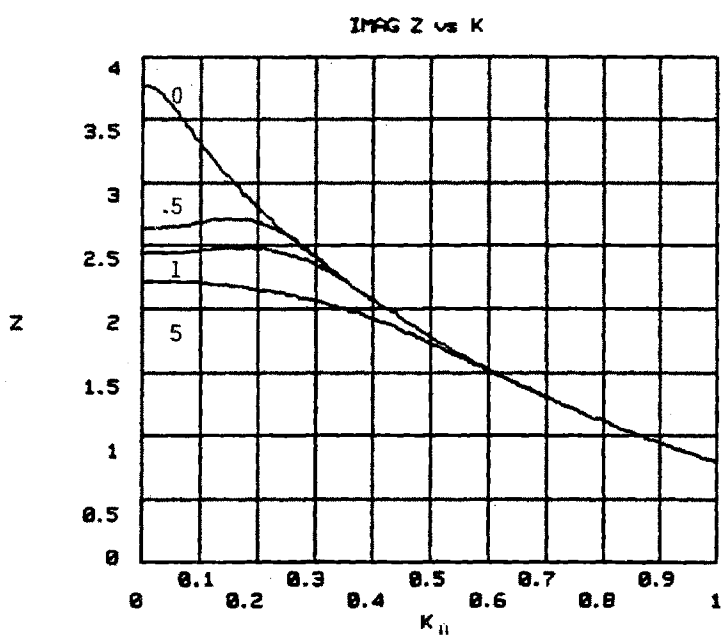

Figure 4

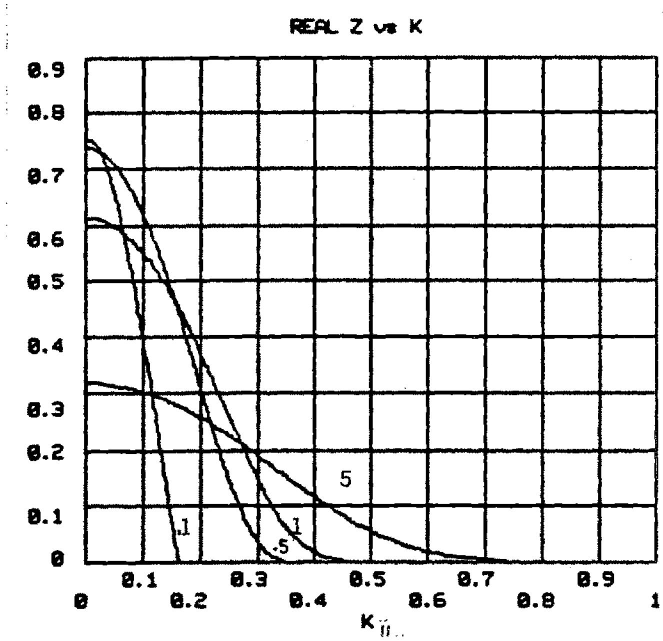

Figure 5

mu= 1.000 omega= 2.000 f=.20000E+09
rw=12.500 ra=11.000 rp= 9.000 ww= 3.000
n0=.00000E+00 zintr= 0.000 zinti= 4.544
n0=.50000E+14 zintr= 0.263 zinti= 4.298
n0=.10000E+15 zintr= 0.275 zinti= 4.172
n0=.50000E+15 zintr= 0.219 zinti= 3.935

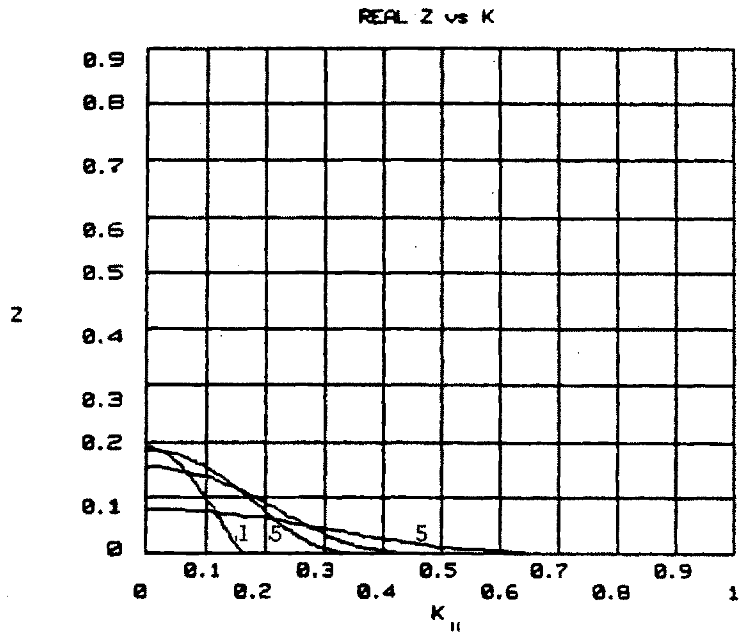

mu= 1.000 omega= 2.000 f=.20000E+09
rw=12.500 ra=11.750 rp= 9.000 ww= 3.000
n0=.10000E+14 zintr= 0.037 zinti= 2.442
n0=.50000E+14 zintr= 0.066 zinti= 2.392
n0=.10000E+15 zintr= 0.068 zinti= 2.363
n0=.50000E+15 zintr= 0.053 zinti= 2.306

d = .75 cm Figure 6

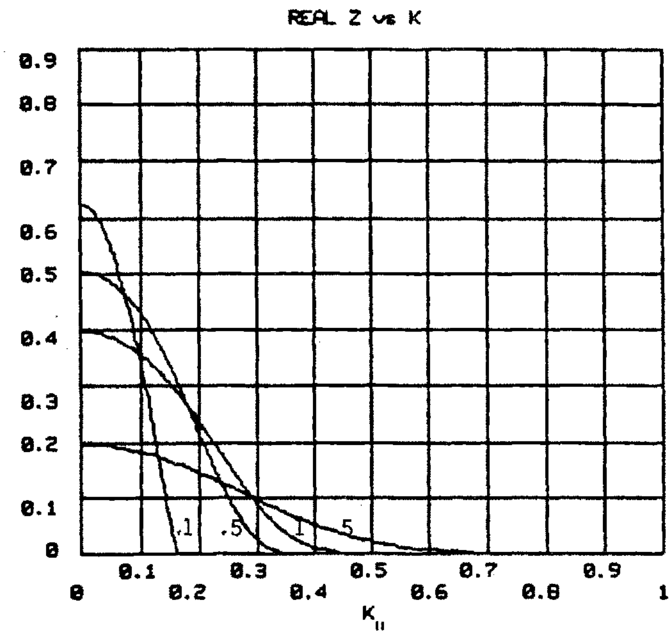

mu= 1.000 omega= 2.000 f=.20000E+09
rw=12.500 ra=11.000 rp= 8.000 ww= 3.000
n0=.10000E+14 zintr= 0.125 zinti= 3.832
n0=.50000E+14 zintr= 0.183 zinti= 3.678
n0=.10000E+15 zintr= 0.177 zinti= 3.604
n0=.50000E+15 zintr= 0.121 zinti= 3.480

r_p = 8 cm Figure 7

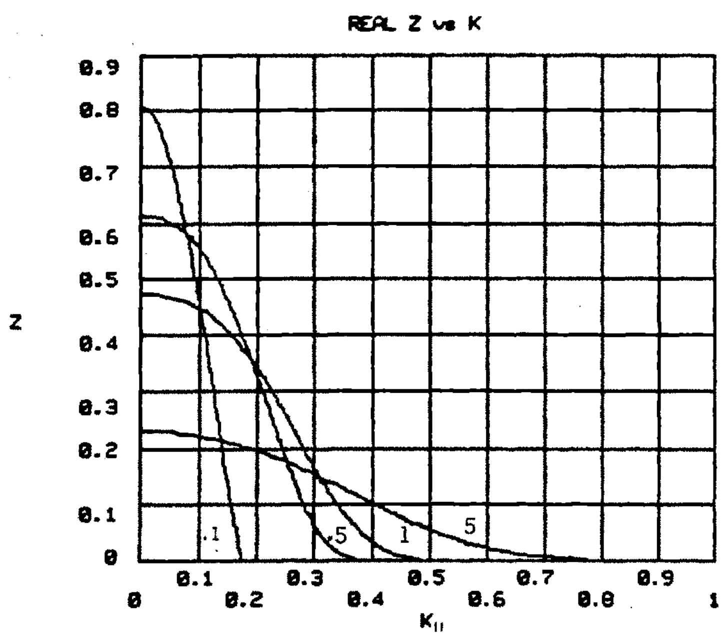

mu= 2.000 omega= 4.000 f=.20000E+09
rw=12.500 ra=11.000 rp= 9.000 ww= 3.000
n0=.10000E+14 zintr= 0.168 zinti= 3.802
n0=.50000E+14 zintr= 0.249 zinti= 3.575
n0=.10000E+15 zintr= 0.244 zinti= 3.461
n0=.50000E+15 zintr= 0.174 zinti= 3.250

D_2 at 200 MHz Figure 8

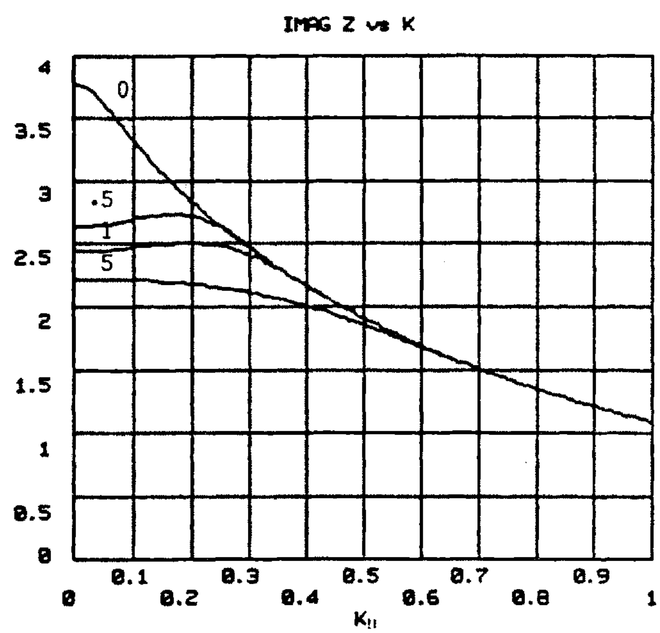

mu= 1.000 omega= 2.000 f=.20000E+09
rw=12.500 ra=11.000 rp= 9.000 ww= 1.500
n0=.00000E+00 zintr= 0.000 zinti= 5.545
n0=.50000E+14 zintr= 0.264 zinti= 5.290
n0=.10000E+15 zintr= 0.278 zinti= 5.172
n0=.50000E+15 zintr= 0.224 zinti= 4.929

w = 1.5 cm Figure 9

IV-7.2. Group velocity and simple ray tracing

The normalized fast wave dispersion relation is well approximated by (IV-2.2.(21))

$$(1) \quad N_\perp^2 + (1 + \Omega)\, N_\parallel^2 = 1$$

$$(2) \quad k_\perp^2 = k_x^2 + k_y^2 = \frac{\omega^2}{V_A^2} - (1 + \Omega)\, k_\parallel^2$$

The group velocity in the y direction (θ) is[144]

$$(3) \quad v_{gy} = \frac{\partial\omega}{\partial k_y} = \left(\frac{\partial k_y}{\partial\omega}\right)^{-1}$$

Combining (2) and (3), we have

$$(4) \quad \frac{1}{v_{gy}} = \frac{\partial k_y}{\partial\omega} = \frac{1}{2k_y}\left[\frac{2\omega}{V_A^2} - \frac{k_\parallel^2}{\omega_{ci}}\right]$$

and similarly for v_{gx}, so that

$$(5) \quad \frac{v_{gy}}{v_{gx}} = \frac{k_y}{k_x} << 1$$

For practical purposes, this means that in the perpendicular plane, energy leaves the antenna at nearly right angles to the vacuum wall, as shown in Figure 1. The wave energy (rays) can even be slightly focused to the plasma center,due to the k_r gradient ($n(r)$). In the single perpendicular pass regime, as opposed to eigenmode coupling, the antenna must of course be fed in the push-pull mode for plasma center heating.

Substituting $k_\perp \to k_y$ in(4)gives the compact form

$$(6) \quad v_{g\perp} = \frac{N_\perp}{1 - \frac{\Omega}{2} N_\parallel^2}\, V_A$$

$$= \frac{N_\perp}{1 - N_\parallel^2}\, V_A \quad \text{for } \Omega = 2$$

$$= V_A \qquad \text{for } k_\parallel = 0$$

Similarly[11],

$$(7)\quad v_{g_\parallel} = \frac{(1+\Omega)N_\parallel}{1-\frac{\Omega}{2}N_\parallel^2} V_A$$

$$= \frac{3N_\parallel}{1-N_\parallel^2} V_A \quad \text{for } \Omega = 2$$

$$= \frac{(1+\Omega)^{3/2}}{1+\Omega/2} V_A \text{ for } k_\perp = 0$$

and finally, dividing (6) by (7), we have

$$(8)\quad \frac{v_{g\perp}}{v_{g_\parallel}} = \frac{1}{1+\Omega} \quad \frac{N_\perp}{N_\parallel}$$

Figure 2 shows a graph of the normalized N_{2x2} fast wave dispersion relation (IV-2.2.(18)), the normalized N elliptical (1) approximation, the normalized 1/N wave normal surface (normalized phase velocity), and the group velocity for $\Omega = 2$. The normalized phase velocity ω/kV_A, is simply $\frac{1}{|N|}$ in the direction of k. Locuses labeled by the number 4 for example, all refer to the case

$$(9)\quad k_\perp = k_\parallel = .5k_A$$

$$N_\perp = N_\parallel = .5$$

$$v_{p\perp} = v_{p_\parallel} = \sqrt{2}\ V_A$$

$$v_{g_\parallel} = 3v_{g\perp} = 2.0\ V_A$$

Simple ray tracing can be done graphically, as shown in Figure 3, by plotting the local group velocity on the wave normal surfaces for different times. The calculation and plot need to be done only once, since the copy can be photostatically reduced. The rays are then conformed to the group velocity vector field.

For the more realistic inhomogeneous plasma of the previous Section, we saw that almost all the power was coupled to small $k_{\parallel}$, due to the evanescent edge. Thus, outside the 45° wedge drawn in Figure 3, $k_{\parallel} > k_{\perp}$, and we need not worry about the more complicated boundary conditions at the plasma edge and vacuum chamber wall. Inside this wedge, our simple model is qualitatively correct, and we note in particular, how the phase fronts propagate at nearly right angles with the magnetic field. The group velocity, and thus the rays, on the other hand, have a very strong tendency to diverge in the parallel direction. The density gradient again tends to focus the rays by increasing $k_{\perp}$, so that most of the single pass energy at the plasma center should be enclosed in the 45° wedge, not that this wedge is in either k (wave normal) or x (wave front) space.

Since the fast wave is electromagnetic (Section IV-2.7.), power flow can also be followed with the Poynting flux vector (IV-1.3.)

(10) $S = \frac{E \times H}{2}$

and assuming $k_y = E_z = 0$

(11) $S_x = \frac{k_x}{2\omega\mu_o} E_y^2$

$S_y = 0 \qquad$ since $E_x \propto i\, E_y$

$S_z = \frac{k_z}{2\omega\mu_o}\left(E_x^2 + E_y^2\right)$

and

(12) $\frac{S_{\perp}}{S_{\parallel}} = \frac{E_y^2}{E_x^2 + E_y^2} \; \frac{k_{\perp}}{k_{\parallel}}$

From the first line of the wave tensor equation, II-2.2.(14)

$$(13) \quad \frac{E_x^2}{E_y^2} = \left[\frac{\Omega\, S}{S - n_{\parallel}^2}\right]^2$$

which combined with (12), gives the energy propagation direction

$$(14) \quad \frac{S_{\perp}}{S_{\parallel}} = \frac{1}{\left(\frac{\Omega}{1 - (1-\Omega^2)\, N_{\parallel}^2}\right)^2 + 1} \quad \frac{N_{\perp}}{N_{\parallel}}$$

$$= \frac{1}{5} \; \frac{N_{\perp}}{N_{\parallel}} \quad \text{for } \Omega = 2 \text{ and } N_{\parallel} = 0 \qquad (90°)$$

$$= \frac{1}{2.4} \; \frac{N_{\perp}}{N_{\parallel}} \quad \text{for } \Omega = 2 \text{ and } N_{\parallel} = .478 \quad (45°)$$

$$= \frac{1}{2} \; \frac{N_{\perp}}{N_{\parallel}} \quad \text{for } \Omega = 2 \text{ and } N_{\parallel} = .58 \quad (0°)$$

in qualitative agreement with the simple elliptical approximation of equation (8).

Perpendicular Ray Training

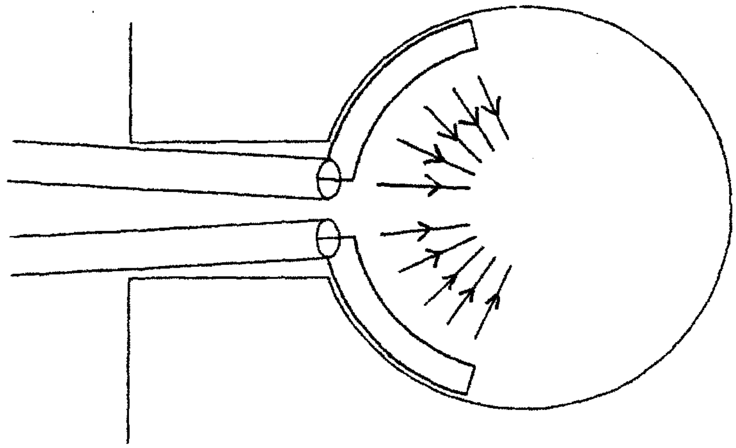

Figure 1

First Order Phase and Group Velocities for $\Omega = 2$

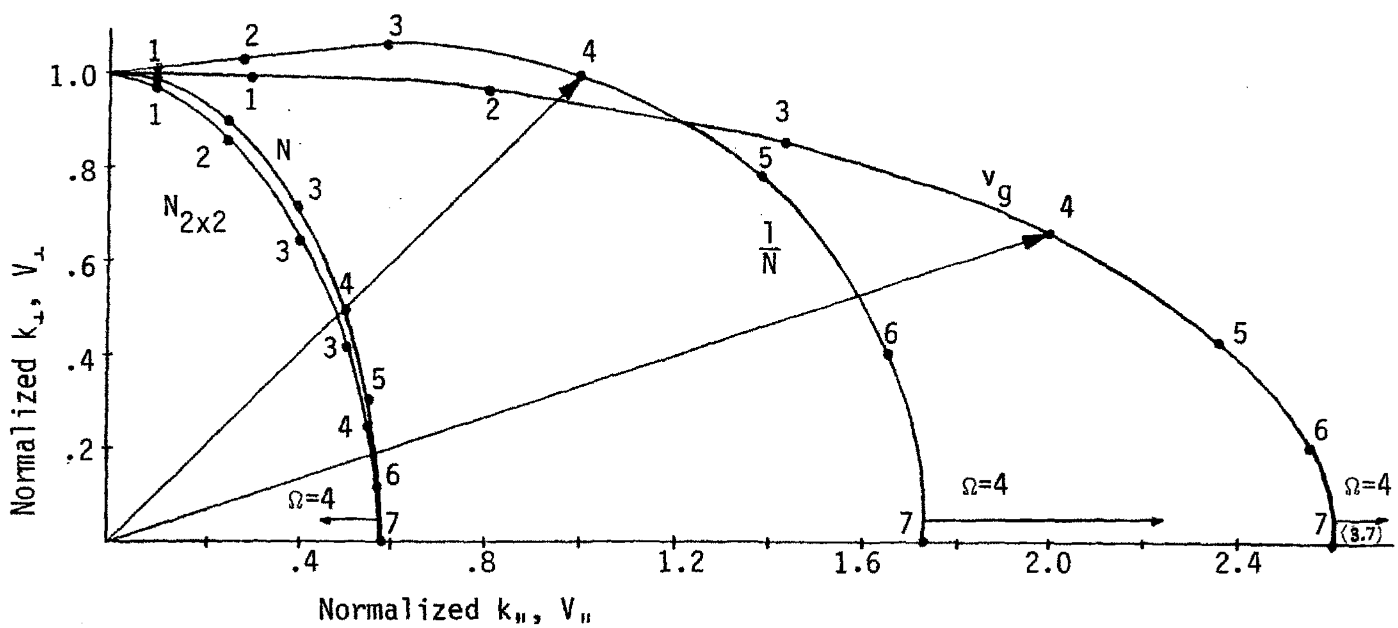

Figure 2

Phase Fronts and Simple Ray Tracing

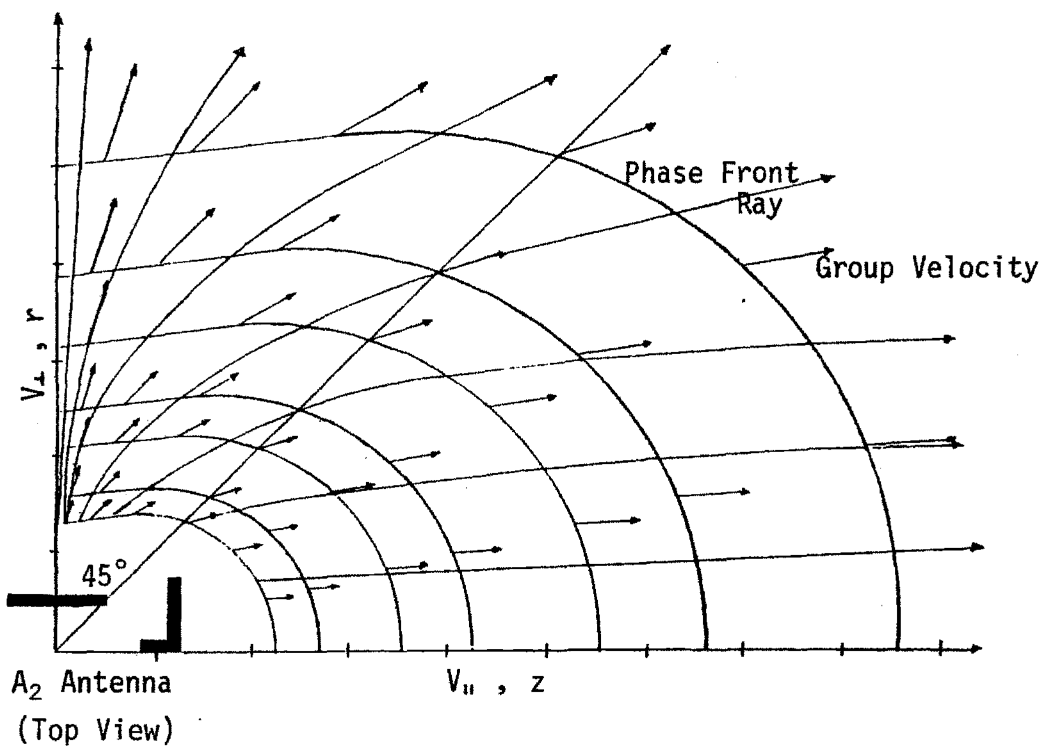

Figure 3

IV-7.3. Tunneling and poloidal magnetic field effects in the TIIH regime

Near the two ion-ion hybrid resonance, the wave equation can be approximated by[10,48]

(1) $$\frac{d^2E}{d\,r^2} + \left[\frac{a}{-r} + b\right] E = 0$$

where from equation IV-2.3.(17)

(2) $$\frac{a}{-r} + b = k_\perp^2(r)$$

and from simple curve fitting at and away from the TIIH layer.

(3) $$b = k_\perp^2(r \to \infty) \approx 1$$

(4) $$a = \Delta rb \approx .5$$

Where Δr is the thickness of the evanescent layer. Figure 1 is a close up of Figure IV-2.5.(3), and is in good agreement with Figure 2, which is a plot of equation (2).

Equation (1) can be solved using confluent hypergeometric functions[81,131] (instead of trigonometric functions, for $k^2(r)$ = constant). From principles of geometrical optics, we can define reflection (R), transmission (T), and absorption coefficients (A) at the TIIH layer. The tunneling coefficient

(5) $$\eta = \Delta r\ k_\perp(\infty) \ = \ .5$$

is independent of damping and direction of propagation through the resonant layer. A wave incident from the high field side sees a resonance first, no reflection occurs, and most of the power is absorbed.

(6) $R = 0$

(7) $T = e^{-\pi\eta/2} = .46$

(8) $A_H = 1 - R^2 - T^2 = 1 - e^{-\pi\eta} = .8$

A wave incident from the low field side, on the other hand, encounters an evanescent layer, and most of the power is reflected.

(9) $R = 1 - e^{-\pi\eta} = .8$

(10) $T = e^{-\pi\eta/2} = .46$

(11) $A_L = e^{-\pi\eta} - e^{-2\pi\eta} \approx .16$

Figure 3 shows how absorption from the high field side (A_H) is always greater than from the low field side (A_L).

We might wonder how power is absorbed if the mechanism is independent damping. The answer resides in the fact that the perpendicular group velocity tends to zero near the resonance. Even for a small change in ω, the resonant layer $k_\perp$ can change drastically, so that

(12) $\frac{\partial k_\perp}{\partial \omega} \to \infty$ and $v_{g\perp} \to 0$

The parallel group velocity, on the other hand, is weakly dependent on ω, so that energy is diverted along the parallel direction, and slowly dissipates over many wavelengths. Of course, mode conversion occurs here, so that this treatment is only approximate.

Another major difference between low and high field side incidence is the difference in species heated. High field incidence lets $k_\perp \to \infty$ so that, from equation IV-2.6.(5), E_z is increased manyfold, and electron Landau damping (equation IV-4.3.(5)) can become very large. The inclusion of rotational transform effects (Figure 4) also increases $k_\parallel$

(13) $k_\parallel \approx k_z + \frac{B_\theta}{B_0} k_\perp$

and further enhances electron heating through increased E_z and v_{the} / v_p.

At low minority concentrations, the TIIH layer becomes part of the finite thickness (IV-4.2.(36)), fundamental and second harmonic resonance layers and hot plasma effects swamp out the resonances, and electron heating stays small compared to ion heating.

Detail of TIIH Resonance Layer Dispersion Relation

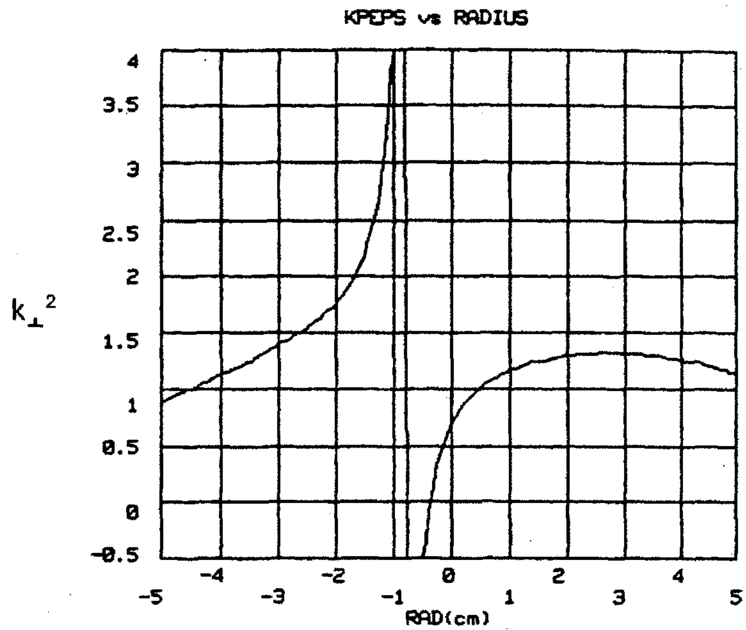

kpar= 0.300 f=.90000E+08 mua= 2.000 mub= 1.000

nahat=.50000E+15 nbhat=.25000E+14 rmax= 5.000 rmaj=54.000

nstep= 203 b0=.60000E+05

Figure 1

Simplified TIIH Resonance Layer Dispersion Relation Model

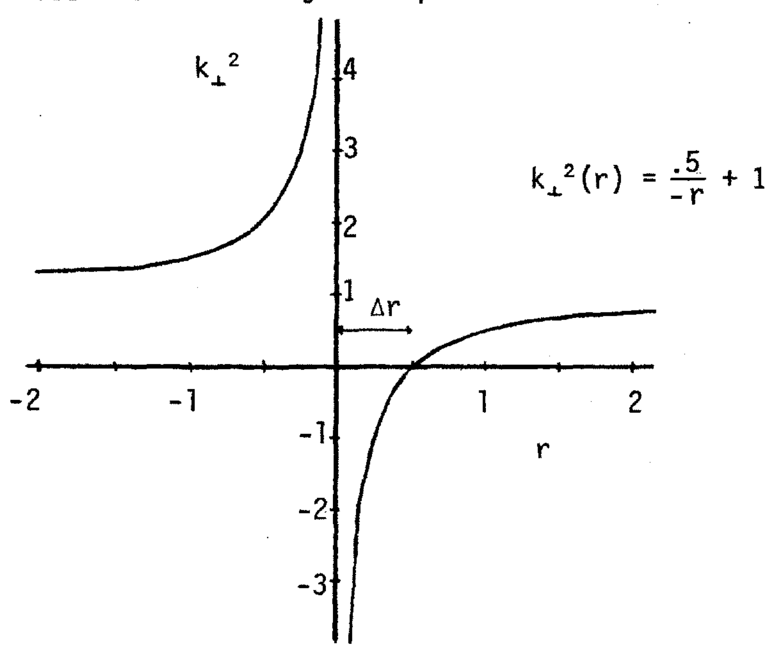

Figure 2

Power absorption from high and low field side

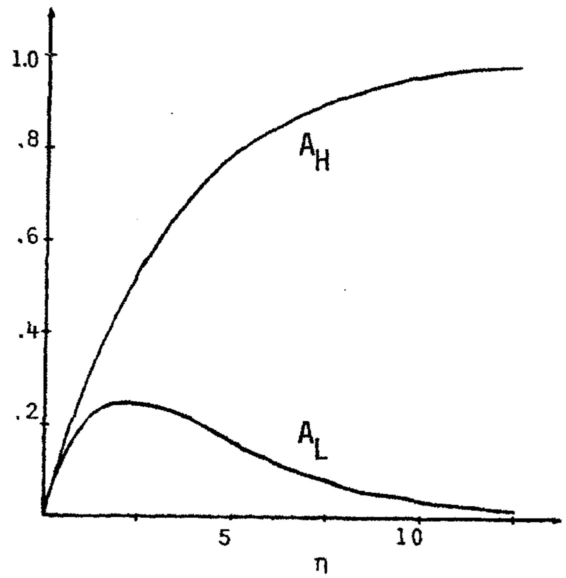

Figure 3

k_z to $k_\parallel$ transformation

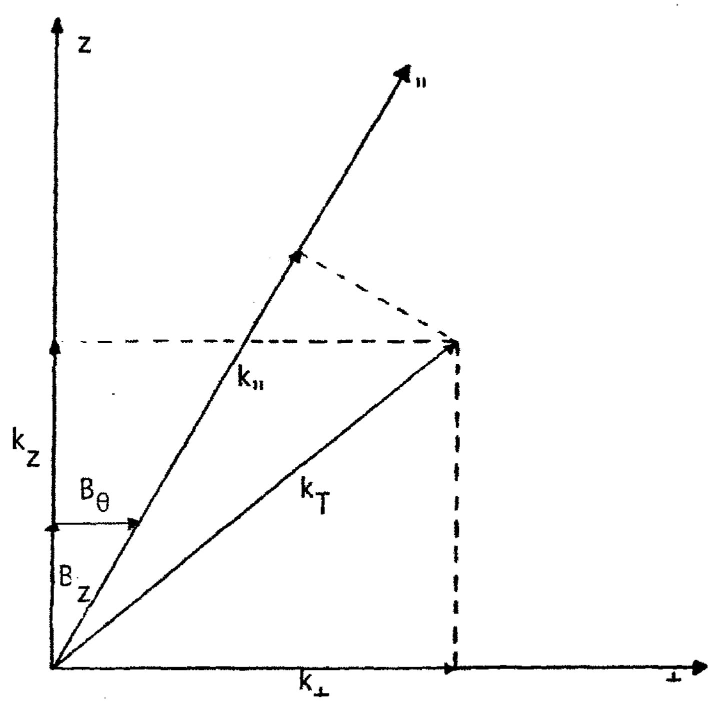

Figure 4

V. Synthesis, Recommendations for Further Work, and Conclusions

V-1. Synthesis

The Alcator A ICRF experiment can be schematically summarized by the block diagram of Figure 1. Some of the main controllable and uncontrollable input variables are shown with the most important ICRF propagation and damping processes. A certain number of wave measurements, products, and by-products are also shown.

From a theoretical point of view, one is interested in understanding the processes, so that an efficient heating scheme can be devised. From a more near-sighted, practical point of view, we need only to produce heating (product) with as little plasma deterioration as possible (by-products). Unfortunately, neither point of view has seemed encouraging up until now for ICRF at high density. Although significant amounts of RF power were coupled to the plasma without any significant plasma deterioration, no evidence of any bulk heating was observed.

Although unpromising (unrealistically high goals were set), many important new results were observed at high density. Before the Alcator experiment, one could not have made a single statement about the effect of any input variable on any of the output measurements, products or by-products of Figure 1. This work has experimentally mapped out most of the different parameter correlations in conjunction with plausible, simple theories.

The most important new scaling law is

$$(1)\quad R_R \;\alpha\; d^{2}\, \ell^{1.5}\, \phi^{\circ}\, F^{\circ}\, n_e^{1}\, \omega_{\circ}^{2}\, P^{\circ} m^{.5}\, z^{-2}\, I_p^{\circ}\, B_{\circ}^{\circ}$$

where we have successively listed the effect of center conductor to wall spacing, antenna length, antenna phasing, Faraday shield, plasma density, transmitter frequency, P power, ion mass, ion charge, plasma current, and toroidal field. Most other results, on the other hand, cannot be cast in such condensed form.

In the fundamental regime, cyclotron or cyclotron harmonic damping were obviously important processes, as shown by the dramatically different probe signal and radiation resistance spikes behavior during a toroidal field scan. At second and fourth harmonic, no such behavior was observed, and some other strong damping mechanism must be accounted for. Collisional damping is a possibility since edge neutral density is unknown, but similar results were observed with gas puffed at the antenna port and 90° away.

A likely source of problems are the trapped particles in the port ripple. Trapped particles were the major concern of the Alcator lower hybrid experiment. Figures 2 and 3 show typical lower hybrid heating shots (data taken by the author in October, 1976). Essentially the same symptoms as in ICRF were observed; energetic ion tail, fast decay time, no plasma deterioration, and no bulk heating. After extensive parameter scanning, a very narrow density window was found where thermonuclear neutron production was dramatically increased, but again, without bulk heating.

Most of the ICRF wave measurements were made far away from the antenna (except for the near-field, which is too close), and it is possible (and even likely) that the observed probe signals are not representative of the bulk power leaving the antenna. There could be, of course, near-field absorption, but also single perpendicular and parallel pass absorption. In all three cases, R_R would be independent of toroidal field (damping strength) as experimentally observed. This idea is especially supported by the surprising fact that $k_\parallel$, away from the antenna, is very large, in contradiction with good mode coupling (small evanescent edge), but consistent with weakly damped ($2\omega_{ci}$) low $k_\perp$ modes. This may explain why the probe eigenmodes are independent of layer position. Put concisely, these eigenmodes are not necessarily representative of bulk power flow and absorption.

All three regimes of damping (single perpendicular pass, single toroidal pass and stochastic mode stacking) at high density can be used to explain the basic behavior of the radiation resistance (equation(1)) and probe signal background. For example, R_R theoretically scales as d^2 independently of damping, ℓ^1 for single perpendicular pass and ℓ^1 to ℓ^4 for perpendicular eigenmodes, and is independent of antenna phasing, etc.

Comparing available parameter space with the space that was actually carefully investigated immediately reveals a large discrepancy; the low density fundamental regime which has been proven successful on the two largest ICRF experiments (TFR,PLT). Three main factors contributed to the brevity of the investigations of this regime; first, the extremely unfavorable power coupling scaling law ($R_R \propto n_e\omega^2$). Second, Alcator is a high density experiment, and considerably more scientific impact could be obtained by heating a high density plasma (commercial reactors will undoubtedly operate above $n_e \approx 10^{14}/cm^3$). Third, the tokamak operators have little experience in low density work, the machine is difficult to run, and diagnostitians are usually not interested in this regime. In hindsight, not fully investigating the fundamental regime has been a mistake, although preliminary results with proper antenna phasing (push-pull in single pass regime) low minority concentration, and fully shielded antenna (A_4), proved unsuccessful.

We are now left with the dilemma of pinpointing the source of the problem. Antenna design is the most unlikely since A_4 is all metal and fully shielded. Trapped particles clearly need further investigation (even simple up-down charge exchange scans were never done), and could be the sole problem, explaining everything. Either high density, field or frequency could also be at the heart of the problem, as they are significantly higher than the TFR and PLT experiments (the evanescent edge is many times worse in Alcator). PLT always stays at very low density while TFR has shown good results up to $10^{14}/cm^3$.

Tokamak size has also been suggested, since the large PLT, TFR and Macrotor tokamaks are easily heated, while the smaller Microtor and Alcator have not been heated. The "Magic Touch" can be ruled out since both Microtor and Macrotor are at the same laboratory. A major difference, caused by tokamak size increase at a given central density, is the much lower plasma edge density. In PLT, the plasma density near the Faraday shield is of the order of 10^{10} - $10^{11}/cm^3$, and reaches $10^{12}/cm^3$, only several centimeters into the plasma. In Alcator, on the other hand, the plasma edge density starts immediately at the $10^{13}/cm^3$ level, at least two orders of magnitude larger than PLT. We could, of course, suggest the counter-argument that A_2 and A_4 behaved the same. If edge density was the problem, an unshielded antenna would have undoubtedly been much worse. Antenna current shorted out by plasma is also ruled out by the same argument. It was most unfortunate that no time was available to use the Langmuir probe installed in the A_4 Faraday shield after so much work went into implementing the intricate design.

Schematic Diagram of the Alcator ICRF Experiment

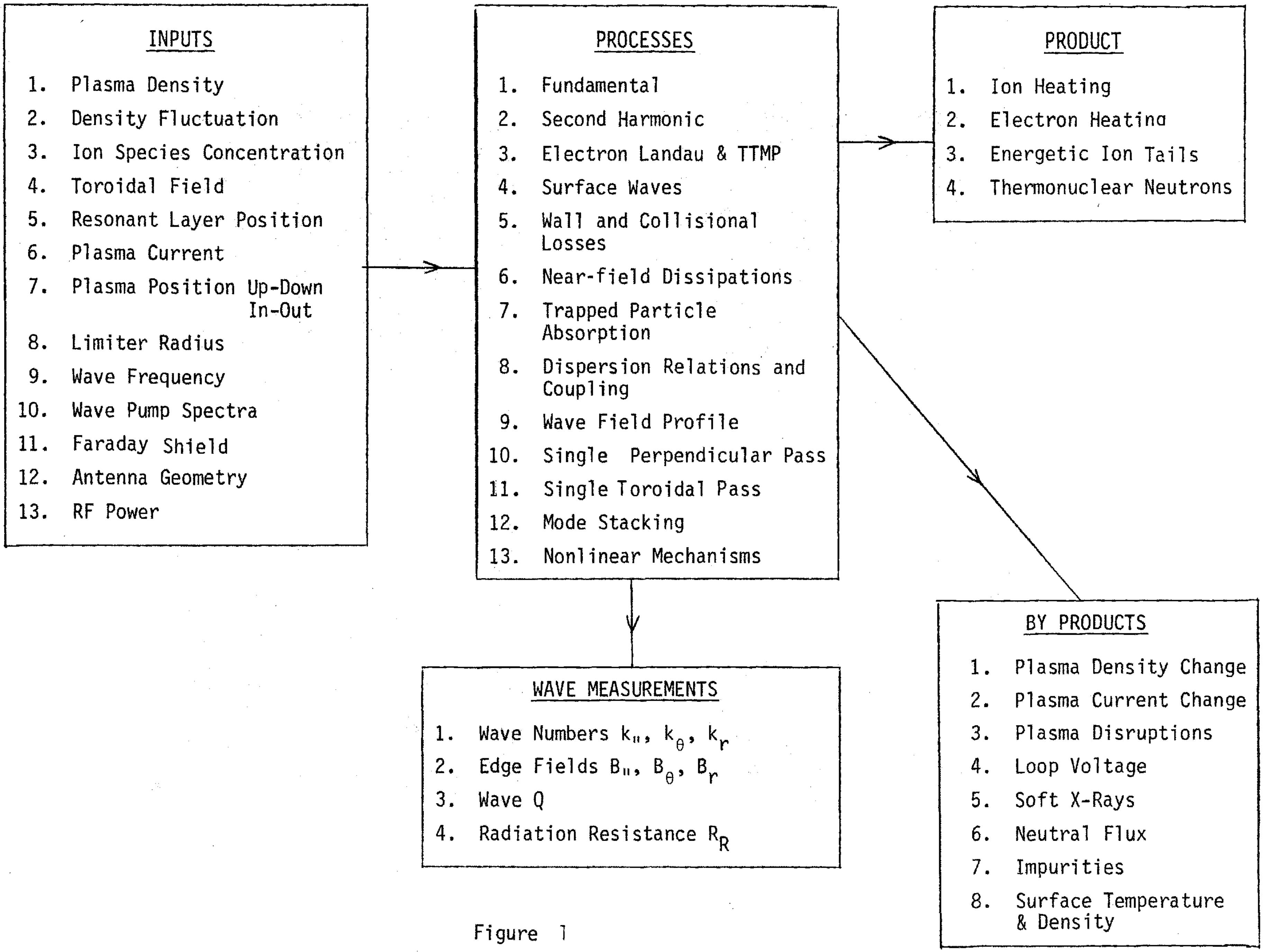

Figure 1

Lower Hybrid Data
10/7/76

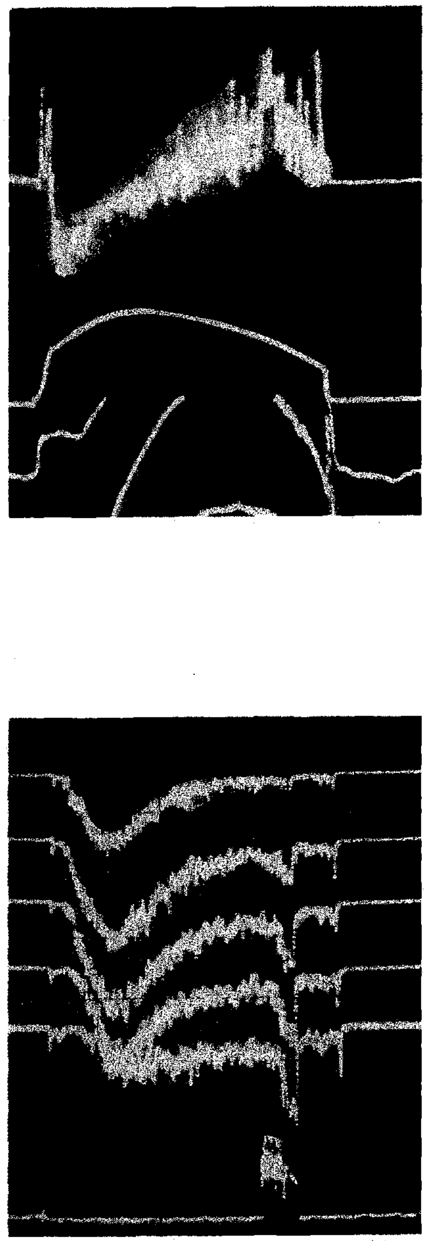

Figure 2

Lower Hybrid Data
10/28/76

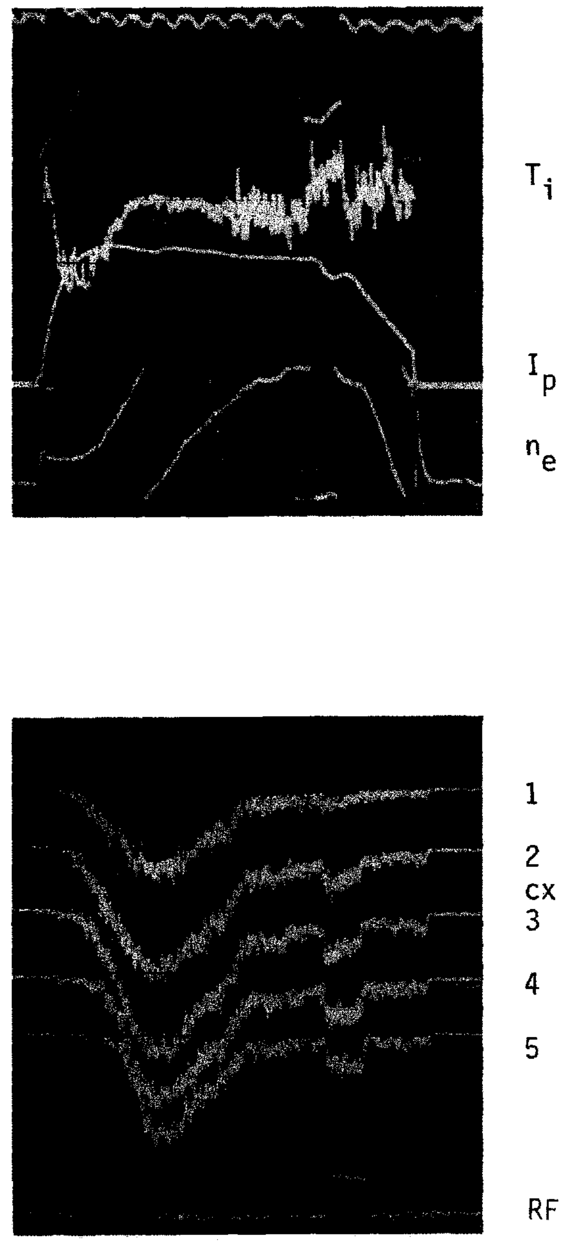

Figure 3

V-2. Recommendations for Further Work

The next theoretical investigations should include an in depth study of hot plasma effects in the TIIH regime at high density and a realistic description of the antenna near-fields, including density gradient and a very strong, localized absorption mechanism similar to those modeled by Y. Lapierre.[120,121] The most important, urgent, and possibly difficult problem is producing a good model of the trapped particle power absorption.

The next stage of experiments on Alcator "A" or "C" should definitely be done with shielded antennas until some evidence of bulk heating has been achieved, since there is no reason to believe that Faraday shields have any detrimental effects (except mechanical, which is of secondary importance at this point), and may in fact be necessary (PLT and TFR groups claim they are). A_6 is an excellent overall design, and only the vacuum breaks (and multipactor) need further investigation.

In the area of diagnostics, much initial work, discussed in Chapter III, needs to be finished, particularly the A_4 Langmuir probe, capacitive probe radial scans, trapped particle detector, high speed stainless steel foil bolometer, antenna breakdown detectors, and most importantly, the antenna viewer. More complete $k_{\parallel}$ array and electron heating (soft X-ray and electron cyclotron emission) diagnostics, as well as less cumbersome data acquisition, are also in order.

The next generation of experiments should concentrate on the more well-known and proven minority regime at low density (Note again that Microtor has not yet been heated successfully). Second harmonic experiments should also concentrate on the lower density with close attention given to power balance and wave activity at the antenna port instead of far away from it.

Of course, any promising results at higher density on Alcator C would completely change these recommendations.

The most important parameter scans are minority concentration, in-out position and up-down charge exchange and, of course, resonant layer position. Of more academic importance are the d^2, $l^{1.5}$, ϕ° and ω^2 scaling laws, which would be very easily investigated (except for d^2) with the A_6 antenna system.

V-3. Conclusions

With a nearly complete comprehensive study of the theoretical foundation of ICRF at high density, and through comparison with experimental data over a wide range of parameters, a more enlightened understanding of the physics of launching, propagation, and absorption has resulted. Even with apparently large discrepancies between theory and experiment, important new scaling laws have been formulated, which can be compared with other experiments and more sophisticated theories.

In any case, many technological advances have been made in the field of antenna design, matching,and diagnostics through careful study of the A_1, A_2, A_4 and A_6 antenna designs and experiments.

In short, this work has tried to substantiate a choice of ICRF schemes for future high field, high density,compact tokamaks, through a broad comparison of different parameter regimes. The outcome is still unclear,and much more experimental and theoretical work is still necessary, continuing, and planned.[143]

APPENDIX 1

Alfvén Regime Approximations

For the purpose of this work, we shall use the usual perturbation technique, and linearize most of the basic equations.[1,45]

(1) $n = n_\circ + n_1 + \ldots$

$\vec{E} = \vec{E}_\circ + \vec{E}_1 + \ldots$

The Fourier transformed first order quantities in a wave are of the form

(2) $A_1 = \bar{A}_1 e^{i(k\cdot r - \omega t)}$

where we will use only the real part of A_1 as measurable quantity. Also

(3) $\vec{k}\cdot\vec{r} = k_x x + k_y y + k_z z$

$k_\perp{}^2 = k_x{}^2 + k_y{}^2$

$k_\parallel{}^2 = k_z{}^2$

$\vec{B}_\circ = \hat{z}B_\circ$

For each species in the plasma, we can write the full fluid equation, i.e., for ions [1]

(4) $Mn \dfrac{d\vec{v}_i}{dt} = en(\vec{E} + \vec{v}_i \times \dfrac{\vec{B}}{c}) - \nabla P_i - \nabla\cdot\pi_i + P_{ie}$

where Mn dv/dt represents the change in momentum, en(E + v_i x B) the electromagnetic forces, ∇P_{ie} the pressure gradients, $\nabla\cdot\pi_i$ the off diagonal shear, and P_{ie} the collisions. For the plasma wave regimes in the near collisionless regime we will be analyzing, the shear and collision terms represent small resistive losses that will be evaluated in Section IV-4.2-5. The pressure term is reactive[1] and would only be important if its corresponding phase velocity, the speed of sound in a plasma ($\approx V_{thi}$ for $T_i \approx T_e$), was of the order of, or greater than, our electromagnetically induced wave phase velocity ($V_p \approx V_A >> V_{thi}$, Appendix 2).

Cancelling the density term on each side, we are then left with the equation of motion of the single particle

(5) $$M \frac{d\vec{v}_i}{dt} = e\left(\vec{E} + \vec{v}_i \times \frac{\vec{B}}{c}\right)$$

with

(6) $$\frac{d\vec{v}}{dt} = \frac{\partial \vec{v}}{\partial t} + (\vec{v}_\circ \cdot \nabla)\vec{v}_1$$

The term on the right is usually called the connective derivative and may be neglected if there is no constant drift. Thus,

(7) $$\vec{v} = \vec{v}_\circ + \vec{v}_1 \simeq \vec{v}_1$$

and our equation of motion is then simply

(8) $$M \frac{\partial \vec{v}_1}{\partial t} = e\left(\vec{E} + \vec{v}_1 \times \frac{\vec{B}}{c}\right)$$

which has orthogonal components

(9) $$-i\omega M v_x = e\left(E_x + v_y \frac{B_\circ}{c}\right)$$

(10) $$-i\omega M v_y = e\left(E_y - v_x \frac{B_\circ}{c}\right)$$

For simplicity, we assume for now that $E_y = 0$,and solve for the ion velocities

(11) $$v_{ix} = \frac{-i\Omega}{1-\Omega^2} \frac{Ec}{B_\circ}$$ polarization current

(12) $$v_{iy} = \frac{-1}{1-\Omega^2} \frac{Ec}{B_\circ}$$ EXB current

where we defined

(13) $$\Omega = \frac{\omega}{\omega_{ci}}$$

Substituting for electrons in the relatively low ICRF,where $\omega << \omega_{ce}$

(14) $M \to m$

$e \to -e$

$\omega_{ci} \to -\omega_{ce}$

$\Omega_i \to -\Omega_e << 1$

we thus have for electron velocities

(15) $v_{ex} = i\ \Omega_e \frac{Ec}{B_o} << v_{ix}, v_{iy}, v_{ey}$

(16) $v_{ey} = -\frac{Ec}{B_o}$

and the electron current along E_x (polarization current) may be neglected.

Combining Ampère's and Faraday's laws with the definition of current density,

(17) $\nabla \times \vec{E} = \frac{-\dot{\vec{B}}}{c}$

(18) $c\ \nabla \times \vec{B} = 4\pi\vec{J} + \dot{\vec{E}}$

(19) $\vec{J} = ne(\vec{v}_i - \vec{v}_e)$

we have the wave equation[1]

(20) $\nabla \times (\nabla \times \vec{E}) = -\vec{k}(\vec{k} \cdot \vec{E}) + k^2\vec{E} = \frac{4\pi i\omega}{c^2}\vec{J} + \frac{\omega^2}{c^2}\vec{E}$

We assume for now that $k = k_z$,(an electromagnetic wave since $\vec{k} \cdot \vec{E} = 0$ (Figure 1)), so that

(21) $k^2E = \frac{\omega^2}{c^2}(1 + \varepsilon)\ E$

where we defined an effective plasma dielectric constant

(22) $\varepsilon = \frac{4\pi i}{\omega}\ \frac{J}{E} = \frac{\pi_i^2}{\omega^2_{ci}} = \varepsilon_{Alfvén}$ for $\omega << \omega_{ci}$

In Section IV-2.1. this will correspond to the total dielectric tensor element

(23) $K_{xx} = S = \varepsilon_{vacuum} + \varepsilon_{plasma} = 1 + \varepsilon$

In the very low frequency approximation $\omega << \omega_{ci}$

(24) $v_{iy} = -\frac{Ec}{B_o} = v_{ey}$

$J_y = 0$, and E_x linear polarization is justified, since the other orthogonal linear polarization, E_y, would not couple power to the original wave

(25) $J_{y_1} E_{y_2}{}^* = 0$

Also, since

(26) $\frac{v_{ix}}{v_{iy}} = i\Omega$

the bulk of the particle wave kinetic energy is oscillating in motion perpendicular to both $\vec{B}_o$ and $\vec{E}$, ($E_x X\, B_{oz}$ drift). The phase velocity is simply

(27) $\frac{\omega}{k} = \frac{1}{\sqrt{\mu_o \varepsilon_A}} = c\,\frac{\omega_{ci}}{\pi_i} = V_A$

From Faraday's law (17)

(28) $B_y = E_x \frac{ck_z}{\omega}$

and we note that this B_y, when added to B_{oz}, gives rise to a small $(\vec{B}_1 << \vec{B}_o)$ shear sinusoidal ripple on the confining field (Figure 1). The y component of the velocity of the field line is simply

(29) $v_{By} = -\frac{\omega}{k}\,\frac{B_y}{B_o} = -\frac{E_x c}{B_o}$

which is the same velocity as the fluid $\vec{E}X\vec{B}$ drift motion

(30) $v_{fluid} = -\frac{E_x c}{B_o}$

For all these reasons, this mode is usually called the electromagnetic shear Alfvén wave.

In the frequency regime above the ion cyclotron frequency $\omega_{ci} < \omega << \omega_{ce}$

(31) $$\frac{-v_{iy}}{v_{ey}} \approx \frac{1}{\Omega^2} << 1$$

and our assumption that E_y was zero is not valid anymore, since E_{y1} couples with $J_{y2} \neq 0$. To treat the problem correctly, we must allow E_y to be arbitrary and solve the coupled set of equations (this will be done in Section IV-2.1). In the ion cyclotron range of frequencies, and in particular, for $\Omega \approx 2$,

(32) $$|v_{ix}| \approx |v_{iy}| \approx |v_{ey}| >> |V_{ex}|$$

For $\omega = \omega_{ci}$, we have singularities in the ion currents. These singularities will be removed in hot plasma theory, and give rise to collisionless damping, (Section IV-42).

If we now look at the case where $\vec{E}$, $\vec{k}$, and $\vec{B}_o$ are all perpendicular to each other, i.e., E_x, k_y, B_{oz}, our previous derivations remain unchanged, except that now the $\vec{E} X \vec{B}_o$ drift is along $\vec{k}$, and the plasma will be compressed (instead of sheared), as in a compressional acoustic wave (Figure 2). One could have also kept the pressure term in the fluid equation and achieved a slightly modified result[1].

(33) $$\frac{\omega^2}{k^2} = c^2 \frac{v_s^2 + V_A^2}{c^2 + V_A^2} \approx V_A^2 \quad \text{for } v_s << V_A$$

where v_s is the sound velocity.

We note also that around the cyclotron frequency (ie $\Omega \approx 2$), the magnitude of the dielectric constant ε (S) is smaller than ε_A, and the wave phase velocity is slightly faster than the Alfvén speed. For all these reasons, this mode is usually called the fast wave, fast compressional wave, fast compressional Alfvén wave, or even fast magnetosonic compressional

Alfvén wave. The fact that S is negative for $\Omega > 1$ should be of some concern, but the overall dielectric constant will be positive when E_y will be allowed to be finite. The basic physical picture of the problem is nevertheless correct. A more powerful mathematical formulation will be necessary to get a complete picture at the cost of physical simplicity. This formulation will be the subject of Section IV-2.

The last possibility is $\vec{E}$ parallel to $\vec{B}_o$. This can be simulated by simply setting $B_o = 0$ in (9) or (15)

(34) $v_{ez} = \frac{-ie}{m\omega} E_z \gg v_{iz}$

(35) $\varepsilon_{\parallel} = \frac{-\omega_{pe}^2}{\omega^2}$

which corresponds to an enormous dielectric constant. For many practical purposes,this can be considered a short circuit and $E_z = 0$. This approximation is often called the zero electron mass approximation ($m_e/m_i \to 0$)

We can now qualitatively conclude that,except for the cyclotron frequency singularity, one has a non-isotropic dielectric constant with a perpendicular component of order π_i^2/ω_{ci}^2, and a much larger parallel component ω_{pe}^2/ω^2. In particular, for ICRF

(36) $\frac{\varepsilon_{\parallel}}{\varepsilon_{\perp}} \simeq \frac{m_i}{m_e} \gg 1$

The dispersive character of the wave is essentially controlled by the ion's frequency dependent polarization and $\vec{V}X\vec{B}$ drifts, with respect to the electron's $\vec{V}X\vec{B}$ drift (Figure 3)

Shear Wave

Figure 1

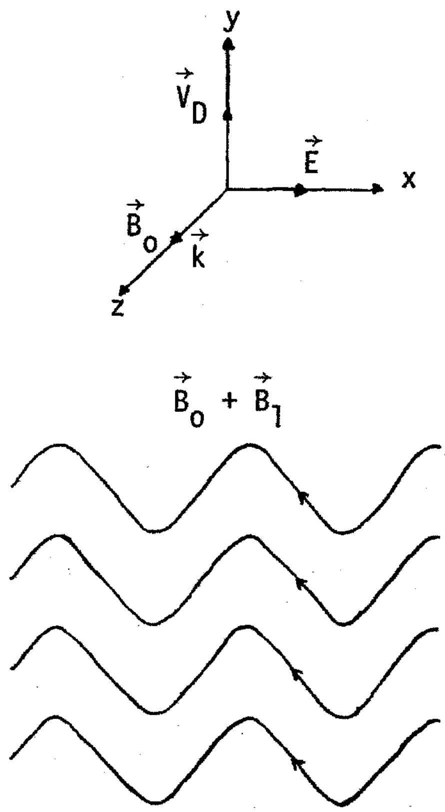

Compressional Wave

Figure 2

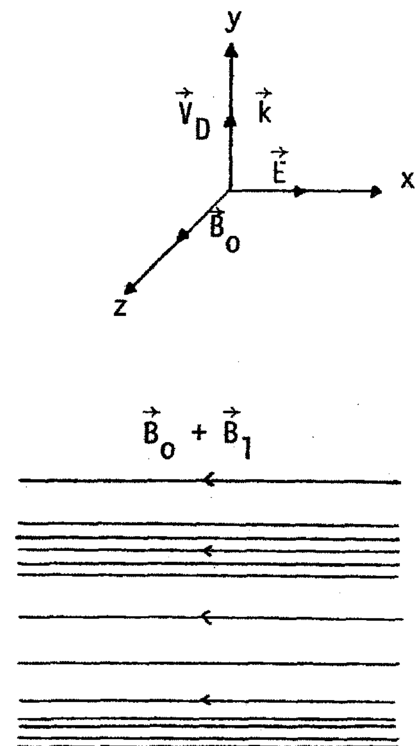

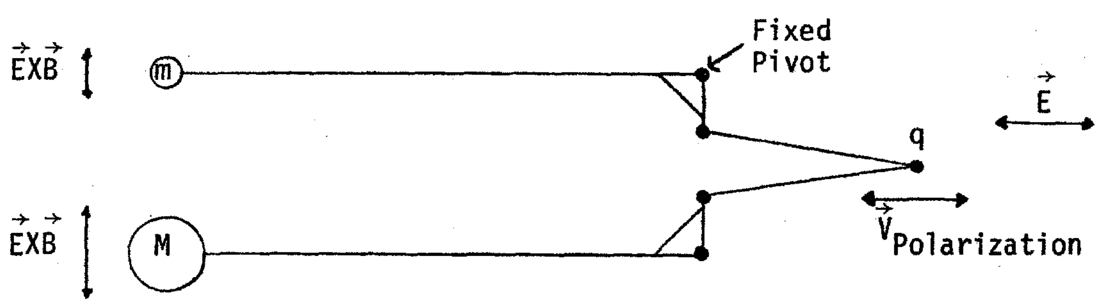

Simple mechanical analogy to $\vec{E}X\vec{B}$ and polarization drift, and energy storage

Figure 3

APPENDIX 2

Table of Formulas and Typical Values[82]

Numerical values are for T_e and T_i in eV, B in gauss, $\mu = m_i/m_p$, n in cm^{-3}. Typical values are for $T_i = T_e = 1$ keV, $\mu = 1$, $n = 3 \times 10^{14}/cm^3$, B = 60 kG, $\lambda_c = 15$, $f_o = 200$ mHz, $k_\parallel = .5$, $k_\perp = 1/cm$.

Name	Symbol	CGS Formula	Numerical Value	Typical Value
FREQUENCIES				
electron gyrofrequency	ω_{ce} =	$\frac{eB}{m_e c}$ =	1.76×10^7 B	$\simeq 10^{12}$/sec
ion gyrofrequency	ω_{ci} =	$\frac{eB}{m_i c}$ =	$\frac{9.58 \times 10^3 \text{ B}}{\mu}$	$\simeq 5.7 \times 10^8$/sec
electron plasma frequency	π_e =	$\sqrt{\frac{4\pi ne^2}{m_e}}$ =	$5.64 \times 10^4 \sqrt{n_e}$	$\simeq 9.8 \times 10^{11}$/sec
ion plasma frequency	π_i =	$\sqrt{\frac{4\pi ne^2}{m_i}}$ =	$1.32 \times 10^3 \sqrt{\frac{n}{\mu}}$	$\simeq 2.3 \times 10^{10}$/sec
electron collision frequency	γ_e =		$2.9 \times 10^{-6}\, n\, \lambda_c\, T_e^{-3/2}$	$\simeq 4.1 \times 10^5$/sec
Ion collision frequency	γ_i =		$4.8 \times 10^{-8}\, n\, \lambda_c\, T_i^{-3/2}$	$\simeq 6.8 \times 10^3$/sec
VELOCITIES				
speed of light	c =			3×10^{10} cm/sec
electron thermal velocity	v_{te} =	$\sqrt{\frac{KT_e}{m_e}}$ =	$4.19 \times 10^7 \sqrt{T_e}$	$\simeq 1.3 \times 10^9$ cm/sec
ion thermal velocity	v_{ti} =	$\sqrt{\frac{KT_i}{m_i}}$ =	$9.79 \times 10^5 \sqrt{\frac{T_i}{\mu}}$	$\simeq 3.0 \times 10^7$ cm/sec
ion sound velocity	v_s =	$\sqrt{\frac{KT_e}{m_i}}$ =	$9.79 \times 10^5 \sqrt{\frac{T_e}{\mu}}$	$\simeq 3.1 \times 10^7$ cm/sec
Alfvén velocity	v_A =	$\frac{B}{\sqrt{4\pi n_i m_i}}$ =	$\frac{2.18 \times 10^{11} \text{ B}}{\sqrt{\mu n_i}}$	$\simeq 7.5 \times 10^8$ cm/sec

Table of Formulas (cont.)

Name	Symbol	CGS Formula	Numerical Value	Typical Value
LENGTH				
electron gyroradius	$\rho_e =$	$v_{te}/\omega_{ce} =$	$\frac{2.38\sqrt{T_e}}{B}$	$\approx 1.2 \times 10^{-3}$ cm
ion gyroradius	$\rho_i =$	$v_{ti}/\omega_{ci} =$	$\frac{1.02 \times 10\sqrt{\mu T_i}}{B}$	$\approx 5.4 \times 10^{-2}$ cm
free space wavelength	$\lambda_o =$	$c/f_o =$		150 cm
Alfvén wavelength	$\lambda_A =$	$V_A/f_o =$		3.8 cm
debye length	$\lambda_D =$	$\sqrt{\frac{KT}{4\pi ne^2}}$	$= 7.43 \times 10^2\sqrt{\frac{T}{n}}$	$\approx 1.4 \times 10^{-3}$ cm
DIMENSIONLESS				
proton/electron mass ratio	$=$	$\frac{m_p}{m_e} =$	1837	
Alfvén refractive index	$\frac{c}{V_A} =$	$\frac{\pi_i}{\omega_{ci}} =$	$\frac{.137\sqrt{\mu n}}{B}$	$\approx$ 40
thermal/magnetic energy ratio	$\beta =$	$\frac{8\pi nKT}{B^2} =$	$\frac{4.03 \; 10^{-11}\; nT}{B^2}$	$\approx 3.4 \times 10^{-3}$

Appendix 3

2 x 2 Dispersion Relation Code

```
                 disper.fortran      04/09/81  1654.0 est Thu

C  NORMALIZED 2X2.
C
C  Calculates and plots the 2X2 dispersion relation
C  nperp**2=(a-Npar**2)+a*(1-Npar**2)/(a-Npar**2)
C  where a =1/(1-omega). Nperp vs Npar is also plotted.
C
      dimension npar(500),nperp(500),npars(500),nperps(500),omeg(10)
      real npar,nperp,npars,nperps,ndel,nmax,nmin,nmin2,nmax2,ndel2
      external plot_$setup(descriptors),plot_$scale(descriptors),
     &  plot_(descriptors)
C
C  Data.
      omega=2.
      nmin=-3.
      nmax=3.
      nstep=200
      omeg(1)=4.
      omeg(2)=3.
      omeg(3)=2.
      omeg(4)=1.5
      omeg(5)=1.25
      omeg(6)=.75
      omeg(7)=.5
      omeg(8)=.25
      omeg(9)=0.
      nmin2=0.
      nmax2=1.
      write(6,25)
25    format(1x,'!wor 30 h !gra 1,35 !ehr b')
C
C  Initial calculations
      a=1./(1.-omega**2)
      ndel=(nmax-nmin)/float(nstep)
      ndel2=(nmax2-nmin2)/float(nstep)
      write(6,30)omega
30    format(/5x,'omega=',f5.3)
C  Beginning of the loop.
      do 100 j=1,nstep
      npars(j)=nmin+float(j-1)*ndel
      nperps(j)=(a-npars(j))+(a*(1.-a)/(a-npars(j)))
      if(nperps(j) .gt. nmax) nperps(j)=nmax
      if(nperps(j) .lt. nmin) nperps(j)=nmin
100   continue
      call plot_$setup("DISPERSION RELATION","NPAR**2",
     &  "NPERP**2",1,0e0,1,0)
      call plot_$scale(-3.,3.,-3.,3.)
      call plot_(npars,nperps,nstep,1," ")
      write(6,25)
      call plot_$setup("DISPERSION RELATION","NPAR","NPERP",1,0e0,1,0)
      call plot_$scale(nmin2,nmax2,nmin2,nmax2)
      write(6,44)
44    format(/4x, 'omega=0., 4., 3., 2., 1.5, 1.25 .75, .5, .25 ')
      do 210 i=1,9
      do 200 j=1,nstep
      a=1./(1.-omeg(i)**2)
      npar(j)=nmin2+float(j-1)*ndel2
      nperps(j)=(a-npar(j)**2)+(a*(1.-a)/(a-npar(j)**2))
      if(nperps(j) .gt. 1.) nperps(j)=1.
      if(nperps(j) .le. 0.) nperps(j)=0.
      nperp(j)=sqrt(nperps(j))
200   continue
      call plot_(npar,nperp,nstep,1," ")
210   continue
      call exit
      end

r 16:55 0.474 9 level 2
```

Appendix 4

Inhomogeneous Plasma Heuristic Code

```
                    hdamp.fortran      04/09/81  1052.3 est Thu

C
C  HEURISTIC
C
C  Heuristic profile calculation of Kperp, Ne, Te, Etheta, and WKB
C  in inhomogenious cartesian plasma.
C
      dimension r(500),n(500),kperp(500),kperps(500),t(500),
     & fint(500),sint(500),etheta(500),kint(500),
     & ewkb0(500),ewkb1(500),rewkb0(500),rewkb1(500),ewkbi0(500),
     & ewkbi1(500),ewkbm0(500),ewkbmi(500),kpari(10)
      real n,npar,nperp,nhat,kpar,kperps,mu,npars,kpeps,kpari
      complex kperp,ewkb0,ewkb1,kint
      external plot_$setup(descriptors)
      external plot_$scale(descriptors)
      external plot_(descriptors)
C
C  Data.
      f=2.e8
      omega=2.
      mu=1.
      nstep=500
      istep=8
      kpari(1)=.6720
      kpari(2)=0.
      kpari(3)=.2
      kpari(3)=.2
      kpari(4)=.4
      kpari(5)=.6
      kpari(6)=.8
      kpari(7)=1.
      kpari(8)=1.2
      nhat=5.e14
      rmax=12.5
      rmin=0.
      pp=9.
      q0=.9
      ql=5.
      t0=1000.
      fint(1)=-1.
      sint(1)=1.
      etheta(1)=1.
      kint(1)=(0.,0.)
C  Nprof=1 for TFR and 2 for Alcator.
      nprof=2
C
C  Initial calculations.
      c=3.e10
6     rdel=(rmax-rmin)/float(nstep)
      w=6.28*f
      ateq=(3./2.)*pp**2*q0/ql
C  Beginning of the loop.
      do 500 i=1,istep
      kpar=kpari(i)
      do 100 j=1,nstep
      r(j)=rmin+float(j)*rdel
C   Temperature profile calculation.
      tnorm=exp(-r(j)**2/ateq)
      t(j)=tnorm*t0
      if(nprof .eq. 1) go to 7
C   Alcator density profile calculation.
      rlim1=9.
      rlim2=9.7
      xpon=12.
      if(r(j) .ge. rlim1) go to 90
      n(j)=nhat*(1.-(r(j)**2./rlim2**2.))
      go to 91
90    n(j)=nhat*.1389*exp(-1.*xpon*(r(j)/9.-1.))
      go to 91
C   TFR density profile calculation.
7     if(r(j) .ge. .9*pp) go to 96
      n(j)=nhat*(1.-(r(j)**2/pp**2))
      go to 91
96    n(j)=nhat*(.04+.15*exp(-12.*(r(j)/pp-.9)))
C   Dispersion relation.
91    npars=(kpar*c/w)**2
      wpi=1.32e3*sqrt(n(j))/sqrt(mu)
      ad=(wpi/w*omega)**2
      s=1.+ad/(1.-omega**2)
      d=-omega*s
      kperps(j)=(w/c)**2*((s-npars)**2-d**2)/(s-npars)
      if(j .eq. 1) go to 100
C   First order integration.
92    fint(j)=fint(j-1)+kperps(j)*etheta(j-1)*rdel
      sint(j)=sint(j-1)+fint(j)*rdel
      etheta(j)=1.-sint(j)
C  0th and 1st order WKB profile.
      kperp(j)=csqrt(cmplx(kperps(j),0.))
      kint(j)=kint(j-1)+kperp(j)*rdel
      ewkb0(j)=cexp((0.,1.)*kint(j))
      ewkb1(j)=ewkb0(j)/csqrt(kperp(j))
      rewkb0(j)=real(ewkb0(j))
      ewkbi0(j)=aimag(ewkb0(j))
      ewkbm0(j)=cabs(ewkb0(j))
      rewkb1(j)=real(ewkb1(j))
      ewkbi1(j)=aimag(ewkb1(j))
      ewkbm1(j)=cabs(ewkb1(j))
100   continue
C  Plotting routines.
      if(i .eq. 1 .or. i .eq. 2) then
```

```
      write(6,16)
16    format(1x,'!wor 30 h !gra 1,35 !shr b')
      write(6,101)nprof,t0,nhat,f,kpari(1),mu,omega
101   format(/4x,'nprof=',i3,3x,'t0=',f8.2,3x,'nhat=',e10.5 /
    & 4x,'f=',e10.5,3x,'kpar(1)=',f8.5,3x,'mu=',f5.2,
    & 3x,'omega=',f5.2)
      end if
      if(i .eq. 2 .or. i .eq. 1) write(6,102)
102   format(/4x,'Kpar= 0., .2, .4, .6, .8, 1.0, 1.2')
      if(i .gt. 1) go to 450
      call plot_$setup("DENSITY PROFILE","RAD(cm)","N",1,0e0,1,0)
      call plot_(r,n,nstep,1," ")
      call plot_$setup("TEMPERATURE PROFILE","RAD(cm)","T",1,0e0,1,0)
      call plot_(r,t,nstep,1," ")
240   call plot_$setup("ETHETA vs RADIUS","RAD(cm)","ETHETA",1,0e0,1,0)
      call plot_(r,etheta,nstep,1," ")
490   call plot_$setup("EWKB0 vs RADIUS","RAD(cm)","EWKB0",1,0e0,1,0)
      call plot_$scale(0.,14.,-3.,3.)
      call plot_(r,ewkbm0,nstep,1," ")
      call plot_(r,rewkb0,nstep,1," ")
      call plot_(r,ewkbi0,nstep,1," ")
      call plot_$setup("EWKB1 vs RADIUS","RAD(cm)","EWKB1",1,0e0,1,0)
      call plot_$scale(0.,14.,-3.,3.)
      call plot_(r,ewkbm1,nstep,1," ")
      call plot_(r,rewkb1,nstep,1," ")
      call plot_(r,ewkbi1,nstep,1," ")
      go to 500
450   if (i .eq. 2) then
      call plot_$setup("KPERP**2","RAD(cm)","KPERP**2",1,0e0,1,0)
      call plot_$scale(0.,14.,-2.,4.)
      end if
      call plot_(r,kperps,nstep,1," ")
500   continue
501   call exit
      end

r 10:53 0.920 52
```

Appendix 5

3 x 3 Analytic Dispersion Relations Code

```
                  kperp.fortran       04/09/81  1221.7 est Thu

C
C  ANALYTIC 3X3.
C
C  Calculates kperp for the fast and the slow waves as
C  Kpeps=(w/c)**2*(s-Npar**2)**2-d**2/(s-Npar**2) and
C  Kpems=(w/c)**2*(p/s)*(s-Npar**2) using one ion species,
C  electrons, no magnetic field dependence, and the TFR
C  density profile.
C
      dimension r(500),n(500),kpeps(500),kpems(500)
      real n,kpar,kpeps,kpems,nhat,npars,mu
      external plot_$setup(descriptors)
      external plot_$scale(descriptors)
      external plot_(descriptors)
C
C  Data.
      f=2.e8
      oma=2.
      mu=1.
      kpar=.5
      nhat=5.e14
      pp=9.
      rmax=12.5
      rmin=0.
      nstep=200
C
C  Initial calculations.
      c0=3.e10
      rdel=(rmax-rmin)/float(nstep)
      w=2.*3.1416*f
      b0=(w/oma)*(mu/9.58e3)
      npars=(kpar*c0/w)**2
C  Beginning of the loop.
      do 100 j=1,nstep
      r(j)=rmin+float(j-1)*rdel
C  Density profile.
      if(r(j)/pp .gt. .9) go to 10
      n(j)=nhat*(1.-(r(j)**2/pp**2))
      go to 20
10    n(j)=nhat*(.04+.15*exp(-12.*(r(j)/pp-.9)))
C  Tensor elements.
20    wpi=1.32e3*sqrt(n(j))/sqrt(mu)
      wpe=5.64e4*sqrt(n(j))
      ad=(wpi/w*oma)**2
      s=1.+ad/(1.-oma**2)
      d=-ad*oma/(1.-oma**2)
```

```
      p=1.-(wpe/w)**2
C  Dispersion relations.
      kpeps(j)=(w/c0)**2*((s-npars)**2-d**2)/(s-npars)
      kpems(j)=(w/c0)**2*p*(s-npars)/s
100   continue
C  Plot Kperp**2.
      write(6,49)
49    format(1x,'!wor 30 h !gra 1,35 !shr b')
      write(6,50) f,oma,b0,kpar,mu
50    format(//1x,'f=',e10.5,3x,'oma=',f6.3,3x,'b0=',
     & e10.5,3x,'kpar=',f6.4,3x,'mu=',f4.2)
      write(6,51) nhat,pp,rmax
51    format(//1x,'nhat=',e10.5,3x,'pp=',f6.3,3x,'rmax=',f6.3//)
      call plot_$setup("KPEPS vs RADIUS","RAD(cm)","KPEPS",1,0e0,1,0)
      call plot_(r,kpeps,nstep,1," ")
      call plot_$setup("KPEMS vs RADIUS","RAD(cm)","KPEMS",1,0e0,1,0)
      call plot_(r,kpems,nstep,1," ")
      call exit
      end

r 12:22 0.432 25
```

Appendix 6

3 x 3, 3 Species Computational B_0/R Dispersion Relations Code

```
                  kperp8.fortran     04/09/81  1633.3 est Thu

C
C  TIIH 3X3.
C
C  Plots kperp squared for the fast and slow waves using the cold
C  plasma 3X3 tensor with two ion species, electrons, and 1/R
C  magnetic field.
C
C   Dimension statements.
      dimension rad(500),na(500),nb(500),kpeps(500),kpems(500),
     & b0z(500),bsq(500),dens(500),mrad(500)
      real mua,mub,nahat,nbhat,na,nb,kpeps,kpems,l,nz,kz,npar,
     & nparn,kpar,mue,mrad
      external plot_$setup(descriptors)
      external plot_$scale(descriptors)
      external plot_(descriptors)
C
C  Data.
      nstep=203
      nprof=1
C    (Nprof=1 for TFR and 2 for Alcator.)
      f=.9e8
      b0=6.08e4
      mua=2.
      mub=1.
      kpar=.3
      nahat=5.e14
      nbhat=2.5e13
      pp=9.
      rmax=15.
      rmaj=54.
C
      write(6,60)
60    format(1x,'!wor 30 h !gra 1,35 !shr b')
      write(6,7) kpar,f,mua,mub,nprof
7     format(/1x,'kpar=',f6.3,2x,'f=',e10.5,2x,'mua=',f6.3,
     & 2x,'mub=',f6.3,2x,'nprof=',i2)
      write(6,8) nahat,nbhat,rmax,rmaj
8     format(/1x,'nahat=',e10.5,2x,'nbhat=',e10.5,2x,'rmax=',f6.3,2x,
     & 'rmaj=',f6.3)
      write(6,9) nstep,b0,pp
9     format(/1x,'nstep=',i5,2x,'b0=',e10.5,2x,'pp=',f8.2)
C  Initial calculations and constants.
      c0=3.e10
      mue=1./1837.
      rmin=-rmax
      rdel=(rmax-rmin)/float(nstep)
```

```
      w=2.*3.141593*f
      npar=kpar*c0/w
C  Start of the loop.
C   Density and magnetic field profiles.
      do 100 j=1,nstep
      rad(j)=rmin+float(j-1)*rdel
      mrad(j)=abs(rad(j))
      if(nprof .eq. 2) go to 14
C  TFR profile.
      if(mrad(j) .gt. .9*pp) go to 10
      dnorm=1.-(mrad(j)**2/pp**2)
      go to 20
10    dnorm=.04+.15*exp(-12.*(mrad(j)/pp-.9))
      go to 20
C  Alcator profile.
14    if(mrad(j) .gt. 9.) go to 15
      dnorm=1.-(mrad(j)**2/9.7**2)
      go to 20
15    dnorm=.1389*exp(-12.*(mrad(j)/9.-1.))
20    na(j)=nahat*dnorm
      nb(j)=nbhat*dnorm
      dens(j)=dnorm
      b0z(j)=b0*rmaj/(rmaj+rad(j))
C   Tensor elements.
      pia=1.32e3*sqrt(na(j))/sqrt(mua)
      pib=1.32e3*sqrt(nb(j))/sqrt(mub)
      pie=1.32e3*sqrt(na(j)+nb(j))/sqrt(mue)
      wca=9.58e3*b0z(j)/mua
      wcb=9.58e3*b0z(j)/mub
      wce=9.58e3*b0z(j)/mue
      r=1.-(pie**2/(w*(w-wce)))-(pia**2/(w*(w+wca)))
     & -(pib**2/(w*(w+wcb)))
      l=1.-(pie**2/(w*(w+wce)))-(pia**2/(w*(w-wca)))
     & -(pib**2/(w*(w-wcb)))
      s=.5*(r+l)
      d=.5*(r-l)
      p=1.-((pie**2+pia**2+pib**2)/w**2)
C   Dispersion relations.
      a=1.
      b=-(p/s+1)*(s-npar**2)+d**2/s
      c=(p/s)*((s-npar**2)**2-d**2)
99    bsq(j)=b**2-4.*a*c
      if(bsq(j) .lt. 0.)bsq(j)=0.
      kpeps(j)=(w/c0)**2*(-b+sqrt(bsq(j)))/(2.*a)
      kpems(j)=(w/c0)**2*(-b-sqrt(bsq(j)))/(2.*a)
C   Plot the dispersion relations.
      if(kpeps(j) .gt. 2.)kpeps(j)=2.
      if(kpeps(j) .lt. -.5)kpeps(j)=-.5
      if(kpems(j) .lt. -3000.) kpems(j)=-3000.
100   continue
      call plot_$setup("KPEPS vs RADIUS","RAD(cm)","KPEPS",1,0e0,1,0)
      call plot_$scale(rmin,rmax,-.5,2.)
      call plot_(rad,kpeps,nstep,1," ")
      call plot_$setup("KPEMS vs RADIUS","RAD(cm)","KPEMS",1,0e0,1,0)
      call plot_$scale(rmin,rmax,-3000.,0.)
      call plot_(rad,kpems,nstep,1," ")
      call exit
      end

r 16:33 0.685 21
```

Appendix 7

TIIH,2 Dimensional Code

```
                 tiih.fortran       04/15/81  1004.1 est Wed

C
C  TIIH 2D
C
C  Calculates the two ion ion hybrid layer position
C  in two dimensions for a simple parabolic
C  density profile, 2 ion species, and a 1/R
C  magnetic field.
C
      dimension rad(200),x(200),y(200),dn(200),bz(200)
      dimension rad2(200),x2(200),y2(200),alpi(10)
      real nehat,nahat,mua,mub,npar,kpar
      external plot_$setup(descriptors)
      external plot_$scale(descriptors)
      external plot_(descriptors)
C
C  Data
C
      nstep=100
      nehat=5.e14
      f0=.97e8
      b0=.7e5
      mua=2.
      mub=1.
      kpar=.1
      rmax=12.5
      rmaj=54.
C
C  Write statements.
      write(6,50)
50    format(1x,' !wor 30 h  !gra 1,35  !shr b')
      write(6,7) f0,mua,mub,b0,nehat
7     format(/1x,'f0=',e10.5,2x,'mua=',f6.3,2x,'mub=',f6.3,2x,
     & 'b0=',e10.5,2x,'nehat=',e10.5)
      write(6,8) rmax,rmaj,kpar,nstep
      write(6,51)
51    format(/1x,'alpha=.05, .1, .2, .3, .45, 1.0')
8     format(/1x,'rmax=',f6.3,2x,'rmaj=',f6.3,2x,
     & 'kpar=',f6.3,2x,'nstep=',i3)
C  Initial calculations and constants.
      c0=3.e10
      rmin=-rmax
      rdel=(rmax-rmin)/float(nstep)
      w=2.*3.1416*f0
      npar=kpar*c0/w
      alpi(1)=.05
      alpi(2)=.1
      alpi(3)=.2
      alpi(4)=.3
      alpi(5)=.45
      alpi(6)=1.
      call plot_$setup("Y vs RADIUS","RAD(cm)","Y",1,0e0,1,0)
      call plot_$scale(-rmax,rmax,0.,2.*rmax)
      do 10 i=1,6
      alp=alpi(i)
      nahat=nehat/(1.+alp)
C  Start of the loop.
      do 200 j=1,nstep+1
      rad(j)=rmin+float(j-1)*rdel
      b0z=b0*rmaj/(rmaj+rad(j))
      bz(j)=b0z
      uca=9.58e3*b0z/mua
      c5=(1./(w**2-uca**2))+((alp*mua/mub)/(w**2-uca**2
     & *(mua/mub)**2))
      dnorm=(1.-npar**2*mua)/(c5*nahat*1.32e3**2)
      dn(j)=dnorm
      x(j)=rad(j)
C  Calculate r (any density profile can be implemented).
      if(dnorm .le. .99 .and. dnorm .ge. .1e-5) then
          r=rmax*sqrt(1.-dnorm)
          if((r**2-x(j)**2) .le. 0.) then
             y(j)=0.
          else
             y(j)=sqrt(r**2-x(j)**2)
          end if
      else
          y(j)=0.
      end if
C  The following loop calculates the large circle of radius rmax.
      rad2(j)=rmin+float(j-1)*rdel
      x2(j)=rad2(j)
      y2(j)=sqrt(rmax**2-x2(j)**2)
200   continue
C  Call the plotting routines.
      call plot_(x2,y2,nstep+1,1," ")
205   call plot_(x,y,nstep+1,1," ")
10    continue
      call exit
      end

r 10:04 0.562 1
```

Appendix 8

Inhomogeneous Plasma Cylindrical Eigenmode Fields and Damping Code

```
                    damp.fortran        04/15/81  0923.0 est Wed

C  TFR - Ez
C
C  Calculates and plots Etheta, Er, Ez, Btheta, Br, Bz,
C  E+**2, E'+**2, Ne, Te, Peld/cm**3, P2wci/cm**3, PHI,
C  P2wci/cm, and radiation resistance for two ion species,
C  inhomogeneous plasma, uniform magnetic field and m from
C  -3 to +3.
C
C  Dimension and format statements.
      dimension y(3),yp(3),q(3,8),eplus(3),rau(3),cep(3)
      dimension rad(200),etheta(200),err(200),bzz(200),btheta(200),
     &  brr(200),phii(200),epsq(200),depsq(200),dens(200),ez(200),
     &  erp(200),tempi(200),tempe(200),peld(200),p2wci(200),
     &    peldpl(200),peldpp(200),p2wpl(200),p2wpp(200)
      real npar,lant,kperps,nperps
      external plot_$setup(descriptors),plot_$scale(descriptors),
     &  plot_(descriptors)
      EXTERNAL SYDELC
      COMMON A,B,C,D,F,G,H,U,R,S,OMAC,OMBC,PM,SOM,ER,IT
     + ,OMCA,OMCB,POM,OMA,OMB,CA
      COMMON /FP/ PP,FA,FB
      common /fix/om,/densty/dnorm
111   format(//12x,'omega a=',f4.1,3x,'omega b=',f4.1,4x,'na=',e10.5,3x,
     &  'nb=',e10.5 / 12x,'ma=',f4.2,8x,'mb=',f4.2,9x,'Ti=',
     &  f6.1,7x,'Te=',f6.1 / 12x,'Kpar=',f6.5,4x,'m=',f4.1,10x,
     &  'rmax=',f5.2,5x,' pp=',f5.2 / 12x,'lant=',f5.2,5x,'f0=',e10.5,
     &  3x,'rmaj=',f5.2,6x,'q0=',f5.2 / 12x,'ql=',f5.2,7x,'rant=',f5.2,
     &  6x,'pas=',f5.3)
      lprnt1=6
1     nt=1
      nimp=1
C
C  Data.
C   For hot plasma effects set:
C   gma=gmb=1.
C   oma=omb=2.
C   pna=. . .
C   pnb=0.
C
       oma=2.
       omb=2.
       pna=5.e14
       pnb=0.
       gma=1.
       gmb=1.
       ti=1000.
       te=1000.
      ca=.60291
      pm=0.
      rm=14.
      pp=9.
      lant=20.
      f0=2.e8
      rmaj=54.
      q0=.9
      ql=5.
      pas=.1
      rant=11.
C  Initial data reduction.
44    c0=3.e10
      w=6.28*f0
      pom=w/c0
      FA=2.E-15*PNA/GMA
      FB=2.E-15*PNB/GMB
      DFA=-2.*FA/PP**2
      DFB=-2.*FB/PP**2
      A=CA**2-POM**2
      OMAC=OMA**2
      OMBC=OMB**2
      OMCA=OMAC-1.
      OMCB=OMBC-1.
      B=OMCA*OMCB
      C=OMAC*OMCB
      D=OMBC*OMCA
      F=A*B
      G=OMA*C
      H=OMB*D
      U=PM**2+1.
      R=OMAC*OMBC*(OMA*OMB-1.)
      S=2.*PM**2*B
      DDR=2.*PAS*NIMP
      write(6,71)
71    format(1x,'!wor 30 h',1x,'!gra 1,35',1x,'!shr b')
      write(lprnt1,111)oma,omb,pna,pnb,gma,gmb,ti,te,ca,pm,
     &  rm,pp,lant,f0,rmaj,q0,ql,rant,pas
C  Poloidal mode number initial conditions.
      Y(1)=0.
      IF(PM.EQ.0.)GO TO12
      NET=ABS(PM)
      GO TO (11,12,13,14),NET
14    Y(2)=0.
      Y(3)=0.
      YP(3)=0.
      GO TO 3
13    Y(2)=0.
      Y(3)=0.
      YP(3)=1.
      GO TO 3
12    Y(2)=0.
```

```
      Y(3)=1.
      YP(3)=0.
      GO TO 3
11    IF(OMA.EQ.1..OR.OMB.EQ.1.)GO TO 10
      Y(2)=1.
      Y(3)=0.
      DELB=A*B+FA*C+FB*D
      DEPB=DFA*C+DFB*D
      DELC=FA*G+FB*H
      DEPC=DFA*G+DFB*H
      DELD=2.*A**2*B+C*(FA*(4.*A**2-2.*FA*OMAC)+2.*DFA)
     1          +D*(FB*(4.*A**2-2.*FB*OMBC)+2.*DFB)-4.*FA*FB*R
      CB=(-DELD+4.*DEPB-2.*PM*DEPC+4.*DELB*(PM*DELC-DELB)/B)/DELB
      YP(3)=-CB/8.
      GO TO 3
10    IF(OMA.EQ.OMB)GO TO 15
      IF(OMA.EQ.1.)GO TO 9
      Z=OMA
      OMA=OMB
      OMB=Z
9     IF(PM.EQ.1.)GO TO 8
      Y(2)=0.
      Y(3)=0.
      YP(3)=1.
      GO TO 3
8     Y(2)=1.
      Y(3)=0.
      YP(3)=A-FA/2.-FB*OMBC*(OMA*OMB-1.)/OMCB
      GO TO 3
15    continue
      GO TO 7
3     IT=4
      ER=0.
      IF(PM.NE.0.)ER=Y(2)/PM
      CALL SYDELC(YP,Y)
      I=0
      IT=0
      SOM=0.
      INI=0
      T=CA/POM
      P=0.25E10*PAS*T
      BR=-T*Y(2)
      BTE=T*ER
      BZ=(Y(2)+Y(1)*Y(3)-PM*ER)/POM
      PHI=P*SOM
      EPLUS(2)=0.
      EPLUS(3)=0.7071*(Y(2)-ER)
      LIGNE=7
      rad(1)=y(1)
      etheta(1)=y(2)
      jj=2
C  Main radius loop.
4     DO 5 LI=1,NIMP
      CALL ADIRKG(3,Y,1,PAS,INI,YP,Q,SYDELC)
      CALL SYDELC(YP,Y)
      IT=0
      INI=INI+1
5     CONTINUE
C  Field components calculation.
      BR=-T*Y(2)
      BTE=T*ER
      BZ=(Y(2)+Y(1)*Y(3)-PM*ER)/POM
      PHI=P*SOM
      EPLUS(1)=EPLUS(2)
      EPLUS(2)=EPLUS(3)
      EPLUS(3)=0.7071*(Y(2)-ER)
      CEPL=EPLUS(3)**2
      DEPL=(EPLUS(3)-EPLUS(1))/DDR
      CDEP=DEPL**2
      RO=Y(1)
      rad(jj)=y(1)
      etheta(jj)=y(2)
      err(jj)=er
      bzz(jj)=bz/y(1)
      brr(jj)=br
      btheta(jj)=bte
      epeq(jj)=cepl
      depeq(jj)=cdep
      phii(jj)=phi
C  Ez calculation.
      err(1)=err(2)
      erp(jj)=-1.*(err(jj-1)-err(jj))/(nimp*pas)
      brack=(err(jj)/rad(jj))+erp(jj)-(pm*etheta(jj)/rad(jj))
      ez(jj)=-(ca*2.8e11)/((pna+pnb)*dnorm)*brack
C  Hot plasma parameters (for 2wci hot plasma case only).
      b0=f0/(2.*1.52e3)
      dens(jj)=pna*dnorm
      atsq=(3./2.)*pp**2*q0/ql
      tnorm=exp(-rad(jj)**2/atsq)
      tempi(jj)=tnorm*ti
      tempe(jj)=tnorm*te
      vti=9.79e5*sqrt(tempi(jj))
      wpi=1.32e3*sqrt(dens(jj))
      r0=(ca*vti/w)*rmaj
      rhoi=(1.02e2/b0)*sqrt(tempi(jj))
      vte=4.19e7*sqrt(tempe(jj))
      alpha=w/(ca*vte)
C  Dispersion relation.
      aa=-1./3.
      npar=ca*c0/(2.*wpi)
      nperps=(aa-npar**2)+(aa*(1.-aa)/(aa-npar**2))
      kperps=nperps*(2.*wpi/c0)**2
C  Power deposition.
      be=4.03e-11*dens(jj)*tempe(jj)/b0**2
      if(alpha .gt. 8.) alpha=8.
      peld(jj)=(w*be/(16.*sqrt(3.14159)))*(kperps*c0**2/w**2)
```

```
      & *alpha*exp(-alpha**2)*etheta(jj)**2
       p2wci(jj)=(wpi**2/(16.*3.14159*w))*(rmaj/(rad(jj)+r0))
      & *rhoi**2*depsq(jj)
       peldpl(1)=0.
       p2wpl(1)=0.
       if(jj .eq. 1) go to 216
       peldpl(jj)=peldpl(jj-1)+2.*3.14159*rad(jj)*peld(jj)
      & *(rad(jj)-rad(jj-1))
       p2wpl(jj)=p2wpl(jj-1)+2.*3.14159*rad(jj)*p2wci(jj)
      & *(rad(jj)-rad(jj-1))
       if(rad(jj) .gt. .99*rant .and. rad(jj) .lt. rant)then
            radres=etheta(jj)**2/2.*lant**2/phii(jj)*9.e11
            elddl=phii(jj)/peldpl(jj)
            p2wdl=phii(jj)/p2wpl(jj)
            write(6,113)radres,elddl,p2wdl
113    format(/12x,'Rr=',e10.5,4x,'elddl=',e10.5,4x,'p2wdl=',e10.5)
       end if
216    jj=jj+1
17     if(y(1)+0.01*pas.lt.rm) go to 4
C  End of the main radius loop. Output statements.
7      continue
       jjm1=jj-1
       go to 198
       call plot_$setup("PELD vs RADIUS","RAD(cm)","PELD",1,0e0,1,0)
       call plot_(rad,peld,jjm1,1," ")
       call plot_$setup("P2WCI vs RADIUS","RAD(cm)","P2WCI",1,0e0,1,0)
       call plot_(rad,p2wci,jjm1,1," ")
       call plot_$setup("PELDPL vs RADIUS","RAD(cm)","PELDPL",1,0e0,1,0)
       call plot_(rad,peldpl,jjm1,1," ")
9000   call plot_$setup("P2WPL vs RADIUS","RAD(cm)","P2WPL",1,0e0,1,0)
       call plot_(rad,p2wpl,jjm1,1," ")
       go to 44
198    call plot_$setup("Ez vs RADIUS","RAD(cm)","Ez",1,0e0,1,0)
       call plot_(rad,ez,jjm1,1," ")
199    call plot_$setup("Etheta vs RADIUS","RAD(cm)","Etheta",1,0e0,1,0)
       call plot_(rad,etheta,jjm1,1," ")
       call plot_$setup("Er vs RADIUS","RAD(cm)","Er",1,0e0,1,0)
       call plot_(rad,err,jjm1,1," ")
       call plot_$setup("Br vs RADIUS","RAD(cm)","Br",1,0e0,1,0)
       call plot_(rad,brr,jjm1,1," ")
       call plot_$setup("Btheta vs RADIUS","RAD(cm)","Btheta",1,0e0,1,0)
       call plot_(rad,btheta,jjm1,1," ")
       call plot_$setup("Bz vs RADIUS","RAD(cm)","Bz",1,0e0,1,0)
       call plot_(rad,bzz,jjm1,1," ")
       call plot_$setup("PHI vs RADIUS","RAD(cm)","PHI",1,0e0,1,0)
       call plot_(rad,phii,jjm1,1," ")
       call plot_$setup("EPSQ vs RADIUS","RAD(cm)","EPSQ",1,0e0,1,0)
       call plot_(rad,epsq,jjm1,1," ")
       call plot_$setup("DEPSQ vs RADIUS","RAD(cm)","DEPSQ",1,0e0,1,0)
       call plot_(rad,depsq,jjm1,1," ")
       go to 44
       go to 44
500    call exit

       END
```



```
C
C  Calculates Runge-Kutta coefficients.
C
      SUBROUTINE  SYDELC(YP,Y)
      DIMENSION  Y(3) , YP(3)
      COMMON A,B,C,D,F,G,H,U,R,S,OMAC,OMBC,PM,SOM,ER,IT
     + ,OMCA,OMCB,POM,OMA,OMB,CA
      common /fix/ om
      common /densty/dnorm
      IT=IT+1
      IF(IT.EQ.1)GO TO 1
      IF(Y(1).EQ.0.)GO TO 10
      CALL CALPI(Y(1),PIA,PIB,DPIA,DPIB)
      RC=Y(1)**2
      APM=A+PM**2/RC
      Z=PIA*C+PIB*D
      DELA=APM*B+Z
      DELB=F+Z
      DELC=PIA*G+PIB*H
      deld=b*a*(a+u/rc)+pia*c*(2.*a-pia*omac+u/rc)+pib*d*(2.*a-pib
     &  *ombc+u/rc)-2.*pia*pib*r
      DEPB=DPIA*C+DPIB*D
      DEPA=DEPB-S/(RC*Y(1))
      DEPC=DPIA*G+DPIB*H
      Z=DEPB/DELB-DEPA/DELA
      IF(PM.EQ.0.)Z=0.
      COA=1./Y(1)+Z
      cob=-deld/delb+z/y(1)+pm*(delc*(2./y(1)+depa/dela)-depc)
     &   /(delb*y(1))
      YP(1)=1.
      YP(2)=Y(3)
      YP(3)=-COA*Y(3)-COB*Y(2)
      IF(IT.EQ.4)RETURN
      ER=PM*B*(Y(3)+Y(2)/Y(1))/(DELA*Y(1))+Y(2)*DELC/DELA
      OM=(ER**2+Y(2)**2)*Y(1)
      IF(IT.EQ.5)GO TO 1
      SOM=SOM+2.*OM
      RETURN
    1 SOM=SOM+OM
      RETURN
10    YP(1)=1.
      YP(2)=Y(3)
      OM=0.
      RETURN
      END
```

adirkg.fortran   04/01/81 1604.2 est Wed

```
      SUBROUTINE ADIRKG(N,Y,KSTEP,H,INI,YP,Q,SYSTEM)
C
C  ROUTINE TO EXECUTE 'KSTEP' RUNGE-KUTTA ITERATIONS.
C
      DIMENSION Y(N),YP(N),Q(N,8),F(4),W(4)
      common /densty/dnorm
      DATA F(1),F(2),F(3),F(4)/.0,.5,.5,1./
      DATA W(1),W(2),W(3),W(4)/1.,2.,2.,1./
C
      DO 1000 NSTEP=1,KSTEP
C FOR EACH STEP, FIRST INITIALIZE:
C Q(I,1) DOESN'T NEED TO BE CLEARED, BECAUSE F(1)=0, BUT DO IT ANYWAY.
C Q(I,6) WILL BE AN ACCUMULATOR, AND Q(I,7) SAVES THE STARTING
C   OF Y.
        DO 10 I=1,N
          Q(I,1)=0.
          Q(I,6)=0.
  10      Q(I,7)=Y(I)
C NOW DO THE 4 DERIVATIVE EVALUATIONS
        DO 100 J=1,4
          DO 20 I=1,N
  20        Q(I,8)=Y(I)+Q(I,J)*H*F(J)
          CALL SYSTEM(YP,Q(1,8))
          DO 30 I=1,N
            Q(I,J+1)=YP(I)
  30        Q(I,6)=Q(I,6)+Q(I,J+1)*W(J)
 100    CONTINUE
C CALCULATE THE NEW Y
        DO 200 I=1,N
 200    Y(I)=Y(I) + Q(I,6)*H/6.
1000  CONTINUE
      RETURN
      END

      SUBROUTINE  CALPI(R,A,B,AP,BP)
C
C   CALCULATES DENSITY AND DENSITY GRADIENT PROFILES.
C
      COMMON  /FP/  PP,FA,FB
      common /densty/dnorm
      RAP=R/PP
      IF(RAP.GT.0.9)GO TO 1
      D=1.-RAP**2
      DP=-2.*RAP/PP
      GO TO 2
1     Z=EXP(-12.*(RAP-0.9))
      D=0.04+0.15*Z
      DP=-1.8*Z/PP
2     A=FA*D
      B=FB*D
      AP=FA*DP
      BP=FB*DP
      dnorm=d
      RETURN
      END
```

<u>List of Symbols used in TFR-EZ</u>

CA = k_z

PM = m

POM = ω/c

OMA = Ω_a

OMB = Ω_b

RM = maximum radius

PP = limiter radius

PNA = n_a cm^{-3}

PNB = n_b cm^{-3}

GMA = M_a

GMB = M_b

E_θ in statvolts

OM = $(E^2_r + E^2_\theta)$ r poynting flux element

PHI = poynting flux -z, +z, erg sec^{-1}

NIMP = # steps between printing intervals

INI = # of applications of ADIRKG during a radius scan

Y(1), Y(2), Y(3), = variables r, E_θ, E'_θ

YP(1), YP(2), YP(3) = derivatives r', E'_θ, E''_θ

others are obvious such ER = E_r etc.

Appendix 9

Stochastic Mode Stacking Code

```
                    phi6.fortran        05/05/81  1701.6 edt Tue

C
C  STOCHASTIC MODE STACKING.
C
C  Calculates and plots the real, imaginary, magnitude, phase,
C  average, and average deviation of the sum of s=1,3,10,20
C  modes as a function of linearly increasing kzr or z, where
C  kzr0 is some random number between .5 and .6/cm with random
C  or fixed initial phase fluctuations and z is the distance
C  from the antenna.
C
      parameter idim=500
      dimension s1(idim),s3(idim),s10(idim),s20(idim),
     &   sre(idim),sim(idim),smag(idim),spha(idim),xarray(idim),
     &   zs(idim),sd(idim)
      dimension kzr0(20),kzrmin(20),kzrmax(20),kzrdel(20),
     &   kzr(20),kz(20),kzm(20),pk(20),f(20),fp(20),fn(20),
     &   pha(20)
      integer s
      real kzr,kzrmin,kzrmax,kzrdel,kzr0,kzi,kzfa,kzff,
     &   kminf,kmaxf,ms,mrs,kmult,ksubt
      complex f,fn,fp,s1,s3,s10,s20,kz,kzm,sd
      external plot_$setup(descriptors),plot_$scale(
     &   descriptors),plot_(descriptors)
      namelist /input/iplot
C
C   Data.
C    scank=1 for k and 0 for z.
C    phase=1 for random and 0 for fixed (0).
C
      s=1
      scank=1.
      phase=0.
      kminf=.9
      kmaxf=1.1
      kmult=1.
      ksubt=0.
      z=0.
      zmin=0.
      zmax=60.
      r=54.
      kzi=.1/r
      p=0.
      n=500
      kzfa=0.
      kzff=1.e3
C
C   Random kzr0.
       kzr0(1)=.5534
       kzr0(2)=.5069
       kzr0(3)=.5110
       kzr0(4)=.5427
       kzr0(5)=.5277
       kzr0(6)=.5779
       kzr0(7)=.5186
       kzr0(8)=.5765
       kzr0(9)=.5965
       kzr0(10)=.5150
       kzr0(11)=.5381
       kzr0(12)=.5609
       kzr0(13)=.5905
       kzr0(14)=.5498
       kzr0(15)=.5184
       kzr0(16)=.5653
       kzr0(17)=.5406
       kzr0(18)=.5516
       kzr0(19)=.5697
       kzr0(20)=.5580
C   Random phase.
       pha(1)=1.048
       pha(2)=4.657
       pha(3)=2.252
       pha(4)=6.162
       pha(5)=.612
       pha(6)=5.349
       pha(7)=5.686
       pha(8)=2.536
       pha(9)=1.256
       pha(10)=.191
       pha(11)=6.259
       pha(12)=4.934
       pha(13)=2.533
       pha(14)=.815
       pha(15)=5.218
       pha(16)=1.805
       pha(17)=2.816
       pha(18)=4.413
       pha(19)=6.160
       pha(20)=.488
C   Initial calculations and initializations.
44     sumr=0.
       sumi=0.
       summ=0.
       sump=0.
       rs=0.
       rrs=0.
       ms=0.
       mrs=0.
       drs=0.
       drrs=0.
```

```
      dms=0.
      dmrs=0.
      if(scank .eq. 1.) then
         scanz=0.
      else
         scanz=1.
      end if
      l=6.2832*r
C  J and I do loops. (increase k or z, different k0 and
C  initial phase).
      do 300 j=1,n
      do 200 i=1,s
C   K(i) calculation.
      kzrmin(i)=kminf*kmult*(kzr0(i)-ksubt)
      kzrmax(i)=kmaxf*kmult*(kzr0(i)-ksubt)
      kzrdel(i)=(kzrmax(i)-kzrmin(i))/float(n)*scank
      zdel=(zmax-zmin)/float(n)*scanz
      zs(j)=zmin+float(j-1)*zdel
      if(scank .eq. 1.) zs(j)=z
      if(scank .eq. 0.) kzrmin(i)=kzr0(i)
      kzr(i)=kzrmin(i)+float(j-1)*kzrdel(i)+kzfa*
     &   cos(kzff*float(j-1)*kzrdel(i))
      pk(i)=p*kzr(i)
      kz(i)=cmplx(kzr(i),kzi)
      kzm(i)=kz(i)+cmplx(pk(i),0.)
C   F+ and F- calculation.
      fp(i)=cexp((0.,1.)*kz(i)*zs(j))/(1.-cexp((0.,1.)*kz(i)*l))
      fn(i)=cexp((0.,1.)*kzm(i)*(l-zs(j)))/(1.-cexp((0.,1.)*kzm(i)*l))
      f(i)=(fp(i)+fn(i))*cexp((0.,1.)*pha(i)*phase)
C   End of I loop.
200   continue
C   Stochastic sum.
      xarray(j)=kzrmin(1)+float(j-1)*kzrdel(1)
      s1(j)=f(1)
      s3(j)=s1(j)+f(2)+f(3)
      s10(j)=s3(j)+f(4)+f(5)+f(6)+f(7)+f(8)+f(9)+f(10)
      s20(j)=s10(j)+f(11)+f(12)+f(13)+f(14)+f(15)+f(16)+f(17)+f(18)
     &  +f(19)+f(20)
      if(s .eq. 1) sd(j)=s1(j)
      if(s .eq. 3) sd(j)=s3(j)
      if(s .eq. 10) sd(j)=s10(j)
      if(s .eq. 20) sd(j)=s20(j)
      sre(j)=real(sd(j))
      sim(j)=aimag(sd(j))
      smag(j)=sqrt(sre(j)**2+sim(j)**2)
      spha(j)=atan2(sim(j),sre(j))
C   Sum and deviation calculation.
      sumr=sumr+sre(j)
      sumi=sumi+sim(j)
      summ=summ+smag(j)
      sump=sump+spha(j)
      rs=rs+abs(sre(j)-s)
      rrs=rrs+abs(sre(j)-sqrt(s))
      ms=ms+abs(smag(j)-s)
      mrs=mrs+abs(smag(j)-sqrt(s))
      drs=drs+(sre(j)-s)**2
      drrs=drrs+(sre(j)-sqrt(s))**2
      dms=dms+(smag(j)-s)**2
      dmrs=dmrs+(smag(j)-sqrt(s))**2
C  End of J loop.
300   continue
C  Average calculation.
      ar=sumr/n
      ai=sumi/n
      am=summ/n
      ap=sump/n
      adrs=rs/n
      adrrs=rrs/n
      adms=ms/n
      admrs=mrs/n
      sdrs=sqrt(drs/n)
      sdrrs=sqrt(drrs/n)
      sdms=sqrt(dms/n)
      sdmrs=sqrt(dmrs/n)
C  Write input and output data.
118   format(1x,' !jum  !hco w')
      write(6,119)
119   format(1x,' !wor 30 h  !gra 1,35  !shr b')
      write(6,120)scank,s,phase,n,r
120   format(//1x,'INPUT',5x,'scank=',f3.1,2x,'s=',i2,2x,
     &   'phase=',f3.1,2x,'n=',i4,2x,'r=',f4.1)
      write(6,121) kzi,p,z,zmin,zmax
121   format(1x,'DATA',6x,'kzi=',f8.6,2x,'p=',f5.2,2x,
     &   'z=',f7.2,2x,'zmin=',f7.2,2x,'zmax=',f7.2)
      write(6,122)kminf,kmaxf,kmult,ksubt
122   format(11x,'kminf=',f5.3,2x,'kmaxf=',f5.3,2x,
     &   'kmult=',f5.2,2x,'ksubt=',f6.3)
      write(6,223)kzfa,kzff,kzr0(1)
223   format(11x,'kzfa=',f4.3,2x,'kzff=',e10.5,2x,
     &   'kzr0(1)=',f7.5/)
      write(6,123)ar,ai,am,ap
123   format(1x,'AVERAGE',3x,'ar=',f8.4,3x,'ai=',f8.4,
     &   3x,'am=',f8.4,3x,'ap=',f8.4)
      write(6,124)adrs,adrrs,adms,admrs
124   format(1x,'AVE DEV',3x,'adrs=',f8.4,2x,'adrrs=',
     &   f8.4,2x,'adms=',f8.4,2x,'admrs=',f8.4)
      write(6,225)sdrs,sdrrs,sdms,sdmrs
225   format(1x,'STAND DEV',1x,'sdrs=',f8.4,2x,'sdrrs=',
     &   f8.4,2x,'sdms=',f8.4,2x,'sdmrs=',f8.4//)
C  Plotting routines.
      write(6,125)
125   format(1x,'iplot=1 to plot real')
      read(5,input)
      if(iplot .eq. 1) then
       if(scank .eq. 1.) then
         call plot_$setup("REAL vs KZR","KZR","RE",1,0)
```

```
      call plot_(xarray,sre,n,1," ")
     else
      call plot_$setup("REAL vs Z","Z","RE",1,0e0,1,0)
      call plot_(zs,sre,n,1," ")
     end if
    end if
    write(6,126)
126 format(1x,'iplot=1 to plot imaginary')
    read(5,input)
    if(iplot .eq. 1) then
     if(scank .eq. 1.) then
      call plot_$setup("IMAGINARY vs KZR","KZR","IM",1,0e0,1,0)
      call plot_(xarray,sim,n,1," ")
     else
      call plot_$setup("IMAGINARY vs Z","Z","IM",1,0e0,1,0)
      call plot_(zs,sim,n,1," ")
     end if
    end if
    write(6,127)
127 format(1x,'iplot=1 to plot magnitude')
    read(5,input)
    if(iplot .eq. 1) then
     if(scank .eq. 1.) then
      call plot_$setup("MAGNITUDE vs KZR","KZR","MAG",1,0e0,1,0)
      call plot_(xarray,smag,n,1," ")
     else
      call plot_$setup("MAGNITUDE vs Z","Z","MAG",1,0e0,1,0)
      call plot_(zs,smag,n,1," ")
     end if
    end if
    write(6,128)
128 format(1x,'iplot=1 to plot phase')
    read(5,input)
    if(iplot .eq. 1) then
     if(scank .eq. 1.) then
      call plot_$setup("PHASE vs KZR","KZR","PHA",1,0e0,1,0)
      call plot_(xarray,spha,n,1," ")
    else
      call plot_$setup("PHASE vs Z","Z","PHA",1,0e0,1,0)
      call plot_(zs,spha,n,1," ")
     end if
    end if
    go to 44
    call exit
    end

r 17:03 1.766 29 level 2
```

Appendix 10

Single Perpendicular Pass Radiation Resistance $k_{\parallel}$ Spectra Code

```
                         imped2.fortran      04/09/81  1108.8 est Thu

C
C  ANTENNA SPECTRUM.
C
C  Calculates the real and imaginary parts of the antenna
C  Kpar spectrum.
C
      dimension zk(500),k(500),rzk(500),zki(500)
      real mu,n0,kmin,kmax,k,npar,nreq,nc,np,kdel,kr
      complex c2,c3,zk
      logical first/.true./
      character cch
      external plot_$setup(descriptors)
      external plot_$scale(descriptors)
      external plot_(descriptors)
      cch=char(33)
C
C  Data.
      zmax=.9
      omega=2.
      mu=1.
      n0=1.e14
      rw=12.5
      ra=11.
      rp=9.
      nstep=500
      kmin=0.
      kmax=2.
      f=2.e8
      ww=3.
C  ispec=1 for real and 2 for imaginary.
      ispec=1
C  Constants.
      pai=3.1415936
      c=3.e10
      nline=36
      write(6,20)cch,cch,cch
20    format(1x,a1,'wor 30 h',a1,'gra 1,35',a1,'shr b')
      if(ispec .eq. 1) then
          call plot_$setup("REAL Z vs K","K","Z",1,0e0,1,0)
      else
          call plot_$setup("IMAG Z vs K","K","Z",1,0e0,1,0)
      end if
      call plot_$scale(0.,1.,0.,zmax)
30    del0=ra-rp
      del2=rw-ra
      w=2.*pai*f
```

Appendix 11

Inhomogeneous Plasma Cylindrical Eigenmode Dispersion Relation Code

eigen.fortran   05/05/81 1553.6 edt Tue

```
C
C  INHOMOGENEOUS EIGENMODE DISPERSION RELATIONS
C
C  Calculates and plots the fast wave eigenmode dispersion
C  relations for mu=1,2,...,n, two ion species, inhomogeneous
C  plasma, uniform magnetic field, and m from -3 to +3.
C
      dimension y(3),yp(3),q(3,8),eplus(3),rau(3),cep(3),etheta(500),
     &   nesol(500),kpsol(500)
      real ne,nesol,nemax,nedel,kpsol,kp,kpar,kpmax,
     &   kpdel
      external plot_$setup(descriptors)
      external plot_$scale(descriptors)
      external plot_(descriptors)
      EXTERNAL SYDELC
      COMMON A,B,C,D,F,G,H,U,R,S,OMAC,OMBC,PM,SOM,ER,IT
     + ,OMCA,OMCB,POM,OMA,OMB,CA
      COMMON /FP/ PP,FA,FB
      common /fix/ om
      common /densty/ dnorm
      write(6,991)
991   format(1x,' !wor 30 h  !gra 1,35  !shr b')
992   format(/3x,'omega a=',f4.2,2x,'omega b=',f4.2,2x,'nb/na=',
     &   f5.3 / 3x,'ma=',f4.2,2x,'mb=',f4.2,2x,'pm=',
     &   f4.2 / 3x,'f0=',e10.5,2x,'rmax=',f5.2,2x,'pp=',f5.2,2x,
     &   'rw=',f5.2)
C
C  Data.
C
      nstep=100
      ne=2.e12
      kpar=.01
      kpmax=1.2
      nemax=6.e14
      pm=0.
      f0=2.e8
      pas=.5
      oma=2.
      omb=2.
      rm=14.
      rw=12.5
      pp=9.
      gma=1.
      gmb=1.
      alpha=1.
C
      zintr=0.
      zinti=0.
      kdel=(kmax-kmin)/float(nstep)
      do 100 j=1,nstep
      k(j)=kmin+float(j)*kdel
      nc=(1.+omega)/omega**2*5.15e14*mu*k(j)**2
      if(nc .lt. .90*n0) go to 50
      del1=rw
      kr=0.
      go to 60
C   Dispersion relation.
50    np=(nc+n0)/2.
      wpisq=1.32e3**2*np/mu
      s=(wpisq/w**2)*(omega**2/(1.-omega**2))
      d=-omega*s
      npar=k(j)*c/w
      nrsq=((s-npar**2)**2-d**2)/(s-npar**2)
      kr=w/c*sqrt(nrsq)
      del1=del0+rp*(1.-sqrt(1.-nc/n0))
60    del3=del1+del2
      c1=exp(k(j)*del2)-exp(-k(j)*del2)
      c2=k(j)*(exp(k(j)*del1)+exp(-k(j)*del1))+(0.,1.)*kr*(exp(k(j)*
     &   del1)-exp(-k(j)*del1))
      c3=k(j)*(exp(k(j)*del3)+exp(-k(j)*del3))+(0.,1.)*kr*(exp(k(j)*
     &   del3)-exp(-k(j)*del3))
      c4=1./(2.*pai)*sin(k(j)*ww/2.)/(k(j)*ww/2.)
      c5=9.e11
      zk(j)=2.*pai*(0.,1.)*w/(k(j)*c**2)*c4*c1*c2*c5/c3
      rzk(j)=real(zk(j))
      zki(j)=aimag(zk(j))
      zintr=zintr+(rzk(j)*kdel)*2.
      zinti=zinti+(zki(j)*kdel)*2.
100   continue
      if(ispec .eq. 1) then
         call plot_(k,rzk,nstep/2,1," ")
      else
         call plot_(k,zki,nstep/2,1," ")
      end if
      write(6,21)cch,nline,cch
21    format(1x,a1,'jum ',i3,1x,a1,'dli 4')
      if (first)  write(6,22)mu,omega,f,rw,ra,rp,ww
22    format(1x,'mu=',f6.3,2x,'omega=',f6.3,1x,'f=',e10.5,/1x,
     & 'rw=',f6.3,1x,'ra=',f6.3,1x,'rp=',f6.3,1x,'ww=',f6.3)
      if (first) nline=nline+2
      first=.false.
      write(6,23)n0,zintr,zinti
23    format(1x,'n0=',e10.5,1x,'zintr=',f6.3,1x,'zinti=',f6.3)
      nline=nline+1
      go to 30
      call exit
      end
```

```
C  Initial data reduction.
      nt=1
      jj=1
      nimp=1
      npunch=0
      pom=6.28*f0/3.e10
      nedel=nemax/float(nstep)
      kpdel=kpmax/float(nstep)
C  Setup for plot.
      write(6,992) oma,omb,alpha,gma,gmb,pm,f0,rm,pp,rw
      call plot_$setup("KPAR vs NE","NE","KPAR",1,0e0,1,0)
      call plot_$scale(0.,nemax,0.,kpmax)
      ca=kpar
41    do 1000 j=1,nstep
      ne=ne+nedel
44    do 7 lt=1,nt
      pna=ne/(1.+alpha)
      pnb=ne*alpha/(1.+alpha)
      FA=2.E-15*PNA/GMA
      FB=2.E-15*PNB/GMB
      DFA=-2.*FA/PP**2
      DFB=-2.*FB/PP**2
      A=CA**2-POM**2
      OMAC=OMA**2
      OMBC=OMB**2
      OMCA=OMAC-1.
      OMCB=OMBC-1.
      B=OMCA*OMCB
      C=OMAC*OMCB
      D=OMBC*OMCA
      F=A*B
      G=OMA*C
      H=OMB*D
      U=PM**2+1.
      R=OMAC*OMBC*(OMA*OMB-1.)
      S=2.*PM**2*B
      DDR=2.*PAS*NIMP
85    y(1)=0.
C  Poloidal mode number initial conditions.
      IF(PM.EQ.0.)GO TO12
      NET=ABS(PM)
      GO TO (11,12,13,14),NET
14    Y(2)=0.
      Y(3)=0.
      YP(3)=0.
      GO TO 3
13    Y(2)=0.
      Y(3)=0.
      YP(3)=1.
      GO TO 3
12    Y(2)=0.
      Y(3)=1.
      YP(3)=0.
      GO TO 3
11    IF(OMA.EQ.1..OR.OMB.EQ.1.)GO TO 10
      Y(2)=1.
      Y(3)=0.
      DELB=A*B+FA*C+FB*D
      DEPB=DFA*C+DFB*D
      DELC=FA*G+FB*H
      DEPC=DFA*G+DFB*H
      DELD=2.*A**2*B+C*(FA*(4.*A**2-2.*FA*OMAC)+2.*DFA)
     1   +D*(FB*(4.*A**2-2.*FB*OMBC)+2.*DFB)-4.*FA*FB*R
      CB=(-DELD+4.*DEPB-2.*PM*DEPC+4.*DELB*(PM*DELC-DELB)/B)/DELB
      YP(3)=-CB/8.
      GO TO 3
10    IF(OMA.EQ.OMB)GO TO 15
      IF(OMA.EQ.1.)GO TO 9
      Z=OMA
      OMA=OMB
      OMB=Z
9     IF(PM.EQ.1.)GO TO 8
      Y(2)=0.
      Y(3)=0.
      YP(3)=1.
      GO TO 3
8     Y(2)=1.
      Y(3)=0.
      YP(3)=A-FA/2.-FB*OMBC*(OMA*OMB-1.)/OMCB
      GO TO 3
15    continue
      GO TO 7
3     IT=4
      ER=0.
      IF(PM.NE.0.)ER=Y(2)/PM
      CALL SYDELC(YP,Y)
      I=0
      IT=0
      SOM=0.
      INI=0
      T=CA/POM
      P=0.25E10*PAS*T
      BR=-T*Y(2)
      BTE=T*ER
      BZ=(Y(2)+Y(1)*Y(3)-PM*ER)/POM
      PHI=P*SOM
      EPLUS(2)=0.
      EPLUS(3)=0.7071*(Y(2)-ER)
      LIGNE=7
C  Main radius loop.
4     DO 5 LI=1,NIMP
      CALL ADIRKG(3,Y,1,PAS,INI,YP,Q,SYDELC)
      CALL SYDELC(YP,Y)
      IT=0
      INI=INI+1
5     CONTINUE
```

```
C  Field components calculation.
      BR=-T*Y(2)
      BTE=T*ER
      BZ=(Y(2)+Y(1)*Y(3)-PM*ER)/POM
      PHI=P*SOM
      EPLUS(1)=EPLUS(2)
      EPLUS(2)=EPLUS(3)
      EPLUS(3)=0.7071*(Y(2)-ER)
      CEPL=EPLUS(3)**2
      DEPL=(EPLUS(3)-EPLUS(1))/DDR
      CDEP=DEPL**2
      LIGNE=LIGNE+1
      LIGNE=0
      IF(NPUNCH.NE.1)GO TO 16
      IF(INI.EQ.NIMP)GO TO 16
      I=I+1
      RAU(I)=RO
      CEP(I)=CDEP
      IF(I.NE.3)GO TO 16
      I=0
16    CONTINUE
      RO=Y(1)
17    if(y(1)+0.01*pas.lt.rw) go to 4
7     continue
C  Crossover point calculation.
900   etheta(j)=y(2)
      if(j .eq. 1) go to 1000
      prod=etheta(j)*etheta(j-1)
      if(prod .le. 0.) go to 500
      nesol(j)=ne
      kpsol(j)=ca
      if(nesol(j) .gt. nemax) nesol(j)=nemax
      if(kpsol(j) .gt. kpmax) kpsol(j)=kpmax
      go to 1000
980   ca=ca+kpdel
      go to 44
1000  continue
      call plot_(nesol,kpsol,nstep,1," ")
      go to 41
500   call exit
      END

r 15:54 1.247 29 level 3
```

Appendix 12

Engineering Drawings

FIRST FLOOR LAYOUT

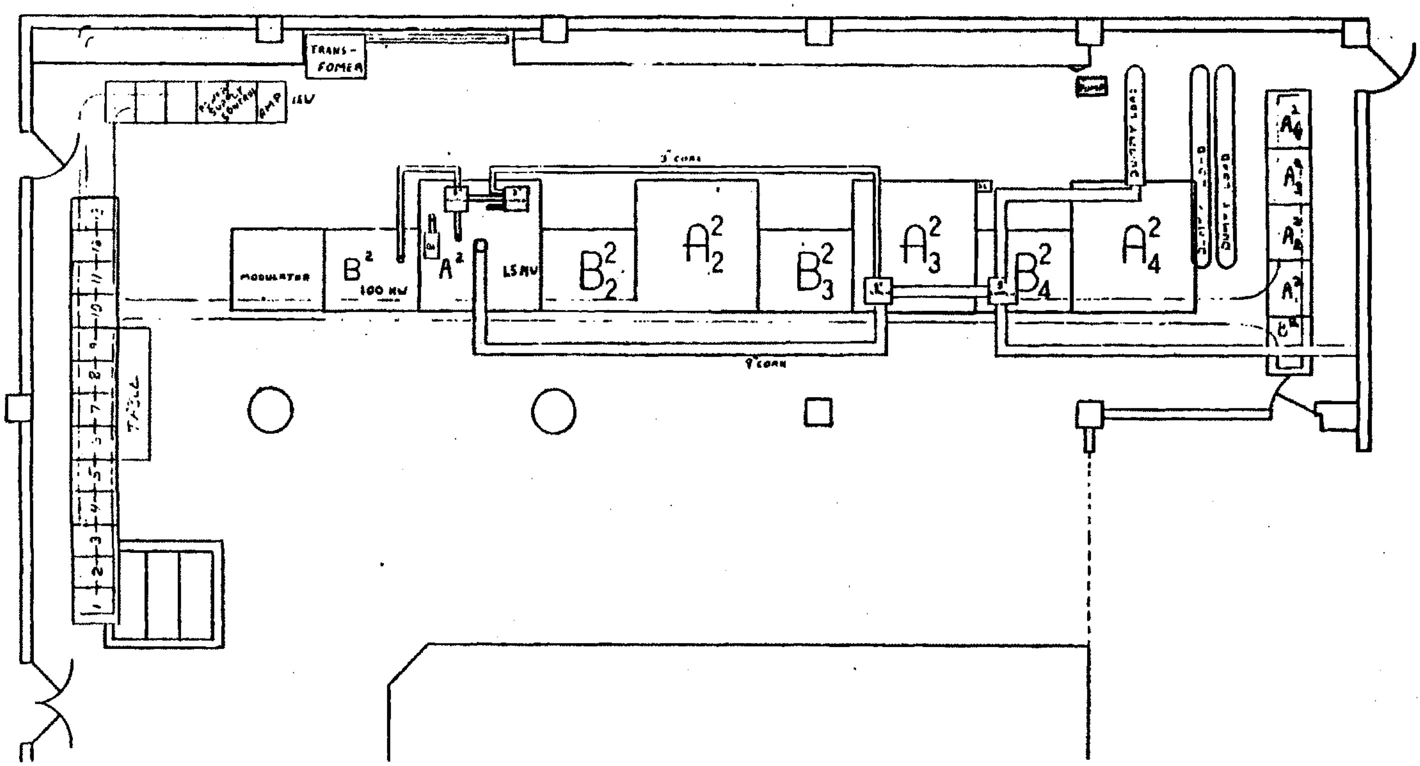

First Floor Layout of Transmitter Room

Figure 1

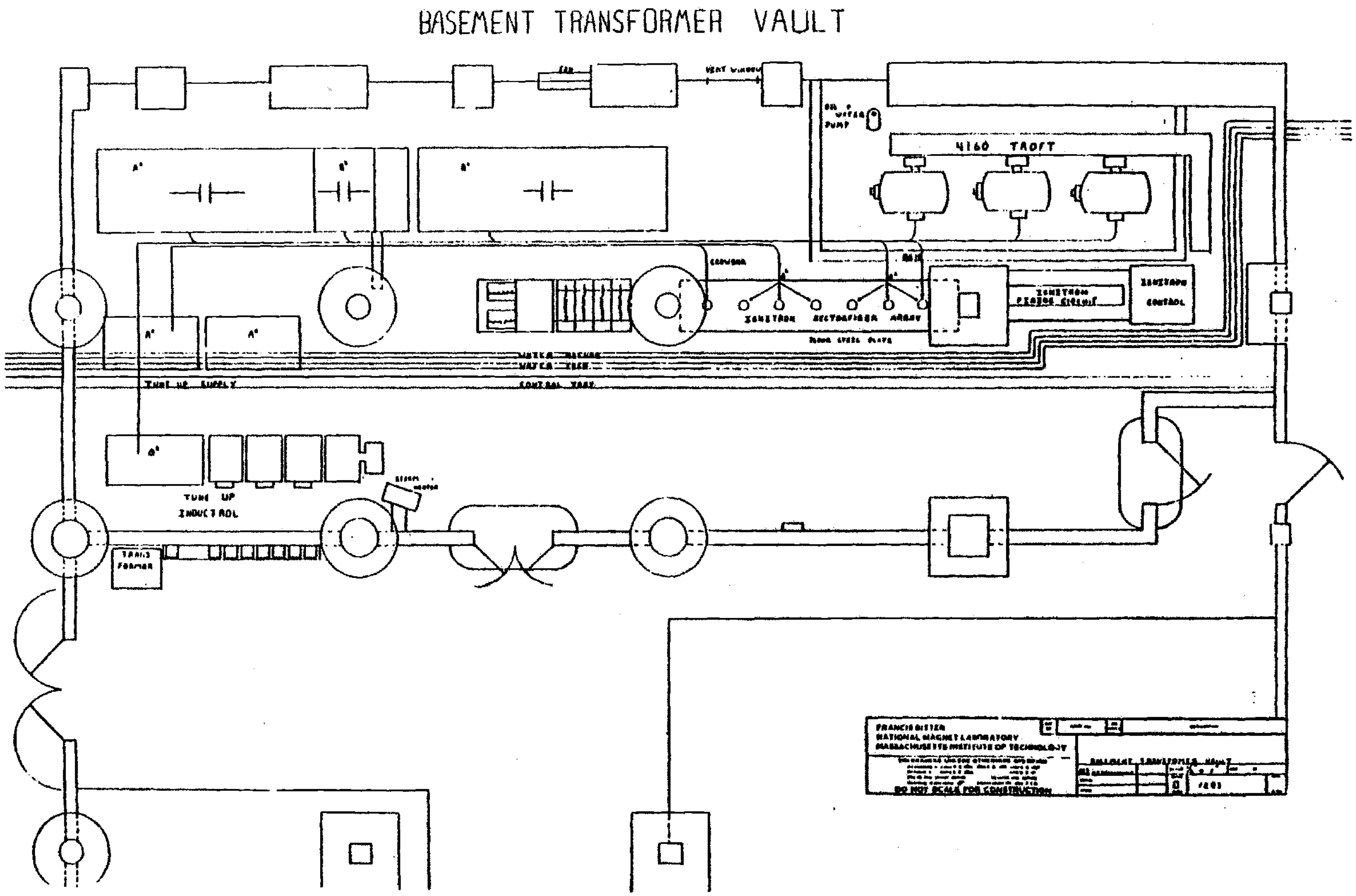

Basement Transformer Vault Layout

Figure 2

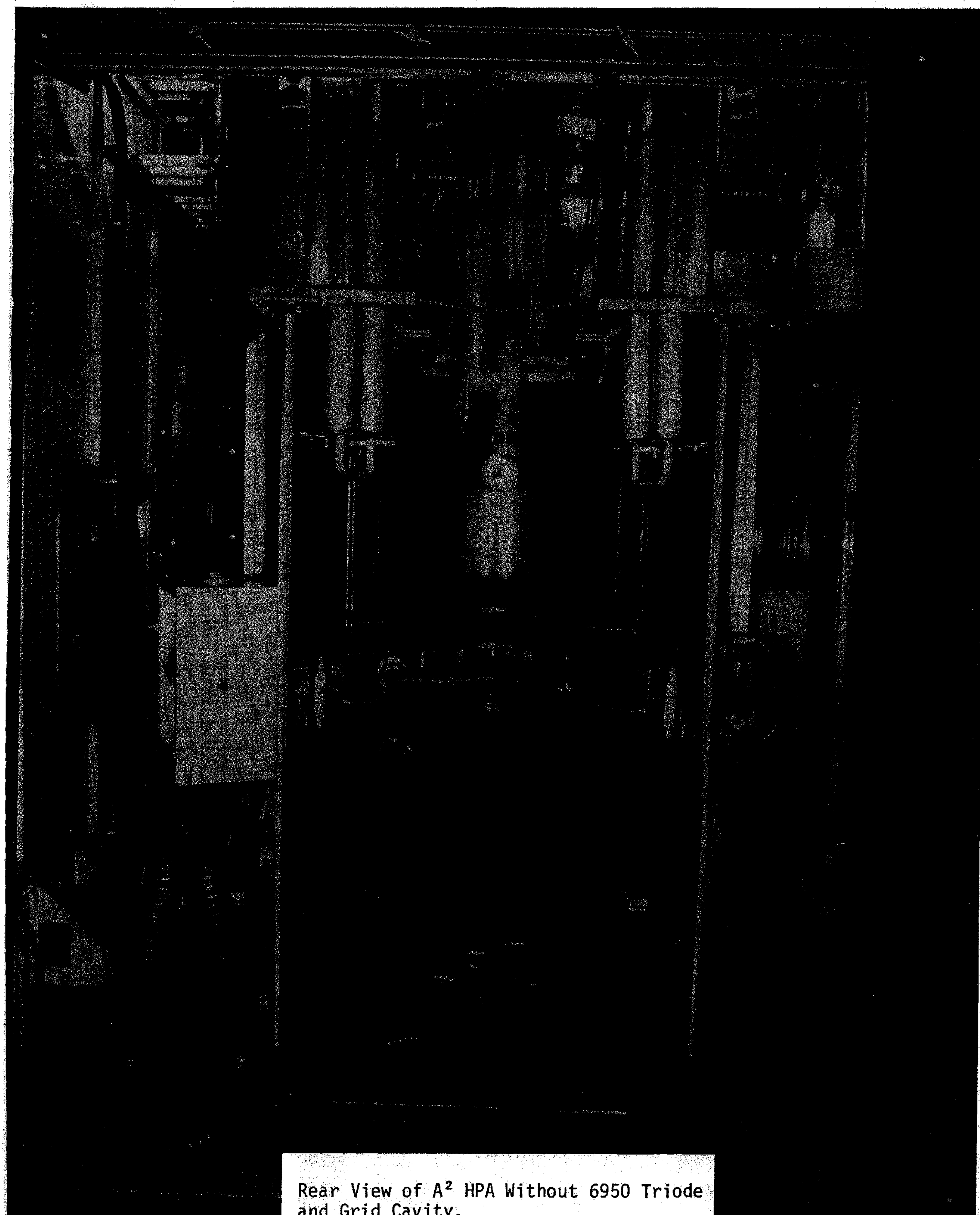

Rear View of A^2 HPA Without 6950 Triode and Grid Cavity.

Figure 3

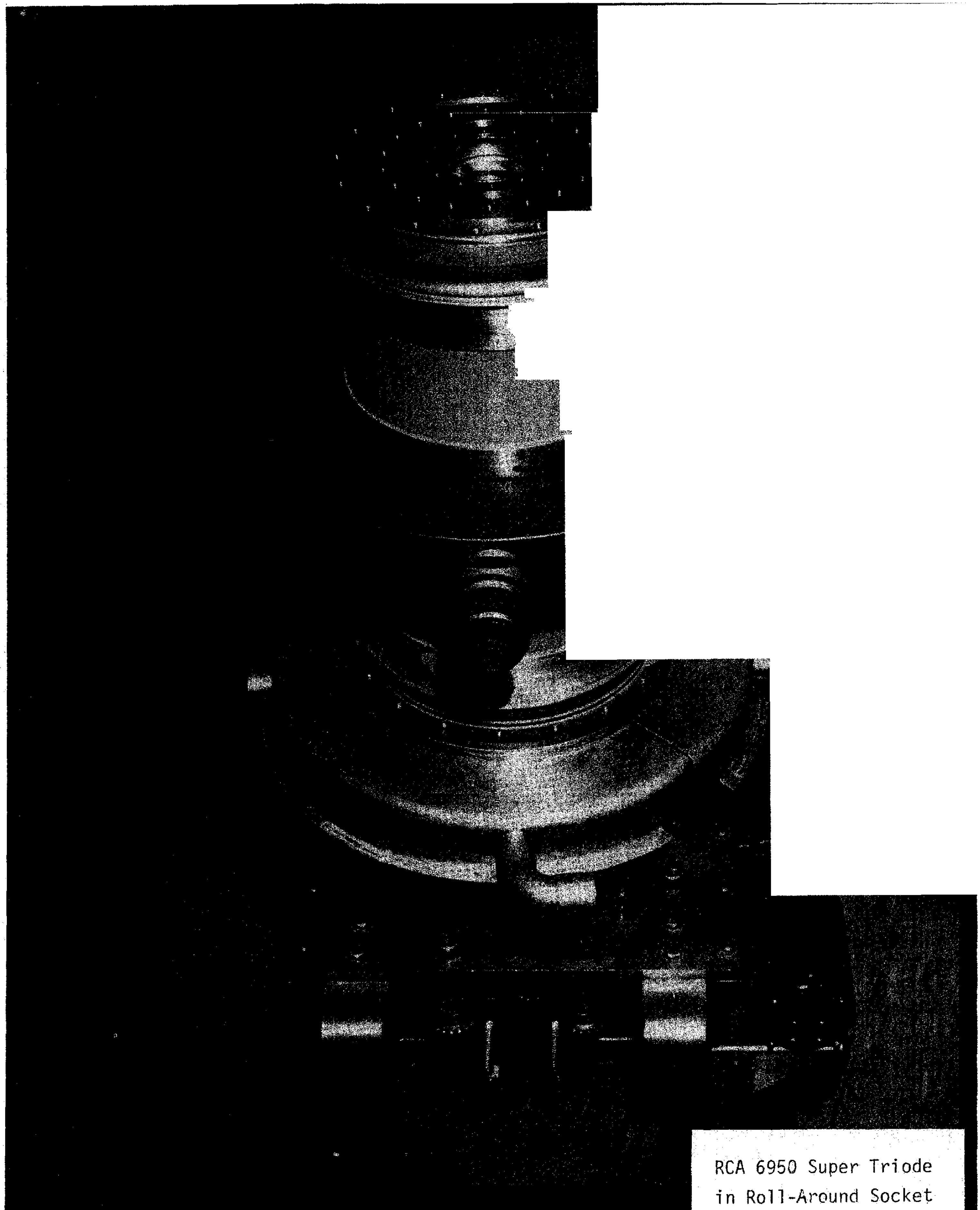

RCA 6950 Super Triode
in Roll-Around Socket

Figure 4

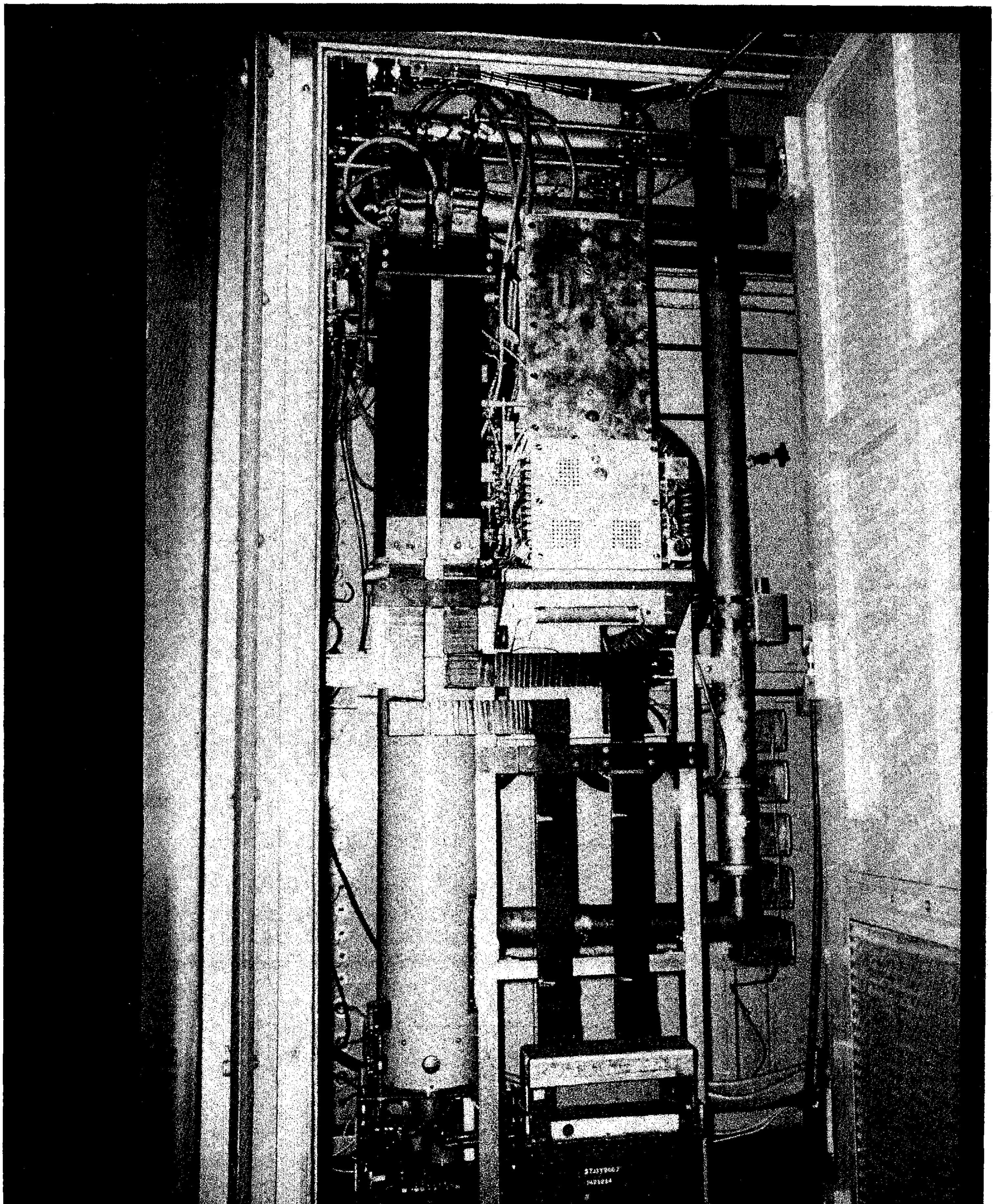

Back of B^2 IPA after 90 MHz Modification.

Figure 5

Simplified Diagram of the High Power

Control and Interlock Systems

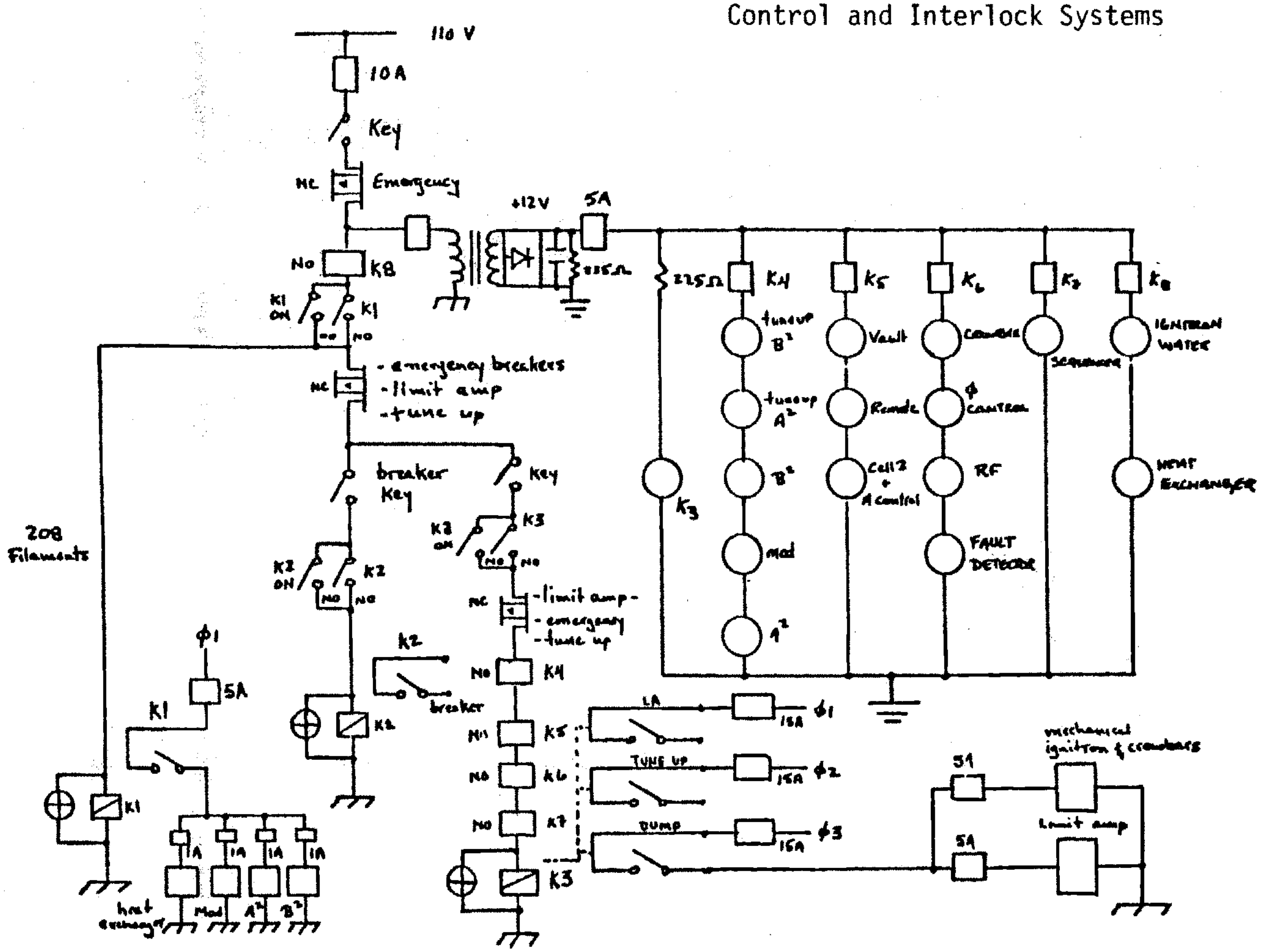

Figure 6

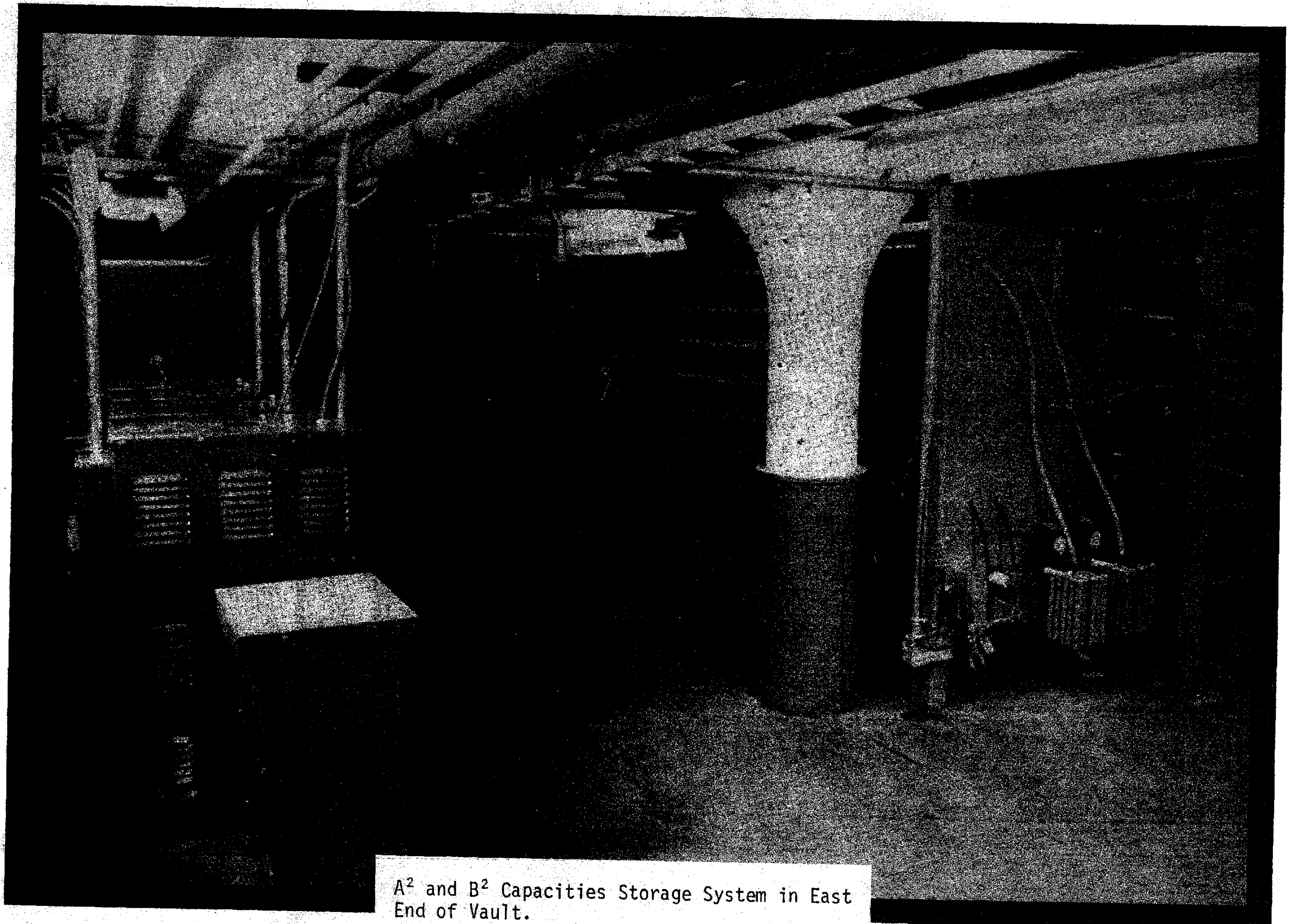

A^2 and B^2 Capacities Storage System in East End of Vault.

Figure 7

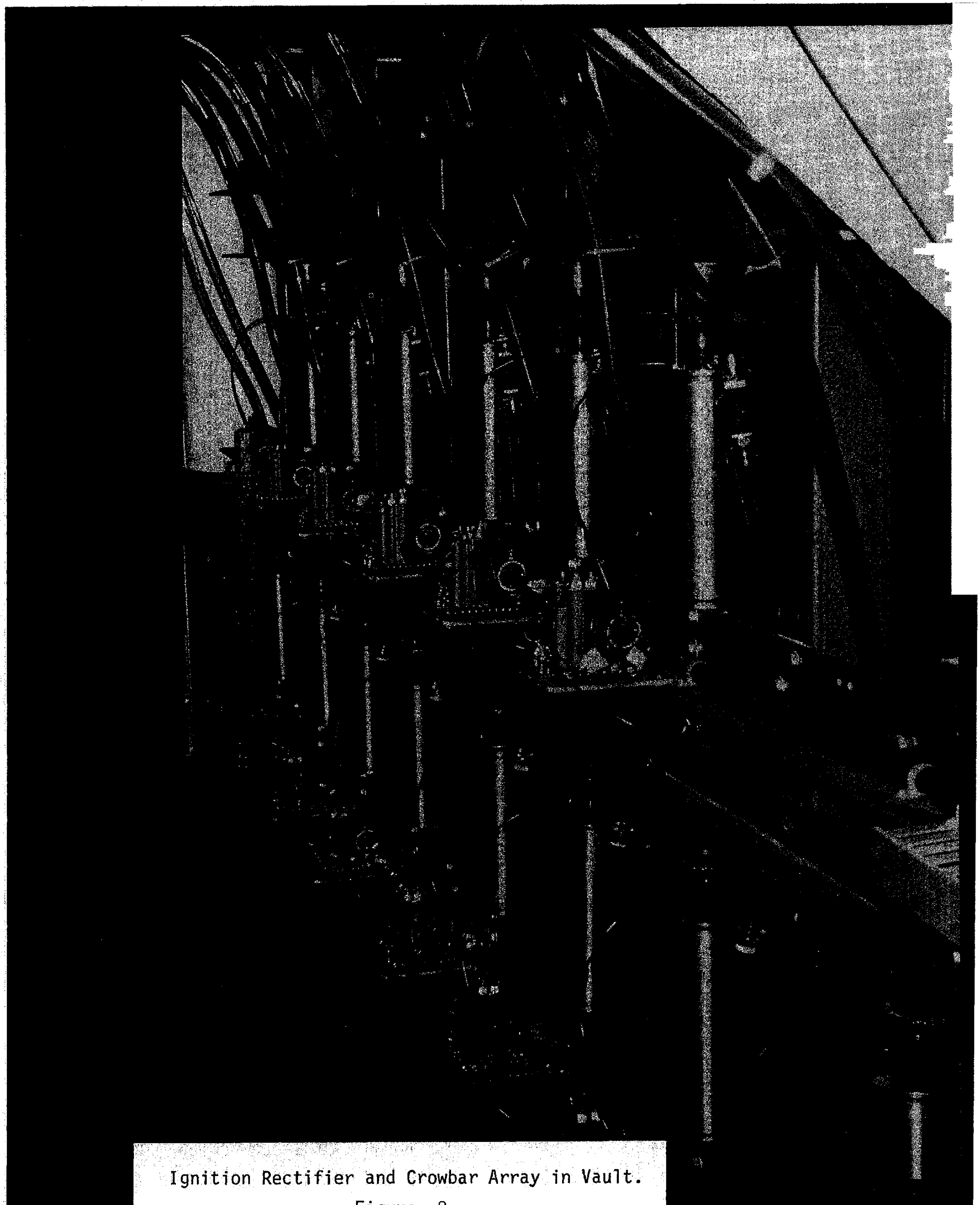

Ignition Rectifier and Crowbar Array in Vault.

Figure 8

REFERENCES

1. Chen, Francis F., Introduction to Plasma Physics, Plenum Press, New York, 1974.

2. Montgomery, D.B., "The Alcator Project," Grenoble Conference, MIT (FBNML), September 1974.

3. Gaudreau, M., et al., "High Density Discharges in the Alcator Tokamak," MIT (FBNML), 1976.

4. "Neutral Beam Energy and Power Requirements for the Next Generation of Tokamaks." ERDA-CTR, ERDA 76-77.

5. TFR Group, "High Power Neutral Injection and Ion Power Balance in TFR," EUR-CEA-FC 915.

6. Hasegawa, A., "Theory of Alfvén Wave Heating," Phys. Rev. Letters 35, (1975) 370.

7. Stix, T.H., "Fast-Wave Heating of a Two-Component Plasma," Nucl. Fusion (1975) 737.

8. Schuss, J.J., et al., "Lower Hybrid Heating in the Alcator A Tokamak," MIT PFC/RR-80-6, PFC/JA-80-11.

9. England, A.C., et al., "High Power Electron Cyclotron Heating in ISX and ORMAK Upgrade at ORNL," ORNL/TM-5425.

10. Takahashi, H., "ICRF Heating in Tokamaks," J. de Physique, Coll. C6, Suppl. au n 12, Tome 38 (1977) 171.

11. Takahashi, H., et al., "Ion Heating in ATC Tokamak in the Ion-Cyclotron Range of Frequencies," Physical Review Letters, Vol. 39, Number 1, July 4, 1977.

12. Hosea, H., "Fast Wave Heating of Two-Ion Plasmas in the Princeton Large Torus Through Minority Cyclotron Resonance Damping," PPPL-1554, July 1979.

13. Gaudreau, M., et al., "Preliminary ICRH Results on the Alcator-A Tokamak," Bull. Am. Phys. Soc. 24 (1979) 1062, Paper 7R7.

14. Coppi, B., et al., "High Temperature Regimes in Magnetically Confined Plasmas in the Alcator Tokamak," MIT, PRR-7524, October 1975.

15. Boxman, G.J., et al., "Low and High Density Operations of Alcator," Invited paper submitted to the VIIth European Conference on Plasma Physics, Lausanne, Switzerland, September 1-5, 1975.

16. Blackfield, D.T., "Numerical Simulations of ICRF Heated Tokamak Plasma," Nucl. Eng. Dept., Univ. of Wisconsin, May 1980.

17. "Rapport D'Activité Du Groupe De Recherches," Association Euratom-CEA, Department dé Recherches sur la Fusion Controlée, EUR-CEA-FC-1047, December 1979.

18. Reed, B.W., et al., "Preliminary Report on the Development of RF Auxiliary Heating Systems for TEPR-1," PPL, 1410 Princeton University, Princeton, N.J. , December 1977.

19. Paoloni, F.J., "Coupling to Fast Eigenmodes in a Non-Uniform Plasma," PPL, Princeton University, Princeton, N.J., Nuclear Fusion 18 3 (1978).

20. Swanson, D.G., "Hot Plasma in a Cylindrical Waveguide," The Physics of Fluid, Vol. 10, No. 2, February 1967.

21. Adams, J., "Etudes des Possibilities de Chauffage du Plasma de TFR par Absorption de L'onde Hydromagnetique Rapide," Report EUR-CEA-FC-711, October 1973.

22. Adams, J., Jacquinot, "Eigenmode Field Structure of the Fast Magnetosonic Wave in a Tokamak and Loading Impedence of Coupling Structures," Report EUR-CEA-FC-886, April 1977.

23. Stix, T.H., "Stochasticity and Superadiabaticity in Radio-Frequency Plasma Heating, PPL, Princeton University, Princeton, N.J., PPPL-1539, April 1979.

24. New College Edition, The American Heritage Dictionary of the English Language, 1978, Houghton Mifflin Company.

25. Rechester, A.B., et al., "Statistical Description of Stochastic Orbits in a Tokamak," Bell Laboratories, Murray Hill, N.J.

26. Mau, T.K., "Preliminary Studies of Collisionless Radiofrequency Heating of Ions in Toroidal Plasmas," Dept. of Electrical and Computer Engineering, University of Wisconsin, Ph.D. Prelim., March 1975.

27. McVey, B.D., "Supplementary RF Heating of a Tokamak Plasma in the Ion Cyclotron Range of Frequencies," Dept. Electrical Engineering, University of Wisconsin, Ph.D. Prelim., February 1977.

28. Overskei, D., "Diffusion and Energy Transport at the Limiter-Shadow Interface," Alcator Internal Memo. #7., MIT, FBNML.

29. Scaturro, L.S., Kusse, B., "Electric Probe Measurements Near the Plasma Edge in Alcator," Alcator Internal Memo. #5., MIT, FBNML.

30. TFR Group, "Damping Mechanisms of the Fast Wave in the Ion Cyclotron Range of Frequency," Third Symposium on Plasma Heating in Toroidal Devices, Varenna, Italy, September 6-17, 1976.

31. Adam., J., Samain, A., Report EUR-CEA-FC- 579, Association Euratom-CEA, (1971), Fontenay-aux-Roses.

32. Paoloni, F.J., "Coupling to Fast MHD Eigenmodes in a Toroidal Cavity," PPL, Princeton University, MATT-1119, May 1975.

33. Gaudreau, M., et al., "Investigation of Fast Atom Fluxes in the High-Density Plasma in Alcator, MIT, Nuclear Fusion 18, 12 (1978) Letters, Journal, April 17, 1978.

34. Alexeev, Yu. A., Gaudreau, M., and Kislayakov, A.U., "Interpretation of the Charge Exchange Measurements of 1976 on Alcator," Alcator Internal Memo. #6., March 1978, MIT.

35. Gaudreau, M., Chihoski, G., Parker, R., Bull. Amer. Phys. Soc. Ser. II 21 (1976) 1141.

36. Cope, D.B., "Passive Charge Exchange Neutral Diagnostics of the Alcator Tokamak Plasma," Dept. of Electrical Engineering, B.S. Thesis, May 1979, MIT.

37. Kilchenmann, M., "A Neutral Particle Spectrometer's Control and Measurement System," Dept. of Electrical Engineering, B.S. Thesis, May 25, 1979, MIT.

38. Besen, P., "Charge Exchange Diagnostic Instrumentation and Data Reduction System," Dept. of Electrical Engineering, B.S. Thesis, May 1978, MIT.

39. Gwinn, D., Granetz, R., "Observation of Neutron and X-Ray Sawteeth in Alcator,"MIT PFC/RR-78-8, June 1978.

40. Pappas, D.S., "Alcator Scaling Laws," for APS Plasma Physics Meeting, St. Petersburg, Florida, November 1975, MIT.

41. Gaudreau, M., et al., "Fast Magnetosonic Wave Structure Measurements in the Alcator A ICRF Experiment," Bull. Am. Phys. Soc. (1980) 4Q5.

42. Gaudreau, M., et al., "Medium Power ICRF Results on the Alcator Tokamak," Bull. Am. Phys. Soc. (1980) 4Q4.

43. Vdovin, V.L., et al., "Excitation of Magnetosonic Resonance in the Tokamak Plasma," ZhETF Pis. Red. 14, No. 4, 228-231 August 20, 1971.

44. Hosea, J., and Sinclair, R.M., "Ion Cyclotron Wave Generation in the Model C Stellarator," PPL, Princeton University, Princeton, N.J., Vol. 13, No. 3, March 1970.

45. Stix, T.H., Theory of Plasma Waves, McGraw-Hill, New York, 1962.

46. Allis, W.P., et al., Waves in Anisotropic Plasmas, MIT Press, Cambridge, MA 1963.

47. Paoloni, F.J., "Boundary Effects on M=0, ± 1 Alfvén Waves in a Cylindrical, Collisionless Plasma," Dept. Electrical Engineering, Texas Tech. University, Lubbock, Texas, July 29, 1974.

48. Perkins, F.W., "Heating Tokamaks Via the Ion-Cyclotron and Ion-Ion Hybrid Resonances," PPL, Princeton University, Princeton, N.J., PPL-1336, April, 1977.

49. Hosea, J.C., and the PLT Group, "Fast Wave Heating in the Princeton Large Torus," PPL, Princeton University, Princeton, N.J., PPL-1588, UC-20f,g, October, 1979.

50. Hosea, J.C., "Regimes of Operation in the Princeton Large Torus," PPL, Princeton University, Princeton, N.J., PPPL-1589, UC-20f, October 1979.

51. Colestock, P.L., et al., "Plasma Heating R&D Assessment," PPPL-1610, September 1979.

52. Adam, J., et al., "Wave Generation and Heating in the St Tokamak at the Fundamental and Harmonic Ion Cyclotron Frequencies," PPL, Princeton University, Princeton, N.J., IAEA-CN-33/A3-2.

53. EQUIPE TFR, "ICRF Heating in TFR Observations with an "All-Metal" Antenna," Nuclear Fusion, Vol. 19, No. 11 (1979).

54. TFR Group, "ICRF Heating in TFR Preliminary Observations and Prospects for Further Developments," Dph-PFC-SCP-STGI, EUR-CEA-FC-970, August 1978.

55. TFR Group, "Magnetosonic Wave Generation and Damping in the TFR Tokamak Near the Ion Cyclotron Frequencies," EQUIPE TFR, Association Euratom-CEA sur la Fusion, Dept. de physique du plasma, et de la fusion controlée, Fontenay-aux-Roses, France. IAEA-CN-35/G8.

56. Parker, R.R., "Excitation and Propagation of Ion-Cyclotron Waves in a Plasma Column," Dept. Electrical Engineering, MIT, August 14, 1967, Ph.D. Thesis.

57. Biddle, A.P., "Ion Heating in the Ion Cyclotron Range of Frequencies in the Wisconsin Tokapole II," University of Wisconsin, DOE-ET53051-7, June 1980.

58. Fusion Experimental Power Reactor (EPR) Design, EPRI, February 1980.

59. Scharer, J.E., et al., "Fast Magnetosonic Wave Heating of the NUWMAK Tokamak Reactor," University of Wisconsin, ECE-78-15, September 1978.

60. Blackwell, B.D. Ph.D. Thesis "Experimental Investigations of Magneto-Acoustic Waves in a Plasma," The University of Sydney.

61. Bernstein, I.B., and Trehan, S.K., "Plasma Oscillations (I)," Project Matterhorn, Princeton University, Princeton, N.J., Nuclear Fusion: 1,3-41 (1960).

62. Eubank, A., (Editor), et al., Course on Plasma Diagnostics and Data Acquisition Systems, Int. School of Plasma Physics, Varenna, Italy, September 3-11, 1975.

63. Schwartz, Mischa, Information Transmission, Modulation, and Noise, Polytechnic Institute of Brooklyn, McGraw-Hill Book Company, 1970.

64. Spiegel, M.R., "Theory and Problems of Probability and Statics," Schaum's Outline Series, McGraw-Hill Book Company. 1975.

65. Surko, C.M., and Slusher, R.E., "Study of Plasma Density Fluctuations by the Correlation of Crossed CO_2 Laser Beams," Bell Laboratories, Murray Hill, N.J., April 1980.

66. Porkolab, M., et al., "Research Proposal for Alcator-C Lower-Hybrid Heating", MIT PFC/RP-78-1, February 1978.

67. Radar Set AN/FPS-17 (V) 2, General Electric Company, Syracuse, New York, April 15, 1959.

68. Fahey, R.E., "Sequencer and Fault Diagnostics for Ion Cyclotron Resonance Heating Experiment on the Alcator Tokamak", Dept. of Electrical Engineering, BS Thesis, May 18, 1979, MIT.

69. Spletter, G.J., "The Design of a Cooling System for the Alcator C Power Supplies," Dept. Mechanical Engineering, BS Thesis, June 1979, MIT.

70. Grearson, P.D., "Fast Reacting R.F. Detector and Shut Down System for the Alcator ICRH Experiments," Dept. Electrical Engineering, BS Thesis, May 1979, MIT.

71. Besen, M.M., "An Antenna and Vacuum Feedthrough System for Ion Cyclotron Radio Frequency Heating of Plasma in the M.I.T. Alcator Tokamak," Dept. Mechanical Engineering, BS Thesis, December 1979, MIT.

72. Abbanat, B.J., "An Ultra-High Power Resonator Matching System for the Ion Cyclotron Radio Frequency Heating Experiment on the M.I.T. Alcator Tokamak," Dept. Mechanical Engineering, BS Thesis, May 23, 1980. MIT.

73. Wolfe, S.M., et al., "Modulated Submillimeter Laser Interferometer System for Plasma Density Measurements, " Applied Optics, Vol. 15, page 2645, November 1976.

74. Fidone, I., et al., "Mode Coupling of Low Frequency Waves," PDh-PFC-STGI, EUR-CEA-FC-876, January 1977.

75. Spitzer, L., Jr., Physics of Fully Ionized Gases. Interscience Publishers A Division of John Wiley and Sons, New York, 1962.

76. Leontovich, M.A., (Editor), Review of Plasma Physicas, Vol. 1, Translated from Russian by Herbert Lashinsky, University of Maryland, Consultants Bureau, New York, 1975.

77. Swift, J.D., and Schwar, M.J.R., Electrical Probes for Plasma Diagnostics, American Elsevier Publishing Co., Inc., New York, 1969.

78. Lotz, W., "Electron Impact Ionization Cross Sections and Ionization Coefficients for Atoms and Ions From Hydrogen to Calcium," Institute for Plasma Physics, Garching, May, 1967.

79. Dean, S.O., et al., Status and Objectives of Tokamak Systems for Fusion Research, U.S. Government Printing Office, Washington, DC.

80. Lafferty, J.M., "Techniques of High Vacuum," General Electric Report No. 64-RL-3791G, Schenectady, New York, November, 1964.

81. Budden, K.G., Radio Waves in the Ionosphere, Cambridge at the University Press, 1966.

82. Book, D.L., NRL Plasma Formulary, Laboratory for Computational Physics, Naval Research Laboratory, Washington, DC, 1978.

83. Blackfield, D.T., "ICRF Heating of Tokamaks," Ph.D. Prelim., University of Madison, January, 1979.

84. McVey, B.D., "A Ray Tracing Analysis of Fast Wave Heating of Tokamaks," Ph.D. Prelim., University of Wisconsin-Madison, May, 1978.

85. Schuss, J.J., "Effect of Magnetic Field Ripple on Energetic Ions in Alcator A," Nuclear Fusion, 20, (1980) 1160.

86. Greenwald, M., Schuss, J.J., Cope, D., "Depletion of Ripple-Trapped Particles in the Alcator Tokamaks," Nuclear Fusion, 20, (1980) 783.

87. Helava, H., Parker, R., "H_α - D_α Measurements in Alcator," Alcator Internal Memorandum #3, March, 1977.

88. Takahashi, H., and Parker, R.R., "A Proposal for ICRF Heating of Alcator-C," MIT - PFC/RR-80-8, December, 1979.

89. Stix, T.H., "The Physics of RF Heating," Symposium on Plasma Heating and Injection, in Varenna Italy, October, 1972.

90. Stix, T.H., "Oscillations of a Cylindrical Plasma," Physical Review, 106, (1957), 1146.

91. Hooke, W.M., et al., "Fast Wave Heating of the PLT and PDX Tokamaks in the Ion Cyclotron Range of Frequencies (ICRF)," Proposal, Princeton University, Plasma Physics Laboratory, April, 1976.

92. Takahashi, H., "ICRF Heating and Wave Generation in the ATC Tokamak," PPPL-1545, April, 1979.

93. Stix, T.H., "Fast-Wave Heating of a Reactor Plasma: Consideration of Two Frequency Regimes," PPPL-1298, Princeton, October, 1976.

94. Paoloni, F.J., "Waveguide and Loop Coupling to Fast MHD Toroidal Eigenmodes," MATT-1173, Princeton, December, 1975.

95. Takahashi, H., "Wave Generation and Heating Near the Ion Cyclotron Frequency in the ST Tokamak," MATT-1140, Princeton, October, 1975.

96. Chung, K., and Rothman, M.A., "Plasma Heating by the Fast Hydromagnetic Wave," The Physics of Fluids, 10, (1967), 2634.

97. Taylor, R.J., et al., "Advances in RF Heating at U.C.L.A.," APS, 1980.

98. Taylor, R.J., and Morales, G.J., "ICRF Heating in Microtor/Macrotor," PPG-509, UCLA, September, 1980.

99. Iizuka, S., et al., "Propagation and Absorption of the Fast Magnetosonic Wave near a Two-Ion Hybrid Resonance Layer," Division of Thermonuclear Fusion Research, Tokai Research Establishment, JAERI, November 9, 1979.

100. Iizuka, S., et al., "Propagation and Absorption of the Fast Magnetosonic Wave in the Ion-Cyclotron Range of Frequencies in the DIVA Tokamak," Physical Review Letters, 45, (1980), 1256.

101. Kimura, H., et al., "High Efficiency ICRF Heating Experiment in DIVA," 8th International Conference on Plasma Physics, IAEA-CN-38, Brussels, July, 1980.

102. Hosea, J., et al., "Fast Wave Ion Cyclotron Heating in the Princeton Large Torus," 8th International Conference on Plasma Physics, IAEA-CN-38, Brussels, July, 1980.

103. Equipe, T.F.R., "T.F.R. Experiments on Superbanana Particle Diffusion, Small Scale Turbulence and Transport," 8th International Conference on Plasma Physics, IAEA-CN-38, Brussels, July, 1980.

104. Equipe, T.F.R., "ICRF Heating in TFR 600," 8th International Conference on Plasma Physics, IAEA-CN-38, Brussels, July, 1980.

105. Taylor, R.J., "ICRF Heating, Particle Transport, and Fluctuations in Tokamaks," 8th International Conference on Plasma Physics, IAEA-CN-38, Brussels, July, 1980.

106. Puri, S., "Alfvén Wave Heating of Fusion Plasmas," 8th International Conference on Plasma Physics, IAEA-CN-38, Brussels, July, 1980.

107. Jacquinot, J., et al., "ICRF Theoretical Progress in Fontenay-aux-Roses", Proceedings of the Fourth Topical Conference on RF Heating in Plasma, University of Texas, February, 1981.

108. Colestock, P.L., PLT, "High Power Ion Cyclotron Heating Experiments on PLT," Proceedings of the Fourth Topical Conference on RF Heating in Plasma, University of Texas, February, 1981.

109. Lapierre, Y., TFR, "Experimental Study of the Fast Wave Propagation in TFR," Proceedings of the Fourth Topical Conference on RF Heating in Plasma, University of Texas, February, 1981.

110. Taylor, R.J., UCLA, "Large Area ICRF Antennas," Proceedings of the Fourth Topical Conference on RF Heating in Plasma, University of Texas, February, 1981.

111. Taylor, R.J., UCLA, "Magnetic Excitation of Electrostatic Slow Modes at ICRF," Proceedings of the Fourth Topical Conference on RF Heating in Plasma, University of Texas, February, 1981.

112. Gaudreau, M.P.J., et al., "Medium Power ICRF Results on the Alcator A Tokamak," Proceedings of the Fourth Topical Conference on RF Heating in Plasma, University of Texas, February, 1981.

113. Blackwell, B.D., et al., MIT, "Numerical Studies of ICRF Heating in Alcator," Proceedings of the Fourth Topical Conference on RF Heating in Plasma, University of Texas, February, 1981.

114. Puri, S., Max Planck-Institut für Plasmaphysik, "Ion Bernstein Wave Heating Using Slow and Fast Wave Coupling," Proceedings of the Fourth Topical Conference on RF Heating in Plasma, University of Texas, February, 1981.

115. Whang, K.W., UCLA, "Effect of Coulomb Collisions on ICRF Heating in Tokamaks," Proceedings of the Fourth Topical Conference on RF Heating in Plasma, University of Texas, February, 1981.

116. Jacquinot, J., Lapierre, Y., "Damping Mechanisms and Heating Scenarii in the ICRF," 2nd Joint Grenoble Varenna International Symposium on heating in toroidal Plasmas (COMO), 3-12 September, 1980.

117. Puri, S., "Faraday Shielding of Surface Dissipation Effects in Alfvén Wave Heating," 2nd Joint Grenoble Varenna International Symposium on heating in toroidal plasmas (COMO), 3-12 September, 1980.

118. Jacquinot, J., "ICRF Heating of a Tokamak in a Proton-Deuteron Mixture," Proceedings of the Joint Varenna-Grenoble International Symposium on Heating in Toroidal Plasmas, Grenoble, July, 1978.

119. Jacquinot, J., "Heating the Various Plasma Species via the Proton-Deuteron Hybrid Resonance," Proceedings of the third Topical Conference on Radio Frequency Plasma Heating - Paper D4 - California Institute of Technology, January 11-13, 1978.

120. Lapierre, Y., "Excitation et Propagation de L'Onde Rapide Dans un Plasma non Uniforme," (EUR-CEA-FC-1043), April, 1980.

121. Lapierre, Y., "Excitation and Propagation of the Fast Wave in a Two Component non Uniform Plasma," English version of EUR-CEA-FC-1043, April, 1980.

122. Bers, A., Jacquinot, J., Lister, G., "Field and Ray Analyses of Antenna Excitations in ICRF Heating of Large Tokamaks," EUR-CEA-FC-1066, September, 1980.

123. Adam, J., Jacquinot, J., Kuus, H., "Physics Aspects and Technical Elements of an ICRF Heating System for Jet," EUR-CEA-FC-1065, September, 1980.

124. Fidone, I., Gomberoff, L., "Fast-Slow Mode Conversion Near the Ion-Ion Hybrid Resonance," EUR-CEA-FC-936, January, 1978.

125. Equipe, TFR, "ICRF Antenna and Heating Studies in High Density TFR Plasmas," EUR-CEA-FC-1046, April, 1980.

126. Adam, J., "Chauffage Cyclotronique et Impedence D'Antenne en Presence D'un Mechanisme de Forte Absorption," EUR-CEA-FC-1004, May, 1979.

127. Arpaci, V.S., Conduction Heat Transfer, Addison-Wesley Publishing Co., Reading, MA, 1966.

128. Jassby, D.L., Towner, H.H., Goldston, R.J., "Reduced Fusion-Neutron Production in Non-Axisymmetric Tokamak Devices," Nuclear Fusion, 18, (1978), 825.

129. Hosea, J.C., "ICRF Heating in Large Tokamaks," Third Symposium on Plasma Heating in Toroidal Devices, Varenna, Italy, September 6-17, 1976.

130. TFR Group, "Damping Mechanisms of the Fast Wave in the Ion Cyclotron Range of Frequency," Third Symposium on Plasma Heating in Toroidal Devices, Varenna, Italy, September 6-17, 1976.

131. Abramowitz, M., Stegun, I.A., Eds., Handbook of Mathematical Functions, United States Department of Commerce, National Bureau of Standards Applied Mathematics Series 55, June, 1964.

132. Hildebrand, F.B., Advanced Calculus for Applications, Prentice-Hall, Inc., New Jersey, 1976.

133. Hayt, W.H., Jr., Kemmerly, J.E., Engineering Circuit Analysis, McGraw-Hill Book Company, 1962.

134. Kraus, J.D., Carver, K.R., Electromagnetics, McGraw-Hill Book Co., 1973.

135. Fink, D.G., Electronics Engineers' Handbook, McGraw-Hill Book Co., 1975.

136. Reference Data for Radio Engineers, Howard W. Sams & Co., Inc., 1973.

137. Beyer, William H., CRC Standard Mathematical Tables, 25th Edition, CRC Press, Inc., 1979.

138. Nesmeyanov, An.N., Vapour Pressure of the Elements, Academic Press, 1963.

139. Arpaci, Vedat S., Conduction Heat Transfer, Addison-Wesley Publishing Co., 1966.

140. Carslaw, H.S., Jaeger, J.C., Conduction of Heat in Solids, Oxford University Press, 1959.

141. Zemansky, Mark W., Heat and Thermodynamics, An Intermediate Textbook, Fifth Edition, McGraw-Hill Book Co., 1968.

142. Weast, Robert C., Melvin J. Astle, Eds., CRC Handbook of Chemistry and Physics: A Ready-Reference Book of Chemical and Physical Data, 59th Edition, CRC Press, Inc., 1979.

143. Sansone, M., MS Thesis, Department of Physics, MIT, in preparation.

144. Jackson, John David, Classical Electrodynamics, John Wiley & Sons, Inc., 1962.

145. Sabersky, Rolf H., Allan J. Acosta, Edward G. Hauptmann, Fluid Flow: A First Course in Fluid Mechanics, Second Edition, The Macmillan Co., 1971.

BIOGRAPHICAL NOTE

The author was born in Black's Harbour, New Brunswick, Canada, in February 1953. He graduated from the private high school (cour classique) of La Pocatière, Province of Quebec, in 1970. In 1972, he received his DEC, (Diplome d'ëtudes collegiales), in physical sciences at the CEGEP of La Pocatière.

In the fall of 1972, the author entered the Physics Department at M.I.T. For his bachelor's thesis, he built the high accuracy charge monitoring system for the new M.I.T. 400 Mev accelerator at the Bates National Laboratory. In May 1974, he received his B.S. degree in physics.

In 1975, the author received his Master's degree in aeronautical and astronomical engineering at M.I.T. His Master's thesis, entitled "An On-Line Technique for Tool-Wear Measurements" was done at the Draper Laboratories under contract with Fiat SPA. An outcome of the thesis was an innovative U.S. patent for heavy industrial automation.

Since 1975, he has been a full time research assistant and temporarily a staff member at the Francis Bitter National Magnet Laboratory at M.I.T. The author worked for two years with several teams of Soviet scientists on a new charge exchange diagnostic for Alcator, and has presented several papers on the subject.

In 1977 he was intensively involved in teaching at M.I.T., having helped teach courses in circuit theory, electrostatics, electromagnetics and linear systems analysis. During this year, he was also the principal implementer of the high power DC systems for Alcator C.

In early 1978, he became extensively involved in high power RF work at M.I.T. In particular, he was the project engineer coordinating the relocation of the Shemya Air Force Base multi-megawatt, long pulse FPS-17 radar. He is coauthor of four research papers on ICRF, presented before the APS Division of Plasma Physics and the 1981 Austin RF workshop.

The author's research interests have been in high power DC and RF systems in the field of nuclear instrumentation and plasma physics, areas in which he remains intensely interested at the present time.

PFC BASE LIST

INTERNAL MAILINGS (MIT)

G. Bekefi
36-213

A. Bers
38-260

D. Cohn
NW16-250

B. Coppi
26-201

R.C. Davidson
NW16-202

T. Dupree
38-172

S. Foner
NW14-3117

J. Freidberg
38-160

A. Gondhalekar
NW16-278

M.O. Hoenig
NW16-176

M. Kazimi
NW12-209

L. Lidsky
38-174

E. Marmar
NW16-280

J. McCune
31-265

J. Meyer
24-208

D.B. Montgomery
NW16-140

J. Moses
NE43-514

D. Pappas
NW16-272

R.R. Parker
NW16-288

N.T. Pierce
NW16-186

P. Politzer
NW16-286

M. Porkolab
36-293

R. Post
NW21-

H. Praddaude
NW14-3101

D. Rose
24-210

J.C. Rose
NW16-189

R.M. Rose
4-132

B.B. Schwartz
NW14-5121

R.F. Post
NW21-203

L.D. Smullin
38-294

R. Temkin
NW16-254

N. Todreas
NW13-202

J.E.C. Williams
NW14-3210

P. Wolff
36-419

T.-F. Yang
NW16-164

Industrial Liaison Office
ATTN: Susan Shansky
Monthly List of Publications
39-513

MIT Libraries
Collection Development
ATTN: MIT Reports
14E-210

B. Colby
PFC Library
NW16-255

EXTERNAL MAILINGS

National

Argonne National Laboratory
Argonne, IL 60439
ATTN: Library Services Dept.

Battelle-Pacific Northwest Laboratory
P.O. Box 99
Richland, WA 99352
ATTN: Technical Information Center

Brookhaven National Laboratory
Upton, NY 11973
ATTN: Research Library

U.S. Dept. of Energy
Washington, D.C. 20545
ATTN: D.O.E. Library

Roger Derby
Oak Ridge National Lab.
ETF Design Center
Bldg. 9204-1
Oak Ridge, TN 37830

General Atomic Co.
P.O. Box 81608
San Diego, CA 92138
ATTN: Library

Lawrence Berkeley Laboratory
1 Cyclotron Rd.
Berkeley, CA 94720
ATTN: Library

Lawrence Livermore Laboratory
UCLA
P.O. Box 808
Livermore, CA 94550

Oak Ridge National Laboratory
Fusion Energy Div. Library
Bldg. 9201-2, ms/5
P.O. Box "Y"
Oak Ridge, TN 37830

Dr. D. Overskei
General Atomic Co.
P.O. Box 81608
San Diego, CA 92138

Princeton Plasma Physics Laboratory
Princeton University
P.O. Box 451
Princeton, NJ 08540
ATTN: Library

Plasma Dynamics Laboratory
Jonsson Engineering Center
Rensselaer Polytechnic Institute
Troy, NY 12181
ATTN: Ms. R. Reep

University of Wisconsin
Nuclear Engineering Dept.
1500 Johnson Drive
Madison, WI 53706
ATTN: UV Fusion Library

EXTERNAL MAILINGS

International

Professor M.H. Brennan
Willis Plasma Physics Dept.
School of Physics
University of Sydney
N.S.W. 2006, Australia

Division of Plasma Physics
Institute of Theoretical Physics
University of Innsbruck
A-6020 Innsbruck
Austria

c/o Physics Section
International Atomic Energy Agency
Wagramerstrasse 5
P.O. Box 100
A-1400 Vienna, Austria

Laboratoire de Physique des Plasmas
c/o H.W.H. Van Andel
Dept. de Physique
Universite de Montreal
C.P. 6128
Montreal, Que H3C 3J7
Canada

Plasma Physics Laboratory
Dept. of Physics
University of Saskatchewan
Saskatoon, Sask., Canada S7N OWO

The Library
Institute of Physics
Chinese Academy of Sciences
Beijing, China

Mrs. A. Wolff-Degives
Kernforschungsanlage Julich GmbH
Zentralbibliothek - Exchange Section
D-5170 Julich - Postfach 1913
Federal Republic of Germany

Preprint Library
Central Research Institute for Physics
H-1525 Budapest, P.O. Box 49
Hungary

Plasma Physics Dept.
Israel Atomic Energy Commission
Soreq Nuclear Research Center
Yavne 70600
Israel

The Librarian (Miss DePalo)
Associazione EURATOM - CNEN Fusione
C.P. 65-00044 Frascati (Rome)
Italy

Librarian
Research Information Center
Institute of Plasma Physics
Nagoya University
Nagoya, 464
Japan

Dr. A.J. Hazen
South African Atomic Energy Board
Private Bag X256
Pretoria 0001
South Africa